Hunting for Fast Radio Transients in the Local Universe and Pulsars Toward the Center of the Milky Way Galaxy

Thesis by
Aaron Benjamin Pearlman

In Partial Fulfillment of the Requirements for the
Degree of
Doctor of Philosophy

Caltech

CALIFORNIA INSTITUTE OF TECHNOLOGY
Pasadena, California

2021
Defended December 29, 2020

Aaron Benjamin Pearlman
ORCID: 0000-0002-8912-0732

Acknowledgements

The work in this thesis would not have been possible without the help and support of many people.

First, I would like to express my gratitude to my advisor, Tom Prince, whose guidance helped to develop me into the scientist that I am today. Tom introduced me to the missing pulsar problem at the Galactic Center (GC), which stimulated my passion for radio astronomy, pulsar searching, developing state-of-art algorithms, and recently fast radio bursts (FRBs). I am incredibly grateful for Tom's willingess to spend time with me each week discussing the latest results from my analysis. Tom's expectation for scientific rigor and excellence has influenced my work greatly, and these standards have strengthened my publications and my overall approach to research. Tom also provided me with extensive advice and wisdom outside of our technical work together, which has been invaluable as a budding young scientist. Tom gave me considerable freedom to work on many projects as a graduate student. I am incredibly grateful for this, as it allowed me to explore and make progress in many different topics in radio and X-ray astronomy simultaneously. I am truly privileged to have had Tom as an advisor.

Next, I would like to thank Walid Majid. Walid has served as a second advisor throughout my graduate career, and none of the work in this thesis would have been possible without his support. Walid spent countless hours teaching me about radio astronomy and the Deep Space Network (DSN) radio telescopes. He nurtured many of my ideas at their infancy, when they were just pictures and back-of-the-envelope calculations that I was trying to communicate on a chalkboard. Walid also gave me incredible freedom to work on a wide range of projects, including pulsar searches, magnetars, radio pulsars, algorithms, and FRBs. Thank you, Walid, for trusting that I could balance a high workload and publish results quickly. It was your willingness to allow me to pursue many research topics that fostered my creativity and exploration of new ideas. Walid also spoiled me with a trip to Australia to help with upgrading the K-band (17–27 GHz) pulsar backend on DSS-43 (the 70 m radio telescope in Tidbinbilla, Australia). This was truly one of the highlights of my time in graduate school. Thank you for an incredible adventure, filled with lots of work but also lots of fun!

To both Tom and Walid: I would like to express my utmost gratitude to both of you. Your unwavering support, guidance, advice, and mentorship has been invaluable to me. Thank you for believing in my scientific abilities and allowing them to grow and flourish under your tutelage. I am indebted to both of you for the opportunities you have provided me.

Next, a special thank you is owed to Barak Zackay, who supported working together on the dynamic programming pulsar search algorithm and the pruning algorithm. My extended visit to Princeton University and the Institute for Advanced Study (IAS), where we worked intensively on algorithms together, was also a highlight of my time in graduate school. You taught me an incredible amount about algorithms, statistics, and critically thinking about a research problem. I am incredibly grateful for your mentorship, friendship, and the opportunity to work together. I am excited about many of our on-going projects, and I hope that we remain lifelong friends and collaborators.

I would like to express my gratitude to all of the members of my thesis committee: Fiona Harrison, Shri Kulkarni, Walid Majid, Sterl Phinney, and Tom Prince. I am incredibly grateful for your advice and support throughout my time as a graduate student. Fiona was the first one to suggest that I should consider working with Tom and Walid on searching for radio pulsars at the Galactic Center with the DSN. I had no idea that this piece of advice would become the seed for all of these projects.

There are many collaborators outside of Caltech that had a profound impact on my scientific development and the work presented in this thesis, either by working together on some aspect of the analysis, sharing data, writing proposals and helping to observe, or through science discussions. In particular, there were many late nights spent talking with Jason Hessels about virtually all aspects of FRBs — mostly because of the time difference between California and Amsterdam! I cherished those conversations, and I look forward to continuing to work together in the future.

I am grateful to Paul Ray for teaching me a great deal about analyzing NICER data and timing pulsars simultaneously at multiple wavelengths with X-ray and radio instruments. It is my pleasure to thank Keith Gendreau and Zaven Arzoumanian for accommodating my requests for NICER observations on short notice. I would also like to thank Charles Naudet, Jonathon Kocz, Shinji Horiuchi, and Jonas Lippuner for helping to support the DSN work presented in this thesis in many ways. I also thank Teruaki Enoto and the Magnetar and Magnetospheres NICER working group for many opportunities to collaborate on various magnetar research projects together. I am extremely grateful to Maura McLaughlin and Brent Shapiro-Albert for help with observing using the Green Bank Telescope (GBT) and preparing science proposals, Vicky Kaspi for her support of DSN observations of repeating FRBs, and Scott Ransom for sharing radio data on globular clusters. I also thank Wenbin Lu, Sterl Phinney, Jim Fuller, Roger Blandford, members of the Caltech radio group, and many faculty members in Caltech's Astronomy and Physics departments for various scientific discussions related to my work.

I am indebted to my undergraduate research advisors and long-time collaborators, Robin Corbet and Katja Pottschmidt. Thank you both for your patience and for explaining various technical research topics to me when I was an undergraduate student learning about research for the first time. I also thank Joel Coley for his friendship and collaboration on various high-energy research projects related to pulsars.

I am happy to thank both Renee Ludlam and Amruta Joadand for providing valuable advice and support while writing my postdoctoral applications.

I acknowledge generous support from the Department of Defense (DoD) through the National Defense Science and Engineering Graduate (NDSEG) Fellowship Program, and also from a National Science Foundation (NSF) Graduate Research Fellowship under Grant No. DGE-1144469. Much of the work presented in this thesis would not have been possible without support from the NASA Jet Propulsion Laboratory (JPL) Spontaneous Concept Research and Technology Development program, and also from NASA JPL's and Caltech's President's and Director's Fund.

I have developed close relationships with many people while in graduate school. I am grateful for their continual support, encouragement, and belief in my abilities. In particular, I met both Jeremy Brouillet and Daniel Brooks while at Caltech, and I greatly cherish their friendship and company.

A very special thank you is owed to my wife, Sheri Pearlman. I don't know where I would be without your constant love, positivity, optimistic point of view, encouragement, friendship, and loyalty. Thank you for bringing joy and happiness into my life! Also, thank you for tolerating my demanding work schedule, especially when I should have been spending more time with you. I owe much of my success to you and your support!

In addition, I would like to thank my mother Hinda Pearlman and my late father David Pearlman for their love, support, always believing in me, and the gift of education.

My father inspired me to become a physicist through long, detailed conversations about the Universe as a young adolescent. I would also like to thank my father-in-law, Dr. Jay Zweier, for his help, support, advice, and wonderfully thought-provoking scientific and academic discussions. I would also like to thank my mother-in-law, Dr. Barrie Zweier, for her love and support throughout this academic journey. I am grateful for the lifelong encouragement and support provided by my family and close friends.

Lastly, I would like to thank my loyal pet companions, Little Bear, Count Fabulous, Coco, and Fancy, who brought me both joy and friendship on a daily basis.

Preface

If I have seen further [than others], it is by standing on the shoulders of giants.

— Isaac Newton

During my graduate school career, I was fortunate to have had a well-rounded research experience. I had the opportunity to build tabletop experiments studying quantum devices and low-temperature, RF (radio frequency) cryogenic experiments exploring the quantum properties of matter, with applications for measuring continuous gravitational-waves from pulsars. I also worked on many research projects in astrophysics, radio astronomy, and X-ray astronomy focused on data analysis and algorithms. I am a stronger scientist today thanks to the lessons I learned along the way in all of these areas.

All of the work presented in this thesis was carried out between May 2016 and December 2020.

Dedication: I dedicate this thesis to my wife, Sheri Pearlman, who supported me in so many ways and remained by my side through it all.

Abstract

The dynamic radio sky is full of fast radio transients that produce emission on timescales ranging from nanoseconds to seconds. The two classes of fast radio transients studied in this thesis are pulsars and fast radio bursts (FRBs). Pulsars are highly magnetized, rotating neutron stars that produce pulses of electromagnetic radiation as a result of charged particles being accelerated along magnetic field lines. FRBs are short-duration, transient radio pulses with extragalactic origins, but the nature of their progenitors still remains a mystery. The extremely high brightness temperatures of pulsars and FRBs indicate that their emission is produced by coherent radiation mechanisms. Bright radio bursts from an extragalactic population of active magnetars (neutron stars with extraordinarily large magnetic fields) may account for at least some fraction of the observed cosmological FRBs. This is supported by the recent detection of a bright, millisecond-duration radio burst, with a fluence of ∼1.5 MJy ms, from the Galactic magnetar SGR 1935+2154 [59, 523].

Although the focus of this thesis is centered around pulsars and FRBs, I cover a broad range of topics, including (1) the emission behavior of radio magnetars, rotation-powered radio pulsars, and repeating FRBs, (2) the development of novel, state-of-the-art algorithms for pulsar searching, (3) a new, sensitive search for pulsars toward the Galactic Center (GC), and (4) the X-ray behavior of wind-accreting high-mass X-ray binaries (HMXBs) displaying superorbital modulation. In this thesis, I explore the emission properties of several radio magnetars in the radio and X-ray bands using the NASA Deep Space Network (DSN) radio telescopes and the *NICER* X-ray telescope. I also study the emission behavior of two repeating FRBs, FRB 121102 and FRB 180916.J0158+65 (also referred to as FRB 20121102A and FRB 20180916B, respectively), at high radio frequencies using the DSN's 70 m radio telescopes. In particular, I show that there is a phenomenological link between the radio pulses observed from radio magnetars and repeating FRB sources. I also describe two novel pulsar search algorithms that have been developed to coherently search for accelerated pulsars in Keplerian orbits. In addition, I describe a new, ongoing survey of the GC region that is being carried out at high radio frequencies to search for GC pulsars using the 70 m DSN radio telescope (DSS-43) in Tidbinbilla, Australia. Lastly, I present the results of a pulsar timing analysis of the wind-accreting HMXB, IGR J16493–4348, which displays a 20.06 day superorbital period of unknown origin.

In Chapter 1, I review some of the essential concepts in radio astronomy and summarize the important properties of pulsars, magnetars, and FRBs that are relevant for this thesis. An overview of the DSN's radio telescopes and the data analysis pipelines used to analyze the radio observations from the DSN is provided in Chapter 2. In Chapter 2, I also describe a novel time-domain based infinite impulse response (IIR) filtering algorithm that I independently developed to remove periodic radio frequency interference (RFI). This algorithm is capable of recovering an underlying astrophysical signal when other strong, undesired periodic signals are present in the data, without significantly impacting the quality of the astrophysical signal of interest. I demonstrate the effectiveness of this IIR filtering algorithm using simulated data and real pulsar data from the DSN. I also describe its potential usefulness in other areas of time-domain astronomy.

Chapters 3–5 describe the results from several magnetar-related studies performed using the DSN radio telescopes and the *NICER* X-ray telescope. In Chapter 3, I present an analysis of simultaneous high frequency radio observations of the transitional magnetar candidate, PSR J1119–6127, at 2.3 and 8.4 GHz with the 70 m DSN radio telescope, DSS-43, following an X-ray outburst in 2016 when the pulsar displayed unusual magnetar-like behavior. PSR J1119–6127 is a high magnetic field ($B_{\rm surf} = 4.1 \times 10^{13}$ G) radio pulsar, with a rotational period of $P_{\rm spin} = 0.41$ s, which had previously only shown behavior similar to other normal radio pulsars. These radio observations of PSR J1119–6127 with DSS-43 demonstrate that there is a smooth transition between the behavior observed from normal radio pulsars and magnetars. Moreover, these observations also help to bridge the gap between these different classes of neutron stars.

In Chapter 4, I present results from an analysis of radio single pulses from the GC magnetar, PSR J1745–2900, which has a projected distance of 0.1 pc from Sgr A*. I found that many of PSR J1745–2900's single pulse emission components display significant frequency structure over bandwidths of $\sim$100 MHz, which is the first observation of such behavior from a radio magnetar. Similar behavior has been observed in the radio spectra of bursts from repeating FRB sources, such as FRB 121102. While the luminosities of radio bursts from FRB 121102 are a factor of $\sim 10^{10}$ larger than the burst luminosities observed from PSR J1745–2900, the spectral properties of the emission from these two classes of objects are remarkably similar. These observations also show that the pulse broadening observed from PSR J1745–2900 is highly variable between different single pulse emission components. This behavior cannot be explained by a thin scattering screen at distances $\gtrsim 1$ kpc. At 8.4 GHz, we measure a characteristic single pulse broadening timescale of $\langle\tau_d\rangle = 6.9 \pm 0.2$ ms, which is more than an order of magnitude larger than previously reported values. This suggests that the temporal broadening observed along the line of sight may substantially change with time.

Chapter 5 describes results from simultaneous radio and X-ray observations of the radio magnetar XTE J1810–197, using the DSN's 34 m radio telescopes in Canberra, Australia and the *NICER* X-ray telescope, after the magnetar's radio reactivation in 2018. Bright, persistent individual X-ray pulses were discovered from XTE J1810–197, and these X-ray pulses were detected during virtually every rotation of the neutron star. Similar behavior has only been previously observed from a magnetar during short time periods following a giant flare. However, these X-ray pulses were detected outside of a flaring state. They are less energetic and display temporal structure that differs from the impulsive X-ray events previously observed from the magnetar class, such as giant flares. These simultaneous radio and X-ray observations also demonstrate that the relative alignment between the magnetar's X-ray and radio pulses varies on rotational timescales. The magnetar's 8.3 GHz radio pulses also display frequency structure, which was not observed in the pulses detected simultaneously at 31.9 GHz. Many of the magnetar's radio pulses were also not detected simultaneously at both of these radio frequencies. This indicates that the underlying emission mechanism producing these pulses is not broadband. The radio bursts detected from XTE J1810–197 display similar spectral properties to radio bursts observed from repeating FRB sources, making it the second Galactic radio magnetar to exhibit such behavior.

Chapters 6 and 7 describe results from long-term multiwavelength radio monitoring observations of two repeating FRB sources, FRB 121102 and FRB 180916.J0158+65, with the DSN's 70 m radio telescopes. In Chapter 6, I present the detection of 6 bursts from FRB 121102 during a 5.7 hr continuous observation with DSS-43 on 2019 September 6, where data were recorded simultaneously at 2.25 and 8.36 GHz. All of these bursts were detected in the 2.25 GHz frequency band, but no radio emission was observed in the 8.36 GHz band, despite the larger bandwidth and greater sensitivity in the higher radio frequency band. This behavior can not be explained by Galactic scintillation. These detections, together with previous multiband experiments, demonstrate that the apparent burst activity of FRB 121102 depends strongly on the radio frequency band that is being observed.

Chapter 7 describes an analysis of multiwavelength radio observations of FRB 121102 and FRB 180916.J0158+65 using the DSN's 70 m radio telescopes (DSS-63 and DSS-14), located in Madrid, Spain and Goldstone, California. The observations of FRB 121102 were performed simultaneously at 2.3 and 8.4 GHz and spanned a total of 27.3 hr between 2019 September 19 and 2020 February 11. A total of 2 radio bursts were detected from FRB 121102 in the 2.3 GHz frequency band, but no evidence of radio emission was found at 8.4 GHz during any of the observations. In addition, the arrival times of the radio bursts detected at 2.3 GHz from FRB 121102 occurred near the predicted peak of the activity cycle, assuming an underlying periodicity of ∼160 days [139, 453]. FRB 180916.J0158+65 was also observed simultaneously at 2.3 and 8.4 GHz, and separately in the 1.5 GHz frequency band, for a total of 101.8 hr between 2019 September 19 and 2020 May 14. The observations of FRB 180916.J0158+65 spanned multiple activity cycles during which the source was known to be active and covered a wide range of activity phases. Several of our observations occurred during times when bursts were detected from the source between 400–800 MHz with the Canadian Hydrogen Intensity Mapping Experiment (CHIME) radio telescope. However, no radio bursts were detected from FRB 180916.J0158+65 at any of the frequencies used during our observations with the DSN radio telescopes. This demonstrates that FRB 180916.J0158+65's apparent activity is strongly frequency-dependent due to the narrowband nature of its radio bursts, which have less spectral occupancy at high radio frequencies ($\gtrsim 2$ GHz). These results also demonstrate that fewer or fainter bursts are emitted from FRB 180916.J0158+65 at high radio frequencies.

In Chapter 8, I present two novel, state-of-the-art pulsar search algorithms that are being used to coherently search for accelerated pulsars in Keplerian orbits. The first algorithm is a time-domain based, top-down implementation of the Fast Folding Algorithm (FFA). Our top-down implementation differs dramatically from bottom-up implementations commonly used in the field of pulsar astronomy and utilizes dynamic programming techniques so that any polynomial-based acceleration search can be performed efficiently. In this thesis, I demonstrate convergence of the dynamic programming algorithm when it is used to carry out an acceleration search. Using radio data from the Parkes radio telescope and the Green Bank Telescope (GBT), I show blind detections of the double pulsar and an assortment of the known pulsars in the globular cluster Terzan 5 when an acceleration search is performed using the dynamic programming algorithm. The second algorithm is a new pruning algorithm, which is capable of efficiently detecting weak pulsations, with respect to the noise, when they are modulated by an arbitrary Keplerian orbit. Together, these algorithms will be a *game-changer* in the field of pulsar searching, and they are expected to discover many new pulsars that would otherwise be challenging or impossible to detect using existing methods.

Chapter 9 focuses on a new, deep 17–27 GHz pulsar survey that we are currently carrying out to search for new pulsars toward the GC using a recently commissioned ultra-wideband pulsar backend outfitted on DSS-43. This survey will have sufficient sensitivity to detect millisecond pulsars (MSPs) for the first time in regions of strong scattering. I describe why the paucity of known pulsars at the GC represents an unsolved enigma in the field of pulsar astronomy and how the detection of MSPs at the GC will provide new insights into the origin of the excess γ-ray emission observed toward the GC by the Large Area Telescope (LAT) on board NASA's *Fermi* Gamma-ray Space Telescope. In addition, I explain how GC pulsars could be used to study the stellar and magneto-ionic environment around Sgr A* and perform a wealth of experiments that would probe new fundamental physics.

Lastly, in Chapter 10, I present results from a pulsar timing analysis of the eclipsing supergiant HMXB IGR J16493–4348. In this system, material is accreted onto the neutron star by the stellar wind of the early B-type companion. Using X-ray data from the *Rossi X-ray Timing Explorer (RXTE)* and *Swift* Burst Alert Telescope (BAT), I analyze the system's X-ray variability and periodic modulation. I perform an observed minus calculated *(O–C)* analysis of the mid-eclipse times to obtain an improved measurement of the system's orbital period. I also provide a refined measurement of the system's superorbital orbital period. A pulsar timing analysis is carried out to precisely measure the neutron star's rotational period and the system's Keplerian binary orbital parameters. I also derive constraints on the mass and radius of the donor, which are used to determine the spectral type of the companion. Since the origin of the superorbital modulation in this wind-accreting system has not been conclusively identified, I discuss potential radiation mechanisms that may be responsible for the observed modulation.

Published Content and Contributions

Lead-Author Publications in Peer-Reviewed Journals:

* These authors contributed equally to both the analysis and writing of the manuscript.

[356] Majid, W. A.* and **Pearlman, A. B.*** et al. (2017). "Post-outburst Radio Observations of the High Magnetic Field Pulsar PSR J1119–6127." In: *ApJL,* 834:L2. 1612.02868 [astro-ph.HE].
A.B.P. discovered the signals, analyzed the data, and co-wrote the manuscript with W.A.M.

[422] **Pearlman, A. B.** et al. (2018). "Pulse Morphology of the Galactic Center Magnetar PSR J1745–2900." In: *ApJ,* 866:160. 1809.02140 [astro-ph.HE].
A.B.P. discovered the signals, analyzed the data, and wrote the manuscript.

[423] **Pearlman, A. B.** et al. (2019). "The Orbital Parameters of the Eclipsing High-mass X-Ray Binary Pulsar IGR J16493-4348 from Pulsar Timing." In: *ApJ,* 873:86. arXiv:1811.06543 [astro-ph.HE].
A.B.P. discovered the signals, analyzed the data, and wrote the manuscript.

[424] **Pearlman, A. B.,** Majid, W. A., and Prince, T. A. (2019). "Observations of Radio Magnetars with the Deep Space Network." In: *Advances in Astronomy,* Vol. 2019, Article ID 6325183. **Invited article for a special issue on magnetars.** 1902.10712 [astro-ph.HE].
A.B.P. developed the Bayesian pulsar timing algorithms, analyzed the data, and wrote the manuscript.

[358] Majid, W. A.* and **Pearlman, A. B.*** et al. (2020). "A Dual-band Radio Observation of FRB 121102 with the Deep Space Network and the Detection of Multiple Bursts." In: *ApJL,* 897:L4. arXiv:2004.06845 [astro-ph.HE].
A.B.P. discovered the signals, performed the majority of the data analysis, and co-wrote the manuscript with W.A.M.

[429] **Pearlman, A. B.** et al. (2020). "Multiwavelength Radio Observations of Two Repeating Fast Radio Burst Sources: FRB 121102 and FRB 180916.J0158+65." In: *ApJL,* 905:L27. arXiv:2009.13559 [astro-ph.HE].
A.B.P. discovered the signals, analyzed the data, and wrote the manuscript.

[430] **Pearlman, A. B.** et al. (2020). "Bright X-ray and Radio Pulses from a Recently Reactivated Magnetar." Submitted. 2005.08410 [astro-ph.HE].
A.B.P. discovered the signals, analyzed the data, and wrote the manuscript.

Co-Author Publications in Peer-Reviewed Journals (with Significant Contributions):

[110] Coley, J. B. et al. (incl. **Pearlman, A. B.**) (2019). "A Study of the 20 day Superorbital Modulation in the High-mass X-Ray Binary IGR J16493-4348." In: *ApJ*, 879:34. 1905.08817 [astro-ph.HE].
A.B.P. contributed to the analysis of the X-ray data, performed the timing analysis, and helped to write the manuscript and interpret the results.

[482] Scholz, P. et al. (incl. **Pearlman, A. B.**) (2020). "Simultaneous X-Ray and Radio Observations of the Repeating Fast Radio Burst FRB 180916.J0158+65." In: *ApJ*, 901:165. 2004.06082 [astro-ph.HE].
A.B.P. analyzed the DSN radio data and helped to write the manuscript and interpret the results.

[27] Bansal, K., **Pearlman, A. B.**, et al. (2021). "Simultaneous Radio and X-ray observations of a Radio Magnetar: Swift J1818.0–1607." Submitted.
A.B.P. analyzed the DSN radio data, helped to analyze the NICER data, and contributed to the interpretation of the results and writing the paper.

In addition to refereed publications, a gauge of success for astronomers is telegrams and circulars that they have issued for quickly disseminating information about discoveries and multiwavelength follow-up observations.

Telegrams/Circulars:

[355] Majid, W. A. et al. (incl. **Pearlman, A. B.**) (2016). "High Frequency Radio Observations of PSR J1119–6127." In: The Astronomer's Telegram #9321. ATel #9321.
A.B.P. contributed to the analysis of the data and helped to write the telegram.

[419] **Pearlman, A. B.** et al. (2016). "Magnetar-like Spectral Index Flattening of the High Magnetic Field Pulsar PSR J1119–6127." In: The Astronomer's Telegram #9870. ATel #9870.
A.B.P. analyzed the data and wrote the telegram.

[421] **Pearlman, A. B.** et al. (2017). "High Frequency Radio Observations of the Reactivated Magnetar PSR J1622–4950." In: The Astronomer's Telegram #10581. ATel #10581.
A.B.P. analyzed the data and wrote the telegram.

[357] Majid, W. A.* and **Pearlman, A. B.*** et al. (2019). "High Frequency Radio Observations of the Reactivated Magnetar XTE J1810–197." In: The Astronomer's Telegram #12353. ATel #12353.
A.B.P. analyzed the data and co-wrote the telegram with W.A.M.

[425] **Pearlman, A. B.** et al. (2019). "Detection of Multiple Radio Bursts from FRB 121102 Using the Deep Space Network." In: The Astronomer's Telegram #13235. ATel #13235.
A.B.P. discovered the signals, analyzed the data, and wrote the telegram.

[361] Majid, W. A.* and **Pearlman, A. B.*** et al. (2020). "Dual Radio Frequency Observations of Swift J1818.0–1607 with the Deep Space Network." In: The Astronomer's Telegram #13649. ATel #13649.
A.B.P. analyzed the data and co-wrote the telegram with W.A.M.

[428] **Pearlman, A. B.** et al. (2020). "A Search for Radio Bursts and Periodic Emission from SGR 1935+2154 at High Radio Frequencies Using the Deep Space Network." In: The Astronomer's Telegram #13713. ATel #13713.
A.B.P. analyzed the data and wrote the telegram.

[360] Majid, W. A.* and **Pearlman, A. B.*** et al. (2020). "Significant Flattening of Swift J1818.0–1607's Spectral Index via Dual Radio Frequency Observations with the Deep Space Network." In: The Astronomer's Telegram #13898. ATel #13898.
A.B.P. analyzed the data and co-wrote the telegram with W.A.M.

[427] **Pearlman, A. B.** et al. (2020). "Detection of Radio Pulsations from Swift J1818.0–1607 Simultaneously at 8.3 and 31.9 GHz with the Deep Space Network." In: The Astronomer's Telegram #13966. ATel #13966.
A.B.P. discovered the signals, analyzed the data, and wrote the telegram.

[359] Majid, W. A.* and **Pearlman, A. B.*** et al. (2020). "DSN Radio and NICER X-Ray Observations of PSR J1846–0258 Following Its Recent Outburst." In: The Astronomer's Telegram #13988. ATel #13988.
A.B.P. analyzed the data and co-wrote the telegram with W.A.M.

[426] **Pearlman, A. B.** et al. (2020). "A Search for Radio Bursts and Periodic Radio Emission from SGR 1830–0645 Using the Deep Space Network." In: The Astronomer's Telegram #14102. ATel #14102.
A.B.P. analyzed the data and wrote the telegram.

Table of Contents

List of Figures

Chapter IV: Pulse Morphology of the Galactic Center Magnetar PSR J1745–2900

Chapter VIII: Novel Algorithms for Detecting Ultracompact Binary Radio Pulsars

Chapter IX: Searches for Radio Pulsars Toward the Center of the Milky Way Galaxy

Chapter X: The Orbital Parameters of the Eclipsing High-mass X-Ray Binary Pulsar IGR J16493–4348 from Pulsar Timing

Chapter XI: A Study of the 20 Day Superorbital Modulation in the High-mass X-Ray Binary IGR J16493–4348

Chapter XII: Simultaneous X-Ray and Radio Observations of the Repeating Fast Radio Burst FRB 180916.J0158+65

List of Tables

Glossary of Selected Acronyms

Acronym	Definition	Acronym	Definition
ACF	Autocorrelation Function	**ADC**	Analog-to-digital Converter
ATNF	Australia Telescope National Facility	**AXP**	Anomalous X-ray Pulsar
BH	Black Hole	**CTFT**	Continuous-time Fourier Transform
DAG	Directed Acyclic Graph	**DEC**	Declination
DFT	Discrete Fourier Transform	**DISS**	Diffractive Interstellar Scintillation
DM	Dispersion Measure	**DNS**	Double Neutron Star
DOF	Degrees of Freedom	**DSN**	Deep Space Network
DSP	Digital Signal Processing	**DTFT**	Discrete-time Fourier Transform
EM	Estimation-maximization	**EoS**	Equation of State
FAP	False Alarm Probability	**FDMT**	Fast Dispersion Measure Transform
FFA	Fast Folding Algorithm	**FFT**	Fast Fourier Transform
FIR	Finite Impulse Response	**FoV**	Field of View
FPGA	Field-programmable Gate Array	**FRB**	Fast Radio Burst
FWHM	Full-width at Half-maximum	**GBT**	Green Bank Telescope
GC	Galactic Center	**GO**	Geometrical Optics
GRB	Gamma-ray Burst	**GW**	Gravitational-wave
HMM	Hidden Markov Model	**HMXB**	High-mass X-ray Binary
HWHM	Half-width at Half-maximum	**IGM**	Intergalactic Medium
IIR	Infinite Impulse Response	**IPS**	Interplanetary Scintillation
ISM	Interstellar Medium	**ISS**	Interstellar Scintillation
KDI	Kirchhoff Diffraction Integral	**KS**	Kolmogorov–Smirnov
LAN	Local Area Network	**LMC**	Large Magellanic Cloud
LMXB	Low-mass X-ray Binary	**LOS**	Line of Sight
LTI	Linear Time-invariant	**MAP**	Maximum A Posteriori
MLE	Maximum Likelihood Estimate	**MS**	Main Sequence
MSP	Millisecond Pulsar	**NS**	Neutron Star
O–C	Observed Minus Calculated	**PBF**	Pulse Broadening Function
PDF	Probability Density Function	**PPA**	Polarization Position Angle
QPO	Quasi-periodic Oscillation	**RA**	Right Ascension
RFI	Radio Frequency Interference	**RISS**	Refractive Interstellar Scintillation
RM	Rotation Measure	**RMS**	Root Mean Square
RRAT	Rotating Radio Transient	**S/N**	Signal-to-noise Ratio
SGHMXB	Supergiant High-Mass X-ray Binary	**SGR**	Soft Gamma Repeater
SMBH	Supermassive Black Hole	**SMC**	Small Magellanic Cloud
SNR	Supernova Remnant	**TOA**	Time of Arrival
TOV	Tolman-Oppenheimer-Volkoff	**ULX**	Ultraluminous X-ray Source
WD	White Dwarf	**XTI**	X-ray Timing Instrument

Table I: **Glossary of selected acronyms.**

Table of Selected Variable Definitions

Symbol	Definition
c	Speed of Light
k_B	Boltzmann Constant
$\mathcal{D}$	Dispersion Constant
A_e	Effective Area
D_{GC}	Distance to the Galactic Center
Δ_{GC}	Distance of the Scattering Screen from the Galactic Center
e	Electron Charge
m_{e}	Mass of the Electron
n_{e}	Electron Number Density
$M_{\oplus}$	Earth Mass
M_{NS}	Neutron Star Mass
n_{chans}	Number of Frequency Channels
ν_{center}	Center Frequency
ν_{p}	Plasma Frequency
$n(\nu)$	Frequency-Dependent Refractive Index
$k(\nu)$	Wavenumber
v_{g}	Group Velocity
R_{NS}	Neutron Star Radius
τ_d	Pulse Broadening Timescale
V_{ISS}	Transverse Velocity Relative to the Plane of the Observer

Table II: **Table of selected variable definitions.**

Part I: Pulsars, Fast Radio Bursts, and the Deep Space Network

Exploration is in our nature. We began as wanderers, and we are wanderers still. We have lingered long enough on the shores of the cosmic ocean. We are ready at last to set sail for the stars.

— Carl Sagan

Chapter I

The Landscape of Pulsars, Magnetars, and Fast Radio Bursts (FRBs)

1.1 A Historical Overview of Pulsar Astronomy

Neutron stars (NSs) and pulsars have led to many landmark discoveries in modern astrophysics, ranging from the discovery of the first radio pulsar to the discovery of the first binary pulsar system, which was dubbed the Hulse-Taylor binary and used to demonstrate the existence of gravitational-waves (GWs). Both of these findings were rewarded with separate Nobel Prizes in Physics. Today, we know of many thousands of pulsar and neutron star systems, and their study continues to capture the interest of many in the astronomical community. Pulsars have emerged as powerful physical tools for probing multiple aspects of fundamental physics, such as the nuclear equation of state (EoS) and testing theories of gravity. Here, I will provide a historical overview of pulsar astronomy and summarize some of the significant breakthroughs in the field.

1.1.1 The Existence of Neutron Stars

The neutron was discovered by James Chadwick in 1932 [89, 90], after separate experiments by Walther Bothe and Hebert Becker in 1930 and Irène Joliot-Curie and Frédéric Joliot-Curie in 1931 found that light elements bombarded by α-particles produced a new type of penetrating radiation. Chadwick was awarded the Nobel Prize in Physics in 1935 for recognizing that this penetrating radiation consisted of particles of mass 1 and of electric charge 0, or neutrons. Shortly after this discovery, Walter Baade and Fritz Zwicky predicted that compact, high density stars comprised primarily of neutrons are formed in supernova explosions [21]. They hypothesized that these neutron stars would be supported from gravitational collapse by the degenerate pressure of their neutrons. This is a consequence of the fact that neutrons are fermions (particles with half-integer spin) and are comprised of 3 fermionic quarks. According to the Pauli exclusion principle, no two fermions can occupy the same quantum state. This forces neutrons to inhabit distinct energy states, rather than all settling into the ground state. Quantum degeneracy pressure is generated when neutrons are squeezed into a small volume, like in neutron stars which have radii of $R_{\mathrm{NS}} \lesssim 20\,\mathrm{km}$. Therefore, the Pauli exclusion principle prevents the densest physical objects (e.g., neutron stars and white dwarfs) from collapsing into black holes (BHs).

The existence of neutron stars was initially met with considerable skepticism, despite theoretical calculations by Richard Tolman, J. Robert Oppenheimer, and George Volkoff that set an upper bound on the mass of cold, non-rotating neutron stars [411, 530]. This bound is now referred to as the Tolman-Oppenheimer-Volkoff (TOV) limit, and it is analogous to the Chandrasekhar limit for white dwarfs (WDs) [93]. At the time, it was believed that it would be very challenging to detect neutron stars, in part because the optical surface emission from neutron stars was thought to be undetectable due to their small size. It was not until radio emission from pulsars was discovered, and then later recognized to originate from rotating neutron stars, that the existence of neutron stars was accepted and mainstreamed.

1.1.2 The Discovery of the First Pulsar

The first pulsar, now known as PSR B1919+21, was serendipitously discovered in 1967 by Jocelyn Bell and Anthony Hewish at the Mullard Radio Astronomy Observatory while Bell was a graduate student working under the supervision of Hewish at Cambridge University. Together, they built a large phased-array dipole antenna, spanning an area of roughly 4.5 acres, which was operated using four beams simultaneously. This instrument was used to scan the entire sky between declinations of $+50^\circ$ and -10° once every four days. The output was recorded on four 3-track pen recorders, which was analyzed visually by Bell. The radio telescope used by Bell and Hewish is now known as the Interplanetary Scintillation Array.

The original scientific motivation for constructing the Interplanetary Scintillation Array was to study the intensity fluctuations from compact radio sources, such as quasars, which scintillate more than extended radio sources. Hewish recognized that interplanetary scintillation (IPS) could be used to identify these compact radio sources since the intensity of the radio emission would appear to fluctuate as the radio waves passed through the turbulent solar wind in interplanetary space due to diffraction. Shortly after the first observations from the survey were recorded, Bell was already able to discriminate between scintillating sources and radio frequency interference (RFI). Bell also noticed that there was also occasionally a bit of "scruff" on the output from her chart recorder, and this "scruff" did not display the characteristics of a scintillating source or terrestrial RFI (see Figure 1.1(a)). However, Hewish initially believed that the signal was produced by terrestrial interference since it failed to repeat at the same right ascension (RA). After repeated observations, the signal reappeared when observing the same part of the sky, RA = 19h:19m, most likely due to scintillation. The signal also displayed a sidereal drift of 4 minutes per day, which was consistent with the drift expected from an astrophysical source. Subsequent observations of the source with higher time resolution revealed that the "scruff" was actually the result of pulsations being detected every 1.34 s, a signature that would later be associated with PSR B1919+21's rotation period (see Figure 1.1(b)).

Shortly afterwards, Bell, Hewish, and their collaborators detected these pulsations using a different telescope. This allowed them to rule out instrumental effects as the source of the signal. They also measured the dispersion of the signal at different radio frequencies, which placed the source outside of our Solar System but within the Milky Way galaxy. Since the pulsations repeated on short timescales with a stable periodicity, they considered both an astrophysical origin and the possibility that the signal could be produced by an extraterrestrial civilization. Roughly a month after the first signal was discovered, Bell had detected pulsations from a second source (PSR B1133+16) from a different part of the sky. When a similar signal from a second source was identified, it was clear that they had found a new class of astrophysical objects. Two additional pulsars, now referred to as PSR B0834+06 and PSR B0950+08, were also discovered by Bell shortly afterwards.

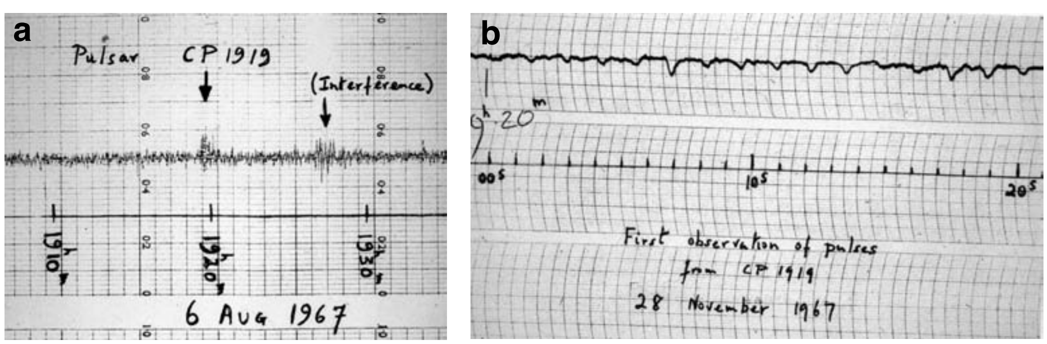

Figure 1.1: **Discovery of PSR B1919+21 by Jocelyn Bell and Anthony Hewish using the Interplanetary Scintillation Array.** Panel (a): Paper chart recorder output showing the discovery of PSR B1919+21, which was originally called CP 1919. The acronym "CP" was used as an abbreviation for Cambridge Pulsar, and "1919" refers to the right ascension (RA), 19h:19m, at which the pulsar was detected. Panel (b): The paper chart recorder output during a higher time resolution observation of PSR B1919+21, which shows the detection of individual pulses from the pulsar every 1.34 s (the pulsar's rotational period).

The discovery of the first four pulsars was published in 1968 [230, 441], and they concluded that the signals originated from pulsations from a new class of compact astrophysical radio sources. These results provided the first observational evidence for the existence of neutron stars[a]. However, Thomas Gold was the first to correctly recognize that the short-timescale pulsations were being produced by radio emission from rotating neutron stars [203]. We now refer to these objects as "pulsars," a name formed from a portmanteau of "pulsing stars." Anthony Hewish was awarded the 1974 Nobel Prize in Physics for the discovery of pulsars. This prize was shared with Sir Martin Ryle, who developed the aperture synthesis technique.

1.1.3 Milestones in Pulsar Astronomy

Since the discovery of the first pulsars in 1967, there have been a number of significant milestones in the field of pulsar astronomy that have opened up new directions in physics and astrophysics. Here, I summarize some of the major developments over the past ~50 years. The following overview is not intended to be a comprehensive list of all of the breakthroughs in the field.

- **The first binary pulsar:** In 1974, the first binary pulsar (PSR B1913+16) was discovered by Russel Hulse and Joseph Taylor during a survey for new pulsars using the 305 m Arecibo Radio Telescope in Puerto Rico [242]. The rotation period of the pulsar is 59 ms. The orbital period of the binary system is 7.75 hr, and the orbit is highly eccentric ($e = 0.62$). The companion is likely a neutron star (e.g., see [186, 496, 513, 548, 551]), making the system the first example of a double neutron star (DNS) binary. Pulses from the companion neutron star have not yet been detected, but this may be due to an unfavorable viewing angle. PSR B1913+16 has been used to carry out a number of important tests of general relativity and alternative theories of gravity. In particular, it was found that the orbital period is declining, and the two astronomical objects are rotating around their center of mass in an increasingly tight orbit due to the emission of gravitational-waves. This behavior is consistent with the expected behavior predicted by General Relativity to within about 0.2% (see Figure 1.2). Hulse and Taylor were both award the Nobel Prize in Physics in 1993 for their discovery of PSR B1913+16, which has provided new insights into gravitation, stellar evolution, and pulsar formation.

[a] Earlier in 1967, Pacini [413] suggested that a neutron star, formed soon after the supernova explosion, could be the energy source powering the Crab Nebula.

- **Discovery of magnetars:** Magnetars are neutron stars with extremely high magnetic fields ($B_{\mathrm{surf}} \gtrsim 10^{13}$ G). They were initially thought to be divided into two separate source sub-classes: soft gamma repeaters (SGRs) and anomalous X-ray pulsars (AXPs), but are now considered to be part of the same source class. They can produce highly energetic bursts of emission, such as giant flares and short, X-ray and soft gamma-ray bursts (e.g., see [193, 244, 245, 379]), which are thought to be powered by the decay of their strong magnetic fields. In fact, a magnetar (namely, SGR 1806–20 [245]) was responsible for the most luminous transient ever observed in the Milky Way galaxy.

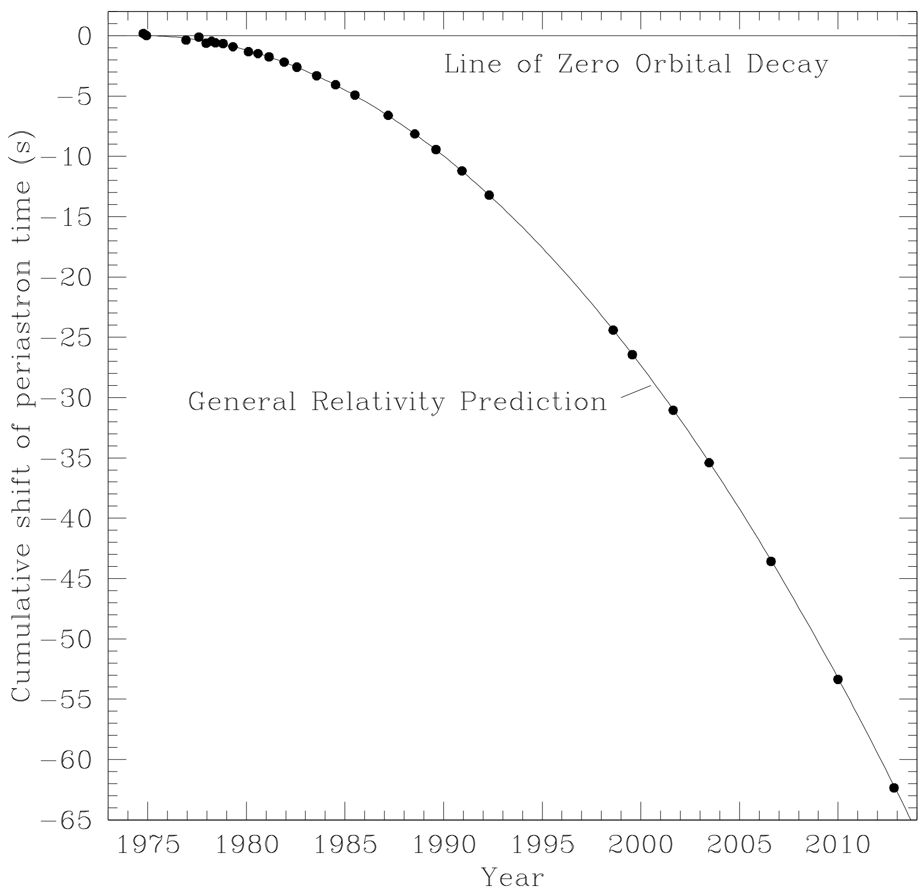

Figure 1.2: **Orbital decay of PSR B1913+16 as a function of time due to gravitational radiation.** The black points correspond to measurements of the change in the periastron time obtained from pulsar timing, which have error bars smaller than the symbol size. The solid parabolic curve shows the orbital phase shift expected from gravitational-wave emission according to General Relativity. The horizontal line shows the predicted behavior if there were no orbital decay in the system. Image credit: Adapted from Figure 3 in [550].

A small fraction of magnetars have also been observed to produce radio pulsations (e.g., see [78, 80, 169, 174, 312]). Studies of magnetars have provided new insights into the nature of young, highly magnetized neutron stars and links with high magnetic field rotation-powered pulsars and, recently, extragalactic fast radio bursts (FRBs) [59, 523].

- **The first millisecond pulsar (MSP):** Don Backer and Shrinivas Kulkarni discovered the first millisecond pulsar (PSR B1937+21) in 1982, while using the 305 m Arecibo Radio Telescope to investigate the nature of 4C21.53, a compact, steep-spectrum, scintillating radio source in the Vulpecula constellation [23]. Their radio observations revealed the presence of a rapidly-rotating pulsar with a spin period of 1.56 ms (642 Hz) that has no binary companion. Subsequent timing measurements of PSR B1937+21 showed that the pulsar exhibited a high degree of rotational stability [24]. This meant that the pulsar could be used as a stable astrophysical clock and compared against Earth-based atomic clocks. At the time of discovery, PSR B1937+21 was the fastest rotating pulsar known, but PSR J1748–2446ad ($P = 1.40$ ms, $\nu = 716$ Hz) in the globular cluster Terzan 5 is presently the fastest spinning pulsar on record [228]. In particular, the discovery of PSR B1937+21 demonstrated the existence of an entirely new class of pulsars, which challenged existing models of pulsar formation and evolution (e.g., see [493, 512]).

- **Discovery of extragalactic pulsars:** Studies of extragalactic pulsars, such as those in the Large Magellanic Cloud (LMC) and Small Magellanic Cloud (SMC), have provided new insights into the pulsar luminosity distribution, astrometry, and the properties of the local intergalactic medium (IGM). Most of the known pulsars in the Milky Way galaxy have relatively low luminosities, which suggests that ultra-sensitive instruments will be needed to detect large numbers of extragalactic pulsars. In 1983, the first extragalactic pulsar (PSR B0529–66) was discovered [380]. PSR B0529–66 is a 0.976-s pulsar located in the LMC. In addition to providing new information about the nature of compact objects in the LMC, measurements of the dispersion measure (DM) and rotation measure (RM) of PSR B0529–66 have allowed us to probe the LMC's magnetic field and the electron density in the IGM along the line of sight (los) in new ways (e.g., see [132]). As of October 2020, there were a total of 31 extragalactic pulsars listed in the Australia Telescope National Facility (ATNF) pulsar catalog, `psrcat`[b] [365]. Additionally, highly magnetized, accretion-powered X-ray pulsars have now been detected in distant galaxies, such as M82 [22], M31 [589], NGC 5097 [250], and NGC 7793 [251], from targeted X-ray observations of ultraluminous X-ray sources (ULXs). These bright X-ray pulsars are continuing to provide new insights into the physical processes through which matter accretes onto magnetized, compact objects.

- **Pulsars in globular clusters:** The central core and interior of globular clusters have the highest stellar densities of any location within the Milky Way galaxy. They produce more MSPs per unit mass than the Galactic disk, most of which are found in binary systems. Many of the exotic binary MSPs discovered in globular clusters would never be found in the Galactic disk since low-mass X-ray binaries (LMXBs), the progenitors of MSPs, are known to be orders-of-magnitude more numerous per unit mass in globular clusters compared to the Galactic disk (e.g., see [102, 268]). The first pulsar (PSR B1821–24A) discovered in a globular cluster was found in the globular cluster M28 while investigating the nature of a compact, steep-spectrum radio source within the cluster [339]. This discovery led to significant new insights into the evolution of MSPs, the role of stellar interactions in their formation, and confirmed that the dense stellar population in globular clusters acts as a nursery for MSPs and binary pulsars. As of October 2020, a total of 157 pulsars have been found in 30 different globular clusters (see Figure 1.3), according to the Globular Cluster Catalog[c].

- **The first exoplanets:** Most exoplanets have been discovered at optical wavelengths using techniques such as Doppler spectroscopy (e.g., see [376]) or transit photometry (e.g., see [94, 227]). Doppler spectroscopy is used to detect periodic variations in the radial velocity of the exoplanet's host star, while transit photometry focuses on detecting the periodic dimming of light as an exoplanet passes in front of its host star. However, the first exoplanets were discovered in 1992 from a pulsar timing analysis of the 6.22 ms pulsar, PSR B1257+12 [564, 565]. This MSP is in a binary system with 3 planetary bodies: (1) a 4.3 $M_\oplus$ planetary body in a 66.54 d orbit, (2) a 3.9 $M_\oplus$ planetary body in a 98.21 d orbit, and (3) a 0.020 $M_\oplus$ planetary body in a 25.26 d orbit [282]. This discovery opened up new avenues for probing the planetary

[b] See https://www.atnf.csiro.au/research/pulsar/psrcat.
[c] See http://www.naic.edu/~pfreire/GCpsr.html.

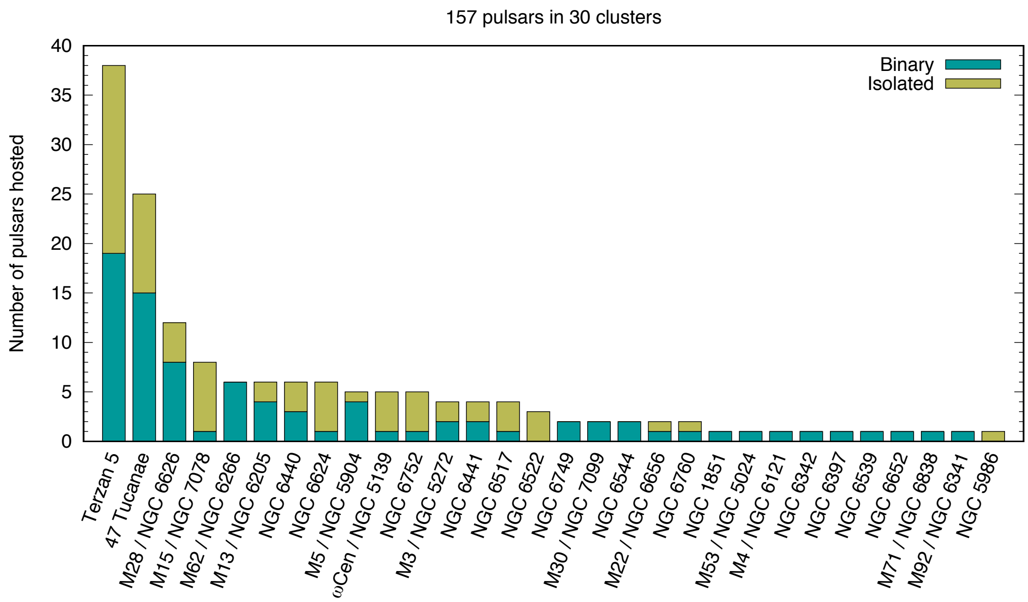

Figure 1.3: **Number of pulsars discovered in globular clusters, as of October 2020.** A total of 157 pulsars have been found in 30 different globular clusters. The number of binary and isolated pulsars discovered in each of these globular clusters are shown using teal and yellow bars, respectively. Image credit: Adapted from the Globular Cluster Catalog[c].

dynamics of planets outside of the Solar System and demonstrated that pulsar timing techniques can be used to make highly precise measurements.

1.2 Pulsars

Main sequence (MS) stars are supported by the balance between the inward-acting force of gravity, due to the star's own mass, and the outward-acting force from radiation pressure created by nuclear fusion in the stellar core. When these forces are balanced, the star is in a state of hydrostatic equilibrium. As the star evolves, its hydrogen reservoir will become depleted as hydrogen atoms are fused together to create helium atoms during nuclear fusion. This process causes the stellar core to shrink and the temperature in the core to increase. The star then enters into a giant phase, where its size and luminosity both increase. Once nuclear fusion in the stellar core has ceased, the star will no longer be able to resist its own self-gravity and will undergo core-collapse. The net result is an extremely energetic supernova explosion, where $\sim 10^{10}\,L_\odot$ is released and most of the star's outer layers are expelled at high velocity (~30,000 km/s). A supernova remnant (SNR) is then formed from the ejected material from the outer layers of the star.

The mass of the progenitor star, prior to core-collapse, determines the type of stellar remnant that is produced after the supernova explosion. A lower mass star ($M \lesssim 8\ M_{\odot}$) will produce a WD, while the collapse of a higher mass star ($M \gtrsim 25\ M_{\odot}$) will result in a BH. Intermediate mass stars ($8\ M_{\odot} \lesssim M \lesssim 25\ M_{\odot}$) will leave behind a NS, but the progenitor star can have a larger mass if its metallicity is sufficiently high. The canonical mass of a NS is typically assumed to be $M_{\rm NS} = 1.4\ M_{\odot}$, but significantly more massive NSs have also been found in the Galaxy (e.g., [136, 150]).

Pulsars are rotating neutron stars that often emit beams of radio waves from regions near their magnetic poles. These objects can also generate high-energy emission as well. A wide range of emission behavior and phenomenology have been observed from pulsars. Despite many decades of intensive research on the subject, there are still many remaining open questions, including how electromagnetic radiation from pulsars is produced. However, much of the observed behavior can be explained using a simplified toy lighthouse model for a rotating neutron star and its magnetosphere, which is shown in Figure 1.4. In this model, the pulsar's magnetic field contains closed and open field lines that thread the light cylinder, an imaginary surface determined by where an object co-rotating with the pulsar would travel at the speed of light. The light cylinder has a radius of:

$$R_{\rm LC} = \frac{c}{\Omega} = \frac{cP_{\rm spin}}{2\pi} \approx 4.77 \times 10^4\ {\rm km} \left(\frac{P_{\rm spin}}{\rm s}\right), \tag{1.1}$$

where $P_{\rm spin}$ is the rotation period of the pulsar and $\Omega_{\rm spin} = 2\pi/P_{\rm spin}$ is the pulsar's rotational angular frequency. This model assumes that the pulsar is surrounded by vacuum and its magnetic field is purely dipolar. In reality, the pulsar is embedded in a dense, plasma-filled environment known as the pulsar magnetosphere [204], and the pulsar's magnetic field may be multipolar, especially near the pulsar surface. The pulsar spins about its rotational axis, which is assumed to be misaligned with its magnetic axis by an angle α, as shown in Figure 1.4. An observer will detect pulses of emission as the pulsar rotates and its emission cone intersects the observer's line of sight (e.g., see Figure 1.5). Therefore, pulsars can be thought of as "cosmic lighthouses," where the radiation is detected with a periodicity that coincides with the rotational period of the NS.

1.2.1 Spin Evolution

Pulsars are born with an initial spin period that is transferred to the neutron star through conservation of angular momentum during the core-collapse of its progenitor supernova. They are also thought to receive a substantial "kick" at birth, which

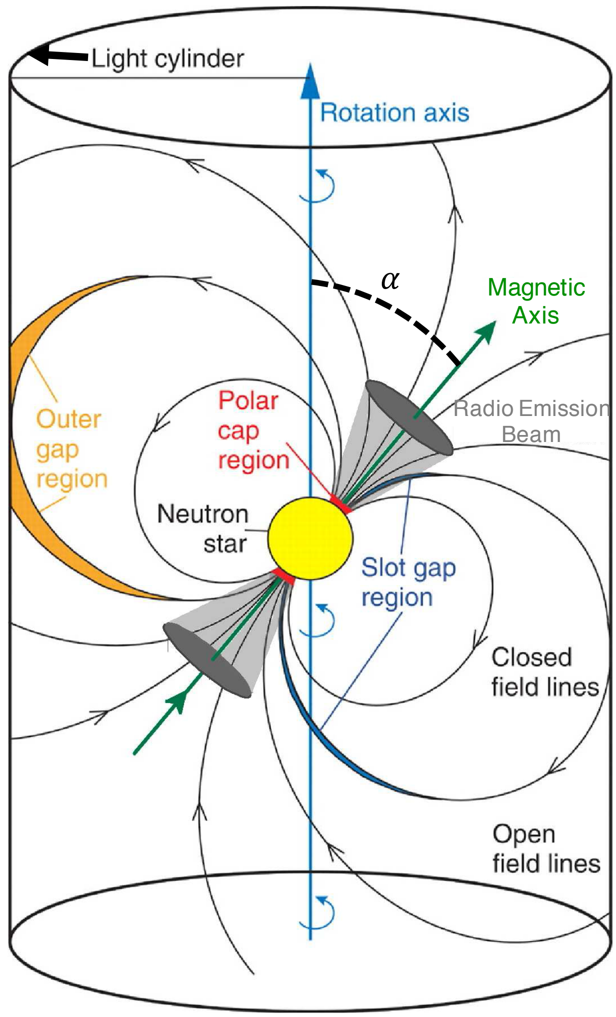

Figure 1.4: **A simplified model of a rotating radio pulsar.** Coherent pulses of radio emission are detected when the pulsar's rotational and magnetic axes are misaligned, and the radio beam crosses the line of sight (los). The light cylinder is an imaginary surface that co-rotates with a pulse propagating at the speed of light. Magnetic field lines that extend beyond the light cylinder are regarded as open field lines. The observed radio emission is produced by charged particles that are accelerated along open field lines. These charge particles are thought to be seeded from the polar caps. Various pulsar emission models also predict that gamma-ray emission can be produced in the polar cap, slot gap, and outer gap regions. Image credit: Adapted from Figure 1.1 in [345].

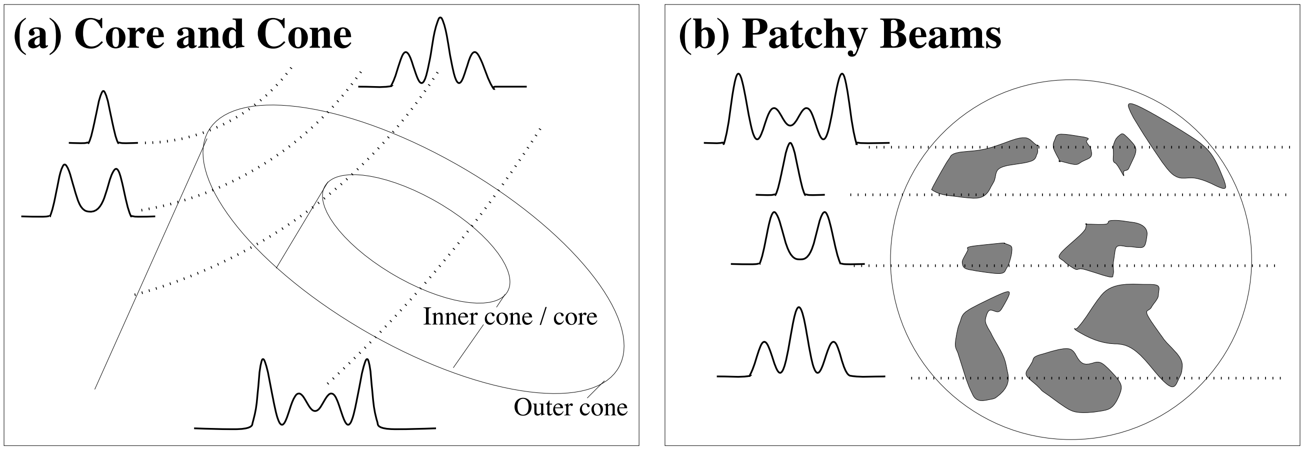

Figure 1.5: **Schematic diagram of the pulse morphology produced by different line of sight (los) slices through different beam models.** Panel (a) shows the observed pulse structure for a beam consisting of an inner cone/core and an outer cone [200, 455]. The pulse profiles for a patchy beam are shown in panel (b) [337]. Image credit: Adapted from Figure 5 in [327].

influences the pulsar's natal rotation period [501]. The spin periods measured from pulsars have been observed to increase with time due to the loss of rotational kinetic energy and other physical processes, such as magnetic dipole radiation, the pulsar wind, and high-energy emission.

The rate at which the pulsar's rotation increases, $\dot{P}_{\rm spin} = dP_{\rm spin}/dt$, can be related to the pulsar's spin-down luminosity, $\dot{E}_{\rm spin}$:

$$\dot{E}_{\rm spin} = -\frac{dE_{\rm rot}}{dt} = -\frac{d(I\Omega^2_{\rm spin}/2)}{dt} = -I\Omega_{\rm spin}\dot{\Omega}_{\rm spin} = 4\pi^2 I\dot{P}_{\rm spin}P^{-3}_{\rm spin}, \tag{1.2}$$

where $I = kM_{\rm psr}R_{\rm psr}$ is the moment of an inertia of the pulsar. Here, $M_{\rm psr}$ and $R_{\rm psr}$ correspond to the mass and radius of the pulsar, respectively. Assuming $k = 0.4$, which corresponds to a sphere of uniform density, and canonical values of $M_{\rm psr} = 1.4\,M_\odot$ and $R_{\rm psr} = 10\,{\rm km}$ for the pulsar, a nominal value for the pulsar's moment of inertia is $I \approx 10^{45}\,{\rm g\,cm^2}$. Substituting this canonical value for the moment of inertia into Equation (1.2) yields a spin-down luminosity of:

$$\dot{E}_{\rm spin} \approx 3.95 \times 10^{31}\,{\rm erg\,s^{-1}} \left(\frac{\dot{P}_{\rm spin}}{10^{-15}}\right)\left(\frac{P_{\rm spin}}{1\,{\rm s}}\right)^{-3}. \tag{1.3}$$

1.2.2 Braking Index

From classical electrodynamics, a rotating magnetic dipole, with a magnetic moment $|\mathbf{m}|$ and an angle α between its magnetic and rotational axes, will produce electromagnetic radiation. The energy loss due to the emission of magnetic dipole radiation is given by:

$$\dot{E}_{\rm dipole} = \frac{2}{3c^3}\,|\mathbf{m}|^2\,\Omega_{\rm spin}^4 \sin^2\alpha. \tag{1.4}$$

Under the assumption that magnetic dipole radiation is the main source of the pulsar's spin-down luminosity, Equations (1.2) and (1.4) can be equated to obtain a formula for the expected evolution of the pulsar's rotational frequency:

$$\dot{\Omega}_{\rm spin} = -\left(\frac{2\,|\mathbf{m}|^2 \sin^2\alpha}{3Ic^3}\right)\Omega_{\rm spin}^3. \tag{1.5}$$

Next, we can generalize the formula in Equation (1.5) as a power-law in terms of $\nu_{\rm spin} = 1/P_{\rm spin}$:

$$\dot{\nu}_{\rm spin} = -K\,\nu_{\rm spin}^n, \tag{1.6}$$

where K is typically assumed to be a constant and n is the braking index. Thus, from Equation (1.5), $n = 3$ in Equation (1.6) corresponds to pure magnetic dipole braking. However, energy losses from other dissipation mechanisms can result in a braking index that deviates from $n = 3$ for a given pulsar.

The braking index can also be determined if the pulsar's second frequency derivative, $\ddot{\nu}_{\rm spin}$, is measured. Differentiating Equation (1.6) with respect to time and using it again to eliminate the constant K gives the following expression for the braking index in terms of the pulsar's spin frequency and its first two time derivatives:

$$n = \frac{\nu_{\rm spin}\,\ddot{\nu}_{\rm spin}}{\dot{\nu}_{\rm spin}^2}. \tag{1.7}$$

It is often difficult to measure $\ddot{\nu}_{\rm spin}$ due to the impact of timing noise and pulsar glitches. Typically, it is only possible to measure $\ddot{\nu}_{\rm spin}$ from young pulsars, which display a high spin-down rate. Currently, there are limited number of braking measurements in the literature, with values ranging between roughly $0.9 \lesssim n \lesssim 2.8$ (e.g., [232]).

1.2.3 Characteristic Age and Rotational Period at Birth

The expression for the braking index in Equation (1.6) can be used to derive the pulsar's approximate age. Rewriting Equation (1.6) in terms of the rotational period yields:

$$\dot{P}_{\rm spin} = K P_{\rm spin}^{(2-n)}. \tag{1.8}$$

Integrating both sides of Equation (1.8) from the time of the pulsar's birth (at $t = 0$) to the current time (at $t = T$), assuming K is constant and $n \neq 1$, we obtain:

$$\int_{P_0}^{P_{\rm spin}} P^{(n-2)} dP = K \int_0^T dt, \tag{1.9}$$

where P_0 is the rotational period of the pulsar at time $t = 0$ and $P_{\rm spin}$ is the pulsar's spin period at time $t = T$. Solving Equation (1.9) yields the following expression for the approximate age of the pulsar:

$$T = \frac{P_{\rm spin}}{(n-1)\dot{P}_{\rm spin}} \left[1 - \left(\frac{P_0}{P_{\rm spin}} \right)^{n-1} \right]. \tag{1.10}$$

Assuming that the current value of the pulsar's spin period is much larger than its rotational period at birth (i.e., $P_{\rm spin} \gg P_0$) and the pulsar's spin-down is due to pure magnetic dipole radiation (i.e., $n = 3$), Equation (1.10) can be simplified to give the pulsar's characteristic age:

$$\tau_{\rm c} = \frac{P_{\rm spin}}{2\dot{P}_{\rm spin}} \approx 15.8\,{\rm Myr} \left(\frac{P_{\rm spin}}{1\,{\rm s}} \right) \left(\frac{\dot{P}_{\rm spin}}{10^{-15}} \right)^{-1}. \tag{1.11}$$

It is important to note that the characteristic age of a pulsar is often not representative of the pulsar's true age since the above mentioned assumptions are typically not valid. For example, MSPs are spun up or "recycled" by the accretion of a matter from a star in a close binary system. Due to the substantially different evolutionary history of MSPs, their rotational properties cannot be characterized by the standard spin-down model. PSR J1938+2012, for instance, is a MSP with a rotational period of 2.6 ms [504]. It has a spin-inferred characteristic age of 55.6 Gyr, which is larger than a Hubble time.

Using Equations (1.10) and (1.11), an expression for the pulsar's birth period can be obtained:

$$P_0 = P_{\rm spin} \left[1 - \frac{(n-1)}{2} \frac{T}{\tau_{\rm c}} \right]^{\left(\frac{1}{n-1}\right)}. \tag{1.12}$$

Therefore, the pulsar's rotational period at birth can be determined from Equation (1.12) if the pulsar's braking index has been measured and the true age of the pulsar, T, is known (e.g., by associating the pulsar with a historical supernova).

1.2.4 Magnetic Fields

Most normal pulsars have magnetic fields ranging between 10^{11}–10^{13} G (see Figure 1.6). While the magnetic field strengths of radio pulsars have not been directly measured, they can be estimated by assuming that the pulsar's spin-down behavior is dominated by dipole braking. The magnetic field strength, B, of a dipole is related to its magnetic moment, $|\mathbf{m}|$, according to:

$$B \approx \frac{|\mathbf{m}|}{r^3}. \tag{1.13}$$

Assuming that the pulsar's spin-down process is entirely due to magnetic braking ($n = 3$), Equation (1.13) can be substituted into Equation (1.4) and equated to Equation (1.2) to obtain an expression for the magnetic field strength at the surface of the neutron star:

$$B_{\text{surf}} = B(r = R_{\text{psr}}) = \sqrt{\frac{3c^3}{8\pi^2} \frac{I}{R_{\text{psr}}^6 \sin^2 \alpha} P_{\text{spin}} \dot{P}_{\text{spin}}}. \tag{1.14}$$

Substituting the canonical values for the moment of inertia ($I = 10^{45}$ g cm^2) and radius ($R_{\text{psr}} = 10$ km) of a neutron star into Equation (1.14), along with $\alpha = 90°$, the above expression simplifies to:

$$B_{\text{surf}} = 3.2 \times 10^{19}\,\text{G} \sqrt{P_{\text{spin}} \dot{P}_{\text{spin}}} \approx 10^{12}\,\text{G} \left(\frac{\dot{P}_{\text{spin}}}{10^{-15}}\right)^{1/2} \left(\frac{P_{\text{spin}}}{1\text{ s}}\right)^{1/2}. \tag{1.15}$$

If the expression in Equation (1.15) is used, it should be treated as an order of magnitude estimate of the pulsar's characteristic surface magnetic field strength. Since the pulsar's moment of inertia and radius are usually uncertain, α is often unknown, and other physical processes may contribute to the pulsar's spin-down, the value obtained using Equation (1.15) can differ from the true surface magnetic field strength of the pulsar.

1.2.5 Types of Pulsars

The pulsar population is comprised of various types of pulsars, including: (1) rotation-powered pulsars, where the star's rotational energy powers the emission, (2) accretion-powered pulsars, where the gravitational potential energy of matter being accreted from a companion produces X-rays and other high-energy emission, and (3) magnetars, where the emission is powered by the decay of extremely strong magnetic fields. There are presently over 2,800 known pulsars listed in the ATNF pulsar catalog[b] [365]. The West Virginia University (WVU) RRATalog[d] lists the properties of Rotating Radio Transients (RRATs) discovered with Parkes, Arecibo, LOFAR, and the GBT. A list of Galactic MSPs, not associated with globular clusters, are

[d] See http://astro.phys.wvu.edu/rratalog.

provided in the WVU MSP catalog[e]. Recently discovered pulsars by the Canadian Hydrogen Intensity Mapping Experiment (CHIME) radio telescope are listed in the CHIME Galactic source catalog[f], and a list of pulsars recently found using the Five-hundred-meter Aperture Spherical radio Telescope (FAST) are provided in the FAST pulsar catalog[g].

In Figure 1.6, I show a $P_{\rm spin}$–$\dot{P}_{\rm spin}$ diagram of the known pulsars. Magnetars inhabit the top-right region of the diagram, and they have longer spin periods and higher spin-inferred magnetic fields than the rest of the pulsar population, on average. MSPs, on the other hand, have shorter rotation periods and smaller magnetic fields. They are mostly distributed in the bottom-left region of the $P_{\rm spin}$–$\dot{P}_{\rm spin}$ diagram. Most normal pulsars have magnetic fields between 10^{11} G $\lesssim B_{\rm surf} \lesssim 10^{13}$ G, and they are shown in the central region of the diagram. Lines of constant magnetic field and characteristic age are also overlaid on this plot, which are derived assuming a constant braking index of $n = 3$.

The different evolutionary scenarios involving binary pulsars are shown in Figure 1.7. The spin-down properties of these systems are strongly influenced by interactions with their companions. As a result, models that assume pure magnetic dipole braking are inadequate for properly characterizing their observed behavior.

Figure 1.8 shows the electron density distribution from YMW16 [577] projected in the plane of the Galaxy, along with the positions of the known Galactic pulsars. The positions of these pulsars are also shown in the cross-section of the Galaxy in Figure 1.9. Most Galactic pulsars have been found to reside in the Galactic disk, and their positions are correlated with the Galactic spiral arms, which are believed to be the birth sites of most Galactic pulsars [183].

1.3 Propagation Effects

Electromagnetic radiation from pulsars, FRBs, and other astrophysical sources are affected by a number of propagation effects as their signals travel through the interstellar medium (ISM). For example, pulse dispersion, Faraday rotation, scintillation, and scattering each imprint a signature on the detected signal. In order to study the underlying properties of the emission, it is critical to understand these effects. In the following subsections, I will describe each of these propagation effects.

[e] See http://astro.phys.wvu.edu/GalacticMSPs/GalacticMSPs.txt.
[f] See https://www.chime-frb.ca/galactic.
[g] See https://crafts.bao.ac.cn/pulsar.

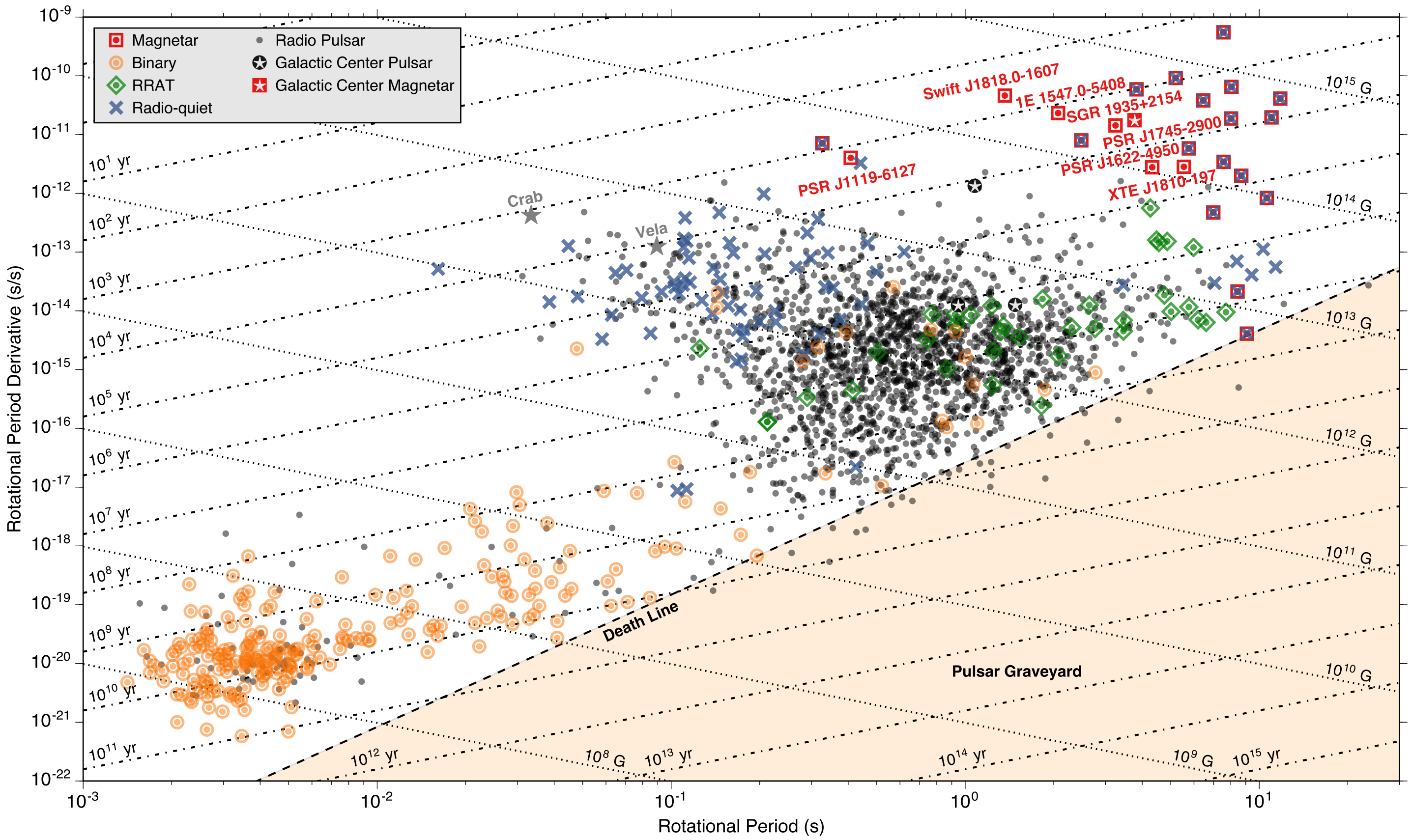

Figure 1.6: **$P_{\rm spin}$–$\dot{P}_{\rm spin}$ diagram of pulsars in the ATNF pulsar catalog[b] [365] and WVU RRATalog[d].** Magnetars (red squares), binary pulsars (orange circles), and RRATs (green diamonds) are shown, along with the population of rotation-powered radio pulsars (black circles). The Crab Pulsar (PSR B0531+21) and the Vela Pulsar (PSR B0833-45) are indicated using black stars. The names of the known Galactic radio magnetars and radio magnetar candidates are labeled explicitly in red. Pulsars detected toward the GC are labeled using a black circle and a white star, and the GC magnetar, PSR J1745-2900, is labeled using a red square and a white star. Radio-quiet pulsars are denoted using blue crosses and include many of the magnetars shown in red. Lines of constant magnetic field (dotted lines) and characteristic age (dot-dashed lines) are derived assuming a constant braking index of $n = 3$. The radio pulsar death line is derived from the model given in Equation (4) of [583], which marks the approximate edge of the pulsar graveyard. Pulsed radio emission is expected to cease from neutron stars that cross into the pulsar graveyard region.

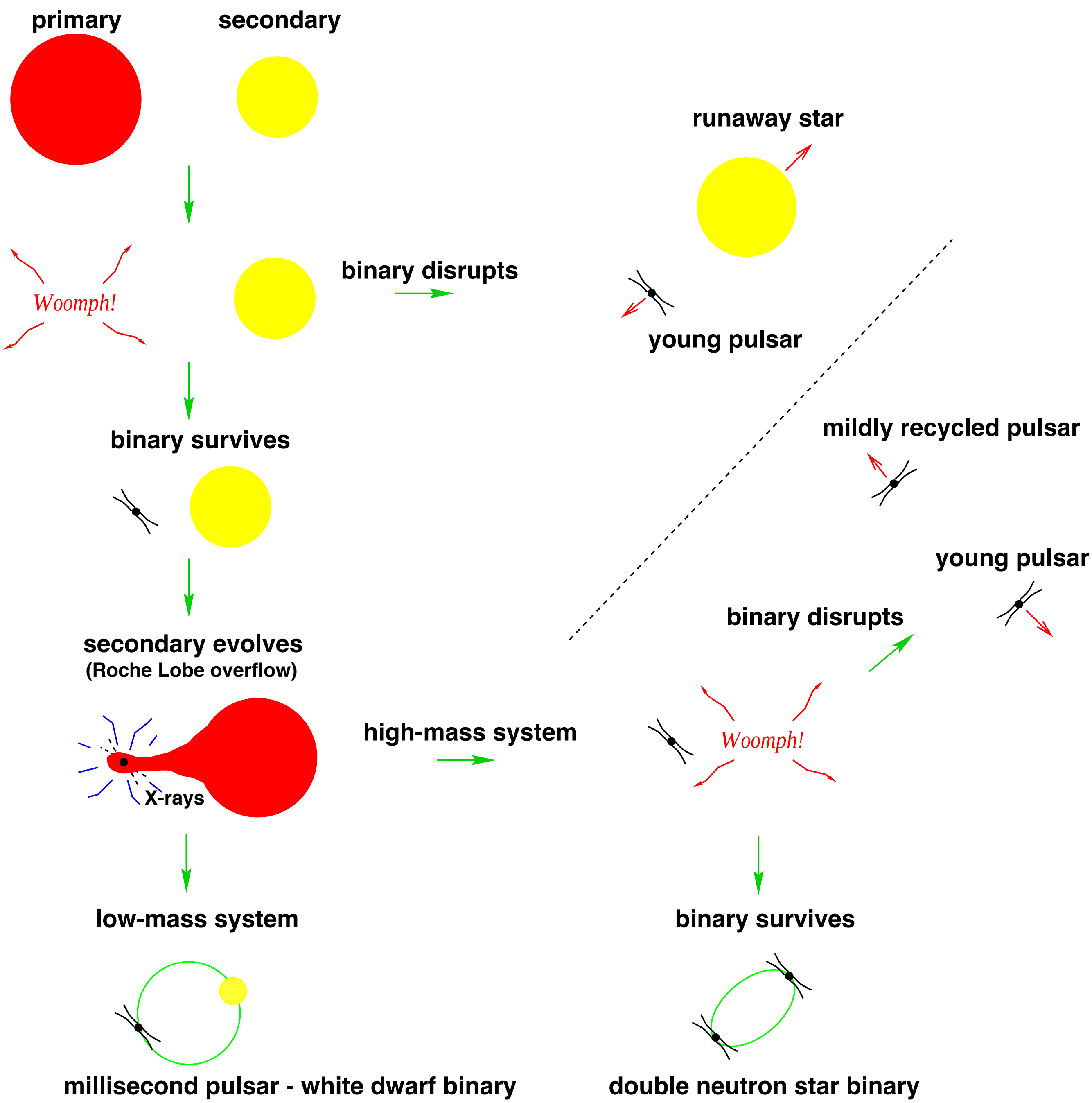

Figure 1.7: **A schematic diagram showing the different formation channels of pulsar binary systems.** Image credit: Adapted from Figure 7 in [327].

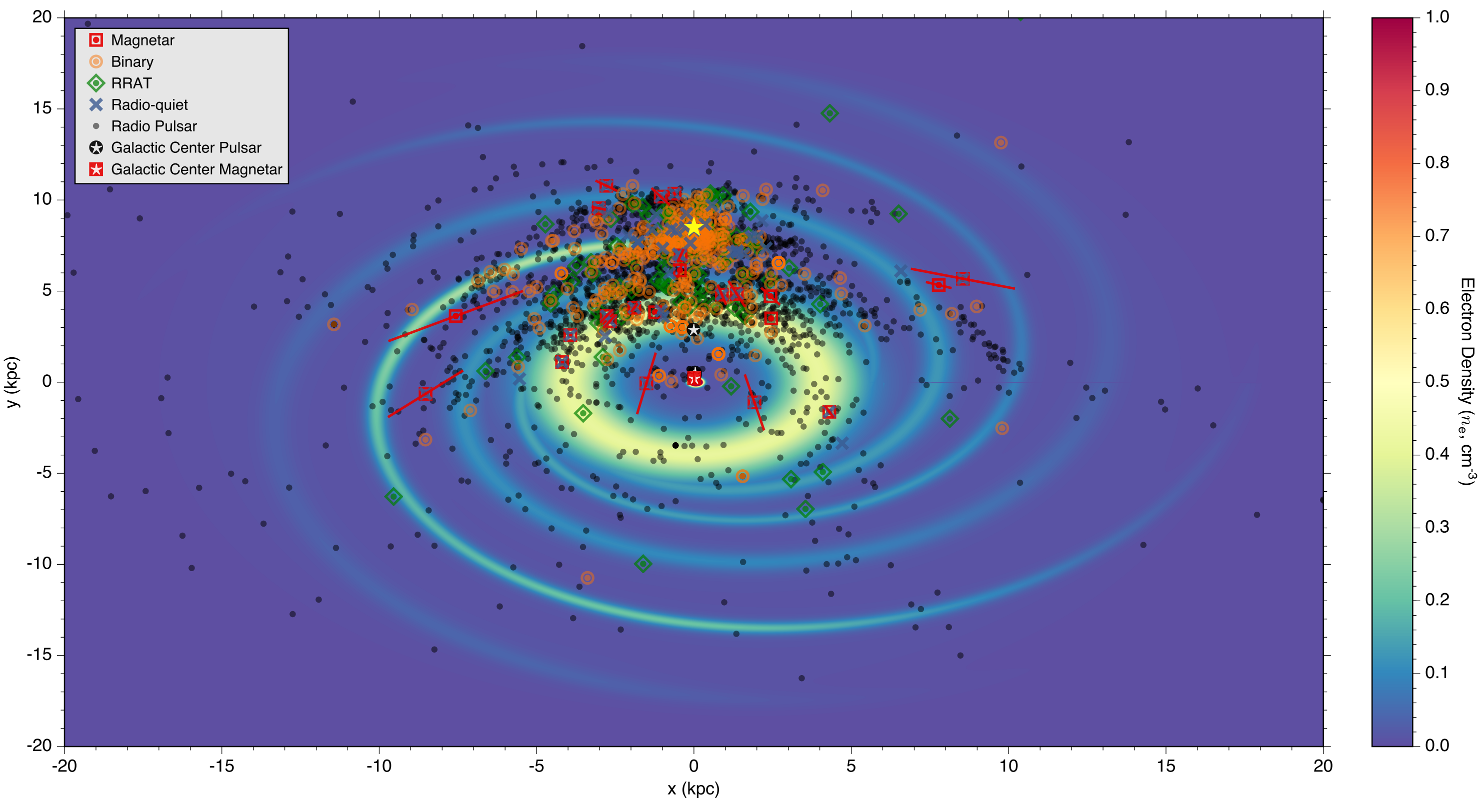

Figure 1.8: **Top-down (x–y plane) view of the Milky Way, where the Galactic Center (GC) is at $(x, y) = (0, 0)$ kpc and the Sun is labeled using a yellow star at $(x, y) = (0, 8.3)$ kpc.** The color bar indicates the electron density in the plane of the Galaxy according to the YMW16 electron density model [577]. The positions of the known magnetars (red squares), binary pulsars (orange circles), and RRATs (green diamonds) are shown together with the population of rotation-powered radio pulsars (black circles). The distance uncertainty associated with each magnetar is indicated using red error bars. Pulsars detected toward the GC are labeled using a black circle and a white star, and the GC magnetar, PSR J1745–2900, is labeled using a red square and a white star. Radio-quiet pulsars are denoted using blue crosses and include many of the magnetars shown in red. All of the known objects in the ATNF pulsar catalog[b] [365], WVU RRATalog[d], WVU MSP catalog[e], CHIME Galactic source catalog[f], and FAST pulsar catalog[g] are labeled in this diagram.

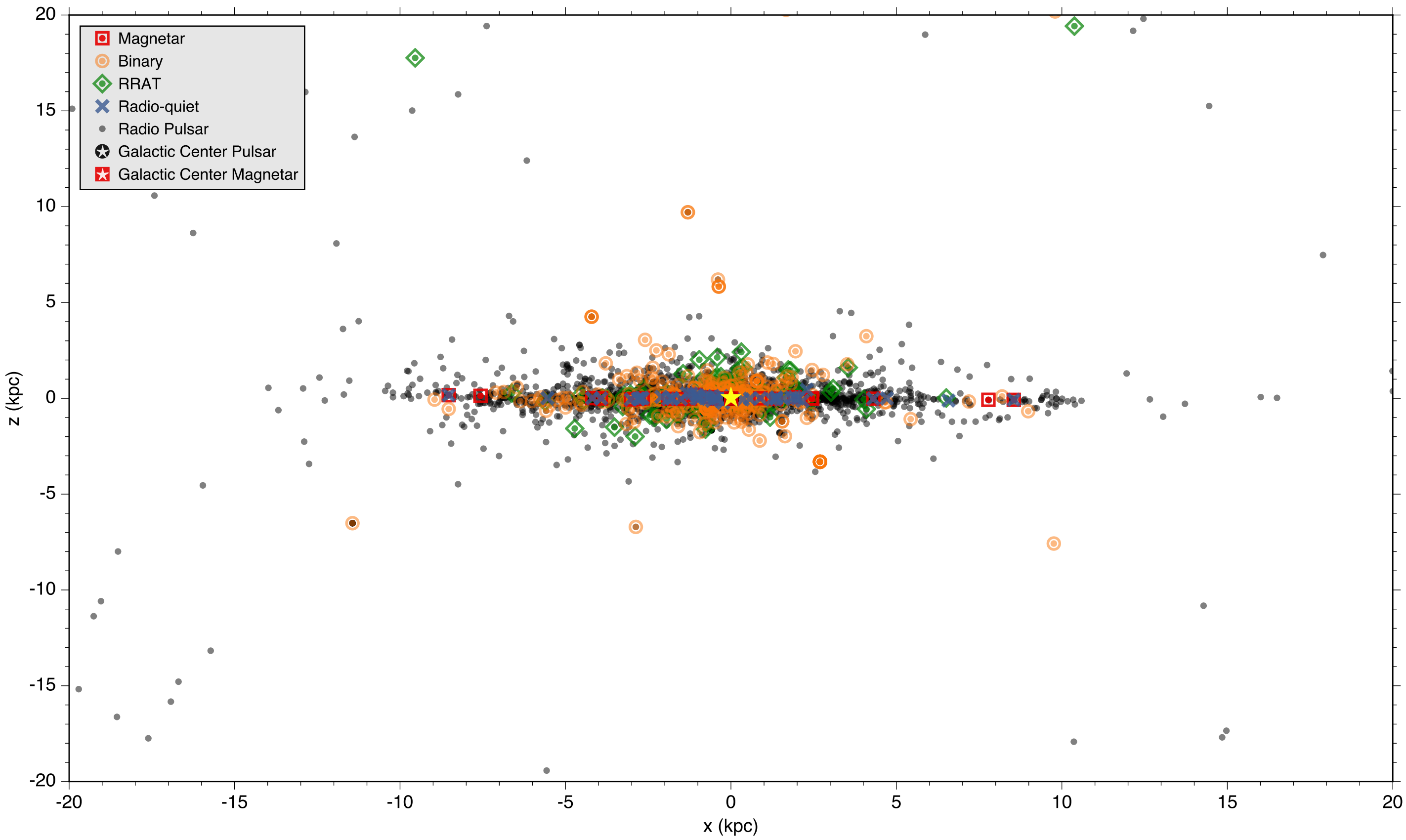

Figure 1.9: **Side (x–z plane) view of the Milky Way, where the Galactic Center (GC) is at $(x, z) = (0, 0)$ kpc and the Sun is labeled using a yellow star at $(x, z) = (0, 0.026)$ kpc [352].** The positions of the known magnetars (red squares), binary pulsars (orange circles), and RRATs (green diamonds) are shown together with the population of rotation-powered radio pulsars (black circles). Pulsars detected toward the GC are labeled using a black circle and a white star, and the GC magnetar, PSR J1745–2900, is labeled using a red square and a white star. Radio-quiet pulsars are denoted using blue crosses and include many of the magnetars shown in red. All of the known objects in the ATNF pulsar catalog[b] [365], WVU RRATalog[d], WVU MSP catalog[e], CHIME Galactic source catalog[f], and FAST pulsar catalog[g] are labeled in this diagram.

1.3.1 Dispersion

When photons propagate through a plasma, they experience frequency-dependent delays in their arrival times due to dispersion. As a result, higher frequency photons from an electromagnetic pulse emitted simultaneously across a broad frequency range will propagate faster than those emitted at lower frequencies. This behavior is commonly observed from radio pulses detected from pulsars and FRBs using radio telescopes on Earth. This phenomenon was first observed by Hewish et al. [230] while studying radio pulses from the first discovered pulsar, PSR B1919+21. In Figure 1.10, I show an example of how dispersion affects the pulses observed from the radio pulsar PSR B1356–60.

As radio waves propagate through the cold, ionized plasma in the ISM, they experience a frequency-dependent change in their group velocity. The group velocity of the wave is given by:

$$v_{\rm g} = c \times n(\nu) = c\sqrt{1 - \left(\frac{\nu_{\rm p}}{\nu}\right)^2}, \tag{1.16}$$

where $n(\nu)$ is the frequency-dependent refractive index, $\nu_{\rm p}$ is the plasma frequency, ν is the observing frequency, and c is the speed of light. The plasma frequency is given by:

$$\nu_{\rm p} = \sqrt{\frac{e^2 n_{\rm e}}{\pi m_{\rm e}}} = 8.5\,{\rm kHz}\left(\frac{n_{\rm e}}{\rm cm^{-3}}\right)^{1/2}, \tag{1.17}$$

where $n_{\rm e}$ is the electron number density, and e and $m_{\rm e}$ are the charge and mass of the electron, respectively. In the ISM, a typical value of $n_{\rm e}$ is roughly $0.03\,{\rm cm}^{-3}$ [6], which corresponds to a plasma frequency of $\nu_{\rm p} \approx 1.5\,{\rm kHz}$. From Equation (1.16), we see that waves with frequencies below the plasma frequency, i.e. $\nu < \nu_{\rm p}$, will not propagate. Therefore, the waves must satisfy $n(\nu) < 1$ in order to propagate.

A radio pulse propagating from the source to Earth, along a path of length d, will experience a time delay compared to a signal at infinite frequency. This delay time can be expressed as:

$$\Delta t_{(\nu,\infty)} = \left(\int_0^d \frac{dl}{v_{\rm g}}\right) - \frac{d}{c}. \tag{1.18}$$

Substituting Equation (1.16) and applying the approximation $\nu_{\rm p} \ll \nu$ yields:

$$\Delta t_{(\nu,\infty)} = \left[\frac{1}{c}\int_0^d \left(1 + \frac{\nu_{\rm p}^2}{2\nu^2}\right) dl\right] - \frac{d}{c} = \frac{e^2}{2\pi m_{\rm e} c}\frac{\int_0^d n_e\, dl}{\nu^2} = \mathcal{D} \times \frac{\rm DM}{\nu^2}. \tag{1.19}$$

The dispersion measure (DM) is defined as:

$${\rm DM} = \int_0^d n_e\, dl, \tag{1.20}$$

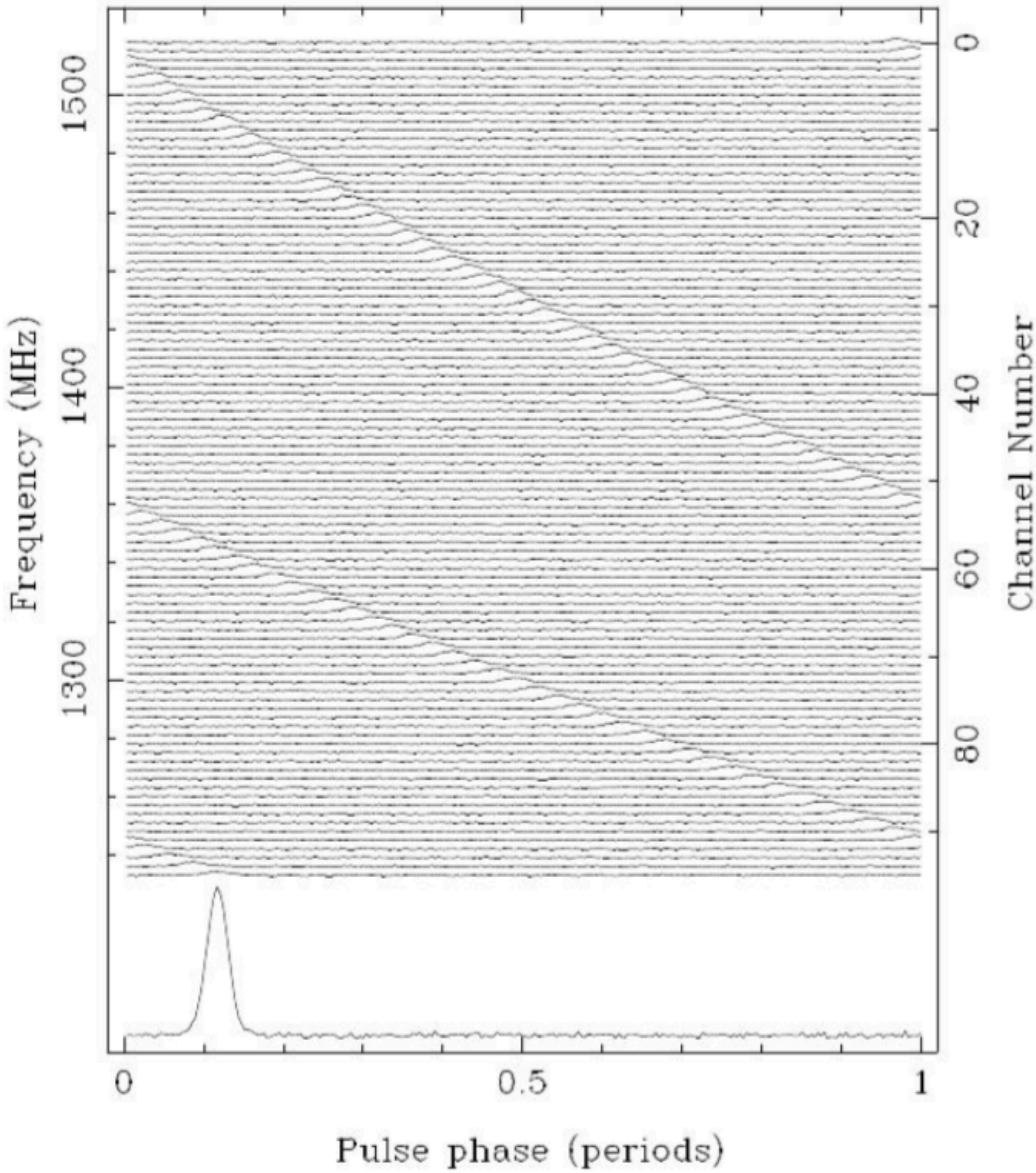

Figure 1.10: **Dispersion delay observed from the 128 ms pulsar PSR B1356–60 during an observation with the Parkes radio telescope.** The DM of the pulsar is 293.736 pc cm^{-3}. Since the dispersion delay across the observing band is so large, the pulses are wrapped around in pulse phase. The integrated pulse profile shown at the bottom is produced by summing the pulses detected at each frequency, after correcting for dispersion. Image credit: Adapted from Figure 1.8 in [328].

and it is typically expressed in units of $\mathrm{pc\,cm^{-3}}$. The DM is a measure of the integrated free electron content along the line of sight to the source, and it is commonly used to characterize the amount of dispersion affecting a signal. The dispersion constant is defined to be:

$$\mathcal{D} = \frac{e^2}{2\pi m_e c} \approx 4.15 \times 10^3\,\mathrm{MHz^2\,pc^{-1}\,cm^3\,s}. \tag{1.21}$$

Throughout this thesis, $1/\mathcal{D} = 2.41 \times 10^{-4}\,\mathrm{MHz^{-2}\,pc\,cm^{-3}\,s^{-1}}$ will be used for the dispersion constant [362], unless otherwise stated.

A broadband signal will experience an arrival time delay between two frequencies, ν_1 and ν_2 (with $\nu_1 < \nu_2$), that is related to the DM by:

$$\Delta t_{(\nu_1,\,\nu_2)} = \mathcal{D} \times \left(\frac{1}{\nu_1^2} - \frac{1}{\nu_2^2}\right) \times \mathrm{DM}. \tag{1.22}$$

Thus, the DM along the line of sight can be inferred by measuring the arrival times of a signal at two or more different frequencies. From Equation (1.20), the DM can also be used to infer the distance to a source, if the electron density, n_e, along the line of sight is known. Models of the Galactic electron density distribution, such as NE2001 [124] and YMW16 [577] (e.g., see Figure 1.8), can be used to estimate the electron density along a given los. These models incorporate local variations in the Galactic n_e distribution from the Galactic disk and spiral arms, where the electron density is typically largest, and they also include contributions from nebulae and supernova remnants. However, calibrated measurements of pulsar distances (e.g., from parallax measurements or H II absorption) can be used to measure the Galactic electron density distribution more accurately.

1.3.2 Faraday Rotation

An electromagnetic wave propagating through an ionized medium that is permeated with a non-zero magnetic field, $B_{\|}$, along the direction of propagation will be affected by Faraday rotation. This will lead to a change in the propagating wave's plane of linear polarization.

This phenomenon can be explained by considering the behavior of free electrons oscillating inside a magnetic field. When $B_{\|} \neq 0$, the electrons will experience a Lorentz force that causes them to rotate in a circular direction. This circular motion will create a local magnetic field, in addition to the external magnetic field, which will cause the two circular polarization states of the wave to propagate at different speeds since they will have group velocities that are determined by different refractive indices. The difference in propagation speeds will result in a change in the relative phase of the two circular polarization states, which is responsible for the change in the angle of linear polarization.

An electromagnetic wave, emitted at a frequency ν, propagating through a cold, ionized and magnetized plasma over a distance d will experience a phase lag given by:

$$\Delta\Psi = -k(\nu)d, \tag{1.23}$$

where $k(\nu) = 2\pi/\lambda = 2\pi\nu n(\nu)/c$ is the wavenumber. In the presence of an external magnetic field, the refractive index is given by:

$$n(\nu) = \sqrt{1 - \frac{\nu_{\rm p}^2}{\nu^2} \mp \frac{\nu_{\rm p}^2 \nu_{\rm B}}{\nu^3}}, \tag{1.24}$$

where the last term in Equation (1.24) has a "–" sign for a left-handed circularly polarized wave and a "+" sign for a right-handed circularly polarized wave. Here, $\nu_{\rm B}$ is the cyclotron or Larmor frequency, which depends on the magnetic field along the los, $B_{||}$:

$$\nu_{\rm B} = \frac{eB_{||}}{2\pi m_{\rm e} c} \approx 3\,{\rm MHz}\left(\frac{B_{||}}{1\,{\rm G}}\right). \tag{1.25}$$

In the Milky Way, the typical value of $B_{||}$ is roughly 1 μG, which corresponds to $\nu_{\rm B} \sim 3\,{\rm Hz}$ in the ISM.

Most radio observations of pulsars and FRBs are performed in the regime where $\nu \gg \nu_{\rm p}$ and $\nu \gg \nu_{\rm B}$. Under these assumptions, Equations (1.23) and (1.24) can be used to calculate the differential phase rotation between the right and left circular polarizations:

$$\Delta\Psi_{\rm Faraday} = \int_0^d (k_{\rm R}(\nu) - k_{\rm L}(\nu))\,dl \approx \frac{e^3}{\pi m_{\rm e}^2 c^2 \nu^2} \int_0^d n_{\rm e} B_{||} dl. \tag{1.26}$$

Here, $k_{\rm R}(\nu)$ and $k_{\rm L}(\nu)$ corresponds to the wavenumber of a right and left circularly polarized wave.

Since the linear polarization position angle (PPA) is periodic on π for phase, rather than 2π, a change in $\Delta\Psi_{\rm Faraday}$ corresponds to half a change in the PPA:

$$\Delta\Psi_{\rm PPA} = \frac{\Delta\Psi_{\rm Faraday}}{2} = \frac{1}{2}\frac{e^3\lambda^2}{\pi m_{\rm e}^2 c^4} \int_0^d n_{\rm e} B_{||} dl = \lambda^2 \times {\rm RM} = \frac{c^2}{\nu^2} \times {\rm RM}, \tag{1.27}$$

where the rotation measure (RM) is defined to be:

$$\mathrm{RM} = \frac{e^3}{2\pi m_\mathrm{e}^2 c^4} \int_0^d n_\mathrm{e} B_{\|} dl. \tag{1.28}$$

Using Equations (1.20) and (1.28), the average magnetic field along the los, weighted by the electron number density, can be inferred from measurements of both the RM and DM:

$$\langle B_{\|} \rangle = \frac{\int_0^d n_\mathrm{e} B_{\|} dl}{\int_0^d n_\mathrm{e} dl} = 1.23\,\mu\mathrm{G} \left(\frac{\mathrm{RM}}{1\ \mathrm{rad\ m^{-2}}}\right) \left(\frac{\mathrm{DM}}{1\ \mathrm{pc\ cm^{-3}}}\right). \tag{1.29}$$

1.3.3 Scattering

The inhomogeneous Galactic ISM is turbulent and contains irregularities that can distort a propagating electromagnetic wave and introduce various effects, such as scattering and scintillation. For example, radio waves traveling through the ISM will get deflected as a result of electron density fluctuations in the intervening medium. Density irregularities in the free electron content along the line of sight cause a change in the refractive index, Δn, which results in different rays traveling along different non-straight optical paths. The deflected rays will experience longer propagation times, which introduces a “tail” into the observed pulse shape. This behavior is known as scattering.

Scattering was first studied by Scheuer [474] using pulsars under the assumption of a thin screen model. Since then, there have been many additional detailed treatments of the subject (e.g., see [46, 293, 317, 467, 558, 559, 560]). Figure 1.11 illustrates how radio waves from a pulsar propagating through a thin screen with density irregularities can form a scatter-broadened image. Let Δn_e denote the electron density fluctuations of the screen in Figure 1.11, where the inhomogeneities have a typical length of a.

Distortions from the turbulent plasma screen will cause the incident radiation to experience a change in its refractive index, Δn. After a wave of frequency ν travels through an inhomogeneity of length a, the wave will experience a phase shift given by:

$$\delta\Phi = \Delta k a, \tag{1.30}$$

where Δk is the change in the magnitude of the wave vector, $\vec{k}$, and $k = 2\pi\nu n/c$. Combining Equations (1.16) and (1.17) and applying the approximation $\nu_\mathrm{p} \ll \nu$, the change in k can be expressed as:

$$\Delta k \approx \frac{2e^2}{m_\mathrm{e}c}\frac{\Delta n_\mathrm{e}}{\nu}. \tag{1.31}$$

Substituting Equation (1.31) into Equation (1.30) then yields a phase shift of:

$$\delta\Phi \approx \frac{2e^2}{m_\mathrm{e}c}\frac{a\Delta n_\mathrm{e}}{\nu}. \tag{1.32}$$

Once a ray traverses a distance d between the source and the observer, the total number of irregularities it encounteres in the electron density content is roughly d/a. This gives rise to a root mean square (RMS) change in phase of:

$$\Delta\Phi \approx \frac{2e^2}{m_\mathrm{e}c}\frac{\sqrt{ad}\Delta n_\mathrm{e}}{\nu}. \tag{1.33}$$

The net effect of this phase difference, $\Delta\Phi$, will be that a screen with scale size a, located midway between the source and the observer, will bend the wavefront by an angle θ_0:

$$\theta_0 \approx \frac{\Delta\Phi}{ka} \approx \frac{\Delta\Phi c}{2\pi a\nu} = \frac{e^2}{\pi m_\mathrm{e}}\frac{\Delta n_\mathrm{e}}{\sqrt{a}}\frac{\sqrt{d}}{f^2}. \tag{1.34}$$

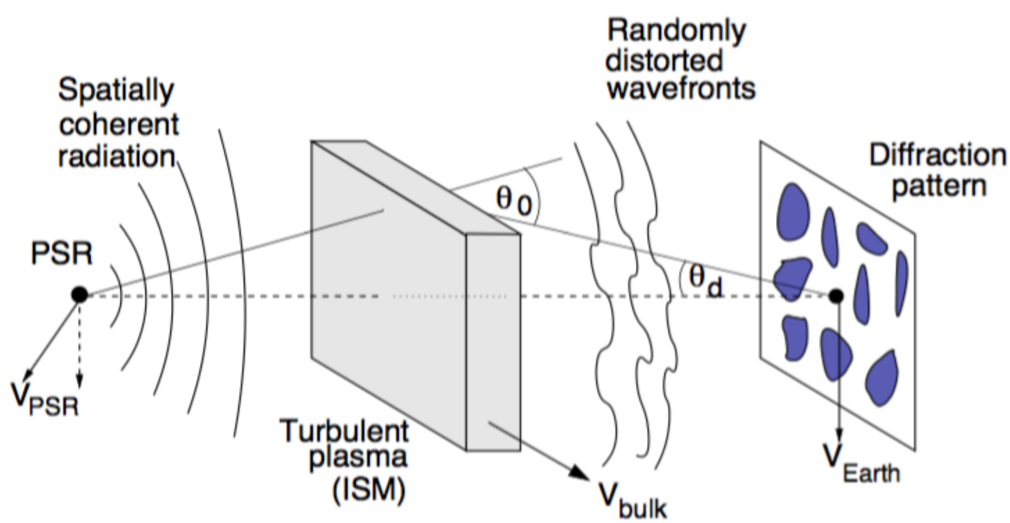

Figure 1.11: **Schematic diagram of emission from a pulsar propagating through a thin screen with density irregularities.** The spatially coherent radiation from the pulsar is randomly distorted by the turbulent plasma screen and deflected by an angle θ_0, which leads to a scatter-broadened image with an angular radius of θ_d. The distorted signals will also produce an interference pattern at the location of a distant observer. If there is relative motion in the system, this results in intensity fluctuations of the signal and a scintillation pattern. Image credit: Adapted from Figure 4.2 in [328].

However, the observer will see a scatter-broadened image as a diffuse disk centered around the location of the source. The angular radius of the scattered image is:

$$\theta_d = \frac{\theta_0}{2} \approx \frac{e^2}{2\pi m_\mathrm{e}} \frac{\Delta n_\mathrm{e}}{\sqrt{a}} \frac{\sqrt{d}}{f^2}. \tag{1.35}$$

In the case of a Gaussian scattering screen, the scattered image will have an angular intensity distribution given by:

$$I(\theta) d\theta \propto \exp\left(-\frac{\theta^2}{\theta_d^2}\right) 2\pi\theta d\theta. \tag{1.36}$$

Rays that are deflected by an angle θ will have longer light travel times and will reach the observer later than undeflected rays that travel directly to the observer. Using the small angle approximation, a ray deflected by an angle θ will experience a geometric time delay of:

$$\Delta t(\theta) = \frac{\theta^2 d}{c}. \tag{1.37}$$

Substitution of Equation (1.37) into Equation (1.36) gives the intensity of the observed wave as a function of time:

$$I(t) \propto \exp\left(-\frac{c\Delta t}{d\theta_\mathrm{d}^2}\right) = \exp\left(-\frac{c\Delta t}{\tau_d}\right), \tag{1.38}$$

where:

$$\tau_d = \frac{\theta_d^2 d}{c} = \frac{e^4}{4\pi^2 m_\mathrm{e}^2} \frac{\Delta n_\mathrm{e}^2}{a} d^2 \nu^{-4}. \tag{1.39}$$

Therefore, a narrow pulse will be measured by a distant observer with an exponential tail. This behavior is often modeled as a convolution of the intrinsic pulse shape with a one-sided exponential function, with a pulse broadening timescale of τ_d (e.g., see [381]). From Equation (1.39), the observed pulse scattering is strongly dependent on the frequency of the wave and the distance to the pulsar:

$$\tau_d \propto \nu^{-4} d^2. \tag{1.40}$$

This basic model can explain the observed scattering behavior from a significant fraction of Galactic pulsars (see Figure 1.12). However, in some cases, the more complicated scattering models are required.

The effects of scattering are most apparent when observing at low radio frequencies (e.g., $\nu \lesssim 1$ GHz). In some cases, the scattering toward the direction of the source can

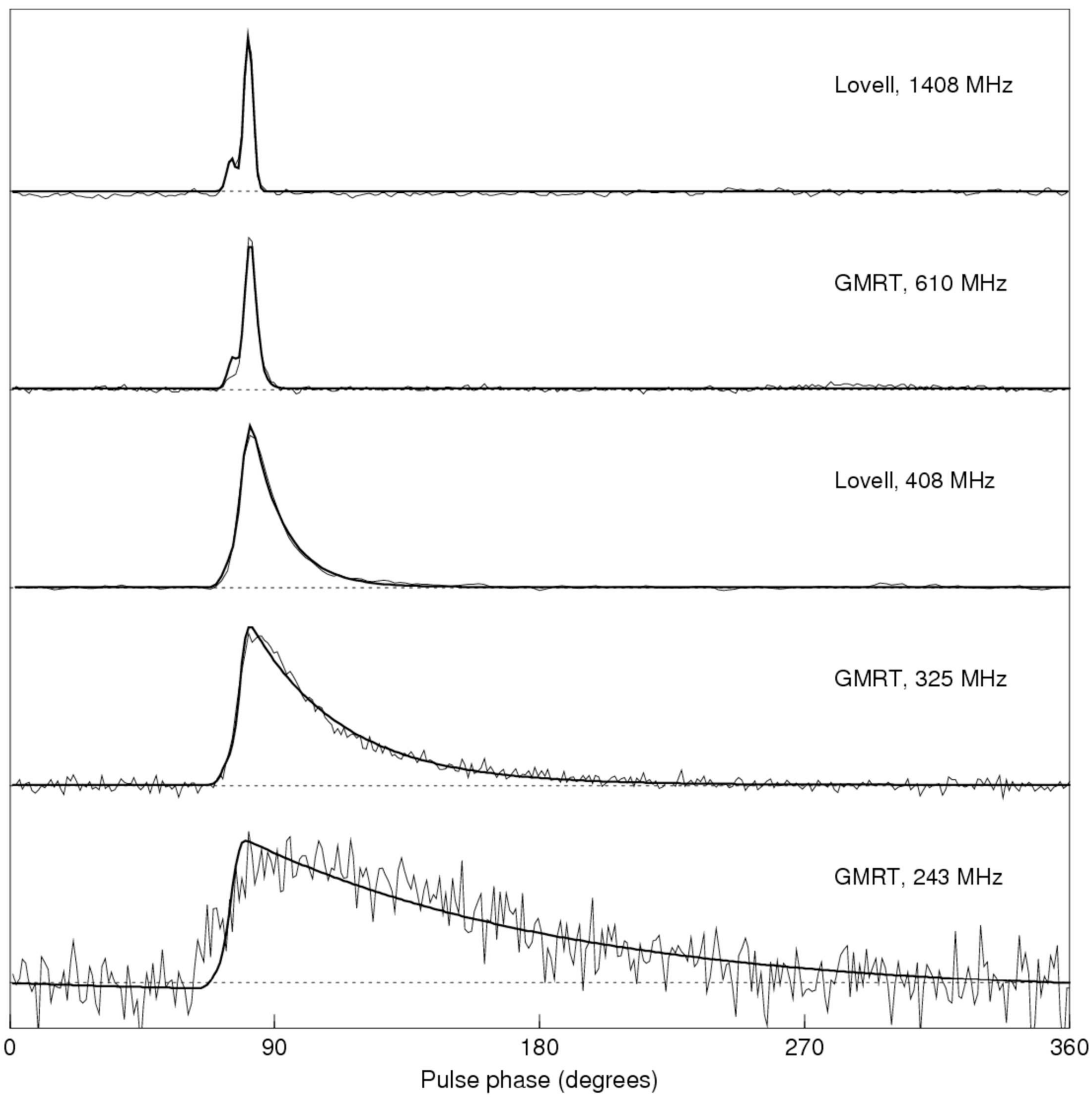

Figure 1.12: **Pulse profiles observed from the 687 ms pulsar PSR B1831–03 using the Lovell radio telescope and the Giant Metre Wave Radio Telescope (GMRT) at five different radio frequencies (1408, 610, 408, 325, and 243 MHz).** These observations show that the effects of scatter broadening increase toward lower frequencies. The solid lines correspond to exponential model fits to the data. Image credit: Adapted from Figure 1.11 in [328].

be so severe that a pulsed signal can be completely smeared out, preventing it from being detected. Thus, observing at higher radio frequencies can help to mitigate the effects of scattering. For Galactic pulsars, the pulse broadening timescale, τ_d, is strongly correlated with DM (see Figure 1.13). Pulsars with large DMs often have a larger measured pulse broadening timescale.

If the scattering medium has complex and anisotropic density fluctuations, the scattering behavior can be complicated (e.g., see [198, 317]). Additional scattering models, describing alternative scattering geometries and spatial distributions of the scattering material, have been explored in detail in previous studies (e.g., see [123, 125]).

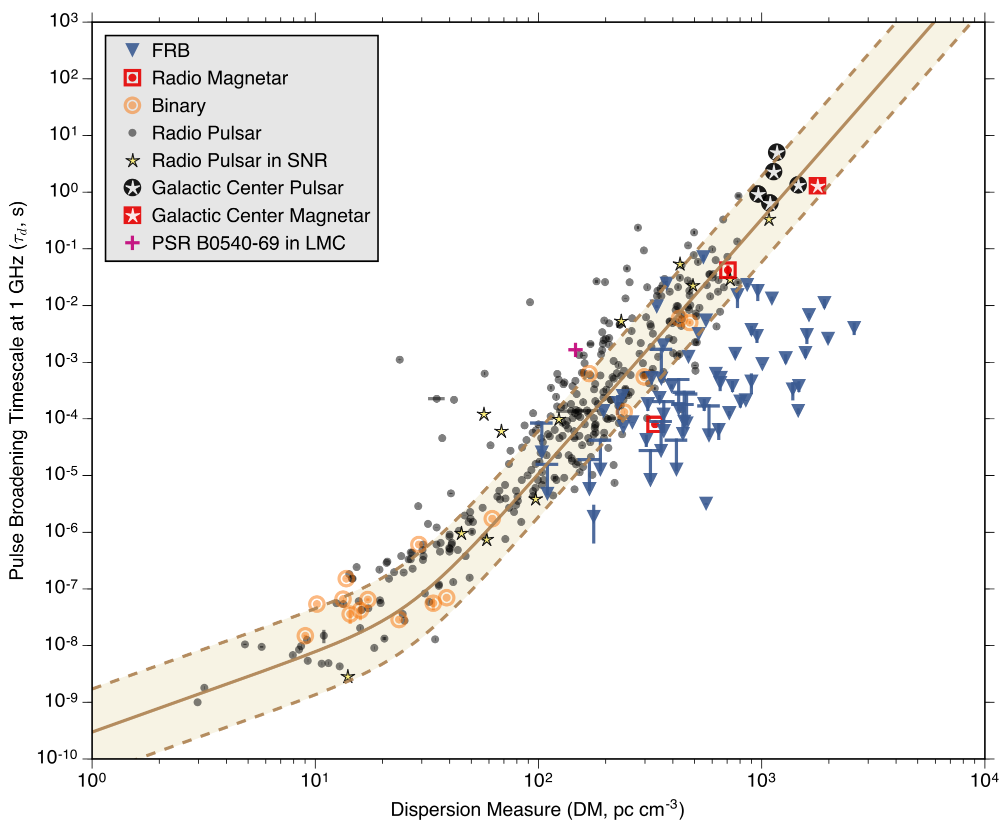

Figure 1.13: **Pulse broadening timescale at 1 GHz for radio pulsars and FRBs versus DM.** The solid brown curve corresponds to a mean scattering model of $\tau_d(\mathrm{DM}) = 2.98 \times 10^{-7}\,\mathrm{ms} \times \mathrm{DM}^{1.4}(1 + 3.55 \times 10^{-5}\,\mathrm{DM}^{3.1})$, obtained from a maximum likelihood fit [130]. The dashed brown curves show the model uncertainty, which is given by $\mathrm{dex}\,[\log \tau_d(\mathrm{DM}) \pm 0.76]$. On average, FRBs display a lower amount of temporal broadening compared to Galactic pulsars with similar DMs.

1.3.4 Scintillation

The relative motion between the source, the scattering medium, and the observer results in an interference pattern at the observer's plane, which causes the observer to detect a variable pattern of intensity from the source (e.g., see Figure 1.11). These intensity variations occur over a characteristic timescale, $\Delta t_{\rm ISS}$, which depends on the relative velocity in the system and the physical properties of the scattering screen. This behavior is referred to as interstellar scintillation (ISS), and it is analogous to the optical twinkling of stars observed through Earth's atmosphere.

In the context of the scattering model presented in Section 1.3.3, a signal detected from an astrophysical source over a time τ_d will experience a variety of phase shifts, given by $\delta\Phi \sim 2\pi\nu\tau_d$. An interference pattern is observed when the phase shifts do not differ by more than roughly 1 radian. The phases of the waves are frequency-dependent, since magnitude of the wave vector is a function of the frequency-dependent refractive index. As a result, only waves within a certain frequency bandwidth will contribute to the interference pattern. This characteristic bandwidth is referred to as the decorrelation bandwidth or scintillation bandwidth, $\Delta\nu_{\rm ISS}$. Interference of the waves occurs when the following condition is met:

$$2\pi\Delta\nu_{\rm ISS}\tau_d \sim 1. \tag{1.41}$$

From Equations (1.40) and (1.41), the scintillation bandwidth scales with frequency as $\Delta\nu_{\rm ISS} \propto \tau_d^{-1} \propto \nu^4$.

Since scintillation produces a pattern of intensity variations that changes as a function of both frequency and time, this behavior can be measured using a dynamic spectrum. The dynamic spectrum is a two-dimensional image containing measurements of the pulse intensity as a function of observation time and frequency. Enhanced regions of flux density, known as scintles, can be identified in the time–frequency plane. The scintle size in frequency, also referred to as the scintillation bandwidth ($\Delta\nu_{\rm ISS}$), is typically defined as the half-width at half-maximum (HWHM) of the autocorrelation function (ACF) of the spectrum. The scintle size in time, also known as the scintillation timescale ($\Delta t_{\rm ISS}$), is defined as the half-width at $1/e$ of the peak along the time axis [128].

There are two scintillation regimes: (1) weak scintillation and (2) strong scintillation. Strong scintillation is further divided into two categories: (1) diffractive scintillation and (2) refractive scintillation, giving a total of three types of scintillation. The size of the electron density inhomogeneities in the screen and the distance to the source influence which kind of scintillation behavior is observed by the observer.

If the screen has a Komologorov spectrum, then the pulse broadening timescale and diffractive scintillation bandwidth scale as:

$$\tau_d \propto \nu^{-\alpha}, \tag{1.42}$$

$$\Delta\nu_{\rm DISS} \propto \nu^{\alpha}, \tag{1.43}$$

where $\alpha = 2\beta/(\beta-2)$ and $\beta = 11/3$ [309]. For a Kolmogorov spectrum, $\alpha = 4.4$, as opposed to $\alpha = 4$ in the case of the thin screen model presented in Section 1.3.3. The relationship between τ_d and $\Delta\nu_{\rm DISS}$ is given by:

$$2\pi\tau_d\Delta\nu_{\rm DISS} = C_1, \tag{1.44}$$

where $C_1 = 1.16$ for a Kolmogorov spectrum [299]. In general, the value of C_1 will change depending on the geometry of the screen and the turbulence of the wavenumber spectrum.

The diffractive scintillation timescale scales as:

$$\Delta t_{\rm DISS} = \frac{s_0}{V_{\rm ISS}} \propto \nu^{1.2} d^{-0.6}, \tag{1.45}$$

where $s_0 = 1/(k\theta_{\rm d})$ is the field coherence scale and $V_{\rm ISS}$ is the transverse velocity of the astrophysical source relative to the plane of the observer. For a Kolmogorov spectrum, $s_0 \propto \nu^{1.2} d^{-0.6}$. Diffractive scintillation occurs when the field coherence scale is much smaller than the Fresnel scale, $l_{\rm F}$, i.e., $s_0 \ll l_{\rm F}$. The Fresnel scale is defined as:

$$l_{\rm F} = \sqrt{\frac{d}{k}} \approx 1.2 \times 10^9\,{\rm m} \left(\frac{d}{\rm kpc}\right)^{1/2} \left(\frac{\nu}{\rm GHz}\right)^{-1/2}. \tag{1.46}$$

From Equation (1.44), the diffractive scintillation bandwidth is given by:

$$\Delta\nu_{\rm DISS} = \frac{1.16}{2\pi\tau_d} \approx 185\,{\rm Hz} \left(\frac{\tau_d}{\rm ms}\right)^{-1}. \tag{1.47}$$

In the strong, diffractive scattering regime, the number of scintles sampled in the time–frequency plane are [121]:

$$N_t \approx 1 + \eta\frac{\Delta t_{\rm obs}}{\Delta t_{\rm DISS}}, \tag{1.48}$$

$$N_\nu \approx 1 + \eta\frac{\Delta\nu_{\rm obs}}{\Delta\nu_{\rm DISS}}. \tag{1.49}$$

Here, N_t is the number of scintles sampled in time, N_ν is the number of scintles sampled in frequency, $\Delta t_{\rm obs}$ is the observation duration, $\Delta\nu_{\rm obs}$ is the recording bandwidth, and $\eta \approx 0.1$–0.2 is an empirically determined constant.

While diffractive scintillation is caused by interference between different components of the angular spectrum, refractive scintillation is associated with larger angular sizes of the scattering disk. Refractive scintillation occurs when the refractive scale, $l_{\rm R}$, is much larger than the Fresnel scale, i.e. $l_{\rm R} \gg l_{\rm F}$. The refractive scale is defined as:

$$l_{\rm R} = d\theta_{\rm d} = \frac{d}{ks_0} = \frac{l_{\rm F}^2}{s_0}. \tag{1.50}$$

For a given transverse velocity between the source and the screen, the refractive scintillation timescale is much longer than the diffractive scintillation timescale. The refractive scintillation timescale, $\Delta t_{\rm RISS}$, is given by:

$$\Delta t_{\rm RISS} = \frac{l_{\rm R}}{V_{\rm ISS}} = \frac{l_{\rm F}^2}{s_0 V_{\rm ISS}} = \frac{l_{\rm F}^2}{s_0^2}\frac{s_0}{V_{\rm ISS}} = u^2\Delta t_{\rm DISS} = \frac{\nu}{\Delta\nu_{\rm DISS}}\Delta t_{\rm DISS} \propto \nu^{-2.2}d^{1.6}, \tag{1.51}$$

where the scintillation strength, u, is defined as [468]:

$$u = \frac{l_{\rm F}}{s_0} = \left(\frac{\nu}{\Delta\nu_{\rm DISS}}\right)^{1/2} \propto \nu^{-1.7}d^{1.1}. \tag{1.52}$$

Strong scintillation occurs when $u > 1$. Weak scintillation, on the other hand, occurs when $s_0 \gg l_{\rm F}$, or when the phase perturbations are small at the position of the observer and $u < 1$. The weak scintillation timescale and scintillation bandwidth are given by:

$$\Delta t_{\rm weak} = \frac{l_{\rm F}}{V_{\rm ISS}} \approx 3.35\,{\rm hr}\left(\frac{d}{\rm kpc}\right)^{1/2}\left(\frac{\nu}{\rm GHz}\right)^{-1/2}\left(\frac{V_{\rm ISS}}{100\,{\rm km\ s^{-1}}}\right)^{-1}, \tag{1.53}$$

$$\Delta\nu_{\rm weak} \propto \nu. \tag{1.54}$$

Therefore, weak scintillations are correlated over a large frequency range.

1.3.5 Pulse Width

The effective width of a detected radio pulse is affected by a combination of propagation effects and instrumental effects from the telescope. The width is often expressed as a quadratic sum of the scattering time, the intrinsic pulse width, the dispersion smearing, the dedispersion error, the receiver's response time, and the scattering time:

$$w_{\rm obs} = \sqrt{\tau_{\rm IGM}^2 + \tau_{\rm ISM}^2 + \tau_{\rm int}^2 + \tau_{\rm DM}^2 + \tau_{\Delta\rm DM}^2 + \tau_{\Delta\nu}^2}. \tag{1.55}$$

Here, $\tau_{\rm IGM}$ and $\tau_{\rm ISM}$ are scattering times due to propagation of the signal through the IGM and ISM, respectively, $\tau_{\rm int}$ is the intrinsic width of the pulse, $\tau_{\Delta{\rm DM}}$ is the dedispersion error, $\tau_{\Delta\nu} = \Delta\nu_{\rm MHz}^{-1}\ \mu$s is the receiver's response time, and $\Delta\nu_{\rm MHz}$ is the bandwidth of the receiver. The dispersion smearing, $\tau_{\rm DM}$, is given by:

$$\tau_{\rm DM} \approx 8.3 \times {\rm DM} \times \frac{\Delta\nu_{\rm MHz}}{\nu_{\rm GHz}^3}\ \mu{\rm s}. \tag{1.56}$$

1.4 Magnetars

Magnetars are a distinct class of young NSs, whose energetic emission is believed to be powered predominantly by the decay of their extremely strong magnetic fields ($B_{\rm surf} \approx 10^{14}$–$10^{16}$ G). They possess the strongest magnetic fields in the Universe and have longer rotation periods ($P_{\rm spin} \approx 1$–12 s) than most of the pulsar population. The term "magnetar" is derived from a portmanteau of "magnetar stars," which was first coined by Duncan and Thompson [165]. These objects often exhibit dramatic variability across the electromagnetic spectrum, particularly at X-ray and soft γ-ray energies. They are capable of emitting transient X-ray and soft γ-ray bursts, which can last just a few milliseconds. In some cases, magnetars can display a wide range of activity during their outbursts, which can last for months–years, and sometimes produce highly energetic giant flares. There are presently ~30 known magnetar sources, but it is believed that magnetars may comprise at least 10% of the young NS population. Of the known magnetars and magnetar candidates, 6 bona fide magnetars (XTE J1810–197, PSR J1622-4950, 1E 1547.0–5408, PSR J1745–2900, Swift J1818.0–1607, and SGR 1935+2154) [59, 78, 80, 169, 174, 312, 523] and one transitional magnetar candidate (PSR J1119–6127) [18, 356] have been found to produce radio pulsations during their active states. While magnetars and radio pulsars do seem to be powered by different mechanisms, these two groups of pulsars share some similarities. An overview of the phenomenology of magnetar emission can be found in several review articles (e.g., see [175, 263, 264]).

At the initial phase of magnetar outbursts, the X-ray luminosity reaches $L_{\rm x} \sim 10^{35}$–10^{36} erg s^{-1} and short high-energy bursts may be sporadically emitted. As the outburst ends, the magnetar will decay back to its quiescence level of $L_{\rm x} \lesssim 10^{33}$ erg s^{-1}. Recent observations suggest that all highly magnetized neutron stars may behave like dormant magnetars and have the ability to display magnetar-like emission behavior.

The GC magnetar, PSR J1745–2900, is arguably the most scientifically-significant magnetar discovered to date. PSR J1745–2900 lies within ~3 arcsec of Sgr A*, the supermassive black hole (SMBH) at the center of the Milky Way galaxy, and

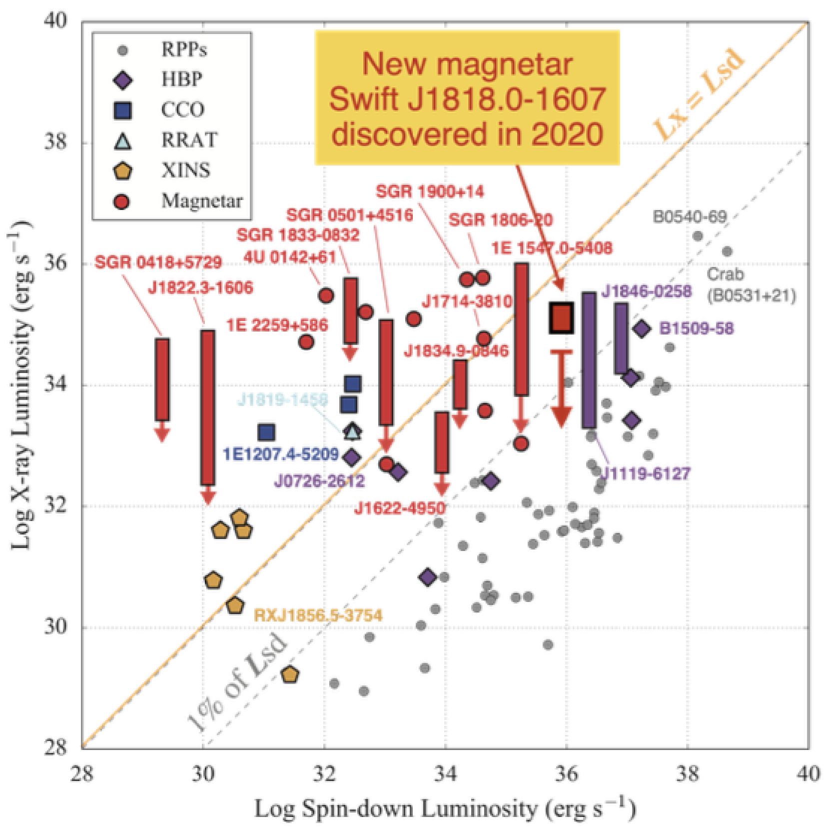

Figure 1.14: **Observed X-ray luminosity (L_x) compared with the spin-down luminosity (L_{sd}) of pulsars based on their timing behavior.** Rotation-powered pulsars (RPPs), high magnetic field pulsars (HBPs), central compact objects (CCOs), rotating radio transients (RRATs), X-ray isolated neutron stars (XINs), and magnetars are labeled using gray circles, purple diamonds, blue squares, teal triangles, orange pentagons, and red circles, respectively. RPPs have values of L_x that are less than ~1% of their spin-down luminosity. Most persistent magnetars, XINs, and COOs appear above the $L_x = L_{sd}$ line. The filled boxes indicate the decaying X-ray luminosity of the source, and the red arrows indicate the quiescent X-ray luminosity level of the source, below which the source was not detectable during X-ray monitoring. Image credit: Adapted from Figure 12 in [173].

it is likely in a bound orbit around Sgr A*. This may allow the magnetar to be used as a rare probe of the BH's surrounding environment. PSR J1745–2900 has also been detected at higher radio frequencies (up to 291 GHz) than any other radio pulsar [533], which may provide additional insights into the mechanisms powering the radio emission observed from both magnetars and ordinary pulsars. In general, magnetars also tend to have larger DMs and RMs than most Galactic pulsars (see Figure 1.15). In fact, PSR J1745–2900 has the highest RM of any known Galactic object (RM $\approx -6.7 \times 10^4$ rad m^{-2}) [154, 169], other than Sgr A*. The high RM

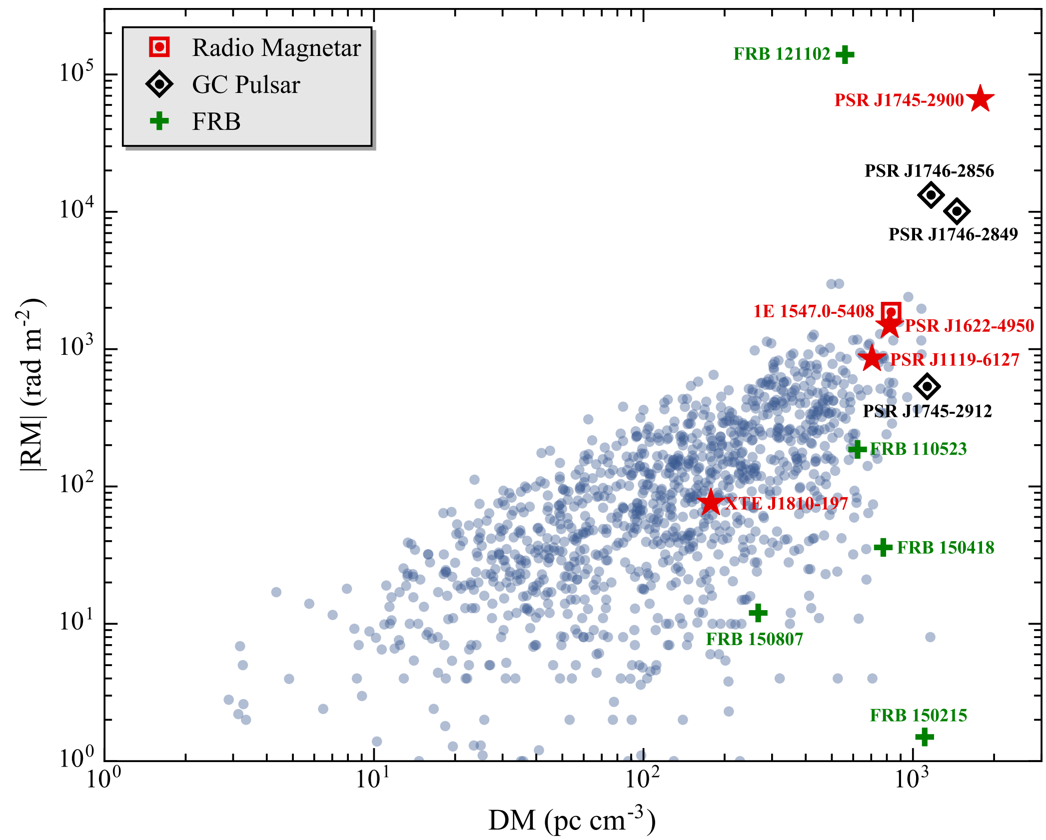

Figure 1.15: **Magnitude of RM versus DM of Galactic pulsars, magnetars, and FRBs known as of January 2019.** Radio pulsars are indicated using blue circles. Radio magnetars (red squares and red stars), Galactic Center (GC) pulsars (black diamonds), and FRBs (green pluses) are labeled explicitly. Image credit: Adapted from Figure 2 in [424].

measured from PSR J1745–2900 is attributed to the magneto-ionic environment of the GC.

1.4.1 Soft Gamma-ray Repeaters (SGRs) and Anomalous X-ray Pulsars (AXPs)

When magnetars were first discovered, they were believed to be divided into two separate source classes: soft gamma repeaters (SGRs) and Anomalous X-ray pulsars (AXPs). SGRs were discovered in 1979 when short, hard X-ray/soft γ-ray bursts were detected by the interplanetary space probes, Venera 11 and 12 [379]. These bursts were initially classified as a subset of the gamma-ray burst (GRB) population [377]. The repeating nature of SGRs was subsequently demonstrated by Laros et al. [300] when a cluster of bursts were detected from SGR 1806–20 in 1983. These repetitive bursts also displayed softer spectra than GRBs, which led to their designation as SGRs — a new class of Galactic high-energy sources.

During the decay of a giant flare from SGR 0526–66, extremely energetic pulsations were detected with a period of 8.00 ± 0.05 s, which was associated with the neutron star's rotational period [518]. Multiple gamma-ray bursts were subsequently discovered from SGR 1900+14 shortly afterwards in 1979 [378], and a giant flare was later detected on 1998 August 27 [244]. These giant flares shared similar phenomenology, including a sharp rise time, followed by a decaying tail (lasting ~5 min during the 1998 giant flare from SGR 1900+14), and prominent pulsations that were visible in the tail of the flare. The extreme energetics of the flares indicated that the release of magnetic energy was responsible for the production of these events. This has been explained in the context of the magnetar model [525] (see Section 1.4.3). It was also determined that such events are rare, and they may occur at any time during a magnetar's activity cycle. An additional giant flare was detected from SGR 1806–20 on 2004 December 27 [245], and short, soft gamma-ray bursts have been detected from several additional sources (e.g., see [249, 463, 567]).

Around the same time, X-ray pulsations were detected from the X-ray source at the center of the Galactic SNR CTB 109 [178]. However, it was determined that the X-ray emission was too bright to be powered by rotational energy [286]. Similar sources were later found and initially associated with accretion-powered LMXBs (e.g., see [383, 488, 556]). However, these pulsars (1E 2259+586, 1E 1048.1–5937, and 4U 0412+61) displayed no evidence of orbital motion and were located in young environments, i.e. in SNRs and in the Galactic plane. They also had softer X-ray spectra than the majority of X-ray binaries and did not have optical counterparts. These characteristics are inconsistent with the properties of LMXBs, and this led to their temporary classification as a new subclass of pulsars, known as "anomalous X-ray pulsars" or AXPs. Thompson and Duncan [525] proposed that AXPs, like SGRs, may be powered by the decay of their high magnetic fields ($B_{\rm surf} \approx 10^{14}$–$10^{16}$ G).

Additional AXPs were subsequently discovered (e.g., see [506, 541]), and short X-ray/soft gamma-ray bursts were detected from several AXP sources (e.g., see [193, 266, 569]). X-ray pulsations, similar to those seen from AXPs, were also detected from SGRs during a state of high persistent X-ray flux [284, 285]. These observations indicated that SGRs and AXPs both share similar observational properties and should be considered as a single source class.

1.4.2 Radiative and Timing Behavior of Magnetars

Magnetars display a wide variety of emission behavior over a range of timescales. In particular, they can produce giant flares, short magnetar bursts, and display extended periods of outburst.

The most extreme type of emission observed from magnetars is a giant flare. Only three giant flares have been detected in the past several decades [244, 245, 379]. These events occurred on 1979 March 5 from SGR 0526–66 [379], 1998 August 27 from SGR 1900+14 [244], and 2004 December 27 from SGR 1806–20 [60, 245, 384]. The peak X-ray luminosities of these giant flares ranged between 10^{44} and 10^{47} erg s^{-1}. The total energy release of each flare was $> 10^{44}$ erg s^{-1} in the X-ray and soft gamma-ray bands. The third flare from SGR 1806–20 is the most luminous transient yet observed in our Galaxy. It was roughly 100 times more energetic than the other two giants flares, and it briefly outshone all of the stars in our Galaxy put together by a factor of ∼1,000.

Short magnetar bursts are another type of phenomenon observed from magnetars. These bursts have durations between roughly a few milliseconds and a few seconds. Their burst profiles are often single-peaked, but not always, with a rise time that is faster than the decay timescale. The luminosities of magnetar bursts span a broad spectrum, which typically ranges between 10^{36} and 10^{44} erg s^{-1}. Their luminosities can exceed the Eddington limit, but short magnetar bursts have also been detected near the sensitivity limit of currently operating X-ray instruments. The energy distributions of the bursts are well-described by a power-law model ($dN/dE \propto E^{\alpha}$), with indices (α) between –1.6 and –1.8 [194, 214, 215].

Magnetar outbursts are usually heralded by short X-ray bursts or a giant flare. At the beginning of the outburst, the magnetar's persistent X-ray flux will increase and then decline rapidly on a timescale of days. This is followed by a slower decay in the magnetar's X-ray flux on timescales of months to years. The magnetar's persistent X-ray spectrum usually hardens near the beginning of the outburst and then softens as the X-ray flux decays (e.g., see [477]). An increase in the number of short magnetar bursts is often observed during the outburst. Transient magnetars in quiescence (i.e., not in outburst) have 2–10 keV X-ray luminosities between $\sim 10^{30}$–10^{35} erg s^{-1}. Their spectra are well-modeled by a soft blackbody component, with blackbody temperatures typically ranging between $kT \approx 0.4$–0.5 keV [409], and a hard power-law. These blackbody temperatures are significantly higher than those observed from high magnetic field pulsars [409]. This suggests that there is an additional source of heating in quiescent magnetars, which may be related to its radiation mechanism.

Magnetars also often display extremely variable timing behavior, including rotational glitches (nearly instantaneous increases in the pulsar's rotational frequency), large changes in their rotational torques, and dramatic pulse profile variability. Phase-coherent pulsar timing techniques have revealed large variations in the rotational properties of magnetars (e.g., see [478, 481]). Changes in the rotational torque (proportional to $\dot{P}_{\rm spin}$) and the effects of timing noise and are usually much larger in magnetars than in rotation-powered pulsars (e.g., see [192, 568]). Torque variations in magnetars can occur on timescales of ~100–1,000 days, with variations in $\dot{P}_{\rm spin}$ ranging from a few percent up to an order of magnitude [158, 481].

Glitches are nearly instantaneous increases in the pulsar's rotational frequency. They are often observed during magnetar outbursts [158], but they can also occur when these objects are in a quiescent state (e.g., see [159]). In the case of rotation-powered pulsars, glitches have been attributed to the transfer of angular momentum from the neutron star's superfluid inner crust to the slower-spinning outer crust [12, 321, 442]. However, it is not yet clear whether or not glitches in magnetars and rotation-powered pulsars are caused by the same underlying physical processes. In at least one case, an anti-glitch (a decrease in the pulsar's rotational frequency) has been observed from the magnetar 1E 2259+586, which was inconsistent with previously proposed models invoked to explain neutron star glitches.

Another interesting timing phenomenon observed from magnetars is the presence of quasi-periodic oscillations (QPOs) in the pulsating tails of magnetar giant flares. QPOs have been detected at a frequency of ~ 92.5 Hz in the tail of the giant flare detected on 2004 December 27 from SGR 1806–20 [248] and also at a frequency of 84.5 Hz during specific rotational phase intervals following the onset of the giant flare detected on 1998 August 27 from SGR 1900+14 [505]. Additional periodic signals associated with QPOs were later reported in the 2004 giant flare from SGR 1806–20 [547]. These QPOs have been associated with vibrations in the neutron star's crust, and they may also provide a new means for testing the neutron star equation of state and studying the crustal breaking strain and magnetic field configuration.

1.4.3 Magnetar Model

The magnetar model [165, 524, 525] was developed to explain the observed behavior of SGRs and AXPs, which were thought to be two separate classes of sources at the time. This model posits that the large magnetic field ($B_{\mathrm{surf}} \approx 10^{15}$ G) of a newborn, rapidly rotating magnetar is generated by a fast, transient dynamo. The high magnetic field serves as an enormous magnetic energy reservoir, which explains why slowly rotating magnetars can produce the wide range of energetic radiation behavior described in Section 1.4.2. The decay of the magnetic field heats the interior of the neutron star and creates internal stresses on the stellar crust, which can lead to sudden fractures of the crust and sufficient energy release to power magnetar bursts and other types of extreme emission if the crust is resistant to these strains [524]. On the other hand, if the crust is elastic, shear strains can shift parts of the crust and build up twists in the magnetosphere [525].

X-ray pulsations observed from magnetars are thought to be produced by hot spots formed on the stellar surface when the magnetospheric twists are confined to a bundle of field lines. Heating of the stellar surface at the footprints of the field lines is caused by relativistic particles in the magnetosphere bombarding the stellar surface. Magnetospheric twists, caused either by “starquakes” [524] or built up slowly over time, cam accelerate particles into the magnetosphere. The magnetar’s thermal spectrum is then modified with a power-law tail component due to the transfer of energy from these particles to thermal photons in a process known as resonant Compton scattering [28, 526]. Crustal quakes [524] or magnetic reconnection events may explain the short bursts and long-term outbursts observed from magnetars since energy injected into the magnetosphere can cause rearrangement of the magnetic field and dissipation of electric currents.

It was initially thought that magnetars could be distinguished from normal pulsars if their magnetic fields exceed B_{QED}, the magnetic field strength at which the first electron Landau level becomes equal to the electron rest mass:

$$B_{\mathrm{QED}} = \frac{m_{\mathrm{e}}^2 c^3}{e\hbar} \approx 4.4 \times 10^{13}\,\mathrm{G}. \tag{1.57}$$

However, the discovery of magnetars with low surface dipolar magnetic fields (e.g., SGR 0418+572; $B_{\mathrm{surf}} \approx 6 \times 10^{12}$ G [464, 466]) that are comparable to average high magnetic field pulsars, such as Swift J1822.3–1606 which has a magnetic field of $B_{\mathrm{surf}} \approx 1.35 \times 10^{13}$ G, has challenged this definition. In addition, magnetar-like behavior has now been observed from high magnetic field rotation-powered pulsars, such as PSR J1846–0258 [17, 195] and PSR J1119–6127 [18, 356] (e.g., see Chapter 3).

1.5 Fast Radio Bursts

FRBs are bright, impulsive bursts of coherent radio emission, with durations ranging between nanoseconds and milliseconds and fluences (time-integrated flux densities) of 0.01–1,000 Jy ms [492] (e.g., see [120, 436] for recent reviews). Their origins and physical nature are both largely a mystery. The radio emission from FRBs arrives later at lower frequencies due to dispersive delays from the intervening ionized material. The dispersive delay is proportional to the DM, which is the integrated column density of free electrons between the source and the observer. The DM is often used as a rough proxy for distance. Radio emission from FRBs follows the cold plasma dispersion law and exhibits a quadratic shift in the arrival time of as a function of frequency. FRBs are characterized by their high excess DMs relative to what is expected from the Milky Way along the line of sight at their position on the sky (see Figures 1.16 and 1.17). The excess in the DM may come from the Intergalactic Medium (IGM), which suggests that these bursts originate from sources located at cosmological distances with high inferred redshifts. The pulse broadening times of FRBs, in most cases, are much larger than those measured from pulsars at similar Galactic latitudes (see Figure 1.18). This is consistent with FRB scattering being due to extragalactic material. A catalog of known FRBs can be found at FRBCAT[h] [435], which contains a list of all bursts up to July 2020. The Transient Name Server (TNS) now provides an up-to-date catalog of FRBs. A list of repeating FRBs discovered by CHIME/FRB are provided in the CHIME repeating FRB catalog[i]. FRBs are extremely promising tools for studying the nature of unseen matter in the Universe and for cosmology because their radio signals interact with the intervening medium between the source and the observer.

The first reported FRB, called the "Lorimer Burst" [329] (see Figure 1.19), was discovered in 2007 in archival data from the Parkes radio telescope recorded at 1.4 GHz. Astronomers remained skeptical about whether this signal originated from an extragalactic source until six additional bursts were found [71, 271, 529]. FRBs had not been detected using another radio telescope besides Parkes until Spitler et al. [497] discovered FRB 121102 with the Arecibo radio telescope and Masui et al. [375] reported the discovery of FRB 110523 using the Green Bank

[h] See http://frbcat.org.

[i] See https://www.chime-frb.ca/repeaters.

Telescope (GBT). FRB 121102 would eventually be found to be the first example of a repeating FRB [499]. Later in 2016, five additional FRBs were reported in the High Time Resolution Universe (HTRU) high-latitude survey with the Parkes radio telescope [92]. FRBs appear to be isotropically distributed on the sky (see Figure 1.20), with initial all-sky rate estimates being of order 1.7×10^3 FRBs sky^{-1} day^{-1} above a fluence threshold of 2 Jy ms.

The astrophysical origin of FRBs was disputed when "perytons" were discovered in 2011 at the Parkes radio telescope [72]. These terrestrial signals were detected in all of the beams of the Parkes radio telescope, but they showed some deviations from the cold plasma dispersion law. These signals were later associated with the premature opening of microwave ovens operating at Parkes [434]. It was found that the magnetron shut-down phase produces dispersed, millisecond-duration radio bursts, which can escape if the microwave door is opened prematurely. It is now well-established that FRBs have cosmological origins, thanks to the localization of repeating FRBs to their host galaxies (e.g., see [95, 367, 516]).

FRBs were mostly believed to be one-off events since radio follow-up campaigns failed to detect repeat bursts at the sky locations of previous FRB detections. The first repeating FRB, FRB 121102, was discovered in 2016 [499], four years after it was initially detected. Initial follow-up programs using the Effelsberg and Lovell radio telescopes failed to detect repeat bursts from the source. However, multiple repeat bursts were later detected using the GBT, and the Arecibo and Effelsberg radio telescopes [223, 479]. Using the Very Large Array (VLA) in fast-imaging mode, FRB 121102 was the first FRB source to be localized to milliarcsecond precision [95, 367]. Multiwavelength follow-up of the field associated the source with a low-metallicity dwarf galaxy at a redshift of $z = 0.19$ [516]. A large and variable RM was detected from FRB 121102, which demonstrates that FRB 121102 resides in an extreme magneto-ionic environment. The short durations of the bursts suggest that the source may be a compact object, such as a neutron star. However, the progenitor has not been conclusively identified. Many more repeat bursts have since been detected, for example, using the wide-band receiver outfitted on the GBT as part of the Breakthrough Listen project [191] and the Deep Space Network (DSN) radio telescopes [361, 429].

Recently, many more repeating FRB sources have been discovered, mostly using the CHIME/FRB radio telescope (e.g., see [187, 520, 521]). These repeating FRBs typically produce highly intermittent radio bursts (e.g., see Figure 1.21). Recently, an energetic, multi-component radio burst was detected from the Galactic magnetar SGR 1935+2154, which has bridged the luminosity gap between pulsars, including those that emit giant pulses, and FRBs (see Figure 1.22). A phase space diagram of radio transients is shown in Figure 1.23.

The DM of an extragalactic FRB can be written as the sum of contributions from the Galactic ISM, the IGM, a host galaxy, and intervening material local to the source:

$$\mathrm{DM_{FRB}} = \mathrm{DM_{MW}} + \mathrm{DM_{MW,\,halo}} + \mathrm{DM_{cosmic}}(z) + \mathrm{DM_{host}}, \tag{1.58}$$

where $\mathrm{DM_{MW}}$ and $\mathrm{DM_{MW,\,halo}}$ are the contributions from the Milky Way's ISM and the halo of the Milky Way, respectively, $\mathrm{DM_{cosmic}}(z)$ is the contribution from the intergalactic medium (IGM), and $\mathrm{DM_{host}}$ is the contribution from the ISM and halo of the host galaxy. $\mathrm{DM_{host}}$ can be further divided into two separate components: (1) the host galaxy contribution and (2) the contribution from the host galaxy's halo. There may also be an additional contribution to the DM from interactions between intervening galaxies or halos in the IGM.

The Galactic DM along a given line of sight is often estimated using the NE2001 [124] and YMW16 [577] electron density models. The DM contribution by the host galaxy will depend upon the type and the orientation of the galaxy. The excess DM is what remains after removing these components from the observed FRB DM. The excess DM typically has values between 100 and 2,500 pc cm^{-3}. Thus, many speculate that the excess DM is associated with the IGM between the source and the observer.

1.5.1 Progenitor Models

Many progenitor theories have been proposed to explain the origins of FRBs (see [444][j] for a catalog). Here, I briefly focus on a few possible models:

Hyperflares from magnetars: Magnetars are dense, magnetized neutron stars whose emission is primarily powered by magnetic energy release. These objects are capable of producing extremely energetic flares, which have been linked to "starquakes," where magnetic disconnection and reconnection occurs on the stellar surface. Interaction of the magnetized pulse with the surrounding plasma in the nebula may produce a relativistic forward shock. This model was first proposed to explain the gamma-ray emission observed from SGRs [53, 536]. It was later adapted by Popov and Postnov [446] to explain the millisecond-duration bursts observed from FRBs.

[j] See http://frbtheorycat.org.

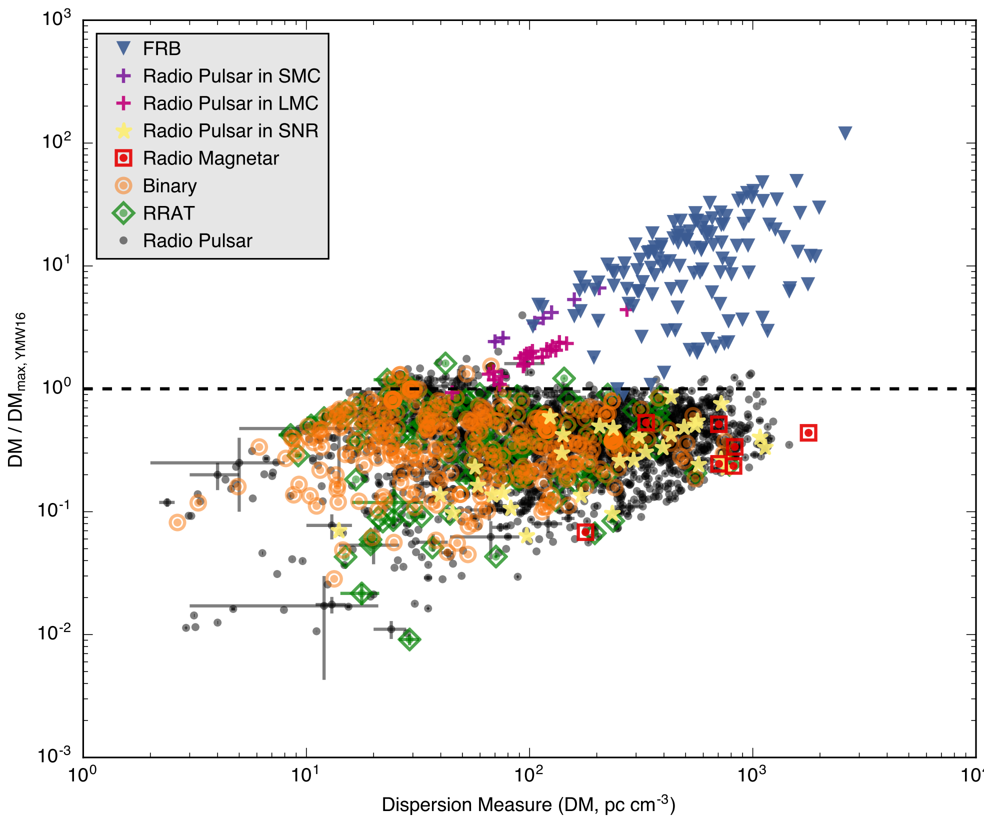

Figure 1.16: **DMs of Galactic radio pulsars, Galactic RRATs (green diamonds), radio pulsars in the SMC (purple pluses) and LMC (magneta pluses), radio pulsars in supernova remnants (SNRs, yellow stars), and FRBs (blue triangles) relative to the maximum Galactic DM along the line of sight predicted by the YMW16 electron density model [577].** Magnetars (red squares) and binary pulsars (orange circles) are also labeled on this diagram. Objects with $\mathrm{DM}/\mathrm{DM}_{\mathrm{max,YMW16}} > 1$ are believed to be located at extragalactic distances since their observed DMs include additional contributions from the intergalactic medium (IGM) and their host galaxies. All of the known objects in the ATNF pulsar catalog[b] [365], WVU RRATalog[d], WVU MSP catalog[e], CHIME Galactic source catalog[f], and FAST pulsar catalog[g] are included in this figure. The DMs of the FRBs shown here were obtained from FRBCAT[h] [435] and the CHIME repeating FRB catalog[i].

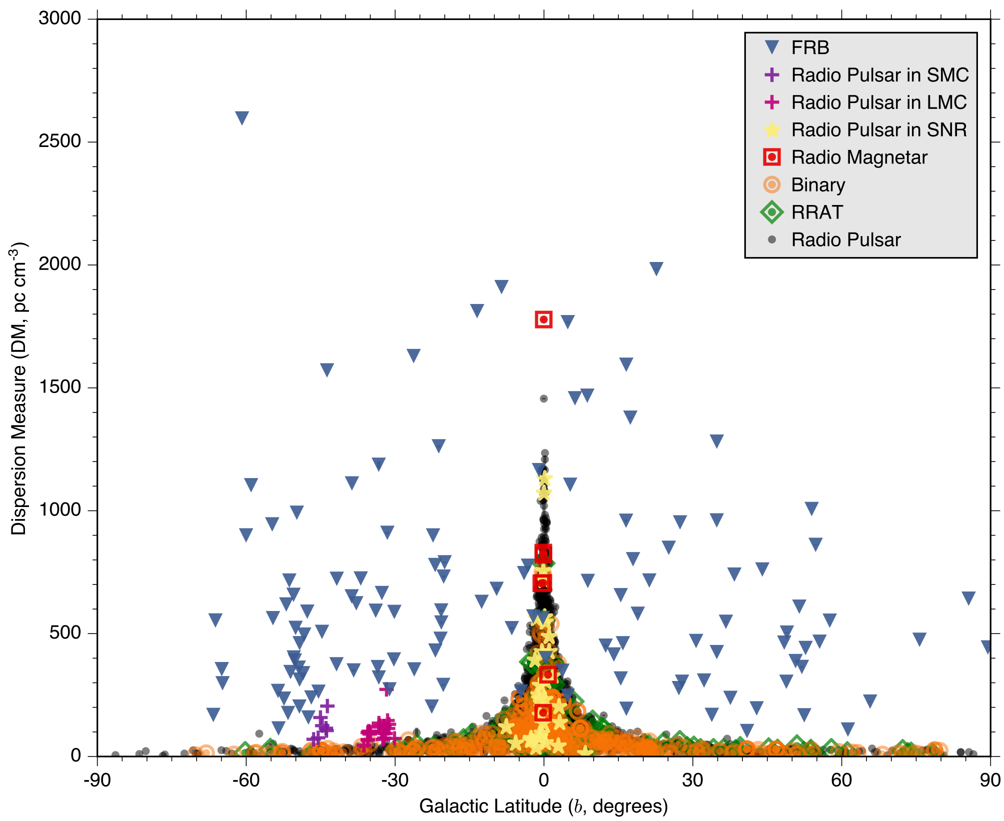

Figure 1.17: **DMs of Galactic radio pulsars, Galactic RRATs (green diamonds), radio pulsars in the SMC (purple pluses) and LMC (magenta pluses), radio pulsars in supernova remnants (SNRs, yellow stars), and FRBs (blue triangles) as a function of Galactic latitude (b).** Magnetars (red squares) and binary pulsars (orange circles) are also labeled on this diagram. FRBs are distinguishable from pulsars by their larger DMs at most Galactic latitudes. The DM envelope of the Milky Way is clearly visible. All of the known objects in the ATNF pulsar catalog[b] [365], WVU RRATalog[d], WVU MSP catalog[e], CHIME Galactic source catalog[f], and FAST pulsar catalog[g] are included in this figure. The DMs of the FRBs shown here were obtained from FRBCAT[h] [435] and the CHIME repeating FRB catalog[i].

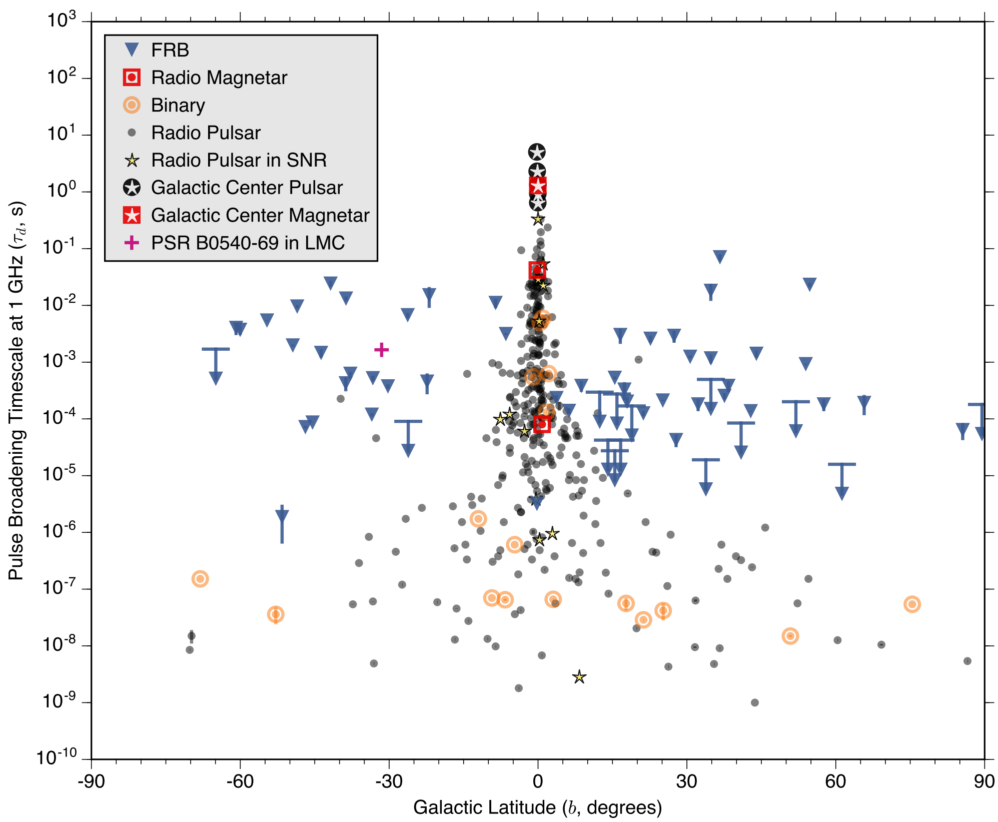

Figure 1.18: **Pulse broadening timescale (τ_d) at 1 GHz of radio pulsars and FRBs versus Galactic latitude (b).** Magnetars (red squares) and binary pulsars (orange circles) are explicitly labeled on this diagram, along with pulsars in supernova remnants (SNRs, yellow stars), Galactic Center (GC) pulsars (black circles with a white star), the GC magnetar (PSR J1745–2900, red square with a white star), PSR B0540–69 in the LMC (magenta plus), and FRBs (blue triangles).

Lyubarsky [341] proposed that coherent synchrotron maser emission from the forward or reverse shock is capable of producing millisecond-duration FRB-like radio bursts. This model is consistent with the high measured brightness temperatures ($T_{\rm b} > 10^{32}$ K) and the inferred all-sky rate of FRBs [296]. If FRBs are associated with magnetar giant flares, then they could leave behind an afterglow, similar to what was observed from the magnetar SGR 1806–20 following the giant flare detected on 2004 December 27. An afterflow was observed between the radio frequencies of 0.84–8.5 GHz, which was present for 20 days following the onset of the outburst [190]. However, no radio emission was detected in archival data of the Parkes radio telescope, which was observing ∼35° away from SGR 1806–20 at the time that the giant flare occurred [515]. An upper limit of 110 MJy was placed at 1.4 GHz at the time of the giant flare.

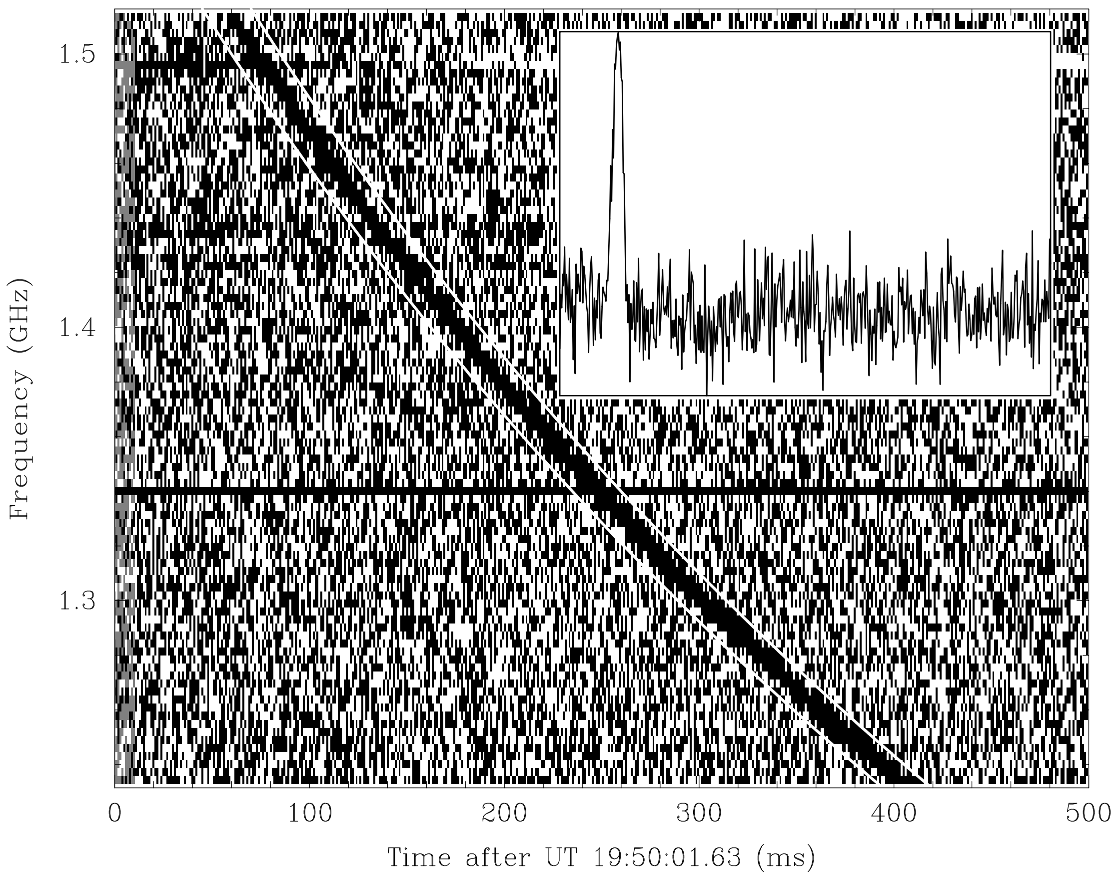

Figure 1.19: **Waterfall plot of FRB 010724 (also referred to as the Lorimer Burst).** The burst sweep across the observing band is due to the dispersive delay from the intervening ionized medium between the source and the observer. The dispersion delay is outlined using white lines. The strong, narrow-band horizontal lines (e.g., at ~1.34 GHz) are a result of RFI. The inset panel shows the burst profile after correcting for dispersion and summing the intensity at each frequency. Image credit: Adapted from Figure 2 in [329].

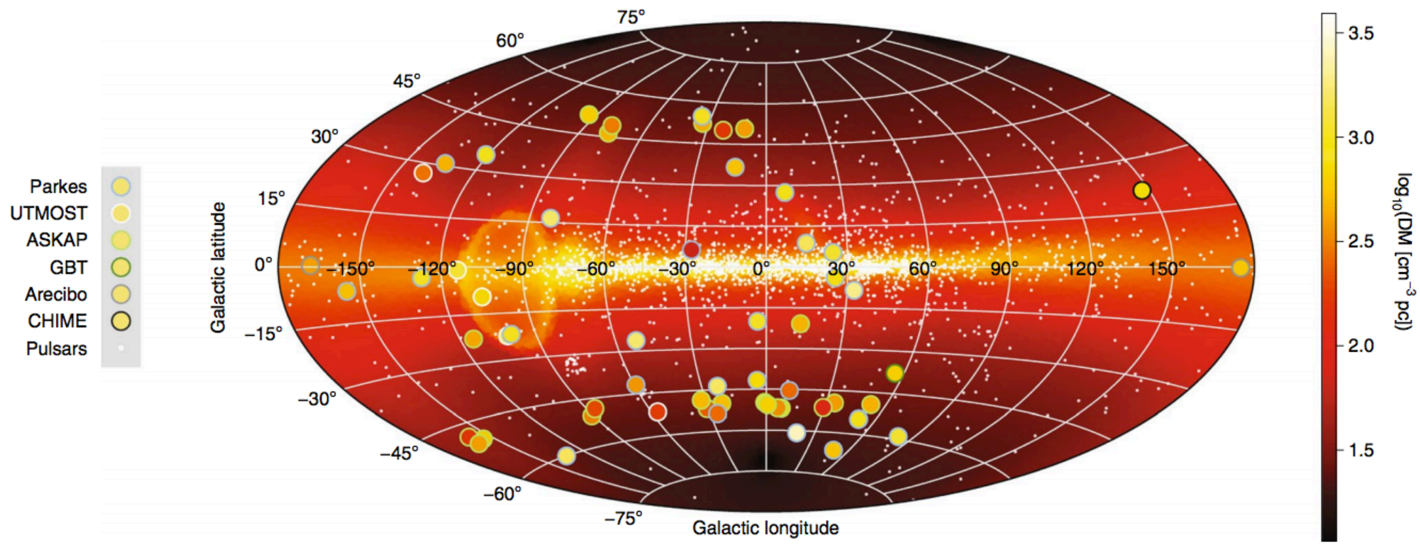

Figure 1.20: **Sky positions of FRBs discovered by the GBT and the Parkes, UTMOST, ASKAP, Arecibo, and CHIME radio telescopes.** The distribution of Galactic pulsars is also overlaid on this figure. A map of the Galactic electron density from the YMW16 model [577] is shown in the background. Image credit: Adapted from Figure 2 in [74].

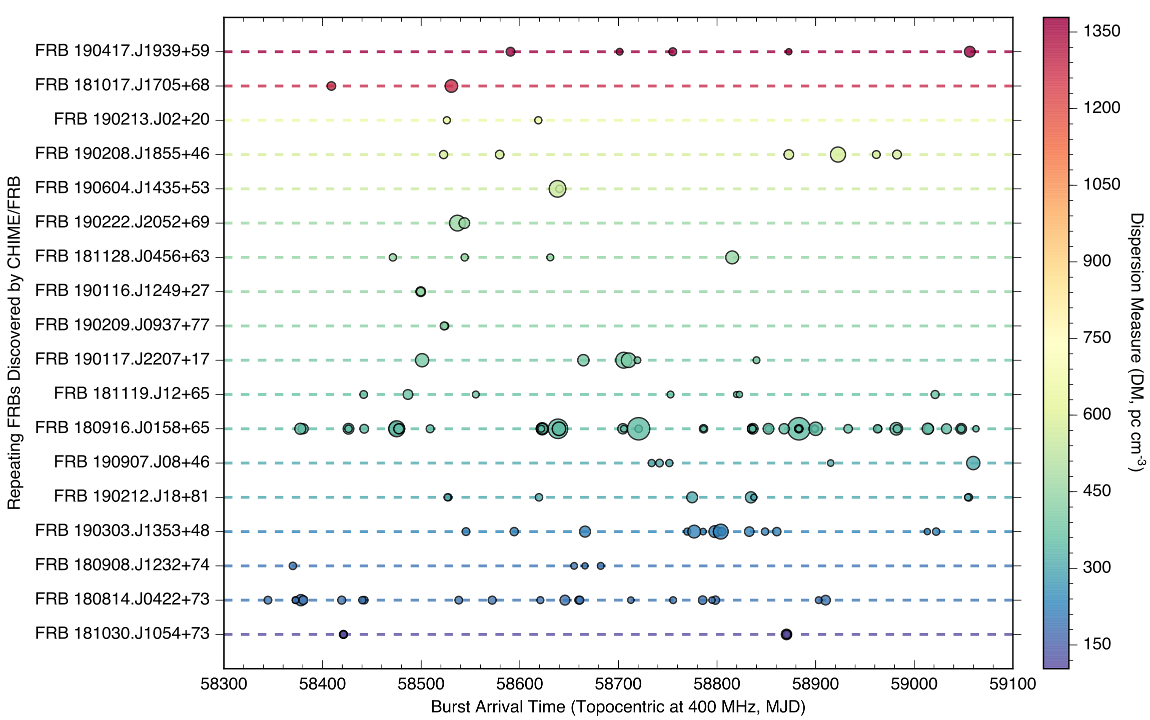

Figure 1.21: **Activity level of repeating FRBs in the 400–800 MHz band, as observed using the CHIME/FRB radio telescope.** Each circle corresponds to the arrival time of an individual radio burst. The size of the circles show the signal-to-noise ratio (S/N) of the bursts, and the color bar indicates the DM of the bursts.

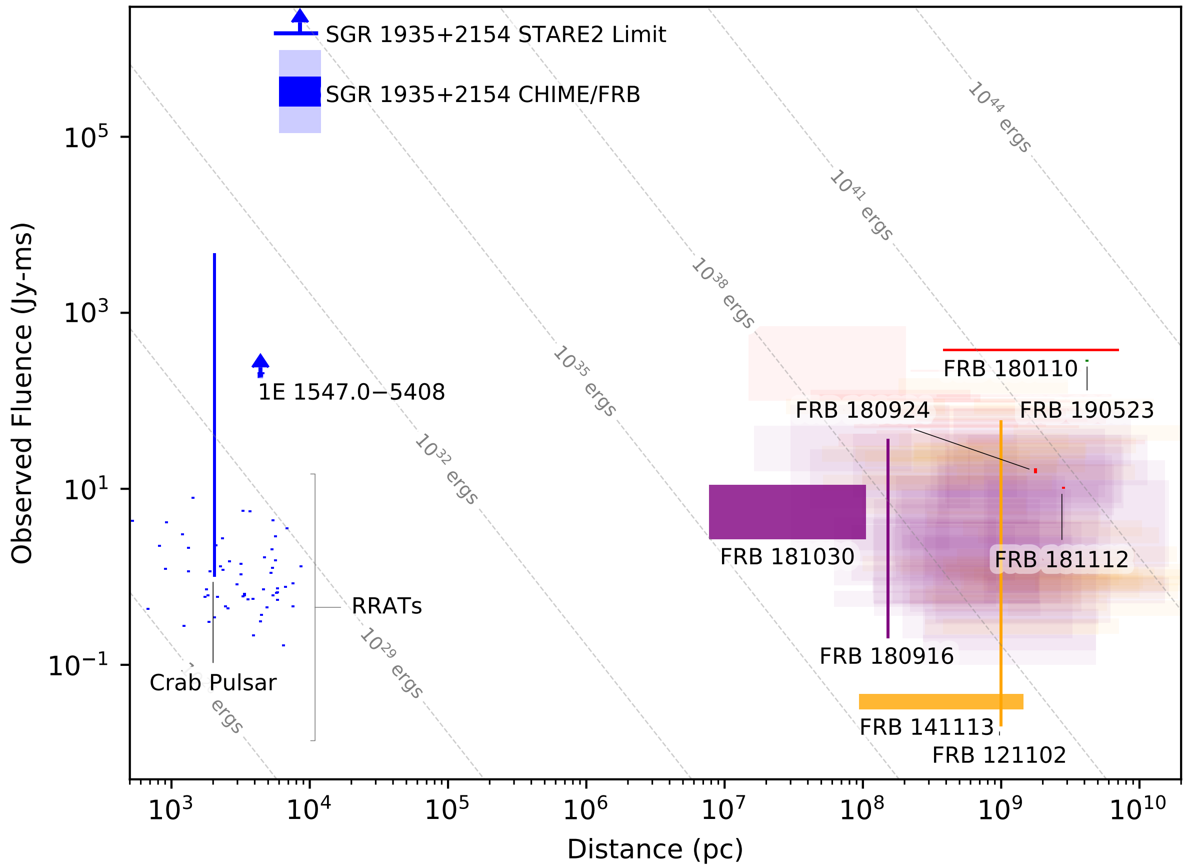

Figure 1.22: **Observed burst fluences of Galactic neutron stars and extragalactic FRBs at radio frequencies from 300 MHz to 1.5 GHz, plotted with their estimated distances.** The fluence ranges include the uncertainties in the fluence measurements, along with the variability in the burst fluences measured from repeating FRBs and pulsars. The colors for each FRB indicate the detection telescope: CHIME/FRB (purple), Australian Square Kilometre Array Pathfinder (ASKAP; red), the Deep Synoptic Array (DSA-10; green, FRB 190523), and the Arecibo and Parkes radio telescopes (orange). Galactic sources are plotted in blue. For SGR 1935+2154, the blue rectange indicates the nominal range of 400–800 MHz fluences measured for the two bursts detected by CHIME/FRB. The light blue region incorporates the possible systemic uncertainty in the CHIME/FRB fluence measurement. The STARE2 lower limit on the fluence at 1.4 GHz is also labeled. The gray diagonal lines correspond to distances of equal isotropic burst energy, assuming a fiducial bandwidth of 500 MHz. FRB distances are estimated from their estimated extragalactic dispersion measure (DM) contribution, including the simulated variance [445], and pulsar distances are based on the NE2001 Galactic electron density model [124]. Objects with accurately measured distances (via parallax or host galaxy redshift measurements) are indicated with vertical lines. The range of fluences observed from rotating radio transients (RRATs) are also labeled. Image credit and caption: Adapted from Figure 2 in [523].

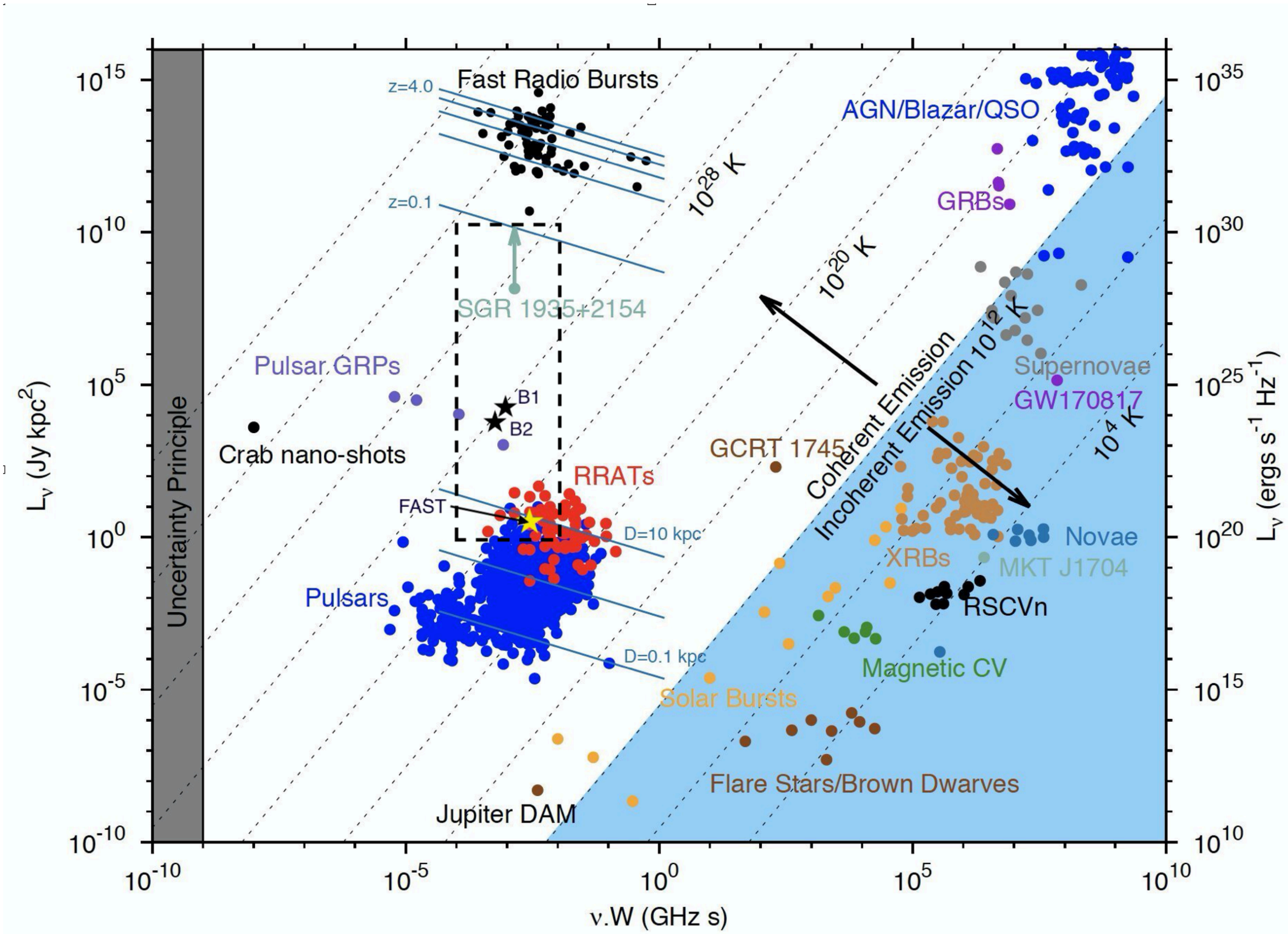

Figure 1.23: **Radio transient phase space diagram.** Astrophysical transients are shown in the νW versus L_{peak} phase space. Various transient phenomena, such as solar bursts, flare stars, active galactic nuclei (AGN), FRBs, RRATs, Jupiter decametric emission (DAM), and giant radio pulses (GRPs), are plotted on this diagram. Lines of constant brightness temperature are shown as diagonal dashed lines. Sources below the Compton catastrophic limit of $T_{\text{b}} = 10^{12}$ K produce radio emission through synchrotron incoherent processes (blue shaded region) while others, above the boundary, arise from coherent emission processes. The dashed box indicates the luminosity distribution of radio bursts detected from SGR 1935+2154, where B1 and B2 are the two bursts reported in Kirsten et al. [277]. For illustrative purposes, sensitivity curves for Galactic distances (0.1, 1, and 10 kpc) and various cosmological redshift values ($z = 0.1$, 1, 2, 3, and 4) are shown and derived based on the sensitivity of MeerKAT. Image credit: Adapted from Figure 1 in [270].

Giant pulses from extragalactic pulsars: Cordes and Wasserman [126] proposed that individual MJy nanoshot-like pulses from extragalactic pulsars may explain FRBs. This model is consistent with the observed energetics and sky rates of FRBs. However, in order to explain a population of FRBs located at high inferred redshifts, the authors invoke gravitational lensing. Instead, they favor a nearby extragalactic population of pulsars, which does not require gravitational lensing and has less stringent requirements on the radiation process. In order to satisfy the apparent FRB rate, such a scenario would require more bursts per object.

Extragalactic, active magnetars: A population of extragalactic magnetars may account for at least some fraction of the FRB population. A 1.5 MJy ms burst was detected from SGR 1935+2154, which has now bridged the large energy gap that previously existed between extragalactic FRBs and Galactic magnetars [59, 523]. However, extragalactic magnetars cannot account for the activity observed from repeating FRBs, so if they are produced by magnetars, they must somehow be different from the known population in the Milky Way [370].

Chapter II

The NASA Deep Space Network (DSN) and Algorithms to Search for Fast Radio Bursts (FRBs), Pulsars, and Other Radio Transients

Section 2.1 of this chapter is based on the following published article:

[424] **Pearlman, A. B.*,** Majid, W. A., and Prince, T. A. (2019). "Observations of Radio Magnetars with the Deep Space Network." In: *Advances in Astronomy,* Vol. 2019, Article ID 6325183. 1902.10712 [astro-ph.HE].

2.1 The NASA Deep Space Network: A Premier Radio Pulsar Observation

The Deep Space Network (DSN) is a worldwide array of radio telescopes that supports NASA's interplanetary spacecraft missions. When the DSN antennas are not communicating with spacecraft, they provide a valuable resource for performing observations of radio magnetars (e.g., see Chapters 3, 4, and 5), observations of FRBs (e.g., see Chapters 6 and 7), searches for new pulsars at the Galactic Center (e.g., see Chapter 9), and additional pulsar-related studies.

The DSN consists of an array of radio telescopes at three locations (Goldstone, California; Madrid, Spain; and Canberra, Australia). Each of these sites is approximately equally separated in terrestrial longitude and situated in a relatively remote location to shield against radio-frequency interference (RFI). With multiple radio antennas at each site, the DSN covers both celestial hemispheres and serves as the spacecraft tracking and communication infrastructure for NASA's deep space missions. The three DSN complexes each include a 70 m diameter antenna, with a surface suitable for radio observations at frequencies up to 27 GHz. In addition, each site hosts a number of smaller 34 m diameter radio telescopes, which are capable of observations as high as 32 GHz. Each antenna is equipped with multiple high efficiency feeds, highly sensitive cryogenically cooled receivers, and dual (circular) polarization capabilities. When the DSN antennas are not communicating with spacecraft, they may be used for radio astronomy and other radio science applications.

Recently, all three sites have been upgraded with state-of-the-art pulsar processing backends that enable data recording with high time and frequency resolution. The DSN telescopes are able to perform radio observations at the following standard frequency bands: L-band (centered at 1.5 GHz), S-band (centered at 2.3 GHz), X-band (centered at 8.4 GHz), and Ka-band (centered at 32 GHz). In addition, the 70 m radio dish in Tidbinbilla, Australia (see Figure 9.8) is outfitted with a dual beam K-band feed covering 17–27 GHz. These capabilities are currently being used in various pulsar-related programs, which include high frequency, ultra-wide bandwidth searches for pulsars in the Galactic Center (GC), high frequency monitoring of radio magnetars [27, 355, 356, 357, 359, 360, 361, 419, 420, 421, 422, 424, 426, 427, 428, 430], multifrequency studies of giant pulses from the Crab pulsar [353, 354], and high frequency searches for FRBs [358, 425, 429, 482].

The DSN radio telescopes are particularly well-suited for monitoring radio magnetars and FRBs. These instruments allow for high cadence observations, which are important for tracking changes in the flux densities, pulse profile shapes, spectral indices, and single pulse behavior of radio magnetars, all of which can vary on daily timescales. High frequency observations are also essential because the spectral indices of radio magnetars are quite flat or inverted on average. The DSN antennas are also capable of providing simultaneous, dual band observations with both circular polarizations, which is essential for accurate spectral index measurements and polarimetric studies. Additionally, since the large 70 m dishes have very low system temperatures, they are ideal for studying the morphology of single pulses from radio magnetars. These capabilities also provide a valuable resource for monitoring the activity and emission properties of repeating FRBs across large spectral bandwidths at multiple radio frequencies simultaneously.

The DSN has served as an excellent facility for performing state-of-the-art pulsar and FRB observations, which will be demonstrated in this thesis. The combination of the excellent sensitivity of the DSN antennas, particularly with the presence of a large 70 m diameter dish at each of the DSN complexes, multifrequency receivers, and the recent deployment of modern pulsar machines, offers an opportunity for pulsar observations that will be a significant addition to the already existing resources in pulsar astronomy. The availability of the 70 m antenna in Canberra, with its southern location, makes it an ideal resource, complementing the Parkes telescope, for observations of Galactic plane sources, including the Galactic Center (GC). In search mode, the DSN's pulsar machines offer high frequency and timing resolution with the ability to record multiple frequencies and incoming polarization bands simultaneously. With precision tracking capabilities available at multiple frequencies, the DSN is particularly well-suited for carrying out observations at shorter wavelengths, which have proven useful for studying objects such as magnetars with flatter spectral indices and high DM pulsars.

2.2 Overview of Data Reduction Pipelines and Algorithms Used to Analyze Pulsar and Fast Radio Burst Observations from the NASA Deep Space Network

After the DSN radio telescopes are used to record radio data from pulsars and FRBs, the bandpass response is flattened, and the data are baseline-corrected to remove low-frequency fluctuations from the time series stored in each frequency channel of the digital search-mode polyphase filterbank. The data are reduced using customized algorithms that I have developed as part of a software suite designed to analyze radio observations from the DSN radio telescopes.

There are several types of analyses that are commonly performed when searching the DSN observations for interesting transient signals from pulsars and FRBs. Single pulse searches are performed using a Fourier domain matched filtering algorithm, where the dedispersed time series data are convolved with boxcar templates with logarithmically spaced widths. A GPU-accelerated machine learning pipeline based on the `FETCH`[k] (Fast Extragalactic Transient Candidate Hunter) software package is used to identify bright bursts from both pulsars and FRBs, when the number of candidates is too large to inspect manually.

Searches for radio pulsations are carried out using: (1) a GPU-accelerated Fast Folding Algorithm (FFA) algorithm and (2) a GPU-accelerated Fourier Domain Acceleration Search (FDAS) pipeline, which employs a matched filtering algorithm to correct for Doppler smearing. In addition, I am also developing novel, state-of-the-art algorithms that are capable of searching for pulsars and other periodic signals with greater sensitivity (e.g., see Chapter 8). In some cases, these algorithms are also used to search the data recorded using the DSN radio telescopes.

2.3 Previous Techniques Used for Mitigating Terrestrial Radio Frequency Interference

Many radio telescopes, such as those comprising the DSN, are located in remote geographical locations in order to reduce the amount of RFI that could potentially adversely impact the observations. However, even in the most secluded locations, terrestrial sources of RFI can have a significant effect on the instrument's ability to

[k] See https://github.com/devanshkv/fetch.

detect periodic radio signals and impulsive radio bursts from astrophysical sources, such as pulsars and FRBs. Mitigation of undesired terrestrial RFI is of paramount importance for detecting these astrophysical sources, especially when their signal strength is close to the nominal sensitivity of the instrument.

Some terrestrial sources of RFI, such as electrical storms, are capable of saturating the radio telescope's receiver. Other RFI sources can produce either narrowband or broadband signals, which can be persistent or transient in time. These signals may be periodic and can even display behavior similar to that of dispersed radio pulses from astrophysical objects like pulsars. These types of signals can originate from nearby electrical devices, such as power lines operating at 60 Hz in the United States or 50 Hz in Australia [364], or external radio communication systems (airport or military radar). Laptop and desktop computers at the observatory are also capable of producing RFI in the radio band. In Figure 2.1, I show a catalog of the various known radio sources in the United States, up to a frequency of 300 GHz[1].

A standard way to identify signals produced by sources of RFI is to exploit the fact that they are not dispersed. Periodic RFI, in particular, can often be identified by analyzing the Fourier transform of the undispersed time series. Previous methods used to mitigate such types of RFI signals include time domain clipping, spectral masking [328], and zero-DM filtering techniques [168].

Time domain clipping is accomplished by setting a threshold above which undesired signals are removed from the data. This threshold is usually determined by comparing the expected mean and standard deviation of the zero-DM time series to the amplitude of the signals that are intended to be removed. This technique can be useful when searching for weak sources, which would otherwise be missed due to sporadic bursts of interference.

Periodic RFI and spurious, impulsive signals can also be filtered out of the data by generating a spectral mask. This is achieved by first dividing the radio data into discrete time and frequency blocks. The data in each of these blocks are then searched for narrowband and wideband RFI by identifying blocks that have strong impulsive or periodic signals in the undispersed data. Strong, impulsive signals are typically removed by masking or clipping data with an amplitude above a specified threshold. Periodic RFI can be identified by calculating Fast Fourier Transforms (FFTs) of each block and identifying Fourier bins with an excess amount of power. These techniques can be used to generate a list of undesired periodic

[1] See https://www.ntia.doc.gov/files/ntia/publications/january_2016_spectrum_wall_chart.pdf.

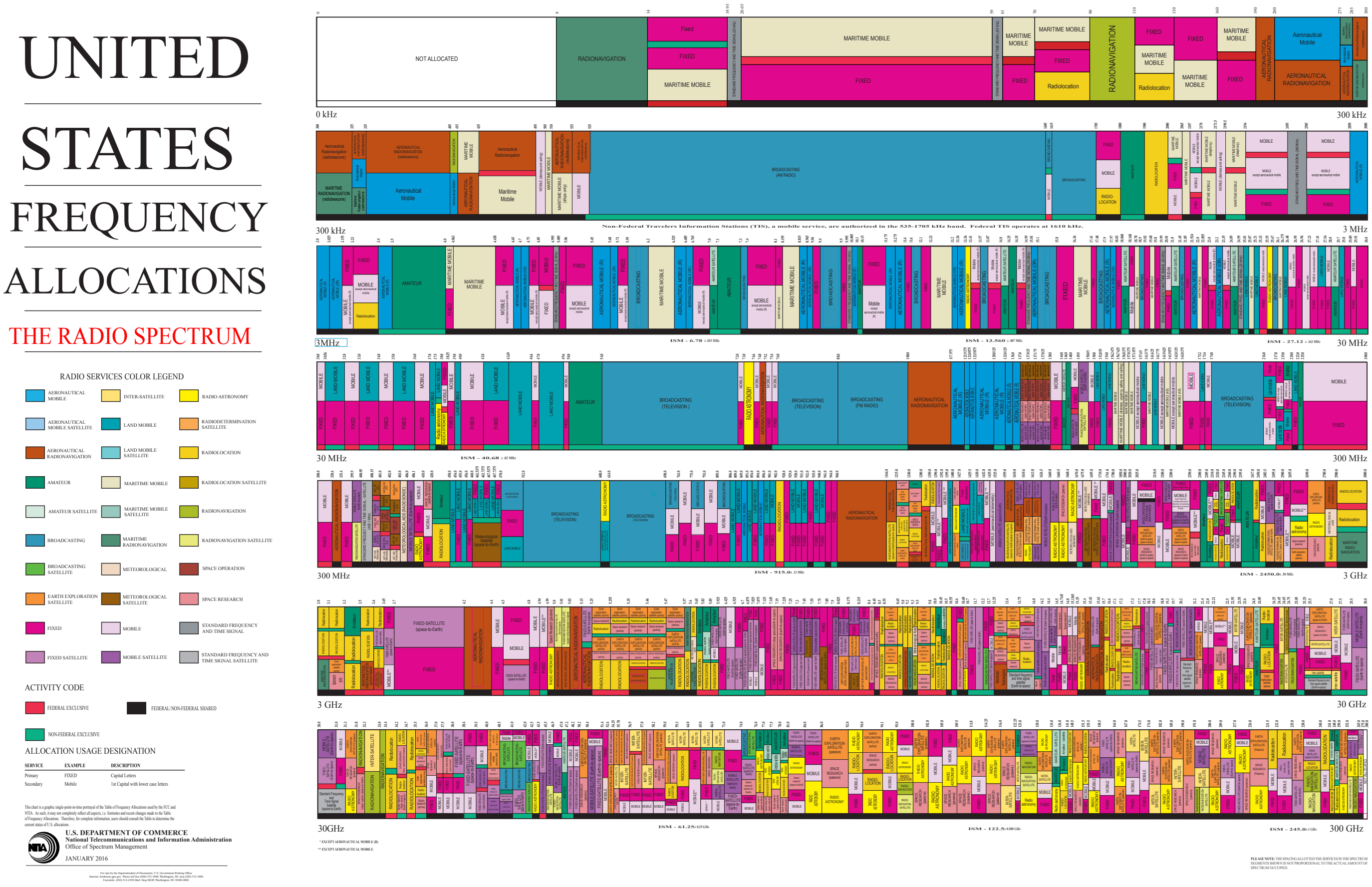

Figure 2.1: **Catalog of known radio sources in the United States, up to a frequency of 300 GHz.** Image credit: United States Department of Commerce, National Telecommunications and Information Administration[l].

signals or chirps, often referred to "RFI birdies," to be excised from the data. This information is then combined to form a "mask," which can be applied, for example, to channelized radio data stored in a digital polyphase filterbank to remove most terrestrial RFI. This method of RFI mitigation has been used extensively in pulsar astronomy, and it is the basis of the `rfifind` algorithm used in the `PRESTO` pulsar search software package[m] [456]. An example of a spectral mask produced by `rfifind`, using data from a 2.3 GHz observation of the Crab pulsar (PSR B0531+21) recorded with the 70 m DSN radio telescope, DSS-63, is shown in Figure 2.2.

Another scheme used to mitigate broadband, undispersed RFI involves employing a technique known as zero-DM filtering [168]. The zero-DM filter is applied to the channelized radio data prior to dedispersion. At each time sample, t_j, a mean value

[m] See https://github.com/scottransom/presto.

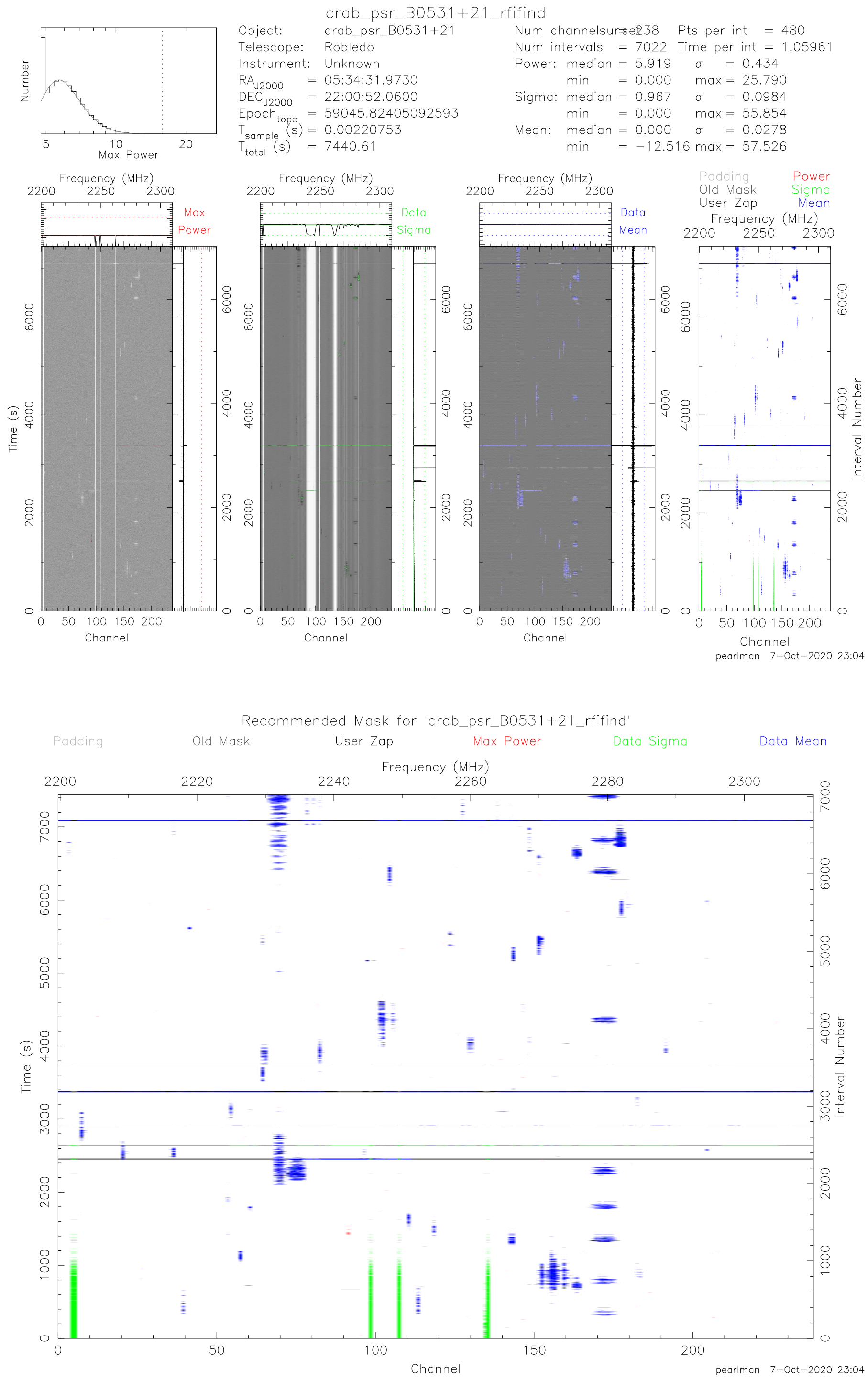

Figure 2.2: **Example of a spectral mask produced by the `rfifind` algorithm, available in the `PRESTO` pulsar search software package[m], using data from a 2.3 GHz observation of the Crab pulsar (PSR B0531+21) recorded with the 70 m DSN radio telescope, DSS-63.** The colored lines indicate the sections of the data that have been masked by the RFI filtering algorithm.

is obtained by averaging the data in all of the frequency channels. This mean value is then subtracted from the corresponding time sample in each frequency channel. This procedure is repeated at each time bin of the observation. The zero-DM filtered data, $S'(f_i, t_j)$, is computed according to:

$$S'(f_i, t_j) = S(f_i, t_j) - \frac{1}{n_{\text{chans}}} \sum_{i=1}^{n_{\text{chans}}} S(f_i, t_j), \tag{2.1}$$

where $S(f_i, t_j)$ is the original data value at time sample t_j of frequency channel f_i and n_{chans} is the number of frequency channels used for channelization. During times when broadband, undispersed RFI is detected, there will be excess power in each frequency channel. By applying Equation (2.1), these signals will be removed from the data. In Figure 2.3, I show a schematic of the effect of the zero-DM filter on a narrow, linearly dispersed pulse in the frequency–time domain. An example application of the zero-DM filter on simulated data is shown in Figure 2.4.

As demonstrated in Figure 2.4, the zero-DM filter is particularly useful for detecting dispersed pulses in the presence of broadband RFI. Most searches for single pulses in the radio band involve convolving the dedispersed time series, $x(t)$, with boxcar functions, $b(t)$, of various widths, if the shape of the pulse is not known in advance. A list of candidates is obtained by searching for peaks above a specified S/N threshold in the convolved data, $x(t) * b(t)$, where $*$ denotes the convolution operator. After applying the zero-DM filter and dedispersing the data, the data are transformed as shown in Figure 2.3(b). The approximate dispersion delay across the receiver bandwidth, B, is given by:

$$\frac{dt}{df} = 2\,\mathcal{D} \times \text{DM} \left(\frac{1}{\nu_{\text{center}}^3} \right) \text{s MHz}^{-1}, \tag{2.2}$$

where $\mathcal{D} = \frac{e^2}{2\pi m_e c}$ is the dispersion constant and ν_{center} is the central observing frequency. After summing the data in each frequency channel after dedispersion, the convolving function, $w(t)$, is obtained, which is shown in Figure 2.3(c). Therefore, the zero-DM filtered time series is given by $x'(t) = x(t) * w(t)$. In the frequency domain, this is equivalent to point-wise multiplying the fluctuation spectrum of the dedispersed time series, $X(\nu)$, by the Fourier transform of $w(t)$, $W(\nu)$, which is given by:

$$W(\nu) = 1 - \text{sinc}^2 \left(\pi B \frac{dt}{dt} \times \nu \right) \tag{2.3}$$

$$= 1 - \text{sinc}^2 \left(\pi B \times 2\,\mathcal{D} \times \frac{\text{DM}}{\nu_{\text{center}}^3} \times \nu \right), \tag{2.4}$$

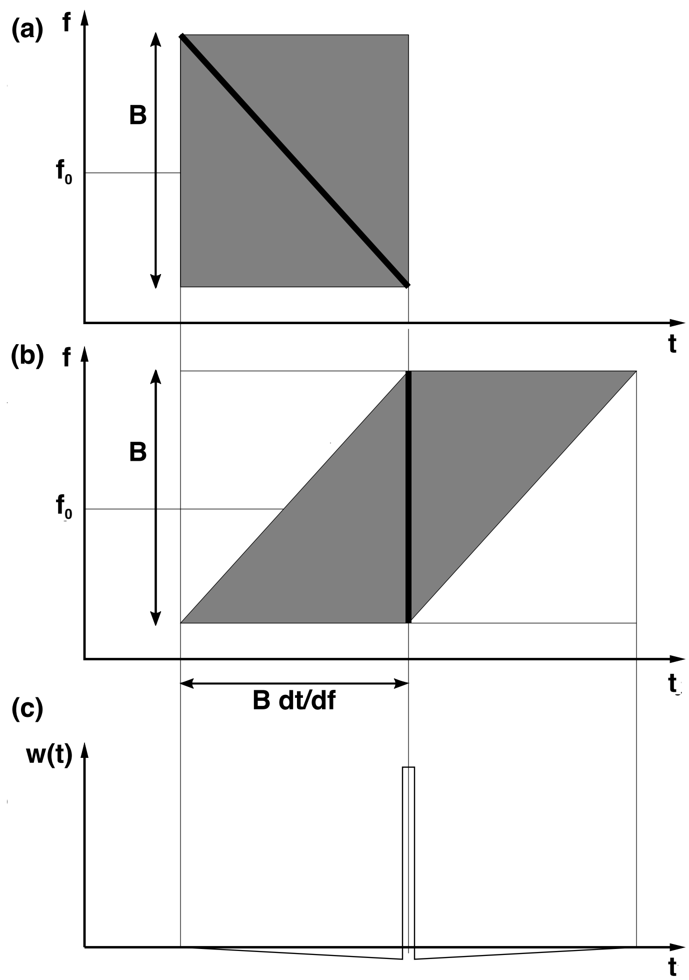

Figure 2.3: **Schematic diagram of the effect of the zero-DM filter on a narrow, linearly dispersed pulse in the frequency–time domain.** The dispersive delay of the pulse ($B\,dt/df$) over the full bandwidth (B) of the receiver is shown in panel (a). After the mean value across the receiver bandwidth is subtracted at each time, t_j, according to Equation (2.1), the non-pulse area (shaded in gray) becomes negative. In panel (b), I show the result after dedispersing the data at the correct DM of the pulse, and panel (c) shows the pulse shape after adding all of the frequency channels at each time sample. Image credit: Adapted from Figure 1 in [168].

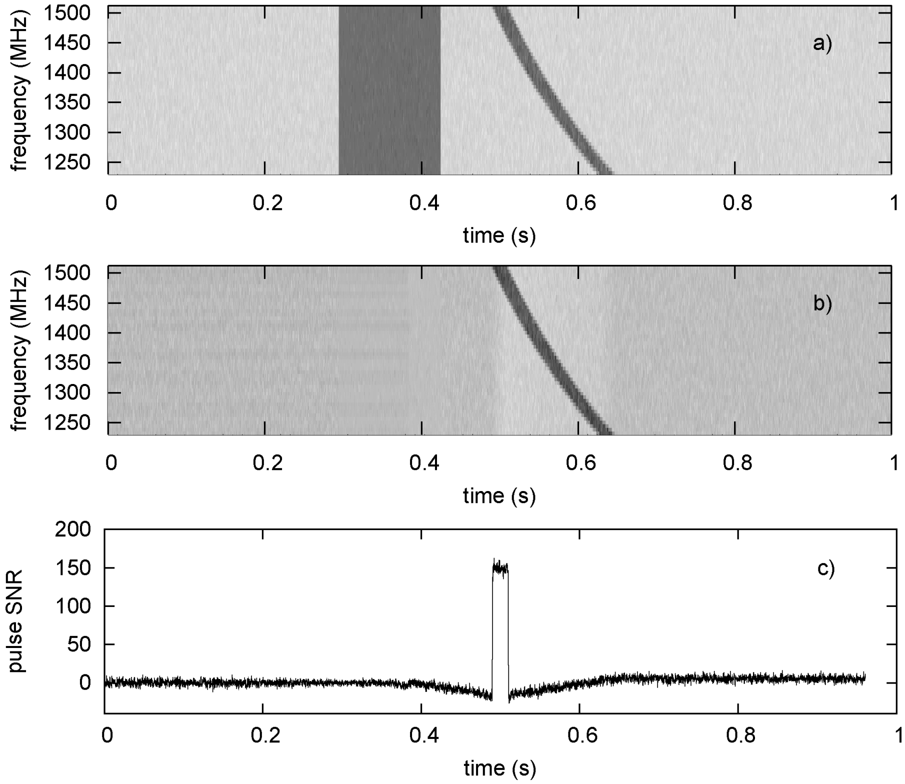

Figure 2.4: **Application of the zero-DM filter on simulated data.** Panel (a): Simulated data of a 130 ms burst of broadband RFI with DM = 0 pc cm^{-3}, followed by a 20 ms dispersed pulse with DM = 150 pc cm^{-3} across 288 MHz of bandwidth at a center frequency of 1374 MHz. Panel (b): The same data shown in panel (a) after applying the zero-DM filter. The broadband RFI is removed, and the non-pulse area underneath the dispersed pulse becomes negative after performing the subtraction in Equation (2.1). Panel (c): The pulse shape after adding all of the frequency channels at each time sample. Image credit: Adapted from Figure 4 in [168].

where ν is the fluctuation frequency of the signal.

While a typical single pulse search algorithm based on matched filtering would normally try to identify peaks in $x'(t) * b(t)$, for an unknown pulse shape, the optimal filter for the zero-DM filtered time series is now $b'(t) = w(t) * b(t)$, rather than a boxcar function. Therefore, peaks should instead be identified in $x''(t) = x'(t) * b'(t)$ $= F^{-1}[X'(\nu) \cdot W'(\nu)] * b(t)$, where F^{-1} denotes the inverse Fourier transform operator, $\cdot$ is the point-wise multiplication operator, and I have used the convolution theorem to evaluate the convolution in the time domain using point-wise multiplication in the frequency domain.

2.4 A Novel Infinite Impulse Response (IIR) Filtering Algorithm for Radio Frequency Interference (RFI) Mitigation

In this Section, I consider the case where an undesired periodic RFI signal is present in the radio data. Such a signal could originate, for example, from the telescope's power lines. One method sometimes used to remove a signal of this kind involves Fourier transforming the data, zeroing specific bins in the frequency domain that are consistent with the frequency of the periodic RFI signal, and then inverse Fourier transforming the data. This technique is equivalent to multiplying the data by a rectangular window function in the frequency domain. Since the Fourier transform of a rectangular function is a sinc function, this method can often introduce unwanted ripples into the filtered time series after inverse Fourier transforming the data. This can be particularly problematic, for example, when performing periodicity or single pulse searches. Here, I describe a novel IIR filtering algorithm that effectively mitigates periodic RFI without significantly degrading the overall data quality.

Filtering is a fundamental aspect of digital signal processing (DSP). This often involves processing a sequence of samples containing a time domain signal in order to alter the characteristics of the data in the frequency domain. This can be achieved by attenuating or filtering selected frequency components from the data using a digital filter. There are two main types of digital filters: (1) nonrecursive, finite impulse response (FIR) filters and (2) recursive, infinite impulse response (IIR) filters.

2.4.1 Finite Impulse Response (FIR) Filters

A block diagram of a generic FIR filter is shown in Figure 2.5. Here, $x(n)$ is the input signal, and $y(n)$ is the output signal. The FIR filter is comprised of several components, which include multiple delay lines, buffers, multipliers, and summing junctions. The output of each delay line block is simply the input, delayed by one sampling period. A delay line is represented by a series of blocks, where each block delays or shifts the input sample by one position (to the right, in Figure 2.5). A delay is implemented using the z-transform (see Section 2.4.2), where z^{-1} applies a delay of one sample. Buffers are used to store the previous input samples. The multipliers are represented using blocks, labeled with filter coefficients, which multiply their inputs by the filter coefficient labeled in each block. The summing junctions are used to add the multiplier outputs and form the filter output, $y(n)$. The filter order is given by N, and there are $N + 1$ terms that are added using summing junctions.

The output of the FIR filter can be described using the difference equation:

$$y(n) = \sum_{k=0}^{N} h(k)x(n-k), \tag{2.5}$$

where $h(k)$ is the value of the impulse response at the k^{th} sampling instant. The impulse response of a FIR filter is equal to its coefficients, but this is not the case for an IIR filter. Equation (2.5) links the input and output signals through the convolution sum of a discrete-time, linear time-invariant (LTI) system, with a FIR given by $h(n)$. The output of any LTI system is obtained by convolving its input signal with its impulse response. In Equation (2.5), I have considered a discrete-time system, but an analogous difference equation can be obtained for continuous-time LTI systems using a convolution integral instead of a convolution sum.

One of the advantages of using FIR filters is that they can be used to implement arbitrary filter characteristics. However, their implementation can also be computationally expensive. Some filter designs may require a large number of filter coefficients to achieve a desired level of accuracy.

2.4.2 Overview of the z-Transform

The z-transform is an important tool in the design and analysis of digital filters. It is used to convert a discrete-time signal, which is a sequence of real or complex numbers, into a complex representation in the frequency domain. The z-transform is considered to be the discrete-time equivalent of the Laplace transform and a generalization of the discrete-time Fourier Transform (DTFT), not to be confused with the discrete Fourier Transform (DFT).

The Laplace transform is a generalization of the continuous-time Fourier Transform (CTFT). It is used to solve continuous-time, linear differential equations by

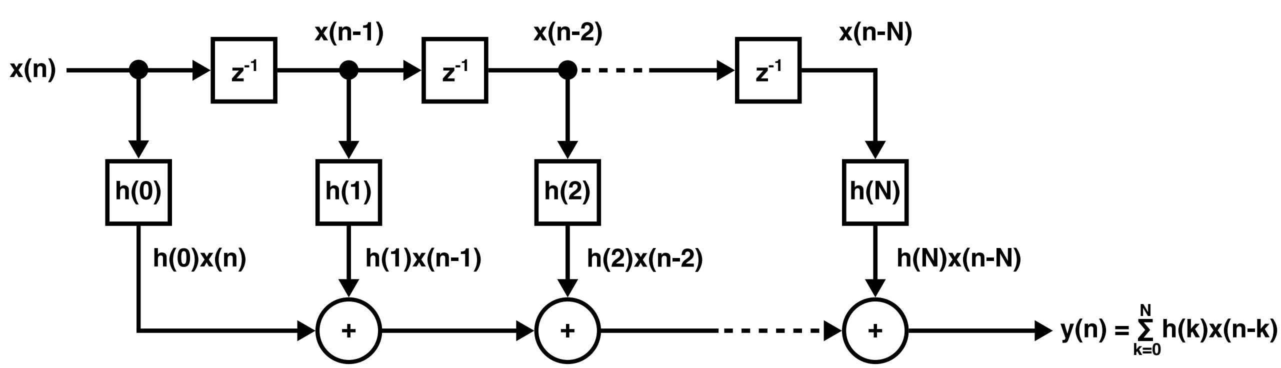

Figure 2.5: **Block diagram representation of a generic FIR filter.**

representing them as algebraic expressions in the complex variable, s, and allows continuous-time LTI systems to be represented using s-transfer functions. Similarly, the z-transform is used to solve discrete-time difference equations by representing them as algebratic expressions in the complex variable, z, and allows discrete-time LTI systems to be represented using z-transfer functions. The Laplace variable, s, can be viewed as an operator, corresponding to differentiation with respect to time. The z variable may also be considered an operator, which applies a shift of one sample position in a sequence.

The z-transform of a discrete-time sequence, $x(n)$, is defined as:

$$X(z) = \mathcal{Z}\{x(n)\} = \sum_{n=-\infty}^{+\infty} x(n) z^{-n}, \tag{2.6}$$

where $z = Ae^{i\phi}$ is a complex number, with a magnitude of A and phase of ϕ, and n is an integer. This form of the z-transform is referred to as the bilateral or two-sided z-transform since $-\infty < n < +\infty$. The unilateral or single-sided z-transform is defined for $n \geq 0$.

From Equation (2.6), it is clear that $X(z)$ is a power series in z, whose number of terms is equal to the number of sample values in the sequence $x(n)$. The corresponding coefficient for each z^{-n} term in $X(z)$ is the n^{th} sample value in $x(n)$. In a discrete-time system, z^{-n} corresponds to the time $t = nT$, where T is the sampling period. $X(z)$ only exists for values of z for which the power series in Equation (2.6) converges, which corresponds to values of z such that $|X(z)| < \infty$.

2.4.3 Infinite Impulse Response (IIR) Filters

The following recursive difference equation describes the input–output relationship of a general IIR filter:

$$y(n) = \sum_{k=0}^{M} b_k x(n-k) - \sum_{j=1}^{N} a_j y(n-j), \tag{2.7}$$

where $x(n)$ is the input signal, $y(n)$ is the output signal, M is the feedforward filter order, b_k are the feedforward filter coefficients, N is the feedback filter order, and a_j are the feedback filter coefficients. Here, the output, $y(n)$, depends on: (1) the input, $x(n)$, at instant n, (2) past inputs, $x(n-1), x(n-2), \ldots, x(n-M)$, and (3) past outputs, $y(n-1), y(n-2), \ldots, y(n-N)$. Equation (2.7) can equivalently be expanded as:

$$\begin{aligned} y(n) = b_0 x(n) + b_1 x(n-1) + b_2 x(n-2) + \cdots + b_M x(n-M) \\ - a_1 y(n-1) - a_2 y(n-2) - \cdots - a_N y(n-N). \end{aligned} \tag{2.8}$$

Here, I consider a right-sided, causal input, $x(n)$, whose z-transform is given by:

$$X(z) = \mathcal{Z}\{x(n)\} = \sum_{n=0}^{+\infty} x(n) z^{-n} = x(0) + x(1) z^{-1} + x(2) z^{-2} + \cdots \tag{2.9}$$

In general, the z-transform of a time-shifted sequence, $x(n-k)$, is given by:

$$\mathcal{Z}\{x(n-k)\} = z^{-k} \sum_{m=1}^{k} x(-m) z^{m} + z^{-k} X(z), \tag{2.10}$$

where k is an integer. If all of the initial conditions are zero, i.e. $x(-m) = 0$ for $m = 1, 2, \ldots, k$, then Equation (2.10) reduces to:

$$\mathcal{Z}\{x(n-k)\} = z^{-k} X(z). \tag{2.11}$$

Under the assumption that all of the initial conditions in Equation (2.8) are zero, then after applying Equation (2.11), its z-transform is given by:

$$\begin{aligned} Y(z) = (b_0 + b_1 z^{-1} + b_2 z^{-2} + \cdots + b_M z^{-M}) X(z) \\ - (a_1 z^{-1} + a_2 z^{-2} + \cdots + a_N z^{-N}) Y(z). \end{aligned} \tag{2.12}$$

The transfer function, $H(z)$, of the IIR filter is obtained after setting $M = N$ in Equation (2.12) :

$$H(z) = \frac{Y(z)}{X(z)} = \frac{b_0 + b_1 z^{-1} + b_2 z^{-2} + \cdots + b_N z^{-N}}{1 + a_1 z^{-1} + a_2 z^{-2} + \cdots + a_N z^{-N}} = \frac{N(z)}{D(z)}, \tag{2.13}$$

where $N(z)$ and $D(z)$ are the polynomials in the numerator and denominator, respectively. Multiplying and dividing Equation (2.13) by z^N yields:

$$H(z) = \frac{b_0 z^N + b_1 z^{N-1} + b_2 z^{N-2} + \cdots + b_N}{z^N + a_1 z^{N-1} + a_2 z^{N-2} + \cdots + a_N} = C \prod_{i=1}^{N} \frac{z - z_i}{z - p_i}, \tag{2.14}$$

where C is a constant. From the right-hand side of Equation (2.14), we see that the transfer function has N zeros and N poles. For an IIR filter to be stable, the magnitude of each of its poles must be less than 1 so that all of the poles of the z-transfer function lie inside the unit circle. Thus, a stable system is obtained when $|p_i| < 1$, so that $h(n) \to 0$ as $n \to \infty$. The system becomes unstable for $|p_i| > 1$

since $h(n) \to \infty$ as $n \to \infty$. The system is marginally unstable and will display an oscillatory response when $|p_i| = 1$.

IIR filters can be implemented using a variety of topologies. Below, we consider a few of the most common types of structures: (1) direct form I, (2) direct form II, and (3) direct form II transpose. Filters designed with these structures will have the same transfer function, but the efficiency will vary depending on which implementation is used.

2.4.3.1 Direct Form I Structure

A block diagram of the direct form I structure is shown in Figure 2.6. It can be used to implement the difference equation in Equations (2.7) and (2.8). The structure shown in Figure 2.6 corresponds to the case when $M = N$, but an analogous design can be constructed for $M \neq N$. An N^{th} order filter requires $2N$ delay elements, which are each represented using blocks that are labeled z^{-1}.

2.4.3.2 Direct Form II Structure

A more efficient implementation of Figure 2.6 can be realized by placing the feedback section before the feedforward section. This rearrangement yields the direct form II structure shown in Figure 2.7, which is one of the most common structures used to represent an IIR filter. The direct form II structure requires half as many delay elements as the direct form I structure, which can be seen by comparing Figures 2.6 and 2.7.

Next, we show that the direct form II structure, shown in Figure 2.7, produces the same transfer function as Equation (2.13). By inspecting Figure 2.7, we see that:

$$w(n) = x(n) - a_1 w(n-1) - a_2 w(n-2) - \cdots - a_N w(n-N) \tag{2.15}$$

and

$$y(n) = b_0 w(n) + b_1 w(n-1) + b_2 w(n-2) + \cdots + b_N w(n-N). \tag{2.16}$$

Taking the z-transform of Equations (2.15) and (2.16), and assuming that all of the initial conditions of $w(n), w(n-1), w(n-2), \ldots, w(n-N)$ are zero, yields:

$$W(z) = X(z) - a_1 z^{-1} W(z) - a_2 z^{-2} W(z) - \cdots - a_N z^{-N} W(z), \tag{2.17}$$

$$X(z) = (1 + a_1 z^{-1} + a_2 z^{-2} + \cdots + a_N z^{-N}) W(z), \tag{2.18}$$

and

$$Y(z) = (b_0 + b_1 z^{-1} + b_2 z^{-2} + \cdots + b_N z^{-N}) W(z). \tag{2.19}$$

Dividing Equation (2.19) by Equation (2.18) gives a transfer function that is identical to Equation (2.13):

$$H(z) = \frac{Y(z)}{X(z)} = \frac{b_0 + b_1 z^{-1} + b_2 z^{-2} + \cdots + b_N z^{-N}}{1 + a_1 z^{-1} + a_2 z^{-2} + \cdots + a_N z^{-N}}. \tag{2.20}$$

We also see that the direct form II structure, in general, can be described equivalently using the following pair of difference equations in Equations (2.15) and (2.16), instead of the form used in Equation (2.7):

$$w(n) = x(n) - \sum_{j=1}^{N} a_j w(n-j), \tag{2.21}$$

$$y(n) = \sum_{k=0}^{M} b_k w(n-k). \tag{2.22}$$

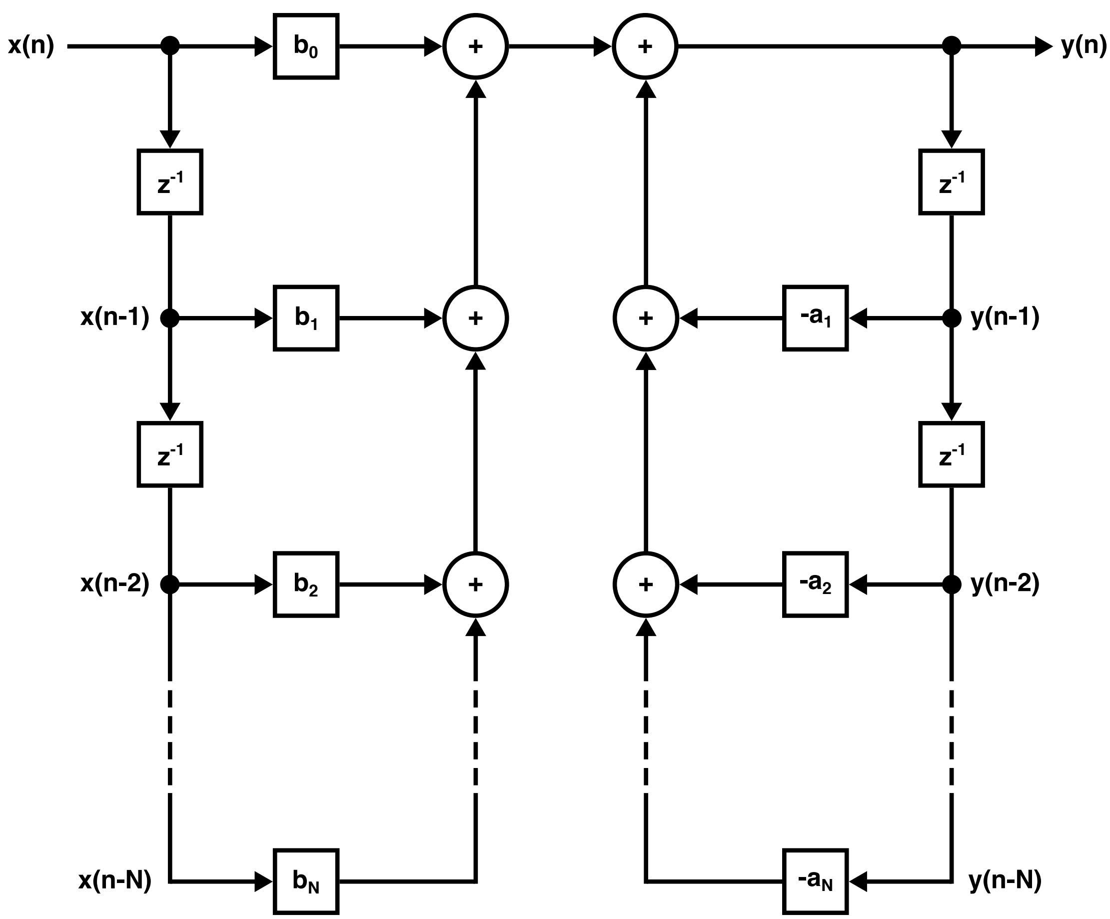

Figure 2.6: **Block diagram representation of the direct form I structure of an IIR filter.**

2.4.3.3 Direct Form II Transpose Structure

In Figure 2.8, we show a block diagram of the direct form II transpose structure, which is a modified version of the direct form II structure. It has the same number of delay elements as the direct form II structure, but requires fewer additions and is therefore more efficient.

From inspection of Figure 2.8, we see that the filter output is given by:

$$y(n) = b_0 x(n) + w_0(n-1). \tag{2.23}$$

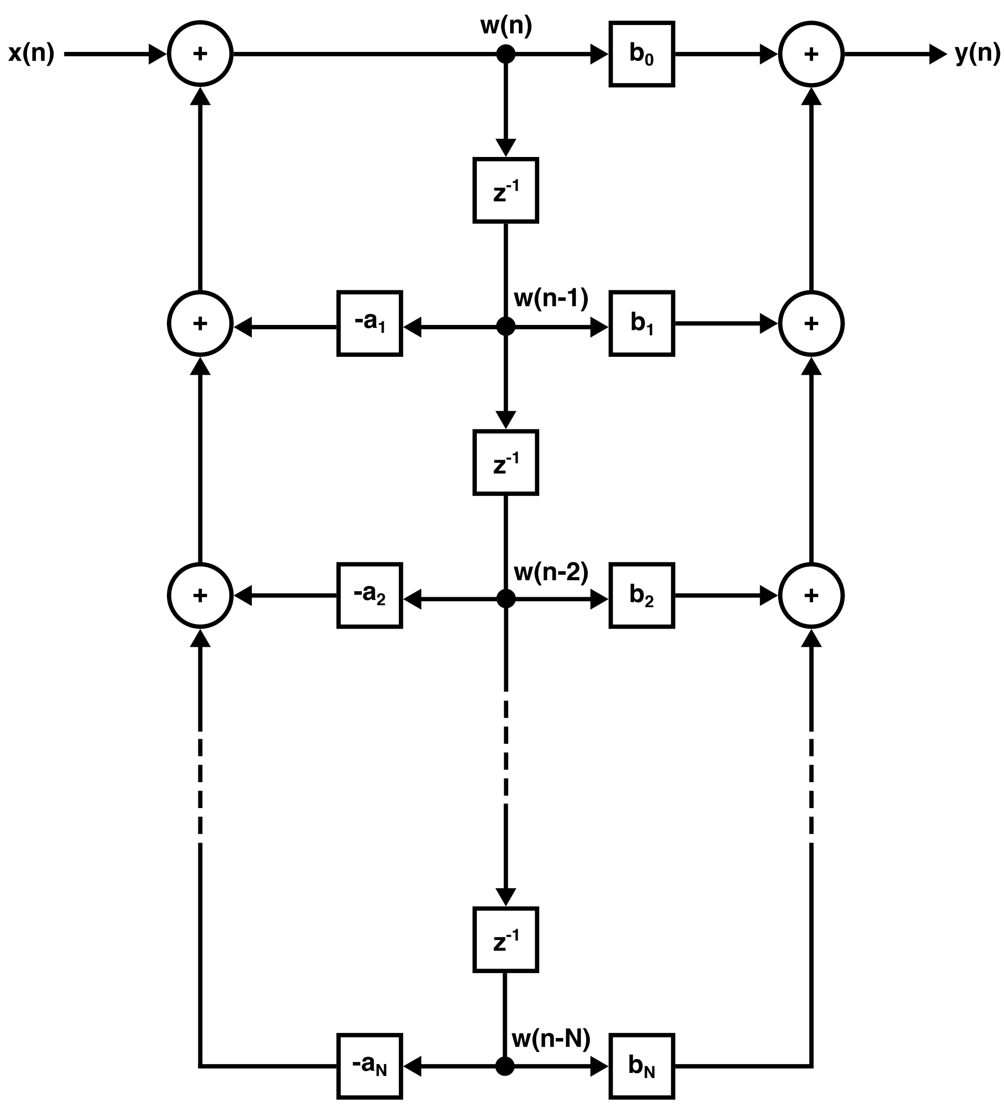

Figure 2.7: **Block diagram representation of the direct form II structure of an IIR filter.**

The input to each delay line is:

$$w_0(n) = b_1 x(n) + w_1(n-1) - a_1 y(n), \tag{2.24}$$

$$w_1(n) = b_2 x(n) + w_2(n-1) - a_2 y(n), \tag{2.25}$$

$$\vdots$$

$$w_{N-1}(n) = b_N x(n) - a_N y(n). \tag{2.26}$$

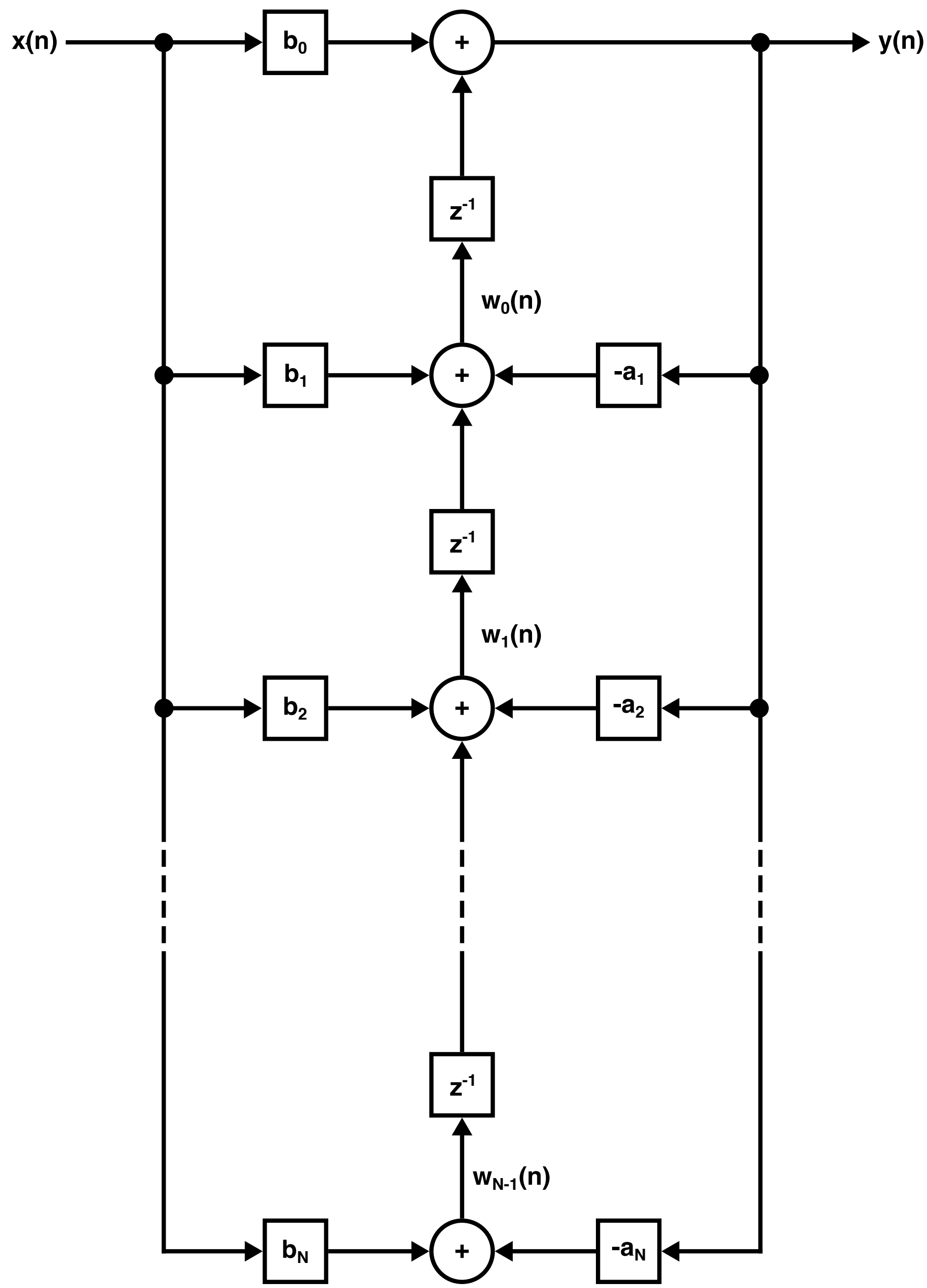

Figure 2.8: **Block diagram representation of the direct form II transpose structure of an IIR filter.**

Equation (2.24) can be used to obtain $w_0(n-1)$:

$$w_0(n-1) = b_1 x(n-1) + w_1(n-2) - a_1 y(n-1). \tag{2.27}$$

Substituting Equation (2.27) into Equation (2.23) yields:

$$y(n) = b_0 x(n) + [b_1 x(n-1) + w_1(n-2) - a_1 y(n-1)]. \tag{2.28}$$

Similarly, Equation (2.25) can be used to find $w_1(n-2)$:

$$w_1(n-2) = b_2 x(n-2) + w_2(n-3) - a_2 y(n-2). \tag{2.29}$$

After substituting Equation (2.29) into Equation (2.28), the following expression is obtained:

$$\begin{aligned} y(n) = b_0 x(n) + [b_1 x(n-1) + [b_2 x(n-2) + w_2(n-3) - a_2 y(n-2)] \\ - a_1 y(n-1)]. \end{aligned} \tag{2.30}$$

If this procedure is continued until Equation (2.26) has been used to obtain $w_{N-1}(n-N)$, then it can be shown that Equation (2.23) can be written as:

$$\begin{aligned} y(n) = b_0 x(n) + b_1 x(n-1) + b_2 x(n-2) + \cdots + b_N x(n-N) \\ - a_1 y(n-1) - a_2 y(n-2) - \cdots - a_N y(n-N). \end{aligned} \tag{2.31}$$

Thus, Equation (2.31) is equivalent to Equations (2.7) and (2.8) for $M = N$, and hence the block diagram in Figure 2.8 is equivalent to the block diagrams shown in Figures 2.6 and 2.7. The direct form II transposed structure implements the zeros of the filter before the poles, whereas the non-transposed direct form II structure implements the poles first. In the design of many digital filters, the poles by themselves produce a large gain at some frequencies. This often occurs for filters with sharp transitions in their frequency response. Since the zeroes are implemented first in the direct form II transposed structure, the zeros help to compensate for this issue by providing attenuation. This is one of the advantages of the direct form II transposed structure.

2.4.3.4 Application of the Infinite Impulse Response (IIR) Digital Filter for Radio Frequency Interference (RFI) Mitigation

Here, I will demonstrate the effectiveness of using an IIR digital filter for mitigating undispersed, periodic RFI from radio data. The filter function is implemented using the direct form II transposed structure described above in Section 2.4.3.3. For

$M = N$, this filter implements the input–output relationship given in Equation (2.31). The transfer function describing this filter, in the z-transform domain, is then equivalent to Equation (2.13). To attenuate undesired frequencies from the data, a linear digital filter is applied forward and background to the signal. This results in zero phase distortion and a filter order that is twice the original filter.

First, I consider a simple example, where there is a 12 Hz sinusoidal signal of interest in the data, along with Gaussian $\mathcal{N}(\mu = 0, \sigma = 0.2)$ noise. The data also contain two strong, undesired periodic signals at 8 and 60 Hz that need to be mitigated in order to recover the noisy 12 Hz signal. In Figure 2.9(a), I show 1 s of simulated data, which contain a combination of Gaussian noise and the 8, 12, and 60 Hz signals. The time resolution of the data is 64 μs, which corresponds to a Nyquist frequency of $f_{\mathrm{nyq}} = f_{\mathrm{s}}/2 = 7812.5$ Hz, where f_{s} is the sampling frequency. Panel (b) of Figure 2.9 shows the result after calculating a discrete Fourier Transform (DFT) of the data in panel (a) using an efficient Fast Fourier Transform (FFT) algorithm. The normalized power spectrum clearly shows strong detections of three signals at 8, 12, and 60 Hz, as expected. The frequency resolution of an n-point DFT is simply $\Delta f = f_{\mathrm{s}} / n$, where n is the number of points used to calculate the Fourier Transform. The DFT in Figure 2.9(b) was calculated using $n = 15625$ points, which results in a frequency resolution of $\Delta f = 1$ Hz in the power spectrum.

The objective here is to mitigate the 8 and 60 Hz periodic signals from the data, in order to recover the noisy 12 Hz sinusoidal signal without introducing artifacts into the filtered data. This is achieved by zero-phase filtering the data by applying an IIR digital filter forwards and backwards through the data in the time domain. In Figure 2.9(c), I show the frequency response of a first-order Butterworth band-stop digital filter, which provides > 100 dB of attenuation at 8 and 60 Hz. I have chosen to use a Butterworth filter here since it has a maximally flat frequency response (i.e., it has no ripples) in the passband and rolls off toward zero in the stopband, but other types of filters can also be used. After the Butterworth filter in Figure 2.9(c) was applied to the simulated data in Figure 2.9(a), the signals at 8 and 60 Hz were attenuated below the noise. This is apparent in Figure 2.9(d), which shows that the 8 and 60 Hz signals have been significantly mitigated in the power spectrum after filtering the data. The filtered time series in Figure 2.9(e) shows that the 12 Hz sinusoidal signal and the Gaussian noise have been successfully recovered. The red curve overlaid in Figure 2.9(e) corresponds to the simulated 12 Hz signal, and it is not a fit to the filtered data. The residuals, obtained by subtracting the simulated 12 Hz signal from the filtered data, are plotted in gray in Figure 2.9(e).

In this example, I have added a modest amount of Gaussian noise ($\sigma = 0.2$), but this technique can also be applied to data with much higher levels of noise. This demonstration (e.g., see Figure 2.9(e)) shows that there is zero phase distortion in the output signal. Another advantage of this technique is that there are no noticable ripples or artifacts introduced into the output as a result of filtering the data. This is one of the benefits of using this algorithm over other filtering methods, such as Fourier transforming the input data, zeroing frequency bins associated with undesired signals, and then inverse Fourier transforming the filtered frequency domain data. Virtually all frequency domain filtering algorithms require a careful choice of the window function in order to reduce spectral leakage and unwanted ripples in the filtered time domain data.

The IIR digital filtering algorithm that I present here can be readily used to mitigate RFI from channelized radio data (e.g., stored in a digital polyphase filterbank). Undesired periodic signals can be identified by searching for frequencies with excess power in the power spectrum of the Fourier-transformed, undispersed radio data. Once a list of frequencies (and their harmonics) have been compiled, digital filters analogous to the Butterworth filter shown in Figure 2.9(c) can be applied to the time series data stored in each frequency channel of the digital filterbank to attenuate these signals. Since each frequency channel can be filtered independently, this allows multiple frequency channels to be filtered simultaneously. Therefore, this algorithm is highly parallelizable when it is applied to channelized radio data.

I have developed an implementation of this algorithm, `fb_iirfilter.py`, which operates fully in Python. This software package will attenuate a list of user-specified frequencies from each frequency channel of a search-mode digital polyphase filterbank. The user can also specify the filter order and filter width (in units of Hz) to mitigate each of the frequencies specified by the user. The default behavior is to use a first-order Butterworth band-stop filter to mitigate the signals at each of the user-specified frequencies, but this code can be easily adapted to use any arbitrary filter design where the filter coefficients can be calculated. This software package filters each of the frequency channels of the digitial polyphase filterbank in parallel on the CPU, and the user can specify how many frequency channels should be filtered simultaneously using independent threads.

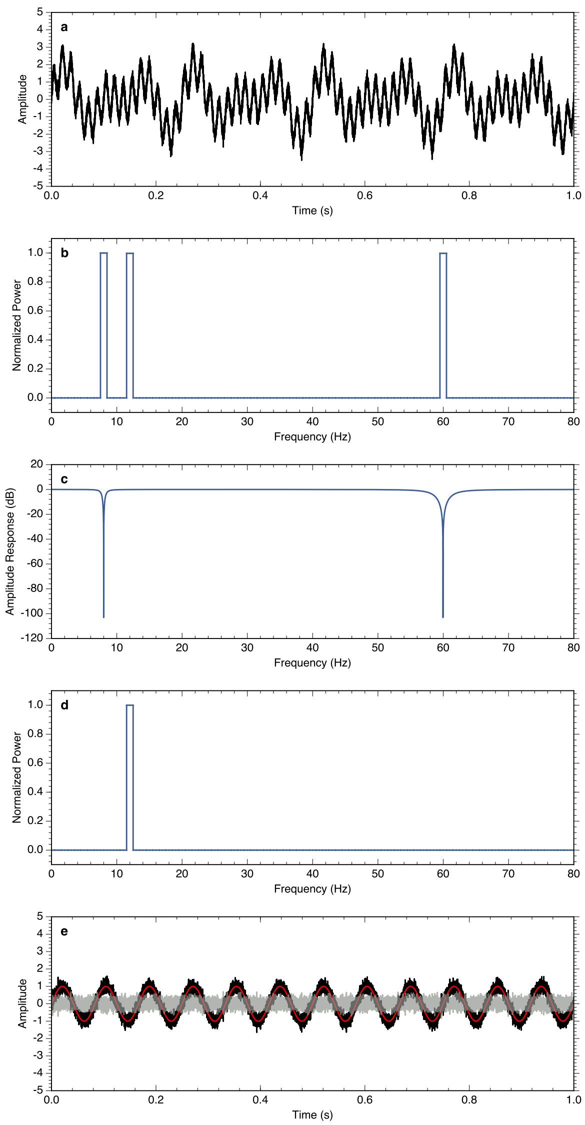

Figure 2.9: **Example application of an infinite impulse response (IIR) response filter, implemented using the direct form II transposed structure, on simulated data.** Panel (a): Simulated data, spanning a total of 1 s, containing a combination of 3 sinusoidal signals with frequencies of 8, 12, and 60 Hz, along with Gaussian $\mathcal{N}(\mu = 0, \sigma = 0.2)$ noise. Panel (b): The normalized power spectrum of the simulated data, which was obtained by calculating a discrete Fourier transform (DFT) of the data shown in panel (a). Panel (c): The frequency response of a first-order Butterworth band-stop filter, which was used to filter out the undesired, periodic signals at 8 and 60 Hz. This Butterworth filter provides > 100 dB of attenuation at 8 and 60 Hz. Panel (d): The normalized power spectrum of the filtered data after applying the Butterworth filter in panel (c) to the data in panel (a). After filtering, the 8 and 60 Hz signals have been attenuated below the noise. Panel (e): The filtered time series showing the recovery of the 12 Hz sinusoidal signal and the Gaussian noise. The red curve corresponds to the simulated 12 Hz signal, and it is not a fit to the filtered data plotted in black. The residuals, calculated by subtracting the simulated 12 Hz signal from the filtered data, are shown in gray.

Next, I demonstrate the effectiveness of applying the `fb_iirfilter.py` software package on radio pulsar data stored in a search-mode digital polyphase filterbank. In this example, I consider an 1 hr observation of the transitional magnetar candidate, PSR J1119–6127 [356, 424], recorded at S-band (2.3 GHz) using the 70 m DSN radio telescope, DSS-43. Throughout this observation, a noise diode, primarily used for flux calibration, is fired on and off continuously at a fundamental frequency of 10 Hz, which causes the power in each frequency channel of the filterbank to abruptly oscillate between a high and low state every 0.1 s. After the radio data are dedispersed at the pulsar's nominal DM of 707.4 pc cm^{-3}, barycentered, and then folded modulo the 0.410 s rotational period of the pulsar, the phaseogram in Figure 2.10(a) shows that the pulsar's periodic emission is concealed by the modulation produced by the noise diode. However, after running the `fb_iirfilter.py` software package to remove the 10 Hz signal, along with all of its harmonics at higher frequencies up to the Nyquist frequency, the effects of the noise diode are very well mitigated and the emission properties of the pulsar can be recovered. The results from folding the barycentered, dedispersed radio data from PSR J1119–6127 after running this algorithm are shown in Figure 2.10(b). The pulsar's periodic radio emission is now clearly visible in the phaseogram shown in the left panel of Figure 2.10(b). This example establishes the effectiveness of this algorithm when applied to real radio pulsar data.

I have developed this algorithm as part of a software suite that is regularly used to reduce radio data recorded with the DSN radio telescopes. This algorithm is typically applied only in cases where there are unwanted sources of periodic RFI that need to mitigated. However, it can also be used on radio data acquired using other radio observatories. In particular, this technique can be used to improve the sensitivity when blindly searching for radio pulsars. Most standard RFI mitigation tools, such as the `rfifind` algorithm available in the available in the `PRESTO` pulsar search software package[m], are unable to remove strong, persistent RFI without masking a significant fraction of the data, which was the case for the example shown in Figure 2.10. I also anticipate that this algorithm will be particularly useful in other areas of time domain astronomy as well, where filtering undesired signals in the time domain is important. I am presently developing a GPU-accelerated implementation of this algorithm that will allow the filtered signal to be calculated more efficiently by parallelizing the direct form II transposed filter structure. Since the direct form II transponse structure has a data dependency (see Figure 2.8), a parallel version of this filtering algorithm is challenging to implement.

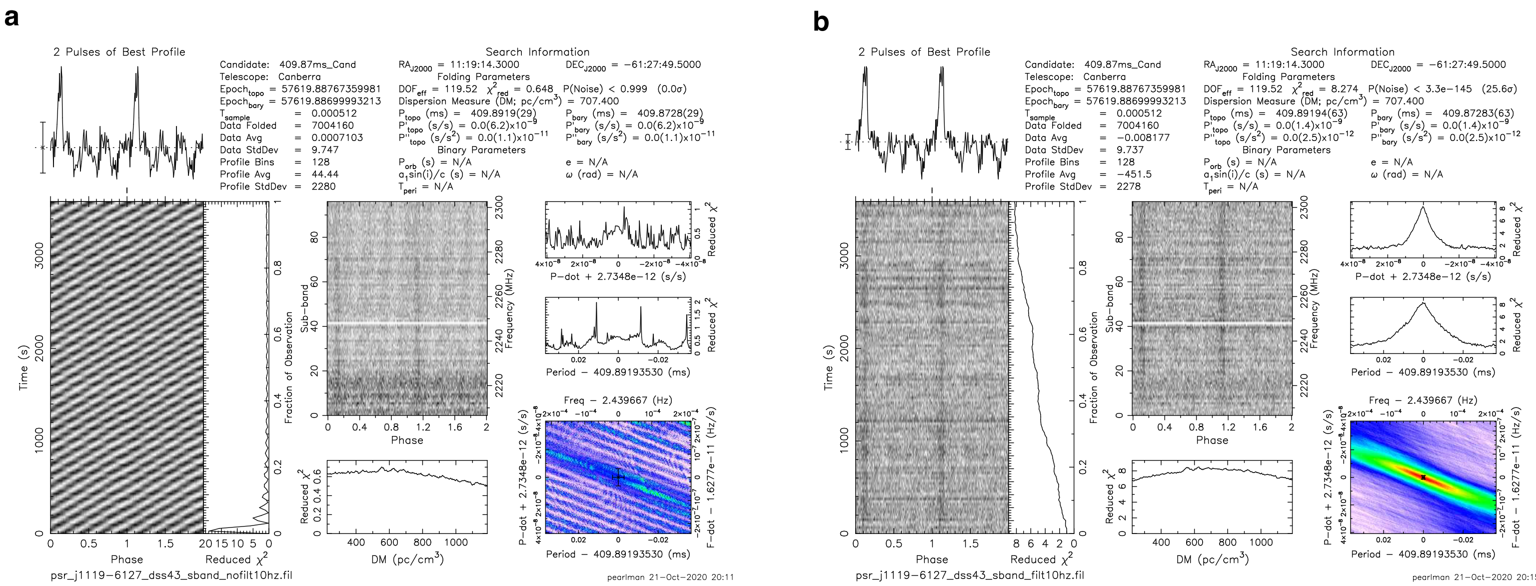

Figure 2.10: **Application of a first-order Butterworth digital filter to mitigate RFI with a fundamental frequency of 10 Hz using radio pulsar data from an observation of PSR J1119–6127 recorded at S-band (2.3 GHz) with the 70 m Deep Space Network (DSN) radio telescope, DSS-43.** The RFI at 10 Hz (and harmonics at higher frequencies) have been mitigated using the `fb_iirfilter.py` software package. The figures in panels (a) and (b) show the results before and after applying the filtering algorithm described in Section 2.4.3.4, respectively. The periodic RFI is clearly mitigated by this filtering algorithm, as shown by the figures in panel (b), which allows the emission properties of the pulsar to be recovered.

Part II: Magnetars and High Magnetic Field Pulsars

The Universe, so far as we can observe it, is a wonderful and immense engine; its extent, its order, its beauty, its cruelty, makes it alike impressive.

— George Santayana

Chapter III

Post-outburst Radio Observations of the High Magnetic Field Pulsar PSR J1119–6127

[356] Majid, W. A.* and **Pearlman, A. B.*** et al. (2017). "Post-outburst Radio Observations of the High Magnetic Field Pulsar PSR J1119–6127." In: *ApJL,* 834:L2. 1612.02868 [astro-ph.HE].

Post-outburst Radio Observations of the High Magnetic Field Pulsar PSR J1119–6127

Walid A. Majid[1,2,*], Aaron B. Pearlman[2,5,6,*], Tatyana Dobreva[1], Shinji Horiuchi[3], Jonathon Kocz[2], Jonas Lippuner[4], and Thomas A. Prince[2,1]

[1] Jet Propulsion Laboratory, California Institute of Technology, Pasadena, CA 91109, USA
[2] Division of Physics, Mathematics, and Astronomy, California Institute of Technology, Pasadena, CA 91125, USA
[3] CSIRO Astronomy and Space Science, Canberra Deep Space Communications Complex, P.O. Box 1035, Tuggeranong, ACT 2901, Australia
[4] TAPIR, Walter Burke Institute for Theoretical Physics, MC 350-17, California Institute of Technology, Pasadena, CA 91125, USA
[5] NDSEG Research Fellow
[6] NSF Graduate Research Fellow
[*] These authors contributed equally to both the analysis and writing of the manuscript.
Corresponding authors: walid.a.majid@jpl.nasa.gov and aaron.b.pearlman@caltech.edu

Abstract

We have carried out high frequency radio observations of the high magnetic field pulsar PSR J1119–6127 following its recent X-ray outburst. While initial observations showed no evidence of significant radio emission, subsequent observations detected pulsed emission across a large frequency band. In this Letter, we report on the initial disappearance of the pulsed emission and its prompt reactivation and dramatic evolution over several months of observation. The periodic pulse profile at S-band (2.3 GHz) after reactivation exhibits a multi-component emission structure, while the simultaneous X-band (8.4 GHz) profile shows a single emission peak.

Single pulses were also detected at *S*-band near the main emission peaks. We present measurements of the spectral index across a wide frequency bandwidth, which captures the underlying changes in the radio emission profile of the neutron star. The high frequency radio detection, unusual emission profile, and observed variability suggest similarities with magnetars, which may independently link the high energy outbursts to magnetar-like behavior.

3.1 Introduction

PSR J1119–6127 is a young radio pulsar with a spin period of $P = 0.410\,\mathrm{s}$ and a period derivative of $\dot{P} = 4.0 \times 10^{-12}$, which is one of the highest reported spin-down rates for a radio pulsar. The pulsar has a characteristic age of 1.6 kyr and an inferred surface dipole magnetic field of $B = 4.1 \times 10^{13}\,\mathrm{G}$, one of the largest among known radio pulsars. PSR J1119–6127 was initially discovered in the Parkes multibeam pulsar survey [77] and is likely associated with the Galactic supernova remnant (SNR) G292.2-0.5 [135] at a distance of 8.4 kpc [87]. This pulsar has been detected in X-rays [205] and gamma-rays [417], and it is also known to glitch [552]. Unusual pulse profile changes, short radio bursts, and irregular timing recoveries [14, 552] have been observed following a glitching event.

On 2016 July 27 13:02:08 UT [578] and 2016 July 28 01:27:51 UT [275], short magnetar-like bursts from PSR J1119–6127 were detected from the *Fermi* Gamma-Ray Burst Monitor (GBM) and the *Swift* Burst Alert Telescope (BAT), respectively. Soon after the announcement of the BAT outburst, the *Swift* X-ray Telescope (XRT) detected a bright X-ray source at the position of this pulsar with pulsed emission at a pulse period of 0.4098627(3) s, consistent with the known rotational period of the pulsar [15]. Prior to the outburst, X-ray pulsed emission was detected only in the soft band (< 2.5 keV). XRT measurements following the outburst showed strong pulsations with a pulsed fraction of 60% across the XRT energy band spanning 2.5–10 keV. A glitch was reported by Archibald et al. [19] using *Swift* XRT, *NuSTAR*, and *Fermi* Large Area Telescope (LAT) data. Archibald et al. [18] observed spectral hardening of PSR J1119–6127 following the high energy outburst, which is suggestive of magnetar-like emission as in the case of the rotation-powered pulsar PSR J1846–0258 [195]. Göğüş et al. [212] uncovered a total of 12 hard X-ray bursts during 2016 July 26–28 using *Fermi* GBM and *Swift* XRT observations and carried out spectral and temporal analyses of the emission.

Adding to this unusual behavior of PSR J1119–6127, immediate radio follow-up of the pulsar at 1465 MHz (L-band) using the Parkes radio telescope on two consecutive days (2016 July 29, starting at 04:59:00 UT and 2016 July 30, starting at 01:08:18 UT) failed to detect radio pulsations, placing an upper limit of 90 μJy [69] on the flux density of this pulsar. Given that the typical flux density at the same frequency is about 1 mJy, with a few percent fluctuations at most, the disappearance of pulsed emission at this frequency implied a reduction of the radio flux by more than a factor of 10 after the high energy outburst. Reactivated radio pulsations were detected on 2016 August 09 03:40:12 UT via continued monitoring of the pulsar at the Parkes telescope [70].

In this Letter, we report our results from high frequency Target of Opportunity (ToO) radio observations of PSR J1119–6127 using the 70 m Deep Space Network (DSN) antenna (DSS-43) in Canberra, Australia, carried out both before and after the return of pulsed emission from this pulsar.

3.2 Radio Observations

Following the reported X-ray outburst, we observed PSR J1119–6127 on four separate epochs with DSS-43. This antenna is equipped with cryogenically cooled dual polarization receivers centered at 2.3 GHz (S-band) and 8.4 GHz (X-band), arranged so that both bands can be used simultaneously with their beams concentric on the sky. The four output signals are then sent to a newly commissioned ultra-wideband pulsar machine, which was specially developed to meet the requirements of searching for short period pulsars at high frequencies with wide bandwidths. The pulsar machine is a digital filterbank system that is capable of processing 16 independent input bands, each up to 1 GHz wide. Spectra for each band have 1024 channels and can be produced with time sampling as short as 32 μs. These are then individually recorded to disk for further processing.

In the observations reported here, we used the pulsar machine with four input bands and simultaneously recorded both S/X-bands in dual circular polarization mode. On-off measurements of a standard calibrator, Hydra A (3C218), were carried out at the start of each observation, which yielded an estimated system temperature of 25/40 K (20% error) at S/X-band. The antenna gain was ~1 K/Jy. The data used in this study spanned 96 and 480 MHz at S-band and X-band, respectively. The data were recorded with a frequency channel spacing of 1 MHz and time sampling of 512 μs at 16 bits per sample. In Table 3.1, we list all four observing epochs with their start times and durations. While epochs 1 and 2 were carried out prior to the reported reactivation of radio pulsed emission [70], the latter two epochs were taken after this reactivation.

As reported in Majid et al. [355], observations during the initial two epochs failed to detect any evidence of either periodic emission or single pulses. Using the calibration data and system configuration, we obtained upper limits of 0.14/0.06 mJy for pulsed emission at S/X-band. The Australia Telescope National Facility (ATNF) pulsar catalog[b] [365] lists flux densities of 0.80/0.44 mJy at 1.4 and 3 GHz, respectively, yielding a relatively flat spectral index of –0.8 over this frequency range. Using this spectral index, the expected flux densities at S/X-band before the X-ray outburst were 0.6/0.2 mJy, respectively. We inferred that the pulsed emission at these higher frequencies during the first two epochs was suppressed by a factor of 3 or more at S-band and X-band following the magnetar-like outburst event. We also searched for single pulses with widths up to 130 ms and detected none with a signal-to-noise ratio (S/N) above 6.0. We place an upper limit of 45/20 mJy on the flux densities of bright single pulses at S/X-band.

Periodicity and single pulse searches were also performed using radio observations during epochs 3 and 4 after the pulsed radio emission was reactivated. We first searched the data for evidence of narrowband and wideband radio frequency interference (RFI) using mild filtering criteria, which required only 5% of the data to be discarded. The contaminated portion of the data was masked and removed from our analysis using the `rfifind` tool from the `PRESTO` pulsar search package[b] [456]. We also corrected for the bandpass slope across the frequency band and removed the baseline using a high-pass filter with a time constant of 1 s. The data were then dedispersed using a dispersion measure (DM) of 707.4 pc cm^{-3} [224]. A problem with the calibration system in epoch 3 prevented us from using data from the RCP (right circular polarization) channel at S-band. For consistency and to avoid introducing any systematic errors, we only used a single polarization channel for all epochs in the analysis presented here. In Section 3.3, we present the results of periodicity searches and the discovery of single pulses at S-band during these latter epochs.

Table 3.1: **Radio Observations of PSR J1119–6127 with the DSN**

Epoch	Start Time[a] (yyyy-mm-dd hh:mm:ss)	Start Time[a] (MJD)	Duration (hr)
1	2016-07-31 23:41:12	57600.98694	0.6
2	2016-08-01 23:37:12	57601.98417	3.7
3	2016-08-19 18:27:34	57619.76914	5.3
4	2016-09-01 17:31:34	57632.73025	3.2

[a] Start time of the observation (UTC).

3.3 Results

3.3.1 Pulse Profiles and Spectral Index

Periodicity searches were performed using the PRESTO pulsar search software package[m] [456] near the spin period of the pulsar, using an updated ephemeris provided by Archibald et al. [18]. We observed bright pulsed emission at S-band during epochs 3 and 4 after the reported reactivation of radio emission at L-band [70]. The best barycentric pulse periods that we find are 409.87281(3) ms and 409.88631(3) ms from S-band observations during epochs 3 and 4, respectively. Pulse profiles were obtained after barycenteric and DM corrections were applied at each epoch. In Figure 3.1, we show the detection of PSR J1119–6127 at S-band and X-band during epochs 3 and 4 after the radio emission was reactivated. The profiles during epoch 3 and epoch 4 were not aligned since the barycentric pulse period changed between the two epochs.

The pulse profile of PSR J1119–6127 had been observed to be single-peaked at 1.37 GHz [77] before the recent high-energy outburst. However, the S-band pulse profile during epoch 3 in Figure 3.1(a) shows a triple-peaked structure, with two prominent peaks following a precursor emission region. We continued to observe significant changes in the profile shape on a timescale of days. By epoch 4, the S-band pulse profile in Figure 3.1(c) had evolved into a strong single-peak, with two of the peaks from epoch 3 diminishing in strength. We marginally detected the pulsar at X-band over a 5 hr observing period in epoch 3, while significant X-band pulsed emission was observed during epoch 4, as shown in Figures 3.1(b) and 3.1(d), respectively.

In Table 3.2, we provide a list of flux density and spectral index measurements at S-band and X-band during epochs 1–4. We estimate the observed S-band flux densities from the LCP (left circularly polarized) channel taken on epochs 3 and 4 to be $S_{2.3} = 1.8(4)$ mJy and $S_{2.3} = 2.0(4)$ mJy, respectively. The S-band flux density

Table 3.2: **Flux Density and Spectral Index Measurements of PSR J1119–6127**

Epoch	$S_{2.3}$[a] (mJy)	$S_{8.4}$[b] (mJy)	α[c]
1	< 0.4(1)	< 0.24(5)	⋯
2	< 0.14(3)	< 0.06(1)	⋯
3	1.8(4)	0.10(2)	–2.2(2)
4	2.0(4)	0.18(4)	–1.9(2)

[a] Mean flux density at 2.3 GHz.
[b] Mean flux density at 8.4 GHz.
[c] Spectral index between 2.3 GHz and 8.4 GHz.

has increased by at least a factor of 10 over the 2-week period of inactivity in pulsed emission. From observations taken on epoch 3, we estimate a mean X-band flux density of $S_{8.4} = 0.10(2)$ mJy, yielding a spectral index of $\alpha = –2.2(2)$, where $S_\nu \propto \nu^\alpha$. Data taken on epoch 4 show an increase in X-band flux density, $S_{8.4} = 0.18(4)$ mJy, yielding a slightly flatter spectral index of $\alpha = –1.9(2)$. The ATNF pulsar catalog[b] [365] reports a spectral index of –0.8 based on flux density measurements at 1.4 and 3 GHz prior to the outburst. To our knowledge, there are no reported flux density measurements of PSR J1119–6127 at or near 8 GHz prior to the recent outburst. If we assume that the reported spectral index is valid up to ~8 GHz frequency, then our measurements indicate a steepening of the spectral index. Our measured spectral index values are in the range expected from the population of radio pulsars, which has a mean index of –1.4 [35], with standard deviation of order unity.

3.3.2 Single Pulses

We present an analysis of the distribution of S-band single pulses during epochs 3 and 4 after the radio emission was reactivated. The raw data for each observation epoch in Table 3.1 were barycentered and dedispersed using a DM of 707.4 pc cm^{-3} after applying a mask to remove RFI. The dedispersed data were then smoothed, normalized, and searched using a matched filtering algorithm, where the full resolution data was convolved with boxcar kernels of varying widths. We searched for individual, bright pulses [552] with widths up to 100 ms and S/Ns above 4.0 in the time domain using the `PRESTO` pulsar search software package[m] [456]. `PRESTO` calculates the S/N of a candidate pulse using:

$$\mathrm{S/N} = \frac{\sum_i (S_i - M)}{\sigma\sqrt{w}}, \tag{3.1}$$

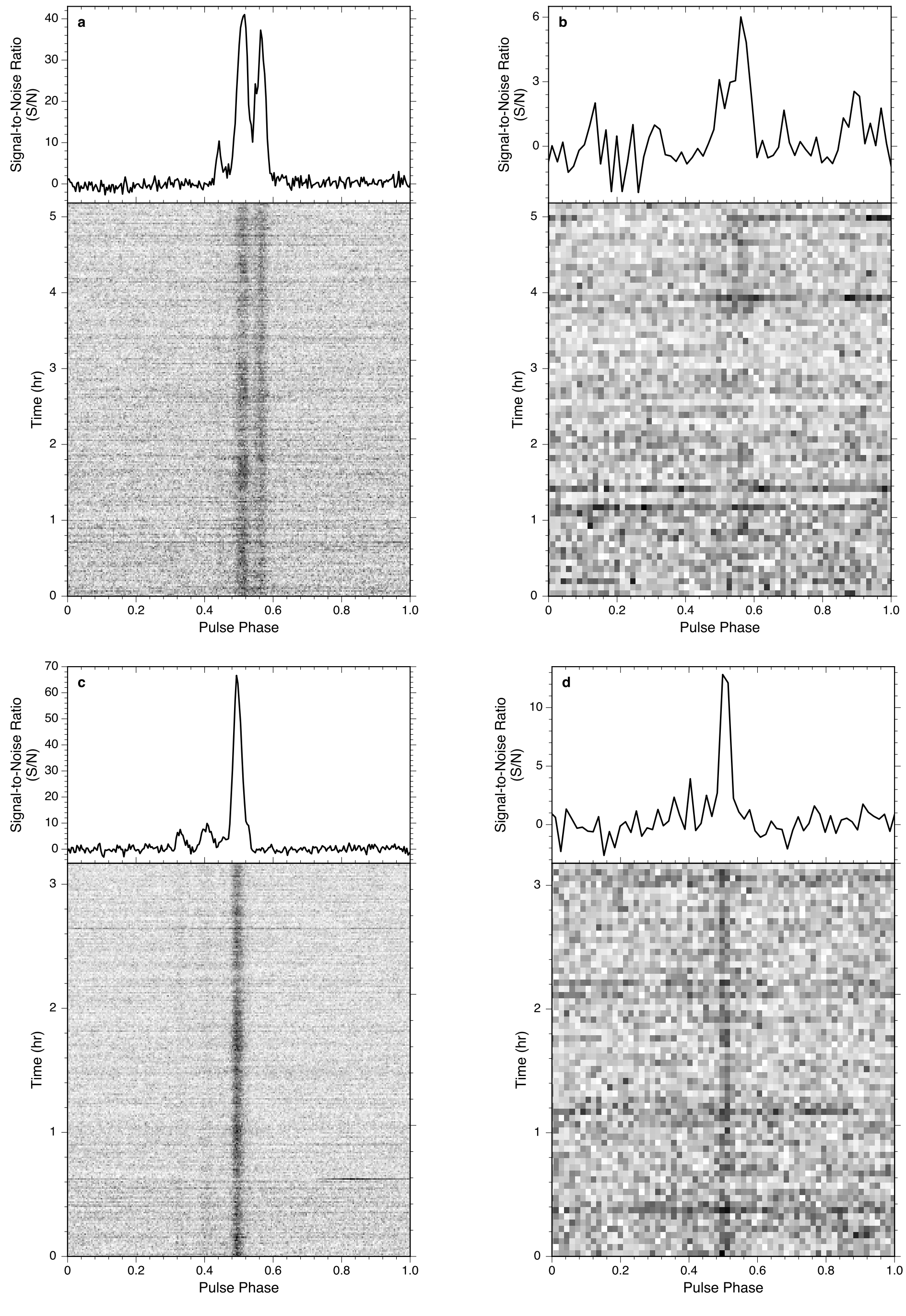

Figure 3.1: **Pulse profiles of PSR J1119–6127 during epoch 3 (top row) and epoch 4 (bottom row) at S-band (left column) and X-band (right column).** The top panels show the integrated pulse profiles in units of signal-to-noise ratio (S/N), and the grayscale bottom panels show the strength of the pulsations as a function of phase and time, where darker bins correspond to stronger pulsed emission. The number of phase bins is 256/64 in the S/X-band profiles.

where the sum is over successive bins S_i in the boxcar function, M is local mean, σ is the root mean square (RMS) noise after normalization, and w is the boxcar width in number of bins. The data were already normalized such that $M \approx 0$ and $\sigma \approx 1$. This definition of S/N has the advantage that it gives approximately the same result regardless of the downsampling factor used for the time series [153].

Single pulses that were found using a DM of 707.4 pc cm^{-3}, which coincided with events obtained without correcting for dispersion, were removed from the candidate list. We also excluded candidates that were falsely identified as a result of our procedure for masking RFI. We chose to restrict our candidate list to pulses with widths less than 16 ms since many of the single pulses with larger widths were determined to be RFI events from their dynamic spectra, which showed the strength of the pulses in frequency and time. No bright single pulses were detected in epochs 1 and 2 before the reappearance of the pulsed radio emission or at X-band during any of the epochs in Table 3.1.

We find a statistically significant population of S-band single pulses during epochs 3 and 4 near the main emission peaks of the pulse profiles. In Figure 3.2, we show the distribution of single pulses in pulse phase using the measured pulse periods from each epoch. With a S/N threshold of 4.0 in Figure 3.2(a) and Figure 3.2(c), which is equivalent to a peak flux density of 0.46 Jy, we detect 573 ± 127 and 1040 ± 73 events above the background during epochs 3 and 4, respectively. This corresponds to a single pulse event rate of 1.2% and 3.7% per stellar rotation during epochs 3 and 4, respectively. The uncertainties were determined from fitting the background rate independently of pulse phase. Figure 3.2(b) and Figure 3.2(d) show single pulses with S/Ns above 4.5 and peak flux densities greater than 0.51 Jy. Using this selection criteria, we find 148 ± 20 and 393 ± 11 single pulses above the background during epochs 3 and 4, respectively, corresponding to a single pulse event rate of 0.3% and 1.4% per stellar rotation during the two epochs. From these event rates, and depending on the chosen value for the S/N threshold cut, we estimate a factor of 3–4 increase in the overall single pulse emission rate in epoch 4 compared to epoch 3. Time of arrivals (ToAs), pulse widths, S/Ns, and false alarm probabilities (FAPs) of individual, bright single pulses in these epochs and additional epochs following these observations will be presented in a later paper (Pearlman et al., in preparation).

3.4 Discussion

PSR J1119–6127 is clearly a transition object, i.e. a high magnetic field neutron star that is normally a rotation-powered pulsar in radio and X-rays, but also shows transient magnetar-like behavior. Such behavior is unlikely to be powered solely by rotation, but also by the release of stored magnetic energy [18]. This was previously suggested because of its unusual pulsed X-ray emission [206], which was hard to reconcile with the thermal emission from the rotation-powered pulsar. This is now dramatically confirmed by clear magnetar-like outbursts [18, 212]. PSR J1119–6127 now joins PSR J1846–0258 as a high magnetic field pulsar with transient magnetar-like behavior [263, 404]. PSR J1119–6127 is similar to PSR J1846–0258 in terms of its magnetic field strength and young characteristic age. However, while PSR J1846–0258 is radio quiet, PSR J1119–6127 shows radio emission both in its "quiescent" rotation-powered state, as well as in its magnetar-like state.

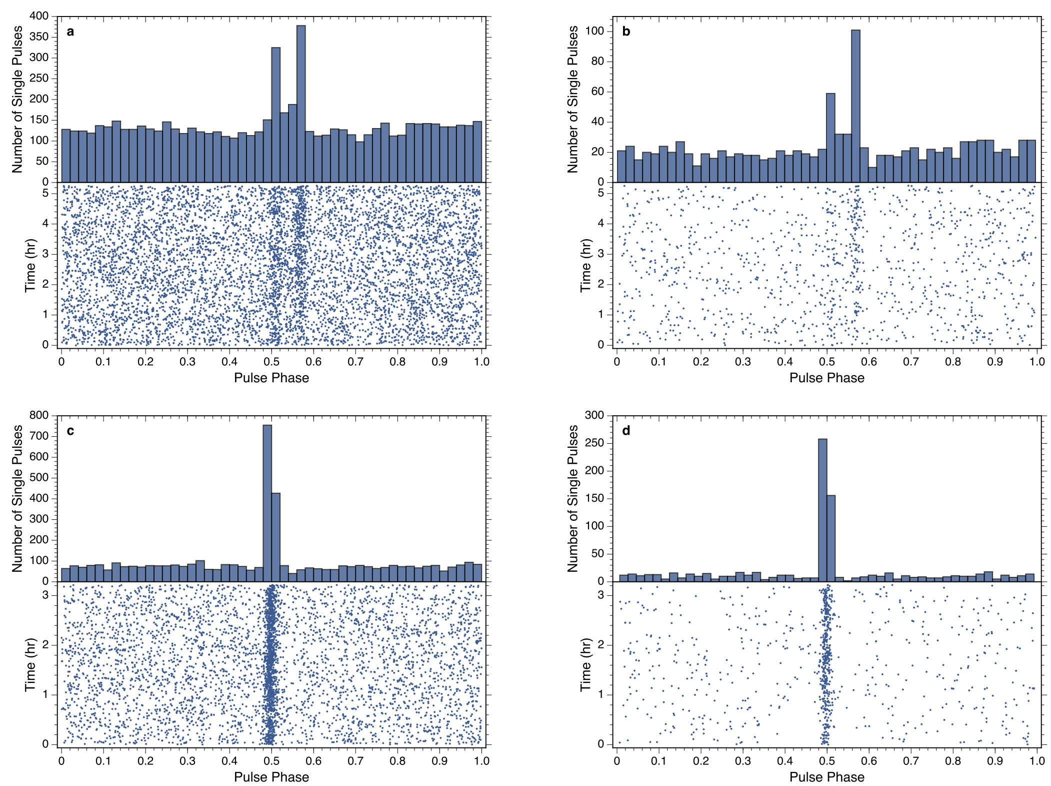

Figure 3.2: **Distribution of S-band single pulses in pulse phase during epoch 3 (top row) and epoch 4 (bottom row).** The top panels of each figure show the number of single pulses detected in each region of the pulse profile, and the bottom panels show the population of single pulses throughout the observation. We show S-band single pulses with S/Ns above 4.0 in (a) and (c), and single pulses with S/Ns above 4.5 are shown in (b) and (d).

Of particular interest is the observation of multi-peaked S-band radio emission shortly after the outburst. In its normal rotation-powered state, PSR J1119–6127 has a single-peaked pulse profile at 1.4 GHz [77] that is aligned with a single-peaked [206], broad profile in the 0.5–2 keV emission band, which is consistent with thermal emission from the polar cap. In γ-rays, PSR J1119–6127 also shows a single-peaked profile consistent with outer gap emission [417]. Our observation of multi-component emission at S-band shortly after the outburst is indicative of a more complex emission geometry and possibly non-dipolar field components near the neutron star surface. Multi-component emission from PSR J1119–6127 was seen only once before and immediately after one of PSR J1119–6127's strong glitches [552], observed only once in 12 years of monitoring. Weltevrede et al. [552] concluded that this emission behavior was extremely rare since it was only observed in 0.1% of their inspected data. In contrast, our observations during epochs 3 and 4 show multiple-peaked emission lasting more than a week. Remarkably, observations in epoch 4 show dramatic changes in both S-band and X-band. The S-band profile seems to be returning to a single peak with reduced emission in the first two emission regions. The X-band emission in epoch 4 is brighter than the previous X-band detection in epoch 3 and seems to be singly peaked.

Weltevrede et al. [552] also reported the detection of a handful of individual pulses during the glitch recovery phase in 2011. We also observe multiple individual pulses in both observations after the reactivation of pulsed radio emission. Additional high frequency radio observations following epoch 4, which are not presented in this Letter, show that the pulse profile at S-band is still evolving. We are continuing to observe PSR J1119–6127 and are finding that the pulse profile is slowly returning to a single-peaked emission structure. These results, along with a detailed study of the mode changes, will be reported in a later work (Pearlman et al., in preparation).

Of the 26 known magnetars [408], 4 have been detected in the radio band: XTE J1810–197 [78], 1E 1547.0–5408 [80], PSR J1622–4950 [313], and PSR J1745–2900 [491], and they all show variability in their pulse profiles, radio flux densities, and spectral indices. Furthermore, both XTE J1810–197 and 1E 1547.0–5408 have exhibited sudden appearance and then fading of their radio emission over timescales of days to months [79, 83]. In addition to an evolving pulse profile, we also report a variable emission flux at X-band showing an increase of roughly a factor of 2 during epoch 4 compared to the observed flux during epoch 3. A similar factor of 3–4 increase is also seen in the single pulse event rate at S-band between these two epochs.

In this respect, PSR J1119–6127 shares many of the properties of the known radio magnetars. However, while the spectral indices of radio magnetars tend to be quite flat, the spectral index of PSR J1119–6127 is more similar to the majority of rotation-powered pulsars, perhaps indicative of the transitional nature of this object.

One possible explanation for the transient radio emission seen in magnetars and similar behavior observed from high magnetic field pulsars, such as PSR J1119–6127, is the dependence of emission on the conditions of the magnetosphere [319, 397]. In this model, toroidal oscillations in the star are excited during an outburst, which then modify the magnetospheric structure and allow radio emission to be produced. Lin et al. [319] suggested that, after a glitch, stellar oscillations enlarge the polar cap angle, and hence also the size of the radiation cone, resulting in multi-component pulse profiles seen along the line of sight to the pulsar. The proposed explanation for such variability is intriguing since the recent outburst of PSR J1119–6127 and some outbursts from soft gamma repeaters (SGRs) and anomalous X-ray pulsars (AXPs) have been associated with glitches [158, 266]. More detailed simulations and long-term monitoring of the pulsar are needed to quantitatively investigate this model.

3.5 Conclusions

We have carried out radio observations of PSR J1119–6127 following its recent X-ray outburst. While initial observations failed to detect the presence of pulsed emission, subsequent observations two weeks later show bright detections of the pulsar at S-band and a significant detection at X-band as the S-band pulse profile returns to a single-peaked shape. From these measurements, we were able to estimate a spectral index over a relatively wide range of radio wavelengths. We also detected an unusual multiple-peaked radio profile and single pulse events at S-band. Since this emission behavior is clearly transitory, further radio monitoring of the source is needed to study both the long-term evolution of the pulse profile and the erratic single pulse emission.

3.6 Acknowledgments

We thank Professor Vicky Kaspi and Robert Archibald for alerting us to the initial outburst and for providing an ephemeris for PSR J1119–6127. We also thank Professor Vicky Kaspi for a careful reading of the manuscript and detailed comments. We acknowledge support from the DSN team for scheduling the observations.

A.B.P. acknowledges support by the Department of Defense (DoD) through the National Defense Science and Engineering Graduate (NDSEG) Fellowship Program and by the National Science Foundation (NSF) Graduate Research Fellowship under Grant No. DGE-1144469. J.L. acknowledges support from the Jet Propulsion Laboratory Graduate Fellowship program.

A portion of this research was performed at the Jet Propulsion Laboratory, California Institute of Technology under a Research and Technology Development Grant and under a contract with the National Aeronautics and Space Administration. U.S. government sponsorship is acknowledged.

Chapter IV

Pulse Morphology of the Galactic Center Magnetar PSR J1745–2900

[422] **Pearlman, A. B.*** et al. (2018). "Pulse Morphology of the Galactic Center Magnetar PSR J1745–2900." In: *ApJ,* 866:160. 1809.02140 [astro-ph.HE].

Pulse Morphology of the Galactic Center Magnetar PSR J1745–2900

Aaron B. Pearlman[1,4,5,*], Walid A. Majid[2,1,*], Thomas A. Prince[1,2], Jonathon Kocz[1], and Shinji Horiuchi[3]

[1] Division of Physics, Mathematics, and Astronomy, California Institute of Technology, Pasadena, CA 91125, USA

[2] Jet Propulsion Laboratory, California Institute of Technology, Pasadena, CA 91109, USA

[3] CSIRO Astronomy and Space Science, Canberra Deep Space Communications Complex, P.O. Box 1035, Tuggeranong, ACT 2901, Australia

[4] NDSEG Research Fellow

[5] NSF Graduate Research Fellow

[*] Lead author of the manuscript.

Corresponding author: aaron.b.pearlman@caltech.edu

Abstract

We present results from observations of the Galactic Center magnetar, PSR J1745–2900, at 2.3 and 8.4 GHz with the NASA Deep Space Network 70 m antenna, DSS-43. We study the magnetar's radio profile shape, flux density, radio spectrum, and single pulse behavior over a ~1 year period between MJDs 57233 and 57621. In particular, the magnetar exhibits a significantly negative average spectral index of $\langle\alpha\rangle = -1.86 \pm 0.02$ when the 8.4 GHz profile is single-peaked, which flattens considerably when the profile is double-peaked. We have carried out an analysis of single pulses at 8.4 GHz on MJD 57479 and find that giant pulses and pulses with multiple emission components are emitted during a significant number of rotations. The resulting single pulse flux density distribution is incompatible with a log-normal distribution. The typical pulse width of the

components is ~1.8 ms, and the prevailing delay time between successive components is ~7.7 ms. Many of the single pulse emission components show significant frequency structure over bandwidths of ~100 MHz, which we believe is the first observation of such behavior from a radio magnetar. We report a characteristic single pulse broadening timescale of $\langle\tau_d\rangle = 6.9 \pm 0.2$ ms at 8.4 GHz. We find that the pulse broadening is highly variable between emission components and cannot be explained by a thin scattering screen at distances $\gtrsim 1$ kpc. We discuss possible intrinsic and extrinsic mechanisms for the magnetar's emission and compare our results to other magnetars, high magnetic field pulsars, and fast radio bursts (FRBs).

4.1 Introduction

Magnetars are a class of slowly rotating neutron stars, with spin periods between ~2 and 12 s, that are thought to be powered by their decaying ultra-strong magnetic fields [165, 524, 525]. More than ~2600 pulsars have now been found, but only 31 magnetars or magnetar candidates are currently known [264] (see the McGill Magnetar Catalog[n] [408]). Most of these are Galactic magnetars, many of which are located in the inner region of the Milky Way [408]. Typical surface dipolar magnetic fields of magnetars range between $\sim 10^{14}$ and 10^{15} G, which exceed the $\sim 10^{12}$ G fields of rotation-powered pulsars. Transient X-ray and gamma-ray outbursts are hallmark features of magnetar emission and have led to the discovery of the majority of new magnetars.

PSR J1745–2900 is one of only four magnetars with detectable radio pulsations [78, 80, 169, 312, 491]. It is unique among the population of magnetars because of its close proximity to the $4 \times 10^6\, M_\odot$ black hole, Sagittarius A* (Sgr A*), at the Galactic Center (GC). The discovery of a rare magnetar near the GC may suggest that the environment around Sgr A* is more conducive for magnetar formation [156]. Observations of PSR J1745–2900 also provide a valuable probe of the interstellar medium (ISM) near the GC (e.g., see [62, 155, 169, 498]), which may shed light on why previous searches for radio pulsars within ~10 arcmin of Sgr A* have been unsuccessful [34, 152, 170, 258, 288, 349, 494]. It is widely believed that these searches may have been hindered by scattering-induced pulse broadening of the pulsed radio emission as a result of large electron densities along the line of sight.

[n] See http://www.physics.mcgill.ca/~pulsar/magnetar/main.html.

The GC magnetar was serendipitiously discovered by the *Swift*[o] Burst Alert Telescope (BAT) following an X-ray flare near Sgr A* and is the most recent addition to the radio magnetar family [169, 274, 491]. Subsequent observations with the *NuSTAR* X-ray telescope uncovered X-ray pulsations at a period of $P = 3.76$ s and a spin-down rate of $\dot{P} = 6.5 \times 10^{-12}$ s s^{-1} [396]. Assuming a dipolar magnetic field, this implies a surface magnetic field of $B_{\rm surf} \approx 1.6 \times 10^{14}$ G, spin-down luminosity of $\dot{E} \approx 5 \times 10^{33}$ erg s^{-1}, and characteristic age of $\tau_{\rm c} \approx 9$ kyr. A series of *Chandra* and *Swift* observations were later performed, which localized the magnetar to an angular distance of 2.4 arcsec from Sgr A* [465]. The proper motion of PSR J1745–2900 was measured relative to Sgr A* using the Very Long Baseline Array (VLBA), which yielded a transverse velocity of 236 km s^{-1} at a projected separation of 0.097 pc [63].

Radio pulsations have been detected from PSR J1745–2900 at frequencies between 1.2 and 291 GHz, and its radio spectrum is relatively flat [169, 498, 532, 533]. Multifrequency radio observations established that the GC magnetar has the largest dispersion measure (DM = 1778 ± 3 pc cm^{-3}) and Faraday rotation measure (RM = –66,960 ± 50 rad m^{-2}) of any known pulsar [169]. Schnitzeler et al. [475] found that its RM had increased to –66,080 ± 24 rad m^{-2} approximately 2 years later, and recent measurements by Desvignes et al. [155] showed that its linear polarization fraction and RM were both significantly variable over a time span of roughly 4 years.

Single pulse radio observations of PSR 1745–2900 have been performed at 8.7 GHz by Lynch et al. [335] with the Green Bank Telescope (GBT) and at 8.6 GHz by Yan et al. [574] using the Shanghai Tian Ma Radio Telescope (TMRT). Lynch et al. [335] showed that the magnetar experienced a transition from a stable state to a more erratic state early in 2014. During this period, significant changes in the magnetar's flux density, radio profile shape, and single pulse properties were observed. Yan et al. [574] presented single pulse observations between 2014 June 28 and October 13, and they performed an analysis of pulses detected during an erratic period on MJD 56836. Yan et al. [573] recently reported on single pulse observations at 3.1 GHz with the Parkes radio telescope, which showed that the magnetar was in a stable state between MJDs 56475 and 56514.

Temporal scatter broadening measurements were performed by Spitler et al. [498] using single pulses and average pulse profiles from PSR J1745–2900 between

[o] The *Swift* Gamma-Ray Burst Explorer was renamed the "Neil Gehrels *Swift* Observatory" in honor of Neil Gehrels, *Swift's* principal investigator.

1.19 and 18.95 GHz. They derived a pulse broadening spectral index of $\alpha_d = -3.8 \pm 0.2$ and a pulse broadening timescale of $\tau_d = 1.3 \pm 0.2$ s at 1 GHz, which is several orders of magnitude lower than the value predicted by the NE2001 electron density model [124]. Observations with the VLBA and phased array of the Karl G. Jansky Very Large Array (VLA) were subsequently performed to measure the angular broadening of PSR J1745–2900 [62]. Bower et al. [62] argued that the observed scattering is consistent with a single thin screen at a distance of $\Delta_{\mathrm{GC}} = 5.8 \pm 0.3$ kpc from the GC. A secondary scattering screen, located ~0.1 pc in front of the magnetar, was recently proposed by Desvignes et al. [155] to explain the magnetar's depolarization at low radio frequencies.

In this paper, we present results from simultaneous observations of PSR J1745–2900 at 2.3 and 8.4 GHz with the NASA Deep Space Network (DSN) antenna, DSS-43. The observations and data reduction procedures are described in Section 4.2. In Section 4.3, we provide measurements of the magnetar's profile shape, flux density, and radio spectrum. We also carry out a detailed single pulse analysis at 8.4 GHz and study the morphology of individual pulses from the magnetar. We discuss and summarize our results in Section 4.4. In this section, we consider the implication of our results on scattering through the ISM toward the GC. We also compare the emission properties of the GC magnetar to other magnetars and high magnetic field pulsars. Lastly, we describe the similarities between the single pulse emission from this magnetar and fast radio bursts (FRBs).

4.2 Observations

High frequency radio observations of PSR J1745–2900 were carried out during four separate epochs between 2015 July 30 and 2016 August 20 using the NASA DSN 70 m antenna (DSS-43) in Tidbinbilla, Australia. A detailed list of these radio observations is provided in Table 4.1. Simultaneous dual circular polarization S-band and X-band data, centered at 2.3 and 8.4 GHz, were recorded during each epoch with a time sampling of 512 μs. The data were channelized, with a frequency spacing of 1 MHz, in a digital polyphase filterbank with 96 and 480 MHz of bandwidth at S-band and X-band, respectively. Polarimetric measurements are not provided since data from a polarimetry calibrator was unavailable.

These observations were performed at elevation angles between 12° and 21°, and the antenna gain was ~1 K/Jy. The total system temperature was calculated at S/X-band

Table 4.1: **Radio Observations of PSR J1745–2900**

Epoch	Date[a]	Time[b] (hh:mm:ss)	Date[b] (MJD)	Duration (hr)	$T_{\rm rec} + T_{\rm atm}$[c] (K)	$T_{\rm rec} + T_{\rm atm}$[d] (K)
1	2015 Jul 30	16:15:00	57233.67708	1.2	34 ± 5	24 ± 4
2	2015 Aug 15	15:25:22	57249.64262	1.3	35 ± 5	25 ± 4
3	2016 Apr 01	12:35:42	57479.52479	0.4	38 ± 6	29 ± 4
4	2016 Aug 20	15:26:28	57620.64338	1.0	36 ± 5	27 ± 4

[a] Start date of the observation (UTC).
[b] Start time of the observation (UTC).
[c] Sum of the instrumental and atmospheric components of the system temperature at S-band.
[d] Sum of the instrumental and atmospheric components of the system temperature at X-band.

for each epoch using:

$$T_{\rm sys} = T_{\rm rec} + T_{\rm atm} + T_{\rm GC}, \tag{4.1}$$

where $T_{\rm rec}$ is the receiver noise temperature, $T_{\rm atm}$ is the atmospheric contribution, and $T_{\rm GC}$ is the contribution from the GC. The atmospheric component was determined from the elevation angle, atmospheric optical depth, and atmospheric temperature during each epoch. In Table 4.1, we list the sum of the instrumental and atmospheric components of the system temperature for each epoch at S/X-band, where we have assumed 15% uncertainties on these values. We modeled $T_{\rm GC}$ using the following empirical relationship derived by Rajwade et al. [451] from calibrated continuum maps of the GC [301]:

$$T_{\rm GC}(\nu) = 568 \left(\frac{\nu}{\rm GHz}\right)^{-1.13} {\rm K}, \tag{4.2}$$

where ν denotes the observing frequency. At the S/X-band central frequencies, the GC adds 227/52 K to the system temperature, giving an average system temperature of 262(3)/78(2) K.

4.2.1 Data Reduction

The raw filterbank data are comprised of power spectral measurements across the band and can include spurious signals due to radio frequency interference (RFI). The first step in the data reduction procedure was to remove data that were consistent with either narrowband or wideband RFI. We searched the data using the `rfifind` tool from the `PRESTO` pulsar search software package[m] [456], which produced a mask for filtering out data identified as RFI and resulted in the removal of less than 3% of the data from each epoch.

Next, we flattened the bandpass response and removed low frequency variations in the baseline of each frequency channel by subtracting the moving average from each data point, which was calculated using 10 s of data around each time sample. The sample times were corrected to the solar system barycenter using the `TEMPO` timing analysis software[p], and the data were then incoherently dedispersed at the magnetar's nominal DM of 1778 pc cm^{-3}.

4.3 Results

4.3.1 Average Pulse Profiles

A blind search for pulsations was performed between 3.6 and 3.9 s using the `PRESTO` pulsar search software package[m] [456]. Barycentric period measurements are provided in Table 4.2 and were derived from the X-band data, where the pulsations were strongest. Average S-band and X-band pulse profiles, shown in Figure 4.1, were obtained after applying barycentric corrections, dedispersing at the magnetar's nominal DM, and folding the data on the barycentric periods given in Table 4.2. These pulse profiles were produced by combining data from both circular polarizations in quadrature. The top panels show the integrated pulse profiles in units of peak flux density and signal-to-noise ratio (S/N). The S/N was calculated by subtracting the off-pulse mean from the pulse profiles and dividing by the off-pulse root mean square (RMS) noise level, $\sigma_{\rm off}$. The bottom panels show the strength of the pulsations as a function of time and pulse phase. The pulse profiles have been aligned such that the peak of the X-band pulse profile lies at the center of the pulse phase window.

The X-band pulse profiles in Figure 4.1 display a narrow emission component during each epoch, and the S-band pulse profiles from epochs 1–3 show broader peaks that are nearly coincident in phase with the X-band peaks. S-band pulsations were only marginally detected during epoch 4. From Figure 4.1, we see that the pulsed emission was stronger at X-band compared to S-band during epochs 2–4, but epoch 1 showed slightly more significant pulsations at S-band. The pulsations also became noticably fainter toward the end of epoch 1, and we found that the pulsed emission was weaker in the right circular polarization (RCP) channel compared to the left circular polarization (LCP) channel during this particular epoch.

[p] See http://tempo.sourceforge.net.

Table 4.2: **Barycentric Period Measurements of PSR J1745–2900**

Epoch	P (s)	$\dot{P}$ ($\mathrm{s\,s^{-1}}$)	T_{ref}[a] (MJD)
1	3.76531(1)	$< 2 \times 10^{-8}$	57233.682318131
2	3.765367(8)	$< 1 \times 10^{-8}$	57249.646691855
3	3.76603(2)	$< 1 \times 10^{-7}$	57479.527055687
4	3.76655(1)	$< 2 \times 10^{-8}$	57620.646961446

Period measurements were derived from the barycentered X-band data.

[a] Barycentric reference time of period measurements.

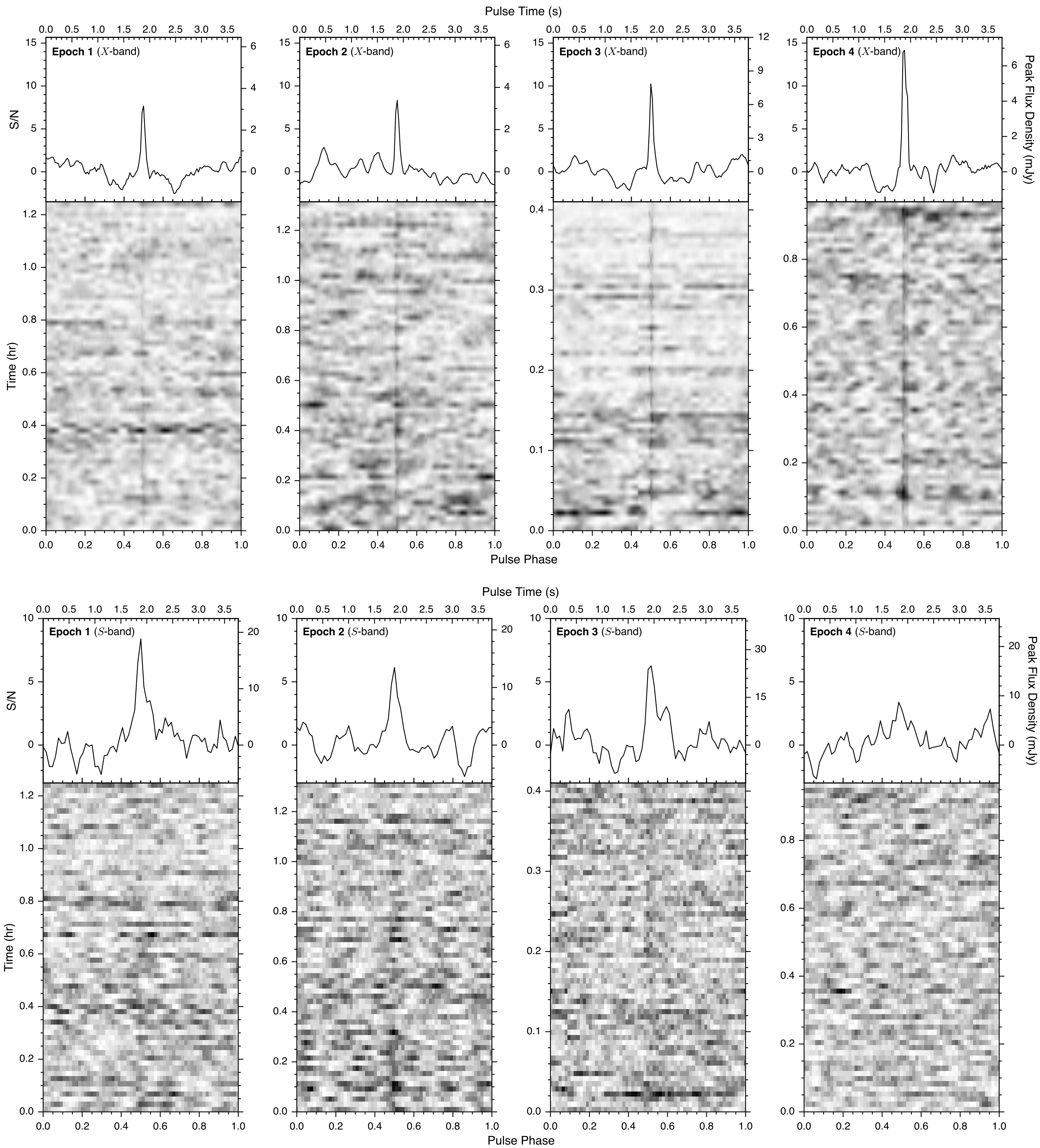

Figure 4.1: **Average pulse profiles of PSR J1745–2900 at (top row) X-band and (bottom row) S-band during epochs 1–4 after combining data from both circular polarizations in quadrature.** The data were folded on the barycentric period measurements given in Table 4.2. The top panels show the integrated pulse profiles using 64/128 phase bins at S/X-band, and the bottom panels show the strength of the pulsations as a function of phase and time, where darker bins correspond to stronger pulsed emission.

4.3.2 Mean Flux Densities and Spectral Indices

Measurements of the magnetar's mean flux density were calculated from the average S-band and X-band pulse profiles in Figure 4.1 using the modified radiometer equation [328]:

$$S_\nu = \frac{\beta\, T_{\rm sys}\, (A_{\rm pulse}/N_{\rm total})}{G\sqrt{\Delta\nu\, n_p\, T_{\rm obs}}}, \tag{4.3}$$

where β is a correction factor that accounts for system imperfections such as digitization of the signal, $T_{\rm sys}$ is the effective system temperature given by Equation (4.1), $A_{\rm pulse}$ is the area under the pulse, G is the telescope gain, $N_{\rm total} = \sqrt{n_{\rm bin}}\,\sigma_{\rm off}$ is the total RMS noise level of the profile, $n_{\rm bin}$ is the total number of phase bins in the profile, $\Delta\nu$ is the observing bandwidth, n_p is the number of polarizations, and $T_{\rm obs}$ is the total observation time. Errors on the mean flux densities were derived from the uncertainties in the flux calibration parameters. In Table 4.3, we provide a list of mean flux density measurements at 2.3 and 8.4 GHz for each epoch. An upper limit is given for the S-band mean flux density during epoch 4 since pulsations were only marginally detected.

The X-band mean flux densities measured on 2015 July 30 and August 15 were smaller by a factor of ~7.5 compared to measurements made roughly 5 months earlier by Torne et al. [533]. Observations performed on 2016 April 1 and August 20 indicate that the magnetar's X-band mean flux density more than doubled since 2015 August 15. The S-band mean flux density was noticably variable, particularly during epoch 4 when a significant decrease in pulsed emission strength was observed. This behavior is not unusual, as large changes in radio flux densities have also been observed from other magnetars on short timescales (e.g., see [313]).

The spectral index, α, was calculated for each epoch using our simultaneous mean flux density measurements at 2.3 and 8.4 GHz, assuming a power-law relationship of the form $S_\nu \propto \nu^\alpha$. These spectral index measurements are listed in Table 4.3. A wide range of spectral index values have been reported from multifrequency radio observations of this magnetar [169, 432, 491, 532, 533]. Torne et al. [533] measured a spectral index of $\alpha = +0.4 \pm 0.2$ from radio observations between 2.54 and 291 GHz between 2015 March 4 and 9, approximately 5 months prior to our observations. However, the radio spectrum derived by Torne et al. [533] was considerably steeper between 2.54 and 8.35 GHz. We performed a nonlinear least squares fit using their total average flux densities in this frequency range and found a spectral index of $\alpha = -0.6 \pm 0.2$. Our spectral index measurements (see Table 4.3) indicate that the magnetar exhibited a significantly negative average spectral index of

Table 4.3: **Flux Density and Spectral Index Measurements of PSR J1745–2900**

Epoch	$S_{2.3}$[a] (mJy)	$S_{8.4}$[b] (mJy)	α[c]
1	1.18 ± 0.02	0.078 ± 0.004	-2.08 ± 0.04
2	0.79 ± 0.02	0.085 ± 0.004	-1.70 ± 0.04
3	1.92 ± 0.04	0.18 ± 0.01	-1.80 ± 0.04
4	< 0.84	0.19 ± 0.01	> -1.12

[a] Mean flux density at 2.3 GHz.
[b] Mean flux density at 8.4 GHz.
[c] Spectral index between 2.3 and 8.4 GHz.

$\langle\alpha\rangle = -1.86 \pm 0.02$ during epochs 1–3 when its 8.4 GHz profile was single-peaked. The spectral index flattened to $\alpha > -1.12$ during epoch 4 when the profile became double-peaked (see Figure 4.2). While our spectral index values suggest a much steeper spectrum than is typical for the other three known radio magnetars, which have nearly flat or inverted spectra [78, 83, 272, 304, 312], a comparably steep spectrum has previously been observed from this magnetar between 2 and 9 GHz [432].

4.3.3 Rotation-resolved Pulse Profiles

The X-band rotation-resolved pulse profiles in Figure 4.2 were produced by folding the barycentered and dedispersed time series data on the barycentric periods given in Table 4.2 and combining the data from both circular polarizations in quadrature. A time resolution of 512 μs was used to define the spacing between neighboring phase bins. The bottom panels show the single pulse emission during each individual pulsar rotation as a function of pulse phase, and the integrated pulse profiles are shown in the top panels. In Figure 4.2, we show a restricted pulse phase interval (0.45–0.55) around the X-band pulse profile peak from each epoch and reference pulse numbers with respect to the start of each observation. S-band rotation-resolved pulse profiles are not shown since the single pulse emission was significantly weaker at 2.3 GHz.

The integrated profiles from epochs 1–3, shown in Figures 4.2(a)–(c), exhibit a single feature with an approximately Gaussian shape, similar to previous observations near this frequency by Spitler et al. [498]. Finer substructure is also seen in the profiles, particularly during epoch 3 when the single pulse emission is brightest. Two main emission peaks are observed in the integrated profile from epoch 4, shown in Figure 4.2(d), with the secondary component originating from separate subpulses delayed by ~65 ms from the primary peak. Yan et al. [574] also found subpulses that were coherent in phase over many rotations during observations with the TMRT at 8.6 GHz between 2014 June and October. We note that the shape of the average

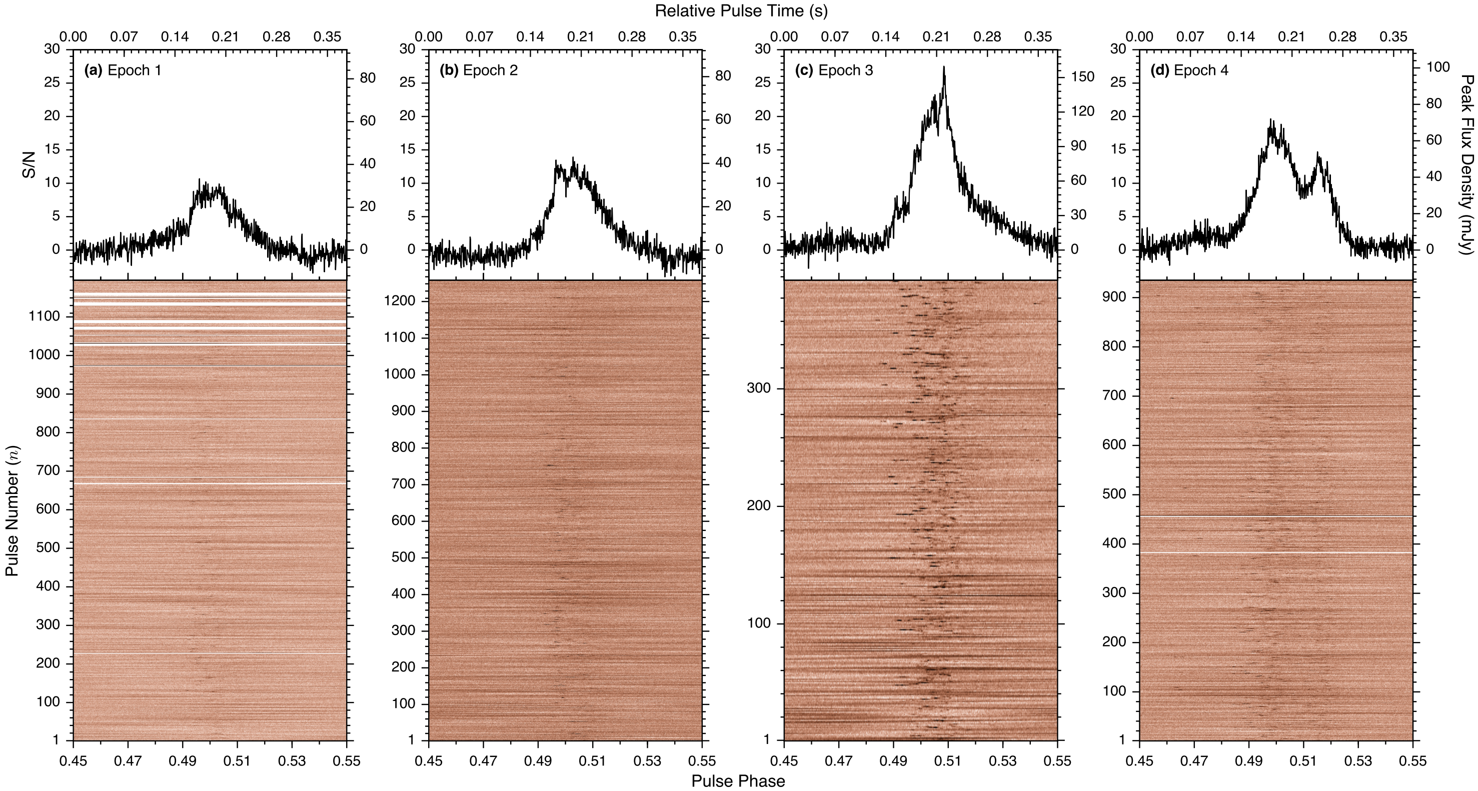

Figure 4.2: **Rotation-resolved pulse profiles of PSR J1745–2900 at X-band during (a) epoch 1, (b) epoch 2, (c) epoch 3, and (d) epoch 4 after folding the data on the barycentric period measurements given in Table 4.2 and combining data from both circular polarizations in quadrature.** The data are shown with a time resolution of 512 μs. The integrated profiles are displayed in the top panels, and the bottom panels show the distribution and relative strength of the single pulses as a function of pulse phase for each individual pulsar rotation, with darker bins signifying stronger emission. Pulse numbers are referenced with respect to the start of each observation.

profile is mostly Gaussian during epoch 1 when the magnetar's radio spectrum is steepest and displays an additional component during epoch 4 after the spectrum has flattened (see Table 4.3), which may suggest a link between the magnetar's radio spectrum and the structure of its pulsed emission.

4.3.4 Single Pulse Analysis

4.3.4.1 Identification of Single Pulses

We carried out a search for S-band and X-band single pulses from each epoch listed in Table 4.1. In this paper, we focus primarily on X-band single pulses detected during epoch 3 since the single pulse emission was brightest during this epoch.

The data were first barycentered and dedispersed at the magnetar's nominal DM of 1778 pc cm^{-3} after masking bad data corrupted by RFI and applying the bandpass and baseline corrections described in Section 4.2.1. The full time resolution time series data were then searched for single pulses using a Fourier domain matched filtering algorithm available through the `PRESTO` pulsar search software package[m], where the data were convolved with boxcar kernels of varying widths.

We used 54 boxcar templates with logarithmically spaced widths up to 2 s, and events with S/N ≥ 5 were recorded for further analysis. If a single pulse candidate was detected with different boxcar widths from the same section of data, only the highest S/N event was stored in the final list. The S/N of each single pulse candidate was calculated using:

$$\mathrm{S/N} = \frac{\sum_i (f_i - \bar{\mu})}{\bar{\sigma}\sqrt{w}}, \tag{4.4}$$

where f_i is the time series value in bin i of the boxcar function, $\bar{\mu}$ and $\bar{\sigma}$ are the local mean and RMS noise after normalization, and w is the boxcar width in number of bins. The time series data were detrended and normalized such that $\bar{\mu} \approx 0$ and $\bar{\sigma} \approx 1$. We note that the definition of S/N in Equation (4.4) has the advantage of giving approximately the same result irrespective of how the input time series is downsampled, provided the pulse is still resolved [153].

4.3.4.2 X-band Single Pulse Morphology

4.3.4.2.1 Multiple Emission Components

An analysis was performed on the X-band single pulse events from epoch 3 that were both detected using the Fourier domain matched filtering algorithm described in Section 4.3.4.1 and showed resolvable dispersed pulses in their barycentered dynamic spectra. We measured the times of arrival (ToAs) of the emission components comprising each single pulse event by incoherently dedispersing the barycentered dynamic spectra at the magnetar's nominal DM of 1778 pc cm^{-3} and then searching for local maxima in the integrated single pulse profiles after smoothing the data by convolving the time series with a one-dimensional Gaussian kernel. The Gaussian kernel used in this procedure is given by:

$$K(t;\,\sigma) = \frac{1}{\sqrt{2\pi}\sigma}\exp\left(-\frac{t^2}{2\sigma^2}\right), \tag{4.5}$$

where σ is the scale of the Gaussian kernel and t corresponds to the sample time in the time series. A modest Gaussian kernel scale of 819 μs was used to smooth the data, which did not hinder our ability to distinguish between narrow, closely spaced peaks. Individual emission components were identified as events displaying a dispersed feature in their dynamic spectrum along with a simultaneous peak in their integrated single pulse profile.

The structure and number of X-band single pulse emission components varied significantly between consecutive pulsar rotations (e.g., Figure 4.2). These changes were observed on timescales shorter than the magnetar's 3.77 s rotation period. An example is shown in the top row of Figure 4.3 from pulse cycle $n = 239$ of epoch 3, where at least six distinct emission components can be resolved. While the overall structure of this particular single pulse is similar in the LCP and RCP channels, the emission components at later pulse phases are detected more strongly in the RCP data. Measurements performed near this epoch at 8.35 GHz with the Effelsberg telescope indicate that the magnetar likely had a high linear polarization fraction [155]. This suggests that some of the magnetar's emission components may be more polarized than others.

Other single pulse events contained fewer emission components. The middle row of Figure 4.3 shows a single pulse event detected during pulse cycle $n = 334$ of epoch 3 with four independent emission components in the LCP and RCP channels. The two brightest components are separated by ~6.8 ms and ~8.6 ms in the LCP and RCP data, respectively. Another example from pulse cycle $n = 391$ of epoch 3 is provided in the bottom row of Figure 4.3, which shows two emission components in the LCP data and three components in the RCP data.

Using the threshold criteria described in Section 4.3.4.1, single pulse emission components were significantly detected in at least one of the polarization channels during 72% of the pulse cycles in epoch 3 and were identified in the LCP/RCP data during 69%/50% of the pulse cycles. Faint emission components were often seen in many of the single pulses, but at a much lower significance level. In Figure 4.4, we show the distribution of the number of significantly detected emission components during these pulse cycles. More than 72%/87% of the single pulses in the LCP/RCP data contained either one or two distinct emission components. The number of single pulses with either one or two emission components was approximately equal in the LCP data, and 59% more single pulses in the RCP channel were found to have one emission component compared to the number of events with two components.

Most of the X-band single pulses detected during epochs 1 and 2 displayed only one emission component, whereas the single pulses from epochs 3 and 4 showed multiple emission components. Single pulses with multiple emission components have also been previously detected at 8.7 GHz with the phased VLA [62] and at 8.6 GHz with the TMRT [574]. In both studies, the number of emission components and structure of the single pulses were found to be variable between pulsar rotations.

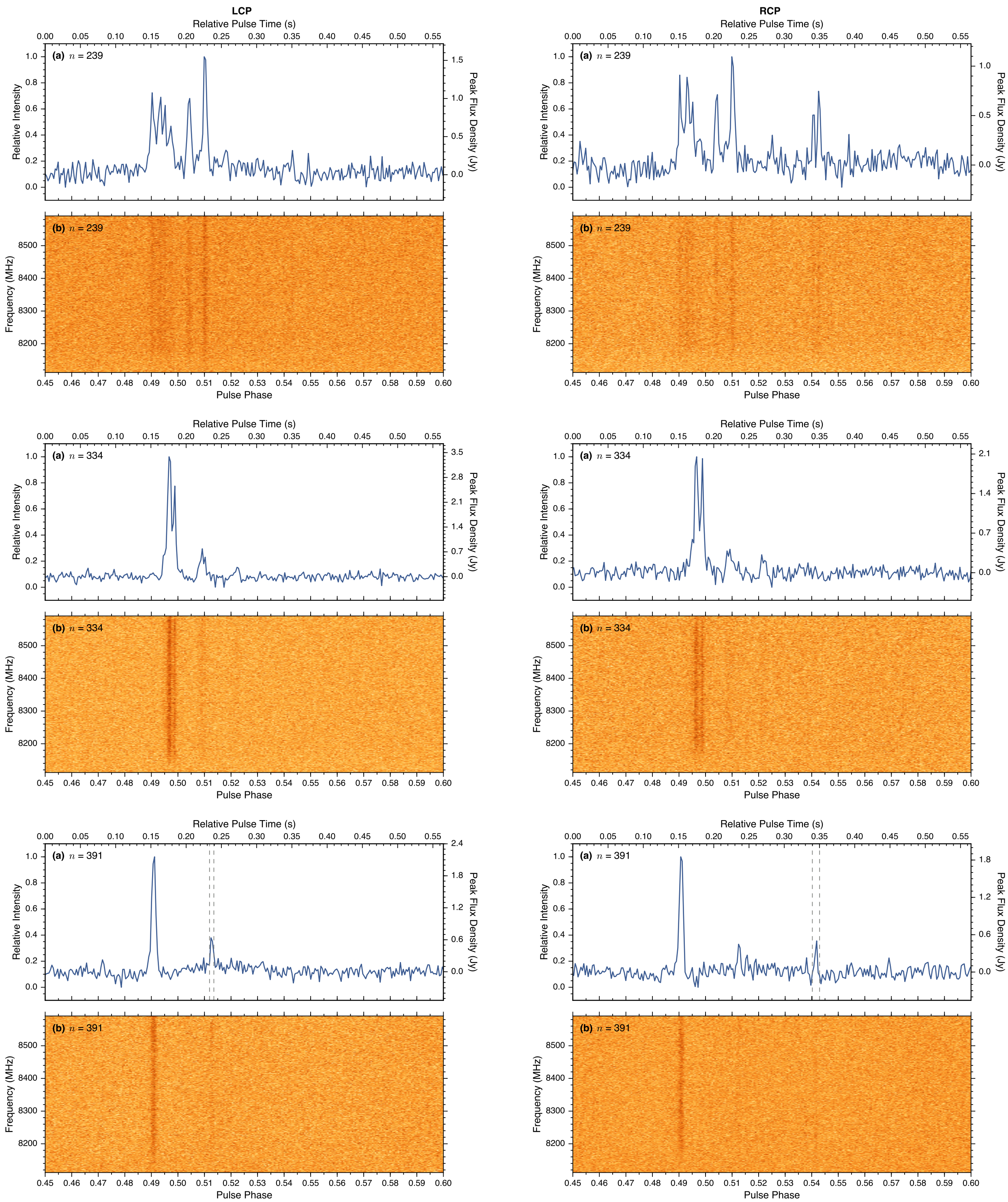

Figure 4.3: **Examples of bright X-band single pulse events displaying multiple emission components during pulse cycles (top row) $n = 239$, (middle row) $n = 334$, and (bottom row) $n = 391$ of epoch 3.** The plots in the left and right columns show detections of the single pulses in the left circular polarization (LCP) and right circular polarization (RCP) channels, respectively. We show the (a) integrated single pulse profiles and (b) dynamic spectra dedispersed using a DM of 1778 pc cm^{-3} from both polarizations with a time resolution of 2 ms.

Figure 4.3 *(continued)*: During pulse cycle $n = 239$, the emission components at later pulse phases are significantly detected in the RCP channel, but are only marginally detected in the LCP data. The two dominant emission components detected during pulse cycle $n = 334$ are separated by $\sim$6.8 ms and $\sim$8.6 ms in the LCP and RCP data, respectively. The secondary emission components detected during pulse cycle $n = 391$ show gaps across the frequency band in the dynamic spectra, but no frequency structure is observed in the primary component's emission. In Figure 4.5, we show the frequency structure of the secondary components indicated by the dashed vertical lines.

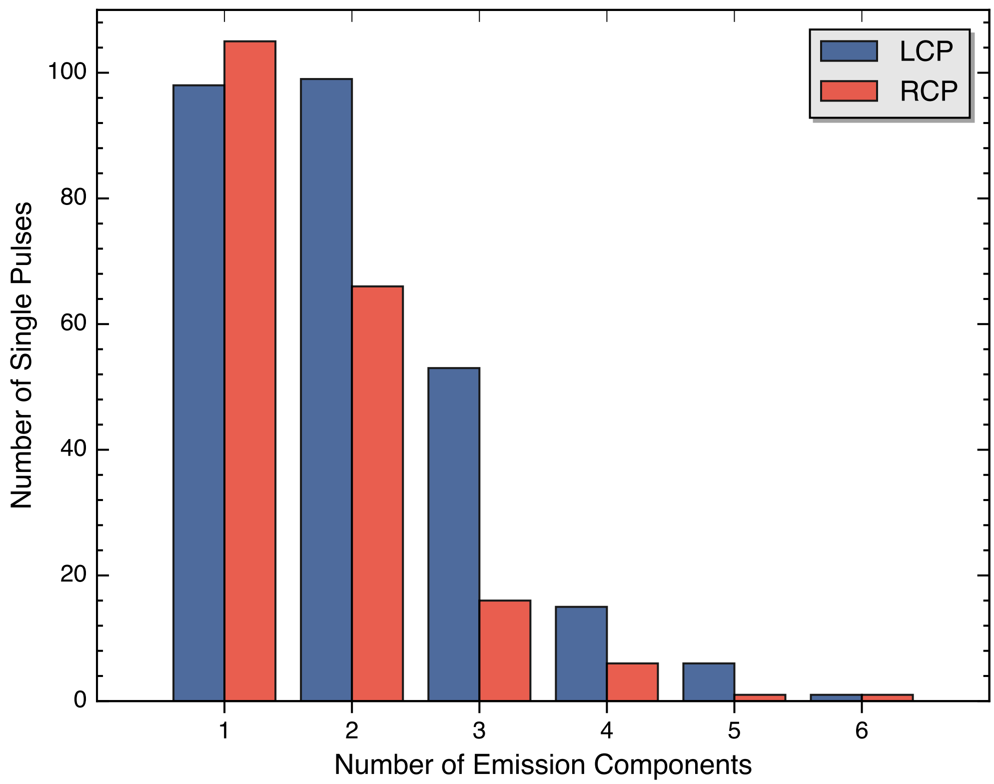

Figure 4.4: **Number of X-band single pulse emission components detected during epoch 3 in the (blue) left circular polarization (LCP) and (red) right circular polarization (RCP) channels.**

4.3.4.2.2 Frequency Structure in Emission Components

Many of the X-band single pulse emission components from epoch 3 displayed frequency structure in their dynamic spectra. These events were characterized by a disappearance or weakening of the radio emission over subintervals of the frequency bandwidth. The typical scale of these frequency features was approximately 100 MHz in extent, and the location of these features often varied between components in a single pulse cycle. The flux densities of these components also varied by factors of $\sim$2–10 over the affected frequency ranges. From a visual inspection of the data, we find that approximately 50% of the pulse cycles exhibited this behavior, and the LCP/RCP data showed these features during 40%/30% of the pulse cycles. While these effects were often more pronounced in one of the polarization channels, approximately 20% of the pulse cycles displayed events with these features in both channels simultaneously. This behavior was usually observed in the fainter emission components, but frequency structure was also sometimes seen in the primary component. These effects are not instrumental in origin since only a subset of the components were affected during a given pulse cycle.

We show an example single pulse from pulse cycle $n = 391$ of epoch 3 in the bottom row of Figure 4.3, where gaps in the radio emission were observed in the secondary emission components. We selected two secondary components displaying this behavior, which we indicate with dashed vertical lines in Figure 4.3, and show their frequency structure in Figure 4.5. We used a one-dimensional Gaussian kernel with $\sigma = 25$ MHz, defined in Equation (4.5), to smooth the frequency response of these secondary components. The uncertainty associated with each data point was calculated from the standard error and is indicated by the blue shaded regions in Figure 4.5. The selected emission component in the LCP data displays a frequency gap centered at ∼8.4 GHz spanning ∼100 MHz. The emission component from the RCP data exhibits more complex frequency structure with a gap near ∼8.3 GHz.

Next, we investigate whether the observed frequency structure could be produced by interstellar scintillation. Assuming a scattering timescale of $\tau_d \approx \nu^{-4}$, where ν is the observing frequency in GHz, we estimate the diffractive interstellar scintillation bandwidth using:

$$\Delta\nu_{\mathrm{DISS}} = \frac{C_1}{2\pi\tau_d}, \tag{4.6}$$

where $C_1 = 1.16$ for a uniform medium with a Kolmogorov wavenumber spectrum [125]. At the X-band observing frequency of 8.4 GHz, a scattering timescale of $\tau_d \approx 0.2$ ms corresponds to a predicted scintillation bandwidth of $\Delta\nu_{\mathrm{DISS}} \approx 1$ kHz, which is well below the frequency scale associated with these features. The scintillation bandwidth decreases if we adopt a larger scattering timescale, such as the ∼7 ms characteristic single pulse broadening timescale reported in Section 4.3.4.2.5. Therefore, interstellar scintillation cannot explain the frequency structure observed in the emission components. This behavior is likely caused by propagation effects in the magnetar's local environment, but may also be intrinsic to the magnetar.

4.3.4.2.3 Flux Density Distribution of Emission Components

We performed a statistical analysis of the distribution of peak flux densities from the X-band single pulse emission components detected during epoch 3. For each emission component, the peak S/N was calculated by dividing the barycentered, integrated single pulse profiles by the off-pulse RMS noise level after subtracting the off-pulse mean. The peak flux density of each emission component was determined from [382]:

$$S_{\mathrm{peak}} = \frac{\beta\, T_{\mathrm{sys}}\, (\mathrm{S/N})_{\mathrm{peak}}}{G\sqrt{\Delta\nu\, n_p\, t_{\mathrm{peak}}}}, \tag{4.7}$$

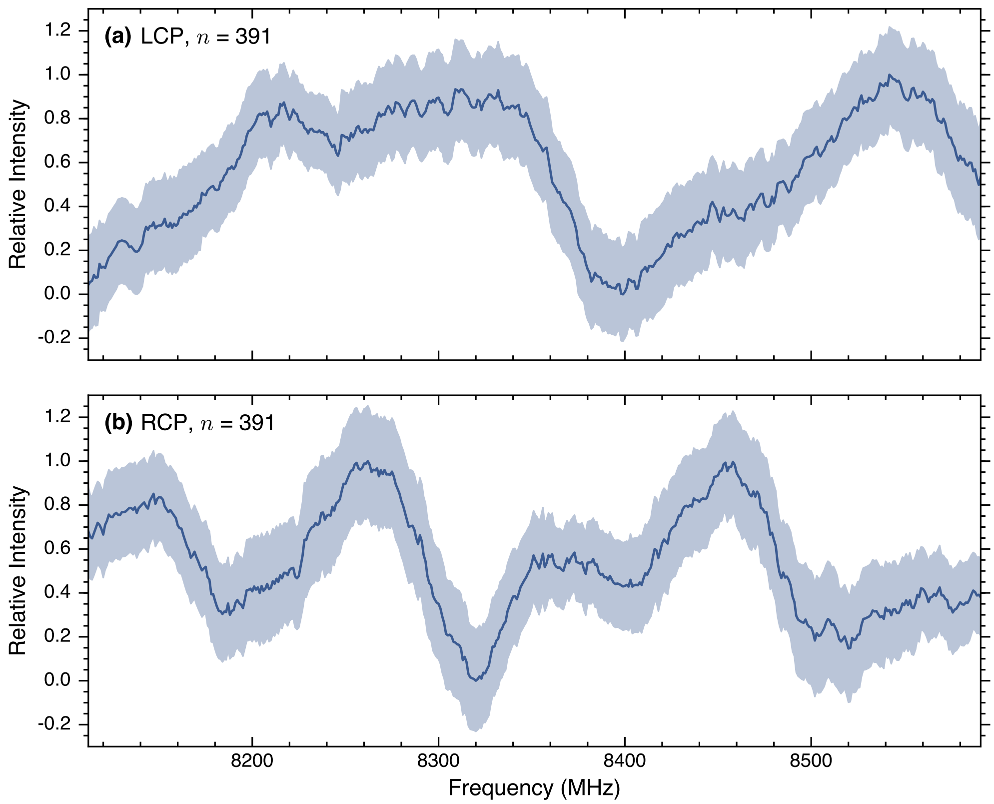

Figure 4.5: **Examples of frequency structure in the secondary emission components of the X-band single pulse event during pulse cycle $n = 391$ of epoch 3.** The frequency structure in the (a) left circular polarization (LCP) and (b) right circular polarization (RCP) channels correspond to the secondary components labeled by the dashed vertical lines in the bottom row of Figure 4.3. The frequency response of the components is smoothed using a one-dimensional Gaussian kernel with $\sigma = 25$ MHz, and thus neighboring points are correlated. The blue shaded regions indicate the standard errors on the data points. The secondary component in the LCP data shows a frequency gap centered at ~8.4 GHz spanning ~100 MHz. The frequency structure of the secondary component from the RCP data is more complex and shows a gap near ~8.3 GHz.

where $(\mathrm{S/N})_{\mathrm{peak}}$ is the peak S/N of the emission component and t_{peak} denotes the integration time at the peak.

Following the analyses in Lynch et al. [335] and Yan et al. [574], the peak flux density of each single pulse emission component was normalized by the peak flux density of the integrated rotation-resolved profile in Figure 4.2(c), $S_{\mathrm{int,peak}} = 0.16$ Jy. A histogram of the distribution of normalized peak flux densities for all 871 emission components is shown in Figure 4.6. We investigated whether the normalized peak flux densities could be characterized by a log-normal distribution with a probability density function (PDF) given by:

$$P_{\mathrm{LN}}\left(x = \frac{S_{\mathrm{peak}}}{S_{\mathrm{int,peak}}}\right) = \frac{1}{\sqrt{2\pi}\sigma_{\mathrm{LN}} x} \exp\left[-\frac{(\ln x - \mu_{\mathrm{LN}})^2}{2\sigma_{\mathrm{LN}}^2}\right], \tag{4.8}$$

where μ_{LN} and σ_{LN} are the mean and standard deviation of the distribution, respectively. A nonlinear least squares fit to the normalized peak flux densities using Equation (4.8) gave a best-fit log-normal distribution with $\mu_{\mathrm{LN}} = 1.33 \pm 0.03$ and $\sigma_{\mathrm{LN}} = 0.58 \pm 0.02$, which is overlaid in red in Figure 4.6.

A Kolmogorov–Smirnov (KS) test [318] yielded a p-value of 0.044, which revealed that the normalized flux densities were marginally inconsistent with the fitted log-normal distribution. This is primarily due to the moderate number of bright emission components with $S_{\mathrm{peak}} \gtrsim 15\, S_{\mathrm{int,peak}}$. These components form a high flux tail in the observed flux density distribution, which is underestimated by the derived log-normal distribution. After removing these events and repeating the KS test, we obtained a p-value of 0.057 and best-fit log-normal mean and standard deviation values that were consistent with our previous fit. This indicates that emission components with $S_{\mathrm{peak}} \lesssim 15\, S_{\mathrm{int,peak}}$ can be described by the log-normal distribution shown in red in Figure 4.6.

Our best-fit log-normal mean and standard deviation values are consistent to within 1σ with the single pulse flux density distribution derived from measurements with the TMRT at 8.6 GHz on MJD 56836 [574]. However, Yan et al. [574] found that the distribution was consistent with log-normal and no high flux tail was observed. In contrast, a high flux tail was seen in the distribution of single pulse flux densities measured at 8.7 GHz with the GBT [335]. Single pulse energy distributions at 1.4, 4.9, and 8.35 GHz from the radio magnetar XTE J1810–197 also showed log-normal behavior along with a high energy tail, which was modeled with a power-law [487]. Here, we fit a power-law to the flux densities in the tail of the distribution and find a scaling exponent of $\Gamma = -7 \pm 1$ for events with $S_{\mathrm{peak}} \geq 15\, S_{\mathrm{int,peak}}$.

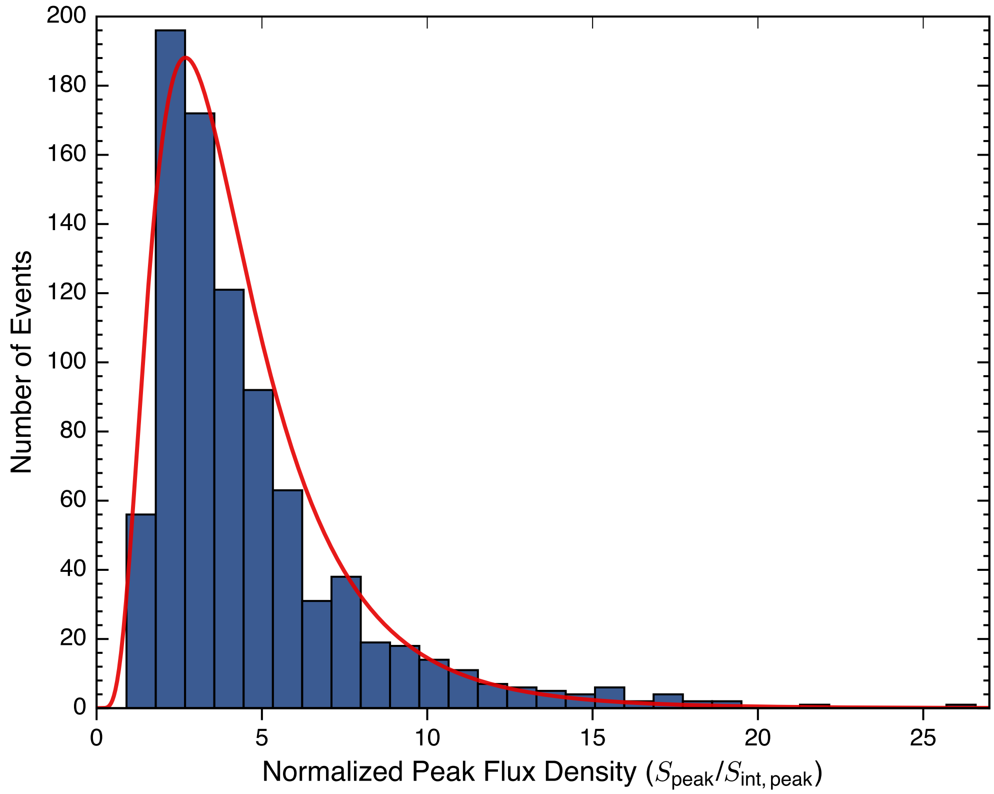

Figure 4.6: **Distribution of peak flux densities from the single pulse emission components detected at X-band during epoch 3.** The flux densities are normalized by $S_{\rm int,peak} = 0.16\,{\rm Jy}$, the peak flux density from the integrated rotation-resolved profile in Figure 4.2(c). The best-fit log-normal distribution is overlaid in red. A high flux tail is observed in the distribution due to bright emission components with $S_{\rm peak} \gtrsim 15\,S_{\rm int,peak}$.

Giant radio pulses are characterized by events with flux densities larger than ten times the mean flux level. We detected a total of 61 emission components with $S_{\rm peak} \geq 10\,S_{\rm int,peak}$, which comprised 7% of the events. Giant pulses were seen during 9% of the pulse cycles, and 72% of these events occurred during the second half of the observation. No correlation was found between the flux density and number of components in these bright events. Previous studies of single pulse flux densities at X-band also showed some evidence of giant single pulses from this magnetar, but at a much lower rate [574].

4.3.4.2.4 Temporal Variability of Emission Components

The X-band single pulses from epoch 3 exhibited significant temporal variability between their emission components. To study this behavior, we folded the ToAs associated with the emission components on the barycentric period given in Table 4.2. The distribution of these events in pulse phase is shown in Figure 4.7 for both polarization channels. A larger number of components were detected at later phases in the RCP channel compared to the LCP channel. This produced a tail in the phase distribution of events from the RCP data, which can be seen in the top panel of Figure 4.7(b). No tail was observed in the phase distribution of the components from the LCP data since emission components at later phases were generally not detected as strongly (e.g., see top row of Figure 4.3).

A bright single pulse with one emission component was detected much earlier in pulse phase (near phase ~0.4) relative to the other events and is indicated by a cross in the bottom panels of Figure 4.7. Only two other single pulses were found at similarly anomalous phases during epoch 4. All of these pulses displayed a single, narrow emission component, and their observed pulse widths ranged between 1.5 and 3.1 ms based on the boxcar widths used for detection in the matched filtering algorithm (see Section 4.3.4.1). This suggests that these pulses are either atypical for this magnetar or unrelated to the pulsar. Excluding this deviant event from our epoch 3 analysis, we measure pulse jitter values of $\sigma_{\rm LCP} \approx 28$ ms and $\sigma_{\rm RCP} \approx 44$ ms from the standard deviation of the emission component pulse phases in each polarization channel.

Approximately 41%/38% of the components in the LCP/RCP data were detected at larger pulse phases than the peak phase of the integrated rotation-resolved profile in Figure 4.2(c). We also found that 29%/41% of the components in the LCP/RCP channels were delayed by more than 30 ms from the profile peak, which indicates that the emission components in the LCP data are more tightly clustered in phase.

In Figure 4.8, we show the pulse phase and peak flux density of the brightest emission component in each pulse cycle from Figure 4.7, where larger and darker circles in the bottom panels correspond to larger peak flux densities. A tail is again observed in the phase distribution of the components from the RCP channel, and no tail is produced by components from the LCP data. Pulse jitter values of $\sigma_{\rm LCP} \approx 26$ ms and $\sigma_{\rm RCP} \approx 43$ ms were found from the LCP and RCP phase distributions shown in Figure 4.8, and these values are similar to those obtained from the distributions in Figure 4.7.

The relative time delays between the single pulse emission components also varied between pulsar rotations. During some pulse cycles, the single pulses showed a multicomponent structure with two bright components separated by $\lesssim 10$ ms, along with additional emission components with larger time delays. An example is shown in the middle row of Figure 4.3, where different time delays between the two

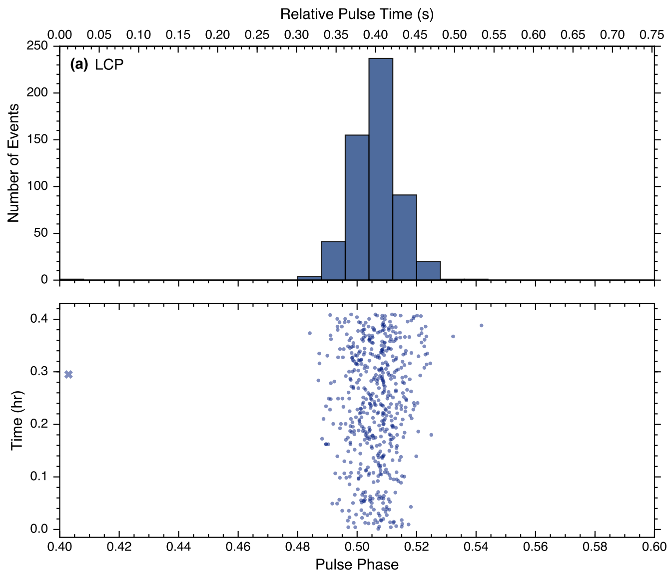

Figure 4.7: **Pulse phase distribution of the X-band single pulse emission components detected during epoch 3 in the (a) left circular polarization (LCP) and (b) right circular polarization (RCP) channels.** Histograms of the number of events detected at each pulse phase are shown in the top panels, and the bottom panels show the phase distributions of the components from folding their times of arrival (ToAs) modulo the barycentric period in Table 4.2. A bright single pulse, indicated with a cross, was detected earlier in pulse phase (near phase ~0.4) relative to the other events.

brightest components were found in the two polarization channels. In other cases, only one dominant emission component was detected and the time delays between neighboring components were much larger (e.g., see bottom row of Figure 4.3).

We calculated characteristic time delays between the single pulse emission components by measuring time differences between adjacent components. We denote the emission component detected earliest in pulse phase during a given pulse cycle by “1” and sequentially label subsequent emission components during the same pulse cycle. The distribution of time delays between the first two emission components was bimodal (see Figure 4.9(a)), which we associate with two distinct populations of single pulses. We report characteristic time delays of $\langle\tau_{12}\rangle_\alpha = 7.7$ ms and $\langle\tau_{12}\rangle_\beta = 39.5$ ms between the first two emission components from the mean delay of these separate distributions. Additionally, we measured a characteristic time delay of $\langle\tau_{23}\rangle = 30.9$ ms from the distribution of time delays between the second two components in Figure 4.9(b). We find that $\langle\tau_{12}\rangle_\alpha$ is comparable to the ~10 ms separation between components in the single pulses detected by the phased VLA at 8.7 GHz [62].

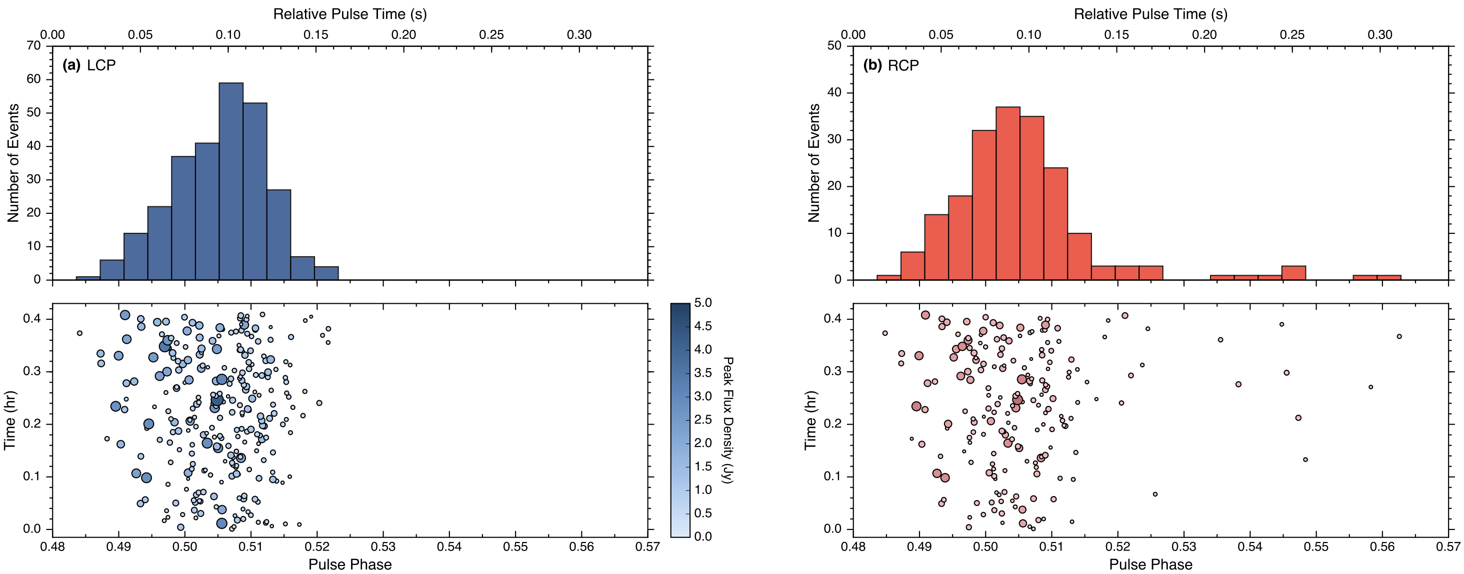

Figure 4.8: **Brightest X-band single pulse emission component detected during each pulsar rotation in Figure 4.7.** Events exceeding the threshold criteria defined in Section 4.3.4.1 in the (a) left circular polarization (LCP) and (b) right circular polarization (RCP) channels are shown in blue and red, respectively. The top panels show histograms of the number of events at each pulse phase. Phase distributions of the components, determined from folding the times of arrival (ToAs) modulo the barycentric period in Table 4.2, are shown in the bottom panels, where larger and darker circles correspond to events with larger peak flux densities. We excise the single pulse event near pulse phase ∼0.4 from both polarization channels to show the distributions over a narrower phase range.

4.3.4.2.5 Pulse Broadening

The X-band single pulses detected during epochs 1–4 displayed features characteristic of pulse broadening. In particular, many of the single pulse events showed significant evidence of exponential tails in their emission components (e.g., see Figure 4.10), which is typically attributed to multipath scattering through the ISM [558]. Strong exponential tails were sometimes observed in only a subset of the emission components during a given single pulse, with no pulse broadening in the other components (e.g., see bottom row of Figure 4.12). A reverse exponential tail structure was also seen in some single pulse emission components (e.g., see top and bottom rows of Figure 4.12), which may be due to more exotic pulse broadening mechanisms. The observed pulse broadening behavior could be explained by scattering from plasma inhomogenities, either local to or distant from the magnetar, or by unresolved low amplitude emission components.

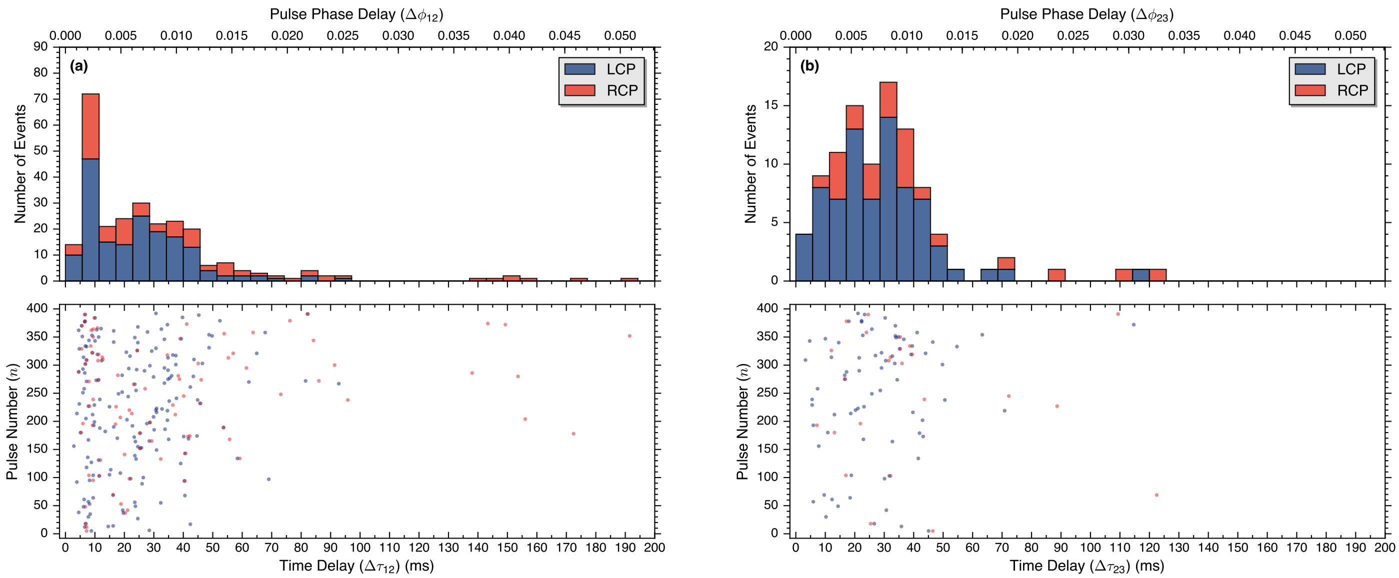

Figure 4.9: **Time delays between the X-band single pulse emission components detected in the (blue) left circular polarization (LCP) and (red) right circular polarization (RCP) channels during epoch 3.** The emission component detected earliest in pulse phase during a given pulsar rotation is denoted by "1" and emission components with later times of arrival (ToAs) during the same pulse cycle are labeled sequentially. We show the time delays between emission components (a) "1" and "2" and (b) "2" and "3." Histograms of the time delays between the emission components are shown in the top panels, and the bottom panels show the distribution of the time delays measured from each polarization channel. Pulse numbers are referenced with respect to the start of the observation.

Here, we measure a characteristic single pulse broadening timescale, τ_d, at X-band (8.4 GHz) using the bright single pulse event shown in Figure 4.10 from epoch 3. The amount of pulse broadening observed in this pulse is representative of other pulses with strong exponential tails. We use a thin scattering screen model, described in detail in Section 4.5, to characterize the intrinsic properties of the pulse and the pulse broadening magnitude.

We fit the single pulse profiles in both polarization channels, shown in Figure 4.10(a), with Equation (4.15). A Bayesian Markov chain Monte Carlo (MCMC) procedure was used to perform the fitting and incorporate covariances between the model parameters into their uncertainties. We assumed uninformed, flat priors on all of our model parameters and used a Gaussian likelihood function, $\mathcal{L} \propto \exp(-\chi^2/2)$, such that the log-likelihood is given by:

$$\ln \mathcal{L} = -\frac{1}{2}\left[\sum_{i}^{N}\left(\frac{P_{\mathrm{obs},\,i} - P_{\mathrm{model},\,i}}{\sigma_i}\right)^2 + \ln(2\pi\sigma_i^2)\right], \tag{4.9}$$

where N is the number of time bins in the single pulse profile, and $P_{\mathrm{obs},i}$ and $P_{\mathrm{model},i}$ are the measured and predicted values of the single pulse profile at bin i, respectively. Each data point in the fit was weighted by the off-pulse RMS noise level, σ_i.

The posterior PDFs of the model parameters in Equation (4.15) were sampled using an affine-invariant MCMC ensemble sampler [207], implemented in `emcee`[q] [188]. The parameter spaces were explored using 200 walkers and a chain length of 10,500 steps per walker. The first 500 steps in each chain were treated as the initial burn-in phase and were removed. Best-fit values for the model parameters were determined from the median of the marginalized posterior distributions using the remaining 10,000 steps in each chain, and uncertainties on the model parameters were derived from 1σ Bayesian credible intervals.

The best-fit scattering model is overlaid in red on the single pulse profiles in Figure 4.10(a) for each polarization channel, and we show the marginalized posterior distributions in the corner plots in Figure 4.11 from individually fitting the LCP and RCP data. Pulse broadening timescales of $\tau_d^{\mathrm{LCP}} = 7.1 \pm 0.2$ ms and $\tau_d^{\mathrm{RCP}} = 6.7 \pm 0.3$ ms were obtained for this single pulse event from the single parameter marginalized posterior distributions, and they are consistent with each other to within 1σ. We report a characteristic pulse broadening timescale of $\langle\tau_d\rangle = 6.9 \pm 0.2$ ms from averaging these two independent polarization channel measurements. These values are comparable to the characteristic time delay $\langle\tau_{12}\rangle_\alpha$ of 7.7 ms between the leading two single pulse emission components reported in Section 4.3.4.2.4, which may indicate that the exponential tails observed in the single pulses could be formed from multiple adjacent emission components.

Pulse broadening measurements by Spitler et al. [498] between 1.19 and 18.95 GHz yielded a spectral index of $\alpha_d = -3.8 \pm 0.2$ and a scattering timescale of $\tau_d = 1.3 \pm 0.2$ s at 1 GHz, which implies $\tau_d \approx 0.4$ ms at 8.4 GHz. If the exponential tail structure in the single pulse events were produced by scattering through a thin screen in the ISM, then our characteristic pulse broadening timescale of 6.9 ms suggests that individual single pulse events can have scattering timescales that are more than an order of magnitude larger than the scattering predicted at this frequency by Spitler et al. [498]. We also point out that our pulse broadening measurements are significantly larger than the scattering timescale predicted at this frequency by Bhat et al. [46], where a mean spectral index of $\alpha_d = -3.9 \pm 0.2$ was derived from integrated pulse profiles between 0.43 and 2.38 GHz of low Galactic latitude pulsars with moderate DMs.

[q] See https://dfm.io/emcee/current.

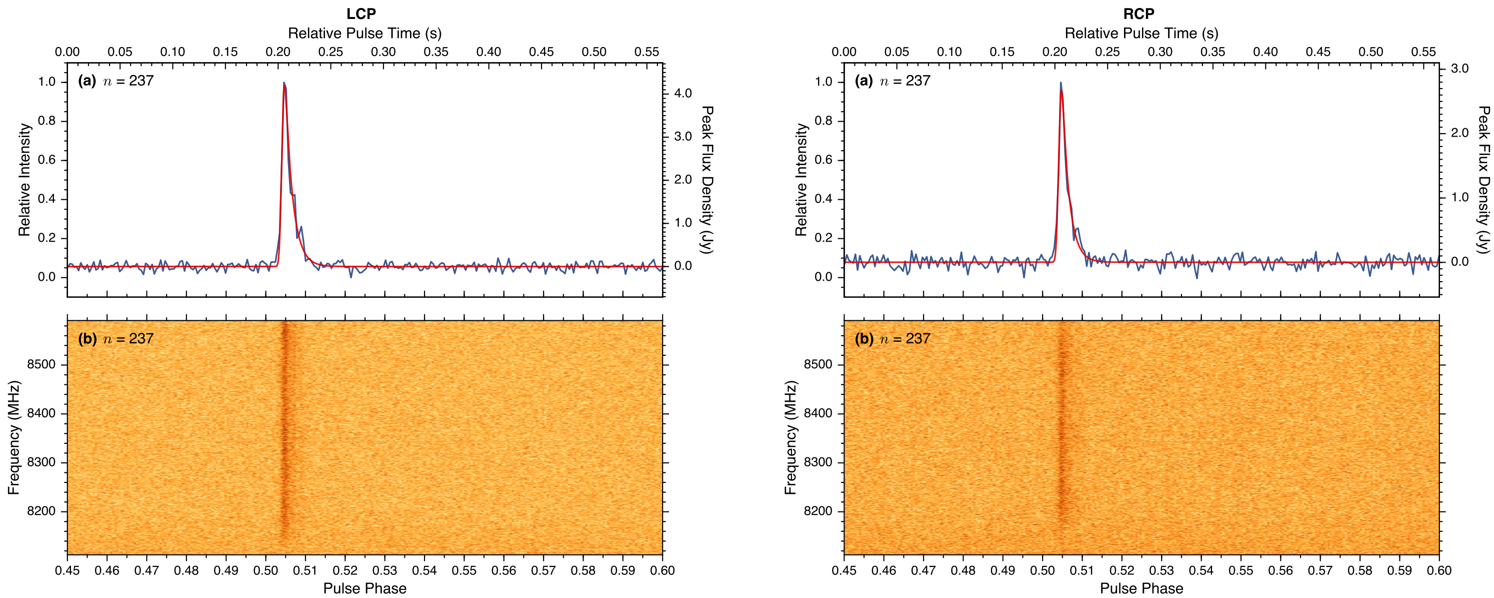

Figure 4.10: **Bright X-band single pulse event displaying significant pulse broadening during pulse cycle $n = 237$ of epoch 3.** The left and right plots show the detection of the single pulse in the left circular polarization (LCP) and right circular polarization (RCP) channels, respectively. We show the (a) integrated single pulse profiles and (b) dynamic spectra dedispersed using a DM of 1778 pc cm^{-3} from both polarizations with a time resolution of 2 ms. The best-fit scattering model, obtained by individually fitting the LCP and RCP data with Equation (4.15), is overlaid in red. The pulse broadening timescales measured for this event in each of these two polarization channels are $\tau_d^{\mathrm{LCP}} = 7.1 \pm 0.2$ ms and $\tau_d^{\mathrm{RCP}} = 6.7 \pm 0.3$ ms, respectively.

An earlier study of nine highly dispersed pulsars between 0.6 and 4.9 GHz yielded a spectral index of $\alpha_d = -3.44 \pm 0.13$ [325], but this is also too steep to account for the amount of single pulse broadening seen here at X-band. Additionally, the level of pulse broadening reported here is inconsistent with a pure Kolmogorov spectrum, which has an expected spectral index of $\alpha_d = -4.4$ [309].

4.4 Discussion and Conclusions

4.4.1 Intrinsic and Extrinsic Emission Characteristics

There are various timescales observed from the data that describe the emission: (1) the typical intrinsic width of individual emission components ($w = 1.8$ ms), (2) a characteristic pulse broadening timescale ($\langle \tau_d \rangle = 6.9$ ms), (3) a prevailing delay time between successive components ($\langle \tau_{12} \rangle_\alpha = 7.7$ ms), (4) the envelope of pulse delays between successive components ($\Delta_{12} \approx 50$ ms), (5) the spread of component arrival times relative to the magnetar rotation period ($\Delta_{\mathrm{comp}} \approx 100$ ms), and (6) the magnetar rotation timescale ($P = 3.77$ s).

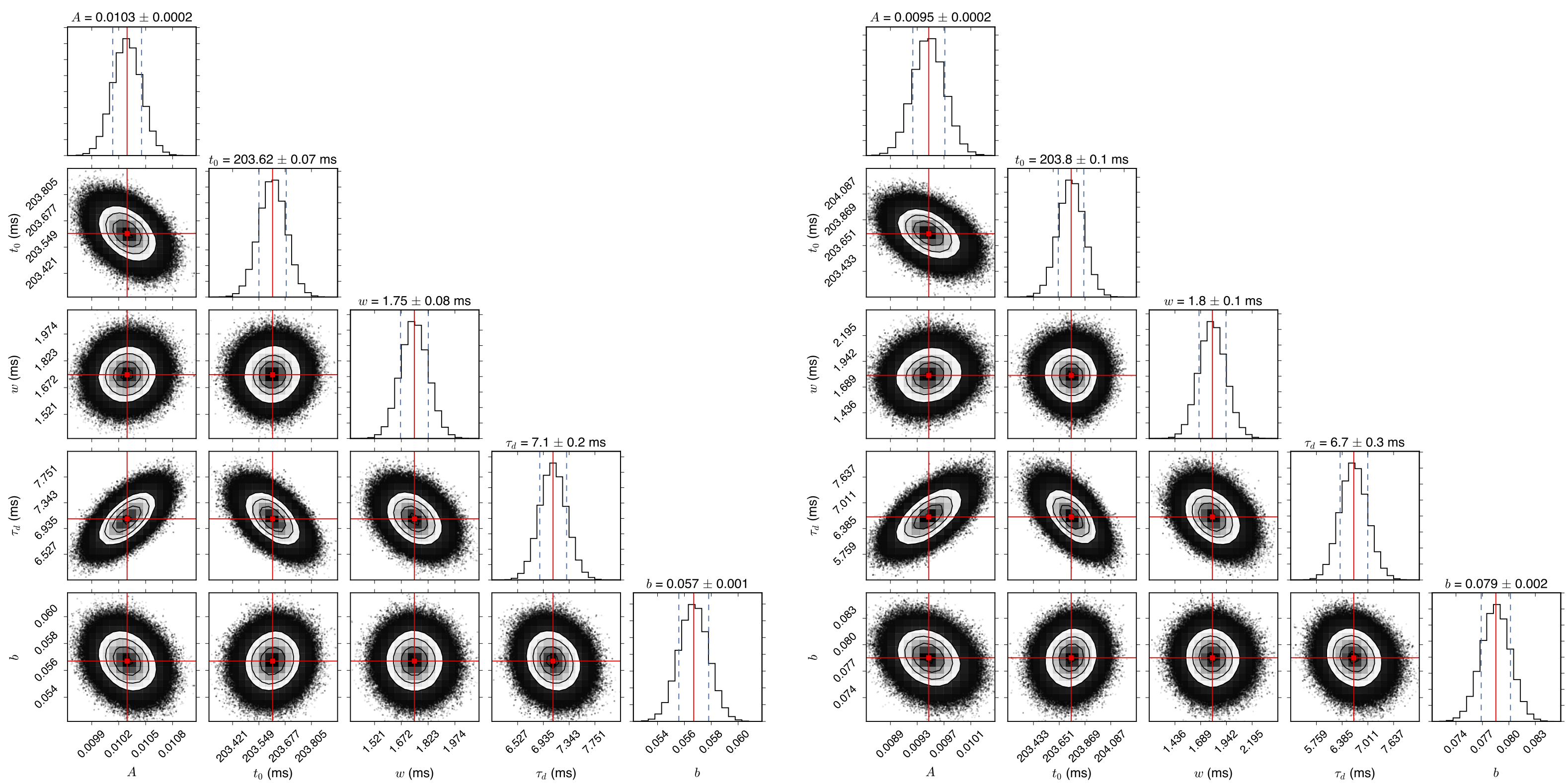

Figure 4.11: **Corner plots showing the marginalized posterior distributions obtained by independently fitting the integrated single pulse profiles from the left circular polarization (LCP) and right circular polarization (RCP) channels in Figure 4.10(a) with the scattering model in Equation (4.15).** The posterior distributions shown on the left and right are derived from fitting the LCP and RCP data, respectively. Single parameter projections of the posterior probability distributions and best-fit values are shown along the diagonal, and the off-diagonal plots are the marginalized two-dimensional posterior distributions. Covariances between the model parameters are indicated by a tilted error ellipse. The red lines correspond to the best-fit values for the model parameters derived from the median of the single parameter posterior distributions, and the dashed blue lines indicate 1σ Bayesian credible intervals.

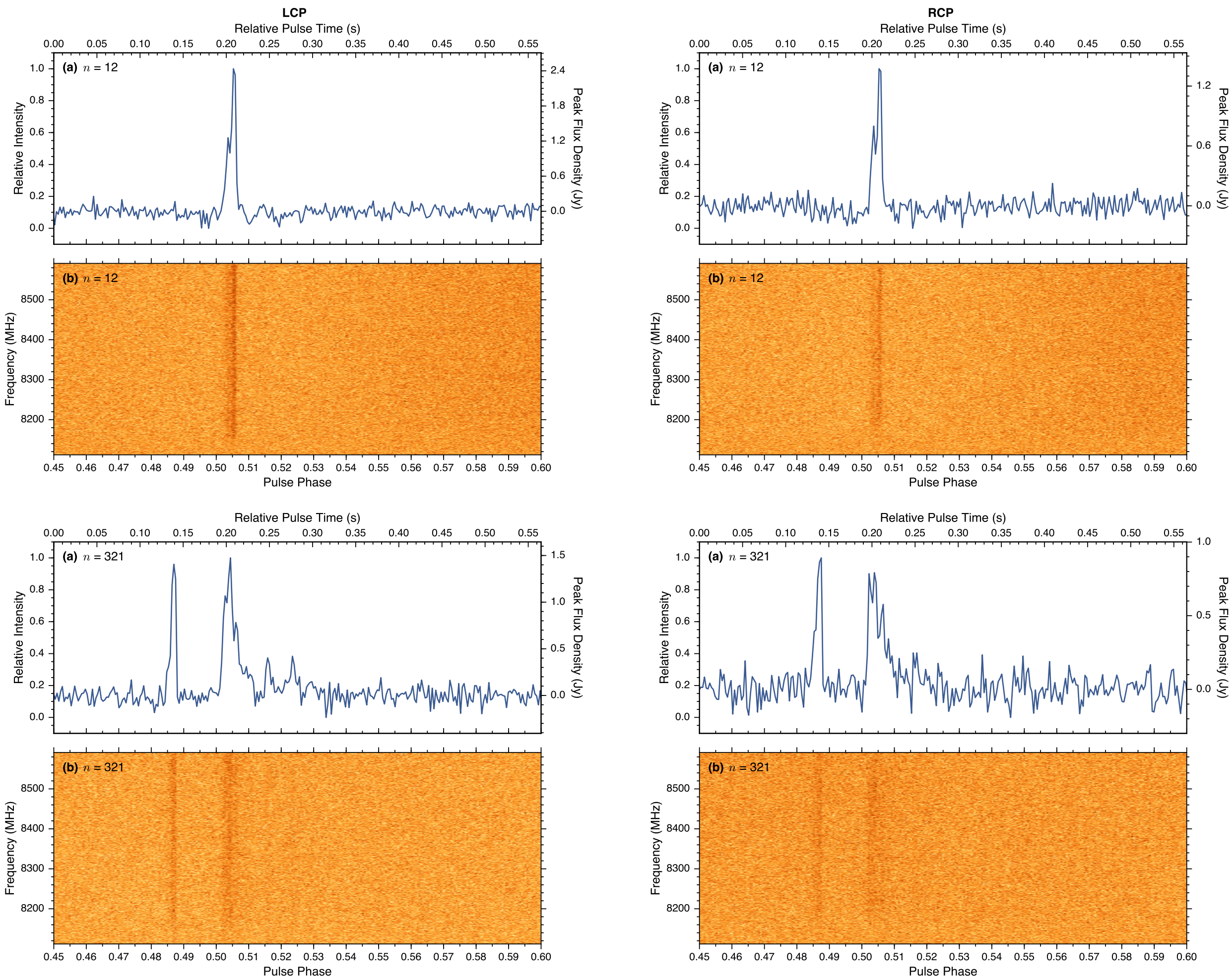

Figure 4.12: **Examples of bright X-band single pulse events displaying exotic pulse broadening behavior during pulse cycles (top row) $n = 12$ and (bottom row) $n = 321$ of epoch 3.** The plots in the left and right columns show detections of the single pulses in the left circular polarization (LCP) and right circular polarization (RCP) channels, respectively. We show the (a) integrated single pulse profiles and (b) dynamic spectra dedispersed using a DM of 1778 pc cm^{-3} from both polarizations with a time resolution of 2 ms. The pulse shapes of the dominant emission components from pulse cycles $n = 12$ and $n = 321$ resemble a reverse exponential tail. The secondary emission component detected during pulse cycle $n = 321$ has a traditional scattering tail shape, which is not observed in the other emission components.

The single pulse morphology may be caused by processes that are either intrinsic or extrinsic to the magnetar. The variability in pulse structure between emission components argues for an intrinsic origin, though external scattering or refractive lensing could also be responsible. Extrinsic mechanisms would have to produce fast line of sight changes on millisecond to second timescales, which suggests that such structures are located near the magnetar.

Pulses were observed during more than 70% of the magnetar's rotations, but often not at precisely the same phase (see Figures 4.7–4.9). This implies that the active site of the emission must emit pulses fairly continuously since pulses were seen during almost all rotations. The 3–50 ms timescale between successive components is likely indicative of the pulse repetition rate. The width of the distribution of pulse components is approximately ±0.02 in phase units (see Figure 4.7). These observations are most naturally explained by fan beam emission with a width of about ±7°. The data are consistent with a single primary active region of emission since pulse components were generally not detected outside of a narrow phase range, except in a few cases.

Figure 4.4 shows that most rotations exhibited multiple pulse components, although single components were not uncommon. Giant pulses were detected primarily during the second half of epoch 3, which indicates that these bright events are transient in nature. There is some evidence that the brightest pulse component appears first during a given rotation, occasionally followed by weaker components. This may indicate that the active region can have outbursts that trigger additional bursts. Alternatively, the dimming of later pulse components may be due to effects from tapering of the fan beam.

Recent measurements of PSR J1745–2900's linear polarization fraction showed large variations as a function of time (see Figure 3 in Desvignes et al. [155]). We note that the strength of the single pulse emission during epochs 1–4 seems to roughly coincide with changes in the polarization fraction. In particular, the third epoch showed the strongest emission components during one of the periods of maximum linear polarization. Desvignes et al. [155] discuss whether the frequency dependent polarization behavior could be intrinsic or extrinsic to the magnetar.

4.4.2 Scattering Regions

Hyperstrong radio wave scattering from pulsars near the GC has typically been modeled by a single thin scattering screen [122, 305]. The amount of pulse broadening produced by multipath propagation through the screen depends on its distance from the GC (Δ_{GC}), which can be calculated from [122]:

$$\Delta_{\text{GC}} = \frac{D_{\text{GC}}}{1 + \left(\frac{\tau_d}{6.3\,\text{s}}\right)\left(\frac{8.5\,\text{kpc}}{D_{\text{GC}}}\right)\left(\frac{1.3\,\text{arcsec}}{\theta_{1\,\text{GHz}}}\right)^2\left(\frac{\nu}{1\,\text{GHz}}\right)^4}, \tag{4.10}$$

where τ_d is the temporal scattering timescale at an observing frequency ν, $D_{\text{GC}} = 8.3 \pm 0.3\,\text{kpc}$ is the distance to the GC [201], and $\theta_{1\,\text{GHz}} = 1075 \pm 50\,\text{mas}$ is the angular size of PSR J1745–2900 scaled to 1 GHz [62]. Assuming the pulse broadening reported in Section 4.3.4.2.5 is entirely due to temporal scattering from diffraction through a single thin screen, Equation (4.10) can be used to determine the screen's distance from the GC. We find that a scatter broadening timescale of $\langle\tau_d\rangle = 6.9 \pm 0.2\,\text{ms}$ at 8.4 GHz would require a screen at a distance of $0.9 \pm 0.1\,\text{kpc}$ from the GC.

The number of scattering screens and their locations is an important consideration, which has strong implications on searches for pulsars toward the GC. A screen is thought to exist at a distance of ~5.8 kpc from the GC based on temporal broadening measurements between 1.2 and 8.7 GHz [62]. Wucknitz [570] argued that most of the temporal and angular scattering from this magnetar are produced by a single thin scattering screen ~4.2 kpc from the pulsar. However, a single screen at either of these distances is incompatible with the single pulse broadening reported here at 8.4 GHz if the broadening is attributed to thin screen scattering. A distant, static scattering screen also cannot account for the variations in broadening between components on short timescales. Scattering from regions much closer to the GC (< 1 kpc) have also been proposed [157, 305], but a single sub-kiloparsec screen overestimates the amount of scattering reported by Spitler et al. [498] between 1.19 and 18.95 GHz.

Recently, Desvignes et al. [155] observed rapid changes in the magnetar's RM and depolarized radio emission at 2.5 GHz. They attributed the variations in RM to magneto-ionic fluctuations in the GC and explained the depolarization behavior by invoking a secondary scattering screen at a distance of ~0.1 pc in front of the magnetar, assuming a screen size of ~1.9 au and a scattering delay time of ~40 ms. A two-scattering-screen model, consisting of a local screen (< 700 pc from the GC) and a distant screen (~ 5 kpc from the GC), has also been proposed to explain the angular and temporal broadening from other GC pulsars, which cannot be accounted for by a single scattering medium [157]. In the case of PSR J1745–2900, Dexter et al. [157] argued that a local screen would not significantly contribute to the temporal broadening. On the other hand, a two component scattering screen, with a strong scattering central region and weak scattering extended region, may explain both the $\tau_d \propto \nu^{-3.8}$ temporal scattering at lower frequencies [498] and larger broadening times at higher frequencies. Depending on the scattering strengths and sizes of the regions, the spectrum of pulse broadening times can flatten at higher frequencies (e.g., see Figure 3 in Cordes and Lazio [123]).

Strong variability in the single pulse broadening times was seen on short timescales between pulse cycles and individual emission components within the same pulse cycle (see Figures 4.3, 4.10, and 4.12). Ultra-fast changes in the scattering media on roughly millisecond to second timescales would be required to explain this variability using multiple screens. Scattering regions formed from turbulent, fast-moving plasma clouds in close proximity to the magnetar might be one possible mechanism that could produce this variability. Similar models have been used to explain the temporal structure of pulses from the Crab pulsar [138, 338]. Alternatively, this behavior could be explained by an ensemble of plasma filaments near a strong scattering screen close to the magnetar, where these filaments create inhomogeneities in the scattering medium [123].

We also consider the possibility that the single pulse broadening is intrinsic in origin. Pulsed radio emission from magnetars is known to be highly variable, and strong spiky single pulses have been observed from other radio magnetars, such as PSR J1622–4950 [313]. The similarity between the time delay between single pulse emission components, $\langle \tau_{12} \rangle_\alpha \approx 8$ ms, and the single pulse broadening timescale, $\langle \tau_d \rangle \approx 7$ ms, suggests that exponential tails in the single pulses may be comprised of multiple unresolved adjacent components.

4.4.3 Plasma Clouds and Plasma Lenses

First, we describe how multipath propagation through compact, high density plasma clouds may give rise to variable pulse broadening between pulse components. This behavior could be produced during pulse cycles where one or more of these clouds traverse the radio beam at high velocities. Inhomogeneities in the clouds could result in different observed scattering shapes. These objects would also have to be transient to explain the differences in broadening between components in the same pulse cycle, which argues for locations near the pulsar magnetosphere. These plasma clouds are postulated to exist in the physical environment of the magnetosphere.

We provide estimates of the temperature (T_{PC}) of the plasma cloud (PC), smallest elementary thickness of the inter-plasmoid current layer (δ), and distance from the magnetar ($D_{\rm PC}$) where these structures are expected to exist. Our calculations follow the model in Uzdensky and Spitkovsky [538], which assumes magnetic reconnection occurs in the pulsar magnetosphere and allows for strong optically thin synchrotron radiative cooling inside the layer. We assume a canonical neutron star mass of $M_\star = 1.4\,M_\odot$, with radius $R_\star = 10\,\mathrm{km}$ and moment of inertia $I = 10^{45}\,\mathrm{g\,cm^2}$. The magnetar's surface dipolar magnetic field is $B_{\rm surf} \approx 3.2 \times 10^{19} (P\dot{P})^{1/2}\,\mathrm{G}$ $\approx 2.6 \times 10^{14}\,\mathrm{G}$ [335], which is ~6 times larger than the quantum critical magnetic field, $B_{\rm Q} = m_e^2 c^3 / e\hbar \approx 4.4 \times 10^{13}\,\mathrm{G}$. If we assume the magnetic field is approximately dipolar inside the light cylinder (LC), we can estimate the magnetic field at distances $D_{\rm PC} \leq R_{\rm LC} = cP/2\pi \approx 1.8 \times 10^5\,\mathrm{km}$ using $B_{\rm PC} \approx B_{\rm surf}(R_\star/R_{\rm PC})^3$. Magnetic reconnection likely occurs at distances much smaller than the light cylinder radius since the predicted magnetic field is considerably weaker at the edge of the light cylinder ($B_{\rm LC} \approx 2.9 \times 10^8 P^{-5/2} \dot{P}^{1/2}\,\mathrm{G} \approx 45\,\mathrm{G}$). Following the analysis in Uzdensky and Spitkovsky [538], we find that, at a distance of $D_{\rm PC} = 5000\,\mathrm{km} = 500 R_\star \sim 0.03 R_{\rm LC}$, the magnetic field inside the magnetosphere is $B_{\rm PC} \approx 2 \times 10^6\,\mathrm{G}$. If this field is comparable to the reconnecting magnetic field in the comoving frame of the relativistic pulsar wind, then plasma clouds formed in the pulsar's magnetosphere can have densities of $n_{\rm PC} \sim 10^{12}\,\mathrm{cm^{-3}}$, with temperatures of $T_{\rm PC} \sim 50\,\mathrm{GeV}$, and plasma scales of order $\delta \sim 150\,\mathrm{cm}$ or larger (in the comoving frame).

Scattering from plasma clouds may give rise to pulse broadening by an amount $\tau_d \sim L_{\rm PC}^2/2cD_{\rm PC}$, where $L_{\rm PC}$ is the cloud size. In order to explain a broadening timescale of ~7 ms, such clouds can be no larger than $L_{\rm PC} \sim 4600\,\mathrm{km}$, assuming a distance of $D_{\rm PC} = 5000\,\mathrm{km}$ to the cloud. Although different cloud geometries are possible, these estimates suggest that high density plasma clouds in close proximity to the pulsar wind could produce changes on the short timescales needed to explain the pulse broadening variations between emission components.

Next, we discuss possible mechanisms responsible for the frequency structure observed in the single pulse emission components. During most magnetar rotations, individual pulse components showed variations in brightness with frequency, but all of the components were not strongly affected simultaneously during pulse cycles where the emission was multipeaked. In many cases, the pulsed radio emission vanished over a significant fraction of the frequency bandwidth (e.g., see Figures 4.3 and 4.5). We argue that these effects are likely extrinsic to the magnetar and can be produced by strong lensing from refractive plasma structures, but may also be intrinsic to the magnetar.

Lensing from structures near the magnetar may account for the variations in brightness between closely spaced components. This mechanism has also been proposed to explain echoes of radio pulses from the Crab pulsar [25, 216] and bursts from FRB sources [131]. Applying the model in Cordes et al. [131], we find that a one-dimensional Gaussian plasma lens at a distance of $d_{\rm sl} = R_{\rm LC} = 1.8 \times 10^5$ km from the magnetar, with a scale size of $a \sim 5300$ km and lens dispersion measure depth of $\mathrm{DM}_\ell \sim 10\,\mathrm{pc\,cm^{-3}}$, can produce frequency structure on scales of ∼1–500 MHz near a focal frequency of ∼8.4 GHz. Caustics can induce strong magnifications, with changes in gain spanning 1–2 orders of magnitude for this particular lens configuration (see Figure 4.15). Frequency dependent interference effects are most prominent near the focal frequency and become attenuated at higher frequencies. Larger dispersion depths would result in higher focal frequencies, which is certainly a possibility for plasma lenses located near the GC. Multiple plasma lenses may be responsible for the observed behavior, and they may have a variety of sizes, dispersion depths, and distances from the source that could differ from the parameter values considered here. Alternatively, this behavior could be intrinsic, possibly similar in nature to the banded structures observed in one of the components of the Crab pulsar, namely the High-Frequency Interpulse [221].

4.4.4 Comparison with Other Magnetars and High Magnetic Field Pulsars

PSR J1745–2900 shares remarkable similarities with the three other radio magnetars: XTE J1810–197, 1E 1547.0–5408, and PSR J1622–4950 [78, 80, 312]. They all exhibit extreme variability in their pulse profiles, radio flux densities, and spectral indices, which are quite anomalous compared to ordinary radio pulsars. Their average pulse shapes and flux densities can also change on short timescales of hours to days (e.g., see [83, 84, 312, 432]). Radio pulses from these magnetars are typically built up of multiple spiky subpulses with widths on the order of milliseconds [313, 487] and can be exceptionally bright, with peak flux densities exceeding 10 Jy in the case of XTE J1810–197 [78]. The flux densities of these events are unlike the giant pulses observed from the Crab pulsar [129], which have an energy flux distribution that follows a power-law [354].

These magnetars tend to have relatively flat or inverted radio spectra, while ordinary radio pulsars have much steeper spectra on average (mean spectral index $\langle\alpha\rangle = -1.8 \pm 0.2$ [372]). This makes the detection of normal radio pulsars challenging at frequencies above a few gigahertz. To date, only seven ordinary pulsars have been detected at frequencies above 30 GHz [287, 326, 398, 557]. In contrast, two of these radio magnetars (PSR J1745–2900 and XTE J1810–197) have been detected at record high frequencies (291 and 144 GHz, respectively [81, 533]). Daily changes in the spectral indices of these four radio magnetars have also been observed (e.g., see [11, 304]). Unusually steep radio spectra have been obtained from PSR J1745–2900 and XTE J1810–197 [84, 432], with negative spectral indices comparable to those reported here in Table 4.3.

The pulsed radio emission from magnetars is often highly linearly polarized [82, 313], but large variations in polarization have been seen [155]. With the exception of XTE J1810–197, the other radio magnetars have RMs that fall in the top 1% of all known pulsar RMs, indicating that they inhabit extreme magneto-ionic environments. Radio emission from magnetars can also suddenly shut off, and quiescence periods can last for many hundreds of days (e.g., see [84, 481]), but no such behavior has yet been reported for the GC magnetar. However, PSR J1745–2900 was not detected during searches for compact radio sources in the GC or in X-ray scans of the Galactic plane prior to its discovery (e.g., see [39, 306]), which suggests that it was quiescent before its initial X-ray outburst in 2013 April [274].

PSR B1931+24, an ordinary isolated radio pulsar, has exhibited quasi-periodic deactivation and reactivation of its radio emission on timescales of 25–35 days [290], but this is extremely atypical of radio pulsars. Normal rotation-powered pulsars with high magnetic fields, such as PSR J1119–6127, have displayed mode changes over days to weeks following magnetar-like X-ray outbursts, which resemble the emission characteristics of radio magnetars [143, 356]. This suggests an underlying connection between ordinary pulsars and magnetars. To our knowledge, our observations of frequency dependent variations in the individual pulses of PSR J1745–2900 (see Section 4.3.4.2.2) are the first examples of such behavior from a radio magnetar.

4.4.5 Similarities with Fast Radio Bursts

As pointed out in various papers (e.g., see [387, 391, 431]), an extragalactic magnetar near a massive black hole could be the progenitor of FRBs. There are numerous similarities between the emission from the GC magnetar and FRB sources, such as the repeating FRB 121102. High dispersion measures are observed from both FRB 121102 (DM = 560 pc cm^{-3} [391]) and PSR J1745–2900 (DM = 1778 pc cm^{-3}). These objects also exhibit large, variable RMs (RM $\approx 1.4 \times 10^5$ rad m$^{-2}/(1+z)^2$, where $z \sim 0.2$ for FRB 121102 [391], compared to RM $\approx -7 \times 10^4$ rad m^{-2} for the

GC magnetar [155, 169]). Multicomponent bursts with widths $\lesssim 1$ ms have been reported from FRB 121102 [191, 391]. This is similar to the pulse morphology of the GC magnetar, which shows emission components with comparable pulse widths that are likely broadened. In both cases, the detected burst spectra show frequency structure on similar scales, which may be produced by the same underlying mechanism (e.g., see [191, 391, 499]). Other FRBs, such as FRB 170827 [180], exhibit bursts with frequency structure on much finer scales ($\lesssim 2$ MHz) at frequencies below $\sim$1 GHz.

At a luminosity distance of $\sim$1 Gpc, the energy output of bursts from FRB 121102 is a factor of $\sim 10^{10}$ larger than the single pulse emission from PSR J1745–2900. However, we find that strong focusing by a single plasma lens can produce caustics that may boost the observed flux densities of bursts from FRB 121102 by factors of ~ 10–10^6 on short timescales (see Figure 4.16) [131]. Multiple plasma lenses could yield even larger burst magnifications. We also note that many pulses from the GC magnetar had $\gtrsim 10$ times the typical single pulse intensity, and the emission rate of these giant pulses was time-variable. Therefore, an FRB source like FRB 121102 could possibly be an extreme version of a magnetar, such as PSR J1745–2900.

4.5 Appendix: Thin Scattering Screen Model

Pulse broadening is typically quantified by a characteristic timescale, τ_d, which is related to the pulsar's distance and scattering measure in the case of scattering from the ISM [121]. We assume that the pulse broadening is produced by multipath scattering through a thin scattering screen, infinitely extended transverse to the line of sight [137]. Temporal scattering is modeled by a pulse broadening function (PBF), which describes the electron density in the ISM. If the electron density fluctuations are characterized by a square-law structure function [299], the PBF is given by a truncated, one-sided exponential [45]:

$$\mathrm{PBF}(t) = \frac{1}{\tau_d} \exp\left(-\frac{t}{\tau_d}\right) \Theta(t), \tag{4.11}$$

where $\Theta(t)$ is the unit step function, defined by $\Theta(t \geq 0) = 1$ and $\Theta(t < 0) = 0$.

We model the unbroadened single pulse emission component as a Gaussian pulse:

$$P(t) = \frac{A}{w\sqrt{2\pi}} \exp\left[-\frac{1}{2}\left(\frac{t-t_0}{w}\right)^2\right], \tag{4.12}$$

where A is the amplitude of the pulse, t_0 is the time of the pulse peak, and w is the intrinsic 1σ pulse width. The observed scattered single pulse profile, $P_{\mathrm{obs}}(t)$, is given by the convolution of the intrinsic profile, $P(t)$, with the PBF in Equation (4.11) and the impulse response of the instrument, $I(t)$:

$$\begin{aligned} P_{\mathrm{obs}}(t) &= P(t) * \mathrm{PBF}(t) * I(t) &\quad (4.13)\\ &= P(t) * \mathrm{PBF}(t) * D(t) * S(t) &\quad (4.14)\end{aligned}$$

The instrumental response, $I(t)$, is derived from the convolution of the impulse response, $D(t)$, due to incoherently dedispersing the data over a narrow detection bandwidth, and the impulse response, $S(t)$, produced by the radio telescope's detection circuitry (e.g., from a finite sampling time). Here, we ignore the effect of incoherent dedispersion on the observed pulse shape since the intra-channel dispersion smearing at X-band is 25.3 μs, which is significantly less than the 512 μs sampling time. We also assume that additional instrumental effects are negligible.

The observed pulse shape in Equation (4.14) has an analytical solution [381] in the absence of instrumental effects (i.e., $I(t) = D(t) = S(t) = \delta(t)$, where $\delta(t)$ is the Dirac delta function):

$$P_{\mathrm{obs}}(t) = \frac{A}{2\tau_d}\exp\left(\frac{w^2}{2\tau_d^2}\right)\exp\left[-\frac{(t-t_0)}{\tau_d}\right] \times \left\{1 + \mathrm{erf}\left[\frac{(t-t_0) - \frac{w^2}{\tau_d}}{w\sqrt{2}}\right]\right\} + b, \quad (4.15)$$

where we have added a constant, b, to account for small offsets in the baseline levels of the single pulse profiles. We note that, aside from normalization factors, which can be incorporated into the definition of the amplitude, A, our model in Equation (4.15) differs from Equation (3) in Spitler et al. [498] and Equation (2) in Desvignes et al. [155] by a multiplicative factor of $\exp(t_0/\tau_d)$. This term has a considerable effect on the pulse amplitude when the broadening timescale, τ_d, is small.

4.6 Appendix: Plasma Lensing

The refractive properties of a one-dimensional interstellar plasma lens with a Gaussian profile of free-electron column density were presented in Clegg et al. [106]. They assumed that plane waves are incident on the lens from an infinitely distant point source, which introduce a phase perturbation:

$$\phi_\lambda = -\lambda r_e \mathrm{DM}(x), \quad (4.16)$$

where λ is the radio wavelength, $r_e = e^2/(m_e c^2)$ is the classical electron radius, e is the electron charge, m_e is the electron mass, and c is the speed of light. In their analysis, Clegg et al. [106] also assume that the lens has a Gaussian column density profile, given by:

$$\mathrm{DM}(x) = \mathrm{DM}_\ell \exp\left(-\frac{x^2}{a^2}\right), \tag{4.17}$$

where a is the scale size of the lens and DM_ℓ is the lens' dispersion measure depth. When $\mathrm{DM}_\ell > 0$, the plasma lens is diverging, but caustics can be produced when rays pass through different parts of the lens.

Cordes et al. [131] extended the analysis presented in Clegg et al. [106] to the case where the source is a finite distance from the plasma lens. Following the formalism in Cordes et al. [131], let d_{so} be the distance from the source to the observer and d_{sl} be the distance from the source to the lens. Then, the distance between the lens and the observer is given by $d_{\mathrm{lo}} = d_{\mathrm{so}} - d_{\mathrm{sl}}$. Furthermore, let x_{s}, x, and x_{obs} denote the transverse coordinates in the source, lens, and observer's planes. The dimensionless coordinates $u_{\mathrm{s}} = x_{\mathrm{s}}/a$, $u = x/a$, and $u_{\mathrm{obs}} = x_{\mathrm{obs}}/a$ are obtained by scaling the transverse coordinates by the lens scale, a. The lens is centered on $u = 0$, and the optics of the lens can be expressed in terms of a combined transverse offset:

$$u' = \left(\frac{d_{\mathrm{lo}}}{d_{\mathrm{so}}}\right) u_{\mathrm{s}} + \left(\frac{d_{\mathrm{sl}}}{d_{\mathrm{so}}}\right) u_{\mathrm{obs}}. \tag{4.18}$$

From Equation (4.18), we see that the observer's location will most strongly impact u' when $d_{\mathrm{lo}}/d_{\mathrm{so}} = 1 - d_{\mathrm{sl}}/d_{\mathrm{so}} \ll 1$. When $d_{\mathrm{sl}}/d_{\mathrm{so}} \ll 1$, then offsets or motions of the source will dominate u' for lenses close to the source.

The lens equation in geometric optics corresponds to stationary-phase solutions for u of the Kirchhoff diffraction integral (KDI):

$$u' = u(1 + \alpha e^{-u^2}). \tag{4.19}$$

Here, α is a dimensionless parameter given by:

$$\alpha = \frac{\lambda^2 r_e \mathrm{DM}_\ell}{\pi a^2}\left(\frac{d_{\mathrm{sl}} d_{\mathrm{lo}}}{d_{\mathrm{so}}}\right), \tag{4.20}$$

where DM_ℓ is in units of pc cm^{-3}, a is in units of au, and d_{sl}, d_{lo}, and d_{so} are in units of kpc. Electron density enhancements correspond to positive values of α and produce a diverging lens, while electron density voids are produced when $\alpha < 0$ and give rise to a converging lens. Here, we restrict our focus to electron density enhancements since the phenomenology of their behavior may account for the observed properties of some FRBs. This formalism may also be extended to a two-dimensional plasma lens with an arbitrary phase peturbation, $\mathrm{DM}(\mathbf{x}) = \mathrm{DM}_\ell \psi(\mathbf{x})$, where $\psi(\mathbf{x})$ is a dimensionless function with unity maximum. In this case, the lens equation becomes $\mathbf{u}' = \mathbf{u} + \alpha a \nabla_u \psi(\mathbf{u})$, where a is the characteristic scale of $\psi(\mathbf{u})$. In this section, we restrict our analysis to the case of a one-dimensional Gaussian lens.

In the geometrical optics (GO) regime, focusing or defocusing of the incident wavefronts gives rise to a gain or amplification. The gain is given by the stationary-phase solution of Equation (4.19), where $u = u(\alpha, u')$ [106, 131]:

$$G = \left|1 + \alpha(1 - 2u^2)e^{-u^2}\right|^{-1}. \tag{4.21}$$

The minimum gain is $G_{\min} = 1/(1 + \alpha)$, which occurs when $u = u' = 0$. The focal points can be found where $G \to \infty$, which occurs when:

$$\alpha_\infty = \frac{e^{u^2}}{2u^2 - 1}. \tag{4.22}$$

When α is restricted to positive values, the gain does not approach ∞ for $|u| < 1/\sqrt{2}$ since $G < 1$. The minimum of α_∞ in Equation (4.22) occurs at $\alpha_{\min} = e^{3/2}/2 = 2.24$ when $|u| = \sqrt{3/2} = 1.22$. For $|u| > \sqrt{3/2}$, α_∞ increases exponentially, which may correspond to physically implausible lenses with large electron densities, large distances, or low frequencies.

In the lens plane, the locations where the gain approaches ∞ can be determined by solving for $G^{-1} = 0$, after combining Equations (4.19) and (4.21) to eliminate αe^{-u^2}. This yields the expression $2u^3 - 2u^2u' + u' = 0$, which is satisfied when $u' = 2u^3/(2u^2 - 1)$. Substituting $|u| = \sqrt{3/2}$ into this expression, which coincides with $\alpha_{\min}$ (the minimum of α_∞), yields $|u'| = (3/2)^{3/2} = 1.84$.

Next, we consider a one-dimensional Gaussian plasma lens configuration with $\mathrm{DM}_\ell = 1\,\mathrm{pc\,cm^{-3}}$, $a = 1$ au, $d_{\mathrm{so}} = 1$ Gpc, and $d_{\mathrm{sl}} = 1$ kpc. In this case, $d_{\mathrm{sl}}/d_{\mathrm{so}} = 10^{-6}$, so u' will be dominated by motions of the source. In Figure 4.13, we show the variation of the gain, G, with frequency and transverse location, u'. Horizontal slices through the lens plane are shown in Figure 4.14 at various frequencies.

When the lens–observer distance, d_{lo} is larger than the focal distance, d_{f}, radio bursts passing through the plasma lens will be affected by caustics in the light curves as they reach the observer along multiple paths. The requirement for multiple images, $\alpha > \alpha_{\min}$, gives a focal distance of:

$$d_{\mathrm{f}}(\nu) = d_{\mathrm{lo}}\left(\frac{\alpha_{\min}}{\alpha}\right) = \frac{\pi(a\nu)^2\alpha_{\min}}{r_e c^2 \mathrm{DM}_\ell}\left(\frac{d_{\mathrm{so}}}{d_{\mathrm{sl}}}\right). \tag{4.23}$$

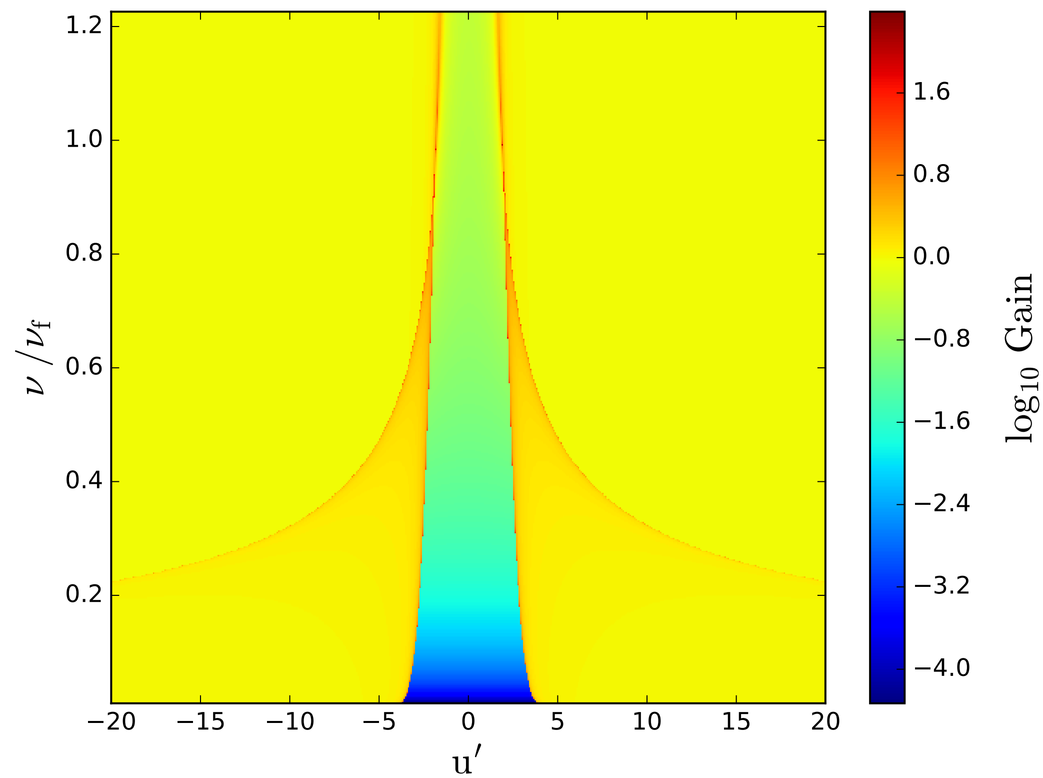

Figure 4.13: **Total gain of a one-dimensional Gaussian plasma lens, summed over all rays that reach an observer, versus frequency (normalized by the focal frequency, ν_f) and transverse location, u'.** The plasma lens considered here has $\mathrm{DM}_\ell = 1\,\mathrm{pc\,cm^{-3}}$, $a = 1$ au, $d_{so} = 1$ Gpc, and $d_{sl} = 1$ kpc. Image credit: Adapted from Figure 3 in [131].

The focal frequency, ν_f, is given by:

$$\nu_f = \nu \left(\frac{\alpha}{\alpha_{\min}}\right)^{1/2} = \frac{c}{a}\left(\frac{r_e \mathrm{DM}_\ell}{\pi \alpha_{\min}} \frac{d_{sl} d_{lo}}{d_{so}}\right)^{1/2}. \tag{4.24}$$

Combining Equations (4.23) and (4.24), the focal frequency can be expressed in terms of the focal distance as:

$$\nu_f = \nu \sqrt{\frac{d_{lo}}{d_f(\nu)}}. \tag{4.25}$$

A one-dimensional Gaussian plasma lens, at a finite distance from PSR J1745–2900, can produce lensing behavior that is qualitatively similar to the frequency structure observed in the radio single pulses from PSR J1745–2900. Applying the model described above, we find that a plasma lens with $\mathrm{DM}_\ell \sim 10\,\mathrm{pc\,cm^{-3}}$, $a = 5300$ km, $d_{so} = 8.3$ kpc, and $d_{sl} = 1.8 \times 10^5$ km can generate frequency structure on scales

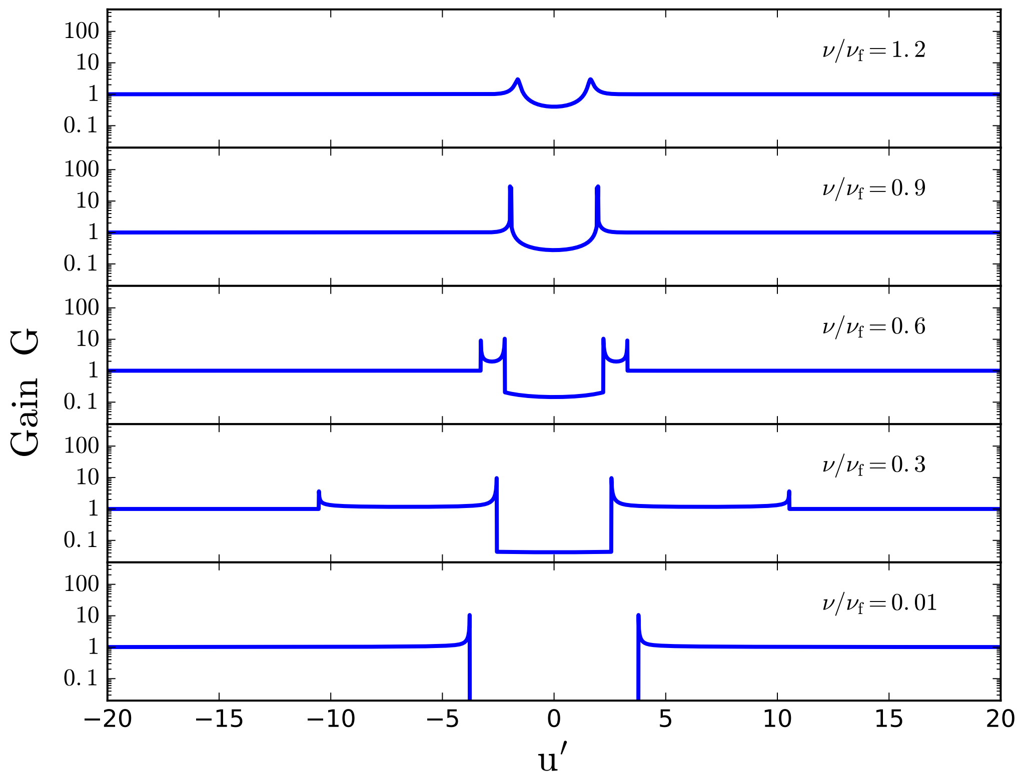

Figure 4.14: **Spatial slices of the gain, G, through the lens plane for a few frequencies (normalized by the focal frequency, ν_f).** The plasma lens considered here has $\mathrm{DM}_\ell = 1\,\mathrm{pc\,cm^{-3}}$, $a = 1$ au, $d_{so} = 1$ Gpc, and $d_{sl} = 1$ kpc. Image credit: Adapted from Figure 4 in [131].

of ∼1–500 MHz near the lens' focal frequency of ∼8.4 GHz. For this particular lens configuration, the observed radio flux density can be amplified by 1–2 orders of magnitude near the focal frequency (see Figure 4.15). The lens parameters considered here are simply for illustrative purposes, and other parameter values may be possible. Alternatively, as discussed in Section 4.4.3, the frequency structure may instead be an intrinsic property of the magnetar's emission mechanism.

Next, we consider a plasma lens with observable properties that are qualitatively similar to the emission observed from the repeating FRB 121102 [131]. We assume that the plasma lens has a dispersion depth of $\mathrm{DM}_\ell = 10\,\mathrm{pc\,cm^{-3}}$ and a scale size of $a = 60$ au, along with distance parameters of $d_{so} = 1$ Gpc and $d_{sl} = 1$ kpc. The focal frequency of this plasma lens is $\nu_f \sim 2$ GHz. This particular configuration can boost the observed radio flux density by factors of ∼10–10^6. In Figure 4.16, we show the total gain versus frequency at a transverse position of $u' = 2.0$ for this particular plasma lens configuration. Plasma lenses in the FRB's host galaxy may have a variety of dispersion depths, sizes, and distances from the source, which could introduce lensing effects with gains and timing perturbations on a wide range of timescales.

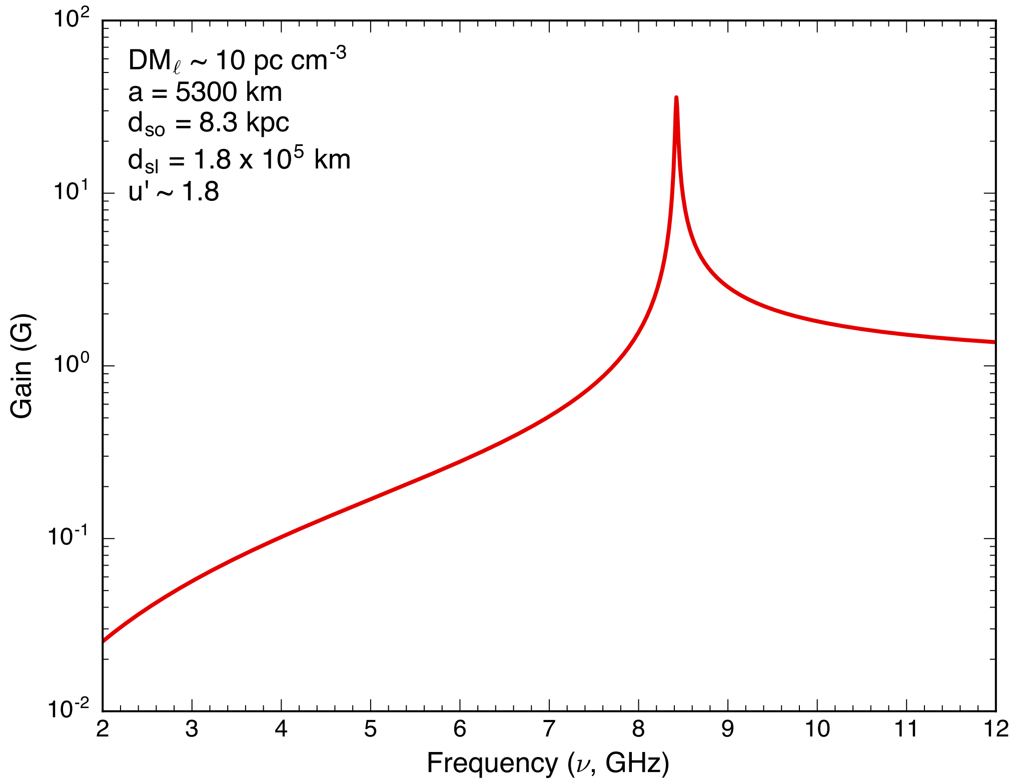

Figure 4.15: **Total gain versus frequency of a one-dimensional Gaussian plasma lens with a transverse position of $u' \sim 1.8$, $\mathrm{DM}_\ell \sim 10\,\mathrm{pc\,cm^{-3}}$, $a = 5300\,\mathrm{km}$, $d_{\mathrm{so}} = 8.3\,\mathrm{kpc}$, and $d_{\mathrm{sl}} = 1.8 \times 10^5\,\mathrm{km}$.** The properties of this plasma lens were chosen so that the lensing behavior is qualitatively similar to the frequency structure observed in the radio single pulses from the Galactic Center magnetar, PSR J1745–2900.

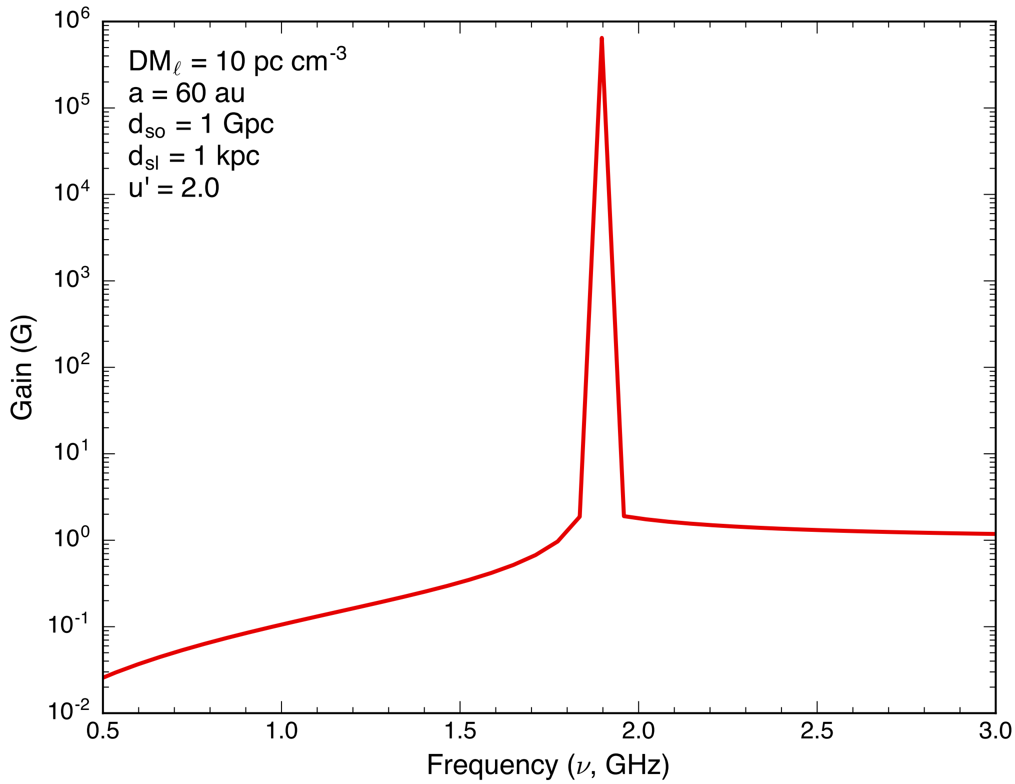

Figure 4.16: **Total gain versus frequency of a one-dimensional Gaussian plasma lens with a transverse position of $u' = 2.0$, $\mathrm{DM}_\ell = 10\,\mathrm{pc\,cm^{-3}}$, $a = 60\,\mathrm{au}$, $d_{\mathrm{so}} = 1\,\mathrm{Gpc}$, and $d_{\mathrm{sl}} = 1\,\mathrm{kpc}$.** The properties of this plasma lens were chosen so that the lensing behavior is qualitatively similar to the emission properties observed from the repeating FRB 121102.

4.7 Acknowledgments

We thank the reviewer for valuable comments that helped us improve this paper. We also thank Professor Roger Blandford for insightful discussions and suggestions.

A.B.P. acknowledges support by the Department of Defense (DoD) through the National Defense Science and Engineering Graduate (NDSEG) Fellowship Program and by the National Science Foundation (NSF) Graduate Research Fellowship under Grant No. DGE-1144469.

We thank the Jet Propulsion Laboratory (JPL) and Caltech's President's and Director's Fund for partial support at JPL and the Caltech campus. We also thank Joseph Lazio and Charles Lawrence for providing programmatic support for this work. A portion of this research was performed at the Jet Propulsion Laboratory, California Institute of Technology and the Caltech campus, under a Research and Technology Development Grant through a contract with the National Aeronautics and Space Administration. U.S. government sponsorship is acknowledged.

Chapter V

Bright X-Ray and Radio Pulses from the Recently Reactivated Magnetar XTE J1810–197

[430] **Pearlman, A. B.*** et al. (2020). "Bright X-Ray and Radio Pulses from a Recently Reactivated Magnetar." Submitted. 2005.08410 [astro-ph.HE].

Bright X-Ray and Radio Pulses from the Recently Reactivated Magnetar XTE J1810–197

Aaron B. Pearlman[1,11,12,*], Walid A. Majid[2,1], Thomas A. Prince[1,2], Paul S. Ray[3], Jonathon Kocz[1,4], Shinji Horiuchi[5], Charles J. Naudet[2], Teruaki Enoto[6], Tolga Güver[7,8], Zaven Arzoumanian[9], Keith C. Gendreau[9], and Wynn C. G. Ho[10]

[1] Division of Physics, Mathematics, and Astronomy, California Institute of Technology, Pasadena, CA 91125, USA

[2] Jet Propulsion Laboratory, California Institute of Technology, Pasadena, CA 91109, USA

[3] Space Science Division, U.S. Naval Research Laboratory, Washington, DC 20375, USA

[4] Department of Astronomy, University of California, Berkeley, CA 94720, USA

[5] CSIRO Astronomy and Space Science, Canberra Deep Space Communications Complex, P.O. Box 1035, Tuggeranong, ACT 2901, Australia

[6] Extreme Natural Phenomena RIKEN Hakubi Research Team, RIKEN Cluster for Pioneering Research, 2-1 Hirosawa, Wako, Saitama 351-0198, Japan

[7] Department of Astronomy and Space Sciences, Faculty of Science, Istanbul University, Beyazıt, 34119 Istanbul, Turkey

[8] Istanbul University Observatory Research and Application Center, Beyazıt, 34119 Istanbul, Turkey

[9] X-ray Astrophysics Laboratory, NASA Goddard Space Flight Center, Greenbelt, MD 20771, USA

[10] Department of Physics and Astronomy, Haverford College, 370 Lancaster Avenue, Haverford, PA 19041, USA

[11] NDSEG Research Fellow

[12] NSF Graduate Research Fellow

[*] Lead author of the manuscript.

Corresponding author: aaron.b.pearlman@caltech.edu

Abstract

Magnetars are young, rotating neutron stars that possess larger magnetic fields ($B \approx 10^{13}$–10^{15} G) and longer rotational periods ($P \approx 1$–12 s) than ordinary pulsars [264, 408]. In contrast to rotation-powered pulsars, magnetar emission is thought to be fueled by the evolution and decay of their powerful magnetic fields. They display highly variable radio and X-ray emission [78, 80, 312, 422], but the processes responsible for this behavior remain a mystery. We report the discovery of bright, persistent individual X-ray pulses from XTE J1810–197, a transient radio magnetar, using the *Neutron star Interior Composition Explorer (NICER)* following its recent radio reactivation [336]. Similar behavior has only been previously observed from a magnetar during short time periods following a giant flare [244, 415]. However, the X-ray pulses presented here were detected outside of a flaring state. They are less energetic and display temporal structure that differs from the impulsive X-ray events previously observed from the magnetar class, such as giant flares [244, 415] and short X-ray bursts [569]. Our high frequency radio observations of the magnetar, carried out simultaneously with the X-ray observations, demonstrate that the relative alignment between the X-ray and radio pulses varies on rotational timescales. No correlation was found between the amplitudes or temporal structure of the X-ray and radio pulses. The magnetar's 8.3 GHz radio pulses displayed frequency structure, which was not observed in the pulses detected simultaneously at 31.9 GHz. Many of the radio pulses were also not detected simultaneously at both frequencies, which indicates that the underlying emission mechanism producing these pulses is not broadband. We find that the radio pulses from XTE J1810–197 share similar characteristics to radio bursts detected from fast radio burst (FRB) sources, some of which are now thought to be produced by active magnetars [57].

5.1 Main Body

XTE J1810–197 was discovered with the *Rossi X-ray Timing Explorer (RXTE)* during an X-ray outburst that began in 2003 [246] and lasted until early 2007 [84]. It is located at a distance of 3.1–4.0 kpc [393], making it one of the nearest magnetars. The pulsar has a rotational period of 5.54 s and a soft X-ray spectrum [246]. Highly linearly polarized radio pulsations were first detected from the magnetar in 2006 using the Parkes telescope, and bright, narrow radio single pulses were observed during each rotation of the neutron star [78]. This discovery established that a relationship exists between magnetars and the larger population of ordinary radio pulsars. XTE J1810–197 has a dispersion measure (DM) of $178 \pm 5\,\mathrm{pc\,cm^{-3}}$ and a spectral index of $-0.5 \lesssim \alpha \lesssim 0$ between 1.4 and 144 GHz [78, 81], with a radio flux density given by $S_\nu \propto \nu^\alpha$. The magnetar's flat radio spectrum has enabled the detection of pulsed radio emission at much higher frequencies than is typically observed from most radio pulsars.

In late 2008, radio pulsations from XTE J1810–197 suddenly ceased [84], and the magnetar remained in a quiescent state for more than a decade [443]. However, on 2018 December 8 (MJD 58460), radio pulsations were redetected from the magnetar using the 76 m Lovell Telescope at Jodrell Bank Observatory [336]. Following the magnetar's reactivation, X-ray and radio follow-up observations were performed (e.g., see [144, 211, 219, 357]).

We carried out observations of XTE J1810–197 with the X-ray Timing Instrument (XTI) on board *NICER* between 2019 February 6 (MJD 58520) and 2019 February 26 (MJD 58540). High frequency radio observations of the magnetar were also performed simultaneously at 8.3 and 31.9 GHz using the NASA Deep Space Network (DSN) [424] 34 m radio telescopes near Canberra, Australia on 2019 February 16 (MJD 58530) and 2019 February 25 (MJD 58539), which included times when *NICER* was also observing the source. These instruments and the data reduction procedures are described in Sections 5.2.1 and 5.2.2 (Methods). A catalog of the X-ray and radio observations presented in this Letter is provided in Table 5.1. Measurements of the magnetar's mean flux density and spectral index at 8.3 and 31.9 GHz are listed in Table 5.2. Unless otherwise stated, all errors quoted in this paper correspond to 1σ uncertainties.

We folded all of the *NICER* barycentric photon arrival times from XTE J1810–197 using an ephemeris derived from contemporaneous radio pulsar timing measurements performed at 8.3 GHz between 2019 February 7 (MJD 58521) and 2019 February 26 (MJD 58540) (see Section 5.2.3; Methods). Relative phase shifts (in phase units) between the folded X-ray pulse profiles in the 1–2, 2–3, 3–4, 4–5, and 5–10 keV energy bands were measured based on sinusoid fits to the pulse profiles in Figure 5.1 (see Table 5.3). Our results indicate that the soft X-ray emission is nearly aligned between 1 and 10 keV. This is consistent with the concentric geometry observed during the magnetar's 2003 outburst [210], where the magnetar's thermal hot spot was surrounded by a larger, warmer emitting region. We measure a relative phase shift of -0.031 ± 0.003 between the 3–5 and 5–10 keV pulse profiles, which is notably smaller in magnitude than the $\Delta\phi \approx 0.1$ phase shift reported in Gotthelf

Table 5.1: **X-ray and Radio Observations of XTE J1810–197**

Instrument	Observation ID	Observation Start Time (UTC)	Observation Start Time (MJD)	Exposure Time (ks)	Count Rate[a] (counts s^{-1})
NICER	1020420130	2019 Feb 06 23:59:20	58520.99954	4.39	48.9
NICER	1020420131	2019 Feb 08 00:29:56	58522.02079	4.83	48.5
NICER	1020420132	2019 Feb 09 15:06:20	58523.62940	1.09	47.1
NICER	1020420133	2019 Feb 10 05:01:40	58524.20949	0.79	45.9
NICER	1020420134	2019 Feb 11 01:07:00	58525.04653	2.00	46.6
NICER	1020420135	2019 Feb 12 07:04:20	58526.29468	1.28	46.0
NICER	1020420136	2019 Feb 13 02:42:41	58527.11297	2.75	46.1
NICER	1020420137	2019 Feb 14 08:08:00	58528.33889	2.13	46.1
NICER	1020420138	2019 Feb 15 02:46:28	58529.11560	1.50	45.5
NICER[†]	1020420139	2019 Feb 16 00:28:00	58530.01944	1.04	45.5
DSN (DSS-34)[†]		2019 Feb 16 18:19:51	58530.76378	7.72	
NICER	1020420140	2019 Feb 17 22:22:11	58531.93207	0.48	46.6
NICER	1020420141	2019 Feb 17 23:54:35	58531.99624	0.52	48.4
NICER	1020420142	2019 Feb 21 02:12:00	58535.09167	2.53	43.7
NICER[†]	1020420143	2019 Feb 25 17:27:40	58539.72755	0.32	44.8
DSN (DSS-35)[†]		2019 Feb 25 18:37:09	58539.77580	6.71	

[a] Average, non-background-subtracted X-ray count rate between 1 and 4 keV.
[†] Data with simultaneous radio and X-ray observations. The overlapping radio and X-ray observations on 2019 February 16 and 2019 February 25 covered a total of ~109 s and ~90 s, respectively.

et al. [211] from a *Nuclear Spectroscopic Telescope Array (NuSTAR)* observation on 2018 December 13 (MJD 58465). If the apparent misalignment between the X-ray pulse profiles in Gotthelf et al. [211] was due to non-coaxial emission components, then our results indicate that the geometry of the X-ray emission has returned to being nearly concentric.

The dynamic energy-resolved folded light curve in Figure 5.1g shows that most of the X-ray photons are detected over a narrow energy range (between 1 and 4 keV). Within this band, a significant fraction of the X-ray photons are detected with energies between roughly 1 and 2.5 keV, where the XTI is most sensitive. The background-subtracted root-mean-squared (RMS) X-ray pulsed fractions in the 0.5–5, 1–2, 2–3, 3–4, 4–5, and 5–10 keV energy bands are listed in Table 5.4. These measurements show that the magnetar's pulsed fraction is increasing linearly as a function of energy between 1 and 5 keV, which is consistent with an earlier *NuSTAR* observation on 2018 December 13 [211].

Bright X-ray pulses were detected from XTE J1810–197 with *NICER* during almost every rotation of the magnetar (e.g., see Figure 5.2). The X-ray pulses were identified by searching for temporal structure in the X-ray light curve using a zero-crossing algorithm. A description of the algorithm is provided in Section 5.2.4.1 (Methods). The X-ray pulses displayed statistically significant temporal variability

Table 5.2: **System Parameters of XTE J1810–197**

Parameter	Value
Fixed Values	
Right Ascension (R.A., J2000)	18 h 09 m 51.08696 s [226]
Declination (Dec., J2000)	–19° 43’ 51.9315” [226]
Dispersion measure (DM)	178.0 pc cm^{-3} [78]
Distance (D)	3.5 kpc [393]
Measured Values	
Mean flux density (S_ν) at 8.3 GHz[a]	4.6 ± 0.9 mJy
Mean flux density (S_ν) at 31.9 GHz[a]	3.7 ± 0.7 mJy
Spectral index (α) between 8.3 and 31.9 GHz[a]	–0.2 ± 0.2
Mean flux density (S_ν) at 8.3 GHz[b]	4.2 ± 0.8 mJy
Mean flux density (S_ν) at 31.9 GHz[b]	2.9 ± 0.6 mJy
Spectral index (α) between 8.3 and 31.9 GHz[b]	–0.3 ± 0.2
Phase-coherent 8.3 GHz timing solution on MJD 58530.8	
Pulse frequency (ν)[c]	0.1804568(1) Hz
Reference epoch (TDB)[d]	MJD 58530.761334907
Observation span (TDB)	MJD 58530.76–58530.85
Number of ToAs	4
Solar system ephemeris	DE405
Timescale	TDB
Weighted root-mean-square (RMS) residual	2.4 ms
Phase-coherent 8.3 GHz timing solution on MJD 58539.8	
Pulse frequency (ν)[c]	0.18045638(5) Hz
Reference epoch (TDB)[d]	MJD 58539.774091226
Observation span (TDB)	MJD 58539.77–58539.85
Number of ToAs	4
Solar system ephemeris	DE405
Timescale	TDB
Weighted root-mean-square (RMS) residual	0.7 ms

[a] Measured value at T_{ref} = MJD 58530.8.
[b] Measured value at T_{ref} = MJD 58539.8.
[c] These values were derived by fitting for a constant rotational frequency, ν.
[d] Reference time corresponding to phase 0.

Table 5.3: **Relative Phase Shifts Between the X-ray Pulse Profiles of XTE J1810–197**

Energy Bands (keV)	Relative Phase Shift
(1–2) / (2–3)	0.010 ± 0.001
(2–3) / (3–4)	0.012 ± 0.001
(3–4) / (4–5)	–0.008 ± 0.002
(4–5) / (5–10)	–0.025 ± 0.003
(3–5) / (5–10)	–0.031 ± 0.003

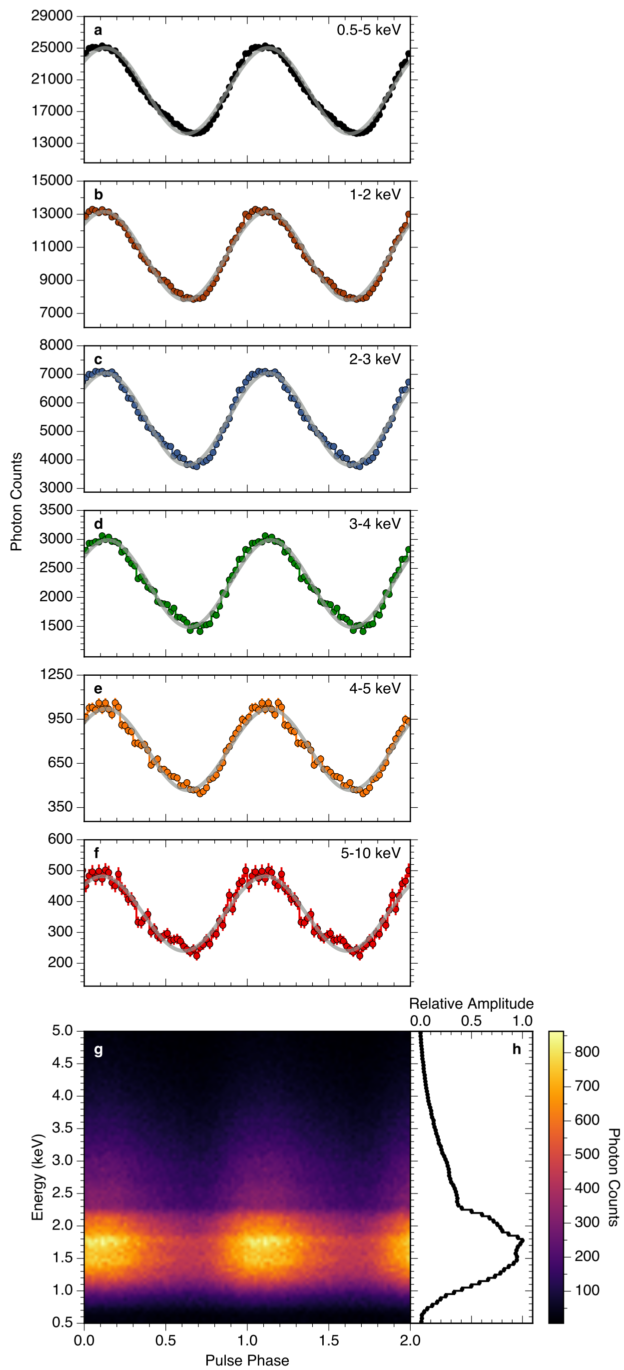

Figure 5.1: **X-ray pulse profiles of XTE J1810–197 in the (a) 0.5–5, (b) 1–2, (c) 2–3, (d) 3–4, (e) 4–5, and (f) 5–10 keV energy bands.** The pulse profiles are derived by combining all of the data from the *NICER* observations listed in Table 5.1. Each pulse profile is folded with 50 phase bins using an ephemeris derived from radio pulsar timing measurements between MJDs 58521 and 58540, where phase 0 corresponds to MJD 58530.761334907 (TDB). Best-fit sinusoids to the pulse profiles are overlaid in gray. The dynamic folded energy-resolved pulse profile is shown in panel (g) with an energy resolution of 0.05 keV. The relative amplitude of the pulse profiles as a function of energy is plotted in panel (h), which shows both the source properties and the detector response.

Table 5.4: **X-ray Pulsed Fractions of XTE J1810–197**

Energy Band (keV)	RMS Pulsed Fraction[a]
0.5–5	0.200 ± 0.001
1–2	0.184 ± 0.001
2–3	0.215 ± 0.002
3–4	0.243 ± 0.003
4–5	0.275 ± 0.005
5–10	0.298 ± 0.009

[a] Background-subtracted RMS pulsed fractions.

on timescales shorter than the magnetar's rotational period, which is not due to Poisson fluctuations (see Section 5.2.4.2; Methods). A single bright X-ray pulse component was detected during most rotations, with a temporal width that varied between pulse cycles. However, X-ray pulses with multiple emission components were detected during ~20% of the rotational cycles, and approximately 20% of the X-ray pulse components had temporal widths that were smaller than 1 s (e.g., see Figure 5.3). The magnetar's individual X-ray pulses also showed pulse-to-pulse energy structure that was stochastically variable in time (e.g., see Figure 5.2d). Similar behavior was observed on 2019 February 25 during separate simultaneous X-ray and radio observations of the magnetar.

The X-ray pulses with larger widths originate from spin-modulated thermal emission from the surface of the magnetar, as the hot spots are swept across the line of sight. The presence of narrow width X-ray pulses indicates that there is also impulsive X-ray emission, which can be produced by external heating from relativistic magnetospheric particles bombarding the stellar surface [42, 412]. This behavior indicates that the X-ray pulses are produced by quasi-thermal emission from one or multiple hot spots on the stellar surface [211, 219]. The X-ray pulses are therefore different from the impulsive, millisecond-wide pulses generated in the radio band (e.g., see Figure 5.8; Methods). These observations show that the thermal hot spots of magnetars can generate individually detectable X-ray pulses, which do not need to be induced by a giant flare.

We find that there is evidence of two different populations of X-ray pulses. In Figure 5.3, we show that the X-ray pulses with larger widths have higher fluences and are emitted over ~60% of the rotational phase range, while the narrow width X-ray pulses have lower fluences and are detected at virtually all rotational phases. The distribution of X-ray pulse fluences in Figure 5.3 reveals a distinct separation between these two groups of X-ray pulses. We ascribe this behavior to anisotropic emission from the thermal regions, which can increase or reduce the apparent luminosity

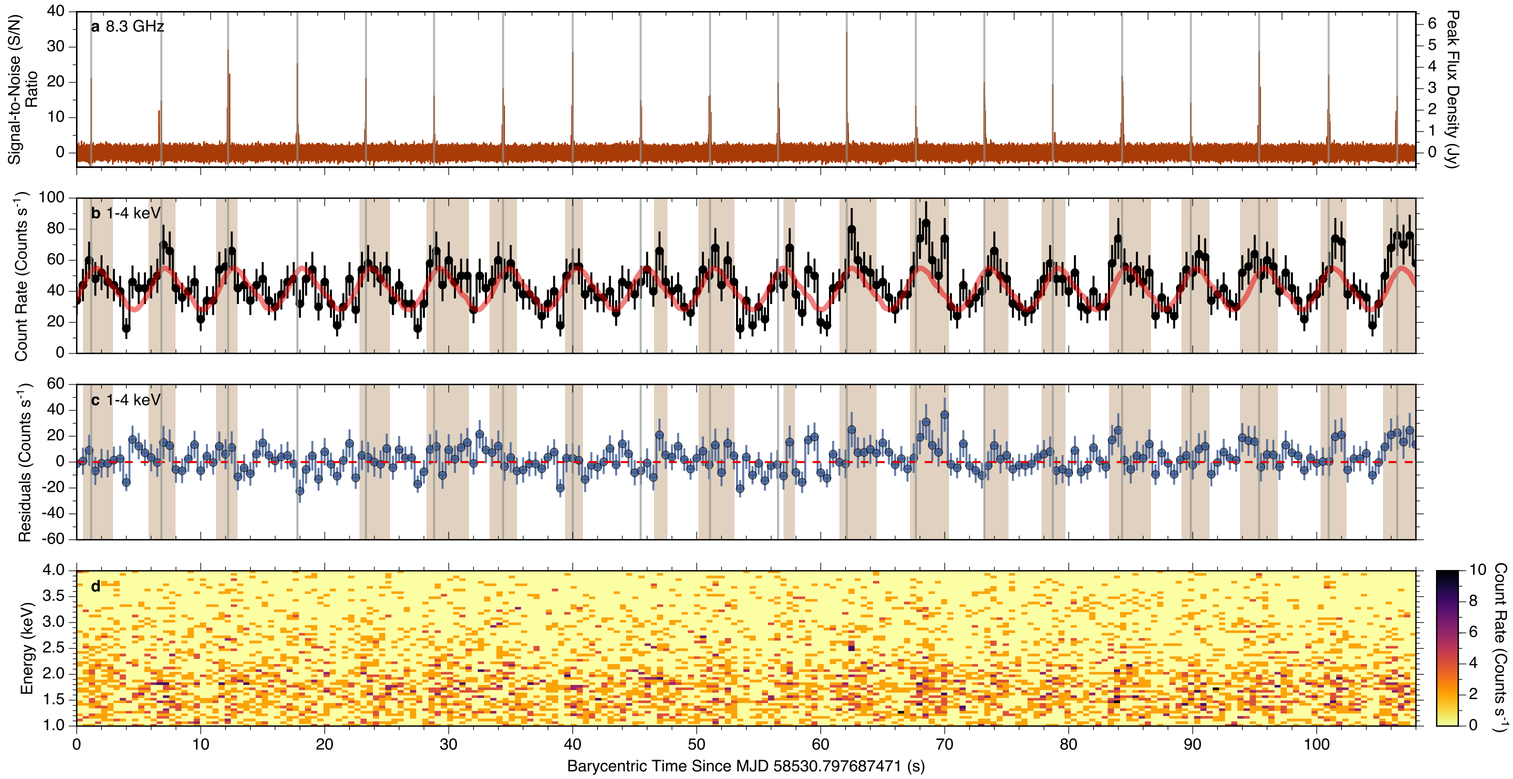

Figure 5.2: **Simultaneous radio and X-ray pulses detected from XTE J1810–197 on MJD 58530.** In panel (a), we show a series of (brown) radio pulses from DSN observations of the magnetar at 8.3 GHz using 512 μs time bins, along with (black) 1–4 keV X-ray pulses simultaneously acquired with *NICER* in panel (b) using 0.5 s time bins. The smoothed, average X-ray pulse profile is overlaid in red in panel (b), after normalizing the pulse profile so that the area under the *NICER* time series and the smoothed profile are equal. The vertical gray lines in panels (a)–(c) indicate the peak time of each radio pulse during each rotation. The beige shaded regions in panels (b) and (c) denote the X-ray pulses identified by the zero-crossing algorithm described in Section 5.2.4.1. The left edge, right edge, and width of the shaded regions correspond to the rising time, falling time, and duration of each X-ray pulse, respectively, as determined by the algorithm. We show the residuals, obtained by subtracting the (red) smoothed X-ray pulse profile from the (black) *NICER* time series, in blue in panel (c). The dynamic spectrum of the X-ray pulses is shown in panel (d) with an energy resolution of 0.05 keV.

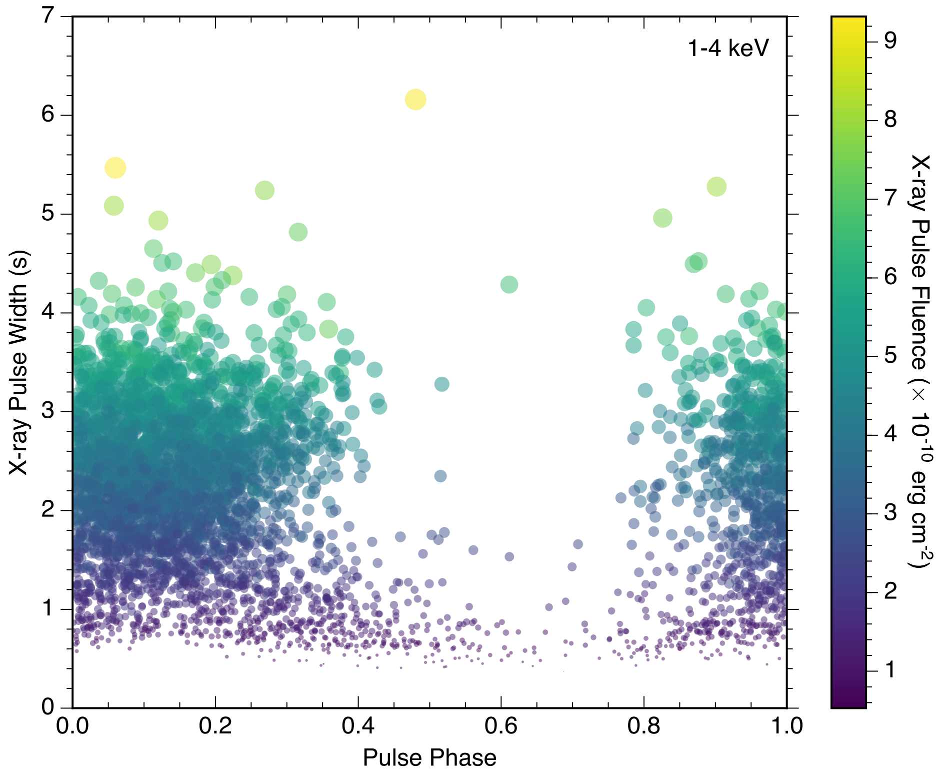

Figure 5.3: **Temporal widths and fluences of the X-ray pulses detected by the zero-crossing algorithm as a function of XTE J1810–197's rotational phase.** These measurements were derived using *NICER* observations between MJDs 58520 and 58540 in the 1–4 keV energy band. The color and size of each data point both represent the fluence of each X-ray pulse.

depending on the opacity in the magnetosphere and the inclination between the hot spots and the line of sight [433].

In Figure 5.2, we show a series of consecutive X-ray and radio pulses from a simultaneous observation with *NICER* and the DSN on 2019 February 16. Although the peak times of the X-ray and radio pulses were nearly aligned during most rotational cycles, the X-ray/radio alignment was variable between subsequent rotations. Some pulse cycles revealed that the radio peak fell slightly before the X-ray peak, while other rotations showed that the radio peak time coincided with the X-ray peak or occurred shortly after. Approximately 65% of the rotations shown in Figure 5.2 had radio and X-ray peak times that agreed to within 0.5 s (the time-resolution of the *NICER* light curve).

The folded 1–4 keV X-ray pulse profiles from 2019 February 16 and 2019 February 25 are shown in Figure 5.4, along with the average pulse profiles from simultaneous radio observations at 8.3 and 31.9 GHz. In order to align the X-ray and radio pulse profiles on each day, we folded the radio and X-ray data using measurements of the magnetar's rotational period during each individual observation, which were derived from a phase-coherent timing solution using pulse times of arrival (ToAs) at 8.3 GHz (see Table 5.2). On 2019 February 16 and 2019 February 25, the 8.3 GHz pulse profile peak was offset from the peak of the X-ray pulse profile by $\Delta\phi = 0.11 \pm 0.05$ and $\Delta\phi = 0.10 \pm 0.05$, respectively. Although these phase shifts are comparable to the X-ray/radio phase alignment reported during XTE J1810–197's 2003 and 2018 outbursts ($\Delta\phi_{2006} = 0.167 \pm 0.006$ [79] and $\Delta\phi_{2018} \approx 0.13$ [211]), we note that these values correspond to the average alignment, which can differ from the alignment during individual rotations. A strong precursor component was also present in the 31.9 GHz pulse profile on 2019 February 25, which was not seen in the profile ~9 days earlier. The phase offset between the 31.9 GHz precursor component and the peak of the 8.3 GHz pulse profile is $\Delta\phi = 0.080 \pm 0.009$. The structure preceding the 31.9 GHz average pulse profile peak on 2019 February 16 is attributed to a population of radio pulses with lower flux densities (see Figure 5.7c; Methods).

Between 2019 February 6 and 2019 February 26 (MJDs 58520–58540), XTE J1810–197's 1–4 keV absorbed X-ray flux decayed from 1.45×10^{-10} to 1.13×10^{-10} erg s^{-1} cm^{-2} at an average rate of $(-1.21 \pm 0.04) \times 10^{-12}$ erg s^{-1} cm^{-2} day^{-1}. During this time period, the peak absorbed X-ray fluxes of the detected X-ray pulses ranged between 1.3×10^{-10} and 2.8×10^{-10} erg s^{-1} cm^{-2}. Assuming that the X-ray emission was produced by a blackbody emitting region at a distance of 3.5 kpc, with an area of $A_{\rm BB} = 213$ km^2 (see Section 5.2.4.3; Methods), we find that the peak X-ray luminosities of the X-ray pulses (averaged over the emitting area; $\langle L_{\rm X} \rangle = L_{\rm X} \left(\frac{A_{\rm BB}}{1\,{\rm km}^2}\right)^{-1}$) were between 0.9×10^{33} and 1.9×10^{33} erg s^{-1} km^{-2}. From the peak X-ray luminosities of the X-ray pulses, we find that the average effective surface temperature over the emitting region ($T_{\rm s} = (\langle L_{\rm X} \rangle / \sigma_{\rm SB})^{1/4}$) is approximately $T_{\rm s} \approx (6\text{–}8) \times 10^6$ K, where $\sigma_{\rm SB} = 5.67 \times 10^{-5}$ erg s^{-1} cm^{-2} K^{-4} is the Stefan-Boltzmann constant. The inferred total radiative energies of the X-ray pulses, averaged over the emitting surface ($\langle E_{\rm total} \rangle = E_{\rm total} \left(\frac{A_{\rm BB}}{1\,{\rm km}^2}\right)^{-1}$), were $(0.4\text{–}6.4) \times 10^{33}$ erg km^{-2}.

The energetics, widths, and morphology of XTE J1810–197's X-ray pulses are remarkably different from those previously observed from giant flares and short X-ray bursts from magnetars. Giant flares from magnetars (e.g., see [244, 415]) are typically characterized by an initial spike lasting ~10–100 ms, followed by an

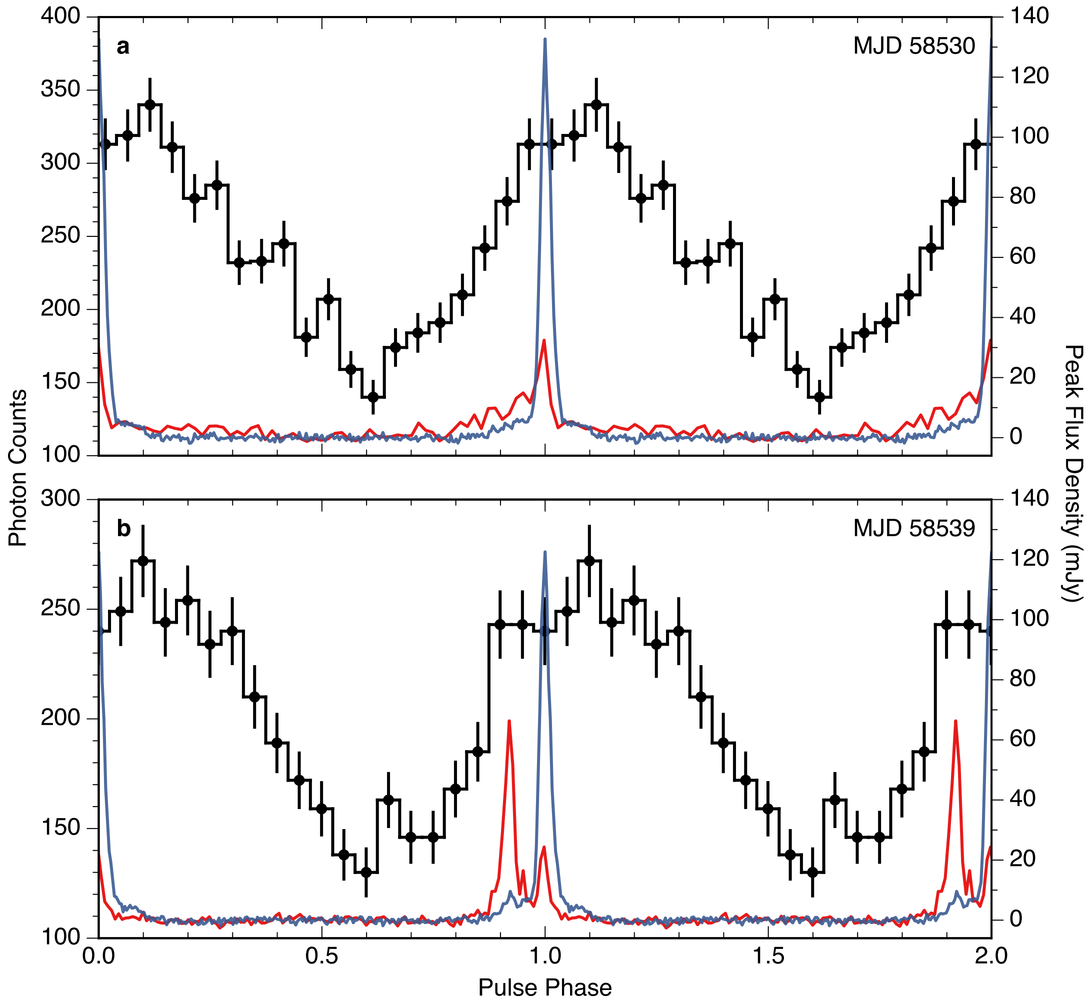

Figure 5.4: **Folded X-ray and radio pulse profiles derived from simultaneous X-ray and radio observations of XTE J1810–197 on MJDs (a) 58530 and (b) 58539.** The blue and red curves correspond to the average 8.3 and 31.9 GHz radio pulse profiles of the magnetar, respectively. The black curves show the *NICER* 1–4 keV pulse profiles, folded with 20 phase bins using a phase-connected radio ephemeris spanning each X-ray observation. Phase 0 in panels (a) and (b) correspond to MJDs 58530.761334907 (TDB) and 58539.774091226 (TDB), respectively.

exponential decaying tail lasting several minutes, with peak X-ray luminosities in the range of 10^{44}–10^{47} erg s^{-1}. These events are rare and occur roughly once per decade. Short X-ray bursts from magnetars (e.g., see [569]) have burst durations that range from a few milliseconds to a few seconds, with tails that can sometimes last several minutes. The peak X-ray luminosities of short X-ray bursts can range between 10^{36} and 10^{43} erg s^{-1}. Therefore, the X-ray pulses reported here from XTE J1810–197 are temporally distinct and less energetic than giant flares and X-ray bursts previously observed from magnetars. Moreover, we find that the pulse-energy distributions of the X-ray and radio pulses are characterized by different statistical distributions (see Section 5.2.5.2 and Figure 5.5).

The persistent emission of X-ray pulses during *NICER* observations spanning ~20 days, along with the derived surface temperatures from the luminosities of the X-ray pulses, indicate that the thermal regions producing the emission are heated quasi-steadily. This behavior can be explained by external heating and is consistent with predictions from the twisted magnetosphere model used in the past to explain XTE J1810–197's radiative behavior during its 2003 outburst [40, 42]. In this model, strong twists and powerful currents in the magnetosphere are generated by the evolution and decay of an ultra-strong magnetic field anchored in the magnetar's crust. The untwisting process forms a current-carrying bundle of field lines, known as the j-bundle, which powers the magnetar's emission on the untwisting timescale of months to years [42]. A hot spot is created at the footprint of the j-bundle as the stellar surface is heated by the bombardment of relativistic magnetospheric particles, and a significant fraction of the dissipated power can be radiated quasi-thermally [42]. The stellar surface is also expected to be thermally heated via anisotropic heat conduction through the neutron star's crust due to the presence of strong sub-surface magnetic fields.

The alignment between the individual X-ray and 8.3 GHz radio pulses suggests that they both originate near the same portion of the neutron star. We attribute the variability in the pulse-to-pulse alignment of the X-ray/radio pulses and the changes in the temporal structure of the X-ray pulses to fluctuations in the thermal emission from the magnetar's hot spots. Particle bombardment from returning magnetospheric currents can externally heat the hot spots on the neutron star's surface on sub-rotational timescales (e.g., see [412]).

We did not find evidence of a correlation between the temporal structure or peak amplitudes of the X-ray and radio pulses (e.g., see Figure 5.2). This indicates that the magnetar's radio emission is uncorrelated with its persistent soft X-ray emission on rotational timescales. Previously, simultaneous suppression of radio emission was reported during short magnetar-like X-ray bursts from PSR J1119–6127, a high magnetic field radio pulsar [20]. This was attributed to the ejection of a pair-plasma fireball into the magnetosphere, which is thought to quench the radio emission by shielding the electric field in the particle accelerating region and then recover on timescales of 10–100 s [572]. However, similar behavior was not detected during our simultaneous X-ray and radio observations of XTE J1810–197.

The radio pulses from XTE J1810–197 share similarities with some of the radio bursts previously detected from repeating FRB sources. In particular, the magnetar's 8.3 GHz radio pulses display frequency structure that is not observed in the radio pulses detected simultaneously at 31.9 GHz. Additionally, some of the magnetar's radio pulses were not simultaneously detected at both radio frequencies (e.g., see Figure 5.8). This indicates that many of XTE J1810–197's radio pulses are not broadband and have a spectral index that varies between pulse components. Similar behavior has been observed in bursts from repeating FRBs, such as FRB 121102. In Section 5.2.7 (Methods), we further describe the morphology of XTE J1810–197's radio pulses and discuss possible links with the emission from repeating FRB sources. Although the luminosities of XTE J1810–197's radio pulses are inconsistent with the energy output of bursts from repeating FRBs, such as those from FRB 121102 and FRB 180916.J0158+65, we note that a $\gtrsim 1.5$ MJy ms radio burst was recently detected from the active magnetar SGR 1935+2154 [57]. This suggests that active magnetars are able to produce sufficiently energetic radio bursts that may explain some extragalactic FRBs. In addition, an X-ray burst was also detected contemporaneously with this high fluence radio burst from SGR 1935+2154 (e.g., see [385]). Therefore, our simultaneous observations of individual radio and X-ray pulses from XTE J1810–197 during its recent outburst are important for characterizing the behavior of active magnetars, which are now thought to be a source of some extragalactic FRBs.

5.2 Methods

5.2.1 X-ray Observations

We observed XTE J1810–197 with the *NICER* X-ray Timing Instrument (XTI) [197] on board the *International Space Station* between 2019 February 6 (MJD 58520) and 2019 February 26 (MJD 58540), soon after the magnetar's position was sufficiently offset from the Sun. The XTI consists of an aligned array of 56 X-ray "concentrator" optics and silicon drift detectors (52 operational on orbit), which is sensitive to soft X-ray photons between 0.2 and 12 keV and has a large effective area of $\sim$1900 cm^2 at 1.5 keV. The precision timing capabilities of the XTI enable the arrival times of individual X-ray photons to be measured to an accuracy better than 100 ns. The X-ray data were processed using the *NICER* data analysis software[r] (DAS version 2018-11-19 V005a). We cleaned the data using the standard *NICER* calibration and filtered out times with a high background count rate using the `niprefilter2` and `nimaketime` routines. We excluded event times near the South Atlantic Anomaly (SAA), when the angular pointing separation was larger than 0.015°, and when the elevation angle was less than 30° above the limb of the Earth or less than 40° above the bright Earth limb. We also removed "hot" detectors from our analysis, which were flagged when an individual detector recorded more events than 3σ above the mean number of events across all of the detectors. The event times were then corrected to the solar system barycenter using the `barycorr` FTOOLS[s] [52] routine and the Jet Propulsion Laboratory (JPL) DE-405 ephemeris.

Since *NICER* is a non-imaging X-ray telescope, the background count rate was estimated using a space weather-based spectral background model derived from observations of "blank sky" fields [219]. A background X-ray spectrum, which incorporated contributions from the time-dependent particle background, optical loading from the Sun, and the diffuse sky background, was used to determine the energy-dependent background count rates. The calculated background count rates in the 0.5-5, 1–2, 2–3, 3–4, 4–5, and 5–10 keV energy bands were 0.486, 0.153, 0.076, 0.054, 0.045, and 0.169 counts s^{-1}, respectively. Between 0.5 and 5 keV, the ratio between the background and source count rates was $\lesssim 1\%$. Since the background is negligible in this energy range, we did not perform further background subtraction. However, the X-ray pulsed fractions of XTE J1810–197, provided in Table 5.4, have been corrected for the energy-dependent background count rate.

5.2.2 Radio Observations

High frequency radio observations of XTE J1810–197 were carried out using the NASA DSN 34 m radio telescopes (DSS-34 and DSS-35) [424] near Canberra, Australia on 2019 February 16 (MJD 58530) and 2019 February 25 (MJD 58539). On both days, dual circular polarization data were simultaneously recorded at central radio frequencies of 8.3 and 31.9 GHz, with roughly 350 MHz of bandwidth. Power

[r] See https://heasarc.gsfc.nasa.gov/docs/nicer/nicer_analysis.html.
[s] See http://heasarc.gsfc.nasa.gov/ftools.

spectral density measurements across the bands were channelized and saved in a digital polyphase filterbank with a time and frequency resolution of 512 μs and $\sim$1 MHz, respectively. The elevation-corrected system temperatures ($T_{\rm sys}$) at 8.3/31.9 GHz during the radio observations on MJDs 58530 and 58539 were 24(5)/46(9) K and 22(4)/41(8) K, respectively. The uncertainties correspond to 20% errors on the system temperature values.

The data were cleaned by first removing spurious signals due to radio frequency interference (RFI) using the `rfifind` tool from the `PRESTO` pulsar search software package[m]. Next, the bandpass response was flattened, and then we subtracted the moving average from each data point using 10 s of data around each sample to remove low frequency variations from the baseline of each frequency channel. We used the `TEMPO` timing analysis software package[p] to correct the sample times to the solar system barycenter and then incoherently dedispersed the data using the magnetar's nominal dispersion measure (DM) of 178 pc cm^{-3}.

5.2.3 Pulsar Timing

Phase-connected timing solutions spanning our radio observations on 2019 February 16 and 2019 February 25 were obtained using 8.3 GHz observations of XTE J1810–197. We derived ToAs by cross-correlating individual measured profiles, which were constructed by folding sub-integrations of the magnetar, in the Fourier frequency domain using a standard template based on the average pulse profile [511]. The ToAs were calculated using the `get_TOAs.py` tool from PRESTO[m] [456] and fit using the `TEMPO2` timing analysis software package[t] [233]. Separate timing solutions were derived for each of our radio observations by fitting only for the magnetar's spin frequency, ν. Additional spin frequency derivatives were not needed to obtain a phase-connected timing solution during each epoch. We fixed the position of the magnetar to the value reported in Helfand et al. [226] from Very Long Baseline Array (VLBA) observations. Due to the variability in the magnetar's pulse intensity at 31.9 GHz, we were unable to carry out a multi-frequency timing analysis. Since the timing models were based on ToAs from a single observing frequency, we set the pulsar DM to be equal to the magnetar's nominal DM in these models. Any alignment error between the 8.3 and 31.9 GHz radio pulse profiles due to uncertainty in the DM is negligible. We also increased the uncertainties on the ToAs by multiplying the error on each ToA by a scaling error factor (EFAC) value, given by $\epsilon = \sqrt{\chi_\nu^2}$, which yielded a reduced chi-squared value of $\chi_\nu^2 = 1$ by construction

[t] See https://www.atnf.csiro.au/research/pulsar/tempo2.

in all of our models. This is a standard technique used in pulsar timing to ensure more realistic parameter uncertainties since the errors on ToAs obtained from cross-correlating profiles with templates are often underestimated [481]. The timing solutions obtained using this procedure are provided in Table 5.2. All reference times are barycentric and scaled to infinite frequency.

These timing solutions were used to derive the phase alignment between the folded X-ray and radio pulse profiles shown in Figure 5.4. The accuracy of XTE J1810–197's X-ray/radio phase alignment was verified using *NICER* and DSN observations of the Crab pulsar, carried out close in time. We confirmed that the peaks in the Crab pulsar's X-ray and radio pulse profiles were phase aligned, which is consistent with previous measurements of the pulsar's X-ray/radio phase alignment (e.g., see [4]). Radio observations, taken close in time, of the Vela pulsar were also carried out using the DSN and the Mount Pleasant 26 m radio telescope, located near Hobart, Tasmania. We found that radio timing measurements of the Vela pulsar from both observatories were in agreement. Both of these independent tests indicate that there are not any significant systematic errors in our absolute timing accuracy that would affect the alignment shown in Figure 5.4.

The X-ray data in Figures 5.1 and 5.7a were folded using an ephemeris derived from spin frequency measurements of XTE J1810–197 on 2019 February 7 (MJD 58521), 2019 February 16 (MJD 58530), and 2019 February 25 (MJD 58539). The rotational frequency on each day was obtained from 8.3 GHz observations of the magnetar using the pulsar timing procedure described above. The ephemeris was constructed by fitting a linear polynomial to these measurements using a non-linear least-squares fitting procedure. The parameters comprising the ephemeris are $\nu_0 = 0.18045678(4)$ Hz and $\dot{\nu} = (-4.8 \pm 0.7) \times 10^{-13}$ Hz s^{-1}, where ν_0 is the rotational frequency of the magnetar on MJD 58530.761334907 (TDB) and $\dot{\nu}$ is the time derivative of the magnetar's spin frequency. We note that our measurement of the magnetar's spin frequency derivative is roughly twice as large in magnitude as the value reported in Levin et al. [314], which is likely explained by variability in the magnetar's spin-down torque. Rapid changes in the neutron star torque have also been observed from other magnetars following an outburst (e.g., see [79, 85, 160, 173, 246]).

5.2.4 X-ray Pulse Analysis

5.2.4.1 Zero-Crossing Algorithm

Since the X-ray pulse structure of XTE J1810–197 was variable between rotational cycles, we used a zero-crossing algorithm to identify individual pulsed emission components containing X-ray temporal structure. We searched for X-ray pulses using the 1–4 keV *NICER* light curve in order to maximize the signal-to-noise (S/N) ratio of each pulse. The cleaned event light curve was first binned to a time resolution of 0.5 s and divided into smaller light curve segments, which each consisted of times when *NICER* was continuously pointed at the magnetar. After subtracting the mean count rate from each of the light curve segments, we searched for times when the product of the count rates in adjacent time bins was negative. This indicated that the relative count rate had changed from a negative to positive value or from a positive to negative value. The slope of the light curve during these time intervals allowed us to determine whether these intervals contained a rising or falling time. The precise rising and falling times were obtained by linearly interpolating between time bins where the relative count rate in the light curve changed sign. The complex variability in Figure 5.2b shows that this technique is superior to searching for pulses by imposing a minimum or maximum count rate threshold. The times when the mean-subtracted signal changes sign are well-behaved, while imposing a threshold in the search algorithm would cause some events to be excluded.

In our analysis, we define the peak amplitude of each X-ray pulse to be the maximum count rate above the mean level during an adjacent set of rising and falling times, and the arrival time of each X-ray pulse corresponds to the time when this maximum occurred. These measurements are displayed in Figure 5.7a. The estimated pulse width of each event is given by the difference between the rising and falling times surrounding the X-ray pulse. The fluence or energy of each pulse is calculated from the time-integrated X-ray flux of each event. The pulse-energy distribution of the X-ray pulses is shown in Figure 5.5c.

5.2.4.2 Monte Carlo Analysis

The X-ray pulses from XTE J1810–197 displayed significant temporal variability between subsequent rotations of the neutron star (e.g., see Figure 5.2b). To demonstrate that the changes in the X-ray pulse structure were not dominated by Poisson fluctuations, we performed a Monte Carlo analysis where we generated 10^6 simulated X-ray pulses for each of the 4,013 X-ray pulses detected by the zero-crossing

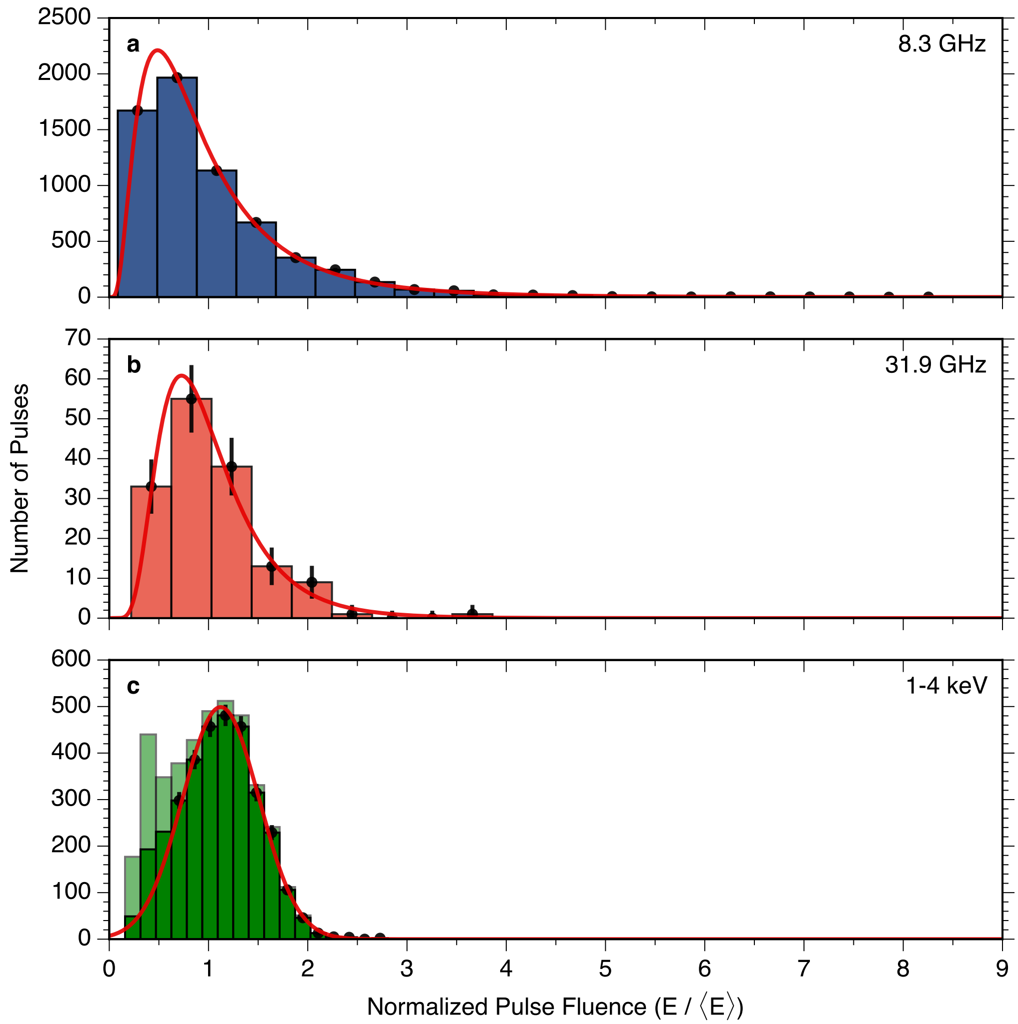

Figure 5.5: **Pulse-energy distributions of the radio and X-ray pulses emitted by XTE J1810–197.** In panels (a) and (b), we show the distribution of (a) 8.3 and (b) 31.9 GHz radio pulses detected with the DSN on MJD 58530 above a S/N threshold of 7.0. Best-fit log-normal distributions are overlaid in red in both of these subpanels. The energy distribution of bright 1–4 keV X-ray pulses detected by *NICER* between MJDs 58520 and 58540 is shown in panel (c). The light green histogram corresponds to the total X-ray pulse distribution, and the dark green histogram shows the distribution derived from including only the brightest X-ray pulse during each rotation. The best-fit Gaussian distribution to the distribution of brightest X-ray pulses with fluences of $E/\langle E\rangle \gtrsim 0.6$ is given by the red curve in panel (c). The error bars shown in all of these panels are derived from Poisson statistics.

algorithm. Each simulated X-ray pulse was derived by Poisson sampling the average 1–4 keV X-ray pulse profile after scaling the profile such that its amplitude was equal to the peak amplitude of an observed X-ray pulse and interpolating the profile to a time resolution of 0.5 s. The number of counts in each time bin of the simulated X-ray pulses was determined by randomly sampling from a Poisson distribution parameterized by the number of counts in the corresponding time bin of the scaled and interpolated average 1-4 keV X-ray pulse profile. The simulated X-ray pulses were then analyzed by the zero-crossing algorithm, and we recorded the rising time, falling time, peak time, and peak amplitude of each significantly detected X-ray pulse component.

A single X-ray pulse component was significantly detected in $> 99.9\%$ of the simulated X-ray pulses analyzed by the zero-crossing algorithm. This demonstrates that the zero-crossing algorithm reliably detects X-ray pulse components with high fidelity. The pulse width of each simulated X-ray pulse component was calculated from the difference between the rising and falling times. In Figure 5.6, we show the observed and simulated X-ray pulse width distributions. The simulated X-ray pulse width distribution is considerably narrower than the observed distribution and peaked at approximately half the magnetar's rotational period. The simulated distribution also shows a small number (0.08%) of pulse components with widths less than 1.5 s, which are attributed to false-positive detections of low amplitude pulse components due to Poisson variability. The observed X-ray pulse width distribution is quasi-bimodal and much broader than the simulated distribution. The notable differences between the observed and simulated X-ray pulse width distributions also demonstrate that there are statistically significant deviations between the temporal structure observed in the individual X-ray pulses and the average X-ray pulse shape.

5.2.4.3 X-ray Flux, Luminosity, and Total Energy

In order to measure the X-ray fluxes of the X-ray pulses, a blackbody plus power-law model was fit to the background-subtracted spectra derived from each of the event light curves used in the zero-crossing analysis. The spectra were formed by first extracting photons in the 1–4 keV energy band. Each spectrum was then binned so that there were at least 50 counts in each spectral channel after background subtraction. We fixed the hydrogen column density (N_{H}) in the fits to be $1.35 \times 10^{22}\,\mathrm{cm}^2$, the same value obtained from the blackbody plus power-law fits in Güver et al. [219]. Conversion factors for each event light curve were determined from the

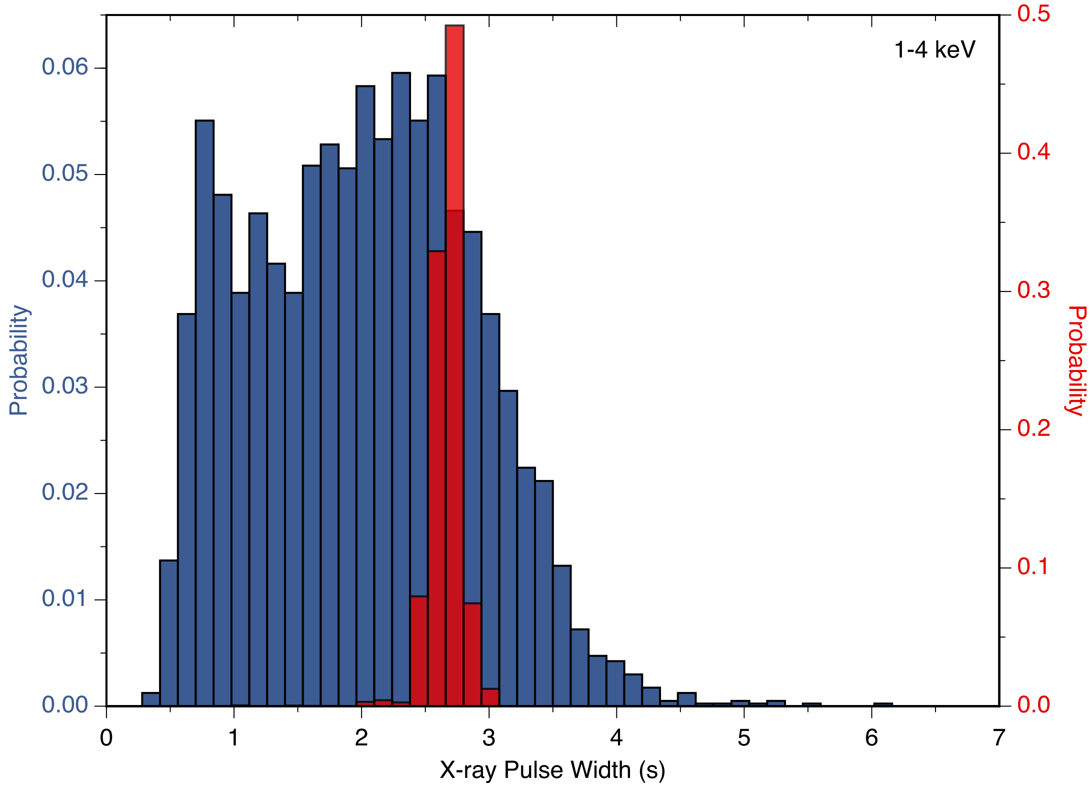

Figure 5.6: **Distribution of X-ray pulse widths determined by the zero-crossing algorithm from *NICER* observations between MJDs 58520 and 58540 in the 1–4 keV energy band.** The observed pulse width distribution is shown in blue, and the simulated distribution derived from Monte Carlo realizations of the X-ray pulses is overlaid in red.

model-predicted absorbed X-ray fluxes and count rates. The peak absorbed X-ray flux of each X-ray pulse was determined by multiplying the peak count rate by its corresponding conversion factor.

We obtained an average blackbody emitting area of $213 \pm 9\,\mathrm{km}^2$ between MJDs 58520 and 58540 from the spectral fits, which implies an average apparent blackbody emitting radius of 5.1 ± 0.1 km. The peak X-ray luminosities and total radiative energies of the X-ray pulses, averaged over the emitting surface, were determined using this blackbody emitting area, assuming a distance of 3.5 kpc to the magnetar.

5.2.5 Radio Single Pulse Analysis

5.2.5.1 Matched Filtering Algorithm

We used a Fourier domain matched filtering algorithm [422, 456] to search for single pulses in our simultaneous 8.3 and 31.9 GHz radio observations of XTE J1810–197.

After masking bad data corrupted by RFI and applying the bandpass and baseline corrections described in Section 5.2.2, we barycentered and incoherently dedispersed the data using the magnetar's nominal DM. The radio pulses were then identified by convolving the full resolution time series data with boxcar functions with widths ranging from 512 μs to 153.6 ms. If a radio pulse from the same section of data was detected with multiple boxcar widths, we only recorded the highest S/N event in the final list. All events with S/N $\geq$ 7.0 were stored for further analysis. The peak flux density of each event was calculated using the radiometer equation [382]:

$$S_{\mathrm{peak}} = \frac{\beta\, T_{\mathrm{sys}}\, (\mathrm{S/N})_{\mathrm{peak}}}{G\, \sigma_{\mathrm{off}} \sqrt{\Delta\nu\, n_p\, t_{\mathrm{peak}}}}, \tag{5.1}$$

where $\beta \approx 1$ is a correction factor that accounts for system imperfections such as digitization of the signal, T_{sys} is the effective system temperature, $(\mathrm{S/N})_{\mathrm{peak}}$ is the peak S/N of the radio pulse, $G = 0.24\,\mathrm{K\,Jy^{-1}}$ is the telescope gain, $\sigma_{\mathrm{off}} = 1$ is the off-pulse standard deviation, $\Delta\nu$ is the observing bandwidth, n_p is the number of polarizations, and t_{peak} denotes the integration time at the peak of the radio pulse. The fluence of each event was determined from the time-integrated flux density.

5.2.5.2 Radio and X-ray Pulse-Energy Distributions

Pulse-energy distributions of the radio pulses detected at 8.3 and 31.9 GHz on MJD 58530 are shown in Figures 5.5a and 5.5b, respectively. Scaled log-normal distributions, given by:

$$P_{\text{log-norm}}\left(x = \frac{E}{\langle E \rangle}\right) = \frac{C}{\sqrt{2\pi}\sigma_{\text{log-norm}} x} \exp\left[-\frac{(\ln x - \mu_{\text{log-norm}})^2}{2\sigma^2_{\text{log-norm}}}\right], \tag{5.2}$$

where x is the normalized energy of each radio pulse, C is a scaling factor, $\mu_{\text{log-norm}}$ is the mean of the distribution, and $\sigma_{\text{log-norm}}$ is the standard deviation of the distribution, were fit to each of these distributions using a weighted nonlinear least-squares fitting procedure. The 8.3 GHz pulse-energy distribution is well-described by a log-normal distribution ($\chi^2_{\mathrm{red}} = 0.98$, dof = 18) with $\mu_{\text{log-norm}} = -0.218 \pm 0.009$ and $\sigma_{\text{log-norm}} = 0.709 \pm 0.008$. We obtained a best-fit log-normal distribution ($\chi^2_{\mathrm{red}} = 0.36$, dof = 6) with $\mu_{\text{log-norm}} = -0.09 \pm 0.05$ and $\sigma_{\text{log-norm}} = 0.48 \pm 0.04$ after fitting the 31.9 GHz pulse-energy distribution. These best-fit log-normal distributions are overlaid in red in Figures 5.5a and 5.5b. We obtained a smaller χ^2_{red} value from the log-normal fit to the 31.9 GHz pulse-energy distribution since fewer radio pulses were detected at this frequency, which resulted in large relative error bars. However, we note that interstellar scintillation (ISS) and/or intrinsic variability (e.g., pulse nulling) may have affected the shape of the 31.9 GHz pulse-energy distribution. For comparison, during the 2003 outburst, XTE J1810–197's single pulse emission displayed both log-normal and power-law behavior between 1.4 and 8.35 GHz [487].

The pulse-energy distribution of all of the X-ray pulse components, along with the distribution derived from selecting only the brightest component during each rotation, is shown in Figure 5.5c. We fit a scaled Gaussian distribution, given by:

$$P_{\rm gauss}\left(x = \frac{E}{\langle E \rangle}\right) = \frac{C}{\sqrt{2\pi}\sigma_{\rm gauss}} \exp\left[-\frac{(x-\mu_{\rm gauss})^2}{2\sigma_{\rm gauss}^2}\right], \tag{5.3}$$

to the pulse-energy distribution of the brightest pulse components with $x \gtrsim 0.6$. The data are well-modeled by a Gaussian distribution ($\chi^2_{\rm red} = 0.91$, dof = 11), with a mean and standard deviation of $\mu_{\rm gauss} = 1.12 \pm 0.01$ and $\sigma_{\rm gauss} = 0.384 \pm 0.009$, respectively. This indicates that the energetics of the brightest X-ray pulses from the magnetar's hot spot are well-described by a Gaussian process. These results also show that the magnetar's X-ray pulse-energy distribution differs from its radio pulse-energy distribution.

5.2.6 Radio Pulse Morphology

Our high frequency radio observations of XTE J1810–197 reveal that the magnetar is emitting bright single pulses with multiple narrow emission components following its recent reactivation. This behavior is similar to the emission characteristics observed during the magnetar's 2003 outburst [78]. Although many of these pulse components were simultaneously detected at 8.3 and 31.9 GHz, not all of the emission components were detected at both frequencies (e.g., see Figure 5.8). This suggests that either a substantial fraction of the magnetar's single pulse components have a steep and variable radio spectrum or they are not all emitted over a broadband frequency range.

We folded the ToAs of the single pulse emission components detected at 8.3 and 31.9 GHz using the radio ephemeris described in Section 5.2.3. The time-phase distributions of these events are shown in Figures 5.7b and 5.7c. The average width of the emission components at 8.3 and 31.9 GHz was 1.7 and 1.8 ms, respectively. These observations are consistent with fan beam emission with an approximate width of $\pm 11^\circ$ (± 0.03 in phase units) at 8.3 GHz and $\pm 7^\circ$ (± 0.02 in phase units) at 31.9 GHz based on the widths of the pulse component distributions. Single pulse emission components were sometimes detected outside of these phase ranges during some rotations (e.g., at earlier phases compared to the pulse profile peak at 31.9 GHz; see Figure 5.7c).

We found that XTE J1810–197's pulse strength at 31.9 GHz was significantly variable on timescales of ∼1000–4000 s and often exhibited extended periods where pulsations were not detected (see Figure 5.7c; Methods). This behavior was intermittent and frequency-dependent, as we did not see similar behavior during our simultaneous observations of the magnetar at 8.3 GHz. This may be an intrinsic effect of the magnetar's emission mechanism at higher radio frequencies or caused by ISS.

The overall emission behavior at 8.3 GHz is similar to the pulse morphology observed from the Galactic Center (GC) magnetar, PSR J1745–2900 [422]. However, in contrast to the GC magnetar, XTE J1810–197 shows a negligible amount of pulse broadening in its single pulse emission components at this frequency. During individual rotations, there is often variability in the frequency structure between the GC magnetar's single pulse emission components [422], whereas the frequency structure in XTE J1810–197's single pulses is typically uniform across all of the pulse components (e.g., see Figure 5.8a). In the case of XTE J1810–197, the extent of these features ranged between ∼1–50 MHz, which is smaller than the ∼100 MHz frequency extent observed from the GC magnetar [422]. However, the 31.9 GHz single pulses from XTE J1810–197 did not show prominent evidence of this structure in any of its single pulse emission components. Similar spectral features have also been observed at lower frequencies (550–750 MHz) in XTE J1810–197's single pulse components [346]. This behavior is likely caused by ISS, but may also be intrinsic to the magnetar's emission mechanism.

If we assume that the frequency structure observed in the 8.3 GHz single pulses is due to diffractive ISS through a uniform Kolmogorov scattering medium, then the scintillation timescale (Δt_d) in seconds is given by [125]:

$$\Delta t_d = A_{\rm ISS} \frac{\sqrt{D \Delta \nu_d}}{V_{\rm ISS} \nu}, \tag{5.4}$$

where $A_{\rm ISS} = 2.53 \times 10^4$ km s^{-1} is the ISS velocity coefficient, D is the distance to the source in kpc, $\Delta\nu_d$ is the scintillation bandwidth in MHz, $V_{\rm ISS}$ is the ISS velocity, and ν is the observing frequency in GHz. Letting $V_{\rm ISS}$ be equal to the pulsar's transverse velocity ($V_\perp = 212 \pm 35$ km s^{-1}) [226], $D = 3.5 \pm 0.5$ kpc [393], $\Delta\nu_d = 50$ MHz, and $\nu = 8.3$ GHz, we obtain a scintillation timescale of $\Delta t_d = 190 \pm 34$ s. The magnetar's

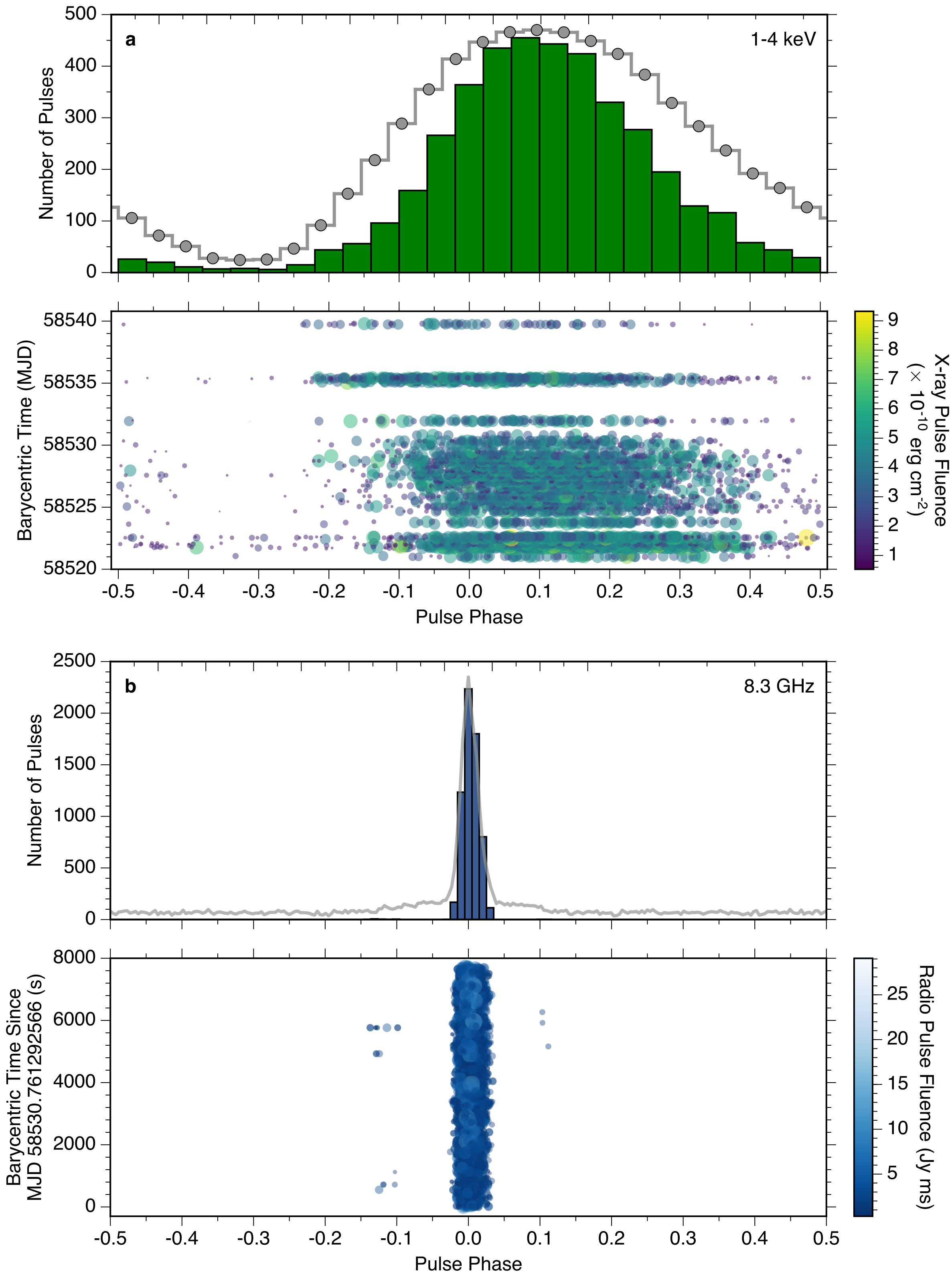
a
1-4 keV
Number of Pulses
Barycentric Time (MJD)
Pulse Phase
X-ray Pulse Fluence
(× 10^-10 erg cm^-2)
b
8.3 GHz
Number of Pulses
Barycentric Time Since
MJD 58530.761292566 (s)
Pulse Phase
Radio Pulse Fluence (Jy ms)

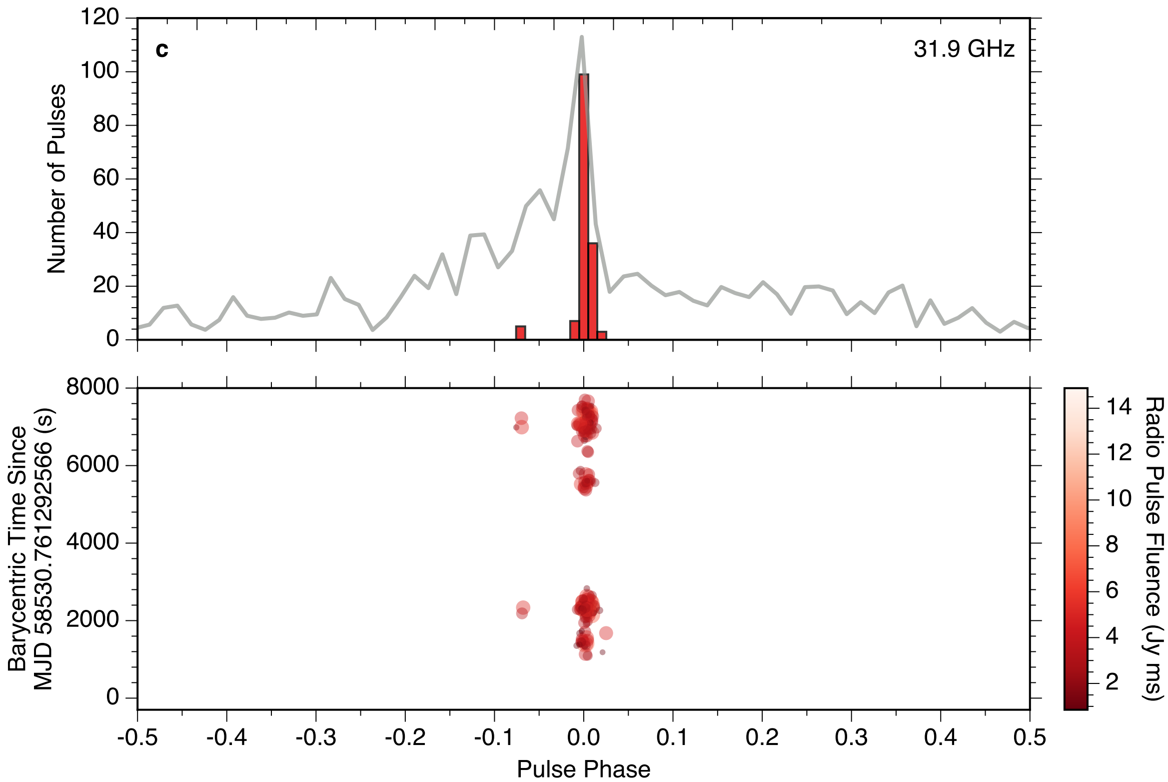

Figure 5.7: **Distribution of X-ray and radio pulses as a function of time and XTE J1810–197's rotational phase.** In panel (a), we show the distribution of X-ray pulses detected in the 1–4 keV energy band between MJDs 58520 and 58540 with *NICER*. The distribution of 8.3 and 31.9 GHz radio pulses detected with S/N $\geq$ 7.0 on MJD 58530 using the DSN are shown in panels (b) and (c), respectively. The color and size of each data point in the bottom panels both indicate the fluence of each pulse. Histograms of the number of pulses as a function of pulse phase are provided in the top panels, and the bottom panels show their time-phase distribution. The folded pulse profiles are overlaid in gray in the top panels. The *NICER* data shown in panel (a) are not continuous, unlike the radio observations, and gaps along the time axis in the bottom panel indicate times when *NICER* was not observing the source.

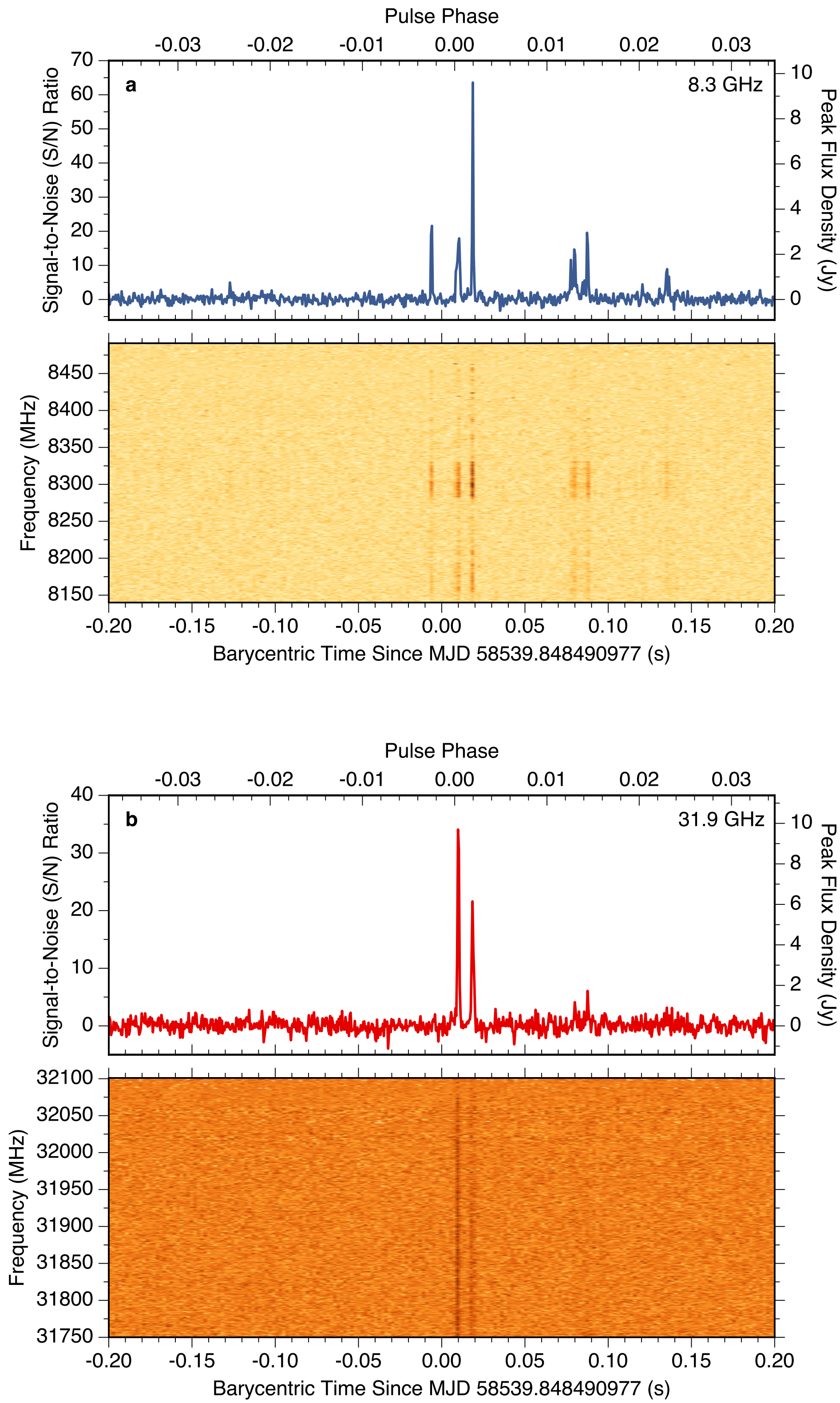

Figure 5.8: **Example of bright radio pulses detected simultaneously at (a) 8.3 and (b) 31.9 GHz from XTE J1810–197 on MJD 58539 during the same rotation of the neutron star.** The top panels show the Stokes I integrated single pulse profiles, and the Stokes I dedispersed dynamic spectra are displayed in the bottom panels.

radio pulse components displayed similar frequency structure over multiple consecutive rotations. The timescale over which we observed variations in the frequency structure is comparable to the predicted scintillation timescale. Additionally, the estimated pulse broadening timescale [125] at 8.3 GHz for a scintillation bandwidth of $\Delta\nu_d = 50$ MHz is:

$$\tau_d = \frac{C_1}{2\pi\Delta\nu_d} = 4\,\mathrm{ns}, \tag{5.5}$$

where $C_1 = 1.16$ for a uniform medium with a Kolmogorov wavenumber spectrum. The detection of such a pulse broadening magnitude is beyond the capability of our instrument.

5.2.7 Comparisons with Fast Radio Bursts

Fast radio bursts (FRBs) are bright, coherent pulses of radio emission with $\sim\mu$s–ms durations and fluences between roughly 0.01 and 1,000 Jy ms (e.g., see [120, 436] for recent reviews). They are thought to have extragalactic origins since their DMs exceed the values expected from Galactic free electrons along their lines of sight. Five FRBs have now been localized to host galaxies with redshifts between 0.034–0.66, which has established that their sources are located at extragalactic distances [26, 95, 368, 449, 462]. Thus far, over a hundred distinct FRB sources have been reported [435][h]. A wide variety of models, including cataclysmic and repeating scenarios, have been proposed to explain the progenitors of FRBs (e.g., see [444][j] for a catalog). In particular, extragalactic magnetars have been suggested as one of the possible progenitor types (e.g., see [57, 369, 387, 391, 422, 431]).

Recently, a 1.5 MJy ms fluence radio burst was detected at 1.4 GHz from the Galactic magnetar SGR 1935+2154 with the Survey for Transient Astronomical Radio Emission 2 (STARE2) [58] during a period of enhanced X-ray activity [57, 276, 414, 579]. A less energetic radio burst, with a fluence of a few kJy ms between 400 and 800 MHz, was also detected contemporaneously at lower frequencies using CHIME/FRB [476], along with a bright X-ray burst [385, 386, 586]. We note that the lower apparent fluence of the radio burst detected by CHIME/FRB may be partially explained by the fact that the burst was detected in the telescope's sidelobe. The radio burst shown in Scholz and Chime/Frb Collaboration [476] has two prominent emission components, which are separated by ~30 ms and have widths of ~5 ms. The dynamic spectrum of these emission components displays evidence of band-limited frequency structure that is variable between the two components [476].

Hereafter, we assume a distance of 12.5 kpc to SGR 1935+2154 based on the magnetar's possible association with SNR G57.2+0.8 [283]. However, we note that a range of distances between 4.5 and 12.5 kpc have been suggested (e.g., see [283, 454, 588]). The isotropic radio burst luminosity for a burst duration of $w = 1$ ms, based on the radio fluence reported in Bochenek et al. [57], is $L_\nu \approx 3 \times 10^9$ Jy kpc$^2 \approx 3 \times 10^{29}$ erg s^{-1} Hz^{-1}. This value far exceeds the luminosities of typical pulses from Galactic radio pulsars, rotating radio transients (RRATs), and giant radio pulses from Galactic pulsars, such as the Crab pulsar, by several orders of magnitude [270]. The inferred brightness temperature, T_B, of SGR 1935+2154 at 1.4 GHz during the time of the radio burst detected by STARE2 was $T_B \gtrsim \left(\frac{4}{\pi}\right) \frac{L_\nu}{2k_\mathrm{B}(\nu w)^2} \approx 7 \times 10^{32}$ K, where $k_\mathrm{B} \approx 1.38 \times 10^{-23}$ J K^{-1} is Boltzmann's constant. This implies that the radio burst discovered by STARE2 would have been detected with a fluence of $\gtrsim 10$ mJy ms at a luminosity distance of 149 Mpc (the luminosity distance of FRB 180916.J0158+65, which is currently the nearest localized FRB). Multiple radio bursts from FRB 180916.J0158+65 have already been detected with fluences above this level (e.g., see [96, 521, 522]). This suggests that active magnetars can generate radio bursts with enough energy to be detected from low redshift host galaxies. If the apparent brightness of such bursts is magnified via extrinsic propagation effects, such as plasma lensing [131, 422], then extragalactic magnetars at high redshifts may also be a source of FRBs.

The radio emission from repeating FRB sources, such as FRB 121102 and FRB 180916.J0158+65, and the radio pulses detected from XTE J1810–197 during its recent outburst have similar characteristics. Multicomponent radio pulses, with roughly millisecond widths, have been observed from both types of objects (e.g., see [191, 229, 358]). Significant frequency structure has also been observed in the radio pulses of both XTE J1810–197 [346] and the Galactic Center magnetar, PSR J1745–2900 [422], with a frequency extent that is similar to the spectral scales seen in bursts from repeating FRBs, such as FRB 121102 [191, 391, 499]. We also found that some of XTE J1810–197's radio pulse components were not detectable over a broad radio frequency range, which also resembles the behavior seen in radio bursts from repeating FRBs [302, 358].

While these similarities may indicate a common underlying emission mechanism between radio magnetars and FRBs, we note that there are several important differences between the radio emission from XTE J1810–197 and FRBs. We did not find evidence that XTE J1810–197's radio subpulses drifted downward in frequency as time progressed. This "sad trombone" behavior is a characteristic feature in many radio bursts detected from repeating FRB sources (e.g., see [229, 521]), but has thus far not been observed from radio magnetars. Additionally, the fluences of the 8.3 and 31.9 GHz radio pulses from XTE J1810–197 did not exceed ~30 Jy ms (see Figures 5.7b and 5.7c), which is incompatible with the energy output from FRB 180916.J0158+65. At a luminosity distance of 149 Mpc, FRB 180916.J0158+65 produces radio bursts that are a factor of $\sim 10^8$ more energetic than the radio single pulse emission from XTE J1810–197. However, we note that a faint (30 mJy) radio pulse was detected from SGR 1935+2154 approximately 2 days after the arrival time of the $\gtrsim 1.5$ MJy ms radio burst [584]. The high fluence radio burst reported in Bochenek et al. [57] may have been produced by energy release as a result of a fast reconnection event in the magnetar's over-twisted magnetosphere [342, 343]. Less energetic radio bursts from magnetars, such as those from XTE J1810–197 and SGR 1935+2154, may instead be powered through a combination of magnetic and rotational energy.

5.3 Acknowledgments

The authors would like to thank Ben Stappers for providing a radio ephemeris of the Crab pulsar and Jim Palfreyman for supplying a radio ephemeris of the Vela pulsar. We are also grateful to Wenbin Lu for valuable discussions.

A.B.P. acknowledges support by the Department of Defense (DoD) through the National Defense Science and Engineering Graduate (NDSEG) Fellowship Program and by the National Science Foundation (NSF) Graduate Research Fellowship under Grant No. DGE-1144469. T.E. is supported by JSPS/MEXT KAKENHI grant number 18H01246.

We thank the Jet Propulsion Laboratory's Research and Technology Development program and Caltech's President's and Director's Fund for partial support at JPL and the Caltech campus. A portion of this research was performed at the Jet Propulsion Laboratory, California Institute of Technology and the Caltech campus under a Research and Technology Development Grant through a contract with the National Aeronautics and Space Administration (NASA). U.S. government sponsorship is acknowledged. We acknowledge support from the DSN team for scheduling and carrying out the radio observations. We also thank Charles Lawrence for providing programmatic support for this work.

This work was supported by NASA through the *NICER* mission and the Astrophysics Explorers Program, and made use of data and software provided by the High Energy Astrophysics Science Archive Research Center (HEASARC). Portions of this work performed at the United States Naval Research Laboratory (NRL) were supported by NASA.

Part III: Fast Radio Bursts

Curiosity demands that we ask questions, that we try to put things together and try to understand this multitude of aspects as perhaps resulting from the action of a relatively small number of elemental things and forces acting in an infinite variety of combinations.

— Richard P. Feynman, The Feynman Lectures on Physics, Volume I

Chapter VI

A Dual-band Radio Observation of FRB 121102 with the Deep Space Network and the Detection of Multiple Bursts

[358] Majid, W. A.* and **Pearlman, A. B.*** et al. (2020). "A Dual-band Radio Observation of FRB 121102 with the Deep Space Network and the Detection of Multiple Bursts." In: *ApJL,* 897:L4. arXiv:2004.06845 [astro-ph.HE].

A Dual-band Radio Observation of FRB 121102 with the Deep Space Network and the Detection of Multiple Bursts

Walid A. Majid[1,2,*], Aaron B. Pearlman[2,6,7,*], Kenzie Nimmo[3,4], Jason W. T. Hessels[3,4], Thomas A. Prince[2,1], Charles J. Naudet[1], Jonathon Kocz[2], and Shinji Horiuchi[5]

[1] Jet Propulsion Laboratory, California Institute of Technology, Pasadena, CA 91109, USA
[2] Division of Physics, Mathematics, and Astronomy, California Institute of Technology, Pasadena, CA 91125, USA
[3] Anton Pannekoek Institute for Astronomy, University of Amsterdam, Science Park 904, 1098 XH Amsterdam, The Netherlands
[4] ASTRON, Netherlands Institute for Radio Astronomy, Oude Hoogeveensedijk 4, 7991 PD Dwingeloo, The Netherlands
[5] CSIRO Astronomy and Space Science, Canberra Deep Space Communications Complex, P.O. Box 1035, Tuggeranong, ACT 2901, Australia
[6] NDSEG Research Fellow
[7] NSF Graduate Research Fellow
[*] These authors contributed equally to both the analysis and writing of the manuscript.
Corresponding authors: walid.a.majid@jpl.nasa.gov and aaron.b.pearlman@caltech.edu

Abstract

The spectra of repeating fast radio bursts (FRBs) are complex and time-variable, sometimes peaking within the observing band and showing a fractional emission bandwidth of about 10–30%. These spectral features may provide insight into the emission mechanism of repeating fast radio bursts, or they could possibly be

explained by extrinsic propagation effects in the local environment. Broadband observations can better quantify this behavior and help to distinguish between intrinsic and extrinsic effects. We present results from a simultaneous 2.25 and 8.36 GHz observation of the repeating FRB 121102 using the 70 m Deep Space Network (DSN) radio telescope, DSS-43. During the 5.7 hr continuous observing session, we detected 6 bursts from FRB 121102, which were visible in the 2.25 GHz frequency band. However, none of these bursts were detected in the 8.36 GHz band, despite the larger bandwidth and greater sensitivity in the higher-frequency band. This effect is not explainable by Galactic scintillation and, along with previous multiband experiments, clearly demonstrates that apparent burst activity depends strongly on the radio frequency band that is being observed.

6.1 Introduction

Fast radio bursts (FRBs) are bright (fluence ~0.1–400 Jy ms), short duration ($\sim\mu$s–ms) radio pulses with dispersion measures (DMs) that are well in excess of the expected Galactic contribution along their line of sights (see, e.g. [120, 436] for recent reviews). The DMs, which are derived from frequency-dependent delays in the arrival times of the bursts due to the passage of the radio waves through the cold plasma between the source and the observer, are used as a proxy for the distances of these bursts. The high DM values have long suggested that the sources of FRBs are located at extragalactic distances. The localization of a subset of FRBs to host galaxies at redshifts of 0.034–0.66 has confirmed the extragalactic nature of FRBs [26, 95, 368, 449, 462]. FRBs have peak flux densities that are similar to those of radio pulsars, and their extragalactic distances imply total burst energies that are $\sim 10^{10}$–10^{14} times those of pulsars, if similar beaming fractions are assumed. There is currently no well-established progenitor theory that can explain this phenomenon, though dozens of hypotheses have been proposed (e.g., see [444][j] for a catalog of theories).

Since the initial FRB discovery by [329], over a hundred distinct sources have been reported (e.g., see [435][h] for a catalog). Interestingly, a subset of these sources have shown repeat bursts, which has provided an opportunity to study this enigmatic phenomenon in more detail through post-facto localization of the sources to a host galaxy (e.g., [368]), studies of burst properties (e.g., [213]), and multiwavelength searches for potential counterparts (e.g., [480, 482]). Whether or not all FRBs are capable of repeating remains an active debate, though it has been argued that the high overall event rate requires that a large fraction of the population are repeaters [460]. FRBs are now also being localized precisely using the initial burst discovery data [26]. This will help greatly in determining whether FRBs that have only been detected once come from a physically distinct progenitor type.

FRB 121102 is the first known repeating FRB [497, 499] and has been localized to a faint dwarf galaxy at a redshift of $z = 0.19$ [95, 367, 516]. Since the discovery of FRB 121102, hundreds of bursts have been detected by the Arecibo telescope and other instruments (e.g., [213]). Many of these detections were made at L-band (1–2 GHz), but FRB 121102 has also been detected at a wide range of radio frequencies using various radio telescopes (e.g., with CHIME/FRB at 0.4–0.8 GHz [259]; the Green Bank Telescope (GBT) at 1.6–2.4 GHz [479, 480]; the NASA Deep Space Network (DSN) 70 m radio telescope, DSS-43, at 2.25 GHz [425]; the Very Large Array (VLA) at 2.5–3.5 GHz [95, 302]; the Arecibo telescope at 4.1–4.9 GHz [391]; the Effelsberg 100 m telescope at 4.6–5.1 GHz [500]; and the GBT at 4–8 GHz [191, 587]).

Since the progenitor population of FRBs is still unknown, broadband and high-frequency radio observations of FRBs are important for understanding the underlying emission mechanism(s). In particular, simultaneous measurements across wide bandwidths are more robust against temporal evolution of scintillation and scattering as the interference patterns change over time because of the relative motion between the source, the scattering screen, and the observer.

In this Letter, we present results from a simultaneous observation of FRB 121102 at 2.25 and 8.36 GHz with the NASA DSN 70 m telescope, DSS-43, and expand upon the initial results reported in Pearlman et al. [425]. The observation and data analysis procedures are described in Section 6.2. In Section 6.3, we provide measurements of the detected bursts, including the DM, width, flux density, and fluence of each burst. In Section 6.4, we discuss our measurements of the burst spectra, previous multifrequency measurements of FRB 121102, the impact of intrinsic and extrinsic effects on the burst properties, and the morphologies of the brightest bursts detected during this observation.

6.2 Observation and Data Analysis

We observed FRB 121102 continuously for 5.7 hr on 2019 September 06, 17:27:54 UTC (MJD 58732.727708) using DSS-43, the NASA DSN 70 m radio telescope located at the Canberra Deep Space Communication Complex (CDSCC) in Tidbinbilla, Australia. This observation was carried out as part of a recently initiated monitoring program of repeating FRBs at high frequencies with the DSN's large 70 m radio telescopes. DSS-43 is equipped with cryogenically-cooled, dual circular polarization receivers, which are capable of recording data simultaneously at S-band and X-band. The center frequencies of the recorded S-band and X-band data were 2.25 and 8.36 GHz, respectively. The S-band system has a bandwidth of 115 MHz, with an effective bandwidth of ~100 MHz after masking bad channels contaminated by radio frequency interference (RFI). The X-band receivers provide 450 MHz of bandwidth, with ~430 MHz of usable bandwidth. Data from both polarization channels were simultaneously received and recorded at each frequency band with two different recorders at the site's Signal Processing Center. The primary recorder is the ultra-wideband pulsar machine, described previously in Majid et al. [356], which provides channelized power spectral densities in filterbank format with a frequency resolution of 0.98 MHz and a time resolution of 64.5 μs.

Data in both circular polarizations were also recorded at S-band using the stations's very-long-baseline interferometry (VLBI) baseband recorder in six non-contiguous sub-bands. Each sub-band spanned 8 MHz in bandwidth and provided a total bandwidth of 48 MHz. The center frequency of the data was 2.24 GHz. A detailed analysis of the baseband data will be presented in an upcoming publication. Most of the results in this Letter are derived from data obtained using the ultra-wideband pulsar machine, with the exception of the autocorrelation analysis (see Section 6.3).

The data were flux calibrated by measuring the system temperature, $T_{\rm sys}$, at both frequency bands using a noise diode modulation scheme at the start of the observation, while the antenna was pointed at zenith. The $T_{\rm sys}$ values were corrected for elevation effects, which are minimal for elevations greater than 20 degrees.

The data processing procedures were similar to those described in previous single pulse studies of pulsars and magnetars with the DSN (e.g., [356, 422, 424]). In each data set, we corrected for the bandpass slope across the frequency band and masked bad channels corrupted by RFI, which were identified using the PSRCHIVE software package [239]. We also subtracted the moving average from each data value using 0.5 s around each time sample in order to remove low frequency temporal variability.

Next, the cleaned data were dedispersed with trial DMs between 500 and 700 pc cm^{-3}. A list of FRB candidates with detection signal-to-noise ratios (S/N) above 6.0 were generated using a matched filtering algorithm, where each dedispersed time series was convolved with boxcar functions with logarithmically spaced widths between ~64.5 μs and ~19.4 ms. We used a GPU-accelerated machine learning pipeline based on the `FETCH`[k] (Fast Extragalactic Transient Candidate Hunter) software package to determine whether or not each of these FRB candidates were astrophysical [7]. The same FRB candidates were also searched for astrophysical bursts using an automated classifier[u] [389, 390], after independently filtering each candidate for RFI. Both of these classification pipelines identified the bursts presented in Section 6.3 as genuine FRBs.

In addition, we extracted raw voltages using 4.0 s of data centered on the arrival times of each of the two brightest bursts for the autocorrelation analysis presented in Section 6.3. The data were coherently dedispersed using a DM value of 563.6 pc cm^{-3}, the structure-optimized DM associated with the brightest burst. We then used the coherently dedispersed baseband data to form filterbanks comprised of channelized power spectral densities with temporal and spectral resolutions of 32 μs and 31.25 kHz, respectively. The resulting burst spectra were used to calculate autocorrelation functions (ACFs) for each burst.

6.3 Results

Six bursts were detected at S-band with a DM value near the nominal DM of FRB 121102. In Table 6.1, we list the peak time, peak S/N, DM value that maximized the peak S/N, burst width, peak flux density, spectral energy density, and fluence for each burst. We show the flux-calibrated, frequency-averaged burst profiles, dynamic spectra, and flux-calibrated, time-averaged spectra for all of these bursts in Figure 6.1, after dedispersing each burst with a DM value of 563.6 pc cm^{-3}. For the brightest bursts (B1 and B6), the structure-optimized DM value was consistent with the DM value that maximized the peak S/N. However, the algorithm[v] [489] used to determined the structure-optimized DM performs poorly on low S/N bursts. Therefore, we have chosen to dedisperse all of the burst spectra shown in Figure 6.1 using the structure-optimized DM associated with the brightest burst, B6.

In the left diagram in Figure 6.2, we show the dedispersed S-band and X-band dynamic spectra of the brightest burst, B6, after correcting for the dispersive delay between the two frequency bands. The frequency-averaged burst profiles are shown in the upper panel. Although the burst was detected with high S/N at S-band, there was no detectable signal during the same time at X-band. We also show the peak flux densities of the six detected S-band bursts as a function of time during our observation in the right diagram in Figure 6.2. The X-band and S-band 7σ

[u] See https://github.com/danielemichilli/SpS.

[v] See https://github.com/danielemichilli/DM_phase.

detection thresholds are indicated with cyan and orange lines, respectively. Since no bursts were detected at X-band, we place a 7σ upper limit of 0.20 Jy on the flux density of the emission at 8.36 GHz during this observation, assuming a nominal pulse width of 1 ms. If we further assume that the flux density scales as a power-law (i.e., $S(\nu) \propto \nu^{\alpha}$, where $S(\nu)$ denotes the flux density at an observing frequency ν and α is the spectral index), which is typical of most pulsar radio spectra, then we can place an upper limit of $\alpha < -2.6$ on the spectral index of the emission process using burst B6. However, we note that previous observations of bursts from FRB 121102 show that they may not be well-modeled by a power-law (e.g., [302, 479, 499]).

The two brightest bursts, B1 and B6, show remarkably similar temporal profiles, with two prominent central components and a precursor component. In addition, B1 shows evidence of an additional component towards the tail of the main burst envelope. Both bursts also show spectral-temporal features that are reminiscent of other FRBs (e.g., FRB 170827 [180]) and other bursts from FRB 121102 (e.g., [229]).

The diffractive interstellar scintillation (DISS) bandwidth roughly scales with frequency as:

$$\Delta\nu_{\rm DISS} \propto \nu^4. \tag{6.1}$$

The scintillation bandwidth of FRB 121102 was previously measured to be 58.1 ± 2.3 kHz at 1.65 GHz [229]. The burst dynamic spectra in Figure 6.1 show narrowband frequency structure. These structures are particularly evident in both B1 and B6 between 2.24 and 2.28 GHz. If we attribute the frequency structure in the burst spectra to DISS, then based on the scintillation bandwidth measured at 1.65 GHz, Equation (6.1) would predict a scintillation bandwidth of $\Delta\nu_{\rm DISS} \approx 200$ kHz at $\nu = 2.24$ GHz. We note that the data recorded from the pulsar machine is insufficient to resolve the predicted scintillation bandwidth due to its 1 MHz spectral resolution. Therefore, to study the frequency-dependent brightness variations that arise due to scintillation, we used the baseband data to perform an ACF analysis on the burst spectra from B1 and B6. The procedure used to carry out the ACF analysis is described in detail in Marcote et al. [368]. We measure the scintillation bandwidth of B1 to be 177 ± 17 kHz and that of B6 to be 280 ± 13 kHz, both at a center frequency of 2.24 GHz. We were unable to compute ACFs for the other four bursts because they did not have sufficient S/N.

The ACFs of both B1 and B6 are shown in Figure 6.3 up to frequency lags of 8 MHz. We also show Lorentzian fits to the central bump in the ACFs, which corresponds to frequency lags up to 0.84 MHz, after removing the zero lag noise spike. The

Table 6.1: **Radio Bursts Detected from FRB 121102 with DSS-43**

Burst ID	Peak Time [a,b] (MJD)	DM [c] ($\mathrm{pc\,cm^{-3}}$)	Burst Width [b,d] (ms)	Peak Flux Density [b,e] (Jy)	Spectral Energy Density [b,f] (10^{30} erg $\mathrm{Hz^{-1}}$)	Fluence [b,e,f] (Jy ms)
B1	58732.8213572248	564.1 ± 0.1	2.94 ± 0.06	2.6 ± 0.5	7.5 ± 1.5	6.7 ± 1.3
B2	58732.8523084187	564.2 ± 0.1	1.05 ± 0.18	0.8 ± 0.2	0.5 ± 0.1	0.4 ± 0.1
B3	58732.8639729023	565.0 ± 0.1	1.65 ± 0.09	1.4 ± 0.3	2.1 ± 0.4	1.8 ± 0.4
B4	58732.8655320626	564.2 ± 0.1	0.63 ± 0.07	1.0 ± 0.2	0.6 ± 0.1	0.5 ± 0.1
B5	58732.8681642140	564.2 ± 0.1	1.23 ± 0.19	0.7 ± 0.1	0.6 ± 0.1	0.5 ± 0.1
B6	58732.9317656593	563.6 ± 0.1	2.10 ± 0.03	5.9 ± 1.2	10 ± 2.0	8.8 ± 1.8

[a] Barycentric time of the center of the burst envelope, determined after removing the time delay from dispersion using a DM value of 563.6 $\mathrm{pc\,cm^{-3}}$ (structure-optimized DM for the brightest burst, B6) and correcting to infinite frequency. The barycentric times were derived using the position ($\alpha_{J2000} = 05^h31^m58^s.698$, $\delta_{J2000} = 33°08'52''.586$) in Marcote et al. [367].
[b] Values are derived after dedispersing each burst using a DM value of 563.6 $\mathrm{pc\,cm^{-3}}$.
[c] DM value that maximized the peak S/N of each burst.
[d] FWHM duration determined using a Gaussian fit.
[e] Uncertainties are dominated by the 20% fractional error on the system temperature, T_{sys}.
[f] Fluence determined using the 2σ FWHM for the duration of the burst. This choice ensures that all of the burst energy is included.

scintillation bandwidth, defined as the half-width at half-maximum (HWHM) of the Lorentzian fit [127], is labeled in the figure for each burst. The baseband data used in this analysis contained 8 MHz frequency gaps between each of the six 8 MHz-wide frequency sub-bands. This introduced noise spikes into the ACF at frequency lags that were close to integer multiples of the sub-band width. This is apparent in the ACFs shown in Figure 6.3 toward frequency lags of 8 MHz. We also include ACFs of the off-burst data in Figure 6.3 to emphasize that the frequency structure is produced by scintillation, rather than instrumental effects. B6 shows a feature in the ACF at a frequency lag of approximately 1.7 MHz, which we highlight using a black arrow in Figure 6.3. Similar behavior is not observed at the same frequency lag in the ACF of B1. We discuss this further in Section 6.4.

6.4 Discussion and Conclusions

To date, FRB 121102 has been detected at radio frequencies from 600 MHz [259] up to 8 GHz [191]. Early observations of FRB 121102 by Spitler et al. [499] and Scholz et al. [479] demonstrated that the bursts have variable spectra that sometimes peak within the observing band and are often not well-modeled by a power-law. This also clarifies the strange inverted spectrum of the discovery detection of FRB 121102 [497], though the detection of that burst in the coma lobe of the receiver likely also affected the apparent spectrum. Broader-band observations (1.15–1.73 GHz) by Hessels et al. [229] demonstrated that the characteristic bandwidth of emission is roughly 250 MHz at 1.4 GHz and the bursts are sometimes composed of sub-bursts with characteristic peak emission frequencies that decrease

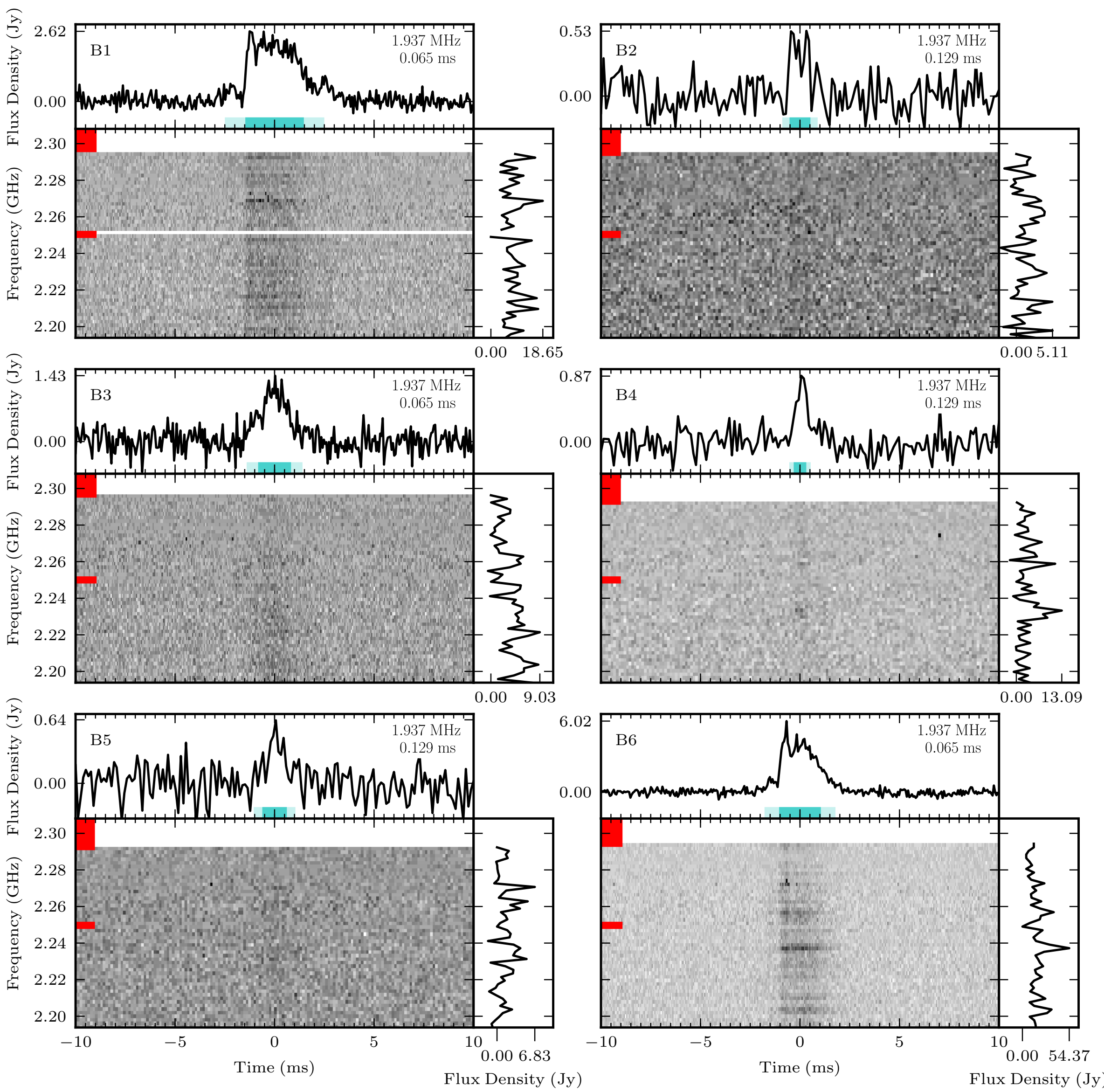

Figure 6.1: ***S*-band bursts detected from FRB 121102 with DSS-43, ordered by increasing arrival time.** The flux calibrated, frequency-averaged burst profiles are shown in the top panels, and the dynamic spectrum associated with each burst is displayed in the bottom panels. The flux calibrated, time-averaged spectra are shown in the right panels. Each burst has been dedispersed using a DM of 563.6 pc cm^{-3}, which corresponds to the structure-optimized DM for the brightest burst (B6). Each burst was fitted with a Gaussian function to determine the full-width at half-maximum (FWHM) burst duration, which is indicated with a cyan bar at the bottom of the top panels. The lighter cyan bar corresponds to a 2σ confidence interval. The red ticks in the dynamic spectrum indicate frequency channels that have been masked as a result of RFI. The data have been downsampled to the frequency and time resolutions specified in the top right corner of the top panels in order to enhance the visualizations of the bursts.

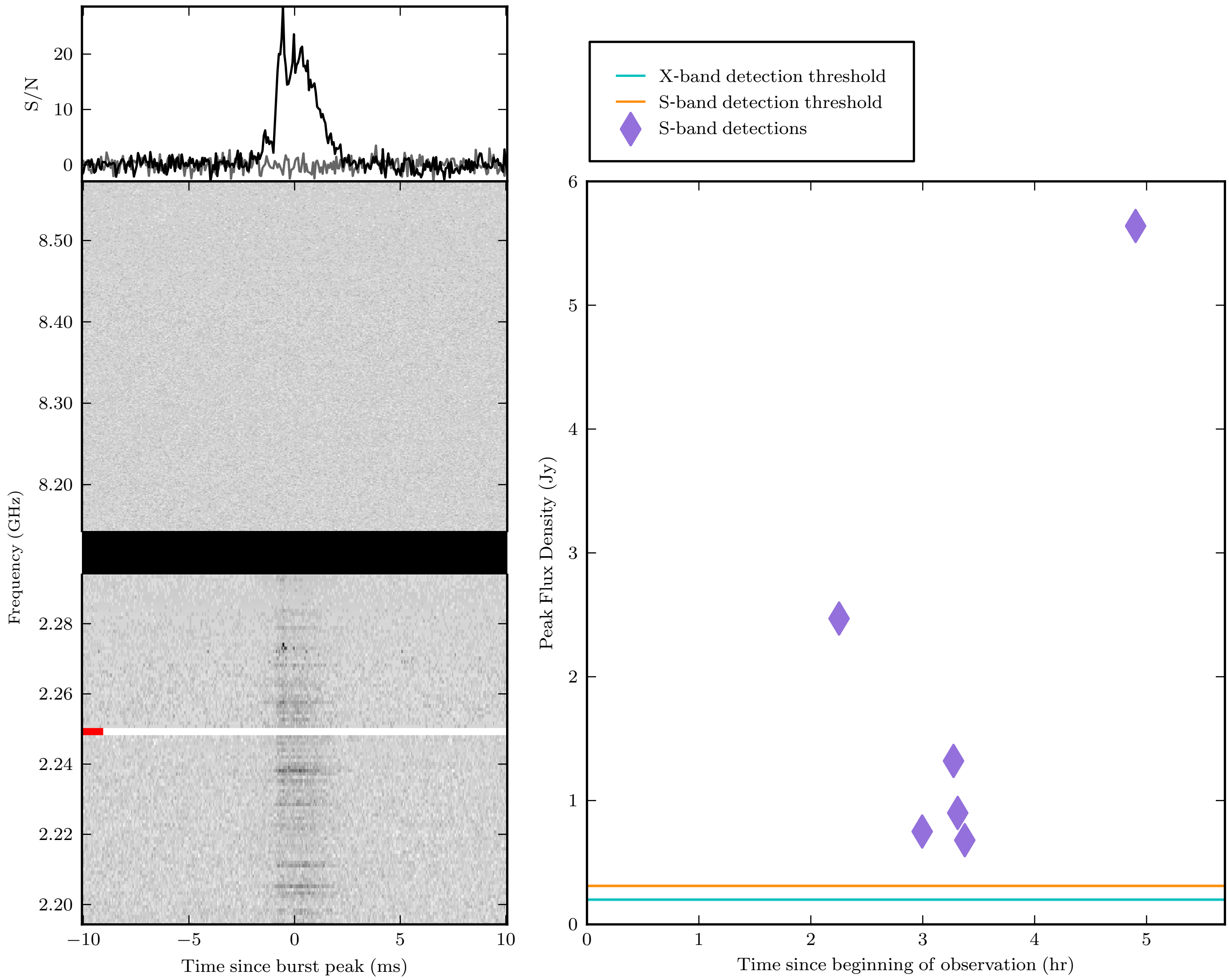

Figure 6.2: **Dynamic spectrum of the brightest S-band burst (B6) detected from FRB 121102 and the peak flux densities of all of the radio bursts as a function of time.** Left panels: Composite dynamic spectrum of the brightest S-band burst (B6), which shows the detection at S-band and the simultaneous non-detection at X-band. The time and frequency resolution plotted here are ~64.5 μs and ~0.98 MHz, respectively. The structure-optimized DM (563.6 pc cm^{-3}) was used for dedispersion and to calculate the dispersive time delay between the S-band and X-band data. The black band indicates the frequency gap between the top of the S-band data and bottom of the X-band data. The red ticks indicate frequency channels that have been masked due to RFI. In the top-left panel, we show the S-band frequency-averaged burst profile in black and the X-band frequency-averaged profile in gray. Right panel: Peak flux densities of the six detected S-band bursts as a function of time during our observation. The cyan line corresponds to the 7σ detection threshold at X-band, and the orange line indicates the 7σ detection threshold at S-band, both determined assuming a burst width of 1 ms.

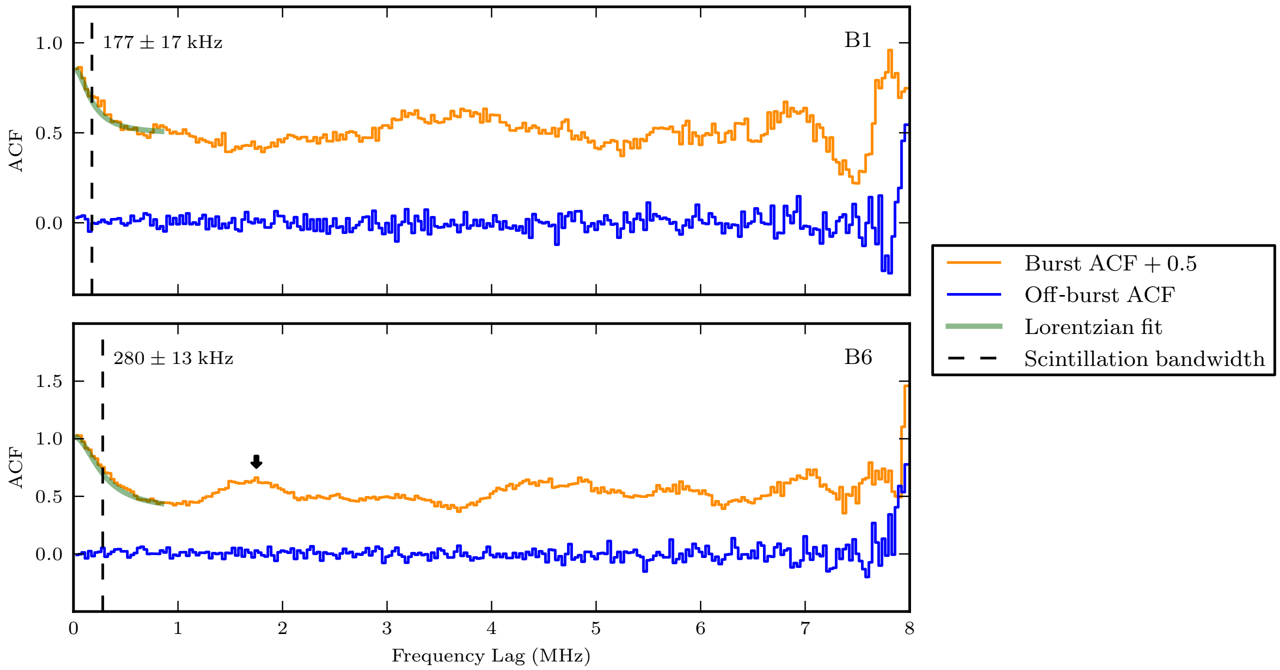

Figure 6.3: **Autocorrelation functions (ACFs) of the spectra associated with the two brightest *S*-band bursts, shown with frequency lags up to 8 MHz.** The ACFs are shown in orange for B1 in the top panel and for B6 in the bottom panel. The zero lag noise spike has been removed. Lorentzian fits to the central bump in the ACFs are shown in green using frequency lags up to 0.84 MHz. The black dashed lines indicate the scintillation bandwidths, defined as the half-width at half-maximum (HWHM) of the Lorentzian fits, and are labeled in the top-left corner of each panel. The ACFs of the off-burst data are shown in blue to aid in distinguishing between frequency structure due to scintillation and instrumental effects. The black arrow in the bottom panel highlights a feature in the ACF of the spectrum of B6 at a frequency lag of ~1.7 MHz.

during the burst envelope at a rate of ~200 MHz ms^{-1} in this frequency band. This "sad trombone" effect appears to be a characteristic feature of repeating FRBs [521], and may be an important clue as to their emission mechanism. The available bandwidth used to detect the 2.25 GHz bursts presented here is insufficient to resolve sub-burst drifts of this type.

Similar narrowband, 100–200 MHz brightness envelopes were also found by Gourdji et al. [213] in a sample of 41 bursts detected using the Arecibo telescope during two ~2 hr observing sessions conducted on consecutive days. They also found tentative evidence for preferred frequencies of emission during those epochs, suggesting that FRB 121102's detectability depends strongly on the radio frequency that is being utilized. In addition, recent simultaneous, multifrequency observations of another repeating FRB, FRB 180916.J0158+65, demonstrated that its apparent activity may also be related to the observing frequency [522]. CHIME/FRB detected two bursts from this source (with fluences of ~2 Jy ms) in the 400–800 MHz band within a 12 min transit. However, no bursts (above a fluence threshold of 0.17 Jy ms) were detected from FRB 180916.J0158+65 with the Effelsberg telescope at ~1.4 GHz during 17.6 hr of observations on the same day, which overlapped the times of the two CHIME/FRB detections. Clearly, the radio emission from repeating FRBs is not instantaneously broadband, which we further demonstrate with our simultaneous 2.25 and 8.36 GHz observations of FRB 121102. Our results show that there was a period of burst activity from FRB 121102, lasting at least 2.6 hr, where radio emission was detected at 2.25 GHz but not at 8.36 GHz.

There are only a few multiband radio observations of FRB 121102 in the literature. Law et al. [302] present results from a multi-telescope campaign of FRB 121102 using the VLA at 3 and 6 GHz, the Arecibo telescope at 1.4 GHz, the Effelsberg telescope at 4.85 GHz, the first station of the Long Wavelength Array (LWA1) at 70 MHz, and the Arcminute Microkelvin Imager Large Array (AMI-LA) at 15.5 GHz. Nine bursts were detected with the VLA, and four of these bursts had simultaneous observing coverage at different frequencies. Only one of these bursts was detected simultaneously at two different observing frequencies with Arecibo (1.15–1.73 GHz) and the VLA (2.5–3.5 GHz). The remaining three bursts were detected solely with the VLA, despite the instantaneous sensitivity of Arecibo being ~5 times better than the VLA. None of the four bursts were detected during simultaneous LWA1, Effelsberg, or AMI-LA observations, though we note that only Effelsberg's sensitivity is comparable to the VLA's. Gourdji et al. [213] describe 41 bursts detected with Arecibo at 1.4 GHz, and no bursts were seen with the VLA during their simultaneous observations. They also report one VLA-detected burst that was not seen in their contemporaneous Arecibo data. Houben et al. [240] performed a search for bursts from FRB 121102 using both Effelsberg (1.4 GHz) and the Low Frequency Array (LOFAR; 150 MHz). In this search, they discovered nine bursts with Effelsberg, but there were no simultaneous detections with LOFAR.

Gajjar et al. [191] reported the detection of 21 bursts above 5.2 GHz during a 6 hr observation with the GBT. It is notable that all of these bursts were detected within a short 1 hr time interval. The peak flux densities of these bursts ranged between ~50 and ~700 mJy. These bursts also showed both large-scale (~1 GHz-wide) and fine-scale frequency structures, none of which spanned the entire 4.5–8.0 GHz frequency band. Assuming a flat spectral index, there are six bursts in Gajjar et al. [191] with peak flux densities that are above our X-band sensitivity limit. Thus, similarly bright bursts would have been detected during our X-band observations, if they were present.

Galactic scintillation cannot explain the observed detection of bursts from FRB 121102 at S-band and the simultaneous absence of detection at X-band. However, the narrowband fluctuations of burst intensity seen at S-band are consistent with scintillation at low Galactic latitude ($b = -0.2°$) expected from the Milky Way foreground ($\Delta\nu_{\rm DISS} = 58.1 \pm 2.3$ kHz at 1.65 GHz, [229]). In this Letter, we have measured $\Delta\nu_{\rm DISS,\,B1} = 177 \pm 17$ kHz and $\Delta\nu_{\rm DISS,\,B6} = 280 \pm 13$ kHz at 2.24 GHz for the two brightest bursts, B1 and B6. Given the expected Galactic scintillation bandwidth of ~200 kHz and scintillation timescale of ~4 minutes at 2.24 GHz, it is not surprising that the measured scintillation bandwidths are different compared to their formal uncertainties. We are sampling a limited number of scintles in each case, and burst self-noise may also contribute to the difference. This likely also explains the other features in the on-burst ACFs, including the prominent 1.7 MHz bump in B6.

Previously, Gajjar et al. [191] reported scintillation bandwidths of $\Delta\nu_{\rm DISS} \sim 10$–100 MHz for bursts detected between 4.5–8.0 GHz. Combining all available measurements, we estimate that the scintillation bandwidth is $\Delta\nu_{\rm DISS} \approx 0.2$–0.3 MHz at 2.25 GHz and $\Delta\nu_{\rm DISS} \approx 30$–90 MHz at 8.36 GHz, where the ranges correspond to assumed scalings of $\Delta\nu_{\rm DISS} \propto \nu^4$ and $\Delta\nu_{\rm DISS} \propto \nu^{4.4}$, respectively. Galactic scintillation therefore cannot explain the clear detections of the 2.25 GHz bursts shown in Figure 6.1 and the lack thereof in our simultaneous 8.36 GHz data, where the bandwidth (430 MHz) at X-band is many times larger than the scintillation bandwidth.

Cordes et al. [131] discuss the possible role of plasma lensing on the burst spectra and apparent brightness of FRBs. They argue that FRBs may be boosted in brightness on short timescales through caustics, which can produce strong magnifications ($\lesssim 10^2$). However, we note that larger spectral gains are possible since this depends strongly on various parameters, such as the geometry of the lens, the lens' dispersion measure depth, and the scale size [131, 422], which are currently poorly constrained. It is therefore possible that the 2.25 GHz detections shown in Figure 6.1 may coincide with a caustic peak. However, it is not clear how plasma lensing could explain the downward-only frequency drifts seen in some FRBs [229]. On the other hand, the synchrotron maser emission model from a decelerating blast wave proposed by Metzger et al. [388] provides a more natural explanation for the downward-only frequency drifts in the case of a constant density model for the upstream medium. Intriguingly, this model also suggests that multiple weaker flares from the source engine in succession could produce clustered bursts over $\sim 10^2$–10^3 s by having each burst run through the same ejecta shell. We note that our sample of faint bursts, B2–B5, are clustered within $\sim 10^3$ s in time, while the most energetic bursts in our sample, B1 and B6, have a temporal separation of $\sim 10^4$ s.

The two brightest bursts (B1 and B6) in Figure 6.1 display remarkably similar morphology: a weak precursor sub-burst, followed by a sharp rise and bright sub-burst (lasting for ~0.5 ms), and thereafter a broader component (lasting for a few milliseconds) perhaps composed of multiple unresolved sub-bursts, followed by a slow decay. The decaying tails of these bursts are far too long to be due to multipath propagation through the Galactic interstellar medium (ISM), which is expected to produce a scattering time of $\tau_d = 1.16/2\pi\Delta\nu_{\rm DISS} \approx 0.7\ \mu$s at 2.25 GHz [125]. Rather, it appears that this structure may either be intrinsic to the burst emission mechanism or originate in FRB 121102's host galaxy and/or local environment. Furthermore, many other bursts from FRB 121102 also show asymmetric burst morphologies, which cannot be explained by scattering (e.g., see [229]). The burst tails observed in B1 and B6 may be caused by the same mechanism responsible for the sub-burst drift rate and the apparent "sad trombone" behavior [229, 259].

A comparison of our structure-maximizing DM of $563.6 \pm 0.1\,\mathrm{pc\,cm^{-3}}$ for B6 at MJD 58732 with the reported DM $= 560 \pm 0.07\,\mathrm{pc\,cm^{-3}}$ at MJD 57644 by Hessels et al. [229] suggests an increase of $\Delta\mathrm{DM} \sim 3.6\,\mathrm{pc\,cm^{-3}}$ over a period of roughly 3 years. This trend agrees roughly with the $\Delta\mathrm{DM} \sim 1$–$3\,\mathrm{pc\,cm^{-3}}$ in 4 years reported by Hessels et al. [229]. The apparent trend, suggesting an increase in the electron column density along the line of sight, could be explained by the source moving in an H II region [576]. Interestingly an FRB source in an expanding supernova remnant (SNR) is expected to primarily result in a decreasing trend in DM over time, which is not borne out by the recent observations. Clearly long term observations of FRB 121102 will be needed to confirm or refute the currently observed trend.

Multifrequency observations that densely cover the ~0.1–30 GHz range can better clarify how the burst activity of FRB 121102 depends on the radio observing frequency. It is currently unclear whether there is an optimal frequency range for observing this source. While many bursts from FRB 121102 appear to span only a few hundred MHz of bandwidth, some appear to span at least ~2 GHz [302]. Multifrequency, broadband measurements can also better quantify the typical emission bandwidth and determine whether or not bursts show multiple brightness peaks at widely separate frequencies, both of which are important for disentangling propagation effects and studying the mechanism(s) responsible for the emission.

Acknowledgments

We thank Jim Cordes for useful discussions.

A.B.P. acknowledges support by the Department of Defense (DoD) through the National Defense Science and Engineering Graduate (NDSEG) Fellowship Program and by the National Science Foundation (NSF) Graduate Research Fellowship under Grant No. DGE-1144469. J.W.T.H. acknowledges funding from an NWO Vici fellowship.

We thank the Jet Propulsion Laboratory's Spontaneous Concept Research and Technology Development program for supporting this work. We also thank Charles Lawrence and Stephen Lichten for providing programmatic support. In addition, we are grateful to the DSN scheduling team (Hernan Diaz, George Martinez, Carleen Ward) and the Canberra Deep Space Communication Complex (CDSCC) staff for scheduling and carrying out these observations.

A portion of this research was performed at the Jet Propulsion Laboratory, California Institute of Technology and the Caltech campus, under a Research and Technology Development Grant through a contract with the National Aeronautics and Space Administration. U.S. government sponsorship is acknowledged.

Chapter VII

Multiwavelength Radio Observations of Two Repeating Fast Radio Burst Sources: FRB 121102 and FRB 180916.J0158+65

[429] **Pearlman, A. B.*** et al. (2020). "Multiwavelength Radio Observations of Two Repeating Fast Radio Burst Sources: FRB 121102 and FRB 180916.J0158+65." In: *ApJL,* 905:L27. arXiv:2009.13559 [astro-ph.HE].

Multiwavelength Radio Observations of Two Repeating Fast Radio Burst Sources: FRB 121102 and FRB 180916.J0158+65

Aaron B. Pearlman[1,6,7,*], Walid A. Majid[2,1], Thomas A. Prince[1,2], Kenzie Nimmo[3,4], Jason W. T. Hessels[3,4], Charles J. Naudet[2], and Jonathon Kocz[1,5]

[1] Division of Physics, Mathematics, and Astronomy, California Institute of Technology, Pasadena, CA 91125, USA

[2] Jet Propulsion Laboratory, California Institute of Technology, Pasadena, CA 91109, USA

[3] Anton Pannekoek Institute for Astronomy, University of Amsterdam, Science Park 904, 1098 XH Amsterdam, The Netherlands

[4] ASTRON, Netherlands Institute for Radio Astronomy, Oude Hoogeveensedijk 4, 7991 PD Dwingeloo, The Netherlands

[5] Department of Astronomy, University of California, Berkeley, CA 94720, USA

[6] NDSEG Research Fellow

[7] NSF Graduate Research Fellow

[*] Lead author of the manuscript.

Corresponding author: aaron.b.pearlman@caltech.edu

Abstract

The spectra of fast radio bursts (FRBs) encode valuable information about the source's local environment, underlying emission mechanism(s), and the intervening media along the line of sight. We present results from a long-term multiwavelength radio monitoring campaign of two repeating FRB sources, FRB 121102 and FRB 180916.J0158+65, with the NASA Deep Space Network (DSN) 70 m radio telescopes (DSS-63 and DSS-14). The observations of FRB 121102 were performed simultaneously at 2.3 and 8.4 GHz, and spanned a total of 27.3 hr between

2019 September 19 and 2020 February 11. We detected 2 radio bursts in the 2.3 GHz frequency band from FRB 121102, but no evidence of radio emission was found at 8.4 GHz during any of our observations. We observed FRB 180916.J0158+65 simultaneously at 2.3 and 8.4 GHz, and also separately in the 1.5 GHz frequency band, for a total of 101.8 hr between 2019 September 19 and 2020 May 14. Our observations of FRB 180916.J0158+65 spanned multiple activity cycles during which the source was known to be active and covered a wide range of activity phases. Several of our observations occurred during times when bursts were detected from the source between 400–800 MHz with the Canadian Hydrogen Intensity Mapping Experiment (CHIME) radio telescope. However, no radio bursts were detected from FRB 180916.J0158+65 at any of the frequencies used during our observations with the DSN radio telescopes. We find that FRB 180916.J0158+65's apparent activity is strongly frequency-dependent due to the narrowband nature of its radio bursts, which have less spectral occupancy at high radio frequencies ($\gtrsim 2$ GHz). We also find that fewer or fainter bursts are emitted from the source at high radio frequencies. We discuss the implications of these results on possible progenitor models of repeating FRBs.

7.1 Introduction

Fast radio bursts (FRBs) are transient pulses of radio emission (see [120, 436] for recent reviews) that have observed temporal widths ranging from microseconds to milliseconds (e.g., see [98, 405]) and fluences between ~0.01–1,000 Jy ms (e.g., see [492]). Their progenitors are mostly believed to be located at extragalactic distances since the observed dispersion measures (DMs) of their radio bursts exceed the expected contribution from the column density of Galactic free electrons along the line of sight. The extragalactic nature of FRBs was definitively confirmed through the sub-arcsecond localization of radio bursts from the first repeating FRB, FRB 121102 (also referred to as FRB 20121102A) [497, 499], to a low-metallicity star-forming dwarf galaxy at a redshift of $z = 0.19$ [95, 367, 516]. Over 100 FRBs have been published to date (see [435] for a catalog[w]), which includes 23 repeating FRB sources [59, 297, 298, 334, 499, 520, 521, 523]. The volumetric occurrence rates of FRBs that have not been observed to repeat thus far suggest that a large fraction of these sources should emit multiple bursts over their lifetimes [460].

A total of 13 extragalactic FRB sources have now been localized to host galaxies at redshifts of 0.034–0.66 [26, 44, 95, 225, 303, 350, 367, 368, 449, 462], which has

[w] See http://frbcat.org.

demonstrated that FRBs can produce radio bursts with a wide range of luminosities from diverse host galaxies and local environments. Radio bursts from repeating FRBs often exhibit hallmark features that typically distinguish their emission from that of apparently non-repeating sources. Repeating FRBs tend to have larger burst widths, on average, compared to non-repeating FRBs [187, 479, 521], as well as bursts with linear polarization fractions approaching 100% and a flat polarization position angle (PA) across their burst envelopes (e.g., see [96, 147, 187, 391, 521]). In some cases, they can also emit bursts with subpulses that drift downward in frequency with time, which has been dubbed the "sad trombone" effect [229, 259, 520, 521]. While these properties suggest that the emission mechanisms and/or local environments of repeating and non-repeating FRB sources may be different, it is not yet clear whether they have different physical origins.

Numerous theoretical models have been proposed to explain the emission behavior of FRBs (see [444] for an overview[j]). Many of these models invoke coherent radiation mechanisms from compact objects, such as young neutron stars or magnetars (e.g., see [41, 247, 331, 387]). Recently, progenitor models involving magnetars have garnered considerable attention thanks to the discovery of an unusually bright millisecond-duration radio burst from the Galactic magnetar, SGR 1935+2154 [59, 523]. This discovery has demonstrated that extragalactic magnetars are responsible for at least some fraction of the cosmological FRB population and has also helped to bridge the large radio energy gap that previously existed between Galactic magnetars and FRBs. In fact, SGR 1935+2154 has emitted radio bursts spanning 7 orders of magnitude in luminosity [59, 277, 523, 584], ranging from "normal" radio bursts from magnetars (e.g., see [422, 430]) to within $\sim$1 order of magnitude of the faintest known FRBs. However, the burst repetition rates and energetics of most active, extragalactic repeating FRB sources indicate that their progenitors are somehow different from the population of known Galactic magnetars. The volume density of active repeating FRBs is also much smaller than the volume density of Galactic magnetars, even if one assumes that active repeating sources are produced by younger versions of Galactic magnetars that are presumed to have larger magnetic fields and higher activity levels. This implies that the progentiors of repeating FRBs must be volumetrically rare [332, 370].

Over the past few years, daily radio observations of the northern hemisphere sky in the 400–800 MHz frequency band with the Canadian Hydrogen Intensity Mapping Experiment (CHIME) transit radio telescope has led to discovery of many new repeating FRB sources [187, 520, 521], enabled by the instrument's large instantaneous field of view (FoV), wide bandwidth, and high sensitivity [519]. In particular, the discovery of FRB 180916.J0158+65 (also referred to as FRB 20180916B) [521], its subsequent localization to a nearby massive spiral galaxy [368], and the detection of a 16.35 d periodicity (or possibly a higher frequency alias of this period) in the burst arrival times [522] has facilitated detailed studies of the source via follow-up observations across multiple wavelengths (e.g., see [482, 517]). Most bursts from FRB 180916.J0158+65 have been detected within a ∼5.4 d interval during cycles when the source was observed to be active (e.g., see [96, 373, 440, 471, 522]), but some bursts have been found to occur slightly outside of this activity window (e.g., see [8]). There is now also tentative evidence for a ∼157 d periodicity in the arrival times of bursts from FRB 121102, with a duty cycle of ∼56 percent for the activity cycle [9, 139, 453].

Most FRB sources have been observed at frequencies below ∼2 GHz due to the smaller FoV of radio telescopes at high frequencies, which limits the instrument's sky survey speed. As a result, the broadband spectral behavior of most FRBs remains largely unexplored at high frequencies since precise sky positions are generally needed for follow-up high frequency radio observations. The precise localization of FRB 121102 to a host galaxy [95, 367, 516] subsequently enabled the detection of numerous radio bursts up to ∼8 GHz (e.g., see [191, 213, 240, 302, 358, 391, 425, 480, 500, 587]). These observations revealed that FRB 121102 emits narrowband bursts, with fractional emission bandwidths of ∼10–30%, across a wide range of radio frequencies. Many of these bursts also display complex time-frequency features. The emission bandwidths and sub-burst drift rates observed from FRB 121102 are typically larger at higher frequencies, on average [191, 229, 587]. In addition, the apparent burst activity of FRB 121102 was shown to strongly depend on the range of radio frequencies that are being observed (e.g., see [213, 240, 302, 358]).

High frequency radio observations of FRBs are especially important for studying sources in the local Universe since the emission from more cosmologically distant sources will be redshifted toward lower radio frequencies [333, 461]. If the intrinsic energy distribution of bursts from FRBs is described by a steep power-law (e.g., $\mathrm{d}N/\mathrm{d}E \propto E^{-\gamma}$, where $\gamma \gtrsim 1.8$), then luminous bursts will be detected more rarely and most repeaters should be found at lower redshifts. Since the progenitor population of FRBs remains poorly constrained, broadband radio observations across a wide range of frequencies are crucial for understanding their underlying emission mechanism(s). Observations at high radio frequencies also offer a valuable resource for studying the circumburst environments of FRBs since some bursts may be rendered undetectable at lower frequencies due to a combination of free-free absorption by thermal electrons in the intervening medium, scatter-broadening produced by multipath propagation through media with electron density fluctuations, plasma lensing [131], and induced Compton scattering [452, 461].

In this Letter, we present results from a series of radio observations of two repeating FRB sources, FRB 121102 and FRB 180916.J0158+65, performed simultaneously at 2.3 and 8.4 GHz, and separately at 1.5 GHz, with the NASA Deep Space Network (DSN) 70 m telescopes, DSS-63 and DSS-14. The radio observations are described in Section 7.2, and the data analysis procedures and algorithms used to search for radio bursts are described in Section 7.3. In Section 7.4, we report the results of our searches for radio bursts from both of these repeating sources and list the measured properties of the bursts detected during our multiwavelength radio campaign. In Section 7.5, we discuss the spectral properties of radio bursts from both of these repeaters and the apparent frequency dependence of the observed burst activity. We also discuss the implications of our results on the activity window and temporal distribution of radio bursts from FRB 180916.J0158+65 and place our results in the context of progenitor models proposed to explain the emission behavior of repeating FRBs. Lastly, we provide a summary of our results and conclusions in Section 7.6.

7.2 Radio Observations

As part of a long-term radio monitoring program of repeating FRBs with the radio telescopes comprising NASA's DSN [424], we carried out high frequency observations of two repeating FRB sources, FRB 121102 and FRB 180916.J0158+65, using two of the DSN's large 70 m radio telescopes (DSS-63 and DSS-14). DSS-63 is located at the Madrid Deep Space Communications Complex (MDSCC) in Robledo, Spain, and DSS-14 is located at the Goldstone Deep Space Communications Complex (GDSCC) in Goldstone, California. Radio observations of FRB 121102 were performed between 2019 September 19 (MJD 58745) and 2020 February 11 (MJD 58890) using DSS-63. Roughly ∼2 weeks prior to the start of these observations, we detected 6 bursts from FRB 121102 in the 2.25 GHz frequency band on 2019 September 6 (MJD 58732) during simultaneous 2.25 and 8.36 GHz observations with the DSN's 70 m radio telescope (DSS-43), located at the Canberra Deep Space Communications Complex (CDSCC) in Tidbinbilla, Australia [358].

We used both DSS-63 and DSS-14 to observe FRB 180916.J0158+65 between 2019 September 19 (MJD 58745) and 2020 May 14 (MJD 58983). The observations of FRB 121102 and FRB 180916.J0158+65 were performed using the positions provided in Marcote et al. [367] and Marcote et al. [368], respectively.

During each radio observation of FRB 121102 and FRB 180916.J0158+65 with DSS-63, we used the telescope's cryogenically cooled dual circular polarization receivers to simultaneously record S-band and X-band data at center frequencies of 2.3 and 8.4 GHz, respectively, except during some observations where only one circular polarization channel was available at S-band. The system's ultra-wideband pulsar backend allowed us to simultaneously receive and save channelized power spectral densities across both frequency bands with a frequency resolution of 0.464 MHz and time resolutions ranging between 0.28 and 2.21 ms. The S-band system has a bandwidth of roughly 120 MHz, and the X-band system has a bandwidth of approximately 400 MHz. The start time, exposure time, center frequency, recorded bandwidth, number of recorded polarizations, and time resolution of each radio observation are provided in Tables 7.1, 7.2, and 7.3. In addition, the very long baseline interferometry (VLBI) baseband recorder at the MDSCC was used to simultaneously record data at S-band and X-band during most observations, which allowed us to search for bursts using high time resolution data. A detailed analysis of the baseband data will be presented in an upcoming publication.

We also observed FRB 180916.J0158+65 at a center frequency of 1.5 GHz (L-band) during 8 epochs using DSS-14 (see Table 7.2). While the L-band system on DSS-14 is capable of recording roughly 500 MHz of total bandwidth, only 250 MHz of the bandwidth was usable after RFI mitigation. The L-band data were recorded with a frequency and time resolution of 0.625 MHz and 102.4 μs, respectively. These L-band observations were also discussed in Scholz et al. [482], along with simultaneous S-band and X-band observations of FRB 180916.J0158+65 using DSS-63 during 7 separate epochs.

The data from each frequency band were flux-calibrated using the elevation-corrected system temperature, $T_{\rm sys}$, and the radiometer equation [382]:

$$S_{\rm peak} = \frac{\beta\, T_{\rm sys}\, ({\rm S/N})_{\rm peak}}{G\sqrt{\Delta\nu\, n_p\, t_{\rm peak}}}. \tag{7.1}$$

Here, $\beta \approx 1$ is a correction factor that accounts for system imperfections, such as digitization of the signal, $({\rm S/N})_{\rm peak}$ is the peak signal-to-noise ratio (S/N), $G \approx 1$ K/Jy is the gain of the DSN's 70 m telescopes (DSS-63 and DSS-14), $\Delta\nu$ is the observing bandwidth, n_p is the number of polarizations, and $t_{\rm peak}$ denotes the integration time at the peak. The system temperature was measured at each frequency at the start of each observation using a noise diode modulation scheme while the antenna was pointed at zenith. The corrections applied to the $T_{\rm sys}$ values for elevations less than 20° were minimal.

7.3 Data Analysis and Searches for Radio Bursts

The channelized filterbank data from DSS-63 and DSS-14 were processed using data reduction procedures similar to those described in previous single pulse studies of pulsars, magnetars, and FRBs with the DSN (e.g., see [356, 358, 422, 424, 425, 430]). We first corrected the bandpass slope across the frequency band in each data set. Then, we identified frequency channels that were corrupted by radio frequency interference (RFI) using an iterative filtering algorithm, where the time-averaged bandpass value of each frequency channel was compared to the moving median of the bandpass values. If the time-averaged bandpass value of an individual frequency channel differed from the moving median value by more than the moving standard deviation of the moving median values, then we flagged the frequency channel for masking. The moving median and moving standard deviation statistics were calculated using a sliding window of 8 frequency channels. This procedure was repeated, after replacing the bandpass value of each flagged frequency channel with its corresponding moving median value at the end of each iteration, until no additional frequency channels were flagged for removal. This algorithm identified most of the frequency channels corrupted by RFI in only a few iterations. A small number of aberrant frequency channels were also identified and masked after visually inspecting the data using the PSRCHIVE software package [239]. Next, in order to remove low frequency temporal variability, the moving average was subtracted from each data value in each frequency channel using a sliding window spanning 0.5 s around each time sample.

Most of the radio bursts previously detected from FRB 121102 have observed DMs between roughly 500–600 pc cm^{-3} (e.g., see [191, 229, 358, 587]). The observed DMs of radio bursts detected thus far from FRB 180916.J0158+65 range between approximately 340–360 pc cm^{-3} (e.g., see [521, 522][x]). Based on this, we dedispersed the cleaned filterbank data from FRB 121102 with trial DMs between 400 and 700 pc cm^{-3}, which were linearly spaced by 5 pc cm^{-3} at S-band and 50 pc cm^{-3} at X-band. The cleaned data from FRB 180916.J0158+65 were dedis-

[x] See https://www.chime-frb.ca/repeaters/180916.J0158+65.

Table 7.1: **Multiwavelength Radio Observations of FRB 121102**

Telescope[a]	Start Time[b] (UTC)	Exposure Time (s)	Center Frequency (GHz)	Bandwidth[c] (MHz)	Number of Polarizations[d]	Time Resolution (ms)	6σ Fluence Threshold ($\mathcal{F}_{\rm min}$)[f] (Jy ms $\sqrt{(w/1\,{\rm ms})}$)
DSS-63	2019-09-19 00:55:25	4379.964	2.25	120.14	1	2.2075	0.34
			8.38	395.68	2		0.14
	2019-09-24 00:07:07	5339.983	2.25	120.14	1	2.2075	0.35
			8.38	395.68	2		0.15
	2019-09-28 00:02:05	5159.923	2.25	120.14	1	2.2075	0.35
			8.38	395.68	2		0.14
	2019-09-28 23:57:05	5339.983	2.25	120.14	1	2.2075	0.35
			8.38	395.68	2		0.14
	2019-10-19 20:52:15	3155.671	2.25	120.14	1	0.2759	0.39
			8.38	395.68	2		0.17
	2019-10-21 22:17:07	5197.230	2.25	120.14	1	0.2759	0.35
			8.38	395.68	2		0.14
	2019-11-09 21:12:15	3596.984	2.25	110.40	2	1.0240	0.27
			8.38	395.68			0.15
	2019-11-20 21:56:53	5459.935	2.25	110.40	2	2.2075	0.25
			8.38	395.68			0.13
	2019-11-21 03:14:05	2799.930	2.25	110.40	2	2.2075	0.24
			8.38	395.68			0.13
	2019-11-25 20:00:45	10641.985	2.25	110.40	2	2.2075	0.27
			8.38	395.68			0.15
	2019-12-02 00:21:19	5159.925	2.25	110.40	2	2.2075	0.24
			8.38	395.68			0.13
	2019-12-02 21:20:55	5339.983	2.25	110.40	2	2.2075	0.25
			8.38	395.68			0.13
	2019-12-06 21:59:03	5339.983	2.25	110.40	2	2.2075	0.24
			8.38	395.68			0.13
	2019-12-10 20:47:43	5339.983	2.25	110.40	2	2.2075	0.25
			8.38	395.68			0.13
	2019-12-13 01:03:31	5119.868	2.25	110.40	2	2.2075	0.24
			8.38	395.68			0.13
	2019-12-16 22:37:57	10499.935	2.26	105.30	2	2.2075	0.25
			8.38	395.68			0.13
	2019-12-21 00:28:03	6119.969	2.26	105.30	2	2.2075	0.25
			8.38	395.68			0.13
	2020-02-10 00:35:01	4199.929	2.25	110.40	2	2.2075	0.25
			8.38	395.68			0.14

FRB 121102 was observed for a total of 27.3 hr between 2019 September 19 and 2020 February 11. During each of the two epochs highlighted in bold, 1 radio burst was detected in the 2.3 GHz frequency band using DSS-63, but there was no evidence of radio emission at 8.4 GHz.

[a] Deep Space Network (DSN) radio antenna used for observations.

[b] Start time of the radio observations in yyyy-mm-dd hh:mm:ss format.

[c] Total usable bandwidth after radio frequency interference (RFI) mitigation.

[d] Number of circular polarizations recorded.

[e] 6σ fluence detection threshold, $\mathcal{F}_{\rm min}$, for an assumed burst width of 1 ms.

Table 7.2: **Multiwavelength Radio Observations of FRB 180916.J0158+65**

Telescope[a]	Start Time[b] (UTC)	Exposure Time (s)	Center Frequency (GHz)	Bandwidth[c] (MHz)	Number of Polarizations[d]	Time Resolution (ms)	6σ Fluence Detection Threshold ($\mathcal{F}_{\rm min}$)[e] (Jy ms $\sqrt{(w/1\ \rm ms)}$)
DSS-63	2019-09-19 02:19:37	12899.948	2.25 8.38	120.14 395.68	1 2	2.2075	0.33 0.13
	2019-09-24 01:41:47	14579.937	2.25 8.38	120.14 395.68	1 2	2.2075	0.33 0.13
	2019-09-28 01:37:03	11279.991	2.25 8.38	120.14 395.68	1 2	2.2075	0.33 0.13
	2019-09-29 01:32:01	11219.933	2.25 8.38	120.14 395.68	1 2	2.2075	0.33 0.13
	2019-10-19 22:24:39	4058.385	2.25 8.38	120.14 395.68	1 2	0.2759	0.33 0.13
	2019-11-20 20:12:03	5639.994	2.25 8.38	110.40 395.68	2	2.2075	0.25 0.13
	2019-11-21 01:29:07	5639.992	2.25 8.38	110.40 395.68	2	2.2075	0.25 0.13
	2019-11-25 23:27:23	11279.991	2.25 8.38	110.40 395.68	2	2.2075	0.24 0.13
	2019-12-02 02:10:35[f]	5939.934	2.25 8.38	110.40 395.68	2	2.2075	0.25 0.14
DSS-14	2019-12-02 05:37:29[f]	5039.997	1.54	250.00	1	0.1024	0.29
	2019-12-02 07:09:03[f]	2474.353	1.54	250.00	1	0.1024	0.29
DSS-63	2019-12-02 22:58:41[f]	5939.934	2.25 8.38	110.40 395.68	2	2.2075	0.24 0.13
	2019-12-03 02:32:47[f]	4242.772	2.25 8.38	110.40 395.68	2	2.2075	0.24 0.13
	2019-12-07 00:20:21	9519.922	2.25 8.38	110.40 395.68	2	2.2075	0.25 0.13
	2019-12-10 22:30:27	5639.992	2.25 8.38	110.40 395.68	2	2.2075	0.24 0.13
	2019-12-12 23:21:31	5339.983	2.25 8.38	110.40 395.68	2	2.2075	0.26 0.14
	2019-12-13 02:47:41	4079.952	2.25 8.38	110.40 395.68	2	2.2075	0.26 0.14
	2019-12-16 20:53:47	5339.983	2.26 8.38	105.30 395.68	2	2.2075	0.25 0.13
DSS-14	2019-12-18 02:22:05[f]	5339.994	1.54	250.00	1	0.1024	0.29
	2019-12-18 04:01:13[f]	5639.994	1.54	250.00	1	0.1024	0.29
	2019-12-18 06:05:43[f]	4619.994	1.54	250.00	1	0.1024	0.29
	2019-12-18 07:30:17[f]	5639.994	1.54	250.00	1	0.1024	0.29
	2019-12-18 09:11:47[f]	5639.994	1.54	250.00	1	0.1024	0.29
	2019-12-18 10:53:33[f]	5099.992	1.54	250.00	1	0.1024	0.29
DSS-63	2019-12-18 20:53:49[f]	5639.992	2.26 8.38	105.30 395.68	2	2.2075	0.26 0.14
	2019-12-18 22:36:31[f]	5639.994	2.26 8.38	105.30 395.68	2	2.2075	0.26 0.14
	2019-12-19 00:18:27[f]	5639.992	2.26 8.38	105.30 395.68	2	2.2075	0.26 0.14
	2019-12-19 02:00:35[f]	6159.892	2.26 8.38	105.30 395.68	2	2.2075	0.26 0.14

Table 7.3: **Multiwavelength Radio Observations of FRB 180916.J0158+65** ***(Continued)***

Telescope[a]	Start Time[b] (UTC)	Exposure Time (s)	Center Frequency (GHz)	Bandwidth[c] (MHz)	Number of Polarizations[d]	Time Resolution (ms)	6σ Fluence Detection Threshold ($\mathcal{F}_{\rm min}$)[e] (Jy ms $\sqrt{(w/1\,{\rm ms})}$)
DSS-63	2019-12-20 20:58:49	5639.994	2.26 8.38	105.30 395.68	2	2.2075	0.25 0.13
	2019-12-20 22:40:45	5639.992	2.26 8.38	105.30 395.68	2	2.2075	0.25 0.13
	2020-01-31 23:01:31	5379.892	2.25 8.38	110.40 395.68	2	2.2075	0.26 0.14
	2020-02-02 00:16:33	11579.930	2.25 8.38	110.40 395.68	2	2.2075	0.27 0.15
	2020-02-03 00:36:33	4679.973	2.25 8.38	110.40 395.68	2	2.2075	0.27 0.15
	2020-02-04 00:26:33	5039.973	2.25 8.38	110.40 395.68	2	2.2075	0.27 0.15
	2020-02-05 20:11:19	7499.864	2.25 8.38	110.40 395.68	2	2.2075	0.25 0.13
	2020-02-06 22:01:27	12779.971	2.25 8.38	110.40 395.68	2	2.2075	0.26 0.14
	2020-02-07 23:01:33	8819.990	2.25 8.38	110.40 395.68	2	2.2075	0.26 0.15
	2020-02-09 21:51:29	9239.977	2.25 8.38	110.40 395.68	2	2.2075	0.26 0.14
	2020-02-10 22:06:29	11399.946	2.25 8.38	110.40 395.68	2	2.2075	0.26 0.14
	2020-03-26 10:58:31	8919.892	2.25 8.38	110.40 395.68	2	2.2075	0.24 0.13
	2020-04-03 11:30:01	3299.942	2.25 8.38	110.40 395.68	2	2.2075	0.25 0.13
	2020-04-03 15:20:01	9359.929	2.25 8.38	110.40 395.68	2	2.2075	0.25 0.13
	2020-04-05 18:26:29	11579.928	2.25 8.38	110.40 395.68	2	2.2075	0.26 0.14
	2020-04-08 09:53:11	14579.953	2.25 8.38	110.40 395.68	2	2.2075	0.24 0.13
	2020-04-15 11:12:29	9778.488	2.25 8.38	110.40 395.68	2	1.0240	0.24 0.13
	2020-05-03 12:18:47	26278.674	2.25 8.38	110.40 395.68	2	1.0240	0.24 0.13
	2020-05-10 17:45:01	5924.631	2.25 8.38	110.40 395.68	2	1.0240	0.27 0.15
	2020-05-13 18:05:01	3719.920	2.25 8.38	110.40 395.68	2	1.0240	0.27 0.15

FRB 180916.J0158+65 was observed for a total of 101.8 hr between 2019 September 19 and 2020 May 14. No radio bursts were detected with DSS-63/DSS-14 in any frequency band during these epochs.

[a] Deep Space Network (DSN) radio antenna used for observations.

[b] Start time of the radio observations in yyyy-mm-dd hh:mm:ss format.

[c] Total usable bandwidth after radio frequency interference (RFI) mitigation.

[d] Number of circular polarizations recorded.

[e] 6σ fluence detection threshold, $\mathcal{F}_{\rm min}$, for an assumed burst width of 1 ms.

[f] These radio observations were also presented in Scholz et al. [482].

persed with trial DMs between 300 and 400 pc cm^{-3} using a linear DM spacing of 2 pc cm^{-3} at L-band, 5 pc cm^{-3} at S-band, and 50 pc cm^{-3} at X-band. This dedispersion scheme was chosen so that the DM smearing was less than the sampling time for each observation.

A list of FRB candidates were generated using a Fourier domain matched filtering algorithm (e.g., see [358, 422, 430]), which was adapted from the `PRESTO` pulsar search software package[m] [456]. Each full time resolution dedispersed time series was convolved with boxcar functions with logarithmically spaced widths between the native time resolution of each observation and ~30.7 ms. We recorded a list of FRB candidates with detection S/Ns above 6.0. If a candidate was detected from the same section of data using multiple boxcar widths, only the highest S/N event was saved in the final list. The detection S/N of each candidate was determined using:

$$\mathrm{S/N} = \frac{\sum_i (f_i - \bar{\mu})}{\bar{\sigma}\sqrt{w}}, \tag{7.2}$$

where f_i is the time series value in bin i of the boxcar function, $\bar{\mu}$ and $\bar{\sigma}$ are the local mean and root-mean-square (RMS) noise after normalization, and w is the boxcar width in number of bins. Before calculating the detection S/N of each candidate, the time series data were detrended and normalized so that $\bar{\mu} \approx 0$ and $\bar{\sigma} \approx 1$. A composite list of FRB candidates was constructed by combining the candidate lists obtained from each DM trial.

We used a GPU-accelerated machine learning pipeline, which incorporates a state-of-the-art deep neural network from the `FETCH`[k] (Fast Extragalactic Transient Candidate Hunter) software package [7], to identify astrophysical bursts from among the large sample of FRB candidates returned by the Fourier domain matched filtering algorithm. Probabilities (p) were assigned to each candidate using the `DenseNet121` Frequency-Time (FT)/`Xception` DM-Time (DMT) "a" model (see Table 4 in [7]), trained using a transfer learning approach. The probability associated with each candidate indicated the likelihood that the candidate was astrophysical. Diagnostic plots of all candidates with $p > 0.3$ were visually inspected for verification.

7.4 Results

7.4.1 FRB 121102

FRB 121102 was observed simultaneously at S-band and X-band with DSS-63 for 27.3 hr between 2019 September 19 (MJD 58745) and 2020 February 11 (MJD 58890) during a recent period of activity from the source. We detected

2 bursts at S-band during these observations. The first burst (B1) was detected on 2019 September 28 (MJD 58754), and the second burst (B2) was detected approximately one day later on 2019 September 29 (MJD 58755). In Figure 7.1, we show the frequency-averaged profiles, dedispersed dynamic spectra, flux-calibrated burst spectra, and DM-time images of each burst. Both bursts were detected in filterbank data recorded with a time resolution of 2.2 ms, and thus they are not temporally resolved. The apparent DM associated with a particular radio burst from a given FRB source can differ depending on the spectral-temporal structure of the burst and whether a signal-to-noise-maximizing or structure-maximizing metric is used to determine the optimal DM. Since we were unable to resolve the spectral-temporal structure of the bursts (B1 and B2) due to the time resolution of the data, we dedispersed both bursts in Figure 7.1 using a DM of 563.0 pc cm^{-3}, which corresponds to the average DM near the time of each burst obtained from long-term monitoring of FRB 121102 with the Arecibo Observatory (A. D. Seymour, private communication).

In Table 7.4, we provide a list of measured properties of each burst, including the barycentric arrival time, peak S/N, burst width, peak flux density, time-integrated burst fluence ($\mathcal{F}$), spectral energy density, and isotropic-equivalent energy. The burst widths were determined by fitting a Gaussian function to the dedispersed burst profile. We quote the full width at half maximum (FWHM) as the temporal width. The burst fluence was determined using the 2σ FWHM for the duration of each burst.

There was no evidence of radio emission at X-band during the times when bursts were detected at S-band. Baseband data was not available at either frequency band during the two epochs when the S-band bursts were detected. We also did not detect any X-band bursts from FRB 121102 at any other times during our observations, despite the fact that the X-band bandwidth was a factor of ~3.5 larger than the bandwidth at S-band and the 6σ fluence detection thresholds were roughly two times lower at X-band than at S-band, on average. In Table 7.1, we list the 6σ fluence detection thresholds ($\mathcal{F}_{\rm min}$) for each observation and each frequency band.

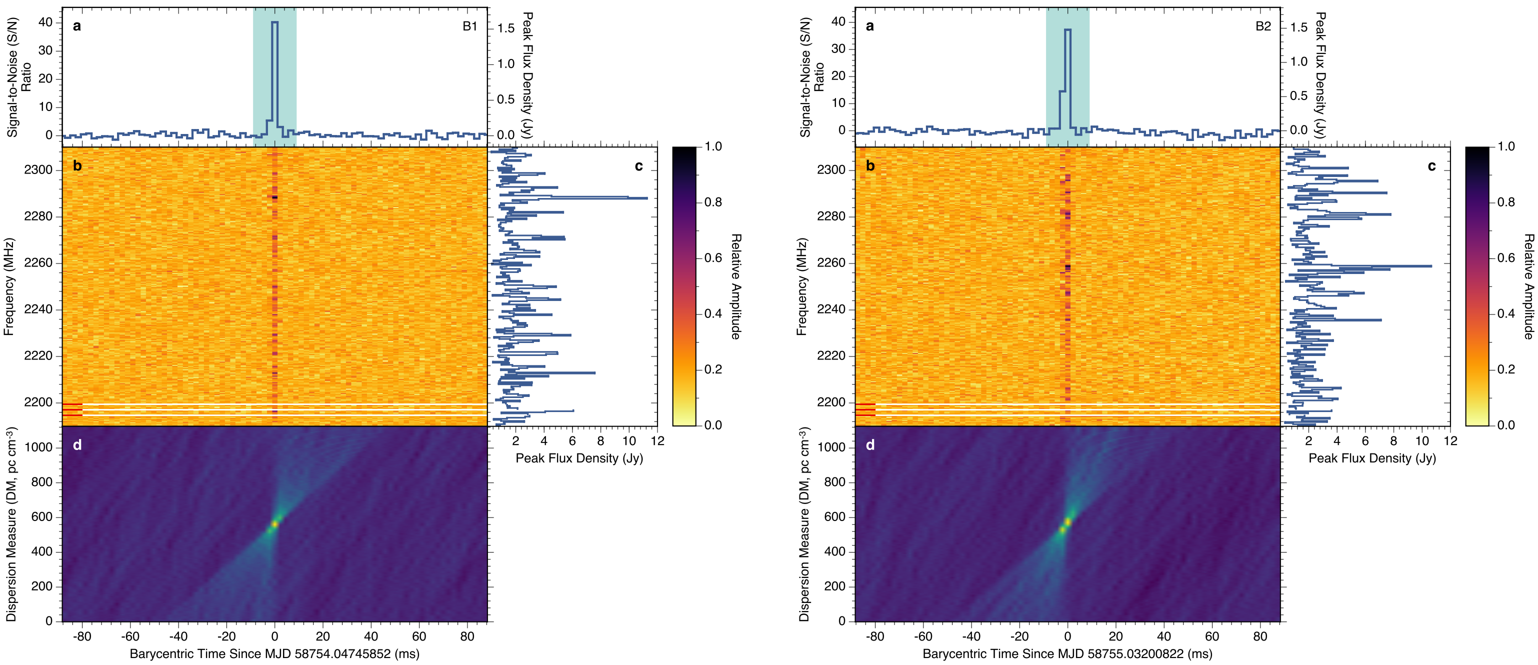

Figure 7.1: ***S*-band radio bursts (B1 and B2) detected from FRB 121102 on (left) 2019 September 28 (MJD 58754) and (right) 2019 September 29 (MJD 58755) using DSS-63.** The frequency-averaged burst profiles are shown in panel (a), and the dedispersed dynamic spectra are displayed in panel (b). The data are shown with a time and frequency resolution of 2.2 ms and 0.464 MHz, respectively. The color bar on the right shows the relative amplitude of the burst's spectral-temporal features. The solid white lines and red markers in panel (b) indicate frequency channels that have been masked due to the presence of radio frequency interference (RFI). The flux-calibrated burst spectra are shown in panel (c). The teal shaded region in panel (a) corresponds to the interval used for extraction of the on-pulse spectrum in panel (c). Both bursts have been dedispersed using a dispersion measure (DM) of 563.0 pc cm^{-3}, which corresponds to the average DM near the time of each burst (A. D. Seymour, private communication). The DM–time images of each burst are displayed in panel (d) and show the signal-to-noise ratio (S/N) of each burst after dedispersion.

Table 7.4: **Radio Bursts Detected from FRB 121102 with DSS-63**

Burst ID	Peak Time[a,i] (MJD)	$(\mathrm{S/N})_{\mathrm{peak}}$[b,i]	DM[c] ($\mathrm{pc\,cm^{-3}}$)	Burst Width[d,i] (ms)	Peak Flux Density[e,i] (Jy)	Fluence ($\mathcal{F}$)[f,i] (Jy ms)	Spectral Energy Density[g,i] (10^{30} erg $\mathrm{Hz^{-1}}$)	Isotropic-Equivalent Energy[h,i] (10^{38} erg)
B1	58754.04745852	40.26	563.0	2.4 ± 0.1	1.6 ± 0.3	3.3 ± 0.5	3.2 ± 0.5	3.8 ± 0.6
B2	58755.03200822	37.27	563.0	2.6 ± 0.2	1.5 ± 0.3	4.6 ± 0.7	3.8 ± 0.5	4.5 ± 0.6

These S-band radio bursts were detected in data recorded with a time resolution of 2.2 ms. We were not sensitive to bursts with narrower widths than the sampling time of our observations (see Table 7.1).

[a] Barycentric time at the peak of the burst, determined after removing the time delay from dispersion using a DM of 563.0 $\mathrm{pc\,cm^{-3}}$ and correcting to infinite frequency. The barycentric times were derived using the position ($\alpha_{\mathrm{J2000}} = 05^{\mathrm{h}}31^{\mathrm{m}}58^{\mathrm{s}}.698$, $\delta_{\mathrm{J2000}} = 33^{\circ}08'52''.586$) in Marcote et al. [367].

[b] Peak signal-to-noise ratio, $(\mathrm{S/N})_{\mathrm{peak}}$.

[c] Average DM near the time of each burst (A. D. Seymour, private communication).

[d] Full width at half maximum (FWHM) temporal duration, determined from a Gaussian fit to the dedispersed burst profile.

[e] Uncertainties are dominated by the 20% fractional error on the system temperature, T_{sys}.

[f] Time-integrated burst fluence ($\mathcal{F}$), determined using the 2σ FWHM for the duration of the burst.

[g] Spectral energy density values were calculated assuming isotropic emission and using the expression $4\pi d_L^2 \mathcal{F}/(1+z)$, where $d_L = 972$ Mpc is the luminosity distance of FRB 121102 [516], $\mathcal{F}$ is the burst fluence, and $z = 0.19273(8)$ is the redshift of the dwarf host galaxy [516].

[h] Isotropic-equivalent energy values were calculated for a bandwidth of 118.75 MHz, which corresponds to the usable portion of the 2.25 GHz frequency band after RFI mitation at the time of the burst.

[i] Values were derived after dedispersing each burst using a DM of 563.0 $\mathrm{pc\,cm^{-3}}$.

7.4.2 FRB 180916.J0158+65

During ~90.8 hr of simultaneous S-band and X-band observations of FRB 180916.J0158+65, carried out between 2019 September 19 (MJD 58745) and 2020 May 14 (MJD 58983) with DSS-63, no radio bursts were detected at either frequency band. We also observed FRB 180916.J0158+65 at L-band with DSS-14 for ~2.1 hr on 2019 December 2 (MJD 58819) and for ~8.9 hr on 2019 December 18 (MJD 58835), but did not detect any radio bursts (see also [482]). The 6σ fluence detection thresholds ($\mathcal{F}_{\rm min}$) associated with each observation and frequency band are listed in Tables 7.2 and 7.3.

In the top panel of Figure 7.2, we show the barycentric mid-time of each of our radio observations of FRB 180916.J0158+65 with DSS-63 and DSS-14 between 2019 September 19 and 2020 May 14, after removing the time delay due to dispersion using a DM of 348.82 pc cm^{-3} and correcting to infinite frequency. This DM corresponds to the average structure-optimizing DM derived from four bursts detected with the CHIME/FRB baseband system [522]. We also show the barycentric times of radio bursts detected from FRB 180916.J0158+65 using the Very Large Array (VLA)/realfast at 1.4 GHz [9], CHIME/FRB instrument between 400–800 MHz [522][x], upgraded Giant Metrewave Radio Telescope (uGMRT) between 550–750 and 300–500 MHz [373, 471], Robert C. Byrd Green Bank Telescope (GBT) between 300–400 MHz [96], and the Sardinia Radio Telescope (SRT) at 328 MHz [440] during this time period. A total of 8 bursts were detected by CHIME/FRB during times when we were simultaneously observing the source with DSS-63/DSS-14 [522][x], which are labeled using green arrows in the top panel of Figure 7.2 (also see Table 7.5). The gray shaded regions correspond to the ±2.7 d activity window around the peak of FRB 180916.J0158+65's activity phase, based on the 16.35 d activity period [522]. The bottom panel of Figure 7.2 shows the total exposure time of the 1.5, 2.3, and 8.4 GHz DSN radio observations as a function of FRB 180916.J0158+65's activity phase.

The barycentric arrival times and properties of the 8 radio bursts detected from FRB 180916.J0158+65 by CHIME/FRB during our DSN observing epochs are listed in Table 7.5. The C1 burst was detected by CHIME/FRB during an overlapping L-band observation of FRB 180916.J0158+65 with DSS-14 (see also [482]), and the other 7 bursts (C2–C8) occurred during epochs when we were simultaneously observing the source at S-band and X-band with DSS-63. We extracted radio data from DSS-14/DSS-63, recorded using the pulsar backend, around each of

Table 7.5: **Radio Bursts Detected from FRB 180916.J0158+65 with CHIME/FRB During Simultaneous Radio Observations with DSS-63/DSS-14**

Burst ID	Peak Time[a] (MJD)	DM (pc cm^{-3})	Burst Width (ms)	Peak Flux Density (Jy)	Fluence ($\mathcal{F}$) (Jy ms)
C1	58835.17721035	349.5 ± 0.5	5.0 ± 0.5	0.4 ± 0.2	2.9 ± 0.7
C2	58882.04838586	349.4 ± 0.3	1.14 ± 0.12	$> 0.5 \pm 0.2$	$> 0.8 \pm 0.3$
C3	58883.02020163	370.4 ± 1.6			
C4	58883.04146680	349.6 ± 0.3	8.6 ± 0.5	$> 0.4 \pm 0.3$	$> 4.3 \pm 1.6$
C5	58883.04307123	349.81 ± 0.05	1.157 ± 0.011	6.1 ± 2.0	16.3 ± 5.0
C6	58883.04556977	349.8 ± 0.5	1.48 ± 0.13	0.5 ± 0.2	1.5 ± 0.6
C7	58883.05523556	348.7 ± 0.6	0.76 ± 0.07	$> 0.5 \pm 0.3$	$> 0.4 \pm 0.1$
C8	58982.76846813	352.6 ± 3.2			

The burst properties are reproduced from The CHIME/FRB Collaboration et al. [522][x]. The burst widths, peak flux densities, and fluences of C3 and C8 have not yet been reported.
[a] Barycentric time at the peak of the burst after removing the time delay from dispersion using the listed DM and correcting to infinite frequency. The barycentric times were determined using the position ($\alpha_{\rm J2000} = 01^{\rm h}58^{\rm m}00^{\rm s}.75017$, $\delta_{\rm J2000} = 65^\circ43'00''.3152$) in Marcote et al. [368].

these times and visually inspected the frequency-averaged profiles and dedispersed dynamic spectra. We found no evidence of radio emission in the pulsar backend data during any of these times.

The C5 burst reported by The CHIME/FRB Collaboration et al. [522] on MJD 58883.04307123 is one of the highest fluence bursts ($\mathcal{F} = 16.3 \pm 5.0$ Jy ms) detected from FRB 180916.J0158+65 in the 400–800 MHz band thus far. In Figure 7.3, we show the frequency-averaged profiles, dedispersed dynamic spectra, and flux-calibrated spectra, spanning ±1 s around the time of the burst, during our simultaneous S-band and X-band observations of FRB 180916.J0158+65 with DSS-63 using the pulsar backend recorder, along with the C5 burst detected by CHIME/FRB. We also extracted baseband data at S-band and X-band around the time of this burst to rule out the presence of faint, narrow-width radio bursts that may have been missed in the pulsar backend data. After inspecting the high time resolution data, no evidence of radio emission was found at either frequency band. A detailed analysis of the baseband data obtained during the epochs listed in Tables 7.2 and 7.3 will be presented in an upcoming publication.

7.5 Discussion

7.5.1 Spectral Properties of Radio Bursts

Multifrequency, broadband radio observations of repeating FRBs have demonstrated that their burst spectra are highly variable and often peak in a narrow frequency band. Some bursts display emission that is limited to a frequency range of tens to hundreds of MHz (e.g., see [213, 229, 298, 358, 521, 522]), while others appear to have a frequency extent that spans at least ∼2 GHz (e.g., see [302]). Many bursts from repeating FRBs also show evidence of downward-drifting subpulses [229, 259, 520, 521]. On average, larger sub-burst bandwidths and drift rates have been observed from repeating FRBs at higher radio frequencies [96, 213, 229, 259]. In many cases, the spectra of FRBs from repeating sources, such as FRB 121102, are not well-modeled by a power-law with a single spectral index (e.g., see [302, 479, 499]). The assortment of spectral behavior may be intrinsic to the source's underlying emission mechanism(s), produced by propagation effects, or generated by a combination of radiation and propagation processes.

While radio bursts from FRB 121102 have been detected up to a frequency of ∼8 GHz [191], no FRB source has yet been observed to produce emission at higher radio frequencies. At 1.4 GHz, bursts from FRB 121102 have characteristic bandwidths of ∼250 MHz, with a 1σ variation of ∼90 MHz [229]. The characteristic bandwidths measured from bursts detected from FRB 121102 between 4.5–8 GHz with the GBT range from ∼1–100 MHz [191]. However, these bursts also display large-scale frequency structure, with a frequency extent of ∼1 GHz, in the 4.5–8 GHz frequency band.

The Galactic pulse broadening timescale predicted along the line of sight to FRB 121102 by the NE2001 Galactic electron density model [124] is:

$$\tau_{d,121102} \;=\; 22\Big(\frac{\nu}{1\,\mathrm{GHz}}\Big)^{-\alpha}\,\mu\mathrm{s}, \tag{7.3}$$

where ν is the observing frequency in GHz and α is the pulse broadening spectral index. The expected diffractive interstellar scintillation (DISS) bandwidth ($\Delta\nu_{\mathrm{DISS}}$) is given by [125]:

$$\Delta\nu_{\mathrm{DISS}} = \frac{C_1}{2\pi\tau_d} = 0.0084\Big(\frac{\nu}{1\,\mathrm{GHz}}\Big)^{\alpha}\,\mathrm{MHz}, \tag{7.4}$$

where $C_1 = 1.16$ for a uniform, Kolomogorov medium, and we have substituted $\tau_{d,121102}$ in Equation (7.3) for τ_d in Equation (7.4). In general, the precise value of C_1 depends on both the geometry and wavenumber spectrum of the electron density. Assuming a pulse broadening spectral index between 4 and 4.4, the DISS bandwidth, $\Delta\nu_{\mathrm{DISS}}$, can range from ∼0.01–133 MHz for observing frequencies between 1 and 9 GHz. These estimates are consistent with previous measurements of the scintillation bandwidth of FRB 121102 in this frequency range (e.g., see [229, 358]). Many bursts from FRB 121102 also display spectral features with a frequency extent that cannot be attributed solely to Galactic DISS.

Radio observations of repeating FRBs over a wide frequency range have revealed bright bursts at lower frequencies that do not have detectable radio emission at higher frequencies. For example, Majid et al. [358] carried out simultaneous radio observations of FRB 121102 at 2.25 GHz (S-band) and 8.36 GHz (X-band) with the 70 m DSN radio telescope, DSS-43, and discovered 6 bursts in the 2.25 GHz frequency band. No radio emission was detected in the 8.36 GHz frequency band at the same time, despite having greater sensitivity and a larger bandwidth at X-band. Both of the S-band bursts (B1 and B2), shown in Figure 7.1, from FRB 121102 also display prominent emission at 2.3 GHz without accompanying radio emission at 8.4 GHz at the same time. The spectral behavior observed in these frequency bands, which are separated by two octaves in frequency, cannot be attributed to Galactic scintillation. Our observations of FRB 121102 further demonstrate that the source's apparent burst activity strongly depends on the radio frequency band that is being utilized.

FRB 180916.J0158+65 is one of the most prolifically bursting repeating FRB sources known and displays a significant 16.35 d periodicity in the arrival times of its bursts [522]. Multiple radio bursts have been detected from FRB 180916.J0158+65 thus far between ~300 MHz and ~1.7 GHz using various radio telescopes (e.g., see [8, 96, 368, 373, 440, 471, 482, 521, 522]). It is surprising that no bursts were detected from FRB 180916.J0158+65 during our 101.8 hr monitoring campaign at 1.5, 2.3, and 8.4 GHz with DSS-14 and DSS-63, considering the high level of activity observed from the source at lower frequencies (e.g., see [522]). Our observations of FRB 180916.J0158+65 further demonstrate that the emission process is strongly frequency-dependent (e.g., see [96, 522]), and its bursts are band-limited, with less spectral occupancy at high frequencies ($\gtrsim$ 2 GHz). These observations also suggest that the source emits fewer or fainter bursts in the 2.3 and 8.4 GHz frequency bands compared to the emission behavior observed at lower radio frequencies. A detailed discussion of the source's burst rates is provided in Section 7.5.3.

Toward the direction of FRB 180916.J0158+65, the Galactic pulse broadening timescale predicted by the NE2001 Galactic electron density model [124] is:

$$\tau_{d,180916} = 21\ \mu s\left(\frac{\nu}{1\,\mathrm{GHz}}\right)^{-\alpha}, \tag{7.5}$$

which is comparable to the estimate obtained from FRB 121102 in Equation (7.3). Substituting $\tau_{d,180916}$ for τ_d in Equation (7.4) and assuming a pulse broadening spectral index between 4 and 4.4, we find that the DISS bandwidth can range from

~0.01–137 MHz for observing frequencies between 1 and 9 GHz, which is consistent with the 0.06 MHz scintillation bandwidth measured from the brightest burst detected at 1.7 GHz with the EVN [368]. Therefore, during the times that bursts were detected from FRB 180916.J0158+65 by CHIME/FRB, the absence of radio emission during our simultaneous observations of the source in the 2.3 and 8.4 GHz frequency bands cannot be explained by Galactic scintillation. Instead, this behavior is likely an intrinsic property of the emission. FRB 180916.J0158+65's low rotation measure (RM) and lack of a luminous, persistent radio source both suggest that its circumburst environment may be less extreme than that of FRB 121102, the only other repeating FRB source localized using VLBI [367, 368]. However, both FRB 121102 and FRB 180916.J0158+65 show similar spectral behavior, which supports the notion that the behavior is intrinsic and not produced by propagation effects. While we find it unlikely that extrinsic effects in FRB 180916.J0158+65's local environment can fully account for the spectral behavior observed at high radio frequencies, they may contribute to some of the characteristic features observed across its radio spectrum. These observations also demonstrate that FRB 180916.J0158+65's apparent burst activity, like FRB 121102, strongly depends on the choice of radio observing frequency.

7.5.2 Correlation between Radio Frequency and Activity Phase of Radio Bursts

After folding the radio burst arrival times from FRB 180916.J0158+65 modulo the 16.35 d activity period, multiple bursts detected at 1.4 and 1.7 GHz were found to occur near the leading edge of the activity cycle [8, 522]. This has led to the suggestion that there may be a correlation between the emission frequency and the source's activity phase (e.g., see [9]), where bursts emitted at higher radio frequencies occur earlier in the activity cycle. However, previous high radio frequency observations of FRB 180916.J0158+65 have not monitored the source across a wide range of activity phases, which is necessary for determining if such a correlation exists.

The cadence of our high frequency radio observations with DSS-63 and DSS-14 across FRB 180916.J0158+65's activity phase is shown in the bottom panel of Figure 7.2. These observations cover a wide range of activity phases, both within the ±2.7 d activity window reported by The CHIME/FRB Collaboration et al. [522] and at phases outside of this range. The DSN observations also cover several activity cycles during which radio bursts were detected at lower frequencies by CHIME/FRB, indicating that the source was active during these epochs. Although our radio observations cover most of the activity phases at which bursts were detected by other instruments during our monitoring campaign, our observing exposures are not uniform across all activity phases, and there are some gaps in the phase coverage. Since no bursts were detected from FRB 180916.J0158+65 in the 1.5, 2.3, or 8.4 GHz frequency bands during our observations with DSS-63 and DSS-14, we were unable to find evidence to support the notion that bursts emitted from the source at higher radio frequencies occur earlier in the activity cycle. However, we cannot presently exclude the possibility that a frequency-phase correlation may exist. Additional high frequency radio observations of FRB 180916.J0158+65, and the detection of bursts above ∼2 GHz, will be able to further address whether or not there is a link between the emission frequency of the bursts and the activity phase at which they are detected.

7.5.3 Temporal Distribution of Radio Bursts

The discovery of a 16.35 d activity period from FRB 180916.J0158+65, together with an activity window during which most of its radio bursts are detected, has enabled dedicated multiwavelength follow-up campaigns to quantify the activity of the source at various wavelengths (e.g., see [8, 96, 368, 373, 440, 471, 482, 522]). We demonstrate here that the apparent burst rate from FRB 180916.J0158+65 is a strong function of radio observing frequency and discuss the temporal distribution of bursts at high radio frequencies.

Assuming Poisson statistics, the probability of randomly detecting exactly n bursts during a time interval, t, is given by:

$$p(n, \lambda) = \frac{\lambda^n e^{-\lambda}}{n!}, \tag{7.6}$$

where λ is the number of bursts that are expected to be detected during this time interval. For a fixed rate parameter, λ, the probability of detecting at least N bursts during a time interval, t, can be computed using:

$$P(n \geq N) = e^{-\lambda} \sum_{k=N}^{\infty} \frac{\lambda^k}{k!} = 1 - e^{-\lambda} \sum_{k=0}^{N-1} \frac{\lambda^k}{k!}. \tag{7.7}$$

From Equation (7.6), if the probability of detecting exactly 0 bursts, $p_0 = p(n = 0, \lambda)$, is known, then the rate parameter, λ, can be calculated analytically using:

$$\lambda = -\ln(p_0). \tag{7.8}$$

We observed FRB 180916.J0158+65 simultaneously at S-band and X-band with DSS-63 for a total of $t = 36.2$ hr during the ±2.7 d interval around the peak of the activity window. In these frequency bands, we assume that the source's emission behavior during the activity window follows Poisson statistics and that there was a non-detection probability of 95%. Using Equation (7.8), we find that the expected number of bursts during this time interval is ~0.051 bursts, which corresponds to a rate of $r \approx 0.0014$ bursts per hour. If the above assumptions hold, then this implies that ~700 hr of radio observations would be needed to detect a single burst in these frequency bands. However, it is possible that the emission process produces bursts with waiting times that may not follow a Poisson distribution [139].

The average 6σ fluence detection thresholds during our L-band, S-band, and X-band observations of FRB 180916.J0158+65 with DSS-14 and DSS-63 were 0.29, 0.26, and 0.14 Jy ms, respectively. We note that 3 of the 4 radio bursts detected at 1.7 GHz from FRB 180916.J0158+65 using the European VLBI Network (EVN) had measured burst widths of ~1.7 ms and fluences exceeding ~0.6 Jy ms [368], which are some of the faintest bursts detected to date. If a similarly bright burst, with a comparable temporal width and fluence, was emitted from the source at 1.5, 2.3, or 8.4 GHz during our radio observations, it would have been detected with S/N > 10.

In the 400–800 MHz frequency band, radio bursts detected from FRB 180916.J0158+65 appear to be clustered in time, and the burst activity is not constant at all activity phases [521, 522]. Assuming that the radio bursts obey Poisson statistics and can be treated as independent events, The CHIME/FRB Collaboration et al. [522] estimated a detection rate of $r = 0.9^{+0.5}_{-0.4}$ bursts per hour above a fluence threshold of 5.2 Jy ms in a ±2.7 d interval around the peak of the activity window, which corresponds to activity phases between ~0.33–0.67. They also estimated detection rates above this fluence threshold in 3 subintervals of the ±2.7 d activity window: (subinterval 1) ±0.9 d around the activity peak, i.e. activity phases ~0.44–0.56; (subinterval 2) between 0.9 and 1.8 d from the activity peak, i.e. activity phases ~0.39–0.44 and ~0.56–0.61; (subinterval 3) between 1.8 and 2.7 d from the activity peak, i.e., activity phases ~0.33–0.39 and ~0.61–0.67. The estimated detection rates in subintervals 1–3 were $r_1 = 1.8^{+1.3}_{-0.8}$, $r_2 = 0.8^{+1.0}_{-0.5}$, and $r_3 = 0.1^{+0.6}_{-0.1}$ bursts per hour above a fluence of 5.2 Jy ms, respectively [522]. The uncertainties associated with these detection rates correspond to 95% confidence limits.

We can also use the formalism described in Houben et al. [240] to calculate the expected burst rates at 1.5, 2.3, and 8.4 GHz with DSS-14 and DSS-63 during the activity intervals defined above. We assume that the differential rate distributions at two frequencies are related by a power-law parameterized by a statistical spectral index, $\alpha_{\rm s}$. The statistical spectral index characterizes the spectrum of the overall burst rate, which is distinct from the instantaneous spectral index of individual bursts. Here, we use $\alpha_{\rm s} = -1.6^{+1.0}_{-0.6}$ for the statistical spectral index of FRB 180916.J0158+65 [96]. We assume that the differential rate distributions at two frequencies are related by a power-law parameterized by a statistical spectral index, $\alpha_{\rm s} = -1.6^{+1.0}_{-0.6}$ [96]. The detection rates, r_{ν_1} and r_{ν_2}, at two frequencies, ν_1 and ν_2, can be determined using:

$$\frac{r_{\nu_1}}{r_{\nu_2}} = \left(\frac{\nu_1}{\nu_2}\right)^{-\alpha_{\rm s}\gamma} \left(\frac{\mathcal{F}_{\nu_1,\rm min}}{\mathcal{F}_{\nu_2,\rm min}}\right)^{\gamma+1}, \tag{7.9}$$

where $\gamma = -2.3 \pm 0.4$ is a power-law index that describes FRB 180916.J0158+65's differential energy distribution [522], and $\mathcal{F}_{\nu_1,\rm min}$ and $\mathcal{F}_{\nu_2,\rm min}$ are the fluence detection thresholds at frequencies ν_1 and ν_2, respectively.

In Table 7.6, we list the predicted burst rates above the average 6σ fluence detection thresholds during our observations in each of these time intervals using Equation (7.9). The total exposure times at S-band and X-band with DSS-63 during subintervals 1–3 were $t_1 = 11.9$ hr, $t_2 = 15.7$ hr, and $t_3 = 8.5$ hr, respectively. The L-band observations with DSS-14 spanned a total of 11.0 hr, which occurred entirely during subinterval 1. Therefore, the expected number of detectable bursts in each of these frequency bands and time intervals is given by $N = r \times t$, where r is the burst rate and t is the total exposure time in each time interval. These values are also provided in Table 7.6. The uncertainties on the burst rates and number of expected bursts are dominated by the large errors on the statistical spectral index, $\alpha_{\rm s}$, which is poorly constrained for FRB 180916.J0158+65.

These estimates are all consistent with our observations, which suggest that fewer or fainter bursts are detectable from FRB 180916.J0158+65 at higher radio frequencies ($\gtrsim 2$ GHz). Intrinsic and extrinsic effects may also affect the observed burst rates. For example, FRB 180916.J0158+65 exhibits periods of apparent inactivity during some activity cycles and, like many other repeating FRB sources, emits narrow-band radio bursts (e.g., see [522]). This behavior is often highly variable between observing frequencies.

We also consider the following less likely explanations for the lack of radio bursts observed from FRB 180916.J0158+65 during our radio monitoring campaign: (1) On average, FRB 180916.J0158+65 emits bursts that have narrower widths at higher frequencies (e.g., see [96, 368, 522]). While it is conceivable that bursts with narrow pulse widths ($\sim$10 μs) and high peak luminosities may not have been detected in the data recorded at S-band and X-band with the pulsar backend, if their fluences did not exceed the fluence detection thresholds listed in Tables 7.2 and 7.3, no evidence of such emission was found during a preliminary inspection of simultaneously recorded high time resolution baseband data during times when bursts were detected between 400–800 MHz with CHIME/FRB. Additionally, our search for bursts using data from the pulsar backend was sufficiently sensitive to detect bursts with similar characteristics to most of those detected at 1.7 GHz with the EVN [368]. (2) If FRB 180916.J0158+65 has a smaller duty cycle at high frequencies ($\gtrsim$ 2 GHz), with a burst rate that is comparable to the rate reported at lower frequencies (e.g., see [522]), then it is possible that many bursts would not be detected unless the observations were performed during activity phases when the source was producing high frequency radio emission. However, we detected no radio bursts during our observations, which spanned $\sim$40% of the FRB 180916.J0158+65's 16.35 d activity cycle and $\sim$50% of the $\pm$2.7 d interval around the peak of the source's activity phase (see Figure 7.2), including 8 times when bursts were simultaneously detected from the source in the 400–800 MHz frequency band (see Table 7.5 and Figure 7.3).

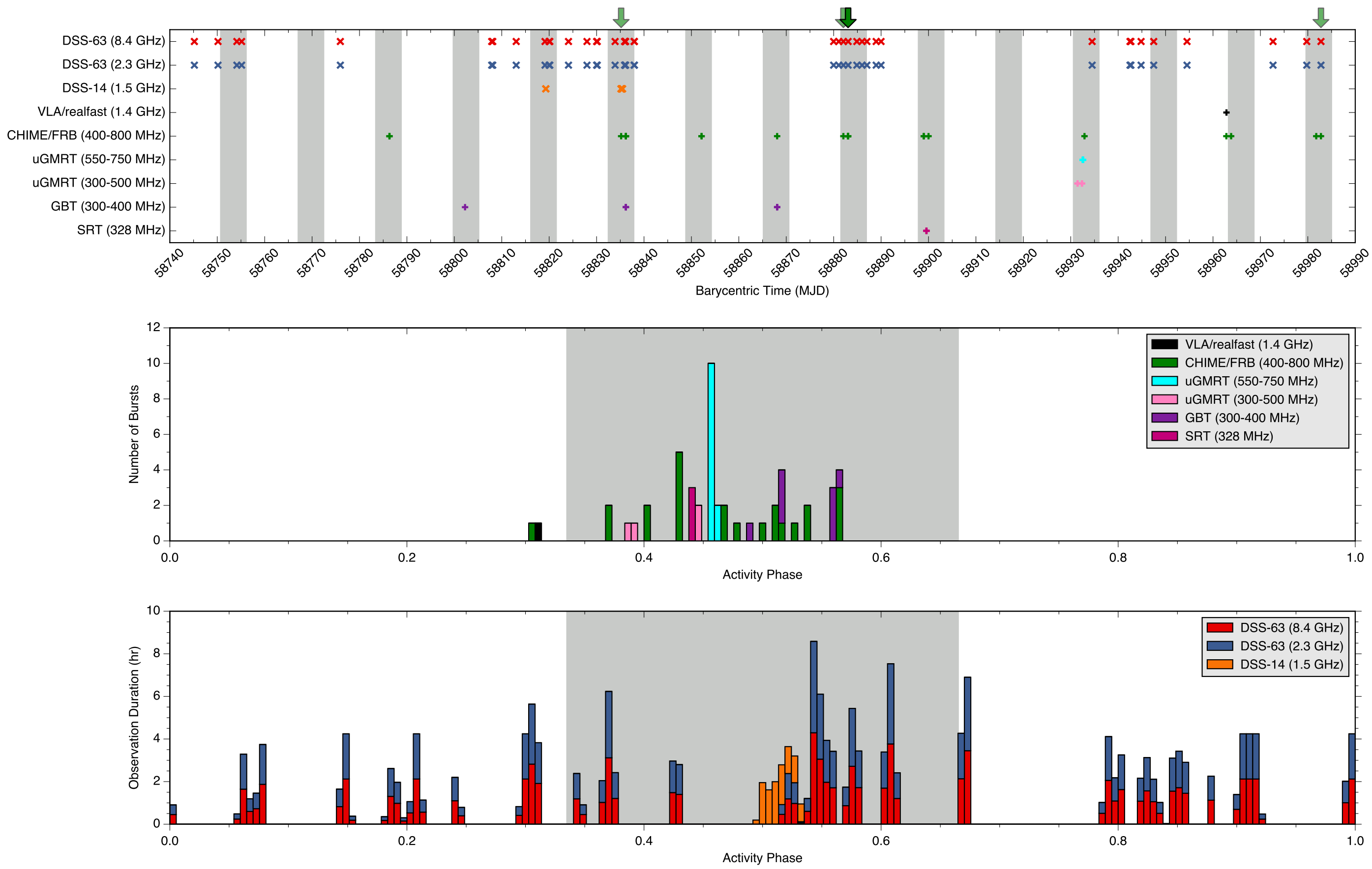

Figure 7.2: **Radio observations and bursts detected from FRB 180916.J0158+65.** Top panel: Radio observations of FRB 180916.J0158+65 between 2019 September 19 (MJD 58745) and 2020 May 14 (MJD 58983). The barycentric time at the middle of the simultaneous 8.4 and 2.3 GHz observations with DSS-63 are labeled using red and blue crosses ($\times$), respectively. The barycentric mid-time of the 1.5 GHz observations with DSS-14 are indicated by orange crosses. The barycentric times of the observations with DSS-63 and DSS-14 were determined by removing the time delay from dispersion using a dispersion measure (DM) of 348.82 pc cm^{-3} and correcting to infinite frequency using the position ($\alpha_{\rm J2000} = 01^{\rm h}58^{\rm m}00^{\rm s}.75017$, $\delta_{\rm J2000} = 65°43'00''.3152$) in Marcote et al. [368]. The duration of each of the DSN observations (see Tables 7.2 and 7.3) is shown using horizontal error bars, which are smaller than the symbol size. The barycentric times of bursts detected from FRB 180916.J0158+65 with the Very Large Array (VLA)/realfast at 1.4 GHz [9], CHIME/FRB radio telescope between 400–800 MHz [522][x], upgraded Giant Metrewave Radio Telescope (uGMRT) between 550–750 and 300–500 MHz [373, 471], Robert C. Byrd Green Bank Telescope (GBT) between 300–400 MHz [96], and the Sardinia Radio Telescope (SRT) at 328 MHz [440] are labeled using black, green, cyan, pink, purple, and magneta pluses (+), respectively. In total, 8 of the radio bursts detected by CHIME/FRB occurred during times when DSS-63/DSS-14 was also observing FRB 180916.J0158+65, and these bursts are labeled using green arrows and listed in Table 7.5. The gray shaded regions correspond to a ±2.7 d window around the peak of FRB 180916.J0158+65's activity phase, assuming an activity period of 16.35 d [522].

Figure 7.2 *(continued)*: Middle panel: Histogram of activity phases at which each of the radio bursts in the top panel were detected. The activity phase of the bursts are shown using colored bars, where each instrument is labeled using the color used in the top panel. Bottom: Exposure times of radio observations of FRB 180916.J0158+65 using DSS-63 and DSS-14 between 2019 September 19 and 2020 May 14 as a function of FRB 180916.J0158+65's activity phase. The exposure times of the 8.4 GHz observations with DSS-63, 2.3 GHz observations with DSS-63, and 1.5 GHz observations with DSS-14 are indicated using red, blue, and orange bars, respectively. In both the middle and bottom panels, the width of each bar is ~0.0054 phase units, which is equal to the average duration (~2.1 hr) of the DSN radio observations. The gray shaded regions, in the middle and bottom panels, correspond to a ±2.7 d window around the peak of FRB 180916.J0158+65's activity phase.

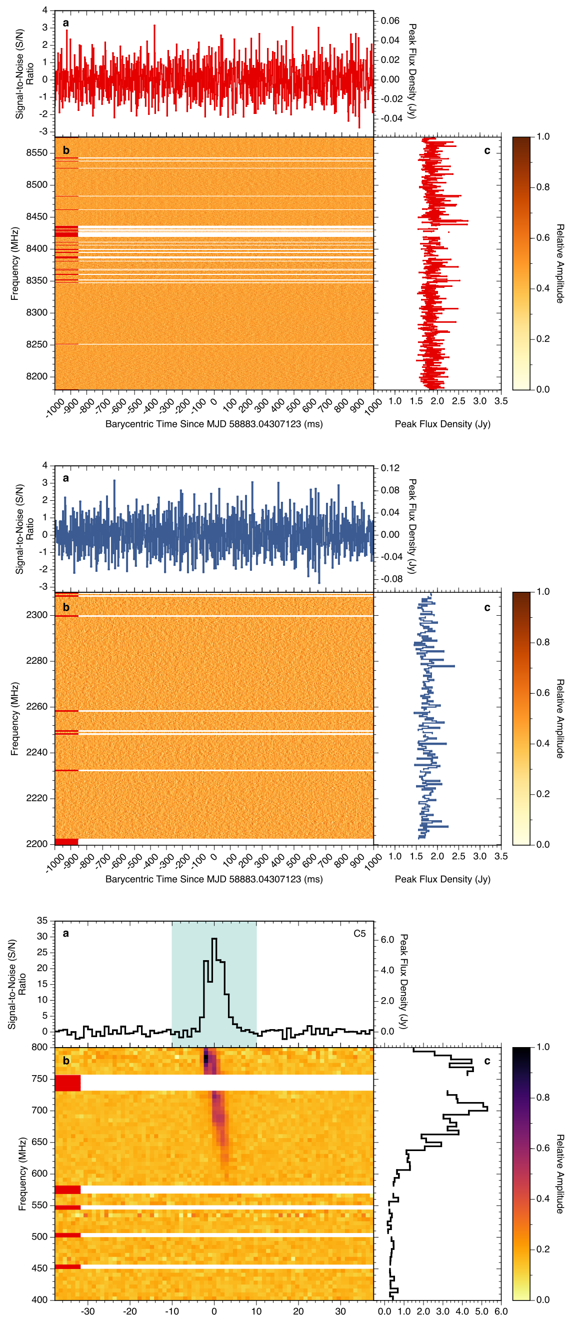

Figure 7.3: **Simultaneous X-band (top) and S-band (middle) observations of FRB 180916.J0158+65 with DSS-63 during the time of a bright burst (C5, see Table 7.5) detected by CHIME/FRB on MJD 58883.04307123, shown in the bottom panels.** The data in each frequency band have been dedispersed using a dispersion measure (DM) of 348.82 pc cm^{-3}, which corresponds to the average structure-optimizing DM derived from four bursts detected with the CHIME/FRB baseband system [522]. The frequency-averaged Stokes I profiles are shown in panel (a), and the dedispersed Stokes I dynamic spectra are displayed in panel (b). The X-band and S-band data are shown with a time and frequency resolution of 2.2 ms and 0.464 MHz, respectively.

Figure 7.3 *(continued)*: The CHIME/FRB data are shown with a time resolution of 0.98304 ms, and we have downsampled the full-resolution data (16,384 channels) into 64 sub-bands, which each have a bandwidth of 6.25 MHz, for better visualization. The color bar on the right shows the relative amplitude of the spectral-temporal features in the dedispersed dynamic spectra. Frequency channels that have been masked due to the presence of radio frequency interference (RFI) are indicated using solid white lines and red markers in panel (b). The flux-calibrated spectra are shown in panel (c). For the burst detected by CHIME/FRB, the teal shaded region in panel (a) corresponds to the interval used to extract the on-pulse spectrum in panel (c).

Table 7.6: **Estimated Number of Radio Bursts Detectable from FRB 180916.J0158+65**

Time Interval	Burst Rate (r) at 1.5 GHz[a] (Bursts Per Hour)	Number of Bursts (N) Detectable at 1.5 GHz[b] (Bursts)	Burst Rate (r) at 2.3 GHz[a] (Bursts Per Hour)	Number of Bursts (N) Detectable at 2.3 GHz[b] (Bursts)	Burst Rate (r) at 8.4 GHz[a] (Bursts Per Hour)	Number of Bursts (N) Detectable at 8.4 GHz[b] (Bursts)
±2.7 d Activity Window[c]	$1.2^{+2.8}_{-1.8}$		$0.3^{+1.0}_{-0.6}$	$12.1^{+37.6}_{-23.1}$	$0.006^{+0.038}_{-0.023}$	$0.2^{+1.4}_{-0.8}$
Subinterval 1[d]	$2.4^{+5.7}_{-3.6}$	$26.5^{+62.2}_{-39.2}$	$0.7^{+2.1}_{-1.3}$	$8.0^{+25.1}_{-15.2}$	$0.01^{+0.08}_{-0.05}$	$0.1^{+0.9}_{-0.5}$
Subinterval 2[e]	$1.1^{+2.7}_{-1.7}$		$0.3^{+1.0}_{-0.6}$	$4.7^{+15.4}_{-9.2}$	$0.006^{+0.034}_{-0.020}$	$0.09^{+0.54}_{-0.32}$
Subinterval 3[f]	$0.1^{+0.9}_{-0.2}$		$0.04^{+0.25}_{-0.08}$	$0.3^{+2.1}_{-0.7}$	$0.0007^{+0.0059}_{-0.0026}$	$0.006^{+0.050}_{-0.022}$

Since the L-band (1.5 GHz) observations of FRB 180916.J0158+65 with DSS-14 occurred entirely during subinterval 1, the number of detectable bursts at this frequency is only estimated in this time interval.

[a] Burst rates at each frequency were calculated by substituting the fluence detection thresholds reported by CHIME/FRB in each time interval [522] and the average 6σ fluence detection thresholds during our L-band, S-band, and X-band observations with DSS-14 and DSS-63 into Equation (7.9), using power-law indices of $\alpha_{\mathrm{s}} = -1.6^{+1.0}_{-0.6}$ [96] and $\gamma = -2.3 \pm 0.4$ [522]. The average 6σ fluence detection thresholds of DSS-14 and DSS-63 at L-band, S-band, and X-band were 0.29, 0.26, and 0.14 Jy ms, respectively.

[b] Expected number of detectable bursts at each frequency band above the average 6σ fluence detection thresholds of DSS-14 and DSS-63. The number of detectable bursts was determined using the formula $N = r \times t$, where r is the calculated rate of detectable bursts and t is the total exposure time in each time interval.

[c] The ±2.7 d interval around the peak of FRB 180916.J0158+65's activity window, defined in The CHIME/FRB Collaboration et al. [522], which corresponds to activity phases between ~0.33–0.67.

[d] Subinterval 1 is defined as ±0.9 d around the activity peak, which corresponds to activity phases between ~0.44–0.56 [522].

[e] Subinterval 2 is defined as times between 0.9 and 1.8 d from the activity peak, which corresponds to activity phases ~0.39–0.44 and ~0.56–0.61 [522].

[f] Subinterval 3 is defined as times between 1.8 and 2.7 d from the activity peak, which corresponds to activity phases ~0.33–0.39 and ~0.61–0.67 [522].

7.5.4 Progenitor Models

Several progenitor models have been proposed that may explain the emission characteristics of repeating FRBs and the periodicity observed thus far from a subset of these sources. For example, the apparent 16.35 d period observed from FRB 180916.J0158+65 could be attributed to eccentric orbital motion of a binary system comprised of a neutron star and a massive O/B-type companion [522], where the emitter could be either a radio pulsar or a magnetar. Other models suggest that the apparent periodicity may arise from free-free absorption in the wind of the massive companion, which could lead to modulated emission that is dependent on the orbital phase [344]. The optical depth in the companion's homogeneous, isothermal wind is expected to decrease with increasing frequency. Under these assumptions, the activity window is predicted to be longer at higher radio frequencies. While some radio bursts detected from FRB 180916.J0158+65 at higher frequencies have been seen to occur earlier in the activity window [8, 522], compared to those detected at lower frequencies, the source's activity had not been well-characterized above ∼2 GHz across a wide range of activity phases, until now. The cadence of our observations of FRB 180916.J0158+65 and the absence of radio emission at 2.3 and 8.4 GHz during times when the source was known to be active together suggest that the duration of the activity window is either not strongly frequency-dependent or narrower at high radio frequencies and possibly systematically shifted in phase.

The binary comb model, proposed by Ioka and Zhang [247], also associates the 16.35 d period observed from FRB 180916.J0158+65 with the orbital period of an interacting neutron star binary system. In this scenario, the FRB emission is produced by a highly magnetized pulsar, whose emission is funneled by the strong wind of a millisecond pulsar or massive stellar companion. The observed activity window then coincides with times when the funnel is directed toward Earth.

Alternatively, FRB 180916.J0158+65's periodicity has been interpreted as arising from the precession of a flaring magnetar or magnetized neutron star [315, 531, 575, 582]. Levin et al. [315] showed that a hyperactive magnetar, driven by a high rate of ambipolar diffusion in the core, can have a precession period ranging from weeks to months, and the viscous damping timescale is orders of magnitude longer than the magnetar's age. Other models suggest that the 16.35 d period observed from FRB 180916.J0158+65 may originate from a 1–10 kyr old magnetar with an ultra-long rotation period and a high internal magnetic field ($B_{\rm int} \gtrsim 10^{16}$ G) at birth [43] or the precession of a jet produced by the accretion disk of a massive black hole [269].

Recently, tentative evidence of a ∼157 d period, with a duty cycle of 56%, was discovered during a search for periodicity in the arrival times of radio bursts from FRB 121102 [453]. This long-term periodicity was also observed by Aggarwal et al. [9] and Cruces et al. [139], and they both found a period that was consistent with the measurement reported in Rajwade et al. [453]. Both of the S-band bursts shown in Figure 7.1 occurred at an activity phase of ∼0.53, determined by folding the burst arrival times modulo the ∼157 d period and using the reference time, $t_{\rm ref}$ = MJD 58200, defined in Rajwade et al. [453]. These bursts were both detected near the peak of the activity window, defined at activity phase 0.5. Although it is not yet clear whether the ∼157 d period is astrophysical in origin, the radio bursts presented here from FRB 121102 are consistent with the observed periodicity. If the ∼157 d period is determined to be astrophysical, it suggests that other repeating FRB sources may display underlying periodic behavior, which would provide important clues about the nature of their progenitors.

Although FRBs and Galactic radio magnetars share some similar emission characteristics, such as prominent frequency-structure in their radio pulses (e.g., see [191, 229, 346, 422, 430]) and extended periods of radio inactivity (e.g., see [85, 314, 481]), there are also notable differences. High frequency radio emission is a hallmark feature of radio magnetars. Bright radio pulses have been detected from several radio magnetars in the Milky Way at record high frequencies, well above 100 GHz in some cases (e.g., see [81, 533, 534]), but no FRB source has yet been detected at radio frequencies above 8 GHz. However, to date, very few searches for FRBs have been carried out at such high radio frequencies [191, 358].

Radio bursts from FRB sources are also considerably more energetic, on average, than radio pulses from Galactic magnetars [229, 422, 430]. The recent detection of a bright radio pulse from SGR 1935+2154 has demonstrated that magnetars can produce radio bursts with a wide range of luminosities, spanning from luminosities comparable to radio pulsars up to about a factor of ∼10 lower than the luminosities of bursts observed from FRB 180916.J0158+65 [59, 277, 523, 584]. However, the apparent burst repetition rate of FRB-like bursts from Galactic magnetars is inconsistent with the repetition rates observed from extragalactic repeating FRBs [332, 370]. For example, for at least the past 7 years, FRB 121102 has been producing radio bursts that are $\sim 10^{10}$ times more energetic than the radio pulses observed from Galactic radio magnetars [497, 499]. No magnetar in the Milky Way has been found to exhibit a similar level of activity. If repeating FRBs are produced by active magnetars, this suggests that they must differ in some way from the Galactic magnetar population.

The short temporal durations of FRB pulses indicate that they originate from compact emitting regions (e.g., see [98, 391]). However, the peculiar spectral properties between sources and the downward-drifting subpulse behavior frequently observed from repeating FRBs are not yet well-explained. Wideband, multifrequency observations of FRBs are therefore crucial for understanding their spectral properties and the underlying emission mechanism(s) powering these sources.

7.6 Summary and Conclusions

We carried out long-term monitoring observations of two repeating FRB sources, FRB 121102 and FRB 180916.J0158+65, at high radio frequencies using the DSN's 70 m radio telescopes (DSS-63 and DSS-14). Radio observations of FRB 121102 were performed between 2019 September 19 (MJD 58745) and 2020 February 11 (MJD 58890), and we observed FRB 180916.J0158+65 between 2019 September 19 (MJD 58745) and 2020 May 14 (MJD 58983). Most of our observations were performed simultaneously at S-band (2.3 GHz) and X-band (8.4 GHz) with DSS-63. We also observed FRB 180916.J0158+65 at L-band (1.5 GHz) during 8 separate epochs using DSS-14.

We detected 2 radio bursts from FRB 121102 at S-band (see Figure 7.1) during periods when the source was predicted to be active. No accompanying radio emission was observed at X-band during the same time. Both of these bursts occurred near the near the peak of the activity window predicted by Rajwade et al. [453]. These detections provide additional examples of the source's narrowband emission behavior at high radio frequencies, which cannot be explained by Galactic DISS [358].

Our radio observations of FRB 180916.J0158+65 span a wide range of activity phases (see Figure 7.2), including several cycles when the source was known to be active at lower frequencies. Until now, FRB 180916.J0158+65's emission behavior had not been explored at frequencies above ~2 GHz across a wide range of activity phases. During our observing campaign, 8 radio bursts were detected from FRB 180916.J0158+65 in the 400–800 MHz band by CHIME/FRB [522][x]. The arrival times of these bursts occurred during times when we were simultaneously observing the source with DSS-14 at L-band or DSS-63 at S/X-band. However, no evidence of radio emission was found in our observing bands during these times (e.g., see Figure 7.3), and no radio bursts were detected from

FRB 180916.J0158+65 during any other times. These observations further demonstrate that FRB 180916.J0158+65's emission process is strongly frequency-dependent (e.g., see [96, 522]), with fewer or fainter bursts emitted from the source at high frequencies. We also find that the radio bursts detected from FRB 180916.J0158+65 are band-limited and have less spectral occupancy at high frequencies. Therefore, the apparent activity of the source, like FRB 121102, strongly depends on the choice of radio observing frequency.

7.7 Acknowledgments

We thank Professor Vicky Kaspi and the CHIME/FRB collaboration for their support of these observations and for providing the CHIME/FRB data used in Figure 7.3. We also thank the reviewer for valuable comments and suggestions.

A.B.P. acknowledges support by the Department of Defense (DoD) through the National Defense Science and Engineering Graduate (NDSEG) Fellowship Program and by the National Science Foundation (NSF) Graduate Research Fellowship under Grant No. DGE-1144469. J.W.T.H. acknowledges funding from an NWO Vici fellowship.

We thank the Jet Propulsion Laboratory's Spontaneous Concept Research and Technology Development program for supporting this work. We also thank Dr. Stephen Lichten for providing programmatic support. In addition, we are grateful to the DSN scheduling team (Hernan Diaz, George Martinez, and Carleen Ward) and the GDSCC and MDSCC operations staff for scheduling and carrying out these observations.

A portion of this research was performed at the Jet Propulsion Laboratory, California Institute of Technology and the Caltech campus, under a Research and Technology Development Grant through a contract with the National Aeronautics and Space Administration. U.S. government sponsorship is acknowledged.

Part IV: Novel Algorithms for Detecting Ultracompact Binary Radio Pulsars and Searches for Radio Pulsars Toward the Galactic Center

The only way to truly understand how an algorithm works is to implement it yourself.

— Barak Zackay

Chapter VIII

Novel Algorithms for Detecting Ultracompact Binary Radio Pulsars

This chapter provides an overview of the scientific content of several papers that are being prepared for publication.

8.1 A Novel Dynamic Programming Algorithm Applied to Pulsar Searching

8.1.1 An Overview of Dynamic Programming

The ideas behind dynamic programming were first introduced in the 1950s by Richard Bellman, an American applied mathematician. Dynamic programming refers to simplifying a complicated problem by breaking it into simpler subproblems in a recursive manner. In cases where this is possible, a relation can be formulated that connects the value of the larger problem to the values of the subproblems. In the optimization literature, this relationship is referred to as the Bellman equation. The name "dynamic programming" is admittedly a misnomer, which was coined by Bellman to hide the fact that he was using mathematics in his work at the RAND Corporation. Many of the principles of dynamic programming have since found many applications in numerous fields, such as mathematics, computer science, astronomy, and biology.

One of the techniques used in some dynamic programming algorithms is memoization. Memoization is an optimization technique, where the results of computationally expensive calculations are stored in cache and returned when the same inputs occur again in order to avoid performing calculations more than once. A simple mathematical problem that demonstrates how dynamic programming and memoization can be highly advantageous is the calculation of the Fibonacci numbers. The sequence, F_n, of Fibonacci numbers are defined by the recurrence relation:

$$F_n = F_{n-1} + F_{n-2}, \tag{8.1}$$

where $F_0 = 0$, $F_1 = 1$, and $n > 1$. The Fibonacci numbers can be calculated using the following recursion algorithm:

Algorithm 1: Recursive algorithm for calculating Fibonacci numbers

Result: $F_n = F_{n-1} + F_{n-2}$

def fib(n):

  if $n \leq 1$ **then**

    return n

  end

  return fib($n - 1$) + fib($n - 2$)

The recursive tree for fib(5) is shown in Figure 8.1, which shows that fib(3) is being calculated two times and fib(2) is computed three times. The computational complexity of this algorithm can be improved by storing the values of fib(k) for $k < n$, rather than recomputing them again.

A memoized version of this algorithm implements a top-down approach, which searches a lookup table for precomputed values before calculating new values and storing them in the lookup table for later use. This dynamic programming algorithm is conceptually similar to the recursive version, except a lookup table is initialized first:

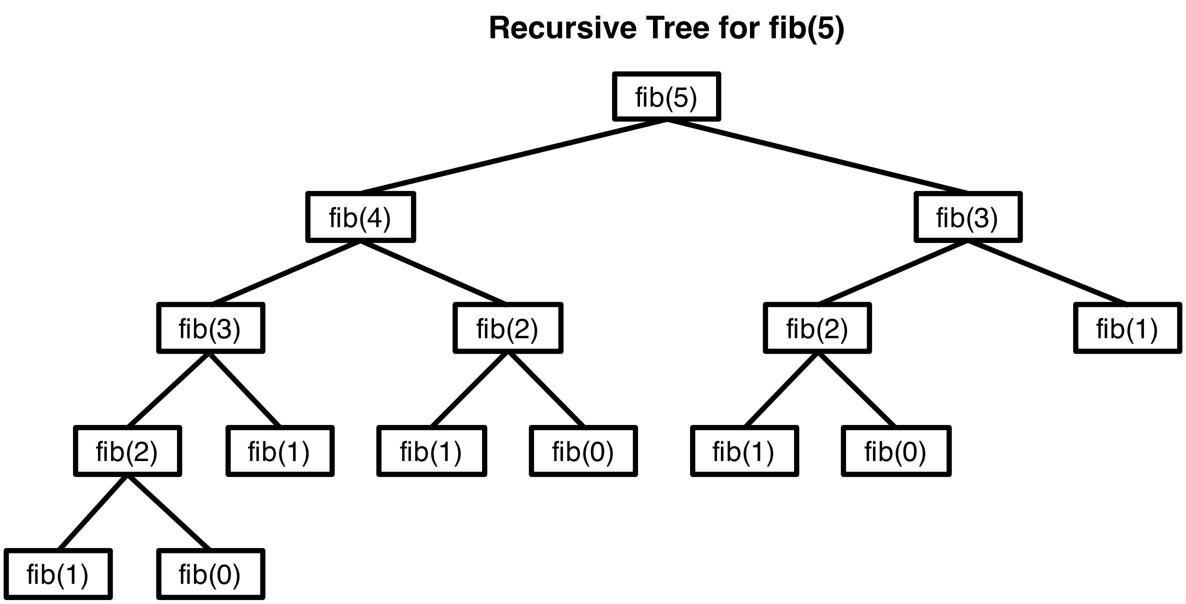

Figure 8.1: **Recursive tree generated by Algorithm 1 when calculating fib(5).**

Algorithm 2: Dynamic programming algorithm for calculating Fibonacci numbers using memoization (top-down approach)

Result: $F_n = F_{n-1} + F_{n-2}$

lookup = np.empty(n)

lookup[:] = np.nan

def fib(n):

  if np.isnan(lookup[n]) **then**

    if $n \leq 1$ **then**

      lookup[n] = n

    else

      lookup[n] = fib($n-1$) + fib($n-2$)

    end

  end

  return lookup[n]

An alternative dynamic programming version of this algorithm can be implemented using a bottom-up design via tabulation. In the bottom-up approach, the lookup table is evaluated iteratively, and the last value in the lookup table is returned:

Algorithm 3: Dynamic programming algorithm for calculating Fibonacci numbers using tabulation (bottom-up approach)

Result: $F_n = F_{n-1} + F_{n-2}$

lookup = np.empty(n)

lookup[:] = np.nan

(lookup[0], lookup[1]) = (1, 1)

def fib(n):

  for i := 2 to n **step** 1 **do**

    lookup[n] = lookup[$n-1$] + lookup[$n+1$]

  return lookup[n]

Although the memoization and tabulation algorithms shown here both store the solutions of the subproblems, the lookup table in the memoization algorithm is filled on demand, while the tabulation algorithm fills all of the entries in the lookup table one-by-one. Tabulation usually outperforms memoization by a constant factor since tabulation has no overhead for recursion, and a preallocated array can be used as the lookup table. However, memoization can be preferrable when only some of the subproblems need to be solved to obtain the solution to the original problem.

The time complexity of the recursive Fibonacci algorithm is $T(n) = T(n-1) + T(n-2) + O(1)$, where $T(n)$ denotes the time complexity of calculating F_n. The $O(1)$ term corresponds to the extra addition needed to sum the results. An upper bound on the complexity of the recursive Fibonacci algorithm is $O(2^n)$, but this is not a tight upper bound. We can find a tight upper bound on the recursive Fibonacci algorithm from the linear recursive function in Equation (8.1). The characteristic equation for this function is given by:

$$x^2 = x + 1. \tag{8.2}$$

The two roots of Equation (8.2) are $r_1 = \frac{1+\sqrt{5}}{2}$ and $r_2 = \frac{1-\sqrt{5}}{2}$, which can be found by solving this equation using the quadratic formula. The solution of the linear recursive function is given by $F_n = \alpha_1 r_1^n + \alpha_2 r_2^n = \alpha_1 \left(\frac{1+\sqrt{5}}{2}\right)^n + \alpha_2 \left(\frac{1-\sqrt{5}}{2}\right)^n$, where $\alpha_1 = \frac{1}{\sqrt{5}}$ and $\alpha_2 = -\frac{1}{\sqrt{5}}$. The coefficients, α_1 and α_2, are obtained using the initial conditions $F_0 = 0$ and $F_1 = 1$. Since $T(n)$ and F_n are asymptotically equivalent, the time complexity of the recursive Fibonacci algorithm is $T(n) = O\left[\left(\frac{1+\sqrt{5}}{2}\right)^n + \left(\frac{1-\sqrt{5}}{2}\right)^n\right]$ $= O\left(\frac{1+\sqrt{5}}{2}\right)^n$. This is a tight upper bound on the time complexity.

The time complexity of the memoization and tabulation algorithms for computing the Fibonacci numbers are both $O(n)$. Thus, both of these dynamic programming implementations provide an exponential speedup over the recursive algorithm, which is very dramatic for large n.

In general, there are three main branches of dynamic programming algorithms: (1) signal processing algorithms, including periodicity search algorithms, such as the FFT or Fast Folding Algorithm (FFA) [502]; (2) string processing algorithms or "stringology" (e.g., DNA sequence alignment algorithms), and (3) graph algorithms (e.g., Dijkstra's algorithm, which finds the shortest paths between nodes on a graph). Historically, many algorithms in these classes were introduced without using dynamic programming, and the computational complexity was later improved dramatically once a dynamic programming design was discovered. Next, I will introduce some examples of dynamic programming algorithm algorithms that are used in fields other than astronomy.

The first non-trivial example that I will describe is the matrix chain multiplication problem, which can be solved efficiently using dynamic programming. Given a sequence of matrices, the goal is to determine the most efficient way to multiply the matrices. The problem is not to actually carry out the matrix multiplication, but rather to determine the order in which the matrices should be multiplied to obtain the result most efficiently. Since matrix multiplication is associative, there are many ways that the multiplication can be performed. For example, for four matrices, A, B, C, and D, the matrix multiplication can be parenthesized in the following ways to give equivalent results: $((AB)C)D = (A(BC))D = (AB)(CD) = A(B(CD))$. If the dimensionality of matrices A, B, and C are 10×100, 100×5, and 5×1000, respectively, then computing $(AB)C$ requires $(10 \times 100 \times 5) + (10 \times 5 \times 1000) = 55000$ operations, whereas computing $A(BC)$ requires $(100 \times 5 \times 1000) + (10 \times 100 \times 1000)$ $= 1500000$ operations. Clearly, the first method is a factor of ~27 times more efficient.

Given a sequence of matrices, the matrix chain multiplication algorithm tries to determine the fewest number of operations needed to compute the product of all the matrices by parenthesizing the chain of matrix multiplications optimally. A brute-force implementation that checks each possible parenthesization would have a complexity that is exponential in the number of matrices. The number of ways to multiply the matrices is given by the n^{th} Catalan number, i.e. $C_n = \binom{2n}{n} - \binom{2n}{n+1} = \frac{1}{n+1}\binom{2n}{n}$ for $n \geq 1$. A more efficient solution is obtained using dynamic programming, where the problem is divided into subproblems and the results from the subproblems are reused.

A top-down dynamic programming solution to this problem identifies the lowest computational cost to compute the full matrix multiplication by splitting the sequence of matrices into subsequences. First, two subsequences are constructed from the full sequence of matrices. Once the minimum cost of multiplying each subsequence is calculated, these costs are added together along with the cost of multiplying the two resulting matrices. This procedure is repeated at each position where the sequence of matrices can be split into subsequences, and the minimum cost is calculated at each stage. For example, given four matrices, A, B, C, and D, the minimum cost to compute $(A)(BCD)$, $(AB)(CD)$, and $(ABC)(D)$ would be determined, and recursion would be used to determine the minimum cost to evaluate BCD, AB, CD, and ABC. The parenthesization and grouping with the lowest minimum cost is returned, which also indicates the best way of performing the matrix chain multiplication.

To improve the computational complexity of this algorithm, it is important to recognize that redundant work is being performed using recursion with this implementation. For example, the result from determining the minimal cost to calculate AB can be reused when the minimal cost of computing ABC is evaluated. Thus, memoization can be used to ensure that unnecessary calculations do not occur. In general, when there are n matrices in the overall sequence, the number of different subsequences (preserving order for matrix multiplication) is $\binom{n}{2} = \frac{n!}{(n-2)!2!} = \frac{n(n-1)}{2}$. It can be shown that a dynamic programming implementation that effectively utilizes memoization will reduce the computational complexity from $O(2^n)$ to $O(n^3)$.

Integer inputs are used in the recursion function to denote the ordering of the subsequences. The recursive function, $f(i, k)$ accepts two integers, (i, k), where i corresponds to a subsequence starting at index i and ending at index k, inclusive. The fewest number of operations required to multiply the subsequence (i, k) is then returned by $f(i, k)$. For a sequence of length n, valid inputs to the recursive function range from $0 \leq i \leq n - 1$ and $0 \leq k \leq n - 1$.

If there is only one matrix in the subsequence, e.g. $f(i, i)$, then zero is returned. Next, suppose we're calculating a matrix subsequence (i, k), and we split the subsequence at index j. The left subsequence, extending from index i to index j, will require $f(i, j)$ operations to evaluate. The matrix product will have the same number of rows (r_i) as the matrix at index i and the same number of columns (c_j) as the matrix at index j. The right subsequence, extending from index $j+1$ to index k will require $f(j + 1, k)$ operations to evaluate. The matrix product will have the same number of rows (r_{j+1}) as the matrix at index $j + 1$ and the same number of columns (c_k) as the matrix at index k. However, the matrix at index $j + 1$ has the same number of rows as the number of columns in the matrix at index j, i.e. $r_{j+1} = c_j$. Therefore, the matrix product in the right subsequence will have dimensions of $c_j \times c_k$. Thus, multiplication of the two resulting matrices from the left and right subsequences will require $r_i \times c_j \times c_k$ operations.

The total number of operations required to multiply the matrices in the overall subsequence is the sum of the three factors described above. This is then minimized over all possible positions where the overall subsequence can be split:

$$\begin{aligned} f(i,i) &= 0 \\ f(i,k) &= \min_{i<j<k} \left[f(i.j) + f(j+1,k) + (r_i \times c_j \times c_k) \right] \end{aligned} \tag{8.3}$$

Alternatively, subsequences in the matrix chain multiplication can be enumerated on a directed acyclic graph (DAG). This leads to a bottom-up dynamic programming implementation that allows subproblems corresponding to subsequences of length l to be solved in increasing order of subsequence length, where $1 < l < n$. This can be carried out in practice, for example, by proceeding in increasing order of the start index, from 0 to $n-l$, inclusive. Proceeding in this manner, the subsequences can be solved in any order since subsequences only depend on shorter subsequences. This method does not require recursion, and it has the same asymptotic computational complexity as the top-down implementation described above.

Another set of well-known classical dynamical programming algorithms include the Viterbi [544, 546], forward-backward [36], and Baum-Welch [36] algorithms. These algorithms allow for tractable inference calculations using hidden Markov models (HMMs) [37, 38]. A Markov model is a type of stochastic signal model that is used to model randomly changing systems, where the Markov property is assumed, i.e. future states depend only on the present state and not on those preceding it. Markov chains (e.g., see Figure 8.2) are often used to model sequential data when the present state, Z_t, represents the complete state of the system and contains all of the information about the system from the current and earlier states, $Z_1, \ldots, Z_t$, where $1 < t < n$. HMMs, on the other hand, assume a Markov process, $X = \{X_1, \ldots, X_n\}$, with unobservable states, $Z = \{Z_1, \ldots, Z_n\}$ (e.g., see Figure 8.3). Here, $X = \{X_1, \ldots, X_n\}$ represent a sequence of observations, and $Z = \{Z_1, \ldots, Z_n\}$ are the "hidden" states, which can be a set of discrete random variables. HMMs are a very powerful tool for modeling a wide range of sequential data, such as speech, written text, genomic data, weather patterns, financial data, and animal behaviors. The Viterbi algorithm can be used to find the most probable sequence of hidden states, while the forward-backward algorithm can be used to perform probabilistic inference and the Baum-Welch algorithm can be used for parameter estimation.

A HMM is a distribution, $p(x_1, \ldots, x_n, z_1, \ldots, z_n)$, that can be represented using the directed graph in Figure 8.3. This distribution can be written as:

$$p(x_{1:n}, z_{1:n}) = p(z_1)p(x_1|z_1) \prod_{t=2}^{n} p(z_t|z_{t-1})p(x_t|z_t). \tag{8.4}$$

Next, we assume that the "transition probabilities", $T_{ij} = p(Z_{t+1} = j|Z_t = i)$ do not depend on the time index, t. This assumption is referred to as "time-homogeneity." The matrix T is referred to as the "transition matrix," which has entries T_{ij} in each position (i, j). For simplicity, if we let $Z_t \in \{1, \ldots, m\}$, then T is an $m \times m$ matrix. In addition, we assume that the "emission probabilities" $\epsilon_i(x_t) = p(x_t|Z_t = i)$ do not depend on the time index, t. We also let π denote the "initial distribution" of Z_1, i.e. $\pi_i = p(Z_1 = i)$. These definitions can be used to rewrite Equation (8.4) as:

$$p(x_{1:n}, z_{1:n}) = \pi_i \epsilon_{z_1}(x_1) \prod_{t=2}^{n} T_{z_t, z_{t-1}} \epsilon_{z_t}(x_t). \tag{8.5}$$

In the Viterbi algorithm and the forward-backward algorithm, it is assumed that the initial distribution (π), transition matrix (T), and emission probabilities (ϵ_i) are all known. The Viterbi algorithm is an efficient method that finds a sequence, $z_1^*, \ldots, z_n^*$, with maximal probability, given $x_1, \ldots, x_n$. In other words, the Viterbi algorithm finds a sequence, $z_{1:n}^*$, such that:

$$z_{1:n}^* \in \underset{z_{1:n}}{\operatorname{argmax}}\, p(z_{1:n}|x_{1:n}), \tag{8.6}$$

where Equation (8.6) means $p(z_{1:n}^*|x_{1:n}) = \max_{z_{1:n}} p(z_{1:n}|x_{1:n})$. Naively maximizing over all sequences would require exponential time, with a time complexity of $O(nm^n)$. However, with dynamic programming, this can be implemented in polynomial time, with a time complexity of $O(nm^2)$.

The forward-backward algorithm allows for a wide range of conditional probabilities to be calculated efficiently, given $x_{1:n}$, including $p(Z_t = i|x_{1:n})$ for each i and t, $p(Z_t = i, Z_{t+1} = j|x_{1:n})$ for each i, j, and t, $p(Z_t \neq Z_{t+1}|x_{1:n})$ for each t, etc... This algorithm can also be used to sample from the distribution of $z_{1:n}$, given $x_{1:n}$. The

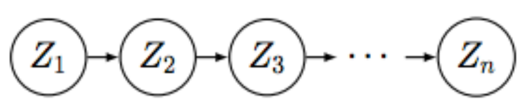

Figure 8.2: **Trellis diagram of a one-dimensional Markov chain.**

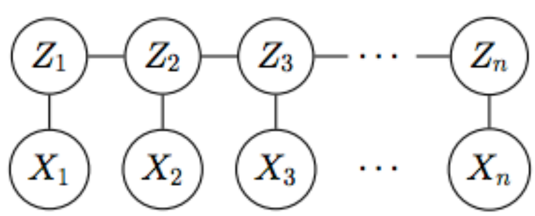

Figure 8.3: **Trellis diagram of a hidden Markov model (HMM).**

forward-backward algorithm tries to efficiently compute the normalization constant, which is the key to being able to easily calculate the quantities of interest. Since $p(z_{1:n}|x_{1:n}) = p(x_{1:n}, z_{1:n})/p(x_{1:n})$, and $p(x_{1:n}, z_{1:n})$ is easy to calculate, the normalization constant is simply given by $p(x_{1:n})$. The expression for the normalization constant can be obtained by deriving recursive formulas that allow this normalization constant to be computed efficiently.

The forward-backward algorithm can be divided into two parts: (1) the forward algorithm and (2) the backward algorithm. In the forward algorithm, we sequentially sum over $z_1, z_2, \ldots, z_n$, in order, and derive a recursion relation for computing $p(x_{1:j}, z_j)$ for each $z_j = 1, \ldots, m$ and $j = 1, \ldots, n$. In the backward algorithm, we sequentially sum over $z_n, z_{n-1}, \ldots, z_1$, in order, and derive a recursion relation for computing $p(x_{j+1:n}|z_j)$ for each $z_j = 1, \ldots, m$ and $j = 1, \ldots, n$. When implemented using dynamic programming, the forward and backward algorithms each take polynomial time, with a time complexity of $O(nm^2)$. Once $p(x_{1:j}, z_j)$ and $p(x_{j+1:n}|z_j)$ are calculated for each z_j and j, many other quantities can be calculated, such as:

$$p(z_j|x_{1:n}) \propto p(x_{1:n}, z_j) = p(x_{1:j}, z_j)p(x_{j+1:n}|z_j), \tag{8.7}$$

and

$$\begin{aligned} p(z_j, z_{j+1}|x_{1:n}) &\propto p(x_{1:n}, z_j, z_{j+1}) \\ &= p(x_{1:j}, z_j)p(z_{j+1}|z_j)p(x_{j+1}|z_{j+1})p(x_{j+2:n}|z_{j+1}), \end{aligned} \tag{8.8}$$

which are used in the Baum-Welch algorithm. Equations (8.7) and (8.8) can also be used to sample from $p(z_{1:n}|x_{1:n})$ by first sampling from $p(z_1|x_{1:n})$ and then from $p(z_{j+1}|z_j, x_{1:n})$ for each $j = 1, \ldots, n-1$, since $p(z_{j+1}|z_j, x_{1:n})$ is easily computed from $p(z_j, z_{j+1}|x_{1:n})$.

Thus far, we have assumed that the initial distribution (π), transition matrix (T), and emission probabilities (ϵ_i) of the HMM are known. The Baum-Welch algorithm [36] is an iterative expectation-maximization (EM) algorithm [151], which uses an efficient dynamic programming procedure to estimate these parameters. At each iteration of the Baum-Welch algorithm, the forward and backward algorithms are used to perform parameter estimation. The EM procedure is used to find a maximum likelihood estimate (MLE) or a maximum a posteriori (MAP) estimate for models with hidden/unobserved variables or data. It is generally advantageous to use EM over standard optimization routines because it exploits the structure of the model to make the optimization computationally efficient. However, it is often difficult to maximize the likelihood of a model with hidden variables, and a global maximum is not guaranteed. EM performs best when the complete data, i.e., the observed and hidden data, can be modeled as an exponential family.

8.1.2 Dynamic Programming Algorithms in Astronomy

Next, I will give an overview of some dynamic programming algorithms that have been used prevalently in astronomy. One of the first algorithms that used dynamic programming to carry out incoherent dedispersion in radio astronomy was the tree dispersion algorithm described in [510]. This algorithm avoids redundant additions when calculating the dedispersed signal in each output channel, similarly to how this is achieved in the FFA [502]. Since tree algorithms efficiently calculate integrals of straight-line paths, they are also similar to the discrete radon transform [65, 220].

The computational cost of incoherent dedispersion with a tree algorithm is $O(N_t N_f \log_2 N_f)$, compared to $O(N_t N_f^2)$ for brute-force incoherent dedispersion algorithms (e.g., see [29, 103, 351, 363]), where N_t and N_f are the number of time and frequency samples, respectively. Recently, improved tree dedispersion algorithms, such as the fast dispersion measure transform (FDMT) [581] and `bonsai` [519], have been implemented to efficiently dedisperse high time and frequency resolution data from state-of-the-art radio telescopes, such as the CHIME/FRB radio telescope. While tree dedispersion is parametrically faster than brute-force dedispersion, it suffers from memory bandwidth bottlenecks, and in some implementations, tree dedispersion makes approximations to the ν^{-2} dispersion delay, which results in reduced S/N.

Dynamic programming has also been used in many other astrophysical subfields, in addition to radio astronomy. For example, an efficient, recursive HMM solver, based on a dynamic programming implementation of the Viterbi algorithm, has been used to search for continuous gravitational-waves (e.g., see [507]). However, the FFT is arguably the most remarkable and well-known numerical algorithm that uses dynamic programming for data analysis. The FFT algorithm has been utilized in numerous areas of astronomy, particularly when searching for periodicity in time series data. Since the FFT algorithm is pervasively used throughout astronomy, I will review how it can be implemented using dynamic programming.

Jean-Baptiste Joseph Fourier was a French mathematician who realized that any continuous function, $x(t)$, can be expressed as a sum of sinusoidal functions, provided each function in the sum is suitably amplified and shifted in phase. The DFT transforms a sequence of N complex numbers, $x_n = \{x_0, x_1, \ldots, x_{N-1}\}$, into another sequence of complex numbers, $X_k = \{X_0, X_1, \ldots, X_{N-1}\}$, according to:

$$\begin{aligned} X_k &= \sum_{n=0}^{N-1} x_n \times \exp\left[-\frac{2\pi ikn}{N}\right] \\ &= \sum_{n=0}^{N-1} x_n \times \left[\cos\left(\frac{2\pi kn}{N}\right) - i\sin\left(\frac{2\pi kn}{N}\right)\right], \end{aligned} \tag{8.9}$$

where Euler's formula has been used to obtain the second expression in Equation (8.9) and $i^2 = -1$. The transformation from $x_n \to X_k$ represents a translation from configuration space to frequency space, which can be useful for determining the power spectrum of a signal and solving certain computational problems more efficiently. The Cooley-Tukey FFT algorithm [111] is a fast dynamic programming algorithm that computes the DFT using a divide-and-conquer procedure. A brute-force implementation of the DFT would require a computational complexity of $O(N^2)$, since N^2 complex multiplications and $N(N-1)$ complex additions are required to evaluate Equation (8.9), assuming that the complex exponentials are precomputed. However, the Cooley-Turkey FFT algorithm allows the DFT to be calculated with a computational complexity of $O(N \log_2 N)$ using dynamic programming by dividing the problem into smaller subproblems, solving the subproblems recursively or iteratively, and then combining the results of the subproblems together to obtain the final result.

The expression for the DFT in Equation (8.9) can be viewed as a linear, matrix-vector multiplication of the vector $\vec{x}$:

$$\vec{X} = M \cdot \vec{x}, \tag{8.10}$$

where the entries in the matrix M are given by $M_{kn} = \exp\left[-\frac{2\pi ikn}{N}\right]$. The entries in the matrix M can also be written as $M_{kn} = \omega^{kn}$, where $\omega = \exp\left[-\frac{2\pi i}{N}\right]$ is a principal N^{th} root of unity and a solution to the equation $x^N = 1$.

Since $\exp(2\pi in) = 1$ for any integer n, from Equation (8.9), we see that the DFT has the following symmetry property:

$$\begin{aligned} X_{k+N} &= \sum_{n=0}^{N-1} x_n \times \exp\left[-\frac{2\pi i(k+N)n}{N}\right] \\ &= \sum_{n=0}^{N-1} x_n \times \exp\left[-\frac{2\pi ikn}{N}\right] \times \exp(-2\pi in) \\ &= \sum_{n=0}^{N-1} x_n \times \exp\left[-\frac{2\pi ikn}{N}\right]. \end{aligned} \tag{8.11}$$

Therefore, Equation (8.11) shows that $X_{k+N} = X_k$, which also implies that $X_{k+i\times N} = X_k$ for any integer i.

Cooley and Tukey showed that the DFT can be computed in two parts:

$$\begin{aligned} X_k &= \sum_{n=0}^{N-1} x_n \times \exp\left[-\frac{2\pi i k n}{N}\right] \\ &= \sum_{m=0}^{N/2-1} x_{2m} \times \exp\left[-\frac{2\pi i k(2m)}{N}\right] + \sum_{m=0}^{N/2-1} x_{2m+1} \times \exp\left[-\frac{2\pi i k(2m+1)}{N}\right] \\ &= \sum_{m=0}^{N/2-1} x_{2m} \times \exp\left[-\frac{2\pi i k m}{(N/2)}\right] + \exp\left[-\frac{2\pi i k}{N}\right] \sum_{m=0}^{N/2-1} x_{2m+1} \times \exp\left[-\frac{2\pi i k m}{(N/2)}\right]. \end{aligned} \tag{8.12}$$

Equation (8.12) shows that the full DFT can be split into two smaller DFTs, one on the odd-numbered values and one on the even-numbered values. Since $0 \leq k < N$ and $0 \leq n < M = N/2$, the symmetry properties obtained from Equation (8.11) can be applied so that only half of the computations need to be performed to evaluate each subproblem. This allows the $O(N^2)$ brute-force computation to be reduced to a computational complexity of $O(M^2)$, where M is half of the size of N. This divide-and-conquer procedure can be repeated, where each of the smaller DFTs are split into two smaller DFTs for even-valued M. At each stage, the computational cost is halved. This process is repeated until the resulting arrays become sufficiently small and it is no longer beneficial to continue forming smaller DFTs. In the asymptotic limit, this approach scales as $O(N \log_2 N)$.

There are many implementations of the FFT. They typically require that N is a composite number, such as a power of 2. However, the radix does not always need to be precisely 2, and mixed radices can be used. This algorithm can be implemented recursively or iteratively, and it is highly parallelizable. In addition to periodicity searches, the FFT can be used for fast convolution, fast polynomial multiplication, and fast multiplication of large integers.

8.1.3 The Fast Folding Algorithm

The FFA is a technique used to search for periodic signals in the presence of noise in the time domain, which was first introduced by David Staelin [502]. The algorithm is fundamentally different from frequency domain techniques used to search for periodicity, such as FFT-based algorithms. The FFA operates by generating a collection of folded profiles by folding a time series modulo a number of trial periods. In pulsar astronomy, these profiles are then assessed to determine whether the resulting profile was produced by a genuine pulsar. The details of the FFA are described in [73, 76, 328, 330, 394, 502], for example. Since a top-down implementation of the FFA is the basis of the novel dynamic programming pulsar search algorithm described in this chapter, I will review the fundamental aspects of the FFA.

8.1.3.1 Bottom-up Implementation of the Fast Folding Algorithm

By avoiding redundant summations and reusing calculations from earlier stages of the algorithm, the FFA is able to more efficiently fold a time series using a range of trial periods. Consider a time series, $\mathcal{T}_j$, consisting of N samples, which we desire search for periodicity. In many analyses aimed at searching for new radio pulsars, for example, $\mathcal{T}_j$ may be a dedispersed time series. The FFA operates by dividing the data into segments of P_0 samples, where $\mathcal{P}_0 = P_0 \times t_{\rm samp}$ is the base period and $t_{\rm samp}$ is the sampling time in the time series. If all of these segments were simply added together, a single folded profile with a period of P_0 samples would be obtained. The FFA efficiently generates N/P_0 folded profiles in a single execution by applying relative offsets to each of the data segments before adding them together. Clearly, a brute-force implementation of this procedure would result in a computational complexity of $\mathcal{O}(N(N/P_0 - 1))$, but the FFA efficiently performs this calculation with a computational complexity of $\mathcal{O}(N \log_2(N/P_0 - 1))$ since it uses memoization to store and reuse redundant results.

In most standard FFA implementations, it is assumed that $N/P_0 = 2^n$, where n is an integer. This condition can be satisfied by either padding or trimming the original data, if this requirement is not automatically satisfied. The FFA uses N/P_0 folded profiles, obtained from folding the time series data modulo the base period, P_0, to generate folded profiles corresponding to a range of trial periods between P_0 and $P_0 + 1$ samples, inclusive. The trial period (in units of samples) of the $i^{\rm th}$ folded profile is given by:

$$P_i = P_0 + \frac{iP_0}{N - P_0}, \tag{8.13}$$

where $0 \leq i \leq (N/P_0) - 1$. The period resolution (in units of samples) between adjacent trial periods is:

$$\Delta P = \frac{P_0}{N - P_0}. \tag{8.14}$$

Next, I describe an easy way to visualize the manner in which the pulse profiles are calculated using the FFA. Let k denote the bin index in the folded profile, where $0 \leq k \leq P_0 - 1$. Assuming that N/P_0 is an integer, the value of the folded pulse profile at bin k, corresponding to a period P_0, can be calculated as [328]:

$$p_{ik} = \sum_{j=0}^{N/P_0-1} \mathcal{T}_{k+jP_0}, \tag{8.15}$$

where $i = 0$ is used as a label for the i^{th} folded profile calculated by the FFA. This expression is obtained by recognizing that the value of the folded profile in bin k can be determined by dividing $\mathcal{T}_j$ into N/P_0 segments. This formalism can be extended for any period P_i, where $P_0 \leq P_i \leq P_0 + 1$, by incorporating the relative shifts required to calculated the value in the k^{th} bin of the i^{th} folded profile [75]:

$$p_{ik} = \sum_{j=0}^{N/P_0-1} \mathcal{T}_{k+jP_0+q_{ij}}, \tag{8.16}$$

where

$$q_{ij} = \lfloor jP_i \rceil \bmod P_0. \tag{8.17}$$

Here, the rounding function, $\lfloor \cdot \rceil$, is used to round q_{ij} to the nearest integer, which ensures that $k + jP_0 + q_{ij}$ is also an integer. The modulo operator is used for wrapping within each segment, $\mathcal{T}_j$, during the addition process. If $k + jP_0 + q_{ij}$ corresponds to an index outside of a given segment, $\mathcal{T}_j$, then the correct index and value for $\mathcal{T}_{k+jP_0+q_{ij}}$ is calculated by wrapping from the end to the beginning of the segment.

A schematic diagram of the FFA procedure, applied to a time series with $N = 12$ samples and a base period of $P_0 = 3$ samples, is shown in Figure 8.4. Using this example, I show how Equations (8.16) and (8.17) handle wrapping when the value in the last bin ($k = 2$) of the folded profile (p_{32}), associated with the period $P_3 = 4$ samples, is calculated. From Equation (8.17), $q_{30} = 0$, $q_{31} = 1$, $q_{32} = 2$, and $q_{33} = 0$. Expanding Equation (8.16) and substituting these values for q_{ij} to evaluate p_{32} gives:

$$\begin{aligned} p_{32} &= \sum_{j=0}^{N/P_0-1} \mathcal{T}_{2+jP_0+q_{3j}} \\ &= \mathcal{T}_{2+0\times P_0+q_{30}} + \mathcal{T}_{2+1\times P_0+q_{31}} + \mathcal{T}_{2+2\times P_0+q_{32}} + \mathcal{T}_{2+3\times P_0+q_{33}} \\ &= \mathcal{T}_{2+0+0} + \mathcal{T}_{2+3+1} + \mathcal{T}_{2+6+2} + \mathcal{T}_{2+9+0} \\ &= \mathcal{T}_2 + \mathcal{T}_6 + \mathcal{T}_{10} + \mathcal{T}_{11} \end{aligned} \tag{8.18}$$

However, since index 6 falls outside of the second segment, $\mathcal{T}_3$ is used as a substitute for $\mathcal{T}_6$ in Equation (8.18) after wrapping around the second segment. Similarly, index 10 falls outside of the third segment, so $\mathcal{T}_7$ is used in place of $\mathcal{T}_{10}$ after wrapping around the third segment. This gives $p_{32} = \mathcal{T}_2 + \mathcal{T}_3 + \mathcal{T}_7 + \mathcal{T}_{11}$, which agrees with the value shown for p_{32} in Figure 8.4.

The FFA has several advantages over FFT-based periodicity search techniques. First off, the FFA coherently sums all of the harmonics of a signal, which differs from searches carried out in the Fourier domain where the harmonics are typically summed incoherently. Generally, FFT-based searches require the user to specify a finite number of harmonics to be summed. This results in reduced sensitivity since the power stored in the higher harmonics is neglected. For this reason, the FFA is a more sensitive method for detecting narrow pulses and yields results that are fully coherent in phase, unlike the FFT. Next, the FFA also offers higher frequency resolution than the FFT, making it more beneficial for detecting signals with long periods.

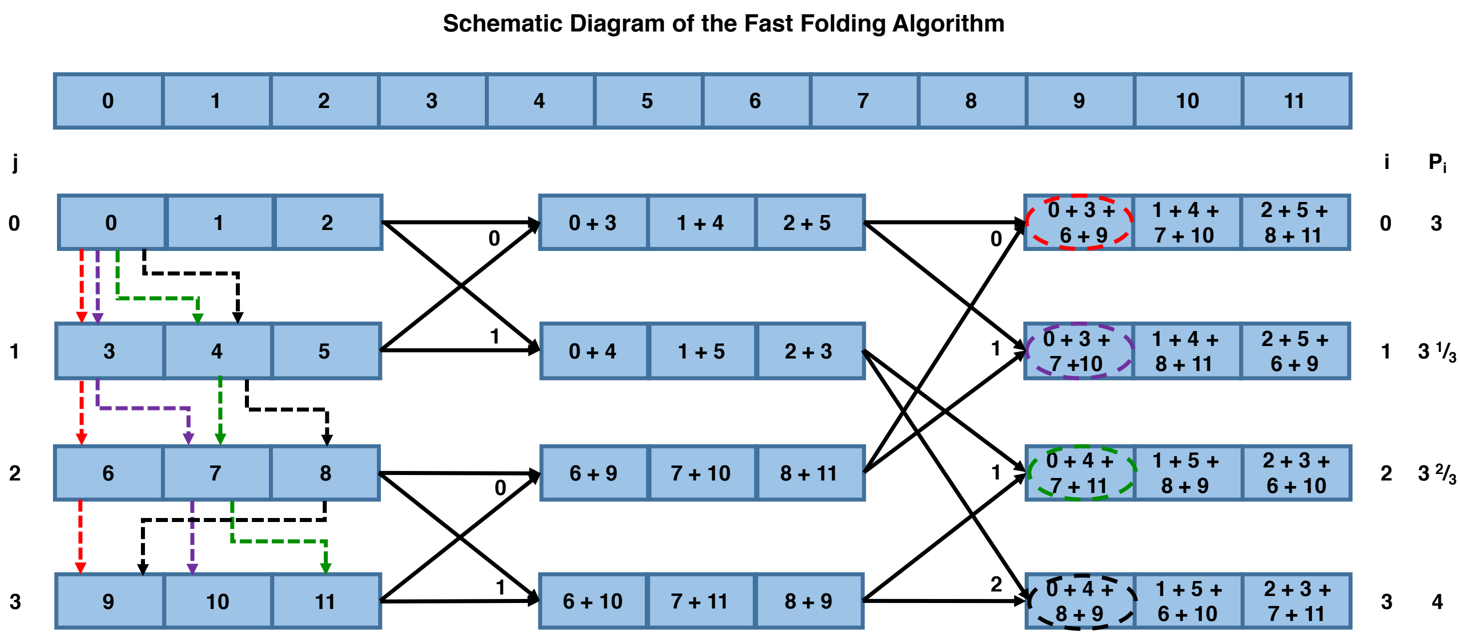

Figure 8.4: **A schematic diagram of the FFA.** In this example, I show a representative illustration of a time series with $N = 12$ samples, folded using the FFA with a base period of $P_0 = 3$ samples. The data are divided into $N/P_0 = 4$ segments, which are indexed by j on the left. The solid black arrows indicate which segments are added together at each step, where the number at each vertex denotes the relative shift applied between the segments before they are added. The FFA produces $N/P_0 = 4$ folded profiles associated with the range of periods $P_0 \leq P_i \leq P_0 + 1$, which are enumerated by index i on the right. A total of $n = 2$ addition steps are required to form each of the folded profiles, where $N/P_0 = 2^n$. The dashed, color arrows show the samples used to calculate the value in the first bin ($k = 0$) of each folded profile, which are indicated by the dashed, colored circles. Image adapted from [75, 328, 502].

Also, since the computational complexity of the FFA is $O(N\log_2(N/P_0 - 1))$, for a fixed number of samples, N, the FFA provides a performance boost over the FFT when carrying out periodicity searches with longer trial periods. However, despite these advantages, the FFA generally requires a large amount of computational power when searching over a wide range of trial periods, which is one of the main reasons why it has not been widely used in large-scale pulsar searches carried out in the past. Given the considerable increase in available computational power over the past decade, phase-coherent techniques, such as the FFA, are beginning to be used in large-scale pulsar searches (e.g., see [418]).

8.1.3.2 Top-down Implementation of the Fast Folding Algorithm

The FFA implementation described in Section 8.1.3.1, and also in many earlier works (e.g., see [76, 502]), relies on a bottom-up design, where the folded segments at each of the $\log_2 P_0$ stages of the algorithm are computed iteratively by performing partial summations starting at the bottom of the tree (see Figure 8.4). However, dynamic programming can be used to implement the FFA using a divide-and-conquer or top-down design. Here, I describe how a top-down implementation of the FFA can be realized by considering the last two stages of the algorithm.

Consider the case where the time series data are divided into two contiguous halves, and assume that there are N samples in each data segment. If the FFA is separately applied to each half of the data, then folded profiles are generated for periods between P_0 and $P_0 + 1$, inclusive, with a resolution of ΔP between periods. When the entire time series is used, folded profiles are also generated for periods in this range, but with a period resolution of $\Delta P/2$ since the data length has been doubled. A top-down implementation of the FFA can be derived by determining how the folded profiles in the two data halves can be combined to obtain the folded profiles at each trial period when the FFA is run on the entire data.

I adopt the convention where the mid-time of each data segment is used as the reference time of each folded profile. First, I consider the case where the trial period used to fold each data half appears exactly in the list of trial periods obtained when applying the FFA to the full data length. For example, let $P_{\rm trial} = P_0 \times t_{\rm tsamp}$. The frequency used to fold the data is then $\nu_{\rm trial} = 1/P_{\rm trial}$. When the data are divided into two halves, the length of each half data segment is $N \times t_{\rm samp}$. The mid-times of the first and second halves of the data then occur at $t_1 = (N/2) \times t_{\rm samp}$ and $t_2 = (3N/2) \times t_{\rm samp}$, respectively. The mid-time of the entire data occurs at

$t_0 = N \times t_{\rm samp}$. Therefore, the time differences between the reference times are $t_1 - t_0 = -(N/2) \times t_{\rm samp}$ and $t_2 - t_0 = (N/2) \times t_{\rm samp}$. The phase-folding relationship, $\Delta\phi = \nu_{\rm trial}(t - t_0)$, can be used to determine how many samples the folded profiles from each half data segment need to be shifted, before adding them together, in order to produce a resolved profile equivalent to folding the entire data modulo the trial period, $P_{\rm trial}$. This phase shift corresponds to shifting the folded profiles by $(t - t_0)/t_{\rm samp} = \Delta\phi \times P_{\rm trial}/t_{\rm samp} = \Delta\phi \times P_0$ samples.

Next, I consider the case where the desired trial period is not in the original list of periods used to derive the folded profiles for each half data segment. This happens roughly half of the time since the full data length is twice as long and the period resolution is twice as fine compared to the period resolution obtained using each half data segment. For example, suppose we want to construct the folded profile associated with a trial period of $P_{\rm trial} = (P_0 + \Delta P/2) \times t_{\rm samp}$ using the folded profiles from each half data segment. For convenience, let $\nu_{\rm trial} = 1/P_{\rm trial}$. At time t, the phase difference between folding with a frequency ν relative to the desired trial frequency, $\nu_{\rm trial}$, is given by $\Delta\phi_\nu = (\nu - \nu_{\rm trial})t$. In order to select which folded profile should be used in each half data segment to generate the desired folded profile associated with $P_{\rm trial}$, we calculate $\Delta\phi_\nu i$ for periods $P_{\rm fold} \in \left[P_0 \times t_{\rm samp}, (P_0 + \Delta P) \times t_{\rm samp}\right]$. If $\Delta\phi_\nu$ is less than half of a sample, i.e. $\Delta\phi_\nu \times P_{\rm fold}/t_{\rm samp} < 0.5 \Rightarrow \Delta\phi_\nu < t_{\rm samp}/(2P_{\rm fold})$ when folding with a period $P_{\rm fold}$, then $P_{\rm fold} \approx P_{\rm trial}$ and the folded profile derived using the period $P_{\rm fold}$ can be used. The phase-folding relationship, $\Delta\phi = \nu_{\rm fold}(t - t_0)$, where $\nu_{\rm fold} = 1/P_{\rm fold}$ and t is the mid-time of the half data segment, can be used to determined the number of required samples that the folded profile from each half data segment needs to be shifted. When the folded profiles are shifted according to this prescription, they can be added together to produce a resolved profile equivalent to folding the entire data modulo the trial period, $P_{\rm trial}$. From this relation, the required phase shift corresponds to shifting the folded profile by $\Delta\phi \times P_{\rm trial}/t_{\rm samp}$ samples, which is analogous to the result obtained above.

A schematic diagram of this top-down dynamic programming implementation, and the procedure described above, is shown in Figure 8.5. As the data chunks are combined together in subsequent iterations, the period resolution scales as $\Delta P \propto 1/t_{\rm seg}$, where $t_{\rm seg}$ is the duration of each data chunk. This is analogous to the frequency resolution, $\Delta\nu = 1/T_{\rm obs} = \nu_{\rm s}/N_{\rm FFT}$, achieved when a FFT is calculated, where $T_{\rm obs}$ is the total duration of the data, $\nu_{\rm s}$ is the sampling frequency, and $N_{\rm FFT}$ is the number of points used to compute the FFT. Since the folded profiles at each iteration are computed by shifting and adding the folded profiles computed during previous stages of the algorithm, this design provides a computational complexity that is similar to the bottom-up implementation of the FFA. Following this prescription, the FFA can be implemented using a top-down dynamic programming design, and it can be extended to handle acceleration, jerk, and other types of searches for binary pulsars.

8.1.4 A New Dynamic Programming Algorithm for Pulsar Searching

The principles described in Section 8.1.3.2 provide a blueprint for a top-down implementation of the FFA. They are also the basis of a new coherent time-domain dynamic programming algorithm that we have developed for pulsar searches using a tree-like scheme. Since the algorithm is implemented in a top-down fashion, it was straightforward to extend its capabilities to allow for acceleration, jerk, and higher-order polynomial searches. For each of these different types of searches, we have implemented parameterized modulation functions that are used to fold each contiguous, non-overlapping segment of data. A schematic diagram of the pulsar search dynamic programming algorithm is shown in Figure 8.6.

At the beginning of the algorithm, the data are divided into non-overlapping segments of length $t_{\mathrm{seg},1} = T$. A data structure is created that is used to store all of the folded profiles obtained by folding each data segment using the grid of parameters passed to the modulation function. For example, when an acceleration search is performed, folded profiles generated using each trial period and trial acceleration are stored in the data structure for each data segment. In subsequent iterations, the folded profiles stored in the data structure from the previous iteration are used to calculate the entries in the data structure for the next iteration, where the data segments are now twice as long, i.e. $t_{\mathrm{seg},2} = 2t_{\mathrm{seg},1} = 2T$. The algorithm proceeds in this fashion until folded profiles corresponding to a single data segment, $t_{\mathrm{seg},N} = \log_2(T_{\mathrm{obs}})$, are formed at iteration N, where T_{obs} is the total duration of the data. As larger data segments are formed at each iteration, the period, acceleration, and jerk resolutions scale as $\Delta P \propto 1/t_{\mathrm{seg},i}$, $\Delta a \propto 1/t_{\mathrm{seg},i}^2$, and $\Delta j \propto 1/t_{\mathrm{seg},i}^3$, respectively, where $t_{\mathrm{seg},i}$ is the length of the data segments at stage i of the algorithm.

An important component of the dynamic programming pulsar search algorithm is the resolving function, which was developed for each type of modulation function. The resolving function translates the parameters of the modulation function from a series of contiguous subsegments at iteration $i-1$ to the parameters of the modulation function associated with a data segment obtained by combining the subsegments together at iteration i, where $1 \leq i \leq N$ denotes the iteration or stage of the algorithm. This mathematical transformation is used to determine how to shift the folded

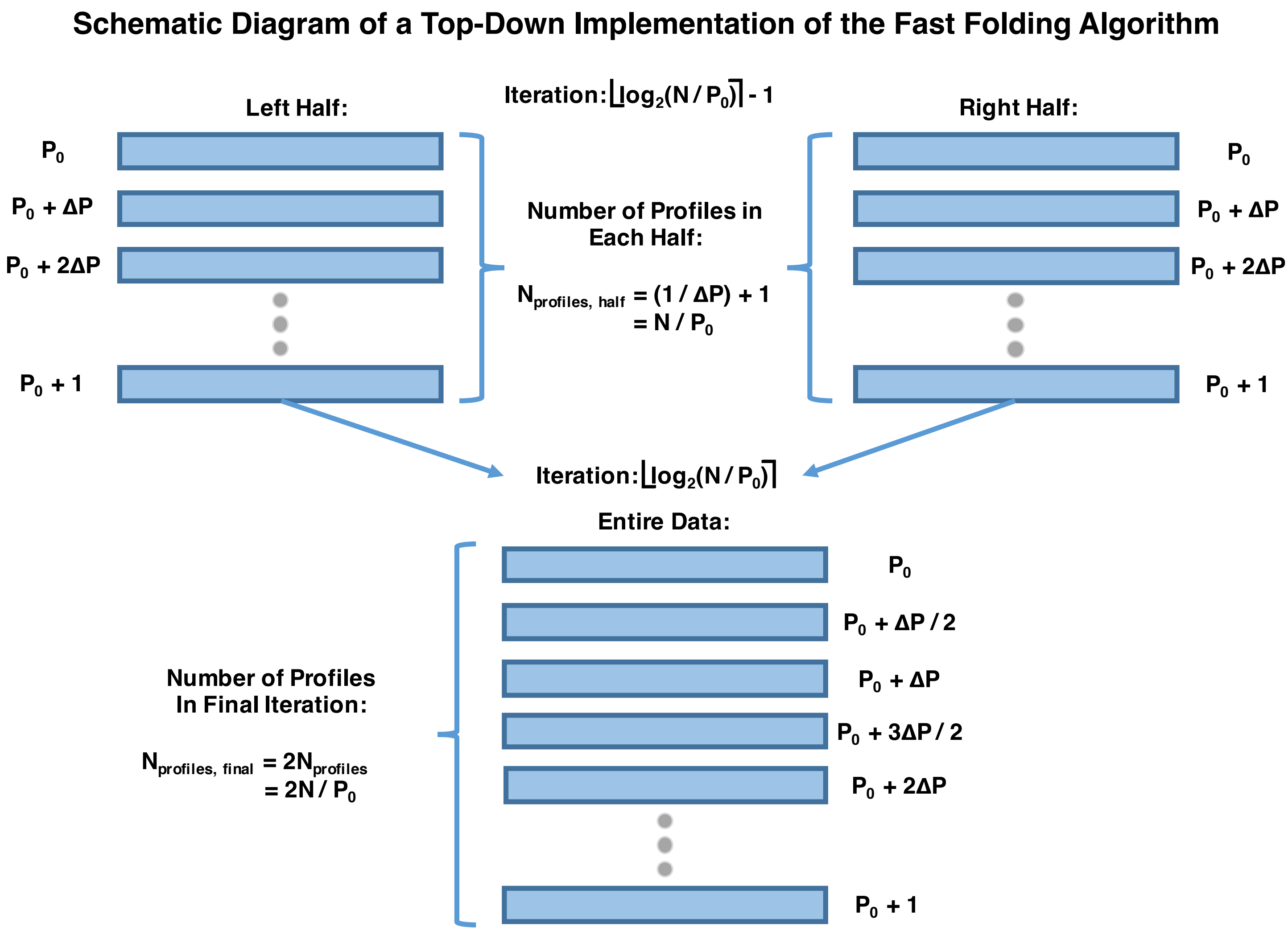

Figure 8.5: **Schematic diagram of a top-down implementation of the FFA.** At iteration $\lfloor \log_2(N/P_0) \rceil - 1$, i.e., the second to last iteration, folded profiles are computed separately using the first half and second half of the data. Assuming N samples in each half, folded profiles corresponding to periods between P_0 and $P_0 + 1$, inclusive, are computed with a period resolution of ΔP. Hence, a total of $N_{\text{profiles, half}} = N/P_0$ folded profiles are generated in each half. In the final iteration, i.e. at iteration $\lfloor \log_2(N/P_0) \rceil$, there are $2N$ samples, and $N_{\text{profiles, final}} = 2N_{\text{profiles, half}} = 2N/P_0$ folded profiles are generated with a period resolution of $\Delta P/2$ for trial periods between P_0 and $P_0 + 1$, inclusive. The folded profiles corresponding to each trial period in the final iteration are obtained by adding the folded profiles from the two data halves in the previous iteration, after shifting the profiles appropriately so that a resolved profile, which is equivalent to folding the entire data modulo the trial period, is obtained.

profiles in the contiguous subsegments before adding them together, in order to properly account for acceleration, jerk, and higher-order polynomial terms.

The resolving function is incredibly delicate, and an error of a single phase bin can be catastrophic to the performance of the algorithm. In Section 8.1.4.2, I will describe how the resolving function is parameterized for an acceleration search. The convergence of the algorithm, when an acceleration search is performed, is demonstrated in Section 8.1.4.3 using simulated data.

At the last stage of the algorithm, folded profiles are computed for each of the trial parameters passed to the modulation function using a data segment of length $t_{\mathrm{seg},N}$. To identify potential pulsar candidates, we use a scoring function that calculates a detection statistic by matched filtering the folded profiles with a single Gaussian function or a double Gaussian function. Matched filtering with a double Gaussian function can be superior, in some cases, when searching for MSPs since many of them display radio pulse profiles with two or more widely separated peaks (e.g., see [265]). Since the fraction of known pulsars that show interpulses in their pulse profiles is only a few percent [281, 347], this matched filter scheme is sufficient in most cases. The threshold used to select potentially interesting pulsar candidates is adjustable, but we typically save all of the parameters associated with a pulsar candidate if the detection significance, obtained after matched filtering the folded profile, has a S/N ≥ 7.

This new time domain-based, dynamic programming algorithm is capable of coherently searching for binary pulsars in an efficient manner, with improved sensitivity compared to existing incoherent techniques used in the pulsar astronomy, such as Fourier domain-based acceleration and sideband searches (e.g., see [457, 458]). The dynamic programming algorithm described here has been tested on simulated data, and it has also been used to recover the known pulsars in the globular cluster Terzan 5 and the double pulsar, PSR J0737–3039A (see Section 8.1.4.4). In all cases, pulsations are detected at the expected theoretical sensitivity level using this algorithm (e.g., see Section 8.1.4.3).

8.1.4.1 Effects of Binary Motion on the Observed Emission from Pulsars

Before describing how the resolving function connects the acceleration, period, and phase of the pulsar in the subsegments at iteration $i-1$ to the parameters in the combined data segment at iteration i, I will first briefly review the effects of orbital motion on an observed pulsar signal.

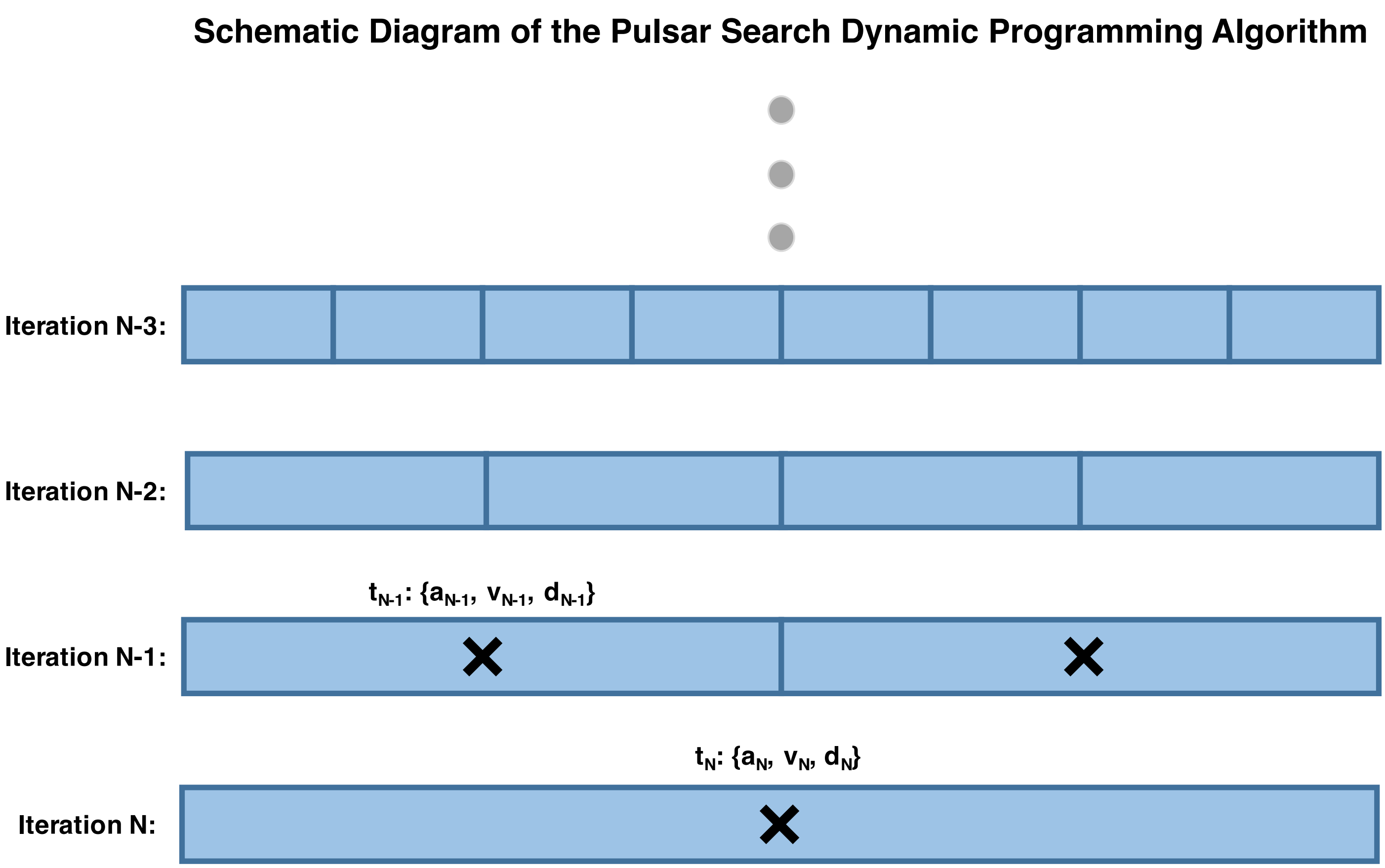

Figure 8.6: **Top-down schematic diagram of an acceleration search for pulsars, implemented using the dynamic programming algorithm.** At iteration $N-1$, the folded data in both data segments are combined in the subsequent iteration N by shifting and adding the folded profiles, such that the desired trial period is obtained after accounting for acceleration at the mid-time of the combined data segment. The acceleration and period at the mid-time of each data segment are calculated using a basis of Chebyshev polynomials. Thus, the folded profile at iteration N is computed using the folded profiles from the data segments in the previous iteration.

The orbital period, $P_{\rm b}$, of a binary pulsar can be assumed to be constant throughout a typical pulsar observation when $P_{\rm b}$ is of the order of days. However, the Doppler effect can result in the pulsar displaying different apparent rotational periods during observations on different days. If the pulsar is in a compact binary, with an orbital period that is of the order of hours or shorter, then this behavior can be often be observed during an individual observation of the pulsar (e.g., see Figure 8.8). The Doppler formula can be used to relate the observed rotational period, $P_{\rm obs}$, of a pulsar moving with a projected line of sight velocity, $v(t)$, as observed by a stationary observer, to its intrinsic rotational period, $P_{\rm int}$, in the pulsar's rest frame:

$$P_{\rm obs}(t) \approx P_{\rm int}\left[1 + \frac{v(t)}{c}\right], \tag{8.19}$$

where c is the speed of light and higher-order terms of (v/c) have been neglected. If the pulsar's projected line of sight velocity is constant in time, i.e., $v(t) = v$, then its rotational period will be shifted from $P_{\rm int}$ to $P_{\rm int}\left(1 + \frac{v}{c}\right)$. For pulsars in compact binary systems (e.g., $P_{\rm b} \approx 10\,T_{\rm obs}$), the projected line of sight velocity is a function of time. The velocity, $v(t)$, can be expanded in a Taylor series, which gives:

$$v(t) = v_0 + a_0 t + j_0 \frac{t^2}{2!} + \cdots, \tag{8.20}$$

where v_0, a_0, and j_0 are the instantaneous line of sight velocity, acceleration, and jerk at time $t = 0$. Substituting Equation (8.20) into Equation (8.19) yields:

$$P_{\rm obs}(t) = P_{\rm int}\left[1 + \frac{1}{c}\left(v_0 + a_0 t + j_0 \frac{t^2}{2!} + \cdots\right)\right]. \tag{8.21}$$

The first term of the Taylor Series expansion in Equation (8.21) gives the apparent change in the pulsar's rotational period when the projected velocity along the line of sight is constant. The second term in the expansion shows that the observed rotational period from the pulsar changes linearly with time due to acceleration. The third term in the Taylor series expansion indicates that there is a quadratic change in the pulsar's rotational period with time as a result of jerk.

For a pulsar in a circular orbit, the line of sight velocity is given by [257]:

$$v(t) = A\cos(\Omega_{\rm b} t + \phi_0), \tag{8.22}$$

where ϕ_0 is the orbital phase at $t = 0$, $\Omega_{\rm b} = 2\pi/P_{\rm b}$ is the angular orbital frequency, and A is the orbital velocity semi-amplitude given by:

$$A = \Omega_{\rm b} \times \frac{m_{\rm c}}{m_{\rm psr} + m_{\rm c}}\left[\frac{G(m_{\rm psr} + m_{\rm c})}{\Omega_{\rm b}^2}\right]^{1/3} \sin i, \tag{8.23}$$

where $m_{\rm psr}$ and $m_{\rm c}$ are the pulsar and companion masses, respectively, and i is the inclination of the binary orbit. The expression for the line of sight velocity, $v(t)$, in Equation (8.22) can be expanded using a Taylor series about $t = 0$, which can be used to calculate the pulsar's velocity, acceleration, and jerk at $t = 0$:

$$v_0 = A \cos \phi_0, \tag{8.24}$$

$$a_0 = -A\, \Omega_{\rm b} \cos \phi_0, \tag{8.25}$$

$$j_0 = -A\, \Omega_{\rm b}^2 \sin \phi_0. \tag{8.26}$$

In general, the pulsar's velocity along the line of sight depends on the orbital parameters of the system, which can be obtained from the system's Keplerian parameters [146, 328]. In general, the pulsar's line of sight velocity is given by:

$$v(A_{\rm T}) = \Omega_{\rm b} \frac{a_{\rm p} \sin i}{\sqrt{1-e^2}} \left[\cos(\omega + A_{\rm T}) + e \cos \omega\right], \tag{8.27}$$

where $A_{\rm T}$ is the true anomaly, which is a function of time, $a_{\rm p} \sin i$ is the projected semi-major axis of the orbit, e is the eccentricity, and ω is the longitude of periastron. If the maximum velocity of the pulsar along the line of sight is small with respect to c, then the observed Doppler-shifted rotational period of the pulsar can be written as [328]:

$$P_{\rm obs}(A_{\rm T}) \approx P_{\rm int} \left[1 + \frac{v(A_{\rm T})}{c}\right], \tag{8.28}$$

where $P_{\rm int}$ is the rotational period of the pulsar in its rest frame. The corresponding acceleration of the pulsar along the line of sight is found by differentiating Equation (8.27):

$$a(A_{\rm T}) = -\Omega_{\rm b}^2 \frac{a_{\rm p} \sin i}{1-e^2} \left[(1 + e \cos A_{\rm T})^2 \sin(\omega + A_{\rm T})\right]. \tag{8.29}$$

When all five of the Keplerian parameters: $\Omega_{\rm b}$, $a_{\rm p} \sin i$, e, ω, and the epoch of periastron, T_0, are blindly searched for in a pulsar search, then the analysis becomes extremely computationally expensive. It is often only possible to carry out such types of pulsar searches by performing the analysis on a distributed volunteer computing system, such as *Einstein@Home* (e.g., see [101]), where tens of thousands of computers are connected across the internet and used to search for pulsations.

Since blind Keplerian pulsar searches require an extreme amount of computational resources, it is often useful to approximate how the orbit of a binary pulsar will affect the pulsations. One common type of search that is carried out using data from large-scale pulsar surveys, such as the Parkes multibeam pulsar survey [171], is an acceleration search (e.g., see [13, 162, 392, 457, 566]), which assumes that the pulsar has a constant orbital acceleration. Acceleration searches are very effective when $T_{\rm obs} \lesssim P_{\rm b}/10$ [458]. In this regime, almost all of the lost sensitivity can be completely recovered using an acceleration search. However, the effects of jerk and higher-order terms are ignored.

Assuming a constant orbital acceleration, the velocity, $v(t)$, can be written as:

$$v(t) = v_0 + a_0 t. \tag{8.30}$$

Under this assumption, from Equation (8.19), the observed rate of change of the rotational frequency, $\dot{\nu}_{\rm obs}$, is given by:

$$|\dot{\nu}_{\rm obs}| = \frac{a_0 \nu_{\rm int}}{c}, \tag{8.31}$$

where $\nu_{\rm int} = 1/P_{\rm int}$ is the intrinsic rotational frequency in the pulsar's rest frame. Over an observation length, $T_{\rm obs}$, the observed change in rotational frequency is given by:

$$|\Delta\nu_{\rm obs}| = |\dot{\nu}_{\rm obs}|\, T_{\rm obs} = \frac{a_0 \nu_{\rm int} T_{\rm obs}}{c} = \frac{a_0 T_{\rm obs}}{P_{\rm int} c}. \tag{8.32}$$

From Equation (8.32), the frequency smearing will be larger if the pulsar has either a larger acceleration or a shorter rotational period. A larger amount of frequency smearing will also be observed when the observation duration is longer.

In the Fourier domain, the width of each spectral bin is $\Delta\nu = 1/T_{\rm obs}$. During an observation of length $T_{\rm obs}$, the number of frequency bins that the pulsar signal will drift in the Fourier domain is:

$$N_{\rm drift} = \frac{|\Delta\nu_{\rm obs}|}{\Delta\nu} = \frac{|\dot{\nu}_{\rm obs}|\, T_{\rm obs}}{\Delta\nu} = \frac{a_0 \nu_{\rm int} T_{\rm obs}^2}{c} = \frac{a_0 T_{\rm obs}^2}{P_{\rm int} c}. \tag{8.33}$$

Hence, the pulsar signal will be smeared across multiple spectral bins when $|\Delta\nu_{\rm obs}|/\Delta\nu > 1$ or $(a_0 T_{\rm obs}^2)/(P_{\rm int} c) > 1$. Higher frequency harmonics often contain a considerable fraction of the pulsar's spectral power. This analysis can be extended by recognizing that the rate of change of the pulsar's rotational frequency scales linearly with harmonic number, $h = 1, 2, 3, \ldots, n$:

$$|\dot{\nu}_{\rm obs}| = \frac{h a_0 \nu_{\rm int}}{c}, \tag{8.34}$$

where $h = 1$ represents the fundamental.

Fourier domain acceleration search algorithms, such as `accelsearch` in the `PRESTO` pulsar search software package[m], use matched filtering to correct for Doppler smearing introduced by the pulsar's acceleration during the observation. This is achieved by accounting for the number of Fourier frequency bins that the pulsar signal drifts over the course of the observation. Let $r = \nu_{\rm obs} T_{\rm obs}$ denote the Fourier bin numbers. Then, $z = \dot{r} = \dot{\nu}_{\rm obs} T_{\rm obs}^2$ corresponds to the number of Fourier frequency bins that the pulsar signal drifts during the observation due to acceleration. Substituting this expression into Equation (8.34), the following relation is obtained under the assumption that the pulsar's acceleration is constant throughout the observation:

$$a_0 = \frac{|\dot{\nu}_{\rm obs}|\, c}{h\nu_{\rm int}} = \frac{zc}{h\nu_{\rm int} T_{\rm obs}^2}. \tag{8.35}$$

This formalism can be extended for jerk searches by defining $w = \dot{z} = \ddot{r} = \ddot{\nu}_{\rm obs} T_{\rm obs}^3$ as the number of Fourier frequency bins that the signal drifts during the observation due to constant jerk. In this case, the pulsar's jerk is given by:

$$j_0 = \dot{a}_0 = \frac{|\ddot{\nu}_{\rm obs}|\, c}{h\nu_{\rm int}} = \frac{wc}{h\nu_{\rm int} T_{\rm obs}^3}. \tag{8.36}$$

Fourier domain-based acceleration and jerk searches often use the r-z-w coordinate system since it is intuitively and computationally advantageous when calculating DFTs [10, 457].

8.1.4.2 Parameterization using Chebyshev Polynomials

A critical component of the dynamic programming algorithm described in Section 8.1.4 involves using the parameters of the modulation function at stage $i-1$ to determine new parameters at stage i after the subsegments are combined. This is important for determining how the folded profiles in the subsegments need to be shifted before they are added together to form the folded profile in the larger data segment. Here, I describe the mathematical transformation that is employed when this algorithm is used to carry out an acceleration search. This formalism is extendable to other types of pulsar searches, such as jerk and higher-order polynomial searches.

During the first iteration of the algorithm, the data in each segment is folded using the formula:

$$\phi(t) = \phi(t_0) + \nu_{\rm fold}(t - t_0) + \frac{1}{2!}\dot{\nu}_{\rm fold}(t - t_0)^2 + \cdots, \tag{8.37}$$

where $\nu_{\rm fold}$ and $\dot{\nu}_{\rm trial}$ are the frequency and frequency derivative values used for folding, respectively. The reference time, t_0, is defined to be the mid-time of each data segment. Folded profiles are generated for each trial period and trial acceleration in the grid of parameters, which are stored in a data structure containing the results for each data segment. Assuming constant orbital acceleration during the observation, the pulsar's velocity along the line sight is $v(t) = v_0 + a_0 t$, and Equation (8.19) can be used to calculate the folding frequency and frequency derivative:

$$\nu_{\rm fold}(t) = \frac{1}{P_{\rm fold}} \approx \nu_{\rm int}\left[1 - \frac{v(t)}{c}\right] = \nu_{\rm int}\left[1 - \frac{v_0}{c} - \frac{a_0 t}{c}\right], \tag{8.38}$$

$$\dot{\nu}_{\rm fold}(t) \approx \nu_{\rm int}\frac{a_0}{c}. \tag{8.39}$$

The distance along the line of sight, $d(t)$, between a binary pulsar and a stationary observer changes with time, t. The pulsar signal emitted at time t is received by the observer at a later time [257]:

$$t' = t + d(t)/c. \tag{8.40}$$

The time-variable distance, $d(t)$, can be expanded in a Taylor series, which gives:

$$d(t) = d_0 + v_0 t + \frac{a_0}{2!}t^2 + \cdots, \tag{8.41}$$

where d_0, v_0, and a_0 are the line of sight distance, velocity, and acceleration to the pulsar at $t = 0$. Expressions for both v_0 and a_0 are given in Equations (8.24) and (8.25).

A basis of Chebyshev polynomials of the first kind, $T_n(x)$, was chosen to transform the velocity and acceleration from the mid-time of a subsegment at stage $i - 1$ to the mid-time of a data segment formed by shifting and adding the folded profiles from two contiguous, adjacent data segments. The Chebyshev polynomials are orthogonal on [–1, 1] with respect to the weighting function $1/\sqrt{1 - x^2}$. That is, for $m \neq n$, the following property holds:

$$\int_{-1}^{1} T_n(x)T_m(x)\frac{1}{\sqrt{1-x^2}}dx = \int_0^{\pi} \cos(n\theta)\cos(m\theta)d\theta = 0. \tag{8.42}$$

This can be proven by setting $x = \cos(\theta)$ and performing a change of variables using the identity $T_n(x) = \cos(n\theta)$. The Chebyshev polynomials have the largest possible leading coefficient, whose absolute value is bounded by 1 on the interval [–1, 1]. This allows the largest deviation from the "correct" solution to be controllable, which is one of the advantages of using Chebyshev polynomials over other polynomial families. The Chebyshev polynomial basis also allows every Keplerian orbit to be uniquely enumerated using this parameterization, with distinct parameter combinations describing distinct curves across each data segment. This is an important property, in particular, for enabling blind Keplerian pulsar searches using a novel pruning algorithm that is being developed (see Section 8.2). The first twelve Chebyshev polynomials of the first kind are listed in Equation (8.43) below:

$$\begin{aligned}
T_0(x) &= 1 \\
T_1(x) &= x \\
T_2(x) &= 2x^2 - 1 \\
T_3(x) &= 4x^3 - 3x \\
T_4(x) &= 8x^4 - 8x^2 + 1 \\
T_5(x) &= 16x^5 - 20x^3 + 5x \\
T_6(x) &= 32x^6 - 48x^4 + 18x^2 - 1 \\
T_7(x) &= 64x^7 - 112x^5 + 56x^3 - 7x \\
T_8(x) &= 128x^8 - 256x^6 + 160x^4 - 32x^2 + 1 \\
T_9(x) &= 256x^9 - 576x^7 + 432x^5 - 120x^3 + 9x \\
T_{10}(x) &= 512x^{10} - 1280x^8 + 1120x^6 - 400x^4 + 50x^2 - 1 \\
T_{11}(x) &= 1024x^{11} - 2816x^9 + 2816x^7 - 1232x^5 + 220x^3 - 11x
\end{aligned} \tag{8.43}$$

Next, I will derive the required mathematical transformation that describes how to shift the folded profiles from the subsegments at iteration $i - 1$ such that, when the profiles are added, the results are equivalent to folding the data segments at stage i with the correct period and acceleration at the mid-times of the combined data segments. To calculate the arrival time of the pulsar's emission at a reference time, $t_{\rm ref}$, the line of sight distance to the pulsar is Taylor expanded about $t = t_{\rm ref}$:

$$d(t - t_{\rm ref}) = d_{t_{\rm ref}} + v_{t_{\rm ref}}(t - t_{\rm ref}) + \frac{a_{t_{\rm ref}}}{2!}(t - t_{\rm ref})^2 + \cdots, \tag{8.44}$$

where $d_{t_{\rm ref}}$, $v_{t_{\rm ref}}$, and $a_{t_{\rm ref}}$ correspond to the distance, velocity, and acceleration of the pulsar along the line of sight at time $t = t_{\rm ref}$. The required time delay is then determined by calculating $d(t - t_{\rm ref})/c$.

Let t_i and t_{i-1} denote the mid-time of a data segment at iteration i and $i - 1$, respectively. These times are treated as the reference time in each of these data segments. For simplicity, I define $t_{i-1} = 0$ in the coordinate system considered here. From Equation (8.44), the line of sight distance of the pulsar at time $t = t_{i-1}$, assuming constant acceleration, is:

$$\begin{aligned} d(t - t_{i-1}) = d(t) &= d_{t_{i-1}} + v_{t_{i-1}}(t - t_{i-1}) + \frac{a_{t_{i-1}}}{2}(t - t_{i-1})^2 \\ &= d_{t_{i-1}} + v_{t_{i-1}} t + \frac{a_{t_{i-1}}}{2} t^2, \end{aligned} \tag{8.45}$$

where $d_{t_{i-1}}$, $v_{t_{i-1}}$, and $a_{t_{i-1}}$ are the distance, velocity, and acceleration at the mid-time of a subsegment in iteration $i - 1$ of the dynamic programming algorithm. To parameterize Equation (8.45) in terms of a basis of Chebyshev polynomails, let $d^*_{t_{i-1}}$, $v^*_{t_{i-1}}$, and $a^*_{t_{i-1}}$ denote the coefficients of first three Chebyshev polynomials in the new basis. This allows Equation (8.45) to be written as:

$$\begin{aligned} d(t - t_{i-1}) = d(t) &= d^*_{t_{i-1}} T_0(t) + v^*_{t_{i-1}} T_1(t) + a^*_{t_{i-1}} T_2(t) \\ &= d^*_{t_{i-1}} + v^*_{t_{i-1}} t + a^*_{t_{i-1}} (2t^2 - 1). \end{aligned} \tag{8.46}$$

The following relations are obtained by equating powers of t in Equations (8.45) and (8.46):

$$\begin{aligned} d^*_{t_{i-1}} &= d_{t_{i-1}} + \frac{a_{t_{i-1}}}{4}, \\ v^*_{t_{i-1}} &= v_{t_{i-1}}, \\ a^*_{t_{i-1}} &= \frac{a_{t_{i-1}}}{4}. \end{aligned} \tag{8.47}$$

Substituting the expressions in Equation (8.47) into Equation (8.46) provides a parameterization in terms of physical units:

$$d(t - t_{i-1}) = d(t) = d_{t_{i-1}} + \frac{a_{t_{i-1}}}{4} + v_{t_{i-1}} t + \frac{a_{t_{i-1}}}{4}(2t^2 - 1). \tag{8.48}$$

Similarly, assuming constant acceleration, the line of sight distance of the pulsar at time $t = t_i$ is given by:

$$d(t - t_i) = d_{t_i} + v_{t_i}(t - t_i) + \frac{a_{t_i}}{2}(t - t_i)^2, \tag{8.49}$$

where d_{t_i}, v_{t_i}, and a_{t_i} are the distance, velocity, and acceleration at the mid-time of the combined data segment in iteration i of the dynamic programming algorithm, which was derived from the subsegment at iteration $i - 1$. Next, Equation (8.49) can be expressed using a basis of Chebyshev polynomials as follows:

$$\begin{aligned} d(t - t_i) &= d^*_{t_i} T_0(t - t_i) + v^*_{t_i} T_1(t - t_i) + a^*_{t_i} T_2(t - t_i) \\ &= d^*_{t_i} + v^*_{t_i}(t - t_i) + a^*_{t_i}\left[2(t - t_i)^2 - 1\right], \end{aligned} \tag{8.50}$$

where $d^*_{t_i}$, $v^*_{t_i}$, and $a^*_{t_i}$ are the coefficients of first three Chebyshev polynomials in the new basis. Equating powers of t in Equations (8.49) and (8.50) gives the following relations:

$$\begin{aligned} d^*_{t_i} &= d_{t_i} + \frac{a_{t_i}}{4}, \\ v^*_{t_i} &= v_{t_i}, \\ a^*_{t_i} &= \frac{a_{t_i}}{4}, \end{aligned} \tag{8.51}$$

which are analogous to the expressions in Equation (8.47). Substituting Equation (8.51) into Equation (8.50) gives the following parameterization in terms of physical units:

$$d(t - t_i) = d_{t_i} + \frac{a_{t_i}}{4} + v_{t_i}(t - t_i) + \frac{a_{t_i}}{4}\left[2(t - t_i)^2 - 1\right]. \tag{8.52}$$

Since the subsegments are coherently combined at each iteration of the dynamic programming algorithm, a mathematical relationship between the distance, velocity, and acceleration along the line of sight at times t_{i-1} and t_i can be obtained from Equations (8.48) and (8.52) by equating powers of t:

$$\begin{aligned} d_{t_i} &= d_{t_{i-1}} + v_{t_i}t_i - \frac{a_{t_i}}{2}t_i^2 = d_{t_{i-1}} + v_{t_{i-1}}t_i + \frac{a_{t_{i-1}}}{2}t_i^2, \\ v_{t_i} &= v_{t_{i-1}} + a_{t_i}t_i = v_{t_{i-1}} + a_{t_{i-1}}t_i, \\ a_{t_i} &= a_{t_{i-1}}. \end{aligned} \tag{8.53}$$

These expressions provide a prescription for obtaining the pulsar's distance (d_{t_i}), velocity (v_{t_i}), and acceleration (a_{t_i}) at time t_i from the corresponding values at time t_{i-1}. They also resemble the Newtonian kinematic equations of motion for a particle moving with constant acceleration. These values are used to calculate the relative phase shift required in order to properly shift the folded profiles from each subsegment due to the pulsar's motion in its binary orbit. The acceleration-corrected period at the mid-time of the combined segment is computed using the expression for v_{t_i} in Equation (8.53), together with Equation (8.19). These calculations are mostly implemented within the resolving function. This computational machinery allows coherent phase-folded profiles to be constructed for any trial period and trial acceleration at each stage of the algorithm. A schematic diagram of this procedure is shown in Figure 8.6. This analysis can be generalized for jerk searches or any type of higher-order polynomial pulsar search, and corresponding mathematical transformations can be derived.

8.1.4.3 Convergence of the Dynamic Programming Algorithm

As mentioned in Section 8.1.4, the resolving function is extremely delicate, and a slight error in the implementation can result in a tremendous sensitivity loss due to improperly shifting the folded profiles when the results from the subsegments are added together at each iteration. In order to demonstrate that the dynamic programming algorithm is converged, we used a simulated time series containing pulsations from an accelerated pulsar with a known period and acceleration. In this section, I will show that the algorithm is converged when an acceleration search is performed.

I generated a simulated time series observation, spanning a duration of $T_{\rm obs} \approx 15$ min with a sampling time of $\Delta t = 32\ \mu$s, which contained Gaussian pulses from a pulsar with a rotational period of $P_{\rm spin} = 12.35$ ms and a projected acceleration along the line of sight of +2000 m/s^2. The Gaussian pulses were derived from a normal distribution with a standard deviation of $\sigma_{\rm psr} = 0.025$. The duty cycle of the pulsar, taken to be the full width at tenth maximum in this case, is $\delta = W_{\rm psr}/P_{\rm spin} \approx 2\sqrt{2\ln(10)}\sigma_{\rm psr} \approx 0.10$, which is comparable to the duty cycles of many of the known Galactic pulsars. The convergence tests shown here were carried out when: (1) a low amount of Gaussian noise, $\mathcal{N}(\mu = 0, \sigma = 0.00001)$, and (2) a modest amount of Gaussian noise, $\mathcal{N}(\mu = 0, \sigma = 0.025)$, were added to the time series.

In the dynamic programming algorithm, we define a tunable tolerance parameter, ξ, which has units of number of time bins across the pulsar's duty cycle ($P_{\rm spin}\delta/\Delta t$). This adjustable tolerance parameter controls the sensitivity of the algorithm. As ξ is reduced, the number of trial periods and trial accelerations in the parameter space $[P_{\rm spin,min}, P_{\rm spin,max}] \times [a_{\rm min}, a_{\rm max}]$ increases linearly with the reduction factor. For example, decreasing ξ by a factor of two increases the period resolution, $\delta P_{\rm spin}$, and the acceleration resolution, δa, both by a factor of two. However, when ξ is decreased, the computational complexity of the algorithm increases since there are more folded profiles that need to be computed for the additional number of trial periods and trial accelerations in the specified search range. The dynamic programming algorithm also has a tunable binning parameter, $\eta = n_{\rm bins}\delta$, which determines how many phase bins should be used to construct the folded profiles at each iteration. In this simulation, I fixed $\eta \approx 34.3$ so that 320 phase bins were always used during the folding process. This ensured that there was minimal sensitivity loss due to binning.

In Figure 8.7, I show that the acceleration search capability of the dynamic programming algorithm is converged. When a low amount of Gaussian noise, $\mathcal{N}(\mu = 0, \sigma = 0.00001)$, was added to the time series, the results in Figures 8.7(a) and (b) are obtained. Figures 8.7(c) and (d) show the results when a modest amount of Gaussian noise, $\mathcal{N}(\mu = 0, \sigma = 0.025)$, was added to the time series. The black curves in Figures 8.7(a) and (c) show the folded pulse profile that is obtained when the data are folded exactly on the pulsar's true rotational period and acceleration. The other curves correspond to the folded pulse profiles that are obtained when the tolerance parameter, ξ, is varied. For each value of ξ, I show the folded pulse profile that gives the highest S/N after matched filtering all of the folded pulse profiles generated for each trial period and trial acceleration with a Gaussian function. In this analysis, the acceleration search was performed blindly using trial periods between 11.11 and 13.59 ms and trial accelerations between –5000 and +5000 m/s^2. As the value of ξ is decreased, the resolution between trial periods and accelerations becomes finer, and the best folded Gaussian pulse profile becomes increasingly narrower until it is fully resolved.

Figures 8.7(b) and (d) show the computational complexity, i.e. runtime in seconds, when the dynamic programming is run with different values of ξ. For relatively small values of ξ, the computational complexity of the algorithm starts to increase dramatically. In this example, for $\xi \gtrsim 10$, the computational complexity plateaus, and increasing the value of ξ further does not significantly decrease the runtime since brute-force folding at the beginning of the algorithm dominates the computational complexity for larger values of ξ. This shows that when the dynamic programming algorithm is used in practice to search for pulsars, the search parameters must be chosen wisely in order to optimize both the desired sensitivity of the algorithm and the computational time required to blindly search the parameter space. Similar demonstrations, showing convergence of the dynamic programming algorithm, can be performed for other types of pulsar searches, such as jerk and higher-order polynomial searches.

8.1.4.4 Demonstrations of Pulsar Searching with the Dynamic Programming Algorithm

The dynamic programming algorithm is currently being used to search new and archival radio observations for undiscovered pulsars. To demonstrate the algorithm's effectiveness, I provide several examples showing that the algorithm is ca-

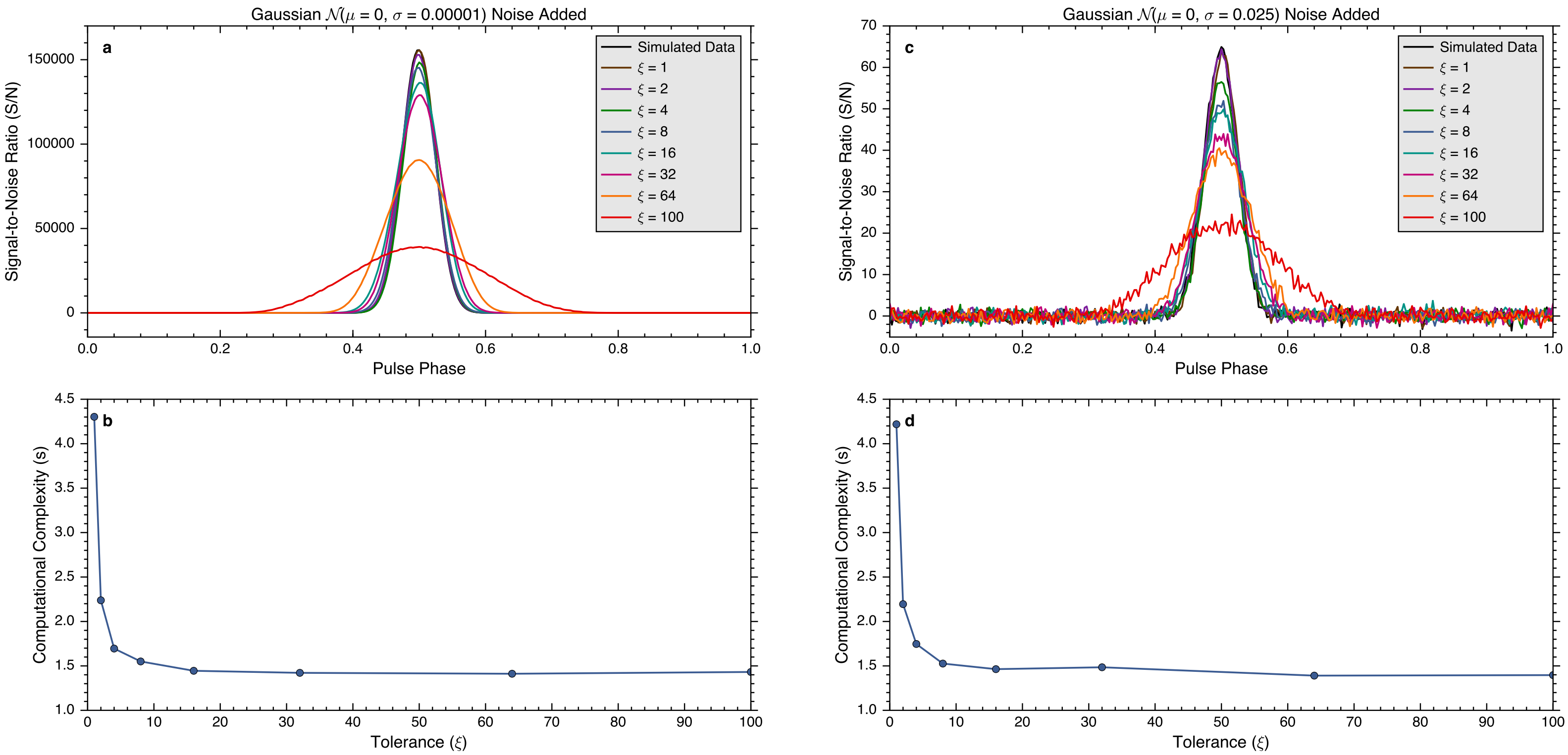

Figure 8.7: **Convergence of the acceleration search capability of the dynamic programming algorithm using simulated pulsar data.** The observation duration of the simulated data is $T_{\rm obs} \approx 15$ min, and the data are sampled at a time resolution of $\Delta t = 32\,\mu$s. The data contain Gaussian pulses, derived from a normal distribution with a standard deviation of $\sigma_{\rm psr} = 0.025$, which have been spaced periodically in time to give a rotational period of $P_{\rm spin} = 12.35$ ms and a projected acceleration along the line of sight of +2000 m/s^2. Panels (a) and (b) show the results when a low amount of Gaussian noise, $\mathcal{N}(\mu = 0, \sigma = 0.00001)$, was added to the data, and panels (c) and (d) show the results when a modest amount of Gaussian noise, $\mathcal{N}(\mu = 0, \sigma = 0.025)$, was added. The black curves in panels (a) and (c) show the folded pulse profiles when the data are folded using the true period and acceleration of the pulsar. The brown, purple, green, blue, teal, magenta, orange, and red curves in panels (a) and (c) show the folded pulses that yield the highest S/N when the tolerance parameter, ξ, is set to values of 1, 2, 4, 8, 16, 32, 64, and 100, respectively. The folded pulse profiles for each value of ξ were obtained by matched filtering all of the folded pulses produced for trial periods and trial accelerations in the specified search range. Panels (b) and (d) show the computational complexity (runtime in seconds) of the dynamic programming algorithm when a low and modest amount of Gaussian noise was added to the simulated data, respectively. When smaller values are used for the tolerance parameter, ξ, the "best" folded pulse profiles become increasingly narrower and approach the result obtained from folding the data with the pulsar's known rotational period and acceleration. However, for $\xi \lesssim 10$, the runtime of the algorithm starts to increase as ξ is to set to a smaller value.

pable of detecting various types of radio pulsars, including binary pulsars, isolated pulsars, and exotic MSPs in compact binary orbits. These results were obtained by performing acceleration searches using the dynamic programming algorithm.

The double pulsar system, PSR J0737–3039A/B, is a highly relativistic double neutron star binary with a 2.4 hr orbital period and a projected semi-major axis of $x = a_x \sin i = 1.42$ lt-s [68, 291, 340]. PSR J0737–3039A is a radio pulsar, which has a rotational period of 22.7 ms, and its binary companion, PSR J0737–3039B, is also a radio pulsar with a rotational period of 2.77 s. I used the dynamic programming algorithm to perform an acceleration search for the double pulsar, in order to demonstrate that the algorithm could blindly detect compact, relativistic binary radio pulsars, such as PSR J0737–3039A. A 2.6 hr *L*-band observation of the double pulsar, recorded with the Parkes radio telescope, was used to search for pulsations using the dynamic programming algorithm. After incoherently dedispersing the data at the pulsar's nominal DM of 48.92 pc cm^{-3}, the algorithm was easily able to detect pulsations from PSR J0737–3039A. The folded pulse profile obtained in the last iteration of the dynamic programming algorithm is shown in the top panel of Figure 8.8 using 64 phase bins. In the middle panel of Figure 8.8, I show measurements of the pulsar's observed rotational period, which is modulated due to Doppler shifts caused by the pulsar's motion in the binary orbit. These measurements were obtained by pausing the algorithm 7 iterations before the end and storing the pulse period that yielded a folded pulse profile with the highest S/N in each data segment. I have excluded rotational period measurements from data segments that significantly deviated from the overall trend in the middle panel of Figure 8.8 for clarity. The plots in the bottom panel of Figure 8.8 show the results when the data are folded using the timing ephemeris in [291].

In addition, I carried out an acceleration search for the known pulsars in the globular cluster Terzan 5 [459] using the dynamic programming algorithm. For this analysis, I used a radio observation spanning 7.1 hr, which was recorded in a polyphase filterbank using the GBT at a center frequency of 2 GHz with 128 frequency channels and a sampling time of 81.92 μs. The width of each frequency channel in the filterbank was 6.25 MHz. Coherent dedispersion was performed across each channel in the filterbank using the average DM of the pulsars in Terzan 5 in order to significantly reduce the effects of DM smearing across the band. The data were then incoherently dedispersed using fine trial DMs spaced around the nominal DMs of the known pulsars in the cluster. Trial DMs were spaced by 0.01 pc cm^{-3} during the incoherent dedispersion process. An acceleration search was then performed using the dedispersed time series associated with each DM trial.

Here, I show blind detections of an assortment of different types of pulsars in Terzan 5. Figure 8.9 shows blind detections of PSR J1748–2446A (Terzan 5A), an eclipsing redback pulsar with a rotational period of 11.56 ms, an orbital period of 1.82 hr, and a projected semi-major axis of 0.12 lt-s. The GBT observations used in this analysis covered ~4 orbital periods of PSR J1748–2446A, which can be directly observed in the middle panel of Figure 8.9 from rotational period measurements obtained when the dynamic programming was paused 8 iterations before the end.

Figures 8.10 and 8.11 show blind detections of two isolated MSPs, PSR J1748–2446C (Terzan 5C) and PSR J1748–2446D (Terzan 5D), which have rotational periods of 8.44 and 4.71 ms, respectively. Since these two pulsars do not reside in a binary, the middle panels of Figures 8.10 and 8.11 do not show significant changes in the pulsar's rotational period during the radio observations.

In Figure 8.12, I show detections of PSR J1748–2446G (Terzan 5G), an isolated pulsar with a rotational period of 21.67 ms. Blind detections of PSR J1748–2446L (Terzan 5L), an isolated 2.24 ms MSP with a duty cycle of ~40%, are shown in Figure 8.13. In addition, detections of the binary MSP, PSR J1748–2446N (Terzan 5N), are shown in Figure 8.14. PSR J1748–2446N has a rotational period of 8.67 ms, an orbital period of 9.3 hr, and a projected semi-major axis of 1.62 lt-s. Since PSR J1748–2446N was detected with lower S/N during this observation, when the dynamic programming was paused 8 iterations before the end, many of the data segments yielded unreliable rotational period measurements due to insufficient S/N in the folded pulse profiles. In the middle panel of Figure 8.14, rotational period measurements from data segments with folded pulse profiles with low S/N have been excluded. Although only ~40% of the data segments yielded credible rotational period measurements, the effects of the pulsar's binary motion can still be clearly observed in the middle panel of Figure 8.14.

8.2 A Novel Pruning Algorithm for Pulsar Searching

We are actively developing a new pruning algorithm that will be used to coherently and efficiently search for weak pulsations, with respect to the noise, when they are modulated by an arbitrary Keplerian orbit. As mentioned in Section 8.1.4.1, blindly searching for new pulsars by searching over all of the possible Keplerian parameters is extremely computationally expensive, and such searches are only possible if

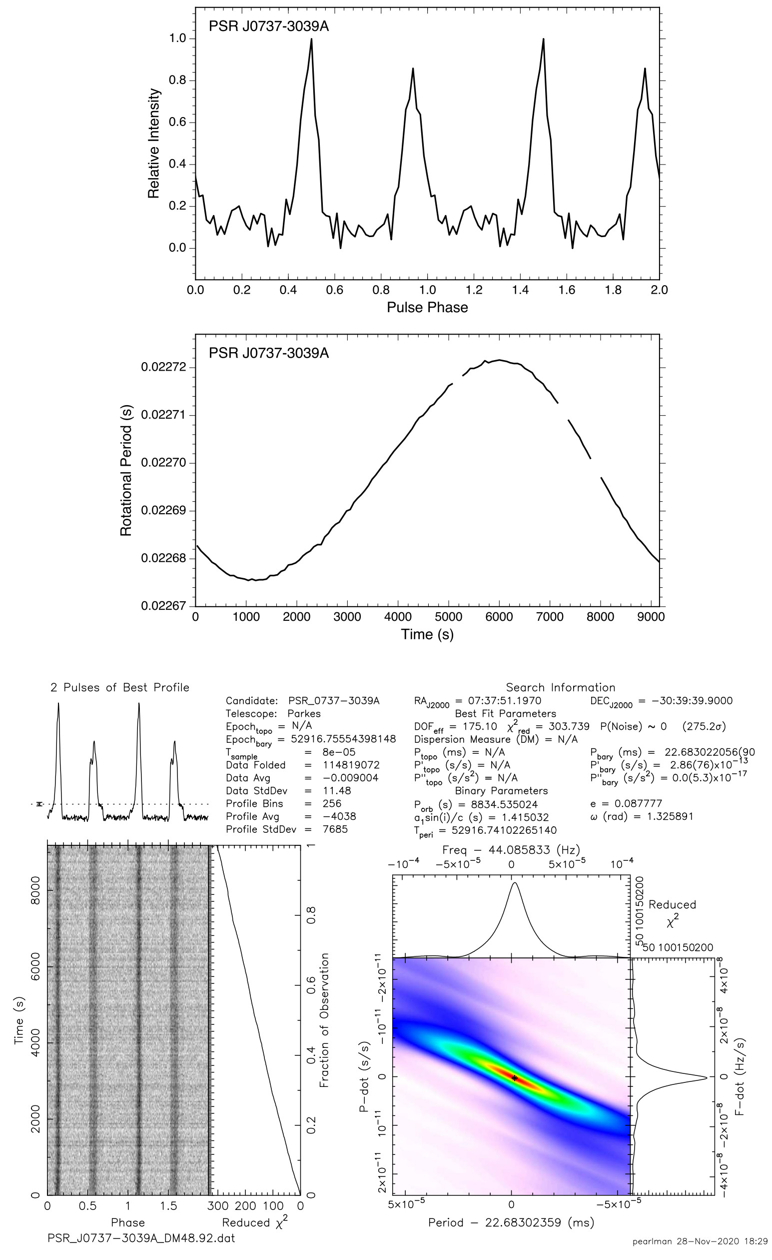

Figure 8.8: **Detection of the double pulsar, PSR J0737–3039A, during a blind acceleration search using the dynamic programming algorithm.** The top panel shows the folded pulse profile obtained during the last iteration of the algorithm, and the middle panel shows the change in the pulsar's measured rotational period due to Doppler shifts as the pulsar orbits its companion during the 2.6 hr observation with the Parkes radio telescope at 1.5 GHz, which covers a full orbital period. In the middle panel, I have excluded measurements from data segments where the measured rotational period significantly deviated from the overall trend, which are indicated by gaps. The bottom panels show the integrated and time-resolved folded pulse profiles after folding the Parkes data on the measured system parameters.

they are carried out on a distributed volunteer computing system over the internet. When the observation duration is longer than the pulsar's orbital period, the pruning algorithm described here will provide a speedup of $\sim 10^5$ when an acceleration search is performed and a speedup of $\sim 10^7$ when a jerk search is carried out. In particular, this technique will be extremely useful for detecting pulsars in tight binary orbits. Compact binary pulsars have already been used to perform some of the most exquisite tests of physics, including general relativity [16, 291, 543].

In order to optimally detect pulsations from an unknown pulsar in a binary orbit, it is necessary to correct for the pulsar's orbital motion. Such corrections typically require knowledge of the orbital parameters to exquisite precision. Blindly searching over all possible parameters associated with different orbital parameter values would require searching over $\sim 10^{15}$–10^{25} different options, in addition to the pulsar's rotational period and DM. Such types of searches are completely infeasible, so current search techniques restrict the length of the observations to be only a small fraction of the orbital period (e.g., see [458]). As a result, current search techniques suffer a tremendous loss in search sensitivity.

The pruning algorithm utilizes partial information that is accumulated during the integration of the data to exponentially narrow the parameter space and detect the faintest statistically significant signals from among a large list of potential orbital models. Here, I will provide a general overview of the pruning technique and the remarkable benefits that it provides when applied to pulsar searching.

The pruning technique that we are developing will be integrated into the dynamic programming algorithm as an additional step after each iteration. During the first iteration of the algorithm, the data is divided into data segments, and pulse profiles are computed by folding the data in each segment using a range of trial periods and Keplerian orbital parameters, for example. These results are stored in a data structure, containing the folded profiles for each set of trial parameters.

Suppose that there is a signal from a pulsar in the data, which has a S/N of $S = 12$ when the entire observation is used for folding in the final iteration. If the data are divided into N subsegments in the first iteration of the algorithm, then the S/N in each data segment after folding will be $S/\sqrt{N}$. Since the S/N in each of the subsegments will not be statistically significant, it is impossible to detect the pulsar using the smaller data segments individually. However, it is possible to decide whether specific folded pulse profiles show evidence of having a signal with a S/N of $S/\sqrt{N}$ buried in the noise. This allows exponential elimination of the search volume, which is achieved by this novel pruning technique.

The pruning algorithm proceeds using a tree-like enumeration scheme, where all of the possible pulsar models are enumerated and then eliminated if they do not pass the required S/N threshold at a given iteration. For instance, in the first iteration of the algorithm, only options that have folded pulse profiles with S/N $\geq S/\sqrt{N}$ are kept in the tree. All other options are eliminated permanently. In the next iteration, folded pulse profiles from pairs of segments are combined using the dynamic programming procedure described in Section 8.1.4. The S/N in the combined segment is now $\sqrt{2}S/\sqrt{N}$ since the results in each segment correspond to an integration time that is twice as long. However, since the data segment is longer, each of the parameters in the model now needs to be searched using higher resolution. In this iteration, only options that were not eliminated during the previous stage are split into new options that are no longer equivalent when integrating a longer section of the data. At the end of the second iteration, all options that did not produce folded pulse profiles with S/N $\geq \sqrt{2}S/\sqrt{N}$ are eliminated from the tree. This process is continued iteratively, where additional data are integrated at each stage and additional parameters are added to the model as the integration times of the data segments become larger, until the entire observation is combined into a single data segment. All options that yield folded pulse profiles with a S/N of $S \geq 12$ are then inspected to determine if they represent a newly discovered pulsar.

A schematic diagram of the pruning algorithm is shown in Figure 8.15. The pruning technique can be thought of as the iterative process of "expansion," where additional data are integrated and the phase space is extended to produce viable sets of parameters over longer integrations, followed by "elimination," where options that are inconsistent with a statistically significant signal are removed from the tree.

For a data segment of length $T_{\mathrm{seg},i}$ at stage i, the number of distinct possible parameterizations of a pulsar signal modulated by a Keplerian orbit scales as $T_{\mathrm{seg},i}^3$ for an acceleration search, $T_{\mathrm{seg},i}^6$ for a jerk search, and $T_{\mathrm{seg},i}^{10}$ for a fourth derivative search. The survival probability of a random option with a statistically significant signal at stage i is given by:

$$p_{\mathrm{survival},i} = \exp\left[-S^2 \frac{T_{\mathrm{seg},i}}{T_{\mathrm{seg},0}}\right], \tag{8.54}$$

which decreases exponentially as the data segment length, $T_{\mathrm{seg},i}$, is increased. This scaling is due to the fact that the detection S/N at stage i is proportional to $\sqrt{T_{\mathrm{seg},i}/T_{\mathrm{seg},0}}$, and the tail probability of a Gaussian variable is proportional to $\exp\left[-(\mathrm{S/N})^2\right] \propto \exp\left[T_{\mathrm{seg},i}/T_{\mathrm{seg},0}\right]$. Therefore, the total volume of options in the tree expands in a polynomial process at the beginning of the algorithm, but it rapidly decreases to zero since the parameter space is pruned exponentially during the elimination process. The elimination process begins to dominate when the integration time reaches $T_{\mathrm{seg},0}$, which corresponds to the required integration time for a S/N of 1.

For a polynomial pulsar search, the computational complexity of the expansion process is $\mathcal{O}(T^k_{\mathrm{seg},i})$, where $k = 3$, 6, and 10 correspond to acceleration, jerk, and fourth derivative pulsar searches. Therefore, the complexity of the pruning algorithm over a polynomial search space can be approximated as:

$$\mathcal{O}(T_{\mathrm{seg},i}, T_{\mathrm{seg},0}, k) \propto \int_0^{T_{\mathrm{seg},i}} t^k \exp\left[-\frac{t}{T_{\mathrm{seg},0}}\right] dt. \tag{8.55}$$

From Equation (8.55), in the limit where $T_{\mathrm{seg},i} \gg T_{\mathrm{seg},0}$, the computational complexity of the pruning algorithm becomes $\mathcal{O}(T_{\mathrm{seg},i}, T_{\mathrm{seg},0}, k) \propto T^{k+1}_{\mathrm{seg},0}\Gamma(k+1)$.

To illustrate the computational benefit of the pruning algorithm, consider the case of a jerk search. Let $C(T)$ denote the computational complexity of carrying out a jerk search on an observation of length $T = T_{\mathrm{obs}}$. Therefore, the computational complexity of a jerk search is $C(T) \propto T^6_{\mathrm{obs}}$. Suppose we stop the pruning algorithm one iteration before the algorithm is completed. In this case, there will be two data segments, which each have length $T_{\mathrm{obs}}/2$. The computational complexity of performing a jerk search in each subsegment is $C(T/2) \propto T^6_{\mathrm{obs}}/2^6$. However, since there are two data segments, the total complexity is $2C(T/2) \propto T^6_{\mathrm{obs}}/2^5$. Thus, there is computational benefit of roughly a factor of 32 in complexity by applying the pruning algorithm one stage before the end. The computational complexity is exponentially reduced when this pruning technique is applied at each iteration.

In general, the threshold scheme utilized in the pruning algorithm needs to be carefully adjusted so that the false alarm probability (Type I error) and false negative probability (Type II error) are optimized. Figure 8.16 shows a schematic diagram describing how the detection threshold is set for the special case where the probability that a pulsar signal is observed in the data, given that there *is* a detectable pulsar present, is $P(S \mid \mathrm{PSR}) = \mathcal{N}(\mu = 1, \sigma = 1)$, and the probability that a pulsar signal is observed in the data, given that there *is not* a detectable pulsar present, is $P(S \mid \mathrm{No\ PSR}) = \mathcal{N}(\mu = 0, \sigma = 1)$. The optimal threshold scheme is non-trivial, and we are currently exploring different strategies for optimizing the pruning process.

The pruning algorithm is under rapid development, and additional details are beyond the scope of this thesis.

8.3 Future Work

We are currently using the dynamic programming algorithm to search archival radio observations for new, exotic radio pulsars. This algorithm is also being used to carry out a sensitive search for new pulsars toward the Galactic Center at high frequencies using data from the DSN 70 m radio telescope, DSS-43. The results from these analyses are the subject of future work.

We are also adding additional features and improvements to the pruning algorithm, which will be used to coherently and efficiently search for new pulsars in Keplerian orbits with weak pulsations in different types of data sets. We anticipate that the pruning algorithm will be useful in other areas of astronomy, including searches for continuous gravitational-waves, detecting planets in complex binary configurations, searching for ultra-compact binary X-ray pulsars, and coherently integrating archival optical data to search for faint objects in the Solar system, such as the possible "Planet Nine."

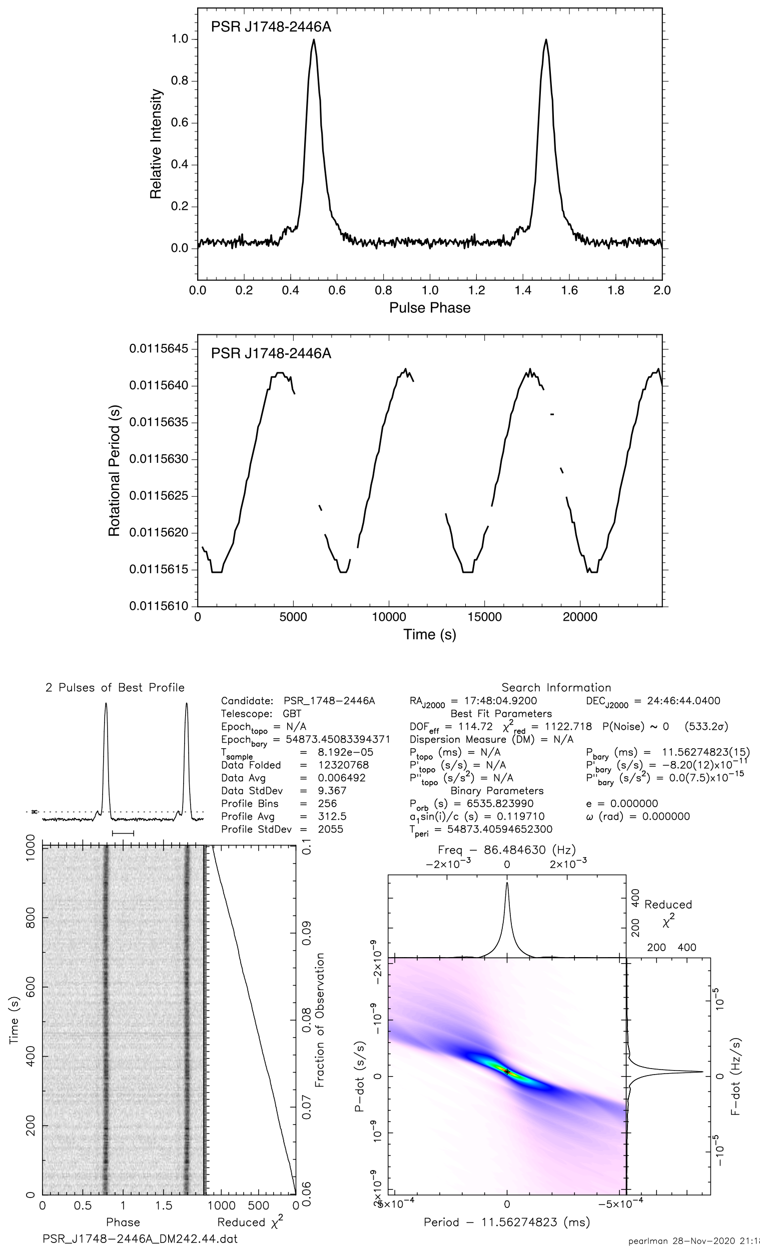

Figure 8.9: **Detection of PSR J1748–2446A (Terzan 5A) during a blind acceleration search for pulsars in Terzan 5 using the dynamic programming algorithm.** The top panel shows the folded pulse profile obtained during the last iteration of the algorithm, and the middle panel shows the change in the pulsar's measured rotational period due to Doppler shifts as the pulsar orbits its companion during the 7.1 hr observation with the GBT radio telescope at 2 GHz, which covers ~4 orbital periods. In the middle panel, I have excluded measurements from data segments where the rotational period significantly deviated from the overall trend, which are indicated by gaps. PSR J1748–2446A is an eclipsing redback pulsar with a rotational period of $P_{\rm spin} = 11.56$ ms, which resides in a binary system with a projected semi-major axis of $x = a_x \sin i = 0.12$ lt-s. The bottom panels show the integrated and time-resolved folded pulse profiles after folding the GBT data on the measured system parameters.

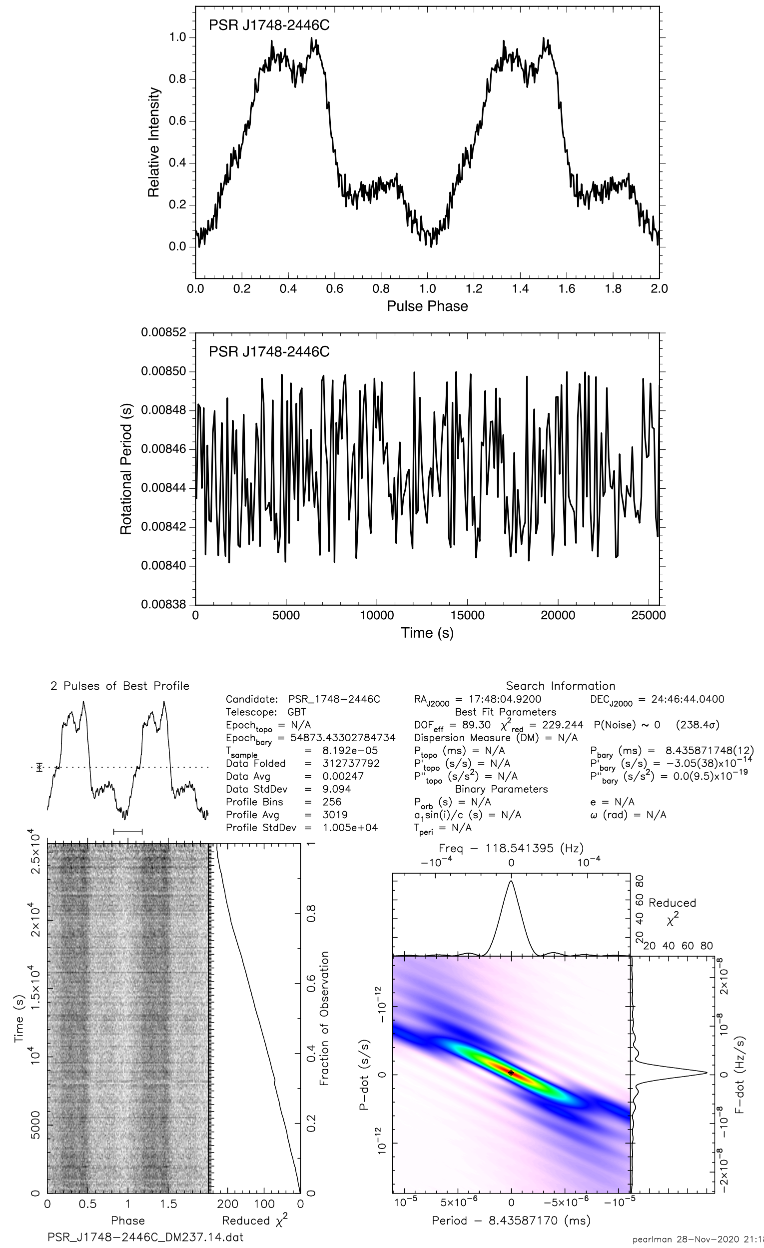

Figure 8.10: **Detection of PSR J1748–2446C (Terzan 5C) during a blind acceleration search for pulsars in Terzan 5 using the dynamic programming algorithm.** The top panel shows the folded pulse profile obtained during the last iteration of the algorithm, and the middle panel shows that there was no significant change in the pulsar's measured rotational period during the 7.1 hr observation with the GBT radio telescope at 2 GHz. PSR J1748–2446C is an isolated MSP in Terzan 5 with a rotational period of $P_{\mathrm{spin}} = 8.44$ ms. The bottom panels show the integrated and time-resolved folded pulse profiles after folding the GBT data on the measured system parameters.

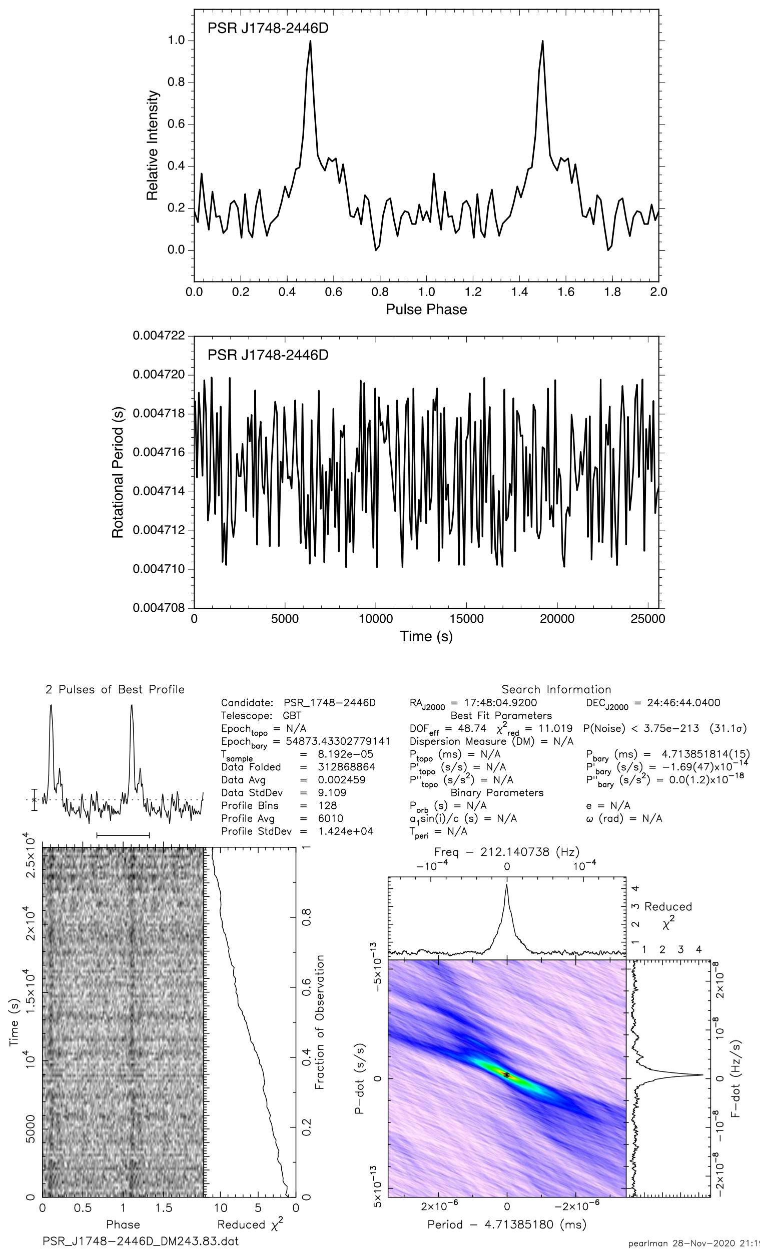

Figure 8.11: **Detection of PSR J1748–2446D (Terzan 5D) during a blind acceleration search for pulsars in Terzan 5 using the dynamic programming algorithm.** The top panel shows the folded pulse profile obtained during the last iteration of the algorithm, and the middle panel shows that there was no significant change in the pulsar's measured rotational period during the 7.1 hr observation with the GBT radio telescope at 2 GHz. PSR J1748–2446D is an isolated MSP in Terzan 5 with a rotational period of $P_{\text{spin}} = 4.71$ ms. The bottom panels show the integrated and time-resolved folded pulse profiles after folding the GBT data on the measured system parameters.

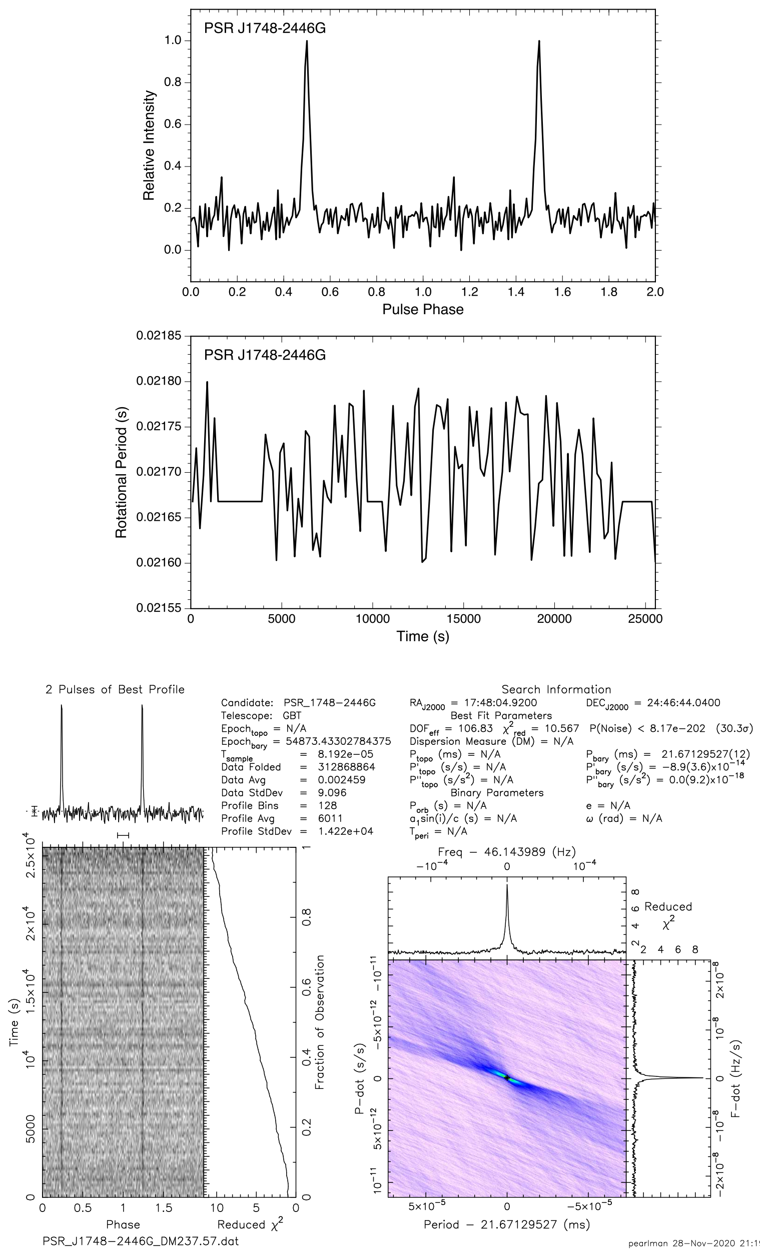

Figure 8.12: **Detection of PSR J1748–2446G (Terzan 5G) during a blind acceleration search for pulsars in Terzan 5 using the dynamic programming algorithm.** The top panel shows the folded pulse profile obtained during the last iteration of the algorithm, and the middle panel shows that there was no significant change in the pulsar's measured rotational period during the 7.1 hr observation with the GBT radio telescope at 2 GHz. PSR J1748–2446G is an isolated pulsar in Terzan 5 with a rotational period of $P_{\rm spin} = 21.67$ ms. The bottom panels show the integrated and time-resolved folded pulse profiles after folding the GBT data on the measured system parameters.

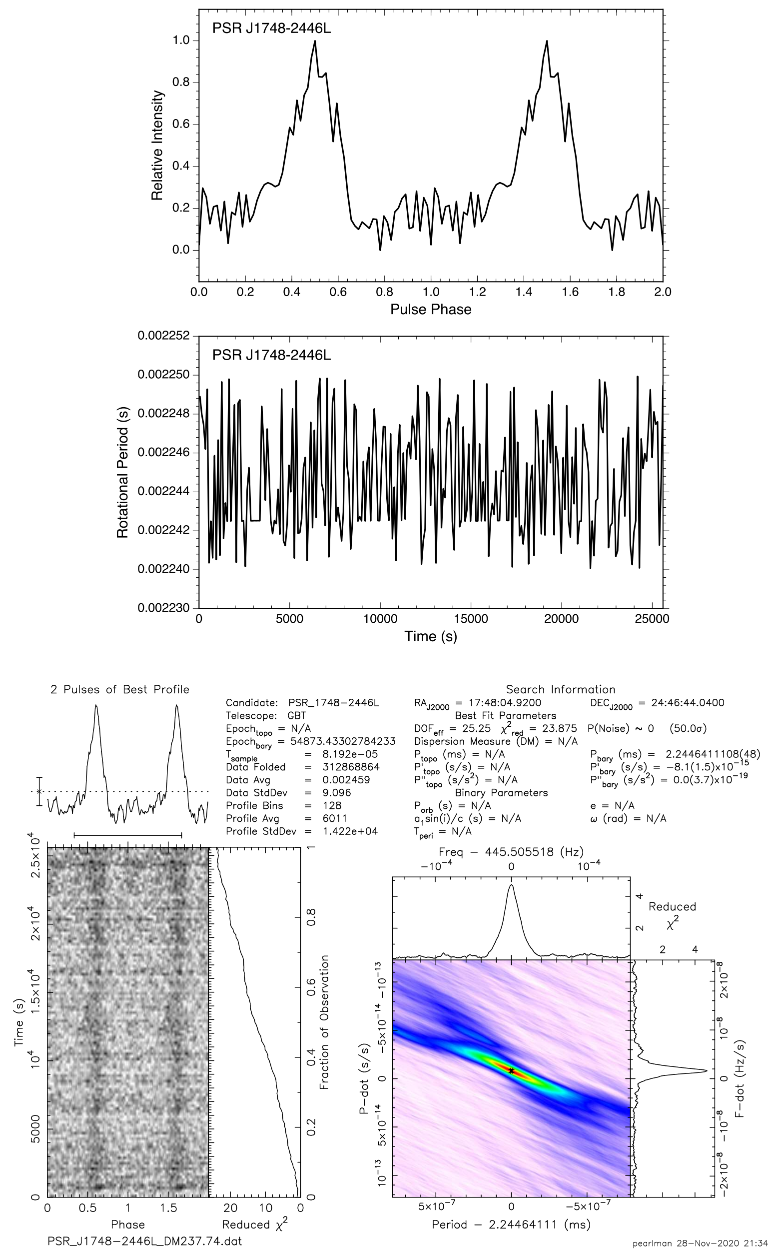

Figure 8.13: **Detection of PSR J1748–2446L (Terzan 5L) during a blind acceleration search for pulsars in Terzan 5 using the dynamic programming algorithm.** The top panel shows the folded pulse profile obtained during the last iteration of the algorithm, and the middle panel shows that there was no significant change in the pulsar's measured rotational period during the 7.1 hr observation with the GBT radio telescope at 2 GHz. PSR J1748–2446L is an isolated MSP in Terzan 5 with a rotational period of $P_{\text{spin}} = 2.24$ ms. The bottom panels show the integrated and time-resolved folded pulse profiles after folding the GBT data on the measured system parameters.

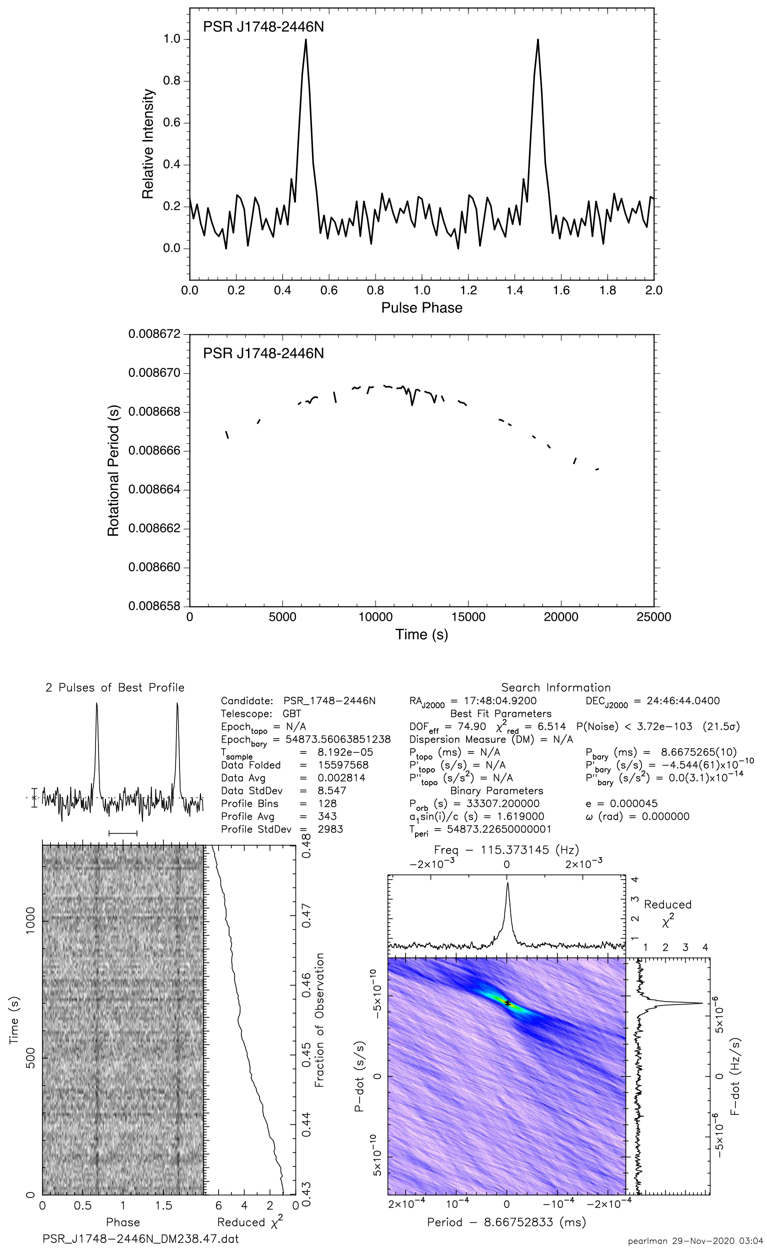

Figure 8.14: **Detection of PSR J1748–2446N (Terzan 5N) during a blind acceleration search for pulsars in Terzan 5 using the dynamic programming algorithm.** The top panel shows the folded pulse profile obtained during the last iteration of the algorithm, and the middle panel shows the change in the pulsar's measured rotational period due to Doppler shifts as the pulsar orbits its companion during the 7.1 hr observation with the GBT radio telescope at 2 GHz. In the middle panel, I have removed data chunks where the measured rotational period significantly deviated from the overall trend, which are indicated by gaps. PSR J1748–2446N is a binary MSP with an orbital period of 9.3 hr. The projected semi-major axis of the binary orbit is $x = a_x \sin i = 1.62$ lt-s, and the pulsar's rotational period is $P_{\rm spin} = 8.67$ ms. The bottom panels show the integrated and time-resolved folded pulse profiles after folding the GBT data on the measured system parameters.

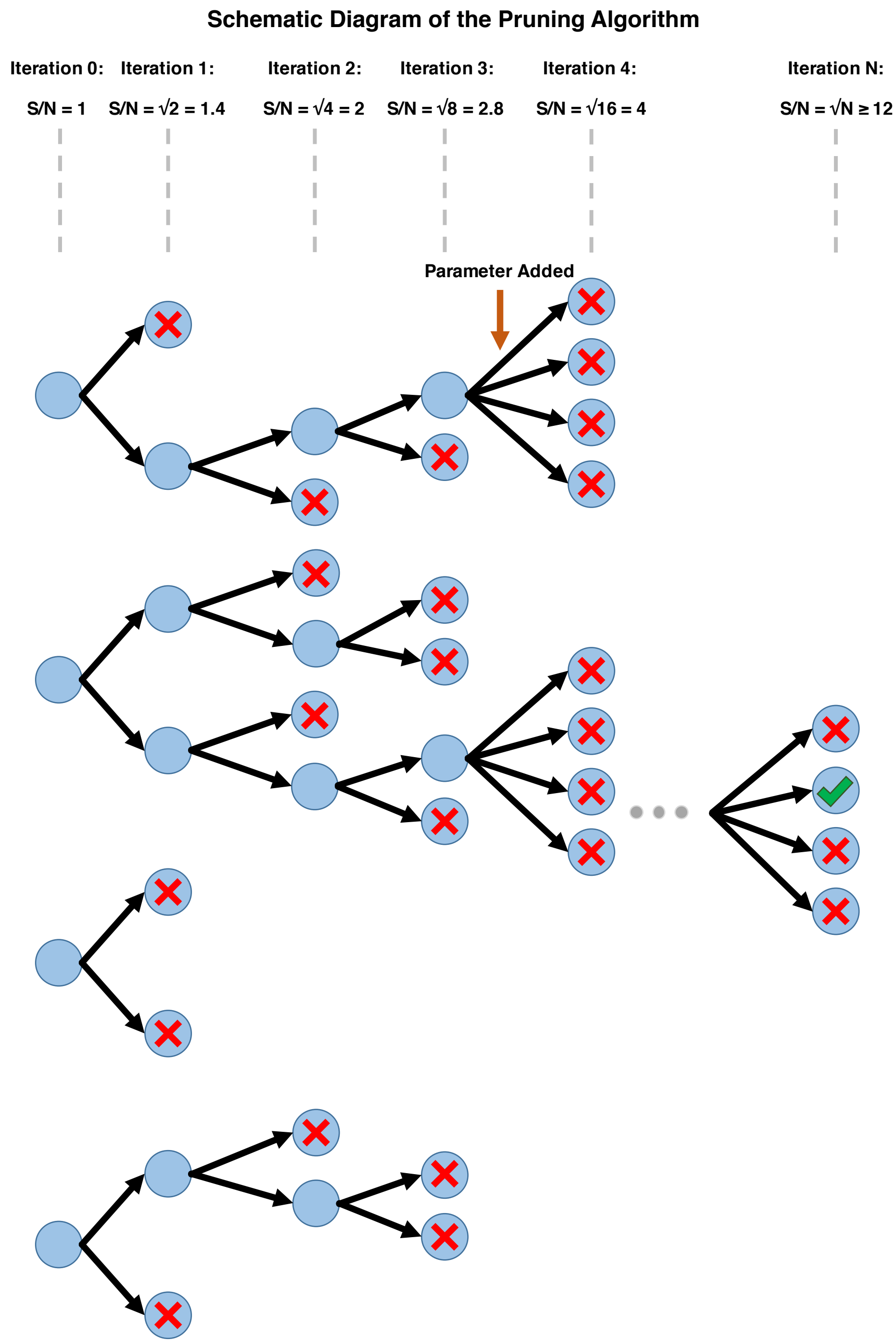

Figure 8.15: **Schematic diagram of the pruning algorithm.** Viable sets of pulsar parameters at each iteration of the pruning algorithm are indicated by blue circles without a red × overlaid. At each iteration, if a particular set of pulsar parameters do not yield a folded pulse profile with a S/N exceeding a specified threshold, it is eliminated from the tree and not used in future iterations. Additional parameters are added to the model, as needed, as the integration time of the data segments becomes larger during successive iterations. After all of the data are combined, pulsar parameters that produce a folded pulse profile with S/N $\geq$ 12 are saved in the final candidate list.

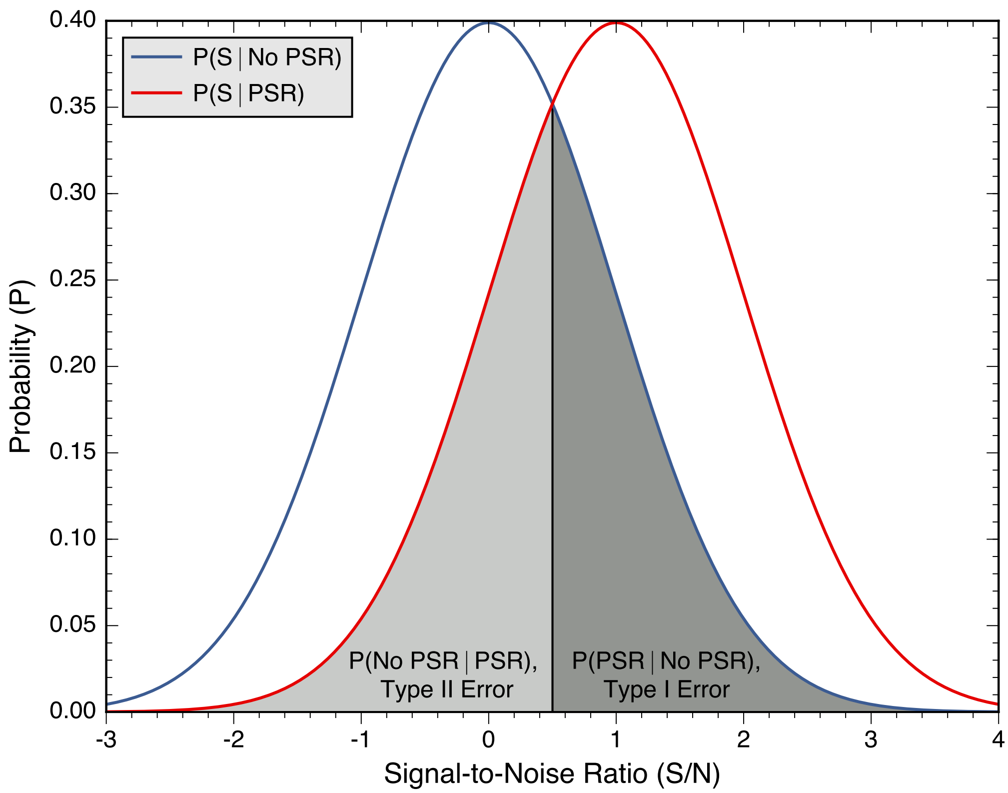

Figure 8.16: **Gaussian probability density functions (PDFs) illustrating the statistical decision theory for determining whether a pulsar is present in a given data chunk during a single iteration of the pruning algorithm.** Here, we assume that a Gaussian PDF, $\mathcal{N}(\mu = 0, \sigma = 1)$, represents the probability distribution of the data, given that there is no detectable pulsar present, $P(S \mid \text{No PSR})$, where S denotes the data. We also assume that a Gaussian PDF, $\mathcal{N}(\mu = 1, \sigma = 1)$, represents the probability distribution of the data, given that there is a detectable pulsar present, $P(S \mid \text{PSR})$. The Type I error and false alarm probability is given by $P_{\text{FA}} = P(\text{PSR} \mid \text{No PSR})$. The Type II error is given by $P(\text{No PSR} \mid \text{PSR})$. The detection threshold at each iteration is set by maximizing the probability of detection, $P_{\text{D}} = P(\text{PSR} \mid \text{PSR})$, subject to the constraint $P_{\text{FA}} = P(\text{PSR} \mid \text{No PSR}) = \alpha$. This is the Neyman-Pearson (NP) approach to signal detection.

Chapter IX

Searches for Radio Pulsars Toward the Center of the Milky Way Galaxy

This chapter provides an overview of the scientific content of several papers that are being prepared for publication.

9.1 A Pulsar Enigma at the Galactic Center

The Galactic Center (GC) harbors a supermassive black hole (SMBH), designated Sgr A*, which has a mass of $4 \times 10^6\, M_\odot$ [199, 202]. Pulsars at the center of our Galaxy can be used to carry out new tests of fundamental physics, including tests of general relativity and black hole (BH) physics, in an ultra strong-field regime of gravity [167, 324]. GC pulsars can also be used to study star formation, stellar dynamics, stellar evolution, the interstellar medium, and the accretion flow of the Milky Way's SMBH (Sgr A*) [61, 100]. In particular, the detection of a single stable pulsar orbiting the SMBH at the GC would enable measurements of the BH's mass, spin, and quadrupole moment with a precision better than any other method [61].

Thousands of pulsars are predicted to exist in the GC based on the high star formation rate and density of massive stars [439]. However, only six pulsars have been detected within 30' (~70 pc) of the central BH [152, 258] (see Figure 9.1), one of which is a rare, highly variable radio magnetar (PSR J1745–2900, dubbed the GC magnetar) orbiting at a projected distance of ~2.4" (0.1 pc) from the massive BH [63]. The GC magnetar cannot be used to study dynamical or strong-field gravity effects near Sgr A* due to its erratic timing stability [267]. All of these pulsars, except for the GC magnetar, are believed to be foreground objects and not gravitationally bound to the central BH. Although a significant population of pulsars is predicted to exist at the GC, the failure to detect radio pulsars is typically attributed to hyperstrong scattering along the line of sight [122]. A radio image of the Galactic Center formed using the MeerKAT array of 64 dishes in South Africa is shown in Figure 9.2. In order to overcome these effects, sensitive high frequency radio observations are needed because the temporal scattering that broadens pulsations is a strong function of frequency ($\tau_d \propto \nu^{-4}$).

The lack of detected pulsars at the Galactic Center (GC) poses an enigma. Previous searches for radio pulsars have yielded no detections within 10' (~25 pc) of Sgr A* [34, 152, 258, 288, 349, 494]. Although a significant population of pulsars orbiting Sgr A* has been predicted [67, 439], the failure to detect any radio pulsars is typically attributed to large temporal scattering and dispersion toward the GC [122, 555]. The GC magnetar is the most recently discovered and nearest radio pulsar to Sgr A*. It was serendipitously found in 2013 after a strong X-ray outburst was observed by the *Swift* X-ray Telescope [274]. Follow-up observations of the

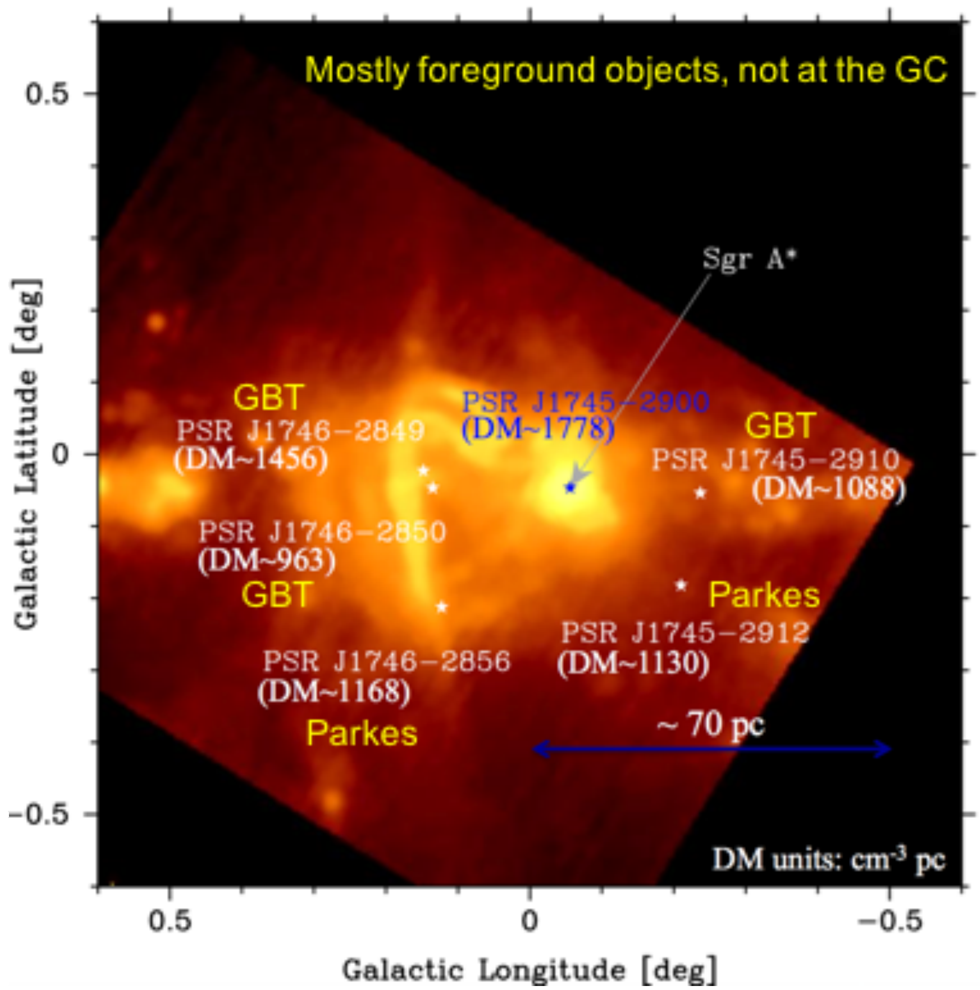

Figure 9.1: **Positions of detected radio pulsars within the central 0.5° of the GC.** The five GC pulsars that are believed to be foreground objects are labeled using white stars, and the GC magnetar is indicated by a blue star. The GC pulsars are overlaid on a 10.55 GHz continuum map from observations with the Effelsberg radio telescope [485]. The DMs and radio telescopes used to discover each GC pulsar are indicated. Assuming a distance of 8.3 kpc to the GC, 0.5° corresponds to a projected distance of ~70 pc. Image adapted from [167].

object using the *NuSTAR* hard X-ray telescope revealed pulsations at a period of 3.76 s [396]. The pulsar was classified as a magnetar, i.e. a neutron star whose emission is powered by the decay of its ultra-high magnetic field, based on the nature of the outburst and its emission properties. Magnetars are exceptionally rare objects and comprise only ~0.2% of the total radio pulsar population, which are mostly normal ("canonical") rotation-powered pulsars.

The detection of the GC magnetar raised many unanswered questions. Why should the first pulsar to be detected in the GC region be a rare magnetar? Second, while the magnetar's dispersion measure (DM) and pulse broadening timescale (τ_d) are large ($\mathrm{DM} = 1778 \pm 3\,\mathrm{pc\,cm^{-3}}$ [169] and $\tau_d = 1.3 \pm 0.2$ s at 1 GHz [498]), they are not so large that they would prevent the detection of other normal radio pulsars with spin periods $\gtrsim 1$ s if they had similar dispersion and scattering properties. If the magnetar's dispersion and scattering properties are representative of other objects in the GC region, then why has a population of normal rotation powered pulsars not been found? This is known as the "missing pulsar problem" [156, 348].

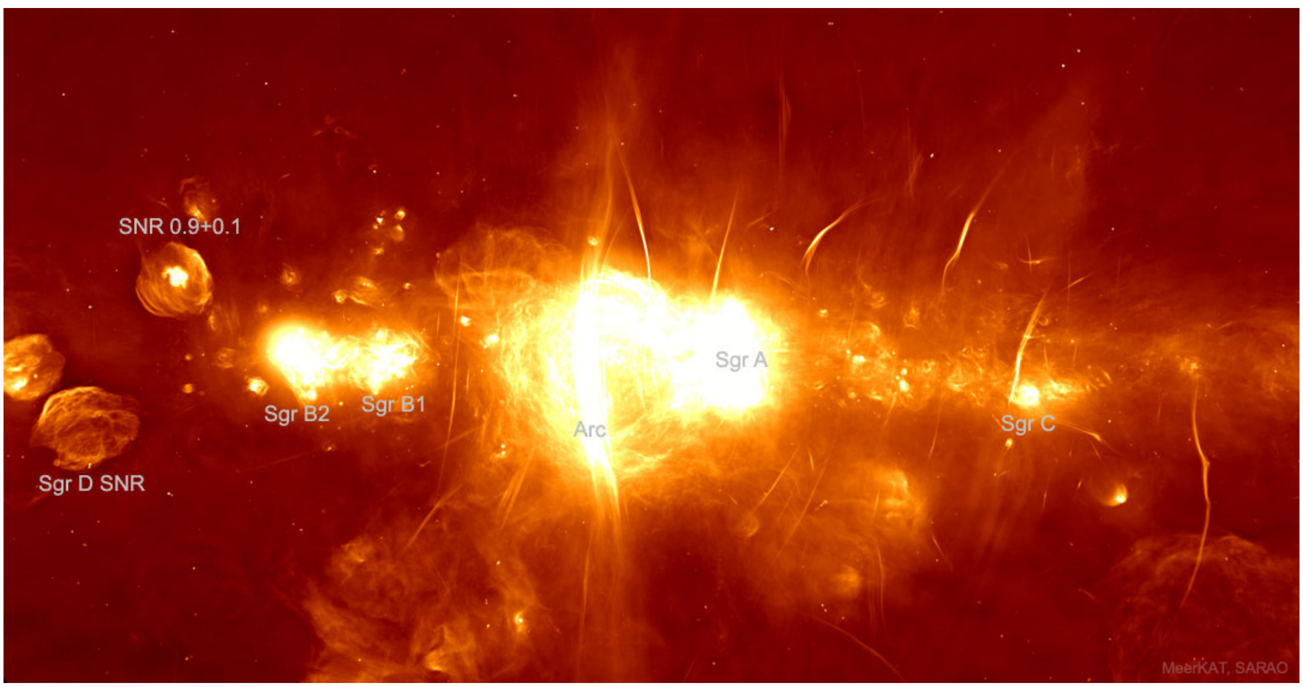

Figure 9.2: **Radio of the image of the Galactic Center region obtained using the MeerKAT array.** The MeerKAT array is comprised of 64 radio antennas, which are each 13.5 m in diameter. They are located on baselines (distances between antenna pairs) of up to 8 km. Image credit: MeerKAT and SARAO.

9.2 The Pulsar Population and Stellar Environment at the Galactic Center

Here, I will summarize a few of the observational and theoretical estimates of the GC pulsar population available in the literature.

• *Multiwavelength estimates:* Wharton et al. [555] discuss multi-wavelength constraints on the pulsar population at the GC, including radio and γ-ray measurements of the diffuse emission, infrared observations of massive star populations in the central few parsecs, estimates of core-collapse supernova rates, etc... Both low- and high-frequency pulsar searches were taken into account, including those mentioned in Section 9.1 [152, 258, 349]. The authors conclude that the observations are consistent with a population of up to 100 canonical pulsars and up to 1000 MSPs in the inner parsec of the GC that are beamed toward Earth.

• *Deficit of canonical pulsars:* Dexter and O'Leary [156] estimate that ∼10 canonical pulsars should have been detected by existing surveys (e.g., at 5 GHz). Based on this, they conclude that the canonical pulsar population in the inner parsec is anomalous.

• *MSPs from disrupted globular clusters:* Brandt and Kocsis [67] discuss a model of a population of MSPs arising from disrupted globular clusters that formed in the nuclear bulge of the Galaxy. They estimate that ∼1000 MSPs should be present with 3 pc of Sgr A*, and about 100 MSPs should reside within 1 pc. Since the beaming fraction for MSPs ($f_{\rm MSP} \gtrsim 0.5$) is thought to be larger than that of canonical pulsars ($f_{\rm PSR} \sim 0.1$), a large fraction of the MSP population may be potentially observable.

To summarize, various studies have estimated a population of perhaps ∼100 potentially observable canonical pulsars within the inner few parsecs of the GC, as well as a population of ∼1000 MSPs. These estimates indicate that there is plausibly a significant population of pulsars in the GC, but this is not yet definitive.

Numerous papers have attempted to explain the dearth of GC pulsars detected thus far. These explanations generally fall into three categories:

• *The scattering toward the magnetar is anomalous.* A significant pulsar population exists at the GC, but most lines of sight are plagued with much higher scattering than the line of sight to the magnetar [498]. This has prevented the detection of canonical radio pulsars.

• *The scattering is not anomalous.* However, the luminosity and luminosity evolution of pulsars in the GC are such that the non-detection of pulsars in previous surveys is not surprising (e.g., see [97]).

• *The radio pulsar population in the GC is anomalous.* The conditions in the GC are conducive to short-lived magnetars, but not longer-lived rotation-powered pulsars. There are several variants of this explanation, some of which invoke high magnetic fields in the GC, an anomalous stellar initial mass function, or dark matter (e.g., see [66, 97, 156]).

Determining the population of normal and MSPs in the GC region and how it is linked to the Milky Way's central BH is a major goal of modern astrophysics.

9.3 Fermi Excess Gamma-Ray Emission

Over the past several years, a number of groups have identified excess γ-ray flux toward the inner 1° of the GC, with even more significant excess emission within 0.2°, using data from the Large Area Telescope (LAT) on board NASA's *Fermi* Gamma-ray Space Telescope [2, 234, 235, 580] (see Figure 9.3). Hooper et al. [236] argued that the excess signal is consistent with dark matter annihilation in a halo distribution around Sgr A*, and no more than ~10% of the emission can be attributed to MSPs in the GC. On the other hand, Abazajian [1] claimed that the spectrum is consistent with γ-ray emission from massive stellar globular clusters containing a population of MSPs. In particular, the spectral index, exponential cutoff, and peak flux energy of the γ-rays in this region is consistent with four of the eight *Fermi*-LAT detected globular clusters reported by Abdo et al. [5]. The γ-ray emission from globular clusters is expected to be dominated by MSP emission due to enhanced binary formation in these systems, where MSPs are spun up by accretion from their binary companions. Five out of eight of the globular clusters detected by the *Fermi*-LAT harbor MSPs [5]. Therefore, it is likely that the detection of the peaked γ-ray spectrum towards the GC stellar cluster is due to a population of MSPs bound within this massive stellar cluster.

As stated by Abazajian and Kaplinghat [2], Occam's razor would dictate a conservative interpretation that strongly prefers an astrophysical source population, particularly a centrally concentrated MSP population. Wharton et al. [555] estimated the MSP population using a similar technique to obtain the number of MSPs in globular clusters [5]. They conclude that $\sim 10^3$ MSPs in the inner tens of parsecs from Sgr A* should contribute to the γ-ray excess reported by Hooper and Goodenough [234].

An important, unanswered question in GC science is whether dark matter or a population of MSPs is responsible for the excess γ-ray emission observed by the

Fermi telescope toward the center of the Galaxy. Numerous papers weigh-in on this debate, including those that: (1) favor dark matter (e.g., see [88, 99, 148, 234, 235, 236, 320]), (2) favor an origin from MSPs (e.g., see [30, 31, 32, 310, 410, 437, 580]), and (3) are neutral or prefer other explanations (e.g., see [2, 3, 209, 237]). The question of whether or not there is a population of MSPs in the GC region is critical because of the astrophysical importance of dark matter.

9.4 Fundamental Physics with Galactic Center Pulsars

The region around Sgr A* is an ideal laboratory for extreme astrophysics. In Figures 9.4 and 9.5, I show a diagram of the distances and mass scales relevant to the GC. Over two decades of infrared (IR) monitoring of ~30 stellar objects in the center of the Galaxy has yielded a mass of $4 \times 10^6\,M_\odot$ for Sgr A* [199, 202], unambiguously classifying the object as a SMBH. The detection of a single stable pulsar in this region at distances similar to these IR stars would serve as a probe of strong-field gravity and allow for novel tests of general relativity in the strong-field regime through measurements of time dilation, gravitational redshifts, frame dragging, Shapiro delays, and possibly even the spin of the BH (e.g., see [324, 439]). Any MSP found within 1 pc of the GC would be highly significant to the field

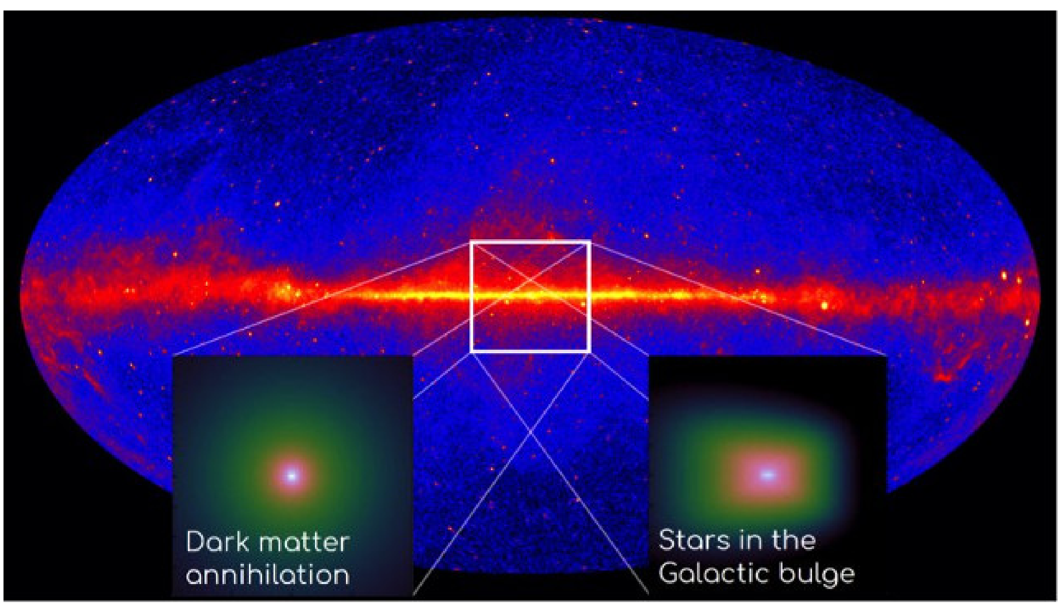

Figure 9.3: **Excess γ-ray emission observed by the Large Area Telescope (LAT) on board NASA's *Fermi* Gamma-ray Space Telescope.** A smooth distribution of high-energy photons is expected to be produced by dark matter annihilation, whereas a clumpy photon distribution is expected for point sources, such as MSPs [310]. Image credit: *Fermi* LAT Collaboration.

of observational astrophysics. Not only would a detection shed light on the origin of the excess γ-ray emission at the GC, but it would also serve as a sensitive probe of the stellar and gravitational environment of the GC, including the stellar mass distribution in the inner parsec.

Pulsar timing measurements of GC pulsars can also be used to track their orbits around the central BH [322]. Currently, astrometric precisions of roughly a few mas (e.g., see [164]) are achievable through IR monitoring of S stars at the GC, which correspond to a positional uncertainty of $\Delta x \approx 10^9$ km at 8.3 kpc. Next generation IR experiments are expected to achieve astrometric precisions of ~10 μas ($\Delta x \approx 10^7$ km at the GC) [554]. Since MSPs are highly precise astrophysical clocks [509], their pulse arrival times can be used to accurately track their orbit and probe information about the space-time around the central BH [63, 100, 324, 439, 585]. However, timing measurements of a GC pulsar with a precision of just a few milliseconds would yield an astrometric precision of $\sim 2 \times 10^{-4}$ μas, which corresponds to a positional uncertainty of $\Delta x \approx 10^3$ km at 8.3 kpc. This represents an improvement of 4–5 orders magnitude over future state-of-the-art IR instruments [554]. Therefore, modest timing measurements of a GC pulsar orbiting Sgr A* would enable an unprecedented study of stellar dynamics at the GC.

Although general relativity is empirically accurate to high precision, most tests that have been conducted are in the weak-field regime, with the exception of compact binary pulsars [16, 291, 513, 514]. Pulsars offer a unique opportunity for probing the space-time environment of a massive BH in the strong-field regime. Due to the large mass of Sgr A*, pulsar timing measurements of even a slowly rotating pulsar in a short-period orbit with the central BH, with a modest timing precision of 100 μs, will be sufficient to: (1) measure the mass of Sgr A* with a precision of $\sim 1\ M_\odot$, (2) test the cosmic censorship conjecture to a precision of about 0.1%, and (3) test the no-hair theorem for black holes to a precision of $\lesssim 1\%$.

Binaries consisting of a pulsar and a BH are considered a "holy grail" of astrophysics due to their significance for stellar evolution and their potential application as probes of strong gravity [184]. In addition to enabling quantitative measurements of the no-hair properties [323, 324, 450] and quadrupole moment of a BH [450, 553], the detection of a pulsar–BH binary would provide new opportunities for probing gravitational theories involving massive scalar and vector fields, as well as gravitational collider physics, by measuring the orbital decay rate (e.g., see [163, 490]). Pulsar–BH binaries could also be used to place new constraints on scalar-tensor gravity [145, 176, 324] and high curvature gravitational theories [571]. In addition, these systems may enable new tests of quantum gravity [177] and allow for limits to be set on the size of extra spatial dimensions [495].

9.5 A New High Frequency Search for Pulsars Toward the Galactic Center

The enigma of the GC pulsar population, as well as the origin of the excess γ-ray emission observed toward the GC, will only be convincingly solved through new observations. Observationally, detecting MSPs at the GC is more challenging than detecting canonical pulsars because of pulse broadening. However, sensitive high frequency radio searches will mitigate these effects (see Figure 9.6).

9.5.1 A Premier Ultra-Wideband K-band Pulsar Search Machine at the Deep Space Network

We are presently carrying out a new, deep high frequency search for radio pulsars at the GC using the DSN's 70 m radio telescope (DSS-43) in Tidbinbilla, Australia [424]. We have recently outfitted this instrument with a state-of-the-art pulsar

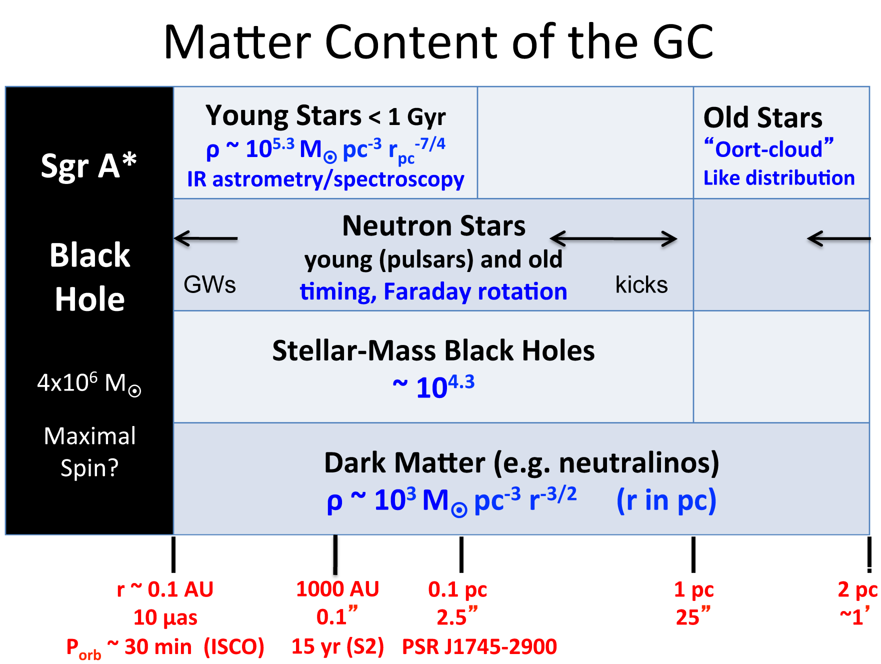

Figure 9.4: **Schematic view of the matter content of the GC. Young stars (e.g., S0-2) are known to approach as close as 0.1" (1000 AU) to Sgr A*.** The combination of young, hot stars in the GC and mass segregation suggests that there are likely to be compact stellar remnants (neutron stars and BHs) at least within 1000 AU and potentially much closer. Image and caption adapted from [167].

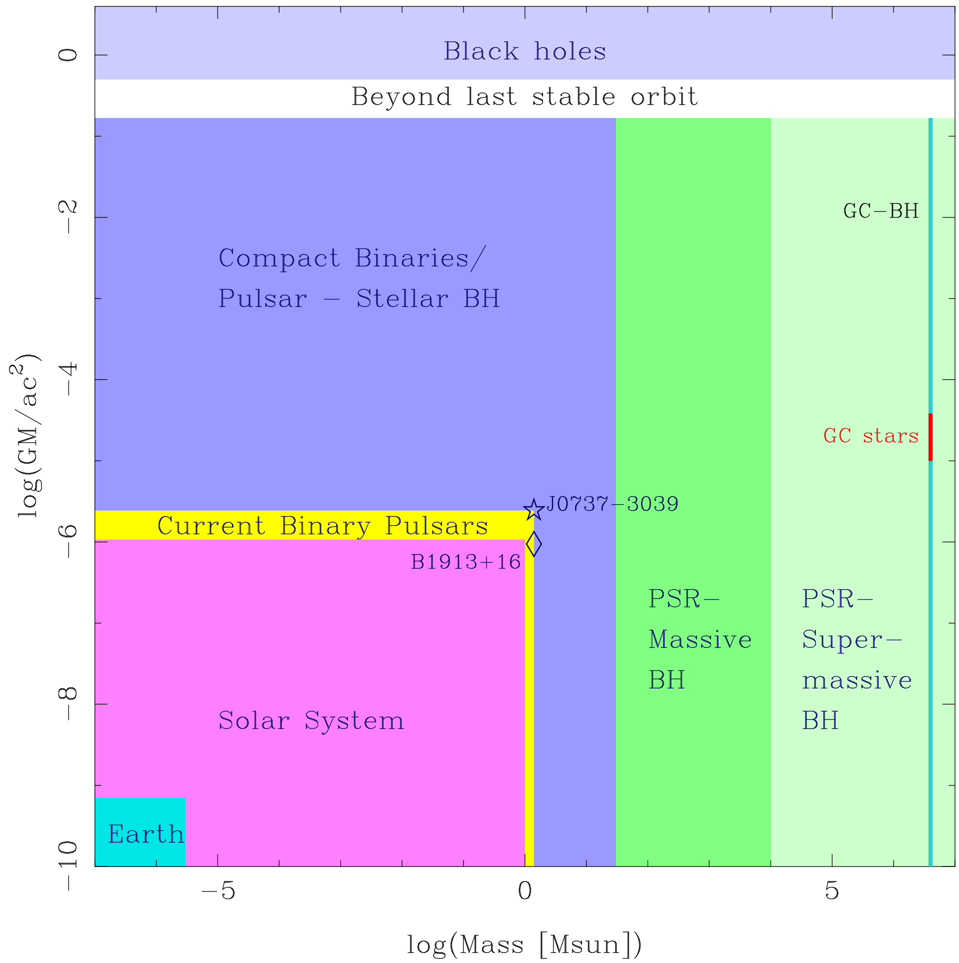

Figure 9.5: **Depth of the gravitational potential (GM/ac^2) probed by an orbit of semi-major axis a as a function of the mass of the binary system, M.** The regions probed by solar system tests and known pulsars in binary system are indicated, with the double neutron star systems PSR B1913+16 and PSR J0737–3039 shown explicitly. The vertical cyan line indicates the mass of Sgr A*. The red line segment shows the region probed by the S stars in the GC. This figure shows that substantially deeper gravitational potentials (larger GM/ac^2) remain to be probed, which could be studied using pulsars and BHs. Image credit and caption adapted from [167, 289].

machine that is capable of performing dual polarization observations of radio pulsars between 17–27 GHz (K-band) with 64 μs time resolution and 16 GHz of total bandwidth.

While observations at high radio frequencies aid in reducing the impact of scattering when searching for new pulsars, the pulsed radio emission observed from pulsars is fainter in most cases since they have steep radio spectra, with a flux density given by $S_\nu \propto \nu^\alpha$, where ν is the observing the frequency and $\langle\alpha\rangle = -1.8$ is the average spectral index [372]. We compensate for this by observing the GC with DSS-43,

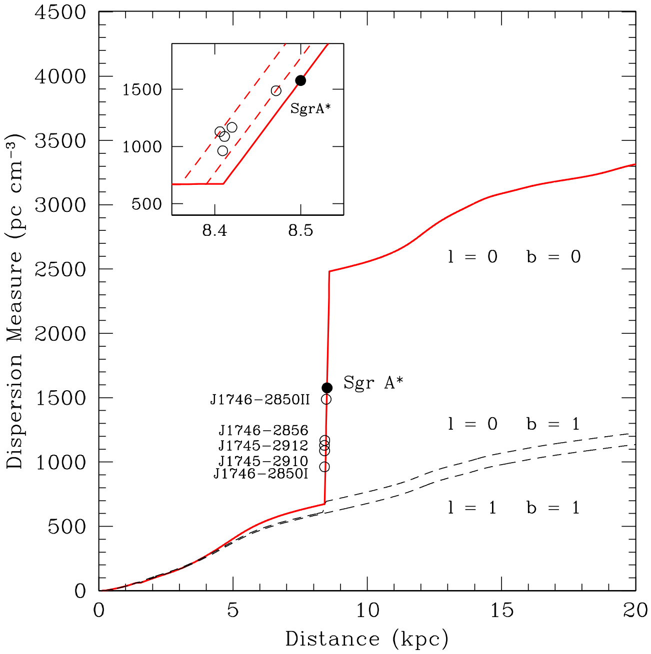

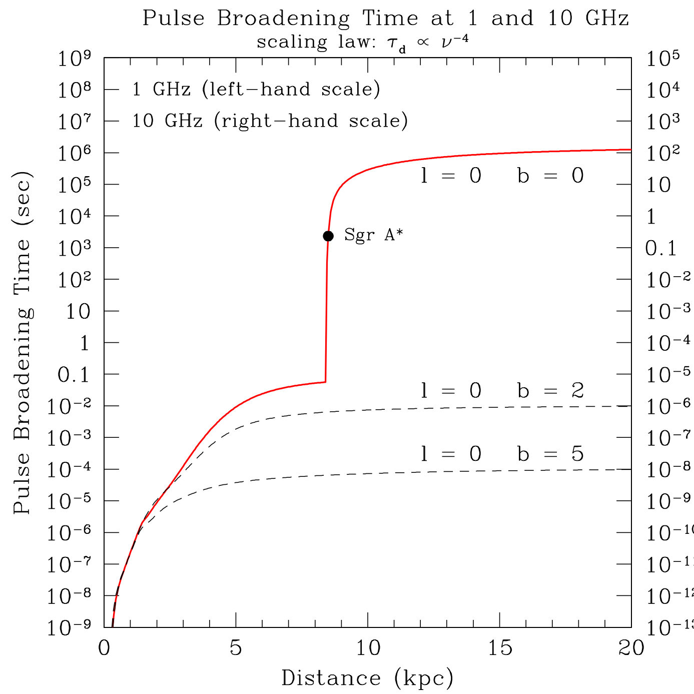

Figure 9.6: **DM and pulse broadening timescale along line of sights toward the inner Galaxy.** Left panel: Expected DM versus distance for several lines of sights toward the inner region of the Galaxy, based on the NE2001 Galactic electron density model [124]. The inset panel shows the expected DM versus distance for lines of sights to five of the known pulsars within 1° of Sgr A*. Objects located near Sgr A* have expected DMs $\gtrsim 1500\,\mathrm{pc\,cm^{-3}}$. Right panel: Pulse broadening timescale versus distance for several lines of sight toward the inner Galaxy. The vertical scale on the left shows the pulse broadening timescale for an observing frequency of $\nu = 1$ GHz, and the vertical scale on the right corresponds to the values for $\nu = 10$ GHz, assuming a $\tau_d \propto \nu^{-4}$ scaling law. In both the left and right panels, the vertical part of the curves, for a line of sight toward Sgr A*, is produced by dense scattering around the GC. Images adapted from [122, 152].

a large, single dish radio telescope with high instantaneous sensitivity, using the *K*-band pulsar backend, which is capable of recording high time resolution data across a large bandwidth.

The analog portion of DSS-43's *K*-band system produces 40 IFs over the 17–27 GHz frequency range. The bandwidth of each IF is 1 GHz [295]. A wideband down converter at DSS-43 is used to distribute these IFs to a new digital spectrometer, which functions as the pulsar backend. The spectrometer consisters of four CASPER Reconfigurable Open Architecture Computing Hardware 2 (ROACH-2) boards, which is capable of processing 16 of the 1 GHz IFs simultaneously.[y]

[y] See https://casper.ssl.berkeley.edu/wiki/ROACH2.

Each ROACH-2 board has two CASPER analog-to-digital converter (ADC) cards, a field-programmable gate array (FPGA), and a PowerPC microprocessor. The ADC cards process 8-bit sampled data at a rate of 5 gigasamples s^{-1}. Each ADC card has two inputs, which provides a total of four inputs to each ROACH-2 board. Four of the 1 GHz IFs are input into each of the ROACH-2 boards.

A Valon 5009 dual frequency synthesizer is used to control the 2 GHz clock for each of the ROACH-2 boards. The input to the Valon synthesizer is a 10 MHz reference signal, which is provided by the Frequency and Timing Standard system available at the DSN complex (CDSCC). The ROACH-2 boards are controlled using a Python-based software suite that is run on a Dell PowerEdge R510 server. The server is connected to the CDSCC's Local Area Network (LAN), and the ROACH-2 boards are connected to the server using a network switch. The ROACH-2 boards form an internal network behind the switch.

The data from each 1 GHz IF are accumulated by the ADC cards to give 32 bit samples in each spectral channel, which are stored in a digital polyphase filterbank with 1024 spectral channels and a frequency resolution of ~0.977 MHz. Thus, each of the two polarization channels is comprised of 8192 frequency channels, which contain 32 bit data recorded at a time resolution of 64 μs. Data from each observation are initially stored on an array of hard disks configured in a RAID array and are later transferred onto high performance computing machines at JPL, where custom data reduction pipelines (see Chapter 2) and novel pulsar search algorithms (see Chapter 8) are used to identify new pulsars. A schematic diagram of the architecture of the K-band digital spectrometer is shown in Figure 9.7. Images of DSS-43 and the various components of the pulsar backend are provided in Figure 9.8.

9.5.2 Pulsar Detections using the K-band Pulsar Machine

While we were commissioning the K-band pulsar machine outfitted on DSS-43 and performing observations of the GC, we routinely observed several known pulsars to calibrate the performance of the system. In Figure 9.9, I show the detection of the Vela pulsar, PSR B0833–45, between 19–23 GHz during a 10 min observation with DSS-43 on 2016 August 27. The folded profiles shown here are derived from data obtained using ~2.5 GHz of the total recording bandwidth from only one of the polarization channels.

To demonstrate the system's capability of detecting MSPs, we observed PSR J0437–4715, a bright MSP with a 5.76 ms rotational period in a nearly circular

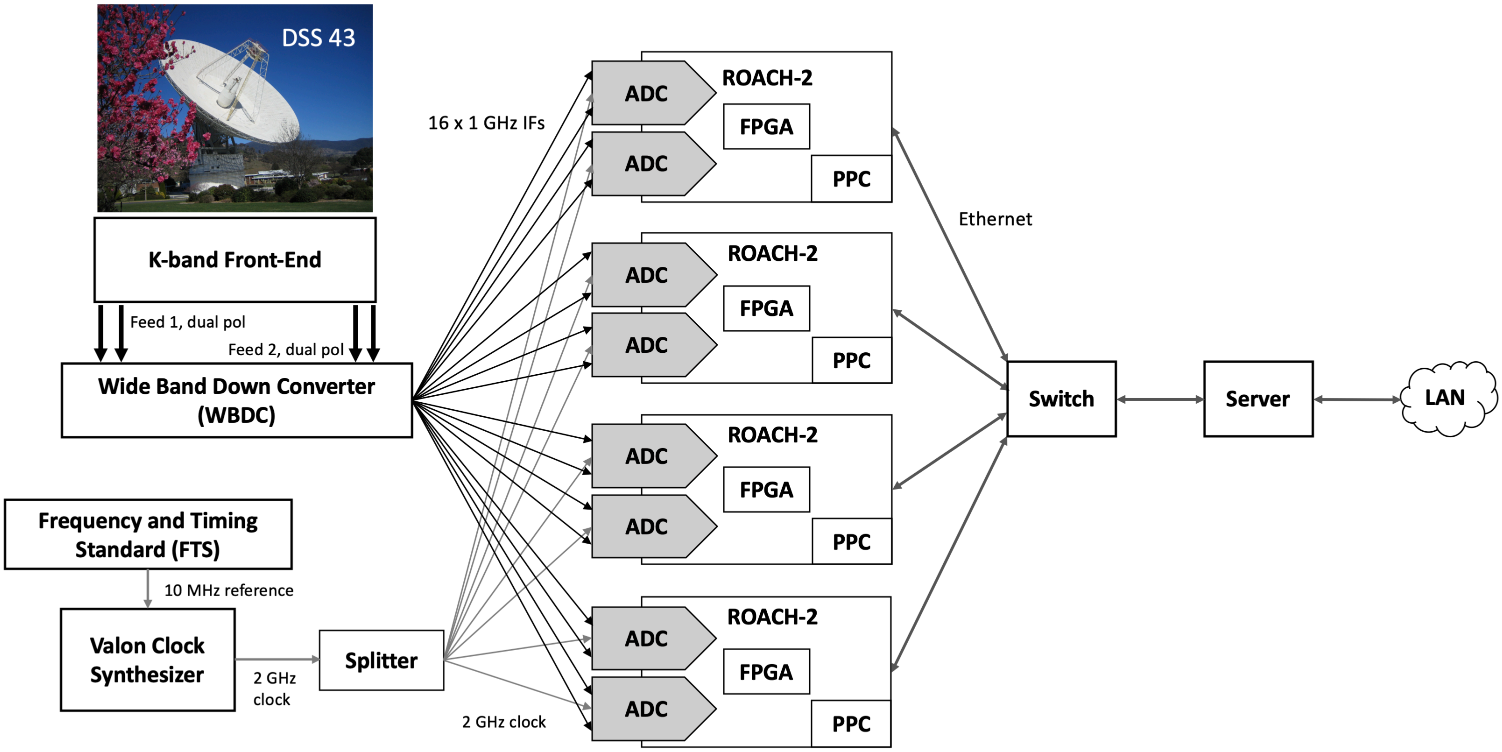

Figure 9.7: **Schematic diagram of the architecture of the K-band digital spectrometer outfitted on DSS-43.** Image credit: Adapted from Figure 1 in [545].

binary orbit. Figure 9.10 shows a bright detection of the pulsar on 2019 April 12 between 20–24 GHz. The folded profiles shown in Figure 9.10 are produced using data from a single polarization channel and ~3 GHz of the total bandwidth. To my knowledge, this detection presently represents the highest radio frequency detection of a MSP to date. The highest radio frequency at which PSR J0437–4715 has been previously detected was 17 GHz [272].

9.5.3 Prospects for Detecting Galactic Center Pulsars with the K-band Pulsar Machine

We are currently carrying out a survey for new GC pulsars within the inner few parsecs of Sgr A* using K-band radio observations of the GC region with DSS-43. Long exposures of the GC are being performed at the positions shown in Figure 9.11. The southern hemisphere location of DSS-43 allows the GC to be viewed continuously for ~12 hours at high elevations, which provides sufficient sensitivity to detect MSPs for the first time in regions of strong scattering.

Our K-band survey of the GC with DSS-43 will have better sensitivity than the most sensitive survey previously performed, which used the GBT's Ku-band re-

Figure 9.8: **Images of several components comprising the K-band pulsar machine at DSS-43.** Panel (a): The exterior of the DSS-43 radio telescope, photographed during a visit to Tidbinbilla, Australia in September 2019 when we upgraded the pulsar backend. Panel (b): The wideband 17–27 GHz down converter. Panel (c): The patch panel used to split the 16 different 1 GHz IFs into the four CASPER ROACH-2 boards. Panel (d): The top four rackmount boxes store the four ROACH-2 boards. The middle rackmount box contains the pulsar timing hardware, and the black rackmount box at the bottom is a switch used to remotely change the observing configuration from K-band to being able to record data simultaneously at S-band and X-band. Panel (e): The RAID array of hard disks where the data are initially stored, and the server used to interface with the ROACH-2 boards and the RAID array.

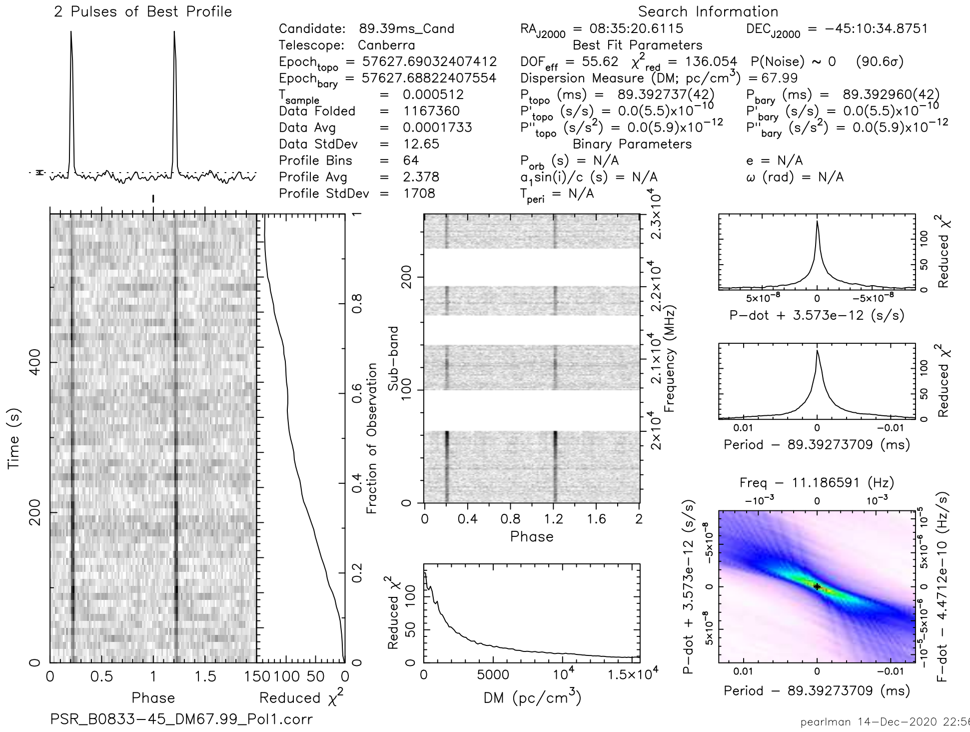

Figure 9.9: **Detection of the Vela pulsar, PSR B0833–45, between 19–23 GHz during a 10 min observation with the K-band system outfitted on the 70 m DSN radio telescope, DSS-43, in Tidbinbilla, Australia.** These observations were carried out on 2016 August 27 (MJD 57627) during a time period when the K-band pulsar backend was being commissioned. The folded pulse profiles shown here are derived from data recorded using only one of the two polarization channels. These results were obtained using ∼2.5 GHz of the total recording bandwidth in a single polarization channel.

ceiver [349]. To calculate our sensitivity to detecting GC pulsars, I consider the sample of known pulsars in the ATNF pulsar catalog[b] [365] and calculate their 1.4 GHz pseudo-luminosity if they were placed at the distance of $D_{\rm GC} = 8.3$ kpc, i.e. the distance of Sgr A*. The pseudo-luminosities have been scaled to a frequency of 1.4 GHz using an average spectral index of $\langle\alpha\rangle = -1.8$ [372].:

$$L_{1.4} = S_{\rm psr}\left(\frac{1.4\,{\rm GHz}}{\nu_{\rm GHz}}\right) D_{\rm GC}^2, \tag{9.1}$$

where $S_{\rm psr}$ is the flux density of the pulsar at an observing frequency of $\nu_{\rm GHz}$. In Figure 9.12, I show the 1.4 GHz pseudo-luminosities of the pulsars in the ATNF pulsar catalog[b] [365], after applying the scaling in Equation (9.1), where normal pulsars are indicated using blue circles and MSPs are shown using red circles. The brightest known MSP, PSR J0437–4715, is shown using a red star.

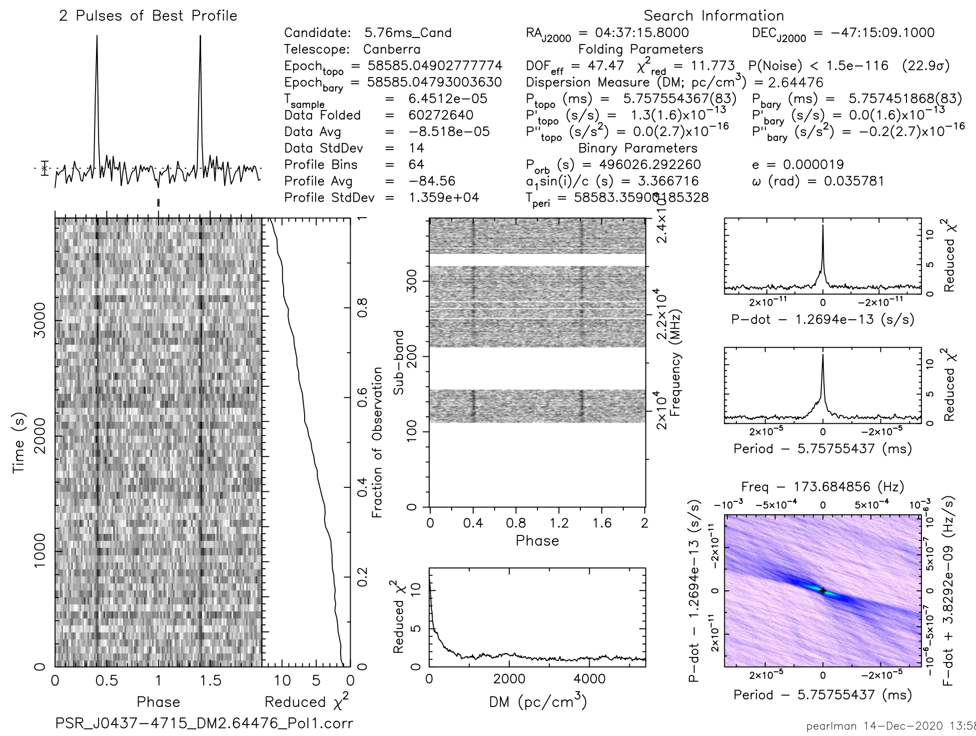

Figure 9.10: **Detection of the bright Galactic MSP, PSR J0437–4715, between 20–24 GHz during a 1.1 hr observation with the K-band system outfitted on the 70 m DSN radio telescope, DSS-43, in Tidbinbilla, Australia.** These observations were carried out on 2019 April 12 (MJD 58585) during a time period when the K-band pulsar backend was being commissioned. The folded pulse profiles shown here are derived from data recorded using only one of the two circular polarization channels. These results were obtained using ∼3 GHz of the total recording bandwidth. To my knowledge, this detection presently represents the highest radio frequency detection of a MSP.

The solid curves in Figure 9.12 show the 10σ sensitivity limits for both a pulsar survey of the GC with DSS-43 at 22 GHz and the most sensitive survey previously carried out using the GBT at 14.6 GHz. The radiometer equation [328] was used to derive the 10σ sensitivity curves:

$$S_{\mathrm{min}} = \frac{(\mathrm{S/N})\,(T_{\mathrm{rec}} + T_{\mathrm{sky}})}{\sqrt{\Delta\nu\, n_p\, T_{\mathrm{obs}}}}\,\frac{\beta}{G}\sqrt{\frac{\delta}{1-\delta}}. \tag{9.2}$$

Here, S_{min} is the sensitivity limit for a specified S/N, T_{rec} and T_{sky} are the receiver noise and sky temperatures, respectively, $\Delta\nu$ is the observing bandwidth, n_p is the number of polarizations, T_{obs} is the observing time, β is a correction factor that

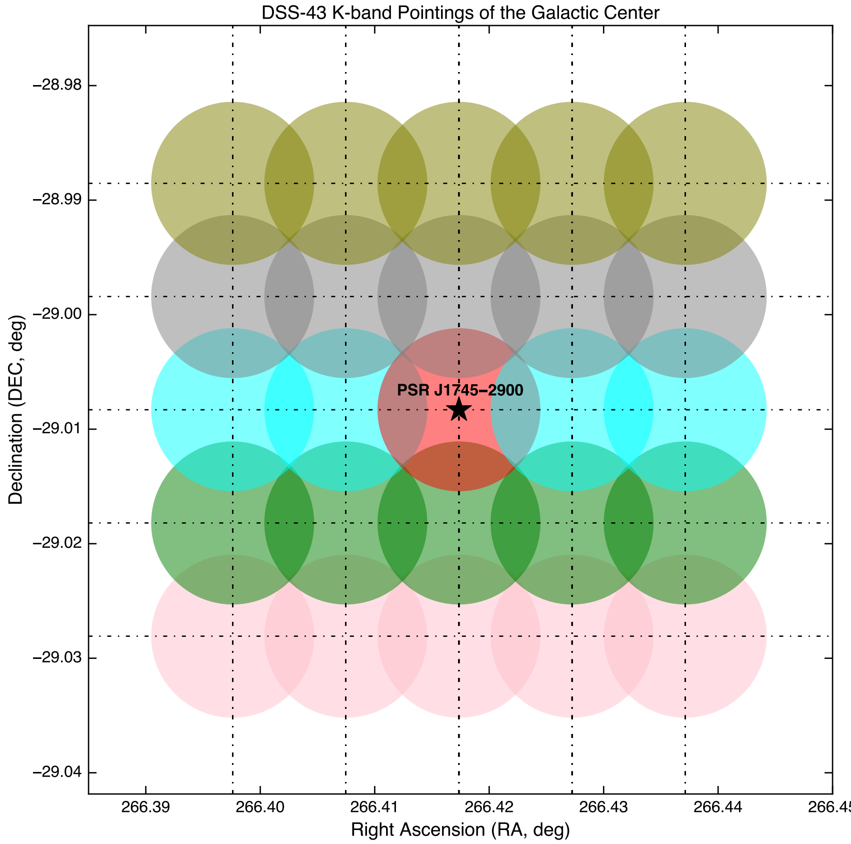

Figure 9.11: **Tiled pointings of the Galactic Center with the K-band system on DSS-43.** The colored circles correspond to the beam size of DSS-43 at 22 GHz. The position of the Galactic Center magnetar, PSR J1745–2900, is overlaid for reference. We are performing deep exposures of the field containing Sgr A* and PSR J1745–2900, along with additional observations at the other pointing positions.

accounts for system imperfections, G is the telescope gain, and $\delta = W_{\rm psr}/P_{\rm spin}$ is the duty cycle of the pulsar. The total system temperature is given by $T_{\rm sys} = T_{\rm rec} + T_{\rm sky}$.

The nominal system temperature of the K-band system on DSS-43 is $T_{\rm rec} = 45$ K, and the Ku-band system on the GBT had a nominal system temperature of $T_{\rm rec} = 35$ K. At each observing frequency, I assume that the sky temperature is given by Equation (4.2). However, at high radio frequencies, the atmosphere contributes significantly to the overall system temperature, especially when the GC is observed at low elevations. Thus, weather can strongly impact the sensitivity during a given observation. The total K-band system temperature of DSS-43 is nominally $T_{\rm sys} = 62.3$ K, and the total system temperature of the Ku-band GC pulsar survey with the GBT was nominally $T_{\rm sys} = 62.5$ K.

The ultra-wideband K-band pulsar backend on DSS-43 has a center frequency of $\nu = 22\,\text{GHz}$, $n_p = 2$ circular polarizations, and a bandwidth of $\Delta\nu = 8\,\text{GHz}$. The Ku-band observations of the GC described in Macquart et al. [349] were carried out using the GBT at a center frequency of $\nu = 14.6\,\text{GHz}$, $n_p = 2$ circular polarizations, and a recording bandwidth 0.8 GHz. The gain of both radio telescopes are given by:

$$G = \frac{A_e}{2k_B}, \tag{9.3}$$

where A_e is the effective area of the telescope and k_B is the Boltzmann constant. The system equivalent flux density (SEFD) is given by SEFD $= T_{\text{sys}}/G$. The K-band system on DSS-43 has a gain of $G = 0.9\,\text{K}\,\text{Jy}^{-1}$, which corresponds to a SEFD of 68.7 Jy. The gain of the Ku-band receiver on the GBT used in Macquart et al. [349] was $G = 1.5\,\text{K}\,\text{Jy}^{-1}$, and the SEFD of the system was 41.6 Jy.

The effective width of each pulsar, W_{psr}, is obtained by combining the pulsar's intrinsic width ($w_{\text{intrinsic}}$) together with contributions from scattering (τ_{ISM}), interstellar dispersion (τ_{DM}), and temporal binning (τ_{res}):

$$W_{\text{psr}} = \sqrt{w_{\text{intrinsic}}^2 + \tau_{\text{ISM}}^2 + \tau_{\text{DM}}^2 + \tau_{\text{res}}^2}. \tag{9.4}$$

The primary source of uncertainty in Equation (9.4) arises from the unknown distance of the scattering screen from the GC, which is expected to be the dominant contributor of temporal smearing for pulsars toward the GC region. Here, I adopt a scattering screen distance of $\Delta_{\text{GC}} = 133^{+200}_{-80}$ pc, which was estimated by Lazio and Cordes [305] using a maximum likelihood analysis by combining all known tracers of ionized gas, such as the scattering diameters of masers and OH/IR stars, free-free emission, and absorption. Under the assumption that the scattering material is confined to a thin screen, the temporal scattering timescale for pulsars near Sgr A* is given by [349]:

$$\tau_{\text{ISM}} = 0.116 \left(\frac{\Delta_{\text{GC}}}{100\,\text{pc}}\right)^{-1} \left(\frac{\nu}{10\,\text{GHz}}\right)^{-4}. \tag{9.5}$$

The temporal scattering due to dispersion, τ_{DM}, can be computed by calculating the uncorrected dispersive smearing across the bandwidth, e.g. due to intra-channel smearing as a result of incoherently dispersing data recorded in a finite number of frequency channels. The temporal binning, τ_{res}, is given by the sampling time. To derive the sensitivity curves in Figure 9.12, I assume a fiducial value of $w_{\text{intrinsic}} = 0.05 P_{\text{spin}}$ since the median duty cycle of pulsars in the ATNF pulsar catalog[b] [365] is roughly 5%.

The dashed and solid brown curves in Figure 9.12 show the 10σ sensitivity limits for a K-band GC pulsar survey with DSS-43 and a total integration time of 20 and 200 hr, respectively. The corresponding 10σ sensitivity limit for the GC pulsar survey in Macquart et al. [349] is indicated by the solid black curve. The dashed green curve shows the 10σ sensitivity limit for a 200 hr GC pulsar survey with the K-band system on DSS-43 under the assumption that the scattering observed from the GC magnetar, PSR J1745–2900, is typical of the GC environment. In this case, instead of Equation (9.5), the following expression is used for τ_{ISM} [498]:

$$\tau_{\mathrm{ISM}} = 1.3\left(\frac{\nu}{1\,\mathrm{GHz}}\right)^{-3.8}. \tag{9.6}$$

The blue dashed curve is obtained if the pulse broadening timescale measured by Pearlman et al. [422] at 8.4 GHz is used instead of Equation (9.5):

$$\tau_{\mathrm{ISM}} = 0.0069\left(\frac{\nu}{8.4\,\mathrm{GHz}}\right)^{-3.8}. \tag{9.7}$$

Figure 9.12 shows that the most sensitive GC pulsar survey previously conducted by Macquart et al. [349] should have been able to detect ~85% of the normal pulsars at the GC, if GC pulsars are similar to those found in the Galactic field. Using the K-band system on DSS-43, we expect to be sensitive to ~83% and and ~98% of the normal pulsar population after integrating for 20 and 200 hr, respectively. Figure 9.12 also demonstrates that the pulsar survey in Macquart et al. [349] would not have been sensitive to detecting a single MSP at the GC if there was a high level of scattering. In contrast, the K-band pulsar survey of the GC region described here should be sensitive to detecting ~10% and ~21% of the MSPs at the GC with an integration time of 20 and 200 hr with DSS-43, respectively, if they are similar to the known MSPs found in other regions of the Milky Way. Thus, our K-band pulsar survey with DSS-43 will provide an opportunity to detect MSPs in regions of strong scattering at the GC for the first time.

9.5.4 Detection of Highly-Accelerated Pulsar–Black Hole Binaries

Our K-band GC pulsar survey has the opportunity to discover exotic objects, such as pulsar–BH binaries, which may only be formed in extreme environments such as the GC. The mass function of a binary pulsar can be computed using the measured Keplerian parameters of the binary system:

$$f(m_{\mathrm{psr}}, m_{\mathrm{c}}) = \frac{(m_{\mathrm{c}}\sin i)^3}{(m_{\mathrm{psr}}+m_{\mathrm{c}})^2} = \frac{4\pi^2}{\mathrm{T}_\odot}\frac{x^3}{P_{\mathrm{orb}}^2}, \tag{9.8}$$

where $m_{\rm psr}$ and $m_{\rm c}$ are the masses of the pulsar and its companion, respectively, i is the inclination angle of the orbit, $\mathrm{T}_\odot = GM_\odot/c^3 \approx 4.925490948\ \mu$s, x is the projected semi-major axis of the orbit, and $P_{\rm orb}$ is the orbital period. Assuming a circular orbit, the maximum acceleration, $|a_{\rm max}|$, expected for a pulsar binary with an orbital period, $P_{\rm orb}$, and pulsar and companion masses of $m_{\rm psr}$ and $m_{\rm c}$ is obtained from Kepler's third law by setting the orbital inclination to be edge-on ($i = 90°$):

$$|a_{\rm max}| = \left(\frac{2\pi}{P_{\rm orb}}\right)^2 xc = \left(\frac{2\pi}{P_{\rm orb}}\right)^{4/3} (\mathrm{T}_\odot f)^{1/3} c. \tag{9.9}$$

In Figure 9.13, I show the maximum acceleration expected from a NS in a circular orbit with several different types of companions, such as a $4 \times 10^6\ M_\odot$ SMBH (similar to Sgr A*), 1000 $M_\odot$ BH, 10 $M_\odot$ BH, 1.4 $M_\odot$ NS, 1 $M_\odot$ white dwarf (WD), and 0.1 $M_\odot$ WD. In order to detect short period binary pulsars, such as systems with $P_{\rm orb} \lesssim 1$ day, a simple acceleration search will likely be inadequate for detecting pulsations that are modulated by the binary's Keplerian orbit. Higher-order polynomial searches will almost certainly be needed to detect pulsars in compact binaries with Sgr A*. The dynamic programming and pruning algorithms described in Chapter 8 will enable sensitive searches for such types of exotic binary systems. These techniques will also be useful for detecting pulsars in tight binaries with a less massive companions than a SMBH since such systems will be highly accelerated at short orbital periods, as shown in the bottom panel of Figure 9.13.

Figure 9.14 shows the line-of-sight acceleration ranges for a selected set of binary pulsars with orbital periods of $P_{\rm orb} < 12$ hr and $|a_{\rm max}| > 1\ \mathrm{m\,s^{-2}}$. At short orbital periods ($P_{\rm orb} \lesssim 1$ hr), there is a paucity of binary pulsars. These rare ultra-compact systems may be abundant in the GC due to the high stellar density in the region, but they may only detectable when higher-order polynomial searches for accelerated pulsars are utilized.

9.6 Future Work

Detailed analyses of the K-band observations of the GC with DSS-43 are still ongoing. The observations are being searched for new pulsars using state-of-the-art pulsar search techniques, such as the dynamic programming algorithm (see Chapter 9), GPU-accelerated Fourier domain algorithms optimized to search for accelerated pulsars, pruning techniques, and a novel single pulse search algorithm designed to detect dispersed pulses at high radio frequencies using a machine learning classifier, trained using a transfer learning approach. The results of these analyses are the subject of future work.

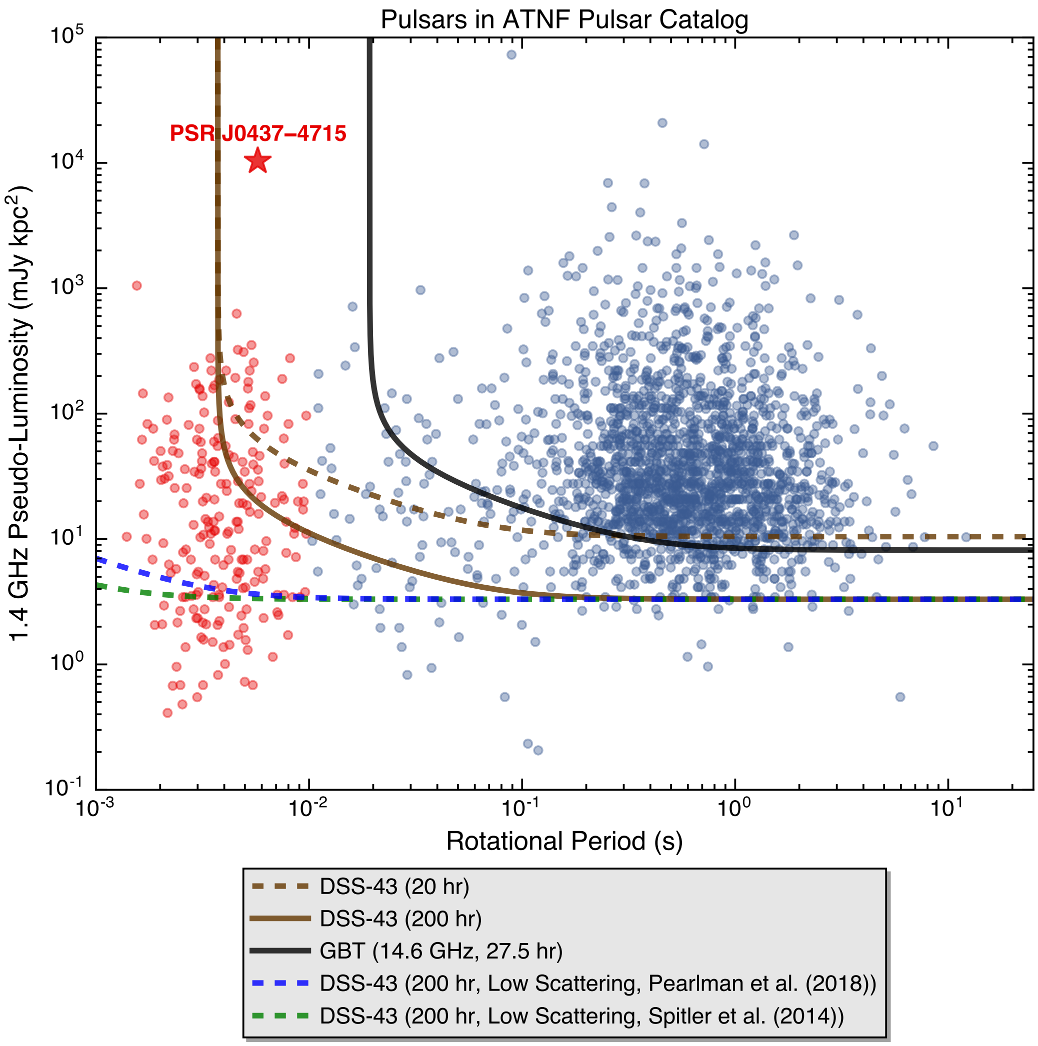

Figure 9.12: **Detectability of pulsars toward the GC.** The blue and red circles show the 1.4 GHz pseudo-luminosities of the known normal and millisecond pulsars in the ATNF pulsar catalog[b] [365], respectively, if they were located at a distance of $D_{\text{GC}} = 8.3$ kpc in the GC. The 1.4 GHz pseudo-luminosities have been scaled using an average spectral index of $\langle\alpha\rangle = -1.8$ [372]. The brown dashed and solid curves show the 10σ sensitivity limits for a 20 and 200 hr pulsar survey using the K-band system outfitted on DSS-43. The solid black curve shows the corresponding sensitivity limit obtained from the 27.5 hr pulsar survey carried out with the GBT at Ku-band by Macquart et al. [349], which was previously the most sensitive pulsar survey of the GC region. The brown and black curves rise at short periods due to significant scattering at shorter periods, which scales as ν^{-4} (see Equation (9.5)). If the scattering observed toward the GC magnetar, PSR J1745–2900, is typical of the GC environment, then the sensitivity curves remain flat at shorter periods. The black and brown sensitivity limits demonstrate that previous searches for GC pulsars would not have been sensitive to detecting MSPs in regions of strong scattering. The brightest known MSP, PSR J0437–4715, is indicated using a red star and would be easily detectable using the K-band system on DSS-43 if it were located at the GC behind a strong scattering screen.

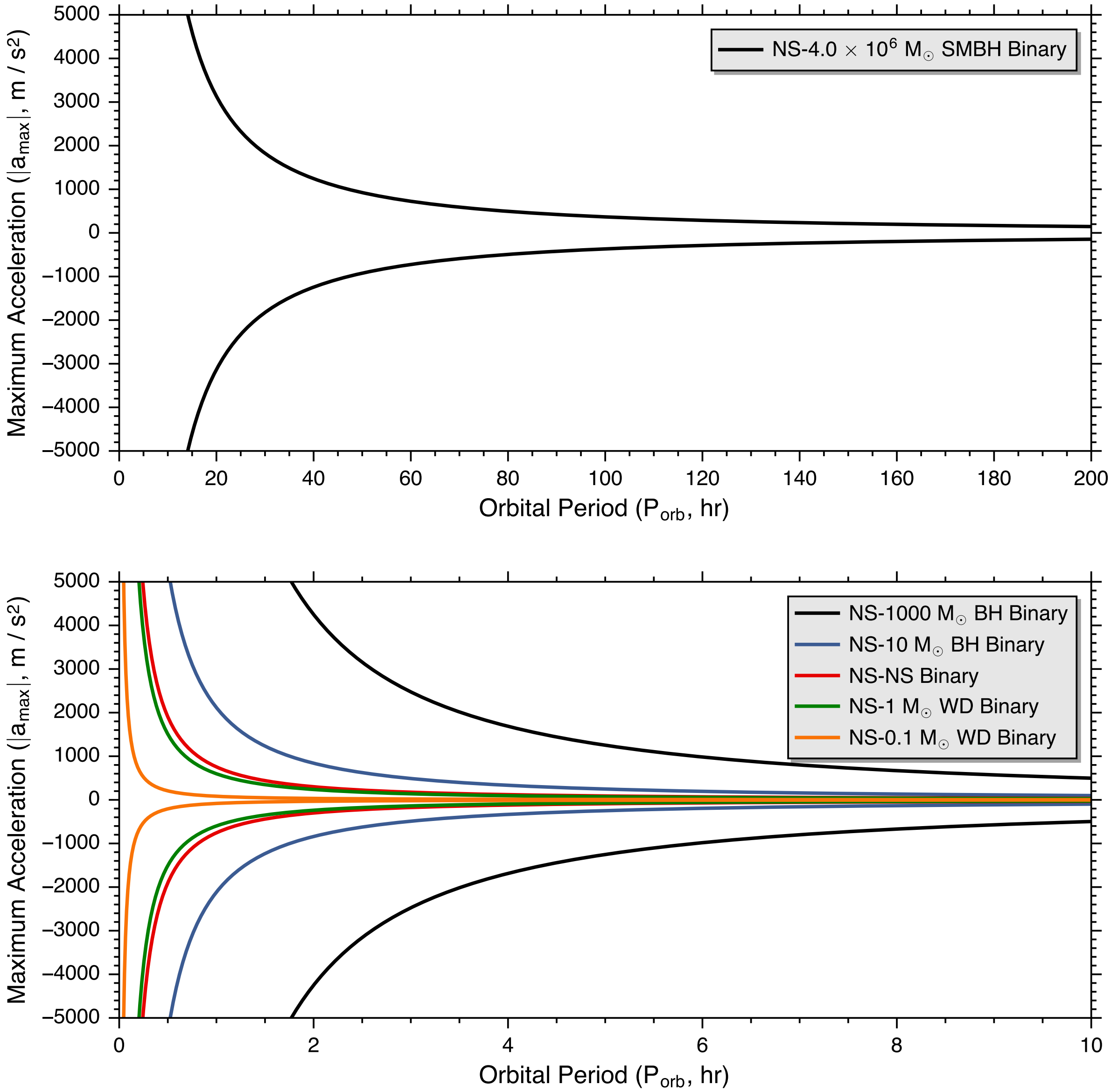

Figure 9.13: **Maximum acceleration of neutron star binaries, assuming a circular orbit and an edge-on configuration, with an inclination angle of $i = 90°$.** Top panel: Maximum acceleration of a 1.4 $M_\odot$ neutron star in a circular orbit with a 4×10^6 $M_\odot$ SMBH, such as Sgr A*, with orbital periods of 0–200 hr. Bottom panel: Maximum acceleration of a 1.4 $M_\odot$ neutron star in a circular orbit with a 1000 $M_\odot$ BH (black curve), 10 $M_\odot$ BH (blue curve), 1.4 $M_\odot$ NS (red curve), 1 $M_\odot$ WD (green curve), and 0.1 $M_\odot$ WD (orange curve), with orbital periods of 0–10 hr.

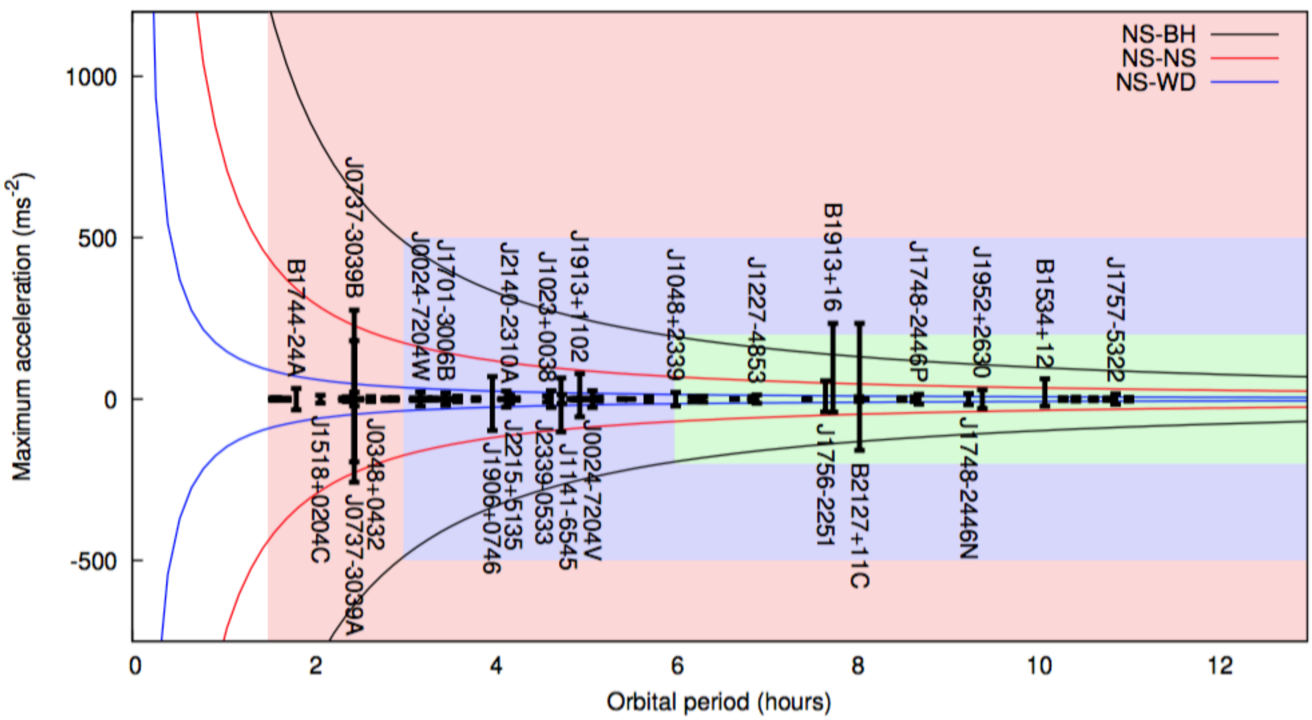

Figure 9.14: **Maximum orbital acceleration for circular binary NS–BH, NS–NS, and NS–WD systems as a function of orbital period.** The black errorbars show the line-of-sight acceleration ranges for a selected set of binary pulsars with $P_{\rm orb} < 12$ hr and $|a_{\rm max}| > 1$ m s^{-2}. The labeled binary pulsars have $|a_{\rm max}| > 20$ m s^{-2}. The colored regions correspond to different parameter spaces probed by previous surveys, such as the High Time Resolution Universe (HTRU) Pulsar Survey, by dividing individual observations into shorter segments [75, 403]. Image and caption adapted from [75, 403].

Part V: X-ray Binaries and Pulsar Timing

The diversity of the phenomena of nature is so great, and the treasures hidden in the heavens so rich, precisely in order that the human mind shall never be lacking in fresh nourishment.

— Johannes Kepler

Chapter X

The Orbital Parameters of the Eclipsing High-mass X-Ray Binary Pulsar IGR J16493–4348 from Pulsar Timing

[423] **Pearlman, A. B.*** et al. (2019). "The Orbital Parameters of the Eclipsing High-mass X-Ray Binary Pulsar IGR J16493-4348 from Pulsar Timing." In: *ApJ,* 873:86. arXiv:1811.06543 [astro-ph.HE].

The Orbital Parameters of the Eclipsing High-Mass X-Ray Binary Pulsar IGR J16493–4348 from Pulsar Timing

Aaron B. Pearlman[1,6,7,*], Joel B. Coley[2,3], Robin H. D. Corbet[4,5], and Katja Pottschmidt[3,5]

[1] Division of Physics, Mathematics, and Astronomy, California Institute of Technology, Pasadena, CA 91125, USA
[2] Department of Physics and Astronomy, Howard University, Washington, DC 20059, USA
[3] CRESST/Mail Code 661, Astroparticle Physics Laboratory, NASA Goddard Space Flight Center, Greenbelt, MD 20771, USA
[4] CRESST/Mail Code 662, X-ray Astrophysics Laboratory, NASA Goddard Space Flight Center, Greenbelt, MD 20771, USA
[5] University of Maryland, Baltimore County, Baltimore, MD 21250, USA
[6] NDSEG Research Fellow
[7] NSF Graduate Research Fellow
[*] Lead author of the manuscript.
Corresponding author: aaron.b.pearlman@caltech.edu

Abstract

IGR J16493–4348 is an eclipsing supergiant high-mass X-ray binary (sgHMXB), where accretion onto the compact object occurs via the radially outflowing stellar wind of its early B-type companion. We present an analysis of the system's X-ray variability and periodic modulation using pointed observations (2.5–25 keV) and Galactic bulge scans (2–10 keV) from the *Rossi X-ray Timing Explorer (RXTE)* Proportional Counter Array (PCA), along with *Swift* Burst Alert Telescope (BAT)

70-month snapshot (14–195 keV) and transient monitor (15–50 keV) observations. The orbital eclipse profiles in the PCA bulge scans and BAT light curves are modeled using asymmetric and symmetric step and ramp functions. We obtain an improved orbital period measurement of 6.7828 ± 0.0004 days from an observed minus calculated *(O–C)* analysis of mid-eclipse times derived from the BAT transient monitor and PCA scan data. No evidence is found for the presence of a strong photoionization or accretion wake. We refine the superorbital period to 20.067 ± 0.009 days from the discrete Fourier transform (DFT) of the BAT transient monitor light curve. A pulse period of 1093.1036 ± 0.0004 s is measured from a pulsar timing analysis using pointed PCA observations spanning ~1.4 binary orbits. We present pulse times of arrival (ToAs), circular and eccentric timing models, and calculations of the system's Keplerian binary orbital parameters. We derive an X-ray mass function of $f_x(M) = 13.2^{+2.4}_{-2.5}\,M_\odot$ and find a spectral type of B0.5 Ia for the supergiant companion through constraints on the mass and radius of the donor. Measurements of the eclipse half-angle and additional parameters describing the system geometry are provided.

10.1 Introduction

IGR J16493–4348 is a persistently accreting supergiant high-mass X-ray binary (sgHMXB), where mass transfer onto the neutron star is driven by the stellar wind from its early B-type companion. It was first detected during a survey of the Galactic plane [47] using the *INTErnational Gamma-Ray Astrophysics Laboratory* (*INTEGRAL*) [562] with the *INTEGRAL* Soft Gamma-Ray Imager (ISGRI) [308] camera of the Imager on Board the *INTEGRAL* Satellite (IBIS) [537] telescope. The source was also detected with *INTEGRAL* during a deep scan of the Norma Arm region [217] and in subsequent IBIS/ISGRI [48, 49, 50, 51] and *Swift* Burst Alert Telescope (BAT) surveys [39, 407].

Pointed *Rossi X-ray Timing Explorer (RXTE)* Proportional Counter Array (PCA) observations of IGR J16493–4348 by Markwardt et al. [371] revealed that the mean spectrum was consistent with a heavily absorbed power-law, with a photon index of $\Gamma = 1.4$ and $N_\mathrm{H} \approx 10^{23}\,\mathrm{cm}^{-2}$. The measured fluxes in the 2–10, 10–20, and 20–40 keV energy bands were 1.0×10^{-11}, 1.3×10^{-11}, and $2.1 \times 10^{-11}\,\mathrm{erg\,cm^{-2}\,s^{-1}}$, respectively. *Chandra* imaging of the field of IGR J16493–4348 was performed by Kuiper et al. [294] using the High Resolution Camera (HRC-I) instrument, which identified 2MASS J16492695–4349090 as the infrared counterpart. A K_S magnitude of 12.0 ± 0.1 was found using the Son of ISAAC (SOFI) infrared camera at the

European Southern Observatory (ESO) 3.5 m New Technology Telescope (NTT), which is consistent with the 11.94 ± 0.04 K_S magnitude reported in the 2MASS catalog and suggests that the source is not highly variable in this band. No optical counterpart was found in the Digital Sky Survey (DSS) maps due to strong absorption along the line of sight.

A spectral type of B0.5-1 Ia-Ib was estimated by Nespoli et al. [401, 402] from K_S-band spectroscopy of IGR J16493–4348's infrared counterpart using observations from the Infrared Spectrometer and Array Camera (ISAAC) spectrograph on UT1 of the ESO Very Large Telescope (VLT). The spectrum showed a strong He I (20581 Å) emission line with He I (21126 Å) in absorption, along with a strong Brγ (21661 Å) absorption line, which are all characteristic features in OB stellar spectra. This led Nespoli et al. [401, 402] to classify the system as an sgHMXB. They also provided an estimate of the interstellar extinction and calculated a hydrogen column density of $N_H = (2.92 \pm 1.96) \times 10^{22}$ cm^{-2}, which they attributed to a significant absorbing envelope surrounding the neutron star. The distance to the source was estimated to be between 6–26 kpc. Romano [470] found that the cumulative luminosity distribution (CLD) and small dynamic range in X-ray flux from *Swift*[o] X-ray Telescope (XRT) observations were also typical of a classical sgHMXB system, rather than a Supergiant Fast X-ray Transient (SFXT).

Hill et al. [231] carried out a spectral analysis of the source using 22–100 keV *INTEGRAL* IBIS/ISGRI and 1–9 keV *Swift* XRT data. They found that the source was best modeled by a highly absorbed power-law, with $\Gamma = 0.6 \pm 0.3$ and $N_H = 5.4^{+1.3}_{-1.0} \times 10^{22}$ cm^{-2}, and a high energy cut-off at $E_{cut} = 17^{+5}_{-3}$ keV. An average source flux of 1.1×10^{-10} erg cm^{-2} s^{-1} was measured in the 1–100 keV energy band. No coherent periodicities were found in their *INTEGRAL* or *Swift* data.

Morris et al. [399] analyzed the 0.2–150.0 keV spectrum of IGR J16493–4348 obtained from *Suzaku* observations with the Hard X-ray Detector (HXD) and X-ray Imaging Spectrometer (XIS) instruments. The spectrum was fit with a power-law modified by a fully and partially covering absorber. The partially covered and fully covered neutral hydrogen column densities were $26^{+9.4}_{-7.9} \times 10^{22}$ and $8.6^{+0.9}_{-1.0} \times 10^{22}$ cm^{-2}, respectively, with a partial covering fraction of $0.62^{+0.06}_{-0.07}$ and photon index of $\Gamma = 2.4 \pm 0.2$. A 6.4 keV Fe emission line, with an equivalent width less than 84 eV, was also included in their spectral model, and a flux of $13.5^{+0.3}_{-2.0} \times 10^{-12}$ erg cm^{-2} s^{-1} was measured between 0.2 and 10 keV.

Spectral analysis in the hard X-ray band was also performed by D'Aì et al. [142] using 15–150 keV *Swift* BAT and *INTEGRAL*/ISGRI data, together with pointed soft X-ray observations from *Suzaku* and the *Swift* XRT. They found that a negative-positive exponential power-law model, with a broad (10 keV width) absorption line at 33 ± 4 keV, yielded the best fit to the broadband spectrum. This absorption feature was interpreted as evidence of a cyclotron resonance scattering feature (CRSF). Assuming cyclotron absorption occurs above the magnetic poles of the neutron star, D'Aì et al. [142] inferred a surface magnetic field of $B_{\rm surf} = (3.7 \pm 0.4) \times 10^{12}$ G from the energy of the cyclotron line for a canonical neutron star with a mass of $1.4\,M_\odot$ and a radius of 10 km.

The 6.8 day binary orbital period was independently discovered by Corbet et al. [117] and Cusumano et al. [140]. Cusumano et al. [140] also found evidence of an eclipse in the folded *Swift* BAT survey light curve lasting approximately 0.8 days. Assuming a neutron star mass of $1.4\,M_\odot$ and a B0.5 Ib companion with a mass and radius of $47\,M_\odot$ and $32.2\,R_\odot$, respectively, Cusumano et al. [140] estimated a semi-major axis of $a \approx 55\,R_\odot$ for the binary orbit and derived an upper limit of $e \leq 0.15$ on the eccentricity.

A 20 day superorbital period was first detected by Corbet et al. [117] in the power spectra of the *Swift* BAT survey and *RXTE* PCA scan light curves. The superorbital period was refined to 20.07 ± 0.01 days using data from the *Swift* BAT transient monitor (15–50 keV), and a monotonic relationship between the superorbital and orbital modulation was suggested [115]. Recently, Coley et al. [110] analyzed *Nuclear Spectroscopic Telescope Array (NuSTAR)* and *Swift* XRT observations near the maximum and minimum of one cycle of the 20 day superorbital modulation. They found that the 3–40 keV spectra were well modeled by an absorbed power-law, with $N_{\rm H} \approx 10^{23}$ cm^{-2}, and a high energy cut-off. Evidence of an Fe Kα emission line was also found at superorbital maximum near 6.4 keV. A comprehensive discussion of possible mechanisms responsible for the superorbital variability is presented in Coley et al. [110], along with a timing analysis characterizing its long term behavior.

A 1069 s period was detected in the power spectrum of the light curve from pointed *RXTE* PCA observations, which was suggested to be linked to the neutron star's rotational period [118]. We find strong evidence for a 1093 s pulse period from pulsar timing measurements using additional archival pointed *RXTE* PCA observations. Pulse phase resolved spectroscopy near the maximum and minimum of the superorbital cycle has recently been carried out by Coley et al. [110] using these pulsar timing results.

In this paper, we present improved measurements of IGR J16493–4348's superorbital, orbital, and pulse periods using *Swift* BAT and *RXTE* PCA observations. We also measure the system's Keplerian binary orbital parameters and study the nature of the supergiant donor and the geometry of the binary. The observations and our data reduction procedure are described in Section 10.2. In Section 10.3, we provide refined period measurements and model the system's eclipse profile. A pulsar timing analysis is presented in Sections 10.4.1–10.4.3, along with pulse times of arrival (ToAs) and orbital timing models. New constraints on the spectral type of the supergiant donor and possible system geometries are given in Section 10.4.4. A discussion of the spectral type of the supergiant companion, eclipse asymmetries, orbital eccentricity, and possible superorbital mechanisms is provided in Section 10.5. We summarize our results and conclusions in Section 10.6.

10.2 Observations

10.2.1 RXTE PCA Pointed Observations

The PCA [253, 254] was the primary instrument on board the *RXTE* satellite. The detector was comprised of five nearly identical Proportional Counter Units (PCUs), with a total effective area of ~6500 cm^2, and was sensitive to X-rays with energies between 2 and 60 keV. The mechanically collimated array had a 1° field of view (FoV) at full width at half maximum (FWHM). Each PCU had a multi-anode main volume filled with xenon and methane and a front propane-filled "veto" volume that was used primarily for background rejection.

We analyzed 24 pointed *RXTE* PCA observations collected at ~0.4 day intervals during 2011 October, which spanned ~9.5 days. The total exposure time was ~160.5 ks, and the exposure times of individual observations ranged between 1.7 and 16.0 ks. A catalog of these observations is provided in Table 10.1, and they are accessible through the High Energy Astrophysics Science Archive Research Center (HEASARC) archive.[z]

Background-subtracted PCA light curves were created using the Standard 2 mode and FTOOLS v6.22[s] [52]. The time resolution of the light curves was 16 s, and we used data obtained from the top xenon layers (1L and 1R) of the PCUs to

[z] See https://heasarc.gsfc.nasa.gov/cgi-bin/W3Browse/w3browse.pl.

maximize the signal-to-noise ratio. The Faint background model[aa] was used to background subtract all of the PCA data since the net count rate did not exceed 40 counts s^{-1} PCU^{-1}. To reduce the uncertainty of the PCA background model, we excluded data: (1) up to 10 minutes immediately following the peak of South Atlantic Anomaly (SAA) passages, (2) with an elevation angle less than 10° above the limb of the Earth, (3) with an electron ratio larger than 0.1 in at least one of the operating PCUs, indicating high electron contamination according to the ratio of veto rates in the detectors, (4) with an offset between the source position and *RXTE*'s pointing position larger than 0.01°, and (5) within 150 s of the start of a PCU breakdown event and up to 600 s following a PCU breakdown event using the PCA breakdown history. A detailed discussion of PCA calibration issues was provided by Jahoda et al. [254]. The light curve times were corrected to the solar system barycenter using the `faxbary` FTOOLS routine and the Jet Propulsion Laboratory (JPL) DE-200 ephemeris [503]. Throughout this paper, Modified Julian Dates (MJDs) refer to the barycentric times.

Data from all available PCUs were used during each pointed observation. The *RXTE* PCA (2.5–25 keV) light curve is shown in Figure 10.1 with count rates normalized by the number of operational PCUs. Orbital phase 0 corresponds to $T_{\pi/2}$ from circular solution 1 in Table 10.6. In Figure 10.2(d), we show the pointed *RXTE* PCA (2–10 keV) light curve, produced using the same data filtering criteria and 128 s time resolution, with nearly simultaneous PCA scan (2–10 keV) observations overlaid in blue.

10.2.2 RXTE PCA Galactic Bulge Scans

From 1999 February to 2011 November, *RXTE* performed raster scans of an approximately 16° × 16° rectangular region near the Galactic Center (GC) using the PCA [508]. The count rates were modulated by the 1° collimators as the source moved into and out of the PCA's FoV during the Galactic bulge scans. These observations were carried out twice weekly, excluding November–January and June when the positions of the Sun and anti-Sun crossed the GC region. A single scan of a source had a typical exposure time of approximately 20 s per observation and was sensitive to 0.5–1 mCrab variations in the source flux. The light curves were generated in the 2–10 keV energy band using only the top layer of the PCA to optimize detections of faint sources. We corrected the light curve times to the solar

[aa] See https://heasarc.nasa.gov/docs/xte/pca_news.html.

Table 10.1: ***RXTE* PCA Pointed Observations of IGR J16493–4348**

Observation ID	Date (UTC)	Observation Time[a] (MJD)	Time Span (ks)	Exposure Time (ks)	Count Rate[b] (Counts s^{-1} PCU^{-1})	Orbital Phase[c]
96358-01-01-01	2011 Oct 09.09–09.19	55843.13981	8.42	5.09	8.04	–1.145
96358-01-01-02	2011 Oct 09.87–09.90	55843.88558	1.87	1.87	2.94	–1.036
96358-01-01-12	2011 Oct 10.07–10.17	55844.11862	8.29	4.91	3.50	–1.001
96358-01-01-03	2011 Oct 10.48–10.57	55844.52174	8.00	5.84	3.44	–0.942
96358-01-01-04	2011 Oct 11.18–11.28	55845.23159	8.85	6.05	6.73	–0.837
96358-01-01-05	2011 Oct 11.44–11.48	55845.46157	3.44	3.44	7.35	–0.803
96358-01-01-00	2011 Oct 11.51–11.61	55845.55934	9.07	6.88	6.31	–0.789
96358-01-01-06	2011 Oct 11.64–11.68	55845.65720	3.42	3.42	5.57	–0.774
96358-01-01-07	2011 Oct 12.09–12.12	55846.10809	2.37	1.71	5.06	–0.708
96358-01-01-08	2011 Oct 12.18–12.33	55846.25345	13.12	7.68	5.22	–0.686
96358-01-01-09	2011 Oct 12.42–12.53	55846.47288	9.02	6.78	5.10	–0.654
96358-01-01-10	2011 Oct 13.27–13.37	55847.32124	9.01	6.72	6.37	–0.529
96358-01-01-11	2011 Oct 13.60–13.70	55847.64742	8.99	6.70	4.63	–0.481
96358-01-02-00	2011 Oct 14.18–14.35	55848.26709	14.61	9.34	4.37	–0.390
96358-01-02-01	2011 Oct 14.44–14.68	55848.56078	20.24	13.29	5.92	–0.346
96358-01-02-02	2011 Oct 15.16–15.33	55849.24572	14.57	9.14	6.36	–0.245
96358-01-02-03	2011 Oct 15.42–15.58	55849.50098	13.57	8.90	6.03	–0.208
96358-01-02-04	2011 Oct 16.14–16.31	55850.22417	14.54	8.83	6.64	–0.101
96358-01-02-05	2011 Oct 16.47–16.63	55850.55044	14.54	9.82	4.89	–0.053
96358-01-02-06	2011 Oct 17.18–17.48	55851.33335	25.81	15.95	3.73	0.063
96358-01-02-09	2011 Oct 17.97–17.99	55851.97617	1.66	1.66	6.56	0.157
96358-01-02-10	2011 Oct 18.03–18.06	55852.04394	2.08	2.08	5.89	0.167
96358-01-02-07	2011 Oct 18.16–18.40	55852.27911	20.16	12.50	7.13	0.202
96358-01-02-08	2011 Oct 18.55–18.58	55852.56585	2.10	1.89	9.55	0.244

Observation IDs in bold were excluded from the pulsar timing analysis since pulsed emission was not strongly detected (see also Figure 10.1).
[a] Mid-time of observation.
[b] Average 2.5–25 keV count rate after background subtraction using all available PCUs.
[c] Orbital phase at the observation mid-time using the refined 6.7828 day orbital period measurement in Section 10.3.2.1. Phase 0 corresponds to $T_{\pi/2}$ from circular solution 1 in Table 10.6.

system barycenter using the tools available through the Ohio State University (OSU) Department of Astronomy website[ab] [166].

We present 524 measurements from a series of PCA Galactic bulge scans between MJDs 53163.8 and 55863.4 (2004 June 7–2011 October 29). The PCA scan (2–10 keV) weighted average light curve is shown in Figure 10.2(a). The Galactic bulge scan data are publicly available[ac].

10.2.3 Swift BAT

The *Swift* BAT [33, 196] is a wide FoV (1.4 sr half-coded), hard X-ray telescope that uses a 2.7 m^2 coded-aperture mask and is sensitive to X-rays in the 14–195 keV band. Although the BAT is primarily designed for studying gamma-ray bursts and their

[ab] See http://astroutils.astronomy.ohio-state.edu/time.
[ac] See https://asd.gsfc.nasa.gov/Craig.Markwardt/galscan/main.html.

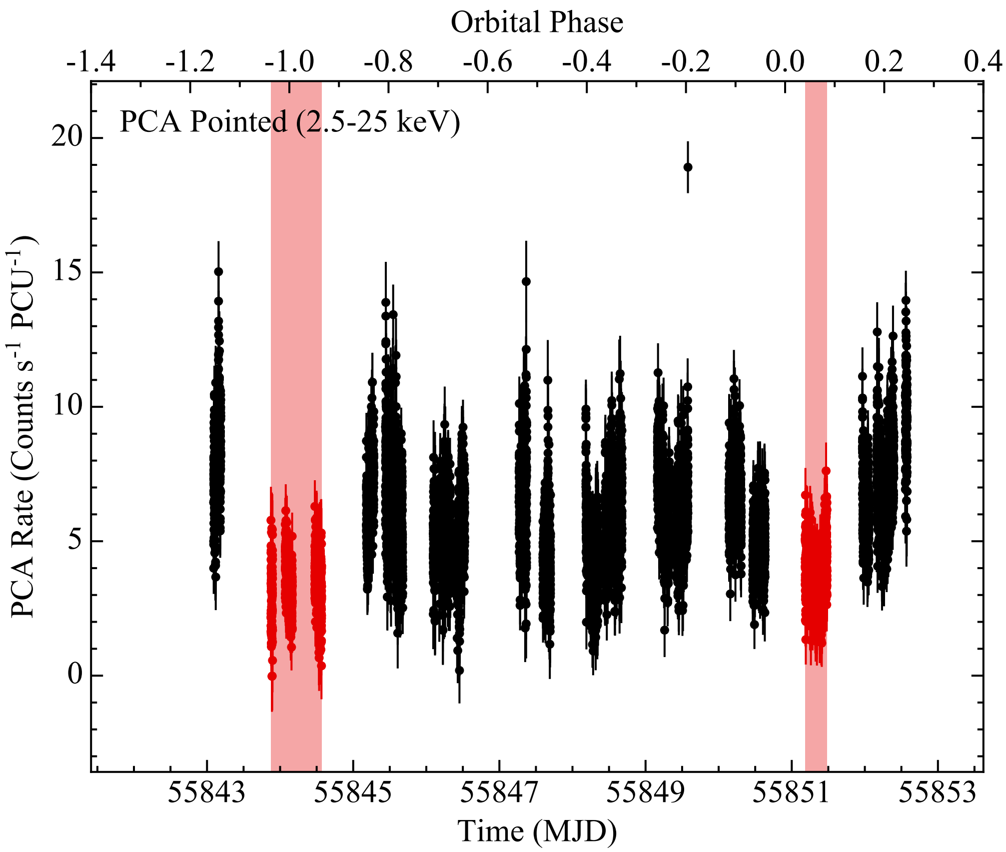

Figure 10.1: **Background-subtracted pointed *RXTE* PCA (2.5–25 keV) light curve of IGR J16493–4348 using all available PCUs with 16 s time resolution.** Orbital phase 0 corresponds to $T_{\pi/2}$ from circular solution 1 in Table 10.6. Data plotted in red were excluded from the pulsar timing analysis since pulsations were not strongly detected.

afterglows, it also serves as a hard X-ray transient monitor [292] and surveys the hard X-ray sky with ~0.4 mCrab sensitivity [39]. Thus, BAT observations of X-ray sources are usually performed in an unpredictable and serendipitous manner. Due to the nonuniform nature of the BAT sky survey, the signal-to-noise ratio of a source during an observation depends strongly on the location of the source within the BAT's FoV. The BAT typically covers 50–80% of the sky each day. The data reduction procedures are described in detail in Krimm et al. [292] and Baumgartner et al. [39].

We analyzed the BAT 70-month snapshot[ad] (14–195 keV) light curve, which is shown in Figure 10.2(b) and spans MJDs 53360.0 through 55470.0 (2004 December 21–2010 October 1). The light curve is comprised of continuous, individual observations pointed at the

[ad] See https://swift.gsfc.nasa.gov/results/bs70mon.

same sky location. Exposure times ranged from 150 to 2679 s, and the mean exposure time was 783 s. The time resolution is determined by the sampling of the individual observations.

We also analyzed the BAT transient monitor (15–50 keV) light curve between MJDs 53416.0 and 57249.8 (2005 February 15–2015 August 15), which is shown in Figure 10.2(c). Orbital and daily averaged light curves are available through the *Swift* NASA Goddard Space Flight Center (GSFC) website[ae] after they have been processed with the data reduction procedures described in Krimm et al. [292]. We used the orbital light curve in our analysis, which had typical exposure times ranging from 64 to 2640 s and a mean exposure time of 720 s. We excluded "bad" times from the light curve, which were indicated by nonzero data quality flag (`DATA_FLAG`) values. A small number of data points with very low fluxes and unusually small uncertainties were also identified and removed, even though they were flagged as "good" [115]. The BAT 70-month snapshot and transient monitor light curve times were corrected to the solar system barycenter using the tools available through the OSU Department of Astronomy website[ab].

10.3 Period Measurements

The *RXTE* PCA scan and *Swift* BAT light curves were used to search for orbital and superorbital modulation since they were longer in duration. A refined superorbital period measurement was obtained from the semi-weighted discrete Fourier transform (DFT) of the BAT transient monitor light curve (see Section 10.3.1). In this paper, uncertainties on period measurements obtained from DFTs were determined according to Horne and Baliunas [238]. We report an improved orbital period from an observed minus calculated *(O–C)* analysis of mid-eclipse times derived from the BAT transient monitor and PCA scan light curves using a Bayesian Markov chain Monte Carlo (MCMC) fitting procedure (see Section 10.3.2.1). Pulsations were detected in the unweighted power spectrum of the pointed PCA light curve after the removal of low frequency noise (see Section 10.3.3). We refine the pulse period using the ToAs derived from the pulsar timing analysis described in Sections 10.4.1–10.4.3.

10.3.1 Superorbital Period

We searched for orbital and superorbital modulation between 1 and 100 days in the power spectra of the PCA scan, BAT 70-month snapshot, and BAT transient monitor

[ae] See https://swift.gsfc.nasa.gov/results/transients.

light curves shown in Figure 10.3. Each of these power spectra was oversampled by a factor of five compared to their nominal frequency resolution, given by the length of the light curve.

The measurements from the PCA scan and BAT light curves showed a wide range of nonuniform error bar sizes. It can be advantageous to use these errors to weight the contribution of each data point when calculating the power spectrum [473]. The semi-weighting technique uses the error bar of each data point and the excess light curve variability to weight the data points in the power spectrum, which is analogous to a semi-weighted mean [107, 108]. Corbet et al. [112, 116] showed that semi-weighting can be very beneficial for faint sources, such as IGR J16493-4348.

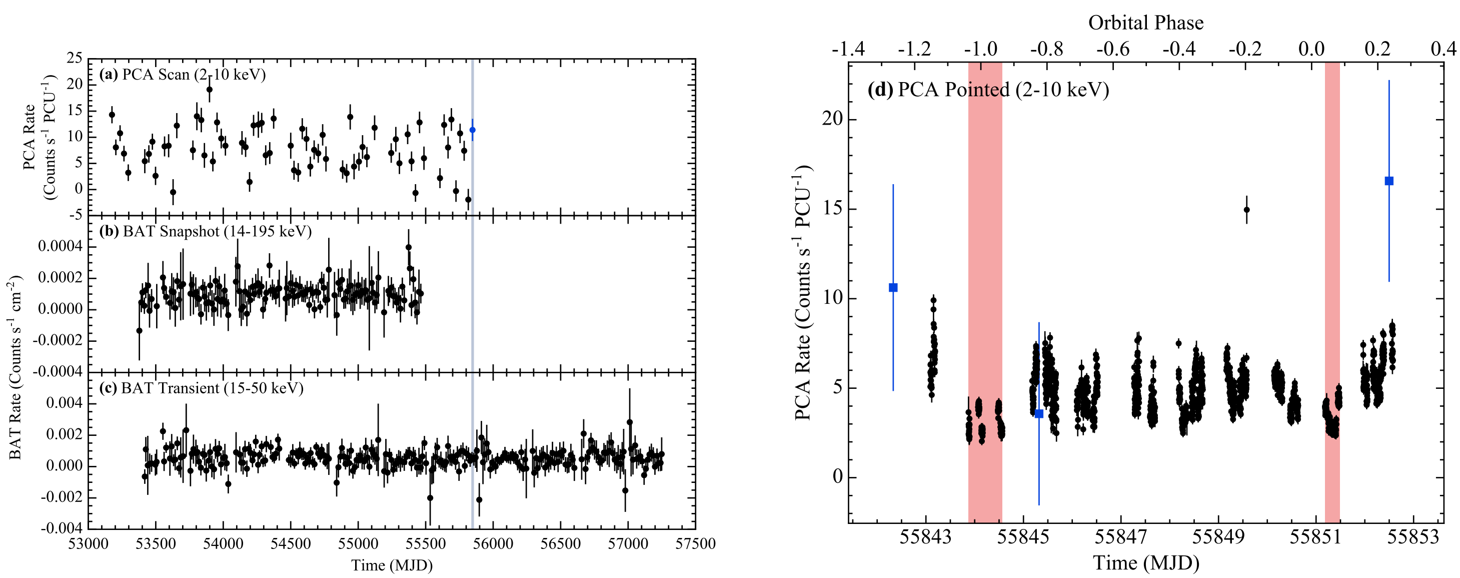

Figure 10.2: **X-ray light curves of IGR J16493–4348.** (a) *RXTE* PCA scan (2–10 keV) weighted average light curve of IGR J16493–4348 using 30 day bin widths. (b) *Swift* BAT 70-month snapshot (14–195 keV) and (c) *Swift* BAT transient monitor (15–50 keV) weighted average light curves of IGR J16493–4348 using bin widths equal to twice the 6.7828 day orbital period. The horizontal uncertainties in Figures 10.2(a)–(c) correspond to the half bin widths in the light curves, and the vertical uncertainties are obtained from the standard error. The pointed PCA observation times are indicated by the blue shaded regions (smaller than the symbol size) in Figures 10.2(a)–(c). (d) Background-subtracted pointed *RXTE* PCA (2–10 keV) light curve of IGR J16493–4348 using all operational PCUs with 128 s time resolution. The red shaded regions correspond to observation times with weak pulsed emission, and nearly simultaneous *RXTE* PCA scan (2–10 keV) observations are overlaid as blue squares. Orbital phase 0 corresponds to $T_{\pi/2}$ from circular solution 1 in Table 10.6.

We used semi-weighting in all of the power spectra in Figure 10.3 since it yielded more significant period detections with smaller uncertainties.

Strong evidence of superorbital modulation near 20.07 days was found in the power spectra of the PCA scan, BAT 70-month snapshot, and BAT transient monitor light curves (see Figure 10.3). The superorbital period was most significantly detected in the power spectrum of the BAT transient monitor light curve in Figure 10.3(c). We refine the superorbital period to 20.067 ± 0.009 days from a semi-weighted DFT of the BAT transient monitor data, which covered an additional 798 days compared to the data in Corbet and Krimm [115]. A coherent signal well above the 99.9% significance level, with a false alarm probability (FAP) [472] of 7×10^{-6}, was found at this period. The power spectrum of the BAT 70-month snapshot data in Figure 10.3(b) showed a peak at 20.07 ± 0.02 days, with a significance level above 99.9% and a FAP of 1×10^{-4}. Evidence of a peak at 20.08 ± 0.02 days, with a FAP of 5×10^{-3}, was also found in the power spectrum of the PCA scan data in Figure 10.3(a), but it was less significant than the corresponding peaks in the BAT power spectra. We note that these superorbital period measurements are all consistent with each other to within 1σ.

In Figure 10.4, we show the PCA scan, BAT 70-month snapshot, and BAT transient monitor light curves folded on our refined superorbital period measurement using 15 bins. Superorbital phase 0 in all of the folded light curves is defined to be the time of maximum flux in the BAT transient monitor data (MJD 55329.65647), which was determined from a sine wave fit to the light curve. The folded PCA and BAT profiles show quasi-sinusoidal variability over many superorbital cycles.

Next, we investigated whether there was an energy dependent phase shift between the superorbital modulation detected in the semi-weighted DFTs of the PCA and BAT light curves by cross-correlating the folded, binned light curves against each other using Equation (10.1), after applying phase offsets to one of the light curves. Linear interpolation was used to determine the count rates of the phase shifted light curve at the phase bins of the unshifted light curve. These linearly interpolated count rates and the count rates from the unshifted light curve were used to compute the cross-correlation statistics. The normalized, linear cross-correlation coefficient between two vectors $\mathbf{u}$ and $\mathbf{v}$ of length N is defined by:

$$r = \mathrm{Re}\frac{\langle \mathbf{u},\mathbf{v} \rangle}{\|\mathbf{u}\| \, \|\mathbf{v}\|}, \tag{10.1}$$

where $\|\mathbf{u}\|$ and $\|\mathbf{v}\|$ are the magnitudes of vectors $\mathbf{u}$ and $\mathbf{v}$, and $\mathbf{u}$ and $\mathbf{v}$ are normalized vectors given by $\mathbf{u} = \mathbf{U} - \bar{U}$ and $\mathbf{v} = \mathbf{V} - \bar{V}$, with $\bar{U}$ and $\bar{V}$ denoting the mean of data vectors $\mathbf{U}$ and $\mathbf{V}$, respectively. The inner product between vectors $\mathbf{u}$ and $\mathbf{v}$ is given by:

$$\langle \mathbf{u},\mathbf{v} \rangle = \sum_{i=1}^{N} u_i v_i^*. \tag{10.2}$$

Each pair of light curves was folded on the superorbital period using $N = 20$, 40, 50, 60, and 80 bins. Phase shifts, in steps of N^{-1}, $0.5N^{-1}$, $0.1N^{-1}$, and $0.01N^{-1}$, were applied to the shifted light curve at each iteration during separate analyses using each

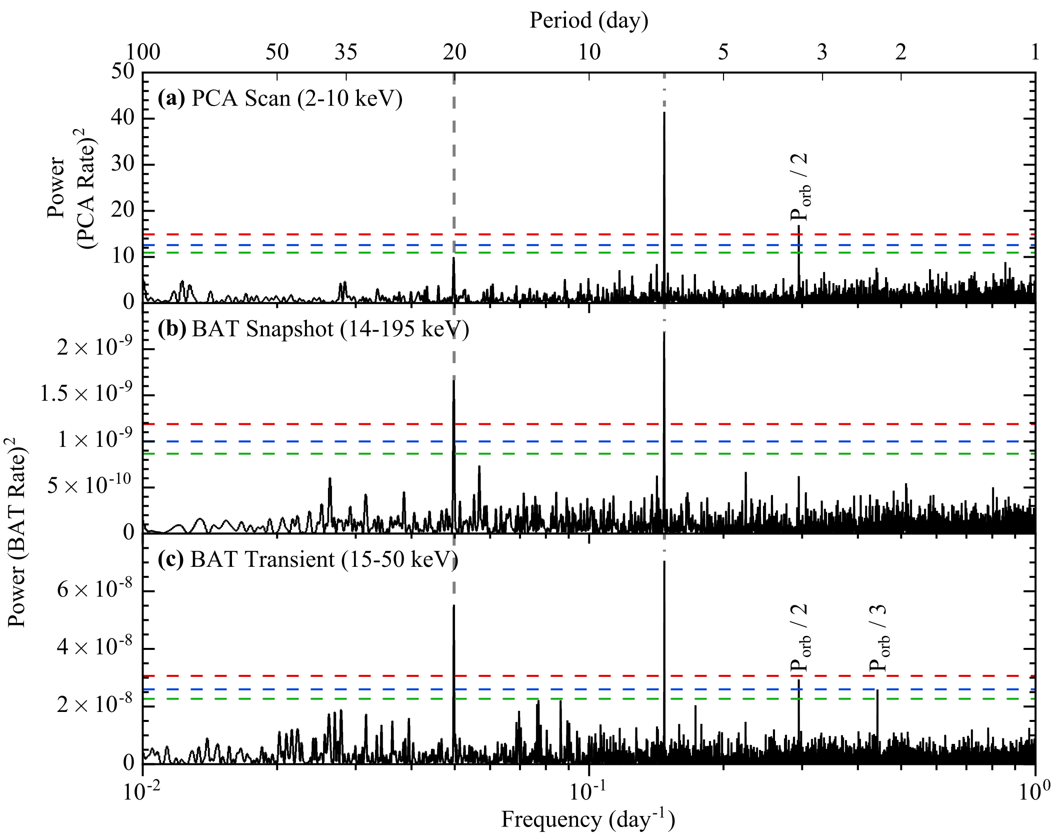

Figure 10.3: **Semi-weighted power spectra of IGR J16493–4348 using the (a) *RXTE* PCA scan (2–10 keV), (b) *Swift* BAT 70-month snapshot (14-195 keV), and (c) *Swift* BAT transient monitor (15–50 keV) light curves.** The horizontal dashed lines indicate 95% (shown in green), 99% (shown in blue), and 99.9% (shown in red) significance levels. The grey vertical dashed line corresponds to the 20.067 day superorbital period from the semi-weighted DFT of the BAT transient monitor data. The 6.7821 day orbital period from the semi-weighted DFT of the BAT transient monitor light curve is indicated by the grey vertical dot-dashed line. Significant harmonics of the orbital period are labeled in each power spectrum.

of these binnings. A total of 20 analyses were performed for each set of light curves, and the superorbital phase corresponding to the maximum cross-correlation value is given by the average of the superorbital phase bins with maximum cross-correlation values from all 20 analyses.

Uncertainties on these measurements were derived from a total of 2,000,000 Monte Carlo simulations, where 100,000 simulations were performed for each binning and phase shift value. At the beginning of each Monte Carlo iteration, we replaced each count rate in both of the unfolded light curves with a value selected randomly from a Gaussian distribution, whose mean was equal to the measured count rate from the unmodified light curves and standard deviation was given by its associated uncertainty. The resultant light curves were then folded on the superorbital period, binned, and cross-correlated using Equation (10.1). The error for each set of Monte Carlo

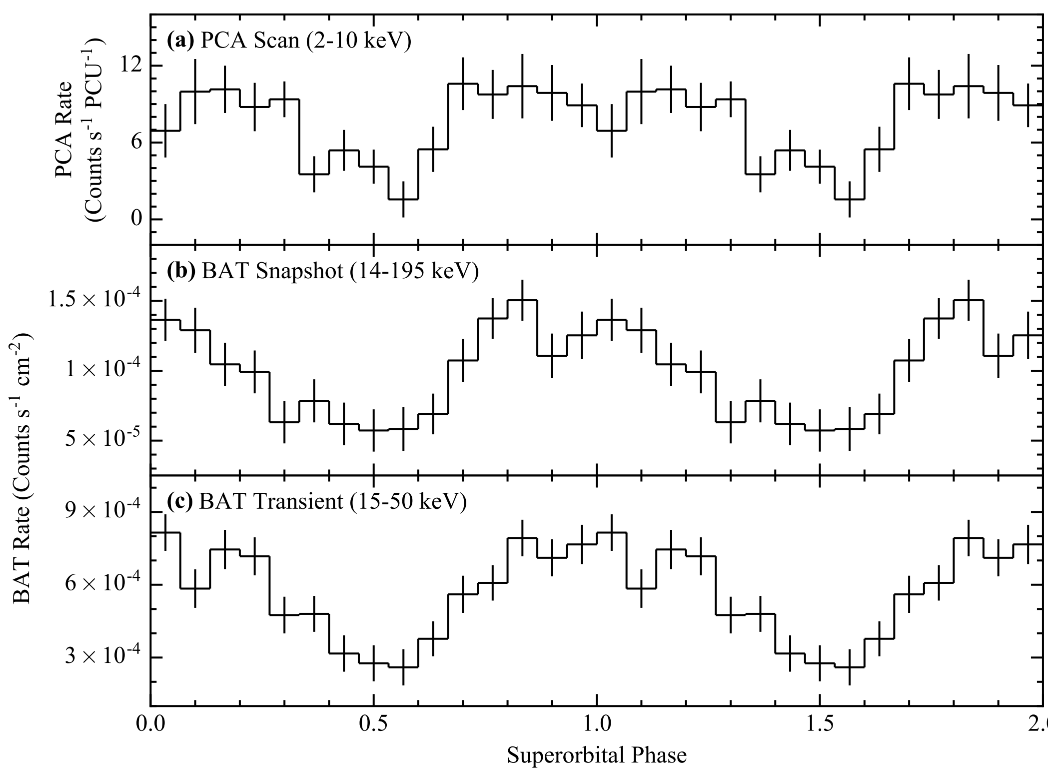

Figure 10.4: **Folded superorbital profiles of IGR J16493–4348.** (a) *RXTE* PCA scan (2–10 keV), (b) *Swift* BAT 70-month snapshot (14–195 keV), and (c) *Swift* BAT transient monitor (15–50 keV) light curves of IGR J16493–4348 folded using 15 bins on the 20.067 day superorbital period measurement from the semi-weighted DFT of the BAT transient monitor data. Superorbital phase 0 corresponds to the time of maximum flux in the BAT transient monitor data (MJD 55329.65647), which was determined from a sine wave fit to the light curve.

analyses was calculated from the standard deviation of the superorbital phase bins with maximum cross-correlation values, and we quote an uncertainty given by the average of all the standard deviations produced by the Monte Carlo procedure.

We find a maximum cross-correlation value between the folded PCA scan and BAT transient monitor light curves at phase 0.02 ± 0.04 of the superorbital period. We repeated this analysis for the PCA scan and BAT 70-month snapshot light curves, and also pairing the BAT 70-month snapshot and transient monitor light curves, and found that the maximum cross-correlation value occured at superorbital phases -0.02 ± 0.04 and 0.00 ± 0.05, respectively. No significantly detected phase offset is observed between the folded PCA and BAT superorbital profiles, which indicates that an energy dependent phase shift is not present.

10.3.2 Orbital Period

Highly significant peaks were detected in the power spectra shown in Figure 10.3 at the previously reported 6.8 day orbital period [117, 140]. We measured orbital periods of 6.784 ± 0.001, 6.788 ± 0.002, and 6.7821 ± 0.0008 days from semi-weighted DFTs of the PCA scan, BAT 70-month snapshot, and BAT transient monitor light curves. The FAPs were 3×10^{-15}, 5×10^{-9}, and 2×10^{-12}, respectively. The orbital period was most significantly detected in the power spectrum of the PCA scan light curve, but the BAT transient monitor data yielded the most precise orbital period measurement due to the longer light curve duration. Harmonics of the orbital period were also significantly detected in the power spectra of the PCA scan and BAT transient monitor light curves and are labeled in Figures 10.3(a) and 10.3(c).

10.3.2.1 Observed Minus Calculated Analysis

We carried out an *O–C* analysis to obtain improved measurements of IGR J16493–4348's orbital period and orbital period derivative using observed mid-eclipse times from the BAT transient monitor and PCA scan light curves. The BAT light curve was divided into six 638 day time intervals, and the PCA light curve was split into two 1348 day segments. At the beginning of the first iteration, we folded each of these divided light curves on the 6.7821 day orbital period from the semi-weighted DFT of the BAT transient monitor light curve. Each divided BAT light curve was folded on the orbital period using 200 bins. Since the PCA light curves were sampled every ~5 days on average, they were not binned to prevent cycle-to-cycle source brightness variations from affecting the folded orbital profiles.

Eclipses were only visible in the BAT and PCA scan light curves after folding the data on the orbital period. We modeled the eclipses in each folded light curve using asymmetric and symmetric step and ramp functions defined in Equation (10.3), where the intensities before ingress, during eclipse, and after egress were assumed to remain constant and change linearly during the ingress and egress transitions [109]. The symmetric model imposes constraints requiring that both the ingress and egress durations and pre-ingress and post-egress count rates be equal. In the asymmetric model, these constraints were removed and the ingress duration, egress duration, and count rates before ingress and after egress were independent free parameters in the model. The adjustable parameters in these models were the: phases corresponding to the start of ingress and start of egress, $\phi_{\rm ing}$ and $\phi_{\rm egr}$, ingress duration, $\Delta\phi_{\rm ing}$, egress duration, $\Delta\phi_{\rm egr}$, pre-ingress count rate, $C_{\rm ing}$, post-egress count rate, $C_{\rm egr}$, and eclipse count rate, $C_{\rm ecl}$. $C_{\rm ing}$ was fit from orbital phase $\phi = -0.2$ to the start of ingress, $C_{\rm ecl}$ was fit during the eclipse, and $C_{\rm egr}$ was fit from the end of egress to orbital phase $\phi = 0.2$. A schematic of the asymmetric eclipse model is shown in Figure 10.5. The eclipse duration was calculated using Equation (10.4), and the mid-eclipse phase was found using Equation (10.5). The eclipse half-angle is defined by Equation (10.6).

$$C(\phi) = \begin{cases} C_{\rm ing}, & -0.2 \leq \phi \leq \phi_{\rm ing} \\ C_{\rm ing} + \left(\frac{C_{\rm ecl}-C_{\rm ing}}{\Delta\phi_{\rm ing}}\right)(\phi - \phi_{\rm ing}), & \phi_{\rm ing} \leq \phi \leq \phi_{\rm ing} + \Delta\phi_{\rm ing} \\ C_{\rm ecl}, & \phi_{\rm ing} + \Delta\phi_{\rm ing} \leq \phi \leq \phi_{\rm egr} \\ C_{\rm ecl} + \left(\frac{C_{\rm egr}-C_{\rm ecl}}{\Delta\phi_{\rm egr}}\right)(\phi - \phi_{\rm egr}), & \phi_{\rm egr} \leq \phi \leq \phi_{\rm egr} + \Delta\phi_{\rm egr} \\ C_{\rm egr}, & \phi_{\rm egr} + \Delta\phi_{\rm egr} \leq \phi \leq 0.2 \end{cases} \tag{10.3}$$

$$\Delta\phi_{\rm ecl} = \phi_{\rm egr} - \left(\phi_{\rm ing} + \Delta\phi_{\rm ing}\right) \tag{10.4}$$

$$\phi_{\rm mid} = \frac{1}{2}\left[\phi_{\rm egr} + \left(\phi_{\rm ing} + \Delta\phi_{\rm ing}\right)\right] \tag{10.5}$$

$$\Theta_e = \Delta\phi_{\rm ecl} \times 180^\circ \tag{10.6}$$

Flares were excluded when fitting the eclipse models to the folded PCA scan light curves, which were identified by data points with count rates above 20 counts s^{-1} PCU^{-1} at orbital phases near the start of ingress or end of egress. This resulted in the removal of approximately 6% of the data from the fitted PCA scan light curves. We chose to remove these data points with high count rates since they increased the fitted χ^2 values, but did not significantly affect the best-fit parameters or their uncertainties.

Observed mid-eclipse times from each folded light curve were determined using Equation (10.5). We fit the observed mid-eclipse times using the orbital change function:

$$T_n = T_{\pi/2} + nP_{\rm orb} + \frac{1}{2}n^2 P_{\rm orb}\dot{P}_{\rm orb}, \tag{10.7}$$

where T_n is the mid-eclipse time in days, n is the nearest integer number of elapsed binary orbits, $P_{\rm orb}$ is the orbital period in days, and $\dot{P}_{\rm orb}$ is the orbital period derivative at $T_{\pi/2}$. Each mid-eclipse time was weighted by its maximum asymmetric error in Table 10.2 during the fitting procedure. After each iteration, the orbital period and $T_{\pi/2}$ were updated with the values obtained from fitting the mid-eclipse times with the orbital change function in Equation (10.7), and these values were used to refold the BAT and PCA light curves in the next iteration. The O–C procedure was repeated until there were no significant changes in the orbital period and $T_{\pi/2}$ between successive iterations.

We observed that many of the parameters in these models were highly covariant from projections of their posterior distributions. A Bayesian MCMC fitting procedure was used to incorporate these covariances into the model parameter uncertainties by marginalizing over multi-dimensional joint posterior distributions. From Bayes' theorem, the posterior probability of a set of model parameters, $\boldsymbol{\theta}$, given the observed data, $\boldsymbol{D}$, and any prior information, $\boldsymbol{I}$, is defined by:

$$p(\boldsymbol{\theta}|\boldsymbol{D},\boldsymbol{I}) = \frac{p(\boldsymbol{D}|\boldsymbol{\theta},\boldsymbol{I})p(\boldsymbol{\theta}|\boldsymbol{I})}{p(\boldsymbol{D}|\boldsymbol{I})}. \tag{10.8}$$

Here, $p(\boldsymbol{D}|\boldsymbol{\theta},\boldsymbol{I}) = \mathcal{L}(\boldsymbol{\theta}|\boldsymbol{D},\boldsymbol{I})$ is the likelihood function, $p(\boldsymbol{\theta}|\boldsymbol{I}) = \pi(\boldsymbol{\theta}|\boldsymbol{I})$ is the prior probability distribution for the model parameters, and $p(\boldsymbol{D}|\boldsymbol{I})$ is the marginal likelihood function. The marginal likelihood function can be thought of as a normalization constant, determined by requiring the posterior probability integrate to unity when integrating over all of the parameters in the model. Marginalized single parameter posterior distributions were obtained by integrating the joint posterior distribution over the remaining parameters:

$$p(\theta_i|\boldsymbol{D},\boldsymbol{I}) \propto \int_{\mathcal{V}} d^n\boldsymbol{\theta}' \mathcal{L}(\boldsymbol{\theta}|\boldsymbol{D},\boldsymbol{I})\pi(\boldsymbol{\theta}|\boldsymbol{I}), \tag{10.9}$$

where $\boldsymbol{\theta}'$ is a parameter vector equal to $\boldsymbol{\theta}$ excluding θ_i and $\mathcal{V}$ is the integration volume of the parameter space. We assumed uninformed, flat priors on all of our model parameters and used a Gaussian likelihood function, such that $\mathcal{L}(\boldsymbol{\theta}|\boldsymbol{D},\boldsymbol{I}) \propto \exp(-\chi^2/2)$.

An affine-invariant MCMC ensemble sampler [207], implemented in `emcee`[q] by Foreman-Mackey et al. [188], was used to sample the posterior probability density functions (PDFs) of the model parameters in Equations (10.3) and (10.7). The parameter spaces were explored using 200 walkers and a chain length of 1,500 steps per walker. The first 500 steps in each chain were treated as the initial burn-in phase and were removed from the analysis. The position of each walker was updated using the current positions of all of the other walkers in the ensemble [207]. We initialized the walkers to start from a small Gaussian ball centered around the parameter values obtained from maximizing the likelihood function subject to the constraints given by the priors. The posterior distributions of the model parameters were calculated using the remaining 1,000 steps in each chain. Best-fit values for the model parameters were derived from the median of the marginalized posterior distributions, and we quote 1σ uncertainties using Bayesian credible intervals.

In Table 10.2, we list the observed mid-eclipse times obtained from the *O–C* analysis using asymmetric and symmetric eclipse models. These measurements are also plotted in the top panels of Figures 10.6(a) and 10.6(b), along with the best-fit orbital change functions. The residuals were derived by subtracting the fits from the mid-eclipse times and are shown in the bottom panels of these figures. We note that our mid-eclipse times are consistent with the mid-eclipse time reported by Cusumano et al. [140] using *Swift* BAT survey (15–50 keV) data, which we indicate with blue triangles in these plots.

We refine the orbital period to 6.7828 ± 0.0004 days using an asymmetric eclipse model and a fiducial mid-eclipse time of $T_{\pi/2} = \mathrm{MJD}\ 55851.3 \pm 0.1$ in our *O–C* analysis. A consistent orbital period of 6.7825 ± 0.0004 days was found using a symmetric eclipse model with $T_{\pi/2} = \mathrm{MJD}\ 55851.21 \pm 0.07$. Orbital period derivatives of $0.01^{+1.74}_{-1.77} \times 10^{-7}\ \mathrm{d\,d^{-1}}$ and $0.09^{+1.69}_{-1.73} \times 10^{-7}\ \mathrm{d\,d^{-1}}$ were measured by fitting the asymmetric and symmetric mid-eclipse times with the orbital change function in Equation (10.7), respectively. These values indicate that there was no significant change in the orbital period over approximately 500 orbital cycles.

We selected the period obtained from using an asymmetric eclipse model in the *O–C* analysis as our preferred orbital period measurement. Since most eclipsing sgHMXBs show evidence of asymmetry in their X-ray eclipses (e.g., see [179]), we argue that an asymmetric eclipse model is more representative of the eclipse behavior in these systems. Additionally, constraints on the eclipse transition durations and count rates outside of the eclipses could introduce systematic errors when fitting the folded light curves with a symmetric eclipse model.

10.3.2.2 Folded Orbital Profiles

Orbital profiles were produced by folding the PCA scan, BAT 70-month snapshot, and BAT transient monitor light curves on the orbital periods from the *O*–*C* analysis in Section 10.3.2.1. Asymmetric and symmetric eclipse models, defined in Equation (10.3), were fit to each of the folded light curves using the Bayesian MCMC

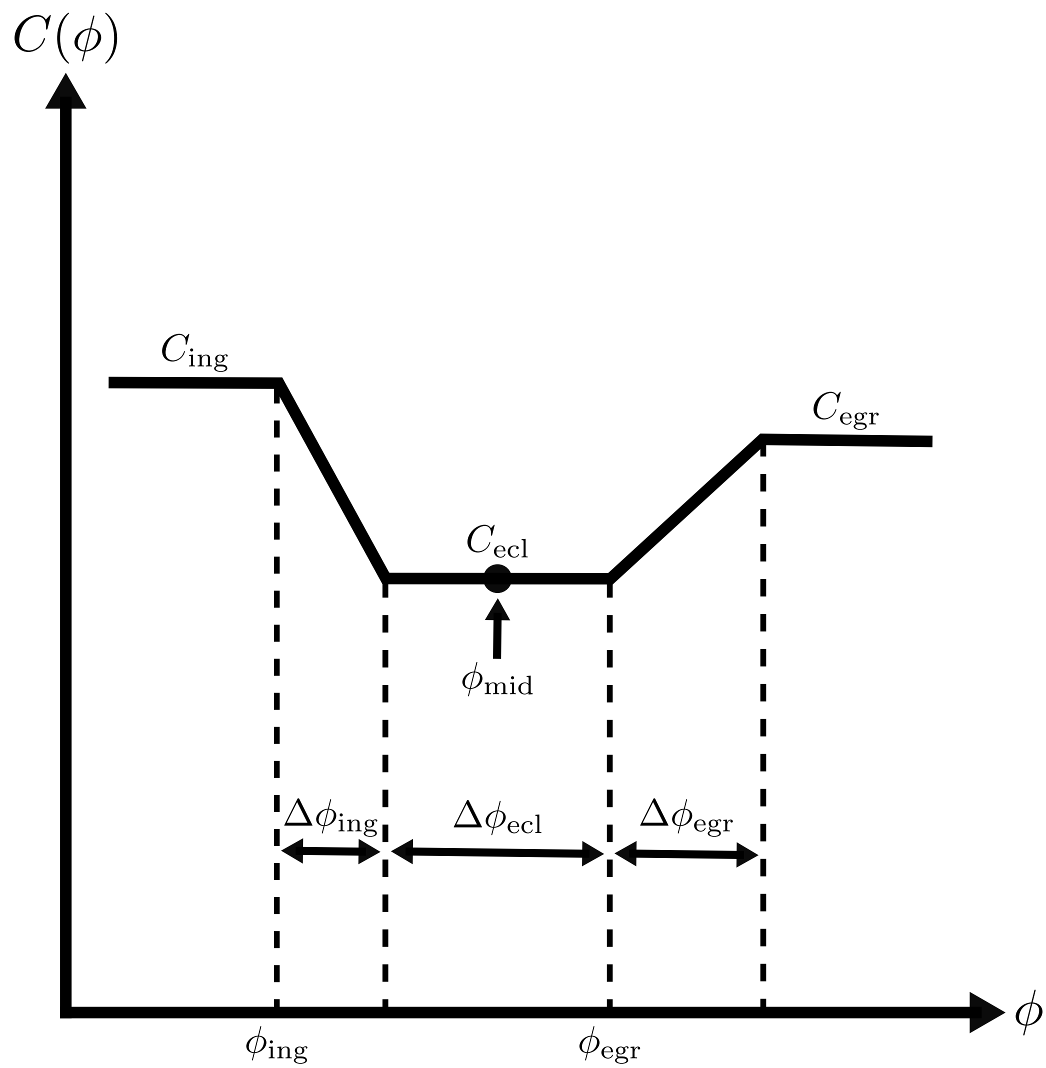

Figure 10.5: **Schematic diagram of the asymmetric step and ramp function in Equation (10.3).** This model was used to characterize the eclipses in the folded *RXTE* PCA scan (2–10 keV), *Swift* BAT 70-month snapshot (14–195 keV), and *Swift* BAT transient monitor (15–50 keV) light curves.

Table 10.2: **Mid-Eclipse Times of IGR J16493–4348 from *O–C* Analysis**

Observation	Orbital Cycle (n)	Mid-Eclipse Time[a] (MJD)	Mid-Eclipse Time[b] (MJD)
BAT Transient Monitor	–312	$53735.2^{+0.2}_{-0.1}$	53735.2 ± 0.1
PCA Scan	–297	$53836.69^{+0.09}_{-0.08}$	$53836.76^{+0.09}_{-0.07}$
BAT Transient Monitor	–217	54379.5 ± 0.2	54379.4 ± 0.2
BAT Transient Monitor	–124	$55010.4^{+0.4}_{-0.3}$	55010.3 ± 0.3
PCA Scan	–98	$55186.51^{+0.10}_{-0.09}$	55186.52 ± 0.06
BAT Transient Monitor	–29	$55654.7^{+0.2}_{-0.3}$	55654.7 ± 0.3
BAT Transient Monitor	65	$56292.2^{+0.4}_{-0.2}$	56292.1 ± 0.3
BAT Transient Monitor	159	$56929.7^{+0.3}_{-0.2}$	$56929.6^{+0.3}_{-0.2}$

We quote 1σ uncertainties using Bayesian credible intervals.
[a] Obtained using an asymmetric eclipse model.
[b] Obtained using a symmetric eclipse model.

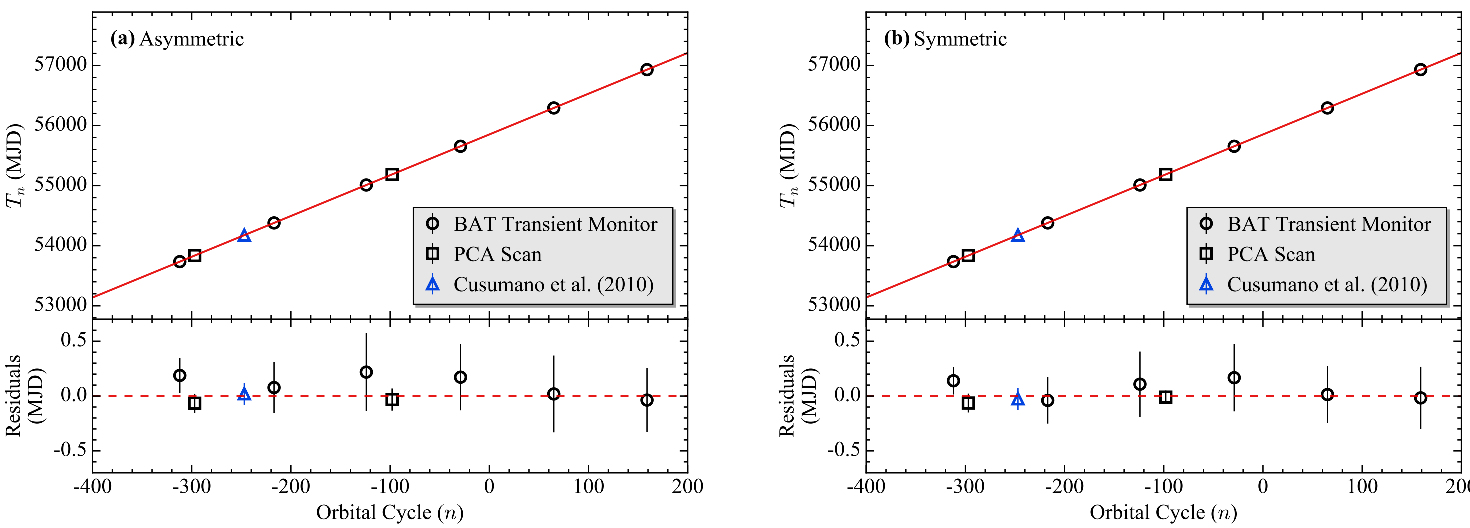

Figure 10.6: **Mid-eclipse times of IGR J16493–4348.** Top panels: Observed mid-eclipse times of IGR J16493–4348 obtained from an *O–C* analysis using the *RXTE* PCA scan (2–10 keV) and *Swift* BAT transient monitor (15–50 keV) light curves and (a) asymmetric and (b) symmetric eclipse models. The solid red line corresponds to the best-fit orbital change function using Equation (10.7). Each mid-eclipse time was weighted by its maximum asymmetric error in Table 10.2 during the fitting procedure. Bottom panels: Residuals determined by subtracting the best fit from the mid-eclipse times. Mid-eclipse times derived from the BAT transient monitor and PCA scan light curves are represented by black open circles and black open squares, respectively. The mid-eclipse time measurement reported by Cusumano et al. [140] is indicated with blue open triangles.

procedure described in Section 10.3.2.1 with the same number of walkers and chain lengths. In Tables 10.3 and 10.4, we list the best-fit eclipse model parameters from the median of the marginalized posterior distributions, along with 1σ uncertainties using Bayesian credible intervals. The folded orbital profiles are shown in Figures 10.7(a)–(c), and the best-fit asymmetric and symmetric eclipse models are overlaid in green and red, respectively.

The mid-eclipse times ($T_{\rm mid}$), calculated in Tables 10.3 and 10.4 using Equation (10.5), are consistent with each other at the 1σ level. Fitting an asymmetric eclipse model to the folded PCA scan, BAT 70-month snapshot, and BAT transient monitor light curves yielded eclipse durations of 0.9 ± 0.1, $0.7^{+0.2}_{-0.3}$, and 0.7 ± 0.3 days, respectively. Using a symmetric eclipse model, we measured eclipse lengths of $0.92^{+0.10}_{-0.09}$, 0.8 ± 0.2, and 0.8 ± 0.2 days, respectively. These eclipse durations are all consistent with each other to within 1σ and agree well with the ~0.8 day eclipse length reported by Cusumano et al. [140] from BAT survey observations. There were no statistically significant differences between the ingress and egress durations or pre-ingress and post-egress count rates obtained from fitting the light curves with an asymmetric eclipse model. This suggests that large-scale structure in the stellar wind from a strong accretion or photoionization wake is unlikely.

10.3.3 Pulse Period

We searched for pulsations with periods between 32 s and 9.5 days in the unweighted power spectrum of the entire pointed *RXTE* PCA (2.5–25 keV) light curve. The power spectrum was oversampled by a factor of five compared to the nominal frequency resolution, which was found to be 1.22×10^{-6} Hz from the length of the light curve. The data in the pointed PCA power spectrum were not weighted since the observations were performed using the same pointing and the light curve had a uniform time resolution of 16 s.

A significant amount of low frequency noise was detected in the power spectrum shown in Figure 10.8(a). We estimated the continuum noise level by fitting polynomials to the logarithm of the power spectrum in Figure 10.8(b) after adding a constant value of 0.25068 to remove the bias from the χ^2 distribution of the log-spectrum [416, 542]. We found that fitting a linear function to the log-spectrum, which would indicate a power-law relationship in the raw power spectrum, was not optimal for describing the power at low frequencies. A quadratic fit significantly overestimated the low frequency power, and we found that a cubic fit to the log-

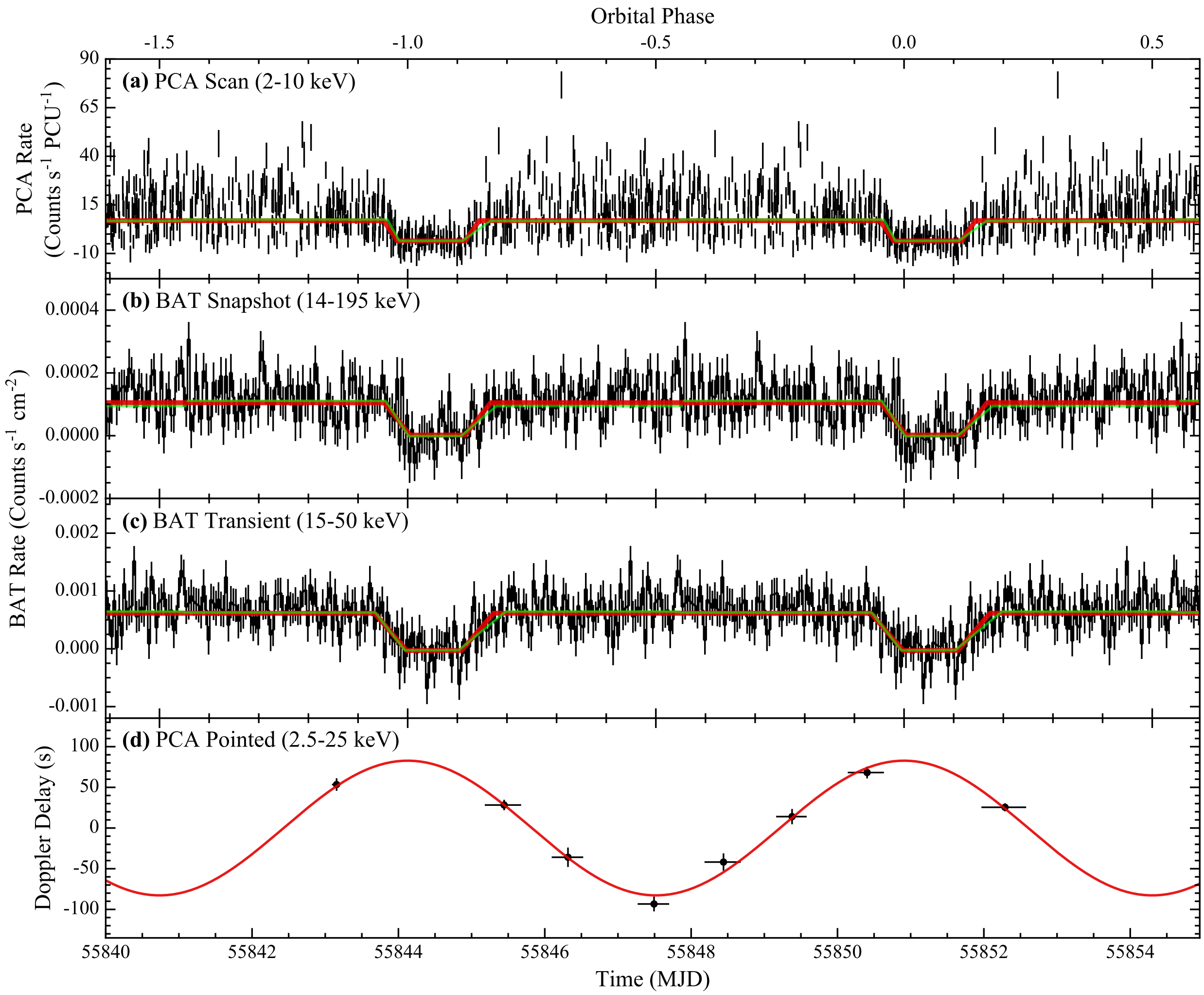

Figure 10.7: **Folded orbital eclipse profiles and Doppler delay times of IGR J16493–4348.** (a) *RXTE* PCA scan (2–10 keV), (b) *Swift* BAT 70-month snapshot (14–195 keV), and (c) *Swift* BAT transient monitor (15–50 keV) light curves of IGR J16493–4348 folded on the refined 6.7828 day orbital period from the O–C analysis in Section 10.3.2.1. The BAT light curves were folded using 200 bins. The PCA scan light curve was not binned to prevent cycle-to-cycle source brightness variations from affecting the folded orbital profile. We overlay the asymmetric (shown in green) and symmetric (shown in red) step and ramp eclipse models from Tables 10.3 and 10.4. Discontinuities in the asymmetric eclipse model are included at half orbital cycles from the mid-eclipse times. (d) Orbital Doppler delay times measured during the final iteration of the pulsar timing analysis using the pointed *RXTE* PCA (2.5–25 keV) light curve of IGR J16493–4348. The uncertainties on the ToAs correspond to the statistical errors obtained from Monte Carlo simulations and do not include the additional 3.1 s systematic uncertainty from circular solution 2 in Table 10.6. The horizontal error bars indicate the duration of the light curve segments used to derive the ToAs. The red curve shows the predicted delay times using the fit from circular solution 1 in Table 10.6, which assumes a constant neutron star rotational period. Orbital phase 0 corresponds to $T_{\pi/2}$ from circular solution 1 in Table 10.6.

Table 10.3: **Asymmetric Eclipse Model Parameters of IGR J16493–4348**

Model Parameter	*RXTE* PCA Galactic Bulge Scans (2–10 keV)	*Swift* BAT 70-month Snapshots (14–195 keV)	*Swift* BAT Transient Monitor (15–50 keV)
$\phi_{\rm ing}$	$-0.092^{+0.005}_{-0.007}$	$-0.10^{+0.02}_{-0.01}$	$-0.12^{+0.01}_{-0.02}$
$\phi_{\rm egr}$	$0.059^{+0.009}_{-0.011}$	$0.06^{+0.02}_{-0.03}$	$0.05^{+0.01}_{-0.03}$
$\Delta\phi_{\rm ing}$	$0.023^{+0.011}_{-0.009}$	$0.05^{+0.03}_{-0.02}$	$0.06^{+0.05}_{-0.03}$
$\Delta\phi_{\rm egr}$	$0.06^{+0.04}_{-0.03}$	$0.07^{+0.05}_{-0.04}$	0.09 ± 0.04
$C_{\rm ing}$	$7.5 \pm 0.8^{\rm a}$	$0.11 \pm 0.01^{\rm b}$	$0.63 \pm 0.07^{\rm b}$
$C_{\rm egr}$	$6.7 \pm 1.1^{\rm a}$	$0.09^{+0.02{\rm b}}_{-0.01}$	$0.64^{+0.10{\rm b}}_{-0.08}$
$C_{\rm ecl}$	$-3.5 \pm 0.6^{\rm a}$	$-0.001^{+0.013{\rm b}}_{-0.014}$	$-0.03^{+0.06{\rm b}}_{-0.07}$
$\Delta\phi_{\rm ecl}$	$0.13^{+0.01}_{-0.02}$	0.11 ± 0.04	$0.11^{+0.05}_{-0.04}$
$P_{\rm orb}{}^{\rm c}$	6.7828 ± 0.0004	6.7828 ± 0.0004	6.7828 ± 0.0004
$\dot{P}_{\rm orb}{}^{\rm d}$	$0.01^{+1.74}_{-1.77}$	$0.01^{+1.74}_{-1.77}$	$0.01^{+1.74}_{-1.77}$
$T_{\rm mid}{}^{\rm e}$	55851.2 ± 0.1	55851.3 ± 0.2	55851.2 ± 0.2
$\Theta_e{}^{\rm f}$	$22.9^{+2.7}_{-2.8}$	$19.0^{+6.4}_{-7.9}$	$19.5^{+9.2}_{-7.3}$
χ^2_ν (dof)	1.22 (197)	1.10 (73)	1.16 (73)

We quote 1σ uncertainties using Bayesian credible intervals. Phase 0 is defined at mid-eclipse.
[a] Units are counts $\rm s^{-1}\,PCU^{-1}$.
[b] Units are 10^{-3} counts $\rm cm^{-2}\,s^{-1}$.
[c] Refined orbital period from *O*–*C* analysis. Units are days.
[d] Orbital period derivative from orbital change function. Units are $10^{-7}\,\rm d\,d^{-1}$.
[e] Units are MJD.
[f] Units are degrees.

spectrum sufficiently characterized the continuum noise level. The red noise was removed by subtracting the cubic fit from the logarithm of the power spectrum, which produced the corrected power spectrum in Figure 10.8(c). We find strong evidence of pulsed emission at a period of 1093.3 ± 0.1 s in the corrected power spectrum, which we associate with the rotational period of the neutron star. This pulse period is labeled by the vertical dot-dashed line in Figure 10.8.

At lower frequencies, there are significant peaks near the ~5800 s orbital period of *RXTE*, which exhibit complex structure. The 95%, 99%, and 99.9% significance levels are labeled in Figure 10.8(c), but do not account for the uncertainty in the model used to fit the continuum or the red noise subtraction. These effects are greatest at low frequencies, and larger power levels would be required to achieve these true levels of statistical significance. We also note that none of the low frequency peaks in the uncorrected power spectrum are statistically significant after the continuum noise was removed.

Table 10.4: **Symmetric Eclipse Model Parameters of IGR J16493–4348**

Model Parameter	*RXTE* PCA Galactic Bulge Scans (2–10 keV)	*Swift* BAT 70-month Snapshots (14–195 keV)	*Swift* BAT Transient Monitor (15–50 keV)
$\phi_{\rm ing}$	$-0.100^{+0.006}_{-0.008}$	$-0.10^{+0.02}_{-0.01}$	-0.12 ± 0.01
$\phi_{\rm egr}$	0.064 ± 0.006	$0.06^{+0.02}_{-0.01}$	0.06 ± 0.01
$\Delta\phi$[a]	0.03 ± 0.01	$0.05^{+0.02}_{-0.03}$	$0.06^{+0.03}_{-0.02}$
C[b]	6.9 ± 0.5[c]	$0.105^{+0.010}_{-0.009}$[d]	0.62 ± 0.05[d]
$C_{\rm ecl}$	-3.6 ± 0.6[c]	$0.002^{+0.012}_{-0.013}$[d]	-0.03 ± 0.06[d]
$\Delta\phi_{\rm ecl}$	$0.14^{+0.02}_{-0.01}$	$0.11^{+0.04}_{-0.03}$	0.11 ± 0.03
$P_{\rm orb}$[e]	6.7825 ± 0.0004	6.7825 ± 0.0004	6.7825 ± 0.0004
$\dot{P}_{\rm orb}$[f]	$0.09^{+1.69}_{-1.73}$	$0.09^{+1.69}_{-1.73}$	$0.09^{+1.69}_{-1.73}$
$T_{\rm mid}$[g]	55851.19 ± 0.09	55851.3 ± 0.1	55851.2 ± 0.1
Θ_e[h]	$24.5^{+2.8}_{-2.5}$	$20.0^{+6.6}_{-6.2}$	$19.9^{+6.1}_{-5.2}$
χ^2_ν (dof)	1.17 (198)	1.25 (75)	0.97 (75)

We quote 1σ uncertainties using Bayesian credible intervals. Phase 0 is defined at mid-eclipse.

[a] $\Delta\phi = \Delta\phi_{\rm ing} = \Delta\phi_{\rm egr}$, assuming equal ingress and egress durations.

[b] $C = C_{\rm ing} = C_{\rm egr}$, assuming equal pre-ingress and post-egress count rates.

[c] Units are counts $\mathrm{s^{-1}}$ $\mathrm{PCU^{-1}}$.

[d] Units are 10^{-3} counts $\mathrm{cm^{-2}\,s^{-1}}$.

[e] Orbital period from O–C analysis. Units are days.

[f] Orbital period derivative from orbital change function. Units are 10^{-7} d $\mathrm{d^{-1}}$.

[g] Units are MJD.

[h] Units are degrees.

10.4 System Geometry

A pulsar timing algorithm was developed to precisely measure the neutron star rotational period and orbital parameters of IGR J16493–4348 by fitting circular and eccentric orbital timing models to the ToAs. These results are presented here, along with a rigorous treatment of the statistical and systematic uncertainties associated with the ToAs. We also provide measurements of additional parameters constraining the system geometry, such as the eclipse half-angle, donor star spectral type, and Roche lobe radius, for different possible inclinations and neutron star masses.

10.4.1 Pulsar Timing Analysis

We carried out a phase-coherent pulsar timing analysis using the pointed *RXTE* PCA (2.5–25 keV) light curve, where each rotation of the pulsar was unambiguously accounted for over the time span of the observations. An iterative epoch folding algorithm [91, 307, 483] was used to derive the ToAs. Epoch folding is useful because of its higher sensitivity to non-sinusoidal pulse shapes and ability to handle gaps in the light curve. The ToAs were obtained by measuring phase offsets between a pulse template and individual measured profiles, which were created by dividing the light curve into smaller segments.

The measured profiles were created by first dividing the pointed PCA light curve into individual segments spanning at least one pulse period in duration. Data within 20 ks of another segment were merged together. Neighboring segments were separated by at least 36 ks, and the segment durations ranged from 8.4 to 52.8 ks. This produced a total of eight segments from which ToAs were derived. We partitioned the data in

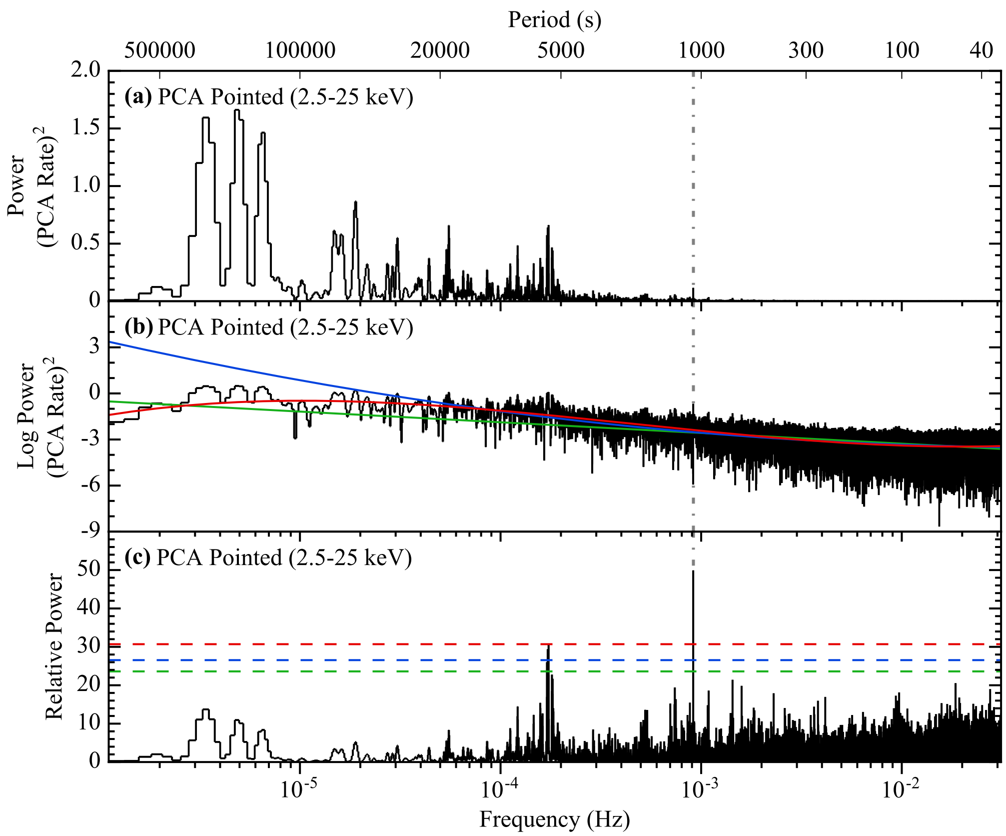

Figure 10.8: **Power spectra of pointed *RXTE* PCA (2.5–25 keV) observations of IGR J16493–4348.** (a) Unweighted power spectrum of IGR J16493–4348 using the pointed *RXTE* PCA (2.5–25 keV) light curve without low frequency noise subtracted from the continuum. (b) Linear (shown in green), quadratic (shown in blue), and cubic (shown in red) fits to the logarithm of the power spectrum. The cubic fit was used to estimate and remove the continuum noise. (c) Corrected power spectrum after subtracting the cubic continuum noise model. The horizontal dashed lines indicate the 95% (shown in green), 99% (shown in blue), and 99.9% (shown in red) significance levels. The vertical dot-dashed line corresponds to the 1093 s pulse period. The statistically significant peaks near ~5800 s are attributed to the orbital period of *RXTE*.

this manner to optimize both the signal-to-noise of the pulsations in each segment and the final number of ToAs.

An initial set of measured profiles were produced by folding each segment on the 1093.3 s pulse period found in the noise subtracted power spectrum of the pointed PCA light curve (see Section 10.3.3). The segments were folded using 68 bins, which provided a time resolution equal to the 16 s sampling rate in the light curve. A preliminary pulse template was created by aligning the measured profiles and averaging the count rates in each bin. The uncertainties on the count rates in the pulse template were calculated by summing the errors in each bin in quadrature and then normalizing by the total number of measured profiles. This method of generating an initial template is beneficial because it incorporates the effects of the binary system's orbital motion, which are neglected when the entire light curve is folded on the pulse period.

Next, the phase offset between the pulse template and each of the measured profiles was determined by cross-correlating the two profiles in the Fourier frequency domain [511]. It is advantageous to calculate the cross-correlation in the frequency domain, as opposed to using time domain techniques, because it circumvents systematic errors due to binning and allows for the ToAs to be measured with greater accuracy. Assuming that the measured profile is a scaled and shifted version of the pulse template, a phase shift is equivalent to multiplying the template by a complex exponential. The phase shift between each measured profile, $d(\phi)$, and the pulse template, $p(\phi)$, was found by minimizing [149, 280, 511]:

$$\chi^2(A,\phi) = \sum_{k=1}^{k_{\max}} \frac{\left|d_k - A p_k e^{-2\pi i k \phi}\right|^2}{\sigma_k^2}, \tag{10.10}$$

where $d_k = \sum_j d(j/N) e^{-2\pi i jk/N}$ is the DFT of $d(\phi)$, $p_k = \sum_j p(j/N) e^{-2\pi i jk/N}$ is the DFT of $p(\phi)$, σ_k^2 is the noise power at each frequency bin of the DFT, and A and ϕ are the measured amplitude and phase shift, respectively.

Several of the observations did not exhibit strong pulsed emission (see the bold entries in Table 10.1) and were excluded from the pulsar timing analysis since their measured profiles yielded phase offsets that could not be well constrained during the cross-correlation procedure. The omitted data spanned MJDs 55843.87475 to 55844.56803 (orbital phases –0.037 to 0.065) and MJDs 55851.18401 to 55851.48269 (orbital phases 0.041 to 0.085), where orbital phase 0 is defined at $T_{\pi/2}$ from circular solution 1 in Table 10.6. The excised data are shown in red in Figure 10.1 and coincide with the eclipse and eclipse transition phases measured from fitting the folded PCA and BAT orbital profiles with asymmetric and symmetric eclipse models (see Section 10.3.2.2).

Pulse time delays were obtained by multiplying the phase differences between each of the measured profiles and the pulse template by the folding period. The ToAs were derived by adding each time delay to the time nearest to the middle of its corresponding observation interval where the pulsar rotational phase was zero. Referencing each ToA relative to the middle of the interval reduces systematic effects that can arise from folding with an inaccurate timing model and is a standard convention used in pulsar timing (e.g., see [316]).

Folding the data with a slightly incorrect pulse period can lead to pulse smearing and produce ToAs that show a drift in pulse phase over the observation duration. At the end of each iteration, a small correction was applied to the pulse period using the drift rate measured from the ToAs. This improved pulse period measurement was then used to refold each of the segments to produce corrected measured profiles and a sharper pulse template in the following iteration. A refined pulse template was constructed by averaging the corrected measured profiles together without any alignment, and a new set of ToAs was produced by cross-correlating the measured profiles with the updated pulse template in the frequency domain. This algorithm was repeated until there was no statistically significant change in the pulse period between successive iterations.

We refine the pulse period to 1093.1036 ± 0.0004 s using the ToAs obtained during the last iteration of the pulsar timing analysis. The final pulse template (2.5–25 keV), shown in Figure 10.9, exhibits sharp features on top of a quasi-sinusoidal template shape. These sharp variations in the pulse template enabled the phase shifts between the measured profiles and the template to be determined more accurately. A list of ToAs measured during the final iteration of the pulsar timing analysis is provided in Table 10.5. Pulse profiles in the 2.5–5, 5–10, 10–25, and 2.5–25 keV energy bands are shown in Figure 10.10 and were obtained by folding the pointed PCA light curves on the final pulse period measurement after correcting for orbital Doppler delays. We define the peak-to-peak pulsed fraction as:

$$\mathcal{P} = \frac{(F_{\max} - F_{\min})}{(F_{\max} + F_{\min})}, \tag{10.11}$$

where $F_{\max}$ and $F_{\min}$ are the maximum and minimum count rates in the pulse profile, respectively. Using Equation (10.11), the pulsed fractions in the 2.5–5, 5–10, 10-25, and 2.5–25 keV energy bands are 0.08 ± 0.02, 0.12 ± 0.02, 0.27 ± 0.04, and 0.13 ± 0.02, respectively. These measurements indicate an increase in pulsed fraction with increasing X-ray energy.

10.4.2 Pulse Time of Arrival Uncertainties

Statistical uncertainties on the ToAs were calculated using 100,000 Monte Carlo simulations [527, 528]. At the beginning of each simulation, the pointed PCA light curve was divided into individual segments according to the procedure described in Section 10.4.1. Each count rate in the segments was replaced with a value selected randomly from a Gaussian distribution, with mean equal to the original background-subtracted count rate and standard devation given by its associated uncertainty. Simulated measured profiles were produced by folding these randomly

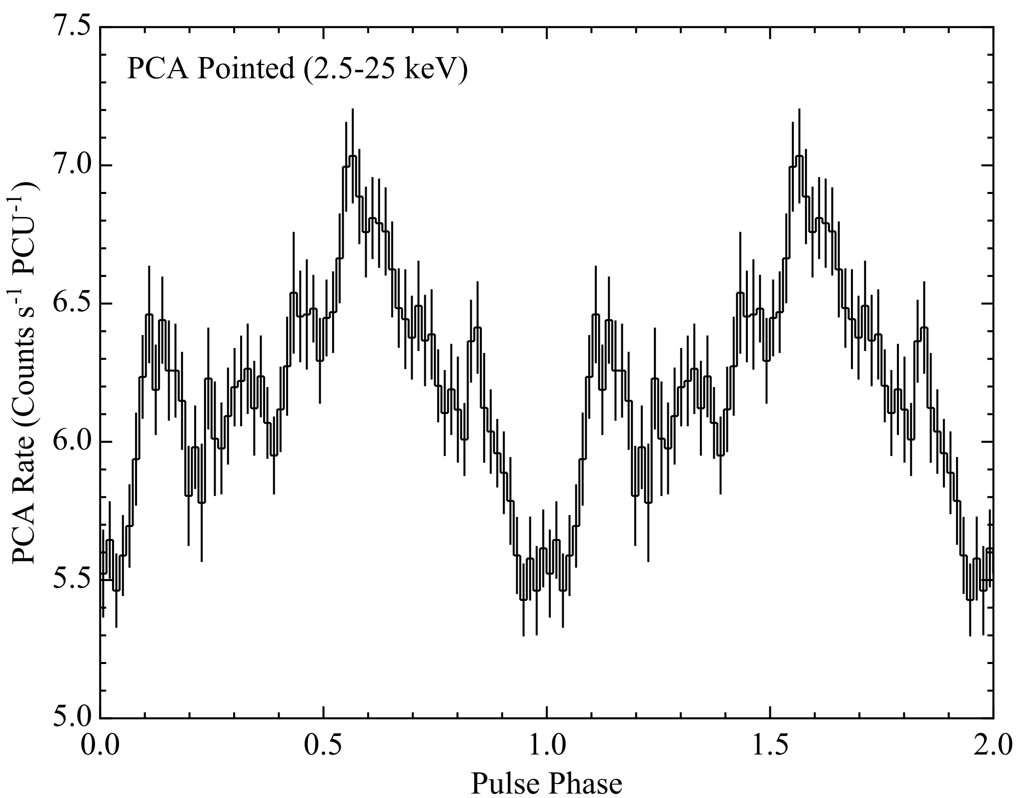

Figure 10.9: **Final pulse template of IGR J16493–4348 obtained during the last iteration of the pulsar timing analysis using the pointed *RXTE* PCA (2.5–25 keV) light curve.** The count rates in each bin were derived by averaging the count rates in the measured profiles. The uncertainties were calculated by summing the errors on the count rates in each bin of the measured profiles in quadrature and then normalizing by the total number of profiles. Phase 0 corresponds to $T_{\pi/2}$ from circular solution 1 in Table 10.6.

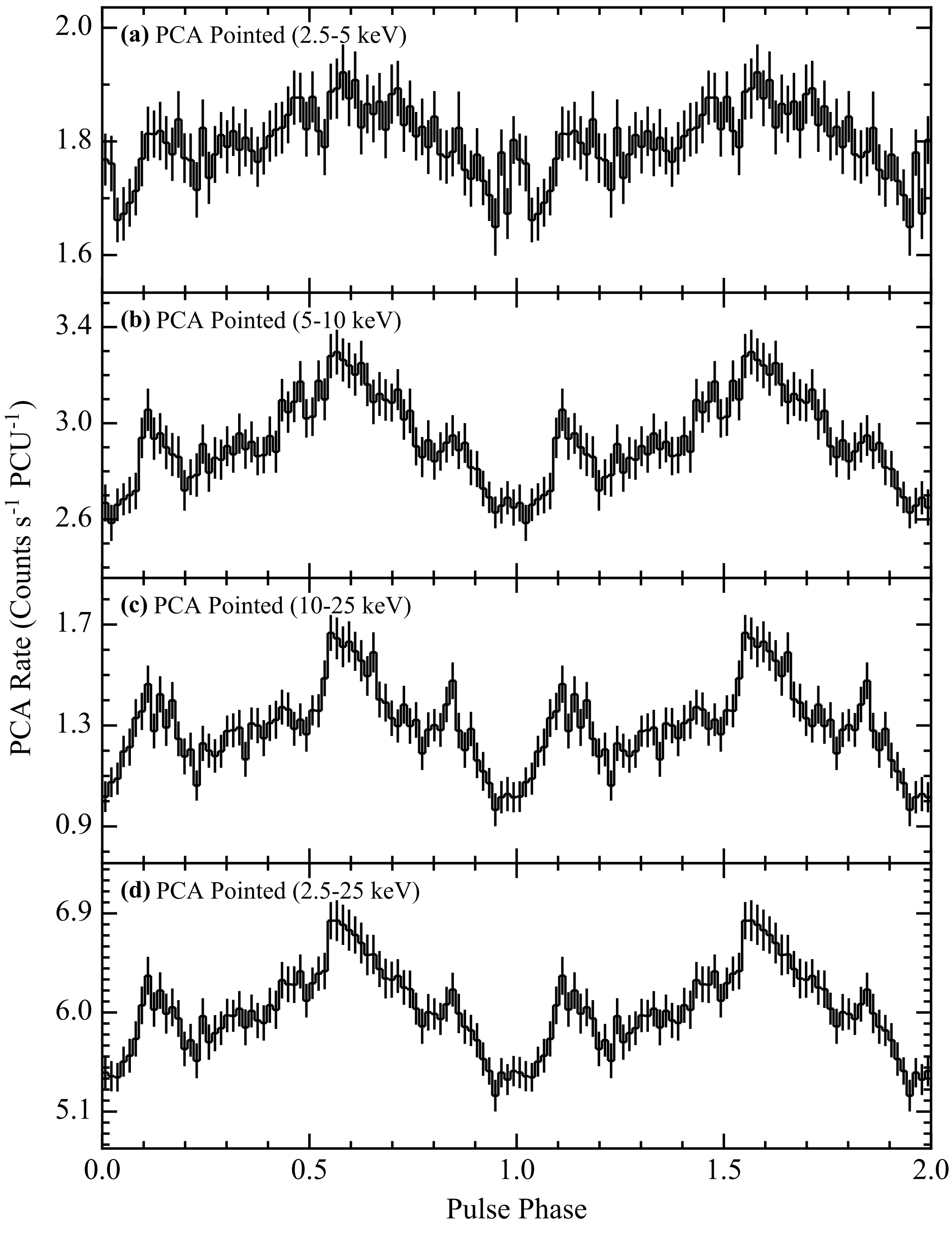

Figure 10.10: **Pulse profiles of IGR J16493–4348 derived from pointed *RXTE* PCA observations in the (a) 2.5–5, (b) 5–10, (c) 10–25, and (d) 2.5–25 keV energy bands.** The profiles were obtained by folding the light curves on the refined 1093 s pulse period measurement from the final iteration of the pulsar timing analysis after correcting for orbital Doppler delays. Phase 0 corresponds to $T_{\pi/2}$ from circular solution 1 in Table 10.6.

Table 10.5: **Pulse Times of Arrival from IGR J16493–4348**

ToA (t_n, MJD)	Pulse Cycle[a] (n)	Statistical Uncertainty[b] (s)	Total Uncertainty[c] (s)	Pulse Phase[d]
55843.15499	5	7.7	8.3	0.09
55845.44465	186	6.4	7.1	0.07
55846.31687	255	11.9	12.3	0.01
55847.49281	348	9.1	9.6	0.96
55848.44228	423	10.7	11.2	0.01
55849.37915	497	9.4	9.9	0.06
55850.40456	578	7.2	7.9	0.11
55852.28917	727	5.0	5.8	0.07

[a] Nearest integer pulse cycle calculated using Equation (10.14) and t_0 = MJD 55843.09111. Pulse cycles are referenced with respect to the start of the pointed PCA observations.
[b] 1σ statistical uncertainties derived from Monte Carlo simulations.
[c] Total uncertainties calculated by adding a systematic uncertainty of 3.1 s from circular solution 2 in Table 10.6 to each statistical uncertainty in quadrature.
[d] Phase 0 corresponds to $T_{\pi/2}$ from circular solution 1 in Table 10.6.

generated segments on the refined 1093 s pulse period measurement from the final iteration of the pulsar timing analysis. During each simulation, phase offsets were measured by cross-correlating each of the simulated measured profiles with the final pulse template in the frequency domain, which were then used to derive an independent set of ToAs. We quote 1σ statistical uncertainties on each ToA listed in Table 10.5 from the median absolute deviation of the distribution of simulated ToAs obtained for each segment. The median absolute deviation is a robust statistic that is more resilient to outliers than the standard deviation. We used this statistic to reduce the effect that tails in the distribution of the simulated ToAs had on the statistical errors. The statistical uncertainties ranged from 5.0 to 11.9 s.

Systematic errors in the ToAs can arise from changes in the average pulse profile due to varying flux levels, absorption along the line of sight, or contamination from nearby sources (e.g., see [527]). We modeled the systematic error as a nuisance parameter when fitting the ToAs with timing models using the Bayesian MCMC procedure described in Section 10.3.2.1. The systematic uncertainty was treated as an additional error that was added in quadrature with the statistical uncertainty in the likelihood function. We marginalized over this systematic uncertainty when constructing posterior PDFs for the model parameters. Due to the limited number of ToAs and few degrees of freedom in the timing solutions, a systematic error was derived only for circular solution 2, which used the same timing model as in circular solution 1 (see Section 10.4.3 and Table 10.5). We find a systematic uncertainty of $\sigma_{\mathrm{sys}} = 3.1^{+3.0}_{-2.3}$ s from the median of the marginalized posterior distribution, and we report 1σ errors on this measurement using Bayesian credible intervals. This systematic uncertainty was added in quadrature with the statistical uncertainty for each ToA, which yielded the total uncertainties listed in Table 10.5. We note that the inclusion of systematic errors as a nuisance parameter increased the reduced χ^2_ν value from 0.88 in circular solution 1 to 1.04 in circular solution 2 without significantly affecting the best-fit orbital parameters.

10.4.3 Pulsar Timing Models

Assuming the pulsar phase varies smoothly as a function of time, a Taylor expansion can be used to approximate the pulse phase, ϕ, at time t:

$$\phi(t) = \phi(t_0) + \nu_{\rm pulse}(t - t_0) + \frac{1}{2}\dot{\nu}_{\rm pulse}(t - t_0)^2 + \cdots, \tag{10.12}$$

where $\nu_{\rm pulse}$ and $\dot{\nu}_{\rm pulse}$ are the neutron star rotational frequency and its time derivative at a reference time t_0, typically chosen to be the start time of the observation. Equation (10.12) can be transformed to give the expected arrival time, t'_n, of the nth pulse:

$$t'_n = t_0 + nP_{\rm pulse} + \frac{1}{2}n^2 P_{\rm pulse}\dot{P}_{\rm pulse} + \cdots, \tag{10.13}$$

where $P_{\rm pulse} = \nu_{\rm pulse}^{-1}$ is the pulse period at time t_0 and $\dot{P}_{\rm pulse}$ is the pulse period derivative. The pulse cycle, n, associated with each ToA is calculated to the nearest integer using:

$$n = \frac{t'_n - t_0}{P_{\rm pulse}} - \frac{1}{2}\frac{\dot{P}_{\rm pulse}}{P^2_{\rm pulse}}(t'_n - t_0)^2. \tag{10.14}$$

Additional time delays are observed from binary pulsars due to their orbital motion. In these systems, the ToAs can be described by:

$$t_n = t'_n + f_{\rm orb}(t'_n), \tag{10.15}$$

where $f_{\rm orb}(t'_n)$ is the orbital Doppler delay time associated with t'_n. For binary pulsars in circular orbits, the orbital Doppler delay times are given by [54, 273]:

$$f_{\rm orb}(t'_n) = a_x \sin i \cos\left[\frac{2\pi(t'_n - T_{\pi/2})}{P_{\rm orb}}\right], \tag{10.16}$$

where $a_x \sin i$ is the projected semi-major axis of the orbit, i is the orbital inclination angle relative to the line of sight, and $T_{\pi/2}$ is the time of maximum delay and mid-eclipse. If the orbit is eccentric, the Doppler delay times are instead given by [54]:

$$f_{\rm orb}(t'_n) = a_x \sin i \left[\sin\omega(\cos E - e) + \sqrt{1 - e^2}\cos\omega \sin E\right], \tag{10.17}$$

where e is the eccentricity, ω is the longitude of periastron, and E is the eccentric anomaly. The eccentric anomaly can be related to the mean anomaly, M, using Kepler's equation:

$$M = E - e \sin E = \frac{2\pi(t'_n - T_{\mathrm{peri}})}{P_{\mathrm{orb}}}, \tag{10.18}$$

where T_{peri} is the time of periastron passage.

The pulse period behavior and orbital parameters were measured by fitting circular and eccentric orbital timing models to the ToAs in Table 10.5. The timing models were constructed using Equations (10.13) and (10.15), together with Equation (10.16) for the circular solutions and Equation (10.17) for the eccentric solutions. To properly account for covariances between the model parameters in the orbital solutions, we used the Bayesian MCMC fitting procedure described in Section 10.3.2.1.

Circular solutions 1 and 2 and eccentric solution 1 were fit assuming a constant neutron star rotational period. Pulse period changes were incorporated into the timing models used to derive circular solution 3 and eccentric solution 2. In all of these models, the orbital period was fixed to the refined 6.7828 day measurement from the O–C analysis in Section 10.3.2.1, and the ToAs were weighted by their corresponding uncertainties during the fitting process.

In Table 10.6, we list the best-fit pulse period and orbital parameter measurements for each timing model, along with 1σ uncertainties derived from Bayesian credible intervals. Circular solution 1 is our favored orbital timing model since the fit yielded an acceptable reduced χ^2_ν value with the greatest number of degrees of freedom compared to the other timing models in Table 10.6. The orbital Doppler delay times measured during the final iteration of the pulsar timing analysis are shown in Figure 10.7(d), along with the predicted delay times from circular solution 1. We find a projected semi-major axis of $a_x \sin i = 82.8^{+5.0}_{-5.2}$ lt-s and a mid-eclipse time of $T_{\pi/2} = \mathrm{MJD}\ 55850.91 \pm 0.05$ from the fit in circular solution 1. A pulse period derivative of $\dot{P}_{\mathrm{pulse}} = -5.4^{+7.9}_{-9.7} \times 10^{-8}\ \mathrm{s\ s^{-1}}$ was obtained in circular solution 3, which indicates that there was no statistically significant long-term change in the pulse period during the pointed PCA observations. In addition, no rapid spin-up or spin-down episodes were observed, which suggests that a transient accretion disk is not present in this system [256, 280].

Table 10.6: **Orbital Parameters of IGR J16493–4348**

Parameter	**Circular Solution 1**	Circular Solution 2	Circular Solution 3	Eccentric Solution 1	Eccentric Solution 2
P_{pulse}[a] (s)	1093.1036 ± 0.0004	1093.1036 ± 0.0001	1093.10 ± 0.02	1093.1036 ± 0.0007	1093.10 ± 0.01
$\dot{P}_{\mathrm{pulse}}$ ($\times 10^{-8}$ s s^{-1})	...	...	$-5.4^{+7.9}_{-9.7}$	...	$-3.0^{+7.5}_{-8.9}$
$a_x \sin i$ (lt-s)	$82.8^{+5.0}_{-5.2}$	82.4 ± 5.5	81.3 ± 5.6	82.9 ± 5.2	82.3 ± 5.5
$T_{\pi/2}$[b] (MJD)	55850.91 ± 0.05	55850.90 ± 0.05	55850.90 ± 0.05	...	...
T_{peri}[c] (MJD)	...	...	...	55847.1 ± 0.5	55847.1 ± 0.5
e	...	...	...	0.17 ± 0.09	$0.17^{+0.08}_{-0.09}$
ω (deg)	...	...	...	251 ± 28	251^{+28}_{-27}
P_{orb}[d] (days)	6.7828	6.7828	6.7828	6.7828	6.7828
σ_{sys}[e] (s)	...	$3.1^{+3.0}_{-2.3}$	...	...	...
$f_x(M)$ ($M_\odot$)	$13.2^{+2.4}_{-2.5}$	13.0 ± 2.6	12.5 ± 2.6	13.3 ± 2.5	13.0 ± 2.6
χ^2_ν (dof)	0.88 (4)	1.04 (3)	1.06 (3)	0.89 (2)	0.98 (1)

We quote 1σ uncertainties on the model parameters using Bayesian credible intervals. We assumed no change in the neutron star's rotational period in circular solution 1, circular solution 2, and eccentric solution 1. We favor circular solution 1 as our preferred timing model for IGR J16493–4348.

[a] Pulse period at $t_0 = \mathrm{MJD}\,55843.09111$.

[b] Time of maximum delay and mid-eclipse in the circular orbital models.

[c] Time of periastron passage in the eccentric orbital models.

[d] Orbital period measurement from the O–C analysis using an asymmetric eclipse model.

[e] Systematic uncertainty measured from the posterior PDF in the Bayesian MCMC fitting procedure.

The X-ray mass function is given by:

$$f_x(M) = \frac{4\pi^2 (a_x \sin i)^3}{G P_{\mathrm{orb}}^2} = \frac{(M_c \sin i)^3}{(M_x + M_c)^2}, \tag{10.19}$$

where M_x is the mass of the neutron star and M_c is the mass of the companion. We find an X-ray mass function of $f_x(M) = 13.2^{+2.4}_{-2.5}\,M_\odot$ using Equation (10.19) and the values of $a_x \sin i$ and P_{orb} from circular solution 1. This mass function provides further evidence that IGR J16493–4348 is an sgHMXB with an early B-type stellar companion. It is also consistent with the mass functions obtained from the other orbital models in Table 10.6 to within 1σ.

An eccentricity of $e = 0.17 \pm 0.09$ and a longitude of periastron of $\omega = 251 \pm 28^\circ$ were measured from eccentric solution 1, and these values are consistent with the results from eccentric solution 2. A time of periastron passage of $T_{\mathrm{peri}} = \mathrm{MJD}\,55847.1 \pm 0.5$ was obtained using the eccentric timing models. The posterior distributions of the periastron passage time and longitude of periastron were both relatively broad due to the limited number of available ToAs, which resulted in large uncertainties on these parameters. Therefore, the results from these eccentric solutions should be interpreted with caution since they were obtained from timing model fits with only a few degrees of freedom.

10.4.4 Supergiant Companion and System Parameters

We present constraints on the mass and radius of the supergiant donor using the orbital parameters from circular solution 1 and eccentric solution 1 (see Table 10.6), together with the asymmetric eclipse model parameters from the BAT transient monitor orbital profile (see Table 10.3). The empirical mass distribution of neutron stars is peaked around a canonical value of 1.4 $M_{\odot}$, and a neutron star mass of 1.9 $M_{\odot}$ is a reasonable upper limit for sgHMXB systems with a B-type companion [262, 540]. Therefore, we assumed neutron star masses of 1.4 $M_{\odot}$ and 1.9 $M_{\odot}$ in these calculations.

For each neutron star mass, the mass of the supergiant was calculated as a function of inclination angle using Equation (10.19) and a fine grid of inclination angles ranging from $i = 0$–$90°$. Assuming a circular orbit ($e = 0$), the separation between the center of masses of the two stars in the binary can be found from Kepler's third law:

$$a = \left[\frac{G P_{\rm orb}^2 (M_x + M_c)}{4\pi^2}\right]^{1/3}. \tag{10.20}$$

For an eccentric orbit, the separation at mid-eclipse is instead given by:

$$a' = a \frac{1 - e^2}{1 + e\cos\omega}. \tag{10.21}$$

The radius of the supergiant was determined as a function of inclination angle from [260]:

$$R_c = a' \sqrt{1 - \cos^2\Theta_e \sin^2 i}, \tag{10.22}$$

where Θ_e is the eclipse half-angle. Equation (10.22) can be used to derive the relationship between the eclipse half-angle and the inclination. The Roche lobe radius was calculated using [172, 208]:

$$\frac{R_L}{a'} = \frac{0.49 q^{-2/3}}{0.6 q^{-2/3} + \ln\left(1 + q^{-1/3}\right)}, \tag{10.23}$$

where $q = M_x/M_c$ is the mass ratio. The inclination angle where the donor star would fill its Roche lobe was found by linearly interpolating between inclination angles where $R_L - R_c$ changed sign. We assumed that Roche lobe overflow occurred at periastron in the eccentric orbital models, where the distance between the two stars is $a' = a(1 - e)$.

In Table 10.7, we list calculated values for the companion mass, mass ratio, companion radius, Roche lobe radius, and Roche lobe filling factor ($\beta = R_c/R_L$) for neutron star masses of 1.4 $M_\odot$ and 1.9 $M_\odot$ using the orbital parameters from circular solution 1. These values were determined at inclination angles corresponding to Roche lobe overflow and an edge-on orbit ($i = 90°$). Assuming a canonical neutron star mass of 1.4 $M_\odot$, we find that the supergiant fills its Roche lobe at an inclination angle of $56.0^{+6.4\circ}_{-5.8}$. At this inclination, the stellar mass and radius of the supergiant companion are $25.8^{+6.3}_{-5.9}\,M_\odot$ and $28.3^{+5.7}_{-5.1}\,R_\odot$, respectively. This yields a mass ratio of $q = 0.05 \pm 0.01$. If we instead consider an edge-on orbit, the stellar mass and radius of the supergiant donor are $15.7^{+2.4}_{-2.5}\,M_\odot$ and $13.0^{+5.9}_{-4.7}\,R_\odot$, respectively. The Roche lobe radius is $22.8 \pm 1.2\,R_\odot$ in this case. We find a mass ratio of $q = 0.09 \pm 0.01$ and a Roche lobe filling factor of $\beta = 0.57^{+0.26}_{-0.21}$ using these values.

If we now consider a more massive 1.9 $M_\odot$ neutron star, the Roche lobe is filled by the donor star at an inclination angle of $58.1^{+5.9\circ}_{-5.1}$. The stellar mass and radius of the supergiant companion are $25.0^{+5.1}_{-4.8}\,M_\odot$ and $27.1^{+5.0}_{-4.4}\,R_\odot$, respectively. This gives a mass ratio of $q = 0.08^{+0.02}_{-0.01}$. For an edge-on orbit, the stellar mass and radius of the supergiant donor are $16.5 \pm 2.5\,M_\odot$ and $13.3^{+6.1}_{-4.8}\,R_\odot$, respectively, and we find a Roche lobe radius of $22.6^{+1.1}_{-1.2}\,R_\odot$. This yields a mass ratio and Roche lobe filling factor of $q = 0.12 \pm 0.02$ and $\beta = 0.59^{+0.27}_{-0.22}$, respectively. These derived masses and radii for the donor star are consistent with a B0.5 Ia spectral type companion from Searle et al. [484], where the Roche lobe is nearly filled at a moderate inclination angle. A complete list of these parameters is provided in Tables 10.9 and 10.10 in Section 10.7 for each pulsar timing solution in Table 10.6 using the asymmetric and symmetric eclipse model parameters in Tables 10.3 and 10.4 from fitting the folded BAT transient monitor and PCA scan orbital profiles.

The constraints on the inclination angle are further visualized in Figure 10.11, together with our measurement of the eclipse half-angle in Table 10.3 from fitting the BAT transient monitor orbital profile. We show the predicted eclipse half-angle of IGR J16493–4348 as a function of inclination angle using Equation (10.22) with supergiant mass and radius values corresponding to an edge-on orbit and where the donor star fills its Roche lobe. This behavior is shown for neutron star masses of 1.4 $M_\odot$ and 1.9 $M_\odot$ using the asymmetric eclipse model parameters from the folded BAT transient monitor light curve and the orbital parameters from circular solution 1 and eccentric solution 1. The allowed parameter space is indicated by the grey shaded regions. For an eclipse half-angle of 19.5°, shown by the solid red lines in Figure 10.11, we find that Roche lobe overflow would occur at inclination angles of $i \approx 57^\circ$ and $i \approx 67^\circ$ using the orbital parameters in circular solution 1 and eccentric solution 1, respectively.

Next, we constrain the spectral type of IGR J16493–4348's supergiant companion using the stellar mass-radius diagrams in Figure 10.12. The relationship between the supergiant's mass and radius is shown for neutron star masses of 1.4 $M_\odot$ and 1.9 $M_\odot$. Constraints are derived using the asymmetric eclipse model parameters from the BAT transient monitor orbital profile and the orbital parameters from circular solution 1 and eccentric solution 1. The grey shaded regions show the allowed parameter space for inclination angles between Roche lobe overflow and an edge-on orbit, and the red shaded areas correspond to the joint-allowed region also satisfying constraints from the asymmetric eclipse and timing models. Supergiant spectral types from Carroll and Ostlie [86], Cox [133], Searle et al. [484], and Lefever et al. [311] are labeled using green circles, orange triangles, blue stars, and magenta crosses, respectively. We spectrally classify the companion of IGR J16493–4348 as a B0.5 Ia supergiant since this is the only spectral type that lies in the joint-allowed regions obtained using the orbital parameters from circular solution 1. This spectral type is consistent with the previous spectral classification by Nespoli et al. [402] from K_S-band spectroscopy of IGR J16493–4348's infrared counterpart. There are no supergiant spectral types from Carroll and Ostlie [86], Cox [133], Searle et al. [484], or Lefever et al. [311] inside the joint-allowed regions derived using eccentric solution 1, which may be due to the few degrees of freedom in the fit.

In Table 10.8, we assume a neutron star mass of 1.4 $M_\odot$ and present supergiant donor parameters for selected spectral types from Carroll and Ostlie [86], Searle et al. [484], and Lefever et al. [311], along with estimates of the source distance and hydrogen column density. The inclination angles were calculated from Equation (10.22) using published values for the companion masses and radii and the measured eclipse half-angle in Table 10.3 from fitting the BAT transient monitor orbital profile. The B0.5 Ia spectral type from Searle et al. [484], which lies in the joint-allowed region of the stellar mass-radius diagrams in Figures 10.12(a) and 10.12(b), is highlighted in bold.

Mass transfer in close eccentric binaries is expected to occur at or near periastron, where the effective Roche lobes of the constituent stars are smallest [486]. We show the variation in the L1 Lagrange point separation from the supergiant companion as a function of orbital phase in Figure 10.13 for a range of eccentricities between 0 and 0.25. The horizontal dashed lines correspond to a companion radius of 27 $R_\odot$

for the B0.5 Ia spectral type from Searle et al. [484]. We find that an eccentric orbit with $e \gtrsim 0.20$ would induce Roche lobe overflow during orbital phases when the L1 Lagrange point is inside the supergiant.

10.5 Discussion

10.5.1 Donor Star Spectral Type

Our measurements of the 6.78 day orbital period and 1093 s pulse period firmly place IGR J16493–4348 in the wind-fed sgHMXB region of the $P_{\rm orb}$–$P_{\rm pulse}$ Corbet diagram [113, 114]. This is further supported by comparing our X-ray mass function of $f_x(M) = 13.2^{+2.4}_{-2.5}\,M_\odot$ to the X-ray mass functions of other sgHMXBs [535]. Nespoli et al. [402] estimated the spectral type of the donor star to be a B0.5-1 Ia-Ib supergiant by comparing the relative strength of He I lines from $K_{\rm S}$-band spectroscopy of IGR J16493–4348's infrared companion to those reported in Hanson et al. [222]. We find a spectral type of B0.5 Ia for the supergiant companion using constraints derived in the stellar mass-radius diagrams shown in Figure 10.12. We assumed neutron star masses of 1.4 $M_\odot$ and 1.9 $M_\odot$ since neither optical nor infrared radial velocity semi-amplitude measurements were available. In both cases, we obtain a spectral type that is consistent with the result in Nespoli et al. [402], but we note that a compact object of 1.9 $M_\odot$ would make it one of the most massive neutron stars in an X-ray binary [262, 540]. Two Galactic B supergiants with spectral types of B0.5 Ia from Searle et al. [484] are shown in Figure 10.12, but constraints on the allowed mass and radius from our timing models exclude the more massive, larger donor. From our spectral classification, we estimate the surface effective temperature and luminosity to be approximately 26,000 K and $3.0 \times 10^5\,L_\odot$, respectively.

We estimate the distance to the source using the supergiant's B0.5 Ia spectral type and the reported parameters in Table 3 of Searle et al. [484]. The infrared counterpart has an apparent K-band magnitude of $m_K = 11.94 \pm 0.04$ from 2MASS photometry [141]. An absolute K-band magnitude of $M_K = –5.93 \pm 0.14$ was derived from the absolute V-band magnitude of $M_V = –6.48 \pm 0.10$ in Searle et al. [484] and the intrinsic $(K - V)_0$ color index of 0.55 ± 0.10 in Wegner [549]. Next, we found the intrinsic $(J - K)_0$ color index to be $–0.12 \pm 0.13$ using the $(J - V)_0$ and $(K - V)_0$ color indices from Wegner [549]. An $E(J - K)$ color excess of 2.78 ± 0.15 was obtained by subtracting the intrinsic color $(J - K)_0$ from the $(J - K)_{\rm 2MASS}$ color. Assuming an average extincition of $R_V = 3.09 \pm 0.03$, we found a V-band extinction magnitude of $A_V = 16.4 \pm 1.3$ from the relation $A_V/E(J - K) = 5.90 \pm 0.36$ [469]. This yielded an extinction magnitude of $A_K = 1.8 \pm 0.1$ at K-band using $A_K/A_V = 0.112$

from Table 3 in Rieke and Lebofsky [469]. From the distance modulus, $M_K = m_K + 5 - 5\log d - A_K$, we find that IGR J16493–4348 lies at a distance of 16.1 ± 1.5 kpc, which is consistent with the 6–26 kpc distance estimate in Nespoli et al. [402]. Our distance measurement is also in agreement with the 7.5–22 kpc distance reported by Hill et al. [231] from infrared spectral energy distribution measurements of the supergiant companion.

Next, we calculate a hydrogen column density of $N_H = (2.93 \pm 0.24) \times 10^{22}$ cm^{-2} from the correlation between visual extinction and hydrogen column density in Predehl and Schmitt [448], which is consistent with the estimate given in Nespoli et al. [402]. If we instead use the more recently measured correlation between optical extinction and N_H in Güver and Özel [218], we obtain a hydrogen column density of $N_H = (3.62 \pm 0.33) \times 10^{22}$ cm^{-2}. Using the procedure in Willingale et al. [561], we find a total hydrogen column density of $N_H = 1.56 \times 10^{22}$ cm^{-2}, which is comparable to the N_H values of 1.42×10^{22} cm^{-2} and 1.82×10^{22} cm^{-2} obtained from the Leiden/Argentine/Bonn survey [261] and Dickey and Lockman [161], respectively, using measurements of H I in the Galaxy. We note that all of these values are smaller than the observed hydrogen column densities measured by Hill et al. [231], Morris et al. [399], D'Aì et al. [142], and Coley et al. [110]. Spectral analyses in the soft and hard X-ray bands have found hydrogen column densities ranging between roughly 5–10×10^{22} cm^{-2} on average. This suggests that there may be an additional component of the hydrogen absorbing column that is intrinsic to the system.

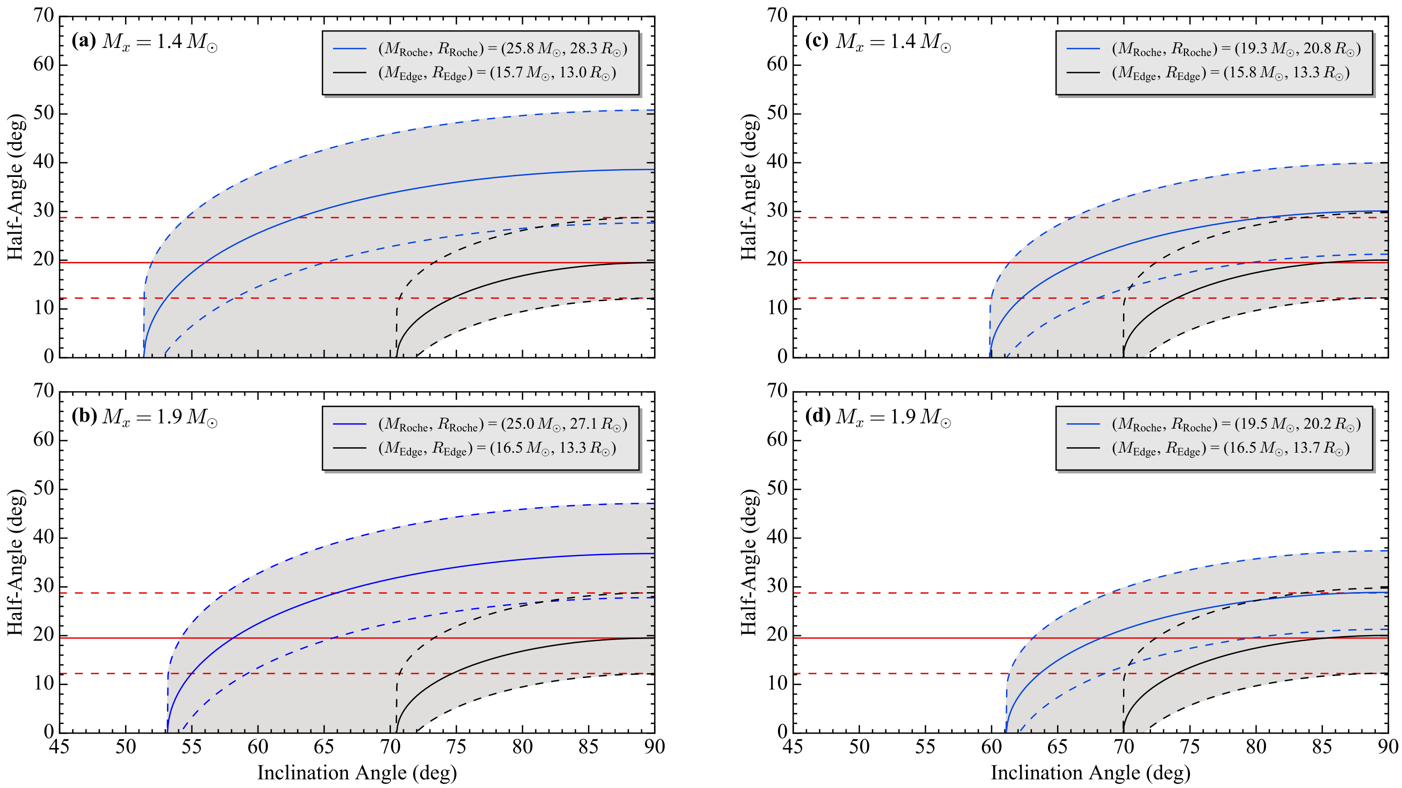

Figure 10.11: **Predicted eclipse half-angle of IGR J16493–4348 as a function of inclination angle, assuming neutron star masses of 1.4 $M_\odot$ in (a) and (c) and 1.9 $M_\odot$ in (b) and (d).** These constraints are obtained using the orbital parameters from (left) circular solution 1 and (right) eccentric solution 1 in Table 10.6, together with the asymmetric eclipse model parameters in Table 10.3 from fitting the *Swift* BAT transient monitor (15–50 keV) orbital profile. The solid blue curves are derived using supergiant mass and radius values corresponding to where the donor fills its Roche lobe, and the solid black curves are obtained using supergiant mass and radius values derived for an edge-on orbit. The solid red lines indicate the measured eclipse half-angle in Table 10.3 from fitting the BAT transient monitor orbital profile. The dashed curves correspond to 1σ uncertainties on the eclipse half-angles. The grey shaded regions show the allowed parameter space.

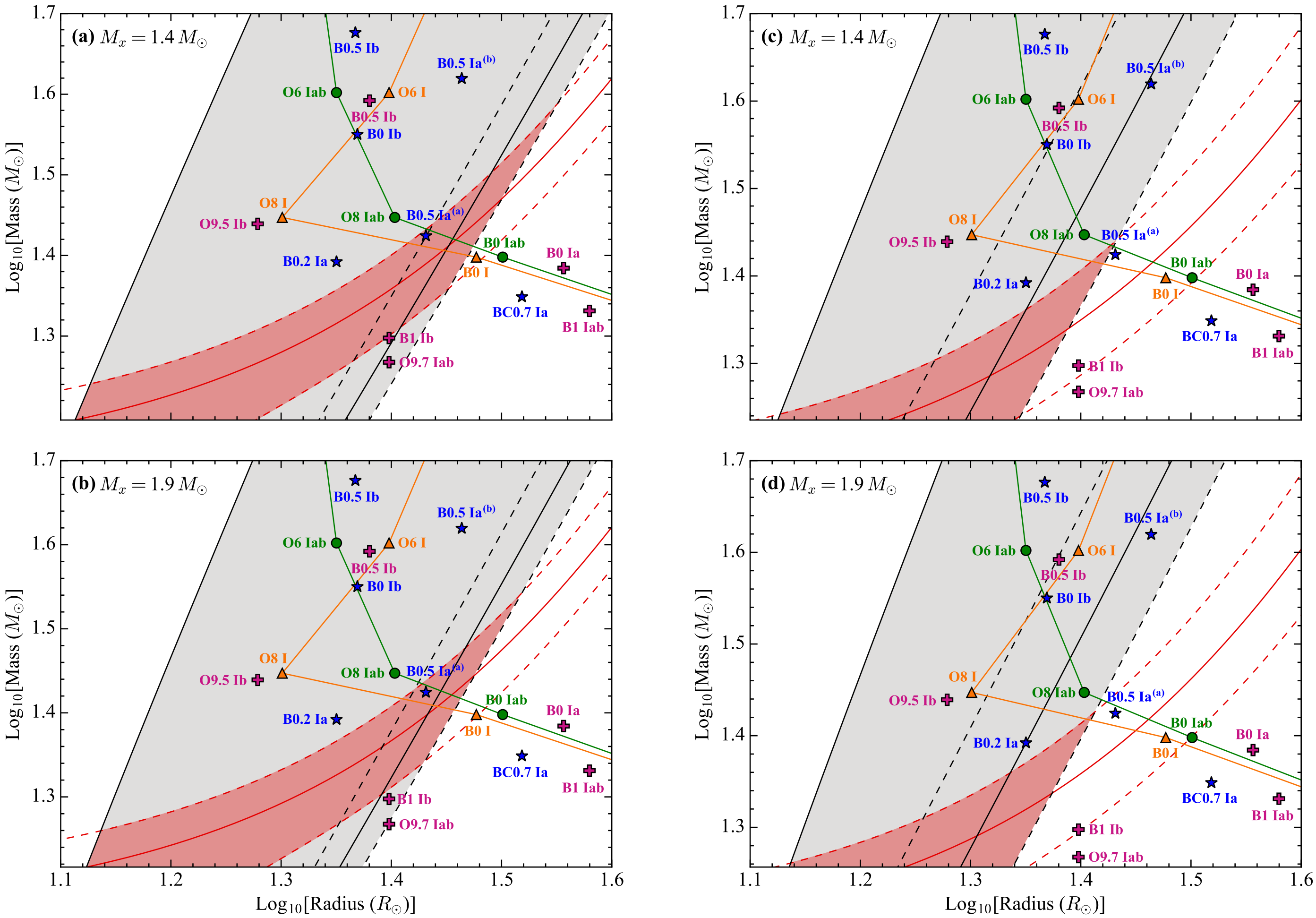

Figure 10.12: **Log-log plots of stellar mass as a function of stellar radius for IGR J16493–4348's supergiant companion using the orbital parameters from (left) circular solution 1 and (right) eccentric solution 1 in Table 10.6.** We assume neutron star masses of 1.4 $M_\odot$ in (a) and (c) and 1.9 $M_\odot$ in (b) and (d). The left and right solid black curves show constraints corresponding to an edge-on orbit and where the supergiant fills its Roche lobe, respectively. The solid red curves show constraints obtained using the orbital parameters in Table 10.6 and the asymmetric eclipse model parameters in Table 10.3 from fitting the *Swift* BAT transient monitor (15–50 keV) orbital profile. The dashed curves indicate 1σ uncertainties on these constraints. The grey shaded regions correspond to the allowed parameter space for inclination angles between Roche lobe overflow and an edge-on orbit, and the red shaded areas indicate the joint-allowed region also satisfying constraints from the asymmetric eclipse and timing models. The green circles, orange triangles, blue stars, and magenta crosses correspond to supergiant spectral types from Carroll and Ostlie [86], Cox [133], Searle et al. [484], and Lefever et al. [311], respectively. The B0.5 Ia$^{(a)}$ and B0.5 Ia$^{(b)}$ labels are used to distinguish between the two B0.5 Ia Galactic B supergiants with different masses and radii in Table 3 of Searle et al. [484]. We favor a spectral type of B0.5 Ia for the supergiant donor since this is the only spectral type that lies in the joint-allowed regions derived using the orbital parameters from circular solution 1.

Table 10.7: **Supergiant Donor Parameters of IGR J16493–4348**

Parameter	Roche Lobe Overflow	Edge-On
i (deg)[a]	$56.0^{+6.4}_{-5.8}$	90.0
M_x ($M_\odot$)[b]	1.4	1.4
M_c ($M_\odot$)[c]	$25.8^{+6.3}_{-5.9}$	$15.7^{+2.4}_{-2.5}$
q[d]	0.05 ± 0.01	0.09 ± 0.01
R_c ($R_\odot$)[e]	$28.3^{+5.7}_{-5.1}$	$13.0^{+5.9}_{-4.7}$
R_L ($R_\odot$)[f]	$28.3^{+2.8}_{-2.6}$	22.8 ± 1.2
β[g]	$1.00^{+0.22}_{-0.20}$	$0.57^{+0.26}_{-0.21}$
i (deg)[a]	$58.1^{+5.9}_{-5.1}$	90.0
M_x ($M_\odot$)[b]	1.9	1.9
M_c ($M_\odot$)[c]	$25.0^{+5.1}_{-4.8}$	16.5 ± 2.5
q[d]	$0.08^{+0.02}_{-0.01}$	0.12 ± 0.02
R_c ($R_\odot$)[e]	$27.1^{+5.0}_{-4.4}$	$13.3^{+6.1}_{-4.8}$
R_L ($R_\odot$)[f]	$27.1^{+2.2}_{-2.1}$	$22.6^{+1.1}_{-1.2}$
β[g]	$1.00^{+0.20}_{-0.18}$	$0.59^{+0.27}_{-0.22}$

Parameter values were obtained using the orbital parameters from circular solution 1 in Table 10.6 and the asymmetric eclipse model parameters from the *Swift* BAT transient monitor (15–50 keV) orbital profile in Table 10.3. We quote 1σ uncertainties on each parameter, if applicable.

[a] Inclination angles where the supergiant donor fills its Roche lobe and where the binary system is viewed edge-on ($i = 90°$).

[b] Assumed mass of the neutron star.

[c] Mass of the supergiant donor calculated using Equation (10.19).

[d] Mass ratio, $q = M_x/M_c$, where M_x is the mass of the neutron star and M_c is the mass of the supergiant companion.

[e] Radius of the supergiant donor obtained using Equation (10.22).

[f] Roche lobe radius calculated using Equation (10.23).

[g] Roche lobe filling factor, $\beta = R_c/R_L$, where R_c is the radius of the supergiant companion and R_L is the Roche lobe radius.

Table 10.8: **System Parameters of IGR J16493–4348 for Selected Spectral Types**

Spectral Type	M_c [a] ($M_\odot$)	q [b]	R_c [c] ($R_\odot$)	R_L [d] ($R_\odot$)	β [e]	i [f] (deg)	M_V [g] (mag)	$(J-K)_0$ [h] (mag)	$E(J-K)$ [i] (mag)	d [j] (kpc)	N_H [k] (10^{22} cm^2)
[l]O8 Iab	28.0	0.05	25.3	29.3	0.86	$62.9^{+6.4}_{-5.0}$	–6.6	-0.18 ± 0.13	2.84 ± 0.15	14.8 ± 1.2	3.00 ± 0.25
[m]B0.2 Ia	24.7 ± 7.1	0.06 ± 0.02	22.4 ± 3.2	27.8 ± 2.7	0.81 ± 0.14	$66.7^{+10.7}_{-9.7}$	-6.07 ± 0.30	-0.13 ± 0.13	2.79 ± 0.15	12.9 ± 2.1	2.94 ± 0.24
[m]B0.5 Ia[(a)]	26.6 ± 2.4	0.053 ± 0.005	27.0 ± 1.2	28.7 ± 0.9	0.94 ± 0.05	$59.0^{+6.1}_{-5.1}$	-6.48 ± 0.10	-0.12 ± 0.13	2.78 ± 0.15	16.1 ± 1.5	2.93 ± 0.24
[m]B0.5 Ia[(b)]	41.6 ± 3.8	0.034 ± 0.003	29.1 ± 1.3	34.7 ± 1.1	0.84 ± 0.05	$62.3^{+6.8}_{-5.6}$	-6.54 ± 0.10	-0.12 ± 0.13	2.78 ± 0.15	16.5 ± 1.6	2.93 ± 0.24
[m]B0.5 Ib	47.5 ± 8.8	0.029 ± 0.005	23.3 ± 2.2	36.6 ± 2.3	0.64 ± 0.07	$74.1^{+12.4}_{-10.2}$	-6.36 ± 0.20	-0.12 ± 0.13	2.78 ± 0.15	15.3 ± 1.9	2.93 ± 0.24
[n]B1 Ib	19.8	0.07	25.0	25.3	0.99	$58.2^{+5.3}_{-4.2}$	–5.8	-0.13 ± 0.13	2.79 ± 0.15	11.9 ± 1.0	2.94 ± 0.24

System parameters for selected spectral types from Carroll and Ostlie [86], Searle et al. [484], and Lefever et al. [311]. We assumed a canonical neutron star mass of 1.4 $M_\odot$ and used the orbital parameters from circular solution 1 in Table 10.6 and the eclipse half-angle in Table 10.3 from fitting the *Swift* BAT transient monitor (15–50 keV) orbital profile with an asymmetric eclipse model. We report 1σ uncertainties on these parameters, if applicable. The favored supergiant spectral type from the stellar mass-radius diagrams in Figure 10.12 is highlighted in bold.

[a] Mass of the supergiant companion from Carroll and Ostlie [86], Searle et al. [484], and Lefever et al. [311].

[b] Mass ratio, $q = M_x/M_c$, where M_x is the neutron star mass and M_c is the mass of the supergiant donor.

[c] Radius of the supergiant companion from Carroll and Ostlie [86], Searle et al. [484], and Lefever et al. [311].

[d] Roche lobe radius calculated using Equation (10.23).

[e] Roche lobe filling factor, $\beta = R_c/R_L$, where R_c is radius of the supergiant donor and R_L is the Roche lobe radius.

[f] Inclination angle calculated using Equation (10.22).

[g] Absolute magnitude from Carroll and Ostlie [86], Searle et al. [484], and Lefever et al. [311].

[h] $(J-K)_0$ intrinsic color index calculated using the $(J-V)_0$ and $(K-V)_0$ color indices from Wegner [549]. The uncertainties on the intrinsic color indices were calculated using Equation (6) in Wegner [549].

[i] Excess color calculated by subtracting the intrinsic $(J-K)_0$ color from the $(J-K)_{\mathrm{2MASS}}$ color.

[j] Distance to the source calculated using the distance modulus with an apparent 2MASS K-band magnitude from Cutri et al. [141] and K-band extinction determined from Rieke and Lebofsky [469].

[k] Hydrogen column density calculated from the correlation with visual extinction in Predehl and Schmitt [448].

[l] Supergiant star from Carroll and Ostlie [86].

[m] Supergiant star from Searle et al. [484].

[n] Supergiant star from Lefever et al. [311].

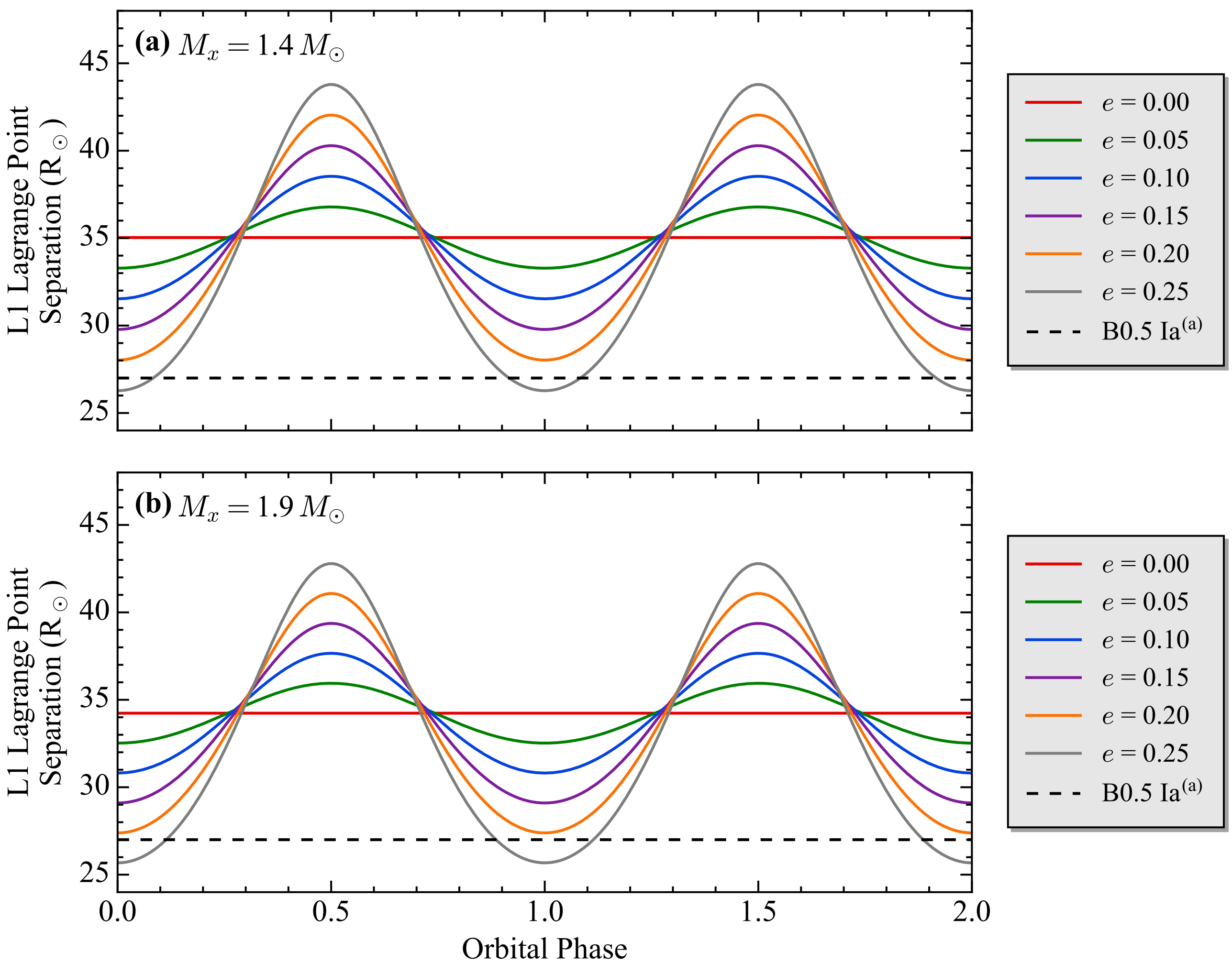

Figure 10.13: **L1 Lagrange point separation from IGR J16493–4348's supergiant companion as a function of orbital phase.** The solid curves indicate the separation for different eccentricities between 0 and 0.25, and the horizontal dashed lines correspond to a supergiant radius of 27 $R_\odot$ for the favored B0.5 Ia spectral type from Searle et al. [484]. For eccentric orbits with $e \gtrsim 0.20$, Roche lobe overflow will be induced during orbital phases where the L1 Lagrange point separation is inside the supergiant.

10.5.2 Eclipse Asymmetry

Asymmetry in the X-ray eclipse profile is often a signature of a photoionization wake [185, 189], accretion bow shock and/or accretion wake trailing the neutron star [55, 56], or other complex structure in the stellar wind. We discuss these phenomena and argue that a strong photoionization or accretion wake is not supported by the X-ray emission observed from IGR J16493–4348.

Mass transfer onto the neutron star occurs through the radiatively powered stellar wind of the supergiant companion. X-ray photoionization can result in collisions between the compressed, ionized gas and the accelerating wind, which causes shocks and dense regions of compressed gas from the wind to trail the X-ray source in its orbit around the supergiant [189, 252]. In systems with high X-ray luminosities, the wind is highly ionized in the vicinity of the X-ray source, and the radiative driving force powering the stellar wind is significantly reduced near the surface of the supergiant [185]. As seen in Vela X-1 [185], the dense gas trailing the photoionization wake can lead to X-ray photoelectric absorption at orbital phases prior to the eclipse and X-ray scattering into the observer's line of sight after eclipse ingress. This can produce ingress durations that are longer than those observed at egress.

Dense regions of compressed gas in the accretion bow shock and/or accretion wake of the compact object can also induce phase-dependent photoelectric absorption [55, 56, 252]. This leads to an enhancement in the hydrogen column density and absorption of the X-ray emission prior to the eclipse [366]. No apparent increase in the hydrogen column density is observable during egress when the accretion wake is located beyond the compact object. We do not find evidence of a strong photoionization or accretion wake since there are no statistically significant differences between the ingress and egress durations or the count rates near ingress and egress in the PCA scan or BAT orbital profiles.

The eclipse profile structure is often dependent on X-ray photon energy. For example, Jain et al. [255] found that the X-ray eclipses from the SFXT IGR J16479–4514 were more evident and exhibited sharper transitions at higher energies using the *Swift* BAT compared to observations at lower energies with the *RXTE* All-Sky Monitor (ASM). This type of behavior has also been observed from various other eclipsing systems in the hard X-ray band (e.g., see [179]). These effects are often linked to the absorbing column density, which causes increased X-ray absorption and scattering at softer X-ray energies. Although the eclipse duration of IGR J16493–4348 was consistent between the PCA scan and BAT orbital profiles, there are observable differences in the eclipse profile structure across the X-ray energy band (see Figure 10.7). While these differences may be indicative of energy dependent structure in the eclipses, systematic effects from binning could also affect the observed eclipse shape.

10.5.3 Orbital Eccentricity

Previous estimates by Cusumano et al. [140] suggest that the orbital eccentricity cannot exceed 0.15 based on IGR J16493–4348's classification as a wind-fed sgHMXB. An eccentricity of $e = 0.17 \pm 0.09$ was measured using the timing model in eccentric solution 1. While this eccentricity is consistent with the upper limit presented in Cusumano et al. [140], we suspect that the orbit is nearly circular since the ToAs are well modeled by circular solution 1 and a B0.5 Ia spectral type fell within the joint-allowed parameter space in the corresponding stellar mass-radius diagrams in Figure 10.12. This spectral type is also consistent with the spectral classification given by Nespoli et al. [402]. Additionally, no spectral types were found inside the joint-allowed regions obtained using eccentric solution 1. If the orbit were highly eccentric ($e \gtrsim 0.20$), then the L1 Lagrange point separation from the supergiant would be located inside the donor during a fraction of the orbit, which would lead to Roche lobe overflow and inhibit mass transfer via the stellar wind. Since the eccentric timing model fits have only a few degrees of freedom, higher cadence pulsar timing observations over multiple orbital cycles are needed to measure the system's eccentricity and longitude of periastron more accurately.

We compare the mid-eclipse time predicted by eccentric solution 1 in Table 10.6 to the measured mid-eclipse times from the PCA scan and BAT orbital profiles in Tables 10.3 and 10.4. To first order in e, the time of mid-eclipse in an eccentric orbit is given by [179, 539]:

$$T_{\mathrm{mid}} = T_{\pi/2} - \frac{eP_{\mathrm{orb}}}{\pi} \cos\omega. \tag{10.24}$$

Here, $T_{\pi/2}$ is calculated from the periastron passage time, T_{peri}, using [539]:

$$T_{\pi/2} = T_{\mathrm{peri}} + \frac{P_{\mathrm{orb}}}{2\pi}\left(\frac{\pi}{2} - \omega\right). \tag{10.25}$$

If the orbit is circular, the values of $T_{\pi/2}$ and T_{mid} will coincide.

Substituting the orbital parameters from eccentric solution 1 into Equations (10.24) and (10.25), we find that $T_{\pi/2} = \mathrm{MJD}\,55850.9 \pm 0.8$ and $T_{\mathrm{mid}} = \mathrm{MJD}\,55851.0 \pm 0.8$

are consistent with each other. The large uncertainties in these calculated values are attributed to the broad posterior distributions measured for the periastron passage time and longitude of periastron in eccentric solution 1. This calculated mid-eclipse time agrees with all of the measured mid-eclipse times in Tables 10.3 and 10.4 to within 1σ. In addition, the value of $T_{\pi/2}$ derived from eccentric solution 1 is consistent with the values of $T_{\pi/2}$ measured using the circular timing models in Table 10.6. This further supports the notion that the orbit is likely not highly eccentric.

10.5.4 Superorbital Mechanisms

IGR J16493–4348 is one of only five wind-fed sgHMXB systems in which superorbital modulation has been definitively observed (e.g., 2S 0114+650, 4U 1909+07, IGR J16418–4532, and IGR J16479–4514 [115]). In addition, Corbet et al. [119] recently reported apparent superorbital modulation from the eclipsing sgHMXB, 4U 1538–52. Superorbital variability from other X-ray pulsar binaries, such as Her X-1, SMC X-1, and LMC X-4, has been linked to mass flow onto the accretion disk of the neutron star via Roche lobe overflow [104, 105]. Accretion flow onto the surface of a freely precessing neutron star with a complex non-dipole magnetic field has also been suggested to explain the 35 day superorbital period of Her X-1 [447]. Alternatively, the periodic superorbital behavior in these systems could be caused by a twisted, warped precessing accretion disk [243, 406, 438, 563].

We detected coherent superorbital modulation at a period of 20.07 days from semi-weighted DFTs of the BAT and PCA scan light curves. While superorbital periods of similar length have been detected in other wind accreting sgHMXBs, such as 2S 0114+650, the mechanism responsible for the variability still has not been clearly identified [181, 182, 241, 374]. It may be possible that tidal oscillations from IGR J16493–4348's B0.5 Ia supergiant companion are driving the variability if the orbit is indeed circular [278, 279, 395]. Using a tidal interaction model, Koenigsberger et al. [279] found that these oscillations would produce modulation on superorbital timescales in binary systems with circular orbits, while orbital period length variability would be observed if these oscillations occurred in eccentric orbits. In both cases, suborbital variability was also predicted on shorter timescales. This may suggest that the mechanism responsible for the superorbital modulation is the structured stellar wind of the supergiant companion, possibly along with X-ray emission generated by strong perturbations on the surface layers of the donor star.

Alternatively, the superorbital variability may be related to the presence of corotating interaction regions (CIRs) in the stellar wind of the supergiant [64]. These structures are thought to form from irregularities on the surface of the donor star and are located at radial distances of tens of stellar radii [134, 400]. We find that IGR J16493-4348's superorbital period is persistently detected in X-ray observations spanning several years, but its strength is variable in time [110]. This implies that these CIRs would have to be stable over long timescales if this is the dominant mechanism driving the variability, which has not yet been established. A detailed discussion of other possible mechanisms responsible for the superorbital modulation is presented in Coley et al. [110].

10.6 Conclusions

IGR J16493–4348 is an eclipsing, wind-fed sgHMXB with an early B-type supergiant companion. We refine the superorbital period to 20.067 ± 0.009 days from a semi-weighted DFT of the BAT transient monitor light curve. An improved orbital period measurement of 6.7828 ± 0.0004 days is obtained from an O–C analysis using the PCA scan and BAT transient monitor data. Asymmetric and symmetric eclipse models were fit to the PCA scan and BAT orbital profiles, and no evidence of a strong photoionization or accretion wake was found.

Pulsations were detected in the unweighted power spectrum of the pointed PCA light curve after the removal of low frequency noise. We refine the pulse period to 1093.1036 ± 0.0004 s from a pulsar timing analysis using the pointed PCA data. The system's Keplerian binary orbital parameters were measured by fitting circular and eccentric timing models to the ToAs. We find that the orbit is likely nearly circular, and no significant change in the rotational period of the pulsar was observed. A mass function of $f_x(M) = 13.2^{+2.4}_{-2.5}\, M_\odot$ was derived from the binary orbital parameters, which allows us to definitively classify IGR J16493–4348 as an sgHMXB. This is further supported by its updated placement in the wind-fed sgHMXB region of the $P_{\rm orb}$–$P_{\rm pulse}$ Corbet diagram. We derive new constraints on the mass and radius of the donor star, which indicate a B0.5 Ia spectral type for the supergiant companion. Additional parameters describing the system geometry are also provided, which give insight into possible inclination angles and Roche lobe sizes.

Although we argue that the binary follows a nearly circular orbit, additional ToAs are needed to provide improved constraints on the system's eccentricity and longitude of periastron. Optical or infrared radial velocity measurements would directly determine the pulsar's neutron star mass, which would allow the system to be classified as a double-lined eclipsing binary. The driving mechanism behind the superorbital modulation remains unexplained, but it is currently thought to be linked with the stellar wind of the supergiant companion.

10.7 Appendix: Calculated System Parameters of IGR J16493–4348

In Tables 10.9 and 10.10, we provide a complete list of calculated values for the companion mass, mass ratio, companion radius, Roche lobe radius, and Roche lobe filling factor using the orbital parameters from each timing solution in Table 10.6 and the asymmetric and symmetric eclipse model parameters in Tables 10.3 and 10.4 from fitting the folded BAT transient monitor and PCA scan orbital profiles. These values were determined at inclination angles corresponding to Roche lobe overflow and an edge-on orbit. We assumed neutron star masses of 1.4 $M_{\odot}$ and 1.9 $M_{\odot}$ in these calculations.

10.8 Acknowledgments

We thank the reviewer for useful suggestions that helped us improve this paper. A.B.P. acknowledges support by the Department of Defense (DoD) through the National Defense Science and Engineering Graduate (NDSEG) Fellowship Program and by the National Science Foundation (NSF) Graduate Research Fellowship under Grant No. DGE-1144469. This work was partially supported by NASA grant NNX15AI74G.

Table 10.9: **Supergiant Donor Parameters of IGR J16493–4348**

Parameter	**Circular Solution 1**		Circular Solution 2		Circular Solution 3		Eccentric Solution 1		Eccentric Solution 2	
Swift BAT Transient Monitor (15–50 keV), Asymmetric Eclipse Model										
i (deg)[a]	$56.0^{+6.4}_{-5.8}$	90.0	$56.0^{+6.1}_{-5.6}$	90.0	$56.4^{+5.9}_{-5.3}$	90.0	$67.8^{+9.2}_{-8.3}$	90.0	$68.2^{+10.7}_{-9.7}$	90.0
M_x ($M_\odot$)[b]	1.4	1.4	1.4	1.4	1.4	1.4	1.4	1.4	1.4	1.4
M_c ($M_\odot$)[c]	$25.8^{+6.3}_{-5.9}$	$15.7^{+2.4}_{-2.5}$	$25.7^{+6.2}_{-5.9}$	$15.6^{+2.8}_{-2.9}$	$24.3^{+5.5}_{-5.2}$	$15.0^{+2.6}_{-2.7}$	$19.3^{+4.2}_{-3.9}$	$15.8^{+2.5}_{-2.6}$	$18.8^{+4.8}_{-4.5}$	15.5 ± 2.7
q[d]	0.05 ± 0.01	0.09 ± 0.01	0.05 ± 0.01	0.09 ± 0.02	0.06 ± 0.01	0.09 ± 0.02	$0.07^{+0.02}_{-0.01}$	0.09 ± 0.01	0.07 ± 0.02	0.09 ± 0.02
R_c ($R_\odot$)[e]	$28.3^{+5.7}_{-5.1}$	$13.0^{+5.9}_{-4.7}$	$28.3^{+5.4}_{-4.9}$	$13.0^{+5.9}_{-4.7}$	$27.6^{+5.1}_{-4.6}$	$12.8^{+5.8}_{-4.6}$	$20.8^{+6.4}_{-5.7}$	$13.3^{+6.2}_{-5.0}$	$20.4^{+7.4}_{-6.5}$	$13.3^{+6.2}_{-4.9}$
R_L ($R_\odot$)[f]	$28.3^{+2.8}_{-2.6}$	22.8 ± 1.2	$28.3^{+2.7}_{-2.6}$	$22.8^{+1.3}_{-1.4}$	$27.6^{+2.5}_{-2.3}$	22.3 ± 1.3	20.8 ± 2.5	$19.0^{+2.2}_{-2.4}$	$20.4^{+2.7}_{-2.8}$	$18.8^{+2.1}_{-2.3}$
β[g]	$1.00^{+0.22}_{-0.20}$	$0.57^{+0.26}_{-0.21}$	$1.00^{+0.22}_{-0.20}$	$0.57^{+0.26}_{-0.21}$	$1.00^{+0.21}_{-0.19}$	$0.57^{+0.26}_{-0.21}$	$1.00^{+0.33}_{-0.30}$	$0.70^{+0.34}_{-0.27}$	$1.00^{+0.39}_{-0.35}$	$0.71^{+0.34}_{-0.28}$
i (deg)[a]	$58.1^{+5.9}_{-5.1}$	90.0	$58.1^{+7.8}_{-6.9}$	90.0	$58.5^{+7.5}_{-6.6}$	90.0	$69.4^{+8.6}_{-7.6}$	90.0	$69.9^{+10.1}_{-9.0}$	90.0
M_x ($M_\odot$)[b]	1.9	1.9	1.9	1.9	1.9	1.9	1.9	1.9	1.9	1.9
M_c ($M_\odot$)[c]	$25.0^{+5.1}_{-4.8}$	16.5 ± 2.5	$24.9^{+7.0}_{-6.6}$	$16.4^{+2.8}_{-2.9}$	$23.6^{+6.2}_{-5.8}$	15.7 ± 2.7	$19.5^{+3.6}_{-3.3}$	16.5 ± 2.6	$19.0^{+4.1}_{-3.9}$	16.3 ± 2.7
q[d]	$0.08^{+0.02}_{-0.01}$	0.12 ± 0.02	0.08 ± 0.02	0.12 ± 0.02	0.08 ± 0.02	0.12 ± 0.02	0.10 ± 0.02	0.11 ± 0.02	0.10 ± 0.02	0.12 ± 0.02
R_c ($R_\odot$)[e]	$27.1^{+5.0}_{-4.4}$	$13.3^{+6.1}_{-4.8}$	$27.0^{+6.6}_{-5.9}$	$13.3^{+6.1}_{-4.8}$	$26.4^{+6.3}_{-5.5}$	$13.1^{+6.0}_{-4.7}$	$20.2^{+5.9}_{-5.1}$	$13.7^{+6.4}_{-5.1}$	$19.9^{+6.8}_{-5.9}$	$13.6^{+6.3}_{-5.0}$
R_L ($R_\odot$)[f]	$27.1^{+2.2}_{-2.1}$	$22.6^{+1.1}_{-1.2}$	$27.0^{+3.0}_{-2.8}$	22.5 ± 1.3	$26.4^{+2.8}_{-2.6}$	22.1 ± 1.2	20.2 ± 2.1	$18.8^{+2.2}_{-2.3}$	$19.9^{+2.3}_{-2.4}$	$18.6^{+2.0}_{-2.3}$
β[g]	$1.00^{+0.20}_{-0.18}$	$0.59^{+0.27}_{-0.22}$	$1.00^{+0.27}_{-0.24}$	$0.59^{+0.27}_{-0.22}$	$1.00^{+0.26}_{-0.23}$	$0.59^{+0.27}_{-0.22}$	$1.00^{+0.31}_{-0.27}$	$0.73^{+0.35}_{-0.28}$	$1.00^{+0.36}_{-0.32}$	$0.73^{+0.35}_{-0.29}$
RXTE PCA Galactic Bulge Scans (2–10 keV), Asymmetric Eclipse Model										
i (deg)[a]	$58.5^{+4.9}_{-5.1}$	90.0	$58.6^{+4.7}_{-4.8}$	90.0	59.0 ± 5.5	90.0	$71.8^{+9.7}_{-10.1}$	90.0	$72.3^{+6.9}_{-7.4}$	90.0
M_x ($M_\odot$)[b]	1.4	1.4	1.4	1.4	1.4	1.4	1.4	1.4	1.4	1.4
M_c ($M_\odot$)[c]	$23.9^{+4.7}_{-4.9}$	$15.7^{+2.4}_{-2.5}$	$23.8^{+4.5}_{-4.6}$	$15.6^{+2.8}_{-2.9}$	$22.5^{+4.9}_{-5.0}$	$15.0^{+2.6}_{-2.7}$	$18.0^{+3.9}_{-4.0}$	$15.8^{+2.5}_{-2.6}$	$17.6^{+2.8}_{-2.9}$	15.5 ± 2.7
q[d]	0.06 ± 0.01	0.09 ± 0.01	0.06 ± 0.01	0.09 ± 0.02	0.06 ± 0.01	0.09 ± 0.02	0.08 ± 0.02	0.09 ± 0.01	0.08 ± 0.01	0.09 ± 0.02
R_c ($R_\odot$)[e]	$27.4^{+3.8}_{-4.0}$	$15.1^{+1.8}_{-1.9}$	$27.3^{+3.6}_{-3.7}$	$15.1^{+1.9}_{-2.0}$	$26.7^{+4.1}_{-4.2}$	$14.9^{+1.8}_{-1.9}$	$20.2^{+5.1}_{-5.3}$	$15.6^{+2.3}_{-2.4}$	$19.8^{+3.6}_{-3.8}$	15.5 ± 2.3
R_L ($R_\odot$)[f]	$27.4^{+2.1}_{-2.2}$	22.8 ± 1.2	$27.3^{+2.0}_{-2.1}$	$22.8^{+1.3}_{-1.4}$	$26.7^{+2.2}_{-2.3}$	22.3 ± 1.3	$20.2^{+2.7}_{-2.8}$	$19.0^{+2.2}_{-2.4}$	$19.8^{+1.8}_{-2.0}$	$18.8^{+2.1}_{-2.3}$
β[g]	$1.00^{+0.16}_{-0.17}$	0.66 ± 0.09	$1.00^{+0.15}_{-0.16}$	0.66 ± 0.09	$1.00^{+0.17}_{-0.18}$	0.67 ± 0.09	$1.00^{+0.29}_{-0.30}$	$0.82^{+0.15}_{-0.16}$	$1.00^{+0.20}_{-0.22}$	$0.82^{+0.15}_{-0.16}$
i (deg)[a]	$60.9^{+4.2}_{-4.4}$	90.0	$60.9^{+5.7}_{-5.9}$	90.0	$61.3^{+4.9}_{-5.0}$	90.0	$73.8^{+7.5}_{-7.8}$	90.0	$74.4^{+7.4}_{-7.9}$	90.0
M_x ($M_\odot$)[b]	1.9	1.9	1.9	1.9	1.9	1.9	1.9	1.9	1.9	1.9
M_c ($M_\odot$)[c]	$23.2^{+3.7}_{-3.9}$	16.5 ± 2.5	$23.1^{+5.1}_{-5.3}$	$16.4^{+2.8}_{-2.9}$	$21.9^{+4.1}_{-4.2}$	15.7 ± 2.7	18.3 ± 2.8	16.5 ± 2.6	17.9 ± 2.8	16.3 ± 2.7
q[d]	0.08 ± 0.01	0.12 ± 0.02	0.08 ± 0.02	0.12 ± 0.02	0.09 ± 0.02	0.12 ± 0.02	0.10 ± 0.02	0.11 ± 0.02	0.11 ± 0.02	0.12 ± 0.02
R_c ($R_\odot$)[e]	$26.2^{+3.1}_{-3.2}$	$15.5^{+1.8}_{-1.9}$	$26.2^{+4.2}_{-4.3}$	$15.5^{+1.9}_{-2.0}$	25.6 ± 3.5	$15.3^{+1.8}_{-1.9}$	$19.7^{+3.7}_{-3.8}$	$15.9^{+2.3}_{-2.4}$	$19.3^{+3.6}_{-3.8}$	$15.9^{+2.3}_{-2.4}$
R_L ($R_\odot$)[f]	$26.2^{+1.6}_{-1.7}$	$22.6^{+1.1}_{-1.2}$	$26.2^{+2.2}_{-2.3}$	22.5 ± 1.3	25.6 ± 1.8	22.1 ± 1.2	$19.7^{+1.9}_{-2.0}$	$18.8^{+2.2}_{-2.3}$	$19.3^{+1.7}_{-2.0}$	$18.6^{+2.0}_{-2.3}$
β[g]	$1.00^{+0.13}_{-0.14}$	0.69 ± 0.09	$1.00^{+0.18}_{-0.19}$	$0.69^{+0.09}_{-0.10}$	$1.00^{+0.15}_{-0.16}$	$0.69^{+0.09}_{-0.10}$	$1.00^{+0.21}_{-0.22}$	0.85 ± 0.16	$1.00^{+0.21}_{-0.22}$	$0.85^{+0.16}_{-0.17}$

We quote 1σ uncertainties on each parameter, if applicable.

[a] Inclination angles where the supergiant donor fills its Roche lobe and where the binary system is viewed edge-on ($i = 90°$).

[b] Assumed mass of the neutron star.

[c] Mass of the supergiant donor calculated using Equation (10.19).

[d] Mass ratio, $q = M_x/M_c$, where M_x is the mass of the neutron star and M_c is the mass of the supergiant companion.

[e] Radius of the supergiant donor obtained using Equation (10.22).

[f] Roche lobe radius calculated using Equation (10.23).

[g] Roche lobe filling factor, $\beta = R_c/R_L$, where R_c is the radius of the supergiant companion and R_L is the Roche lobe radius.

Table 10.10: **Supergiant Donor Parameters of IGR J16493–4348** ***(Continued)***

Parameter	**Circular Solution 1**		Circular Solution 2		Circular Solution 3		Eccentric Solution 1		Eccentric Solution 2	
	Swift BAT Transient Monitor (15–50 keV), Symmetric Eclipse Model									
i (deg)[a]	$56.3^{+5.6}_{-5.4}$	90.0	$56.3^{+5.7}_{-5.5}$	90.0	$56.6^{+6.4}_{-6.1}$	90.0	$68.2^{+7.7}_{-7.4}$	90.0	$68.6^{+9.0}_{-8.8}$	90.0
M_x ($M_\odot$)[b]	1.4	1.4	1.4	1.4	1.4	1.4	1.4	1.4	1.4	1.4
M_c ($M_\odot$)[c]	25.6 ± 5.8	$15.7^{+2.4}_{-2.5}$	25.5 ± 5.9	$15.6^{+2.8}_{-2.9}$	$24.1^{+6.2}_{-6.1}$	$15.0^{+2.6}_{-2.7}$	$19.2^{+3.7}_{-3.6}$	$15.8^{+2.5}_{-2.6}$	$18.7^{+4.3}_{-4.2}$	15.5 ± 2.7
q[d]	0.05 ± 0.01	0.09 ± 0.01	0.05 ± 0.01	0.09 ± 0.02	$0.06^{+0.02}_{-0.01}$	0.09 ± 0.02	0.07 ± 0.01	0.09 ± 0.01	0.08 ± 0.02	0.09 ± 0.02
R_c ($R_\odot$)[e]	$28.2^{+4.9}_{-4.7}$	$13.2^{+4.0}_{-3.4}$	$28.2^{+4.9}_{-4.7}$	$13.2^{+4.0}_{-3.4}$	$27.5^{+5.4}_{-5.1}$	$13.0^{+3.9}_{-3.4}$	$20.7^{+5.2}_{-4.9}$	$13.6^{+4.2}_{-3.7}$	$20.4^{+5.9}_{-5.7}$	$13.6^{+4.2}_{-3.7}$
R_L ($R_\odot$)[f]	28.2 ± 2.5	22.8 ± 1.2	28.2 ± 2.6	$22.8^{+1.3}_{-1.4}$	$27.5^{+2.8}_{-2.7}$	22.3 ± 1.3	$20.7^{+2.3}_{-2.4}$	$19.0^{+2.2}_{-2.4}$	$20.4^{+2.5}_{-2.7}$	$18.8^{+2.1}_{-2.3}$
β[g]	1.00 ± 0.19	$0.58^{+0.18}_{-0.15}$	$1.00^{+0.20}_{-0.19}$	$0.58^{+0.18}_{-0.15}$	$1.00^{+0.22}_{-0.21}$	$0.58^{+0.18}_{-0.15}$	$1.00^{+0.27}_{-0.26}$	$0.72^{+0.24}_{-0.21}$	$1.00^{+0.32}_{-0.31}$	$0.72^{+0.24}_{-0.21}$
i (deg)[a]	$58.4^{+5.7}_{-5.5}$	90.0	$58.4^{+5.3}_{-5.0}$	90.0	$58.8^{+6.4}_{-6.0}$	90.0	$69.9^{+7.9}_{-7.6}$	90.0	$70.3^{+9.3}_{-9.0}$	90.0
M_x ($M_\odot$)[b]	1.9	1.9	1.9	1.9	1.9	1.9	1.9	1.9	1.9	1.9
M_c ($M_\odot$)[c]	24.8 ± 5.3	16.5 ± 2.5	24.7 ± 5.0	$16.4^{+2.8}_{-2.9}$	$23.4^{+5.7}_{-5.5}$	15.7 ± 2.7	$19.4^{+3.5}_{-3.4}$	16.5 ± 2.6	$18.9^{+4.1}_{-4.0}$	16.3 ± 2.7
q[d]	0.08 ± 0.02	0.12 ± 0.02	0.08 ± 0.02	0.12 ± 0.02	0.08 ± 0.02	0.12 ± 0.02	0.10 ± 0.02	0.11 ± 0.02	0.10 ± 0.02	0.12 ± 0.02
R_c ($R_\odot$)[e]	$27.0^{+4.8}_{-4.5}$	$13.6^{+4.1}_{-3.5}$	$26.9^{+4.4}_{-4.2}$	$13.5^{+4.1}_{-3.5}$	$26.3^{+5.2}_{-4.9}$	$13.4^{+4.0}_{-3.4}$	$20.2^{+5.1}_{-4.8}$	$13.9^{+4.3}_{-3.7}$	$19.8^{+6.0}_{-5.7}$	$13.9^{+4.3}_{-3.7}$
R_L ($R_\odot$)[f]	$27.0^{+2.3}_{-2.2}$	$22.6^{+1.1}_{-1.2}$	26.9 ± 2.1	22.5 ± 1.3	$26.3^{+2.5}_{-2.4}$	22.1 ± 1.2	20.2 ± 2.2	$18.8^{+2.2}_{-2.3}$	$19.8^{+2.4}_{-2.6}$	$18.6^{+2.0}_{-2.3}$
β[g]	$1.00^{+0.20}_{-0.19}$	$0.60^{+0.18}_{-0.16}$	$1.00^{+0.18}_{-0.17}$	$0.60^{+0.18}_{-0.16}$	$1.00^{+0.22}_{-0.21}$	$0.60^{+0.18}_{-0.16}$	$1.00^{+0.28}_{-0.26}$	$0.74^{+0.25}_{-0.22}$	$1.00^{+0.32}_{-0.31}$	$0.75^{+0.25}_{-0.22}$
	RXTE PCA Galactic Bulge Scans (2–10 keV), Symmetric Eclipse Model									
i (deg)[a]	$60.0^{+4.4}_{-4.5}$	90.0	60.1 ± 5.7	90.0	$60.5^{+5.1}_{-5.0}$	90.0	$74.4^{+11.2}_{-11.4}$	90.0	$75.0^{+8.3}_{-8.6}$	90.0
M_x ($M_\odot$)[b]	1.4	1.4	1.4	1.4	1.4	1.4	1.4	1.4	1.4	1.4
M_c ($M_\odot$)[c]	$22.9^{+3.8}_{-3.9}$	$15.7^{+2.4}_{-2.5}$	$22.8^{+4.9}_{-5.0}$	$15.6^{+2.8}_{-2.9}$	21.6 ± 4.1	$15.0^{+2.6}_{-2.7}$	17.4 ± 3.7	$15.8^{+2.5}_{-2.6}$	$17.0^{+2.7}_{-2.8}$	15.5 ± 2.7
q[d]	0.06 ± 0.01	0.09 ± 0.01	0.06 ± 0.01	0.09 ± 0.02	0.06 ± 0.01	0.09 ± 0.02	0.08 ± 0.02	0.09 ± 0.01	0.08 ± 0.01	0.09 ± 0.02
R_c ($R_\odot$)[e]	26.9 ± 3.2	$16.1^{+1.9}_{-1.7}$	26.8 ± 4.1	$16.1^{+1.9}_{-1.8}$	$26.2^{+3.6}_{-3.5}$	$15.9^{+1.9}_{-1.7}$	$19.9^{+5.0}_{-5.1}$	$16.6^{+2.4}_{-2.3}$	$19.5^{+3.6}_{-3.7}$	$16.5^{+2.4}_{-2.2}$
R_L ($R_\odot$)[f]	$26.9^{+1.7}_{-1.8}$	22.8 ± 1.2	$26.8^{+2.2}_{-2.3}$	$22.8^{+1.3}_{-1.4}$	26.2 ± 1.9	22.3 ± 1.3	$19.9^{+2.5}_{-2.7}$	$19.0^{+2.2}_{-2.4}$	$19.5^{+1.8}_{-1.9}$	$18.8^{+2.1}_{-2.3}$
β[g]	$1.00^{+0.13}_{-0.14}$	$0.71^{+0.09}_{-0.08}$	1.00 ± 0.17	0.71 ± 0.09	1.00 ± 0.15	0.71 ± 0.09	$1.00^{+0.28}_{-0.29}$	0.87 ± 0.16	1.00 ± 0.21	0.88 ± 0.16
i (deg)[a]	62.5 ± 4.2	90.0	62.5 ± 5.1	90.0	62.9 ± 4.6	90.0	$76.8^{+11.7}_{-11.8}$	90.0	$77.5^{+9.1}_{-9.3}$	90.0
M_x ($M_\odot$)[b]	1.9	1.9	1.9	1.9	1.9	1.9	1.9	1.9	1.9	1.9
M_c ($M_\odot$)[c]	$22.3^{+3.3}_{-3.4}$	16.5 ± 2.5	$22.2^{+4.1}_{-4.2}$	$16.4^{+2.8}_{-2.9}$	21.1 ± 3.5	15.7 ± 2.7	$17.7^{+3.3}_{-3.4}$	16.5 ± 2.6	17.3 ± 2.6	16.3 ± 2.7
q[d]	0.09 ± 0.01	0.12 ± 0.02	0.09 ± 0.02	0.12 ± 0.02	0.09 ± 0.01	0.12 ± 0.02	0.11 ± 0.02	0.11 ± 0.02	0.11 ± 0.02	0.12 ± 0.02
R_c ($R_\odot$)[e]	25.8 ± 2.9	$16.5^{+1.9}_{-1.7}$	25.7 ± 3.5	$16.5^{+1.9}_{-1.8}$	$25.1^{+3.1}_{-3.0}$	$16.3^{+1.9}_{-1.8}$	19.4 ± 4.6	$17.0^{+2.4}_{-2.3}$	19.1 ± 3.5	$16.9^{+2.4}_{-2.3}$
R_L ($R_\odot$)[f]	25.8 ± 1.5	$22.6^{+1.1}_{-1.2}$	25.7 ± 1.8	22.5 ± 1.3	25.1 ± 1.6	22.1 ± 1.2	$19.4^{+2.3}_{-2.4}$	$18.8^{+2.2}_{-2.3}$	$19.1^{+1.6}_{-1.8}$	$18.6^{+2.0}_{-2.3}$
β[g]	1.00 ± 0.13	0.73 ± 0.09	1.00 ± 0.15	$0.73^{+0.10}_{-0.09}$	$1.00^{+0.14}_{-0.13}$	$0.74^{+0.10}_{-0.09}$	1.00 ± 0.27	$0.90^{+0.17}_{-0.16}$	$1.00^{+0.20}_{-0.21}$	$0.91^{+0.16}_{-0.17}$

We quote 1σ uncertainties on each parameter, if applicable.

[a] Inclination angles where the supergiant donor fills its Roche lobe and where the binary system is viewed edge-on ($i = 90°$).

[b] Assumed mass of the neutron star.

[c] Mass of the supergiant donor calculated using Equation (10.19).

[d] Mass ratio, $q = M_x/M_c$, where M_x is the mass of the neutron star and M_c is the mass of the supergiant companion.

[e] Radius of the supergiant donor obtained using Equation (10.22).

[f] Roche lobe radius calculated using Equation (10.23).

[g] Roche lobe filling factor, $\beta = R_c/R_L$, where R_c is the radius of the supergiant companion and R_L is the Roche lobe radius.

Part VI: Other Contributions

Somewhere, something incredible is waiting to be known.

— Carl Sagan

Chapter XI

A Study of the 20 Day Superorbital Modulation in the High-mass X-Ray Binary IGR J16493–4348

[110] Coley, J. B. and Corbet, R. H. D., Fürst, F., Huxtable, G., Krimm, H. A., Pearlman, A. B., and Pottschmidt, K. (2019). "A Study of the 20 Day Superorbital Modulation in the High-mass X-Ray Binary IGR J16493–4348." In: *ApJ,* 879:34. arXiv:1905.08817 [astro-ph.HE].

A Study of the 20 Day Superorbital Modulation in the High-mass X-Ray Binary IGR J16493–4348

J. .B. Coley[1,2,*], R. .H. D. Corbet[3,4], F. Fürst[5], G. Huxtable[3,4], H. A. Krimm[6,7], **A. B. Pearlman[8,9,10],** and K. Pottschmidt[2,3]

[1] Department of Physics and Astronomy, Howard University, Washington, DC 20059, USA
[2] CRESST/Mail Code 661, Astroparticle Physics Laboratory, NASA Goddard Space Flight Center, Greenbelt, MD 20771, USA
[3] University of Maryland, Baltimore County, MD, USA
[4] CRESST/Mail Code 662, X-ray Astrophysics Laboratory, NASA Goddard Space Flight Center, Greenbelt, MD 20771, USA
[5] European Space Astronomy Center(ESA/ESAC), Operations Department, Vilanueva de la Cañada(Madrid), Spain
[6] Universities Space Research Association, Columbia, MD 21046, USA
[7] National Science Foundation, Alexandria, VA 22314, USA
[8] Division of Physics, Mathematics, and Astronomy, California Institute of Technology, Pasadena, CA 91125, USA
[9] NDSEG Research Fellow
[10] NSF Graduate Research Fellow
[*] Lead author of the manuscript.
Corresponding author: joel.coley@howard.edu

Abstract

We report on *Nuclear Spectroscopic Telescope Array (NuSTAR), Neil Gehrels Swift Observatory (Swift)* X-ray Telescope (XRT), and *Swift* Burst Alert Telescope (BAT) observations of IGR J16493–4348, a wind-fed supergiant X-ray binary showing

significant superorbital variability. From a discrete Fourier transform of the BAT light curve, we refine its superorbital period to be 20.058 ± 0.007 days. The BAT dynamic power spectrum and a fractional root mean square analysis both show strong variations in the amplitude of the superorbital modulation, but no observed changes in the period are found. The superorbital modulation is significantly weaker between MJD 55,700 and MJD 56,300. The joint NuSTAR and XRT observations, which were performed near the minimum and maximum of one cycle of the 20 day superorbital modulation, show that the flux increases by more than a factor of two between superorbital minimum and maximum. We find no significant changes in the 3–50 keV pulse profiles between superorbital minimum and maximum, which suggests a similar accretion regime. Modeling the pulse-phase-averaged spectra, we find a possible Fe Kα emission line at 6.4 keV at superorbital maximum. This feature is not significant at superorbital minimum. While we do not observe any significant differences between the pulse-phase-averaged spectral continua apart from the overall flux change, we find that the hardness ratio near the broad main peak of the pulse profile increases from superorbital minimum to maximum. This suggests the spectral shape hardens with increasing luminosity. We discuss different mechanisms that might drive the observed superorbital modulation.

Chapter XII

Simultaneous X-Ray and Radio Observations of the Repeating Fast Radio Burst FRB 180916.J0158+65

[482] Scholz P., Cook A., Cruces M., Hessels, J. W. T., Kaspi, V. M., Majid, W. A., Naidu, A., **Pearlman, A. B.**, Spitler, L. et al. (2020). "Simultaneous X-Ray and Radio Observations of the Repeating Fast Radio Burst FRB 180916.J0158+65." In: *ApJ,* 901:165. arXiv:2004.06082 [astro-ph.HE].

Simultaneous X-Ray and Radio Observations of the Repeating Fast Radio Burst FRB 180916.J0158+65

P. Scholz[1,*], A. Cook[1], M. Cruces[2], J. W. T. Hessels[3,4], V. M. Kaspi[5,6], W. A. Majid[7,8], A. Naidu[5,6], **A. B. Pearlman[8,19,20],** L. Spitler[2], K. M. Bandura[9,10], M. Bhardwaj[5,6], T. Cassanelli[1], P. Chawla[5,6], B. M. Gaensler[1], D. C. Good[11], A. Josephy[5,6], R. Karuppusamy[2], A. Keimpema[12], A. Yu. Kirichenko[13,14], F. Kirsten[15], J. Kocz[8], C. Leung[16,17], B. Marcote[12], K. Masui[16,17], J. Mena-Parra[16], M. Merryfield[5,6], D. Michilli[5,6], C. J. Naudet[7], K. Nimmo[3,4], Z. Pleunis[5,6], T. A. Prince[7,8], M. Rafiei-Ravandi[18], M. Rahman[1], K. Shin[16,17], K. M. Smith[18], I. H. Stairs[11], S. P. Tendulkar[5,6], and K. Vanderlinde[1]

[1] Dunlap Institute for Astronomy & Astrophysics, University of Toronto, 50 St. George Street, Toronto, ON M5S 3H4, Canada

[2] Max Planck Institut für Radioastronomie, Auf dem Hügel 69, D-53121, Bonn, Germany

[3] Anton Pannekoek Institute for Astronomy, University of Amsterdam, Science Park 904, 1098 XH, Amsterdam, The Netherlands

[4] ASTRON, Netherlands Institute for Radio Astronomy, Oude Hoogeveensedijk 4, 7991 PD Dwingeloo, The Netherlands

[5] Department of Physics, McGill University, 3600 rue University, Montréal, QC H3A 2T8, Canada

[6] McGill Space Institute, McGill University, 3550 rue University, Montréal, QC H3A 2A7, Canada

[7] Jet Propulsion Laboratory, California Institute of Technology, Pasadena, CA 91109, USA

[8] Division of Physics, Mathematics, and Astronomy, California Institute of Technology, Pasadena, CA 91125, USA

[9] CSEE, West Virginia University, Morgantown, WV 26505, USA

[10] Center for Gravitational Waves and Cosmology, West Virginia University, Morgantown, WV 26505, USA

[11] Department of Physics & Astronomy, 6224 Agricultural Road, Vancouver, BC V6T 1Z1, Canada

[12] Joint Institute for VLBI ERIC, Oude Hoogeveensedijk 4, 7991 PD Dwingeloo, The Netherlands
[13] Instituto de Astronomía, Universidad Nacional Autónoma de México, Apdo. Postal 877, Ensenada, Baja California 22800, México
[14] Ioffe Institute, 26 Politekhnicheskaya st., St. Petersburg 194021, Russia
[15] Department of Space, Earth and Environment, Chalmers University of Technology, Onsala Space Observatory, SE-43992, Onsala, Sweden
[16] MIT Kavli Institute for Astrophysics and Space Research, Massachusetts Institute of Technology, 77 Massachusetts Avenue, Cambridge, MA 02139, USA
[17] Department of Physics, Massachusetts Institute of Technology, 77 Massachusetts Avenue, Cambridge, MA 02139, USA
[18] Perimeter Institute for Theoretical Physics, 31 Caroline Street N, Waterloo ON N2L 2Y5, Canada
[19] NDSEG Research Fellow
[20] NSF Graduate Research Fellow
[*] Lead author of the manuscript.
Corresponding author: paul.scholz@dunlap.utoronto.ca

Abstract

We report on simultaneous radio and X-ray observations of the repeating fast radio burst source FRB 180916.J0158+65 using the Canadian Hydrogen Intensity Mapping Experiment (CHIME), Effelsberg, and Deep Space Network (DSS-14 and DSS-63) radio telescopes and the Chandra X-ray Observatory. During 33 ks of Chandra observations, we detect no radio bursts in overlapping Effelsberg or Deep Space Network observations and a single burst during CHIME/FRB source transits. We detect no X-ray events in excess of the background during the Chandra observations. These non-detections imply a 5σ limit of $< 5 \times 10^{-10}$ erg cm^{-2} for the 0.5–10 keV fluence of prompt emission at the time of the radio burst and 1.3×10^{-9} erg cm^{-2} at any time during the Chandra observations. Given the host-galaxy redshift of FRB 180916.J0158+65 ($z \sim 0.034$), these correspond to energy limits of $< 1.6 \times 10^{45}$ erg and $< 4 \times 10^{45}$ erg, respectively. We also place a 5σ limit of $< 8 \times 10^{-15}$ erg s^{-1} cm^{-2} on the 0.5–10 keV absorbed flux of a persistent source at the location of FRB 180916.J0158+65. This corresponds to a luminosity limit of $< 2 \times 10^{40}$ erg s^{-1}. Using an archival set of radio bursts from FRB 180916.J0158+65, we search for prompt gamma-ray emission in Fermi/GBM data but find no significant gamma-ray bursts, thereby placing a limit of 9×10^{-9} erg cm^{-2} on the 10–100 keV fluence. We also search Fermi/LAT data for periodic modulation of the gamma-ray brightness at the 16.35 day period of radio burst activity and detect no significant modulation. We compare these deep limits to the predictions of various fast radio burst models, but conclude that similar X-ray constraints on a closer fast radio burst source would be needed to strongly constrain theory.

Bibliography

[1] K. N. Abazajian. The Consistency of Fermi-LAT Observations of the Galactic Center with a Millisecond Pulsar Population in the Central Stellar Cluster. *JCAP*, 2011(3):010, Mar 2011. doi: 10.1088/1475-7516/2011/03/010. (Cited on page: 260)

[2] K. N. Abazajian and M. Kaplinghat. Detection of a Gamma-Ray Source in the Galactic Center Consistent with Extended Emission from Dark Matter Annihilation and Concentrated Astrophysical Emission. *Phys. Rev. D*, 86(8): 083511, Oct 2012. doi: 10.1103/PhysRevD.86.083511. (Cited on pages: 260 and 261)

[3] K. N. Abazajian, N. Canac, S. Horiuchi, and M. Kaplinghat. Astrophysical and Dark Matter Interpretations of Extended Gamma-Ray Emission from the Galactic Center. *Phys. Rev. D*, 90(2):023526, Jul 2014. doi: 10.1103/PhysRevD.90.023526. (Cited on page: 261)

[4] A. A. Abdo, M. Ackermann, M. Ajello, W. B. Atwood, M. Axelsson, L. Baldini, J. Ballet, G. Barbiellini, M. G. Baring, D. Bastieri, K. Bechtol, R. Bellazzini, B. Berenji, R. D. Blandford, E. D. Bloom, E. Bonamente, A. W. Borgland, J. Bregeon, A. Brez, M. Brigida, P. Bruel, T. H. Burnett, G. A. Caliandro, R. A. Cameron, F. Camilo, P. A. Caraveo, J. M. Casandjian, C. Cecchi, Ö. Çelik, A. Chekhtman, C. C. Cheung, J. Chiang, S. Ciprini, R. Claus, I. Cognard, J. Cohen-Tanugi, L. R. Cominsky, J. Conrad, C. D. Dermer, A. de Angelis, A. de Luca, F. de Palma, S. W. Digel, E. d. C. e. Silva, P. S. Drell, R. Dubois, D. Dumora, C. Espinoza, C. Farnier, C. Favuzzi, S. J. Fegan, E. C. Ferrara, W. B. Focke, M. Frailis, P. C. C. Freire, Y. Fukazawa, S. Funk, P. Fusco, F. Gargano, D. Gasparrini, N. Gehrels, S. Germani, G. Giavitto, B. Giebels, N. Giglietto, F. Giordano, T. Glanzman, G. Godfrey, I. A. Grenier, M. H. Grondin, J. E. Grove, L. Guillemot, S. Guiriec, Y. Hanabata, A. K. Harding, M. Hayashida, E. Hays, R. E. Hughes, G. Jóhannesson, A. S. Johnson, R. P. Johnson, T. J. Johnson, W. N. Johnson, S. Johnston, T. Kamae, H. Katagiri, J. Kataoka, N. Kawai, M. Kerr, J. Knödlseder, M. L. Kocian, M. Kramer, F. Kuehn, M. Kuss, J. Lande, L. Latronico, S. H. Lee, M. Lemoine-Goumard, F. Longo, F. Loparco, B. Lott, M. N. Lovellette, P. Lubrano, A. G. Lyne, A. Makeev, M. Marelli, M. N. Mazziotta, J. E. McEnery, C. Meurer, P. F. Michelson, W. Mitthumsiri, T. Mizuno, A. A. Moiseev, C. Monte, M. E. Monzani, E. Moretti, A. Morselli, I. V. Moskalenko, S. Murgia, T. Nakamori, P. L. Nolan, J. P. Norris, A. Noutsos, E. Nuss, T. Ohsugi, N. Omodei, E. Orlando, J. F. Ormes, M. Ozaki, D. Paneque, J. H. Panetta, D. Parent, V. Pelassa, M. Pepe, M. Pesce-Rollins, M. Pierbattista, F. Piron, T. A. Porter, S. Rainò, R. Rando, P. S. Ray, M. Razzano, A. Reimer, O. Reimer, T. Reposeur, S. Ritz, L. S. Rochester, A. Y. Rodriguez, R. W. Romani, M. Roth, F. Ryde, H. F. W.

Sadrozinski, D. Sanchez, A. Sander, P. M. Saz Parkinson, J. D. Scargle, C. Sgrò, E. J. Siskind, D. A. Smith, P. D. Smith, G. Spandre, P. Spinelli, B. W. Stappers, M. S. Strickman, D. J. Suson, H. Tajima, H. Takahashi, T. Tanaka, J. B. Thayer, J. G. Thayer, G. Theureau, D. J. Thompson, S. E. Thorsett, L. Tibaldo, D. F. Torres, G. Tosti, A. Tramacere, Y. Uchiyama, T. L. Usher, A. Van Etten, V. Vasileiou, N. Vilchez, V. Vitale, A. P. Waite, E. Wallace, P. Wang, K. Watters, P. Weltevrede, B. L. Winer, K. S. Wood, T. Ylinen, and M. Ziegler. Fermi Large Area Telescope Observations of the Crab Pulsar and Nebula. *ApJ*, 708(2):1254–1267, January 2010. doi: 10.1088/0004-637X/708/2/1254. (Cited on page: 146)

[5] A. A. Abdo, M. Ackermann, M. Ajello, L. Baldini, J. Ballet, G. Barbiellini, D. Bastieri, R. Bellazzini, R. D. Blandford, E. D. Bloom, E. Bonamente, A. W. Borgland, A. Bouvier, T. J. Brand t, J. Bregeon, M. Brigida, P. Bruel, R. Buehler, S. Buson, G. A. Caliandro, R. A. Cameron, P. A. Caraveo, S. Carrigan, J. M. Casand jian, E. Charles, S. Chaty, A. Chekhtman, C. C. Cheung, J. Chiang, S. Ciprini, R. Claus, J. Cohen-Tanugi, J. Conrad, M. E. Decesar, C. D. Dermer, F. de Palma, S. W. Digel, E. D. C. E. Silva, P. S. Drell, R. Dubois, D. Dumora, C. Favuzzi, P. Fortin, M. Frailis, Y. Fukazawa, P. Fusco, F. Gargano, D. Gasparrini, N. Gehrels, S. Germani, N. Giglietto, F. Giordano, T. Glanzman, G. Godfrey, I. Grenier, M. H. Grondin, J. E. Grove, L. Guillemot, S. Guiriec, D. Hadasch, A. K. Harding, E. Hays, P. Jean, G. Jóhannesson, T. J. Johnson, W. N. Johnson, T. Kamae, H. Katagiri, J. Kataoka, M. Kerr, J. Knödlseder, M. Kuss, J. Lande, L. Latronico, S. H. Lee, M. Lemoine-Goumard, M. Llena Garde, F. Longo, F. Loparco, M. N. Lovellette, P. Lubrano, A. Makeev, M. N. Mazziotta, P. F. Michelson, W. Mitthumsiri, T. Mizuno, C. Monte, M. E. Monzani, A. Morselli, I. V. Moskalenko, S. Murgia, M. Naumann-Godo, P. L. Nolan, J. P. Norris, E. Nuss, T. Ohsugi, N. Omodei, E. Orlando, J. F. Ormes, B. Pancrazi, D. Parent, M. Pepe, M. Pesce-Rollins, F. Piron, T. A. Porter, S. Rainò, R. Rando, A. Reimer, O. Reimer, T. Reposeur, J. Ripken, R. W. Romani, M. Roth, H. F. W. Sadrozinski, P. M. Saz Parkinson, C. Sgrò, E. J. Siskind, D. A. Smith, P. Spinelli, M. S. Strickman, D. J. Suson, H. Takahashi, T. Takahashi, T. Tanaka, J. B. Thayer, J. G. Thayer, L. Tibaldo, D. F. Torres, G. Tosti, A. Tramacere, Y. Uchiyama, T. L. Usher, V. Vasileiou, C. Venter, N. Vilchez, V. Vitale, A. P. Waite, P. Wang, N. Webb, B. L. Winer, Z. Yang, T. Ylinen, M. Ziegler, and Fermi LAT Collaboration. A Population of Gamma-Ray Emitting Globular Clusters Seen with the Fermi Large Area Telescope. *A&A*, 524:A75, Dec 2010. doi: 10.1051/0004-6361/201014458. (Cited on page: 260)

[6] J. G. Ables and R. N. Manchester. Hydrogen-line Absorption Observations of Distant Pulsars. *A&A*, 50:177–184, July 1976. (Cited on page: 21)

[7] D. Agarwal, K. Aggarwal, S. Burke-Spolaor, D. R. Lorimer, and N. Garver-Daniels. FETCH: A Deep-Learning Based Classifier for Fast Transient Clas-

sification. *MNRAS*, 497(2):1661–1674, June 2020. doi: 10.1093/mnras/staa1856. (Cited on pages: 166 and 186)

[8] K. Aggarwal and Realfast Collaboration. VLA/realfast Detection of Burst from FRB180916.J0158+65. *The Astronomer's Telegram*, #13664, April 2020. (Cited on pages: 179, 193, 194, 195, and 204)

[9] K. Aggarwal, C. J. Law, S. Burke-Spolaor, G. Bower, B. J. Butler, P. Demorest, J. Linford, and T. J. W. Lazio. VLA/Realfast Detection of a Burst from FRB 180916.J0158+65 and Tests for Periodic Activity. *RNAAS*, 4(6): 94, June 2020. doi: 10.3847/2515-5172/ab9f33. (Cited on pages: xliii, 179, 190, 194, 199, and 205)

[10] B. C. Andersen and S. M. Ransom. A Fourier Domain "Jerk" Search for Binary Pulsars. *ApJL*, 863(1):L13, August 2018. doi: 10.3847/2041-8213/aad59f. (Cited on page: 233)

[11] G. E. Anderson, B. M. Gaensler, P. O. Slane, N. Rea, D. L. Kaplan, B. Posselt, L. Levin, S. Johnston, S. S. Murray, C. L. Brogan, M. Bailes, S. Bates, R. A. Benjamin, N. D. R. Bhat, M. Burgay, S. Burke-Spolaor, D. Chakrabarty, N. D'Amico, J. J. Drake, P. Esposito, J. E. Grindlay, J. Hong, G. L. Israel, M. J. Keith, M. Kramer, T. J. W. Lazio, J. C. Lee, J. C. Mauerhan, S. Milia, A. Possenti, B. Stappers, and D. T. H. Steeghs. Multi-wavelength Observations of the Radio Magnetar PSR J1622–4950 and Discovery of Its Possibly Associated Supernova Remnant. *ApJ*, 751(1):53, May 2012. doi: 10.1088/0004-637X/751/1/53. (Cited on page: 121)

[12] P. W. Anderson and N. Itoh. Pulsar Glitches and Restlessness as a Hard Superfluidity Phenomenon. *Nature*, 256(5512):25–27, July 1975. doi: 10.1038/256025a0. (Cited on page: 38)

[13] S. B. Anderson, P. W. Gorham, S. R. Kulkarni, T. A. Prince, and A. Wolszczan. Discovery of Two Radio Pulsars in the Globular Cluster M15. *Nature*, 346 (6279):42–44, July 1990. doi: 10.1038/346042a0. (Cited on page: 232)

[14] D. Antonopoulou, P. Weltevrede, C. M. Espinoza, A. L. Watts, S. Johnston, R. M. Shannon, and M. Kerr. The Unusual Glitch Recoveries of the High-Magnetic-Field Pulsar J1119–6127. *MNRAS*, 447:3924–3935, March 2015. doi: 10.1093/mnras/stu2710. (Cited on page: 76)

[15] D. Antonopoulou, G. Vasilopoulos, and C. M. Espinoza. Swift Detection of Pulsations from PSR J1119–6127 Promptly After Its July 27th 2016 Burst. *The Astronomer's Telegram*, #9282, July 2016. (Cited on page: 76)

[16] A. M. Archibald, N. V. Gusinskaia, J. W. T. Hessels, A. T. Deller, D. L. Kaplan, D. R. Lorimer, R. S. Lynch, S. M. Ransom, and I. H. Stairs. Universality of Free Fall from the Orbital Motion of a Pulsar in a Stellar Triple System. *Nature*, 559(7712):73–76, July 2018. doi: 10.1038/s41586-018-0265-1. (Cited on pages: 244 and 262)

[17] R. F. Archibald, V. M. Kaspi, A. P. Beardmore, N. Gehrels, and J. A. Kennea. On the Braking Index of the Unusual High-B Rotation-powered Pulsar PSR J1846–0258. *ApJ*, 810(1):67, September 2015. doi: 10.1088/0004-637X/810/1/67. (Cited on page: 40)

[18] R. F. Archibald, V. M. Kaspi, S. P. Tendulkar, and P. Scholz. A Magnetar-like Outburst from a High-B Radio Pulsar. *ApJL*, 829(1):L21, September 2016. doi: 10.3847/2041-8205/829/1/L21. (Cited on pages: 33, 40, 76, 79, and 83)

[19] R. F. Archibald, S. P. Tendulkar, P. A. Scholz, and V. M. Kaspi. Glitch Observation and Hard X-Ray Power Law Measurement in PSR J1119–6127. *The Astronomer's Telegram*, #9284, July 2016. (Cited on page: 76)

[20] R. F. Archibald, M. Burgay, M. Lyutikov, V. M. Kaspi, P. Esposito, G. Israel, M. Kerr, A. Possenti, N. Rea, J. Sarkissian, P. Scholz, and S. P. Tendulkar. Magnetar-like X-Ray Bursts Suppress Pulsar Radio Emission. *ApJL*, 849(2): L20, November 2017. doi: 10.3847/2041-8213/aa9371. (Cited on page: 143)

[21] W. Baade and F. Zwicky. On Super-Novae. *PNAS*, 20(5):254–259, May 1934. doi: 10.1073/pnas.20.5.254. (Cited on page: 2)

[22] M. Bachetti, F. A. Harrison, D. J. Walton, B. W. Grefenstette, D. Chakrabarty, F. Fürst, D. Barret, A. Beloborodov, S. E. Boggs, F. E. Christensen, W. W. Craig, A. C. Fabian, C. J. Hailey, A. Hornschemeier, V. Kaspi, S. R. Kulkarni, T. Maccarone, J. M. Miller, V. Rana, D. Stern, S. P. Tendulkar, J. Tomsick, N. A. Webb, and W. W. Zhang. An Ultraluminous X-Ray Source Powered by an Accreting Neutron Star. *Nature*, 514(7521):202–204, October 2014. doi: 10.1038/nature13791. (Cited on page: 8)

[23] D. C. Backer, S. R. Kulkarni, C. Heiles, M. M. Davis, and W. M. Goss. A Millisecond Pulsar. *Nature*, 300(5893):615–618, December 1982. doi: 10.1038/300615a0. (Cited on page: 7)

[24] D. C. Backer, S. R. Kulkarni, and J. H. Taylor. Timing Observations of the Millisecond Pulsar. *Nature*, 301:314–315, January 1983. doi: 10.1038/301314a0. (Cited on page: 7)

[25] D. C. Backer, T. Wong, and J. Valanju. A Plasma Prism Model for an Anomalous Dispersion Event in the Crab Pulsar. *ApJ*, 543(2):740–753, November 2000. doi: 10.1086/317150. (Cited on page: 120)

[26] K. W. Bannister, A. T. Deller, C. Phillips, J. P. Macquart, J. X. Prochaska, N. Tejos, S. D. Ryder, E. M. Sadler, R. M. Shannon, S. Simha, C. K. Day, M. McQuinn, F. O. North-Hickey, S. Bhandari, W. R. Arcus, V. N. Bennert, J. Burchett, M. Bouwhuis, R. Dodson, R. D. Ekers, W. Farah, C. Flynn, C. W. James, M. Kerr, E. Lenc, E. K. Mahony, J. O'Meara, S. Osłowski, H. Qiu, T. Treu, V. U, T. J. Bateman, D. C. J. Bock, R. J. Bolton, A. Brown, J. D. Bunton, A. P. Chippendale, F. R. Cooray, T. Cornwell, N. Gupta,

D. B. Hayman, M. Kesteven, B. S. Koribalski, A. MacLeod, N. M. McClure-Griffiths, S. Neuhold, R. P. Norris, M. A. Pilawa, R. Y. Qiao, J. Reynolds, D. N. Roxby, T. W. Shimwell, M. A. Voronkov, and C. D. Wilson. A Single Fast Radio Burst Localized to a Massive Galaxy at Cosmological Distance. *Science*, 365(6453):565–570, August 2019. doi: 10.1126/science.aaw5903. (Cited on pages: 157, 163, 164, and 177)

[27] K. Bansal, A. B. Pearlman, W. A. Majid, T. A. Prince, Y. George, C.-P. Hu, T. Enoto, J. Kocz, and S. Horiuchi. Simultaneous Radio and X-Ray Observations of a Radio Magnetar: Swift J1818.0–1607. *Submitted*, 2021. (Cited on pages: xiv and 52)

[28] M. G. Baring and A. K. Harding. Resonant Compton Upscattering in Anomalous X-Ray Pulsars. *Ap&SS*, 308(1-4):109–118, April 2007. doi: 10.1007/s10509-007-9326-x. (Cited on page: 39)

[29] B. R. Barsdell, M. Bailes, D. G. Barnes, and C. J. Fluke. Accelerating Incoherent Dedispersion. *MNRAS*, 422(1):379–392, May 2012. doi: 10.1111/j.1365-2966.2012.20622.x. (Cited on page: 218)

[30] R. Bartels, S. Krishnamurthy, and C. Weniger. Strong Support for the Millisecond Pulsar Origin of the Galactic Center GeV Excess. *Phys. Rev. Lett.*, 116(5):051102, Feb 2016. doi: 10.1103/PhysRevLett.116.051102. (Cited on page: 261)

[31] R. Bartels, F. Calore, E. Storm, and C. Weniger. Galactic Binaries Can Explain the Fermi Galactic Centre Excess and 511 keV Emission. *MNRAS*, 480(3):3826–3841, Nov 2018. doi: 10.1093/mnras/sty2135. (Cited on page: 261)

[32] R. Bartels, E. Storm, C. Weniger, and F. Calore. The Fermi-LAT GeV Excess as a Tracer of Stellar Mass in the Galactic Bulge. *Nature Astronomy*, 2:819–828, Aug 2018. doi: 10.1038/s41550-018-0531-z. (Cited on page: 261)

[33] S. D. Barthelmy, L. M. Barbier, J. R. Cummings, E. E. Fenimore, N. Gehrels, D. Hullinger, H. A. Krimm, C. B. Markwardt, D. M. Palmer, A. Parsons, G. Sato, M. Suzuki, T. Takahashi, M. Tashiro, and J. Tueller. The Burst Alert Telescope (BAT) on the SWIFT Midex Mission. *Space Sci. Rev.*, 120(3-4):143–164, October 2005. doi: 10.1007/s11214-005-5096-3. (Cited on page: 286)

[34] S. D. Bates, S. Johnston, D. R. Lorimer, M. Kramer, A. Possenti, M. Burgay, B. Stappers, M. J. Keith, A. Lyne, M. Bailes, M. A. McLaughlin, J. T. O'Brien, and G. Hobbs. A 6.5-GHz Multibeam Pulsar Survey. *MNRAS*, 411(3):1575–1584, March 2011. doi: 10.1111/j.1365-2966.2010.17790.x. (Cited on pages: 88 and 257)

[35] S. D. Bates, D. R. Lorimer, and J. P. W. Verbiest. The Pulsar Spectral Index Distribution. *MNRAS*, 431(2):1352–1358, May 2013. doi: 10.1093/mnras/stt257. (Cited on page: 80)

[36] L. E. Baum. An inequality and associated maximization technique in statistical estimation for probabilistic functions of Markov processes. In O. Shisha, editor, *Inequalities III: Proceedings of the Third Symposium on Inequalities*, pages 1–8, University of California, Los Angeles, 1972. Academic Press. (Cited on pages: 215 and 217)

[37] L. E. Baum and J. A. Eagon. An inequality with applications to statistical estimation for probabilistic functions of Markov processes and to a model for ecology. *Bulletin of the American Mathematical Society*, 73(3):360–363, May 1967. (Cited on page: 215)

[38] L. E. Baum and T. Petrie. Statistical inference for probabilistic functions of finite state Markov chains. *Annals of Mathematical Statistics*, 37:1554–1563, 1966. (Cited on page: 215)

[39] W. H. Baumgartner, J. Tueller, C. B. Markwardt, G. K. Skinner, S. Barthelmy, R. F. Mushotzky, P. A. Evans, and N. Gehrels. The 70 Month Swift-BAT All-sky Hard X-Ray Survey. *ApJS*, 207(2):19, August 2013. doi: 10.1088/0067-0049/207/2/19. (Cited on pages: 121, 281, and 287)

[40] A. M. Beloborodov. Untwisting Magnetospheres of Neutron Stars. *ApJ*, 703(1):1044–1060, September 2009. doi: 10.1088/0004-637X/703/1/1044. (Cited on page: 142)

[41] A. M. Beloborodov. A Flaring Magnetar in FRB 121102? *ApJL*, 843(2): L26, July 2017. doi: 10.3847/2041-8213/aa78f3. (Cited on page: 178)

[42] A. M. Beloborodov and X. Li. Magnetar Heating. *ApJ*, 833(2):261, December 2016. doi: 10.3847/1538-4357/833/2/261. (Cited on pages: 137 and 142)

[43] P. Beniamini, Z. Wadiasingh, and B. D. Metzger. Periodicity in Recurrent Fast Radio Bursts and the Origin of Ultralong Period Magnetars. *MNRAS*, 496(3):3390–3401, June 2020. doi: 10.1093/mnras/staa1783. (Cited on page: 204)

[44] S. Bhandari, E. M. Sadler, J. X. Prochaska, S. Simha, S. D. Ryder, L. Marnoch, K. W. Bannister, J.-P. Macquart, C. Flynn, R. M. Shannon, N. Tejos, F. Corro-Guerra, C. K. Day, A. T. Deller, R. Ekers, S. Lopez, E. K. Mahony, C. Nuñez, and C. Phillips. The Host Galaxies and Progenitors of Fast Radio Bursts Localized with the Australian Square Kilometre Array Pathfinder. *ApJL*, 895 (2):L37, June 2020. doi: 10.3847/2041-8213/ab672e. (Cited on page: 177)

[45] N. D. R. Bhat, J. M. Cordes, and S. Chatterjee. A CLEAN-based Method for Deconvolving Interstellar Pulse Broadening from Radio Pulses. *ApJ*, 584(2): 782–790, February 2003. doi: 10.1086/345775. (Cited on page: 122)

[46] N. D. R. Bhat, J. M. Cordes, F. Camilo, D. J. Nice, and D. R. Lorimer. Multifrequency Observations of Radio Pulse Broadening and Constraints on

Interstellar Electron Density Microstructure. *ApJ*, 605(2):759–783, April 2004. doi: 10.1086/382680. (Cited on pages: 25 and 112)

[47] A. J. Bird, E. J. Barlow, L. Bassani, A. Bazzano, A. Bodaghee, F. Capitanio, M. Cocchi, M. Del Santo, A. J. Dean, A. B. Hill, F. Lebrun, G. Malaguti, A. Malizia, R. Much, S. E. Shaw, J. B. Stephen, R. Terrier, P. Ubertini, and R. Walter. The First IBIS/ISGRI Soft Gamma-Ray Galactic Plane Survey Catalog. *ApJL*, 607(1):L33–L37, May 2004. doi: 10.1086/421772. (Cited on page: 281)

[48] A. J. Bird, E. J. Barlow, L. Bassani, A. Bazzano, G. Bélanger, A. Bodaghee, F. Capitanio, A. J. Dean, M. Fiocchi, A. B. Hill, F. Lebrun, A. Malizia, J. M. Mas-Hesse, M. Molina, L. Moran, M. Renaud, V. Sguera, S. E. Shaw, J. B. Stephen, R. Terrier, P. Ubertini, R. Walter, D. R. Willis, and C. Winkler. The Second IBIS/ISGRI Soft Gamma-Ray Survey Catalog. *ApJ*, 636(2):765–776, January 2006. doi: 10.1086/498090. (Cited on page: 281)

[49] A. J. Bird, A. Malizia, A. Bazzano, E. J. Barlow, L. Bassani, A. B. Hill, G. Bélanger, F. Capitanio, D. J. Clark, A. J. Dean, M. Fiocchi, D. Götz, F. Lebrun, M. Molina, N. Produit, M. Renaud, V. Sguera, J. B. Stephen, R. Terrier, P. Ubertini, R. Walter, C. Winkler, and J. Zurita. The Third IBIS/ISGRI Soft Gamma-Ray Survey Catalog. *ApJS*, 170(1):175–186, May 2007. doi: 10.1086/513148. (Cited on page: 281)

[50] A. J. Bird, A. Bazzano, L. Bassani, F. Capitanio, M. Fiocchi, A. B. Hill, A. Malizia, V. A. McBride, S. Scaringi, V. Sguera, J. B. Stephen, P. Ubertini, A. J. Dean, F. Lebrun, R. Terrier, M. Renaud, F. Mattana, D. Götz, J. Rodriguez, G. Belanger, R. Walter, and C. Winkler. The Fourth IBIS/ISGRI Soft Gamma-Ray Survey Catalog. *ApJS*, 186(1):1–9, January 2010. doi: 10.1088/0067-0049/186/1/1. (Cited on page: 281)

[51] A. J. Bird, A. Bazzano, A. Malizia, M. Fiocchi, V. Sguera, L. Bassani, A. B. Hill, P. Ubertini, and C. Winkler. The IBIS Soft Gamma-Ray Sky After 1000 Integral Orbits. *ApJS*, 223(1):15, March 2016. doi: 10.3847/0067-0049/223/1/15. (Cited on page: 281)

[52] J. K. Blackburn. FTOOLS: A FITS Data Processing and Analysis Software Package. In R. A. Shaw, H. E. Payne, and J. J. E. Hayes, editors, *Astronomical Data Analysis Software and Systems IV*, volume 77 of *Astronomical Society of the Pacific Conference Series*, page 367, January 1995. (Cited on pages: 144 and 284)

[53] O. Blaes, R. Blandford, P. Goldreich, and P. Madau. Neutron Starquake Models for Gamma-Ray Bursts. *ApJ*, 343:839, August 1989. doi: 10.1086/167754. (Cited on page: 42)

[54] R. Blandford and S. A. Teukolsky. Arrival-time Analysis for a Pulsar in a Binary System. *ApJ*, 205:580–591, April 1976. doi: 10.1086/154315. (Cited on page: 309)

[55] J. M. Blondin, T. R. Kallman, B. A. Fryxell, and R. E. Taam. Hydrodynamic Simulations of Stellar Wind Disruption by a Compact X-Ray Source. *ApJ*, 356:591, June 1990. doi: 10.1086/168865. (Cited on page: 322)

[56] J. M. Blondin, I. R. Stevens, and T. R. Kallman. Enhanced Winds and Tidal Streams in Massive X-Ray Binaries. *ApJ*, 371:684, April 1991. doi: 10.1086/169934. (Cited on page: 322)

[57] C. Bochenek, S. Kulkarni, V. Ravi, D. McKenna, G. Hallinan, and K. Belov. Independent Detection of the Radio Burst Reported in ATel #13681 with STARE2. *The Astronomer's Telegram*, #13684:1, April 2020. (Cited on pages: 132, 143, 157, 158, and 159)

[58] C. D. Bochenek, D. L. McKenna, K. V. Belov, J. Kocz, S. R. Kulkarni, J. Lamb, V. Ravi, and D. Woody. STARE2: Detecting Fast Radio Bursts in the Milky Way. *PASP*, 132(1009):034202, March 2020. doi: 10.1088/1538-3873/ab63b3. (Cited on page: 157)

[59] C. D. Bochenek, V. Ravi, K. V. Belov, G. Hallinan, J. Kocz, S. R. Kulkarni, and D. L. McKenna. A Fast Radio Burst Associated with a Galactic Magnetar. *Nature*, 587(7832):59–62, November 2020. doi: 10.1038/s41586-020-2872-x. (Cited on pages: viii, 7, 33, 50, 177, 178, and 205)

[60] S. E. Boggs, A. Zoglauer, E. Bellm, K. Hurley, R. P. Lin, D. M. Smith, C. Wigger, and W. Hajdas. The Giant Flare of 2004 December 27 from SGR 1806–20. *ApJ*, 661(1):458–467, May 2007. doi: 10.1086/516732. (Cited on page: 37)

[61] G. Bower, S. Chatterjee, J. Cordes, P. Demorest, J. S. Deneva, J. Dexter, R. Eatough, M. Kramer, J. Lazio, K. Liu, S. Ransom, L. Shao, N. Wex, and R. Wharton. Fundamental Physics with Galactic Center Pulsars. *BAAS*, 51 (3):438, May 2019. (Cited on page: 256)

[62] G. C. Bower, A. Deller, P. Demorest, A. Brunthaler, R. Eatough, H. Falcke, M. Kramer, K. J. Lee, and L. Spitler. The Angular Broadening of the Galactic Center Pulsar SGR J1745–29: A New Constraint on the Scattering Medium. *ApJL*, 780(1):L2, January 2014. doi: 10.1088/2041-8205/780/1/L2. (Cited on pages: 88, 90, 100, 109, and 117)

[63] G. C. Bower, A. Deller, P. Demorest, A. Brunthaler, H. Falcke, M. Moscibrodzka, R. M. O'Leary, R. P. Eatough, M. Kramer, K. J. Lee, L. Spitler, G. Desvignes, A. P. Rushton, S. Doeleman, and M. J. Reid. The Proper Motion of the Galactic Center Pulsar Relative to Sagittarius A*. *ApJ*, 798(2): 120, January 2015. doi: 10.1088/0004-637X/798/2/120. (Cited on pages: 89, 256, and 262)

[64] E. Bozzo, L. Oskinova, A. Lobel, and W. R. Hamann. The Super-orbital Modulation of Supergiant High-mass X-Ray Binaries. *A&A*, 606:L10, October 2017. doi: 10.1051/0004-6361/201731930. (Cited on page: 325)

[65] M. L. Brady. A fast discrete approximation algorithm for the radon transform. *SIAM Journal on Computation*, 27(1):107–119, 1998. (Cited on page: 218)

[66] J. Bramante and T. Linden. Detecting Dark Matter with Imploding Pulsars in the Galactic Center. *Phys. Rev. Lett.*, 113(19):191301, Nov 2014. doi: 10.1103/PhysRevLett.113.191301. (Cited on page: 260)

[67] T. D. Brandt and B. Kocsis. Disrupted Globular Clusters Can Explain the Galactic Center Gamma-Ray Excess. *ApJ*, 812(1):15, Oct 2015. doi: 10.1088/0004-637X/812/1/15. (Cited on pages: 257 and 259)

[68] M. Burgay, N. D'Amico, A. Possenti, R. N. Manchester, A. G. Lyne, B. C. Joshi, M. A. McLaughlin, M. Kramer, J. M. Sarkissian, F. Camilo, V. Kalogera, C. Kim, and D. R. Lorimer. An Increased Estimate of the Merger Rate of Double Neutron Stars from Observations of a Highly Relativistic System. *Nature*, 426(6966):531–533, December 2003. doi: 10.1038/nature02124. (Cited on page: 241)

[69] M. Burgay, A. Possenti, M. Kerr, P. Esposito, N. Rea, F. C. Zelati, G. L. Israel, and S. Johnston. Pulsed Radio Emission from PSR J1119–6127 Disappeared. *The Astronomer's Telegram*, #9286, July 2016. (Cited on page: 77)

[70] M. Burgay, A. Possenti, M. Kerr, P. Esposito, N. Rea, F. C. Zelati, G. L. Israel, and S. Johnston. Pulsed Radio Emission from PSR J1119–6127 Re-activated. *The Astronomer's Telegram*, #9366, August 2016. (Cited on pages: 77, 78, and 79)

[71] S. Burke-Spolaor and K. W. Bannister. The Galactic Position Dependence of Fast Radio Bursts and the Discovery of FRB011025. *ApJ*, 792(1):19, September 2014. doi: 10.1088/0004-637X/792/1/19. (Cited on page: 40)

[72] S. Burke-Spolaor, M. Bailes, R. Ekers, J.-P. Macquart, and I. Crawford, Fronefield. Radio Bursts with Extragalactic Spectral Characteristics Show Terrestrial Origins. *ApJ*, 727(1):18, January 2011. doi: 10.1088/0004-637X/727/1/18. (Cited on page: 41)

[73] W. R. Burns and B. G. Clark. Pulsar Search Techniques. *A&A*, 2:280–287, July 1969. (Cited on page: 221)

[74] M. Caleb, L. G. Spitler, and B. W. Stappers. One or Several Populations of Fast Radio Burst Sources? *Nature Astronomy*, 2:839–841, October 2018. doi: 10.1038/s41550-018-0612-z. (Cited on pages: xxvi and 47)

[75] A. D. Cameron. *Innovative Pulsar Searching Techniques or Fantastic Pulsars and How to Find Them*. PhD thesis, University of Bonn, May 2018. (Cited on pages: xlv, lvi, 222, 223, and 278)

[76] A. D. Cameron, E. D. Barr, D. J. Champion, M. Kramer, and W. W. Zhu. An Investigation of Pulsar Searching Techniques with the Fast Folding Algorithm. *MNRAS*, 468(2):1994–2010, June 2017. doi: 10.1093/mnras/stx589. (Cited on pages: 221 and 224)

[77] F. Camilo, V. M. Kaspi, A. G. Lyne, R. N. Manchester, J. F. Bell, N. D'Amico, N. P. F. McKay, and F. Crawford. Discovery of Two High Magnetic Field Radio Pulsars. *ApJ*, 541:367–373, September 2000. doi: 10.1086/309435. (Cited on pages: 76, 79, and 84)

[78] F. Camilo, S. M. Ransom, J. P. Halpern, J. Reynolds, D. J. Helfand, N. Zimmerman, and J. Sarkissian. Transient Pulsed Radio Emission from a Magnetar. *Nature*, 442(7105):892–895, August 2006. doi: 10.1038/nature04986. (Cited on pages: 7, 33, 84, 88, 96, 120, 132, 133, 135, and 152)

[79] F. Camilo, I. Cognard, S. M. Ransom, J. P. Halpern, J. Reynolds, N. Zimmerman, E. V. Gotthelf, D. J. Helfand , P. Demorest, G. Theureau, and D. C. Backer. The Magnetar XTE J1810–197: Variations in Torque, Radio Flux Density, and Pulse Profile Morphology. *ApJ*, 663(1):497–504, July 2007. doi: 10.1086/518226. (Cited on pages: 84, 140, and 146)

[80] F. Camilo, S. M. Ransom, J. P. Halpern, and J. Reynolds. 1E 1547.0–5408: A Radio-emitting Magnetar with a Rotation Period of 2 Seconds. *ApJL*, 666 (2):L93–L96, September 2007. doi: 10.1086/521826. (Cited on pages: 7, 33, 84, 88, 120, and 132)

[81] F. Camilo, S. M. Ransom, J. Peñalver, A. Karastergiou, M. H. van Kerkwijk, M. Durant, J. P. Halpern, J. Reynolds, C. Thum, D. J. Helfand , N. Zimmerman, and I. Cognard. The Variable Radio-to-X-Ray Spectrum of the Magnetar XTE J1810–197. *ApJ*, 669(1):561–569, November 2007. doi: 10.1086/521548. (Cited on pages: 121, 133, and 205)

[82] F. Camilo, J. Reynolds, S. Johnston, J. P. Halpern, S. M. Ransom, and W. van Straten. Polarized Radio Emission from the Magnetar XTE J1810–197. *ApJL*, 659(1):L37–L40, April 2007. doi: 10.1086/516630. (Cited on page: 121)

[83] F. Camilo, J. Reynolds, S. Johnston, J. P. Halpern, and S. M. Ransom. The Magnetar 1E 1547.0–5408: Radio Spectrum, Polarimetry, and Timing. *ApJ*, 679(1):681–686, May 2008. doi: 10.1086/587054. (Cited on pages: 84, 96, and 120)

[84] F. Camilo, S. M. Ransom, J. P. Halpern, J. A. J. Alford, I. Cognard, J. E. Reynolds, S. Johnston, J. Sarkissian, and W. van Straten. Radio Disappearance of the Magnetar XTE J1810–197 and Continued X-Ray Timing. *ApJ*,

820(2):110, April 2016. doi: 10.3847/0004-637X/820/2/110. (Cited on pages: 120, 121, 132, and 133)

[85] F. Camilo, P. Scholz, M. Serylak, S. Buchner, M. Merryfield, V. M. Kaspi, R. F. Archibald, M. Bailes, A. Jameson, W. van Straten, J. Sarkissian, J. E. Reynolds, S. Johnston, G. Hobbs, T. D. Abbott, R. M. Adam, G. B. Adams, T. Alberts, R. Andreas, K. M. B. Asad, D. E. Baker, T. Baloyi, E. F. Bauermeister, T. Baxana, T. G. H. Bennett, G. Bernardi, D. Booisen, R. S. Booth, D. H. Botha, L. Boyana, L. R. S. Brederode, J. P. Burger, T. Cheetham, J. Conradie, J. P. Conradie, D. B. Davidson, G. De Bruin, B. de Swardt, C. de Villiers, D. I. L. de Villiers, M. S. de Villiers, W. de Villiers, C. De Waal, M. A. Dikgale, G. du Toit, L. J. du Toit, S. W. P. Esterhuyse, B. Fanaroff, S. Fataar, A. R. Foley, G. Foster, D. Fourie, R. Gamatham, T. Gatsi, R. Geschke, S. Goedhart, T. L. Grobler, S. C. Gumede, M. J. Hlakola, A. Hokwana, D. H. Hoorn, D. Horn, J. Horrell, B. Hugo, A. Isaacson, O. Jacobs, J. P. Jansen van Rensburg, J. L. Jonas, B. Jordaan, A. Joubert, F. Joubert, G. I. G. Józsa, R. Julie, C. C. Julius, F. Kapp, A. Karastergiou, F. Karels, M. Kariseb, R. Karuppusamy, V. Kasper, E. C. Knox-Davies, D. Koch, P. P. A. Kotzé, A. Krebs, N. Kriek, H. Kriel, T. Kusel, S. Lamoor, R. Lehmensiek, D. Liebenberg, I. Liebenberg, R. T. Lord, B. Lunsky, N. Mabombo, T. Macdonald, P. Macfarlane, K. Madisa, L. Mafhungo, L. G. Magnus, C. Magozore, O. Mahgoub, J. P. L. Main, S. Makhathini, J. A. Malan, P. Malgas, J. R. Manley, M. Manzini, L. Marais, N. Marais, S. J. Marais, M. Maree, A. Martens, S. D. Matshawule, N. Matthysen, T. Mauch, L. D. McNally, B. Merry, R. P. Millenaar, C. Mjikelo, N. Mkhabela, N. Mnyand u, I. T. Moeng, O. J. Mokone, T. E. Monama, K. Montshiwa, V. Moss, M. Mphego, W. New, B. Ngcebetsha, K. Ngoasheng, H. Niehaus, P. Ntuli, A. Nzama, F. Obies, M. Obrocka, M. T. Ockards, C. Olyn, N. Oozeer, A. J. Otto, Y. Padayachee, S. Passmoor, A. A. Patel, S. Paula, A. Peens-Hough, B. Pholoholo, P. Prozesky, S. Rakoma, A. J. T. Ramaila, I. Rammala, Z. R. Ramudzuli, M. Rasivhaga, S. Ratcliffe, H. C. Reader, R. Renil, L. Richter, A. Robyntjies, D. Rosekrans, A. Rust, S. Salie, N. Sambu, C. T. G. Schollar, L. Schwardt, S. Seranyane, G. Sethosa, C. Sharpe, R. Siebrits, S. K. Sirothia, M. J. Slabber, O. Smirnov, S. Smith, L. Sofeya, N. Songqumase, R. Spann, B. Stappers, D. Steyn, T. J. Steyn, R. Strong, A. Struthers, C. Stuart, P. Sunnylall, P. S. Swart, B. Taljaard, C. Tasse, G. Taylor, I. P. Theron, V. Thondikulam, K. Thorat, A. Tiplady, O. Toruvanda, J. van Aardt, T. van Balla, L. van den Heever, A. van der Byl, C. van der Merwe, P. van der Merwe, P. C. van Niekerk, R. van Rooyen, J. P. van Staden, V. van Tonder, R. van Wyk, I. Wait, A. L. Walker, B. Wallace, M. Welz, L. P. Williams, B. Xaia, N. Young, and S. Zitha. Revival of the Magnetar PSR J1622–4950: Observations with MeerKAT, Parkes, XMM-Newton, Swift, Chandra, and NuSTAR. *ApJ*, 856(2):180, April 2018. doi: 10.3847/1538-4357/aab35a. (Cited on pages: 146 and 205)

[86] B. W. Carroll and D. A. Ostlie. *An Introduction to Modern Astrophysics*. Pearson, Addison-Wesley, 2 edition, July 2006. ISBN 0805304029. (Cited on pages: lxi, 314, 318, and 320)

[87] J. L. Caswell, N. M. McClure-Griffiths, and M. C. M. Cheung. Supernova Remnant G292.2–0.5, Its Pulsar, and the Galactic Magnetic Field. *MNRAS*, 352:1405–1412, August 2004. doi: 10.1111/j.1365-2966.2004.08030.x. (Cited on page: 76)

[88] A. Cesarini, F. Fucito, A. Lionetto, A. Morselli, and P. Ullio. The Galactic Center as a Dark Matter Gamma-Ray Source. *Astroparticle Physics*, 21(3): 267–285, Jun 2004. doi: 10.1016/j.astropartphys.2004.02.001. (Cited on page: 261)

[89] J. Chadwick. Possible Existence of a Neutron. *Nature*, 129(3252):312, February 1932. doi: 10.1038/129312a0. (Cited on page: 2)

[90] J. Chadwick. The Existence of a Neutron. *Proceedings of the Royal Society of London Series A*, 136(830):692–708, June 1932. doi: 10.1098/rspa.1932.0112. (Cited on page: 2)

[91] D. Chakrabarty. *Hard X-Ray Detection and Timing of Accretion-powered Pulsars with BATSE*. PhD thesis, Division of Physics, Mathematics, and Astronomy, California Insititute of Technology, Pasadena, CA, January 1996. (Cited on page: 302)

[92] D. J. Champion, E. Petroff, M. Kramer, M. J. Keith, M. Bailes, E. D. Barr, S. D. Bates, N. D. R. Bhat, M. Burgay, S. Burke-Spolaor, C. M. L. Flynn, A. Jameson, S. Johnston, C. Ng, L. Levin, A. Possenti, B. W. Stappers, W. van Straten, D. Thornton, C. Tiburzi, and A. G. Lyne. Five New Fast Radio Bursts from the HTRU High-latitude Survey at Parkes: First Evidence for Two-component Bursts. *MNRAS*, 460(1):L30–L34, July 2016. doi: 10.1093/mnrasl/slw069. (Cited on page: 41)

[93] S. Chandrasekhar. The Maximum Mass of Ideal White Dwarfs. *ApJ*, 74:81, July 1931. doi: 10.1086/143324. (Cited on page: 3)

[94] D. Charbonneau, T. M. Brown, D. W. Latham, and M. Mayor. Detection of Planetary Transits Across a Sun-like Star. *ApJL*, 529(1):L45–L48, January 2000. doi: 10.1086/312457. (Cited on page: 8)

[95] S. Chatterjee, C. J. Law, R. S. Wharton, S. Burke-Spolaor, J. W. T. Hessels, G. C. Bower, J. M. Cordes, S. P. Tendulkar, C. G. Bassa, P. Demorest, B. J. Butler, A. Seymour, P. Scholz, M. W. Abruzzo, S. Bogdanov, V. M. Kaspi, A. Keimpema, T. J. W. Lazio, B. Marcote, M. A. McLaughlin, Z. Paragi, S. M. Ransom, M. Rupen, L. G. Spitler, and H. J. van Langevelde. A Direct Localization of a Fast Radio Burst and Its Host. *Nature*, 541(7635):58–61, Jan 2017. doi: 10.1038/nature20797. (Cited on pages: 41, 157, 163, 164, 177, and 179)

[96] P. Chawla, B. C. Andersen, M. Bhardwaj, E. Fonseca, A. Josephy, V. M. Kaspi, D. Michilli, Z. Pleunis, K. M. Bandura, C. G. Bassa, P. J. Boyle, C. Brar, T. Cassanelli, D. Cubranic, M. Dobbs, F. Q. Dong, B. M. Gaensler, D. C. Good, J. W. T. Hessels, T. L. Land ecker, C. Leung, D. Z. Li, H. . H. Lin, K. Masui, R. Mckinven, J. Mena-Parra, M. Merryfield, B. W. Meyers, A. Naidu, C. Ng, C. Patel, M. Rafiei-Ravandi, M. Rahman, P. Sanghavi, P. Scholz, K. Shin, K. M. Smith, I. H. Stairs, S. P. Tendulkar, and K. Vanderlinde. Detection of Repeating FRB 180916.J0158+65 Down to Frequencies of 300 MHz. *ApJL*, 896(2):L41, June 2020. doi: 10.3847/2041-8213/ab96bf. (Cited on pages: xliii, 158, 178, 179, 190, 192, 193, 195, 197, 199, 203, and 207)

[97] J. Chennamangalam and D. R. Lorimer. The Galactic Centre Pulsar Population. *MNRAS*, 440:L86–L90, May 2014. doi: 10.1093/mnrasl/slu025. (Cited on pages: 259 and 260)

[98] H. Cho, J.-P. Macquart, R. M. Shannon, A. T. Deller, I. S. Morrison, R. D. Ekers, K. W. Bannister, W. Farah, H. Qiu, M. W. Sammons, M. Bailes, S. Bhandari, C. K. Day, C. W. James, C. J. Phillips, J. X. Prochaska, and J. Tuthill. Spectropolarimetric Analysis of FRB 181112 at Microsecond Resolution: Implications for Fast Radio Burst Emission Mechanism. *ApJL*, 891 (2):L38, March 2020. doi: 10.3847/2041-8213/ab7824. (Cited on pages: 177 and 206)

[99] I. Cholis, D. Hooper, and T. Linden. Challenges in Explaining the Galactic Center Gamma-Ray Excess with Millisecond Pulsars. *JCAP*, 2015(6):043, Jun 2015. doi: 10.1088/1475-7516/2015/06/043. (Cited on page: 261)

[100] P. Christian and A. Loeb. Pulsar Timing Constraints on Cumulative and Individual Mass of Stars in the Galactic Center. *ApJ*, 798(2):78, Jan 2015. doi: 10.1088/0004-637X/798/2/78. (Cited on pages: 256 and 262)

[101] C. J. Clark, H. J. Pletsch, J. Wu, L. Guillemot, M. Kerr, T. J. Johnson, F. Camilo, D. Salvetti, B. Allen, D. Anderson, C. Aulbert, C. Beer, O. Bock, A. Cuéllar, H.-B. Eggenstein, H. Fehrmann, M. Kramer, S. A. Kwang, B. Machenschalk, L. Nieder, M. Ackermann, M. Ajello, L. Baldini, J. Ballet, G. Barbiellini, D. Bastieri, R. Bellazzini, E. Bissaldi, R. D. Blandford, E. D. Bloom, R. Bonino, E. Bottacini, T. J. Brandt, J. Bregeon, P. Bruel, R. Buehler, T. H. Burnett, S. Buson, R. A. Cameron, R. Caputo, P. A. Caraveo, E. Cavazzuti, C. Cecchi, E. Charles, A. Chekhtman, S. Ciprini, L. R. Cominsky, D. Costantin, S. Cutini, F. D'Ammando, A. De Luca, R. Desiante, L. Di Venere, M. Di Mauro, N. Di Lalla, S. W. Digel, C. Favuzzi, E. C. Ferrara, A. Franckowiak, Y. Fukazawa, S. Funk, P. Fusco, F. Gargano, D. Gasparrini, N. Giglietto, F. Giordano, M. Giroletti, G. A. Gomez-Vargas, D. Green, I. A. Grenier, S. Guiriec, A. K. Harding, J. W. Hewitt, D. Horan, G. Jóhannesson, S. Kensei, M. Kuss, G. La Mura, S. Larsson, L. Latronico, J. Li, F. Longo, F. Loparco, M. N. Lovellette, P. Lubrano, J. D. Magill,

S. Maldera, A. Manfreda, M. N. Mazziotta, J. E. McEnery, P. F. Michelson, N. Mirabal, W. Mitthumsiri, T. Mizuno, M. E. Monzani, A. Morselli, I. V. Moskalenko, E. Nuss, T. Ohsugi, N. Omodei, M. Orienti, E. Orlando, M. Palatiello, V. S. Paliya, F. de Palma, D. Paneque, J. S. Perkins, M. Persic, M. Pesce-Rollins, T. A. Porter, G. Principe, S. Rainò, R. Rando, P. S. Ray, M. Razzano, A. Reimer, O. Reimer, R. W. Romani, P. M. Saz Parkinson, C. Sgrò, E. J. Siskind, D. A. Smith, F. Spada, G. Spandre, P. Spinelli, J. B. Thayer, D. J. Thompson, D. F. Torres, E. Troja, G. Vianello, K. Wood, and M. Wood. Einstein@Home Discovers a Radio-quiet Gamma-Ray Millisecond Pulsar. *Science Advances*, 4(2):eaao7228, February 2018. doi: 10.1126/sciadv.aao7228. (Cited on page: 231)

[102] G. W. Clark. X-Ray Binaries in Globular Clusters. *ApJL*, 199:L143–L145, August 1975. doi: 10.1086/181869. (Cited on page: 8)

[103] N. Clarke, L. D'Addario, R. Navarro, and J. Trinh. A Multi-beam Radio Transient Detector with Real-time De-dispersion Over a Wide DM Range. *Journal of Astronomical Instrumentation*, 3(1):1450004, March 2014. doi: 10.1142/S2251171714500044. (Cited on page: 218)

[104] W. I. Clarkson, P. A. Charles, M. J. Coe, and S. Laycock. Long-term Properties of Accretion Discs in X-Ray Binaries - II. Stability of Radiation-Driven Warping. *MNRAS*, 343(4):1213–1223, August 2003. doi: 10.1046/j.1365-8711.2003.06761.x. (Cited on page: 324)

[105] W. I. Clarkson, P. A. Charles, M. J. Coe, S. Laycock, M. D. Tout, and C. A. Wilson. Long-term Properties of Accretion Discs in X-Ray Binaries - I. The Variable Third Period in SMC X–1. *MNRAS*, 339(2):447–454, February 2003. doi: 10.1046/j.1365-8711.2003.06176.x. (Cited on page: 324)

[106] A. W. Clegg, A. L. Fey, and T. J. W. Lazio. The Gaussian Plasma Lens in Astrophysics: Refraction. *ApJ*, 496(1):253–266, March 1998. doi: 10.1086/305344. (Cited on pages: 123, 124, and 125)

[107] W. G. Cochran. Problems Arising in the Analysis of a Series of Similar Experiments. *Supplement to the Journal of the Royal Statistical Society*, 4:102–118, 1937. doi: 10.2307/2984123. (Cited on page: 289)

[108] W. G. Cochran. The Combination of Estimates from Different Experiments. *Biometrics*, 10:101–129, 1954. doi: 10.2307/3001666. (Cited on page: 289)

[109] J. B. Coley, R. H. D. Corbet, and H. A. Krimm. Probing the Masses and Radii of Donor Stars in Eclipsing X-Ray Binaries with the Swift Burst Alert Telescope. *ApJ*, 808(2):140, August 2015. doi: 10.1088/0004-637X/808/2/140. (Cited on page: 294)

[110] J. B. Coley, R. H. D. Corbet, F. Fürst, G. Huxtable, H. A. Krimm, A. B. Pearlman, and K. Pottschmidt. A Study of the 20 Day Superorbital Modulation

in the High-mass X-Ray Binary IGR J16493–4348. *ApJ*, 879(1):34, July 2019. doi: 10.3847/1538-4357/ab223c. (Cited on pages: xiv, 283, 284, 316, 325, and 330)

[111] J. Cooley and J. Tukey. An algorithm for the machine calculation of complex fourier series. *Mathematics of Computation*, 19(90):297–301, 1965. (Cited on page: 219)

[112] R. Corbet, C. Markwardt, L. Barbier, S. Barthelmy, J. Cummings, N. Gehrels, H. Krimm, D. Palmer, T. Sakamoto, G. Sato, J. Tueller, and Swift/BAT Survey Team. Periodicities in X-Ray Binaries from Swift/BAT Observations. *Progress of Theoretical Physics Supplement*, 169:200–203, January 2007. doi: 10.1143/PTPS.169.200. (Cited on page: 289)

[113] R. H. D. Corbet. Be/Neutron Star Binaries: A Relationship Between Orbital Period and Neutron Star Spin Period. *A&A*, 141:91–93, December 1984. (Cited on page: 315)

[114] R. H. D. Corbet. The Three Types of High-mass X-Ray Pulsator. *MNRAS*, 220:1047–1056, June 1986. doi: 10.1093/mnras/220.4.1047. (Cited on page: 315)

[115] R. H. D. Corbet and H. A. Krimm. Superorbital Periodic Modulation in Wind-accretion High-mass X-Ray Binaries from Swift Burst Alert Telescope Observations. *ApJ*, 778(1):45, November 2013. doi: 10.1088/0004-637X/778/1/45. (Cited on pages: 283, 288, 290, and 324)

[116] R. H. D. Corbet, C. B. Markwardt, and J. Tueller. Swift BAT and RXTE Observations of the Peculiar X-Ray Binary 4U 2206+54: Disappearance of the 9.6 Day Modulation. *ApJ*, 655(1):458–465, January 2007. doi: 10.1086/509319. (Cited on page: 289)

[117] R. H. D. Corbet, S. D. Barthelmy, W. H. Baumgartner, H. A. Krimm, C. B. Markwardt, G. K. Skinner, and J. Tueller. A 6.8 Day Period in IGR J16493–4348 from Swift/BAT and RXTE/PCA Observations. *The Astronomer's Telegram*, 2599:1, May 2010. (Cited on pages: 283 and 293)

[118] R. H. D. Corbet, A. B. Pearlman, and K. Pottschmidt. Discovery of the Pulse Period of IGR J16493–4348 from RXTE PCA Observations. *The Astronomer's Telegram*, 2766:1, July 2010. (Cited on page: 283)

[119] R. H. D. Corbet, J. B. Coley, H. A. Krimm, and K. Pottschmidt. Apparent Superorbital Modulation in 4U 1538–52 at Four Times the Orbital Period. *The Astronomer's Telegram*, 11918:1, August 2018. (Cited on page: 324)

[120] J. M. Cordes and S. Chatterjee. Fast Radio Bursts: An Extragalactic Enigma. *ARA&A*, 57:417–465, August 2019. doi: 10.1146/annurev-astro-091918-104501. (Cited on pages: 40, 157, 163, and 177)

[121] J. M. Cordes and T. J. Lazio. Interstellar Scattering Effects on the Detection of Narrow-band Signals. *ApJ*, 376:123, July 1991. doi: 10.1086/170261. (Cited on pages: 31 and 122)

[122] J. M. Cordes and T. J. W. Lazio. Finding Radio Pulsars in and Beyond the Galactic Center. *ApJ*, 475(2):557–564, February 1997. doi: 10.1086/303569. (Cited on pages: liii, 116, 117, 256, 257, and 265)

[123] J. M. Cordes and T. J. W. Lazio. Anomalous Radio-wave Scattering from Interstellar Plasma Structures. *ApJ*, 549(2):997–1010, March 2001. doi: 10.1086/319442. (Cited on pages: 29 and 118)

[124] J. M. Cordes and T. J. W. Lazio. NE2001. I. A New Model for the Galactic Distribution of Free Electrons and Its Fluctuations. *arXiv e-prints*, art. astro-ph/0207156, July 2002. (Cited on pages: xxvii, liii, 23, 42, 48, 90, 192, 193, and 265)

[125] J. M. Cordes and B. J. Rickett. Diffractive Interstellar Scintillation Timescales and Velocities. *ApJ*, 507(2):846–860, November 1998. doi: 10.1086/306358. (Cited on pages: 29, 104, 153, 157, 174, and 192)

[126] J. M. Cordes and I. Wasserman. Supergiant Pulses from Extragalactic Neutron Stars. *MNRAS*, 457(1):232–257, March 2016. doi: 10.1093/mnras/stv2948. (Cited on page: 50)

[127] J. M. Cordes, J. M. Weisberg, and V. Boriakoff. Small-Scale Electron Density Turbulence in the Interstellar Medium. *ApJ*, 288:221–247, January 1985. doi: 10.1086/162784. (Cited on page: 168)

[128] J. M. Cordes, A. Pidwerbetsky, and R. V. E. Lovelace. Refractive and Diffractive Scattering in the Interstellar Medium. *ApJ*, 310:737, November 1986. doi: 10.1086/164728. (Cited on page: 30)

[129] J. M. Cordes, N. D. R. Bhat, T. H. Hankins, M. A. McLaughlin, and J. Kern. The Brightest Pulses in the Universe: Multifrequency Observations of the Crab Pulsar's Giant Pulses. *ApJ*, 612(1):375–388, September 2004. doi: 10.1086/422495. (Cited on page: 120)

[130] J. M. Cordes, R. S. Wharton, L. G. Spitler, S. Chatterjee, and I. Wasserman. Radio Wave Propagation and the Provenance of Fast Radio Bursts. *arXiv e-prints*, art. arXiv:1605.05890, May 2016. (Cited on pages: xxiv and 29)

[131] J. M. Cordes, I. Wasserman, J. W. T. Hessels, T. J. W. Lazio, S. Chatterjee, and R. S. Wharton. Lensing of Fast Radio Bursts by Plasma Structures in Host Galaxies. *ApJ*, 842(1):35, June 2017. doi: 10.3847/1538-4357/aa74da. (Cited on pages: xxxv, 120, 122, 124, 125, 126, 127, 158, 173, and 180)

[132] M. E. Costa, P. M. McCulloch, and P. A. Hamilton. Polarization Observations of 17 Southern Pulsars at 600 MHz. *MNRAS*, 252:13, September 1991. doi: 10.1093/mnras/252.1.13. (Cited on page: 7)

[133] A. N. Cox, editor. *Allen's Astrophysical Quantities*. Springer, AIP Press, 4 edition, 2000. ISBN 0387987460. (Cited on pages: lxi, 314, and 318)

[134] S. R. Cranmer and S. P. Owocki. Hydrodynamical Simulations of Corotating Interaction Regions and Discrete Absorption Components in Rotating O-star Winds. *ApJ*, 462:469, May 1996. doi: 10.1086/177166. (Cited on page: 325)

[135] F. Crawford, B. M. Gaensler, V. M. Kaspi, R. N. Manchester, F. Camilo, A. G. Lyne, and M. J. Pivovaroff. A Radio Supernova Remnant Associated with the Young Pulsar J1119–6127. *ApJ*, 554:152–160, June 2001. doi: 10.1086/321328. (Cited on page: 76)

[136] H. T. Cromartie, E. Fonseca, S. M. Ransom, P. B. Demorest, Z. Arzoumanian, H. Blumer, P. R. Brook, M. E. DeCesar, T. Dolch, J. A. Ellis, R. D. Ferdman, E. C. Ferrara, N. Garver-Daniels, P. A. Gentile, M. L. Jones, M. T. Lam, D. R. Lorimer, R. S. Lynch, M. A. McLaughlin, C. Ng, D. J. Nice, T. T. Pennucci, R. Spiewak, I. H. Stairs, K. Stovall, J. K. Swiggum, and W. W. Zhu. Relativistic Shapiro Delay Measurements of an Extremely Massive Millisecond Pulsar. *Nature Astronomy*, 4:72–76, January 2020. doi: 10.1038/s41550-019-0880-2. (Cited on page: 10)

[137] W. M. Cronyn. Interstellar Scattering of Pulsar Radiation and Its Effect on the Spectrum of NP0532. *Science*, 168(3938):1453–1455, June 1970. doi: 10.1126/science.168.3938.1453. (Cited on page: 122)

[138] J. H. Crossley, J. A. Eilek, T. H. Hankins, and J. S. Kern. Short-lived Radio Bursts from the Crab Pulsar. *ApJ*, 722(2):1908–1920, October 2010. doi: 10.1088/0004-637X/722/2/1908. (Cited on page: 118)

[139] M. Cruces, L. G. Spitler, P. Scholz, R. Lynch, A. Seymour, J. W. T. Hessels, C. Gouiffés, G. H. Hilmarsson, M. Kramer, and S. Munjal. Repeating Behaviour of FRB 121102: Periodicity, Waiting Times, and Energy Distribution. *MNRAS*, 500(1):448–463, January 2021. doi: 10.1093/mnras/staa3223. (Cited on pages: xi, 179, 196, and 205)

[140] G. Cusumano, V. La Parola, P. Romano, A. Segreto, S. Vercellone, and G. Chincarini. The Swift-BAT Hard X-Ray Sky Monitoring Unveils the Orbital Period of the HMXB IGR J16493–4348. *MNRAS*, 406(1):L16–L19, July 2010. doi: 10.1111/j.1745-3933.2010.00872.x. (Cited on pages: lviii, 283, 293, 296, 298, 299, and 323)

[141] R. M. Cutri, M. F. Skrutskie, S. van Dyk, C. A. Beichman, J. M. Carpenter, T. Chester, L. Cambresy, T. Evans, J. Fowler, J. Gizis, E. Howard, J. Huchra,

T. Jarrett, E. L. Kopan, J. D. Kirkpatrick, R. M. Light, K. A. Marsh, H. McCallon, S. Schneider, R. Stiening, M. Sykes, M. Weinberg, W. A. Wheaton, S. Wheelock, and N. Zacarias. *2MASS All Sky Catalog of Point Sources*. June 2003. (Cited on pages: 315 and 320)

[142] A. D'Aì, G. Cusumano, V. La Parola, A. Segreto, T. di Salvo, R. Iaria, and N. R. Robba. Evidence for a Resonant Cyclotron Line in IGR J16493–4348 from the Swift-BAT Hard X-Ray Survey. *A&A*, 532:A73, August 2011. doi: 10.1051/0004-6361/201117035. (Cited on pages: 283 and 316)

[143] S. Dai, S. Johnston, P. Weltevrede, M. Kerr, M. Burgay, P. Esposito, G. Israel, A. Possenti, N. Rea, and J. Sarkissian. Peculiar Spin Frequency and Radio Profile Evolution of PSR J1119–6127 Following Magnetar-like X-Ray Bursts. *MNRAS*, 480(3):3584–3594, November 2018. doi: 10.1093/mnras/sty2063. (Cited on page: 121)

[144] S. Dai, M. E. Lower, M. Bailes, F. Camilo, J. P. Halpern, S. Johnston, M. Kerr, J. Reynolds, J. Sarkissian, and P. Scholz. Wideband Polarized Radio Emission from the Newly Revived Magnetar XTE J1810–197. *ApJL*, 874(2):L14, April 2019. doi: 10.3847/2041-8213/ab0e7a. (Cited on page: 133)

[145] T. Damour and G. Esposito-Farèse. Gravitational-wave Versus Binary-pulsar Tests of Strong-field Gravity. *Phys. Rev. D*, 58(4):042001, August 1998. doi: 10.1103/PhysRevD.58.042001. (Cited on page: 263)

[146] T. Damour and J. H. Taylor. Strong-field Tests of Relativistic Gravity and Binary Pulsars. *Phys. Rev. D*, 45(6):1840–1868, March 1992. doi: 10.1103/PhysRevD.45.1840. (Cited on page: 231)

[147] C. K. Day, A. T. Deller, R. M. Shannon, H. Qiu, K. W. Bannister, S. Bhandari, R. Ekers, C. Flynn, C. W. James, J.-P. Macquart, E. K. Mahony, C. J. Phillips, and J. Xavier Prochaska. High Time Resolution and Polarization Properties of ASKAP-Localized Fast Radio Bursts. *MNRAS*, 497(3):3335–3350, July 2020. doi: 10.1093/mnras/staa2138. (Cited on page: 178)

[148] T. Daylan, D. P. Finkbeiner, D. Hooper, T. Linden, S. K. N. Portillo, N. L. Rodd, and T. R. Slatyer. The Characterization of the Gamma-Ray Signal from the Central Milky Way: A Case for Annihilating Dark Matter. *Physics of the Dark Universe*, 12:1–23, Jun 2016. doi: 10.1016/j.dark.2015.12.005. (Cited on page: 261)

[149] P. B. Demorest. *Measuring the Gravitational Wave Background Using Precision Pulsar Timing*. PhD thesis, University of California, Berkeley, August 2007. (Cited on page: 304)

[150] P. B. Demorest, T. Pennucci, S. M. Ransom, M. S. E. Roberts, and J. W. T. Hessels. A Two-Solar-Mass Neutron Star Measured Using Shapiro Delay. *Nature*, 467(7319):1081–1083, October 2010. doi: 10.1038/nature09466. (Cited on page: 10)

[151] A. P. Dempster, N. M. Laird, and D. B. Rubin. Maximum likelihood from incomplete data via the EM algorithm. *Journal of the Royal Statistical Society: Series B*, 39:1–38, 1977. (Cited on page: 217)

[152] J. S. Deneva, J. M. Cordes, and T. J. W. Lazio. Discovery of Three Pulsars from a Galactic Center Pulsar Population. *ApJL*, 702(2):L177–L181, September 2009. doi: 10.1088/0004-637X/702/2/L177. (Cited on pages: liii, 88, 256, 257, 259, and 265)

[153] J. S. Deneva, K. Stovall, M. A. McLaughlin, M. Bagchi, S. D. Bates, P. C. C. Freire, J. G. Martinez, F. Jenet, and N. Garver-Daniels. New Discoveries from the Arecibo 327 MHz Drift Pulsar Survey Radio Transient Search. *ApJ*, 821 (1):10, April 2016. doi: 10.3847/0004-637X/821/1/10. (Cited on pages: 82 and 98)

[154] G. Desvignes, R. Eatough, M. Kramer, R. Karuppusamy, A. Kraus, A. Lyne, L. Levin, B. Stappers, and M. Mickaliger. High-frequency Observations of the Radio Magnetar XTE J1810–197. *The Astronomer's Telegram*, #12285: 1, December 2018. (Cited on page: 34)

[155] G. Desvignes, R. P. Eatough, U. L. Pen, K. J. Lee, S. A. Mao, R. Karuppusamy, D. H. F. M. Schnitzeler, H. Falcke, M. Kramer, O. Wucknitz, L. G. Spitler, P. Torne, K. Liu, G. C. Bower, I. Cognard, A. G. Lyne, and B. W. Stappers. Large Magneto-ionic Variations Toward the Galactic Center Magnetar, PSR J1745–2900. *ApJL*, 852(1):L12, January 2018. doi: 10.3847/2041-8213/aaa2f8. (Cited on pages: 88, 89, 90, 99, 116, 117, 121, 122, and 123)

[156] J. Dexter and R. M. O'Leary. The Peculiar Pulsar Population of the Central Parsec. *ApJL*, 783(1):L7, March 2014. doi: 10.1088/2041-8205/783/1/L7. (Cited on pages: 88, 258, 259, and 260)

[157] J. Dexter, A. Deller, G. C. Bower, P. Demorest, M. Kramer, B. W. Stappers, A. G. Lyne, M. Kerr, L. G. Spitler, D. Psaltis, M. Johnson, and R. Narayan. Locating the Intense Interstellar Scattering Towards the Inner Galaxy. *MNRAS*, 471(3):3563–3576, November 2017. doi: 10.1093/mnras/stx1777. (Cited on page: 117)

[158] R. Dib and V. M. Kaspi. 16 yr of RXTE Monitoring of Five Anomalous X-Ray Pulsars. *ApJ*, 784(1):37, March 2014. doi: 10.1088/0004-637X/784/1/37. (Cited on pages: 38 and 85)

[159] R. Dib, V. M. Kaspi, and F. P. Gavriil. Glitches in Anomalous X-Ray Pulsars. *ApJ*, 673(2):1044–1061, February 2008. doi: 10.1086/524653. (Cited on page: 38)

[160] R. Dib, V. M. Kaspi, P. Scholz, and F. P. Gavriil. RXTE Observations of Anomalous X-Ray Pulsar 1E 1547.0–5408 During and After Its 2008 and

2009 Outbursts. *ApJ*, 748(1):3, March 2012. doi: 10.1088/0004-637X/748/1/3. (Cited on page: 146)

[161] J. M. Dickey and F. J. Lockman. H I in the Galaxy. *ARA&A*, 28:215–261, January 1990. doi: 10.1146/annurev.aa.28.090190.001243. (Cited on page: 316)

[162] S. Dimoudi, K. Adamek, P. Thiagaraj, S. M. Ransom, A. Karastergiou, and W. Armour. A GPU Implementation of the Correlation Technique for Real-time Fourier Domain Pulsar Acceleration Searches. *ApJS*, 239(2):28, December 2018. doi: 10.3847/1538-4365/aabe88. (Cited on page: 232)

[163] Q. Ding, X. Tong, and Y. Wang. Gravitational Collider Physics via Pulsar–Black Hole Binaries. *ApJ*, 908(1):78, February 2021. doi: 10.3847/1538-4357/abd803. (Cited on page: 262)

[164] T. Do, A. Hees, A. Ghez, G. D. Martinez, D. S. Chu, S. Jia, S. Sakai, J. R. Lu, A. K. Gautam, K. K. O'Neil, E. E. Becklin, M. R. Morris, K. Matthews, S. Nishiyama, R. Campbell, S. Chappell, Z. Chen, A. Ciurlo, A. Dehghanfar, E. Gallego-Cano, W. E. Kerzendorf, J. E. Lyke, S. Naoz, H. Saida, R. Schödel, M. Takahashi, Y. Takamori, G. Witzel, and P. Wizinowich. Relativistic Redshift of the Star S0–2 Orbiting the Galactic Center Supermassive Black Hole. *Science*, 365(6454):664–668, Aug 2019. doi: 10.1126/science.aav8137. (Cited on page: 262)

[165] R. C. Duncan and C. Thompson. Formation of Very Strongly Magnetized Neutron Stars: Implications for Gamma-Ray Bursts. *ApJL*, 392:L9, June 1992. doi: 10.1086/186413. (Cited on pages: 33, 39, and 88)

[166] J. Eastman, R. Siverd, and B. S. Gaudi. Achieving Better Than 1 Minute Accuracy in the Heliocentric and Barycentric Julian Dates. *PASP*, 122(894):935, August 2010. doi: 10.1086/655938. (Cited on page: 286)

[167] R. Eatough, T. J. W. Lazio, J. Casanellas, S. Chatterjee, J. M. Cordes, P. B. Demorest, M. Kramer, K. J. Lee, K. Liu, S. M. Ransom, and N. Wex. Observing Radio Pulsars in the Galactic Centre with the Square Kilometre Array. In *Advancing Astrophysics with the Square Kilometre Array (AASKA14)*, page 45, Apr 2015. (Cited on pages: lii, 256, 257, 263, and 264)

[168] R. P. Eatough, E. F. Keane, and A. G. Lyne. An Interference Removal Technique for Radio Pulsar Searches. *MNRAS*, 395(1):410–415, May 2009. doi: 10.1111/j.1365-2966.2009.14524.x. (Cited on pages: xxix, 54, 55, 58, and 59)

[169] R. P. Eatough, H. Falcke, R. Karuppusamy, K. J. Lee, D. J. Champion, E. F. Keane, G. Desvignes, D. H. F. M. Schnitzeler, L. G. Spitler, M. Kramer, B. Klein, C. Bassa, G. C. Bower, A. Brunthaler, I. Cognard, A. T. Deller, P. B. Demorest, P. C. C. Freire, A. Kraus, A. G. Lyne, A. Noutsos, B. Stappers,

and N. Wex. A Strong Magnetic Field Around the Supermassive Black Hole at the Centre of the Galaxy. *Nature*, 501(7467):391–394, September 2013. doi: 10.1038/nature12499. (Cited on pages: 7, 33, 34, 88, 89, 95, 122, and 258)

[170] R. P. Eatough, M. Kramer, B. Klein, R. Karuppusamy, D. J. Champion, P. C. C. Freire, N. Wex, and K. Liu. Can We See Pulsars Around Sgr A⋆? The Latest Searches with the Effelsberg Telescope. In J. van Leeuwen, editor, *Neutron Stars and Pulsars: Challenges and Opportunities after 80 years*, volume 291, pages 382–384, March 2013. doi: 10.1017/S1743921312024209. (Cited on page: 88)

[171] R. P. Eatough, M. Kramer, A. G. Lyne, and M. J. Keith. A Coherent Acceleration Search of the Parkes Multibeam Pulsar Survey - Techniques and the Discovery and Timing of 16 Pulsars. *MNRAS*, 431(1):292–307, May 2013. doi: 10.1093/mnras/stt161. (Cited on page: 232)

[172] P. P. Eggleton. Aproximations to the Radii of Roche Lobes. *ApJ*, 268: 368–369, May 1983. doi: 10.1086/160960. (Cited on page: 312)

[173] T. Enoto, S. Kisaka, and S. Shibata. Observational Diversity of Magnetized Neutron Stars. *Reports on Progress in Physics*, 82(10):106901, October 2019. doi: 10.1088/1361-6633/ab3def. (Cited on pages: xxv, 34, and 146)

[174] P. Esposito, N. Rea, A. Borghese, F. Coti Zelati, D. Viganò, G. L. Israel, A. Tiengo, A. Ridolfi, A. Possenti, M. Burgay, D. Götz, F. Pintore, L. Stella, C. Dehman, M. Ronchi, S. Campana, A. Garcia-Garcia, V. Graber, S. Mereghetti, R. Perna, G. A. Rodríguez Castillo, R. Turolla, and S. Zane. A Very Young Radio-loud Magnetar. *ApJL*, 896(2):L30, June 2020. doi: 10.3847/2041-8213/ab9742. (Cited on pages: 7 and 33)

[175] P. Esposito, N. Rea, and G. L. Israel. *Magnetars: A Short Review and Some Sparse Considerations*, volume 461, pages 97–142. 2021. doi: 10.1007/978-3-662-62110-3_3. (Cited on page: 33)

[176] G. Esposito-Farèse. *Motion in Alternative Theories of Gravity*, volume 162, pages 461–489. Springer Netherlands, 2011. doi: 10.1007/978-90-481-3015-3_17. (Cited on page: 263)

[177] J. Estes, M. Kavic, M. Lippert, and J. H. Simonetti. Shining Light on Quantum Gravity with Pulsar–Black Hole Binaries. *ApJ*, 837(1):87, March 2017. doi: 10.3847/1538-4357/aa610e. (Cited on page: 263)

[178] G. G. Fahlman and P. C. Gregory. An X-Ray Pulsar in SNR G109.1–1.0. *Nature*, 293(5829):202–204, September 1981. doi: 10.1038/293202a0. (Cited on page: 36)

[179] M. Falanga, E. Bozzo, A. Lutovinov, J. M. Bonnet-Bidaud, Y. Fetisova, and J. Puls. Ephemeris, Orbital Decay, and Masses of Ten Eclipsing High-mass X-Ray Binaries. *A&A*, 577:A130, May 2015. doi: 10.1051/0004-6361/201425191. (Cited on pages: 296, 322, and 323)

[180] W. Farah, C. Flynn, M. Bailes, A. Jameson, K. W. Bannister, E. D. Barr, T. Bateman, S. Bhand ari, M. Caleb, D. Campbell-Wilson, S. W. Chang, A. Deller, A. J. Green, R. Hunstead, F. Jankowski, E. Keane, J. P. Macquart, A. Möller, C. A. Onken, S. Osłowski, A. Parthasarathy, K. Plant, V. Ravi, R. M. Shannon, B. E. Tucker, V. Venkatraman Krishnan, and C. Wolf. FRB Microstructure Revealed by the Real-time Detection of FRB170827. *MNRAS*, 478(1):1209–1217, Jul 2018. doi: 10.1093/mnras/sty1122. (Cited on pages: 122 and 167)

[181] S. A. Farrell, R. K. Sood, and P. M. O'Neill. Super-orbital Period in the High-mass X-Ray Binary 2S 0114+650. *MNRAS*, 367(4):1457–1462, April 2006. doi: 10.1111/j.1365-2966.2006.10150.x. (Cited on page: 324)

[182] S. A. Farrell, R. K. Sood, P. M. O'Neill, and S. Dieters. A Detailed Study of 2S 0114+650 with the Rossi X-Ray Timing Explorer. *MNRAS*, 389(2): 608–628, September 2008. doi: 10.1111/j.1365-2966.2008.13588.x. (Cited on page: 324)

[183] C.-A. Faucher-Giguère and V. M. Kaspi. Birth and Evolution of Isolated Radio Pulsars. *ApJ*, 643(1):332–355, May 2006. doi: 10.1086/501516. (Cited on page: 16)

[184] C.-A. Faucher-Giguère and A. Loeb. Pulsar–Black Hole Binaries in the Galactic Centre. *MNRAS*, 415(4):3951–3961, Aug 2011. doi: 10.1111/j.1365-2966.2011.19019.x. (Cited on page: 262)

[185] A. Feldmeier, U. Anzer, G. Boerner, and F. Nagase. Vela X–1: How to Produce Asymmetric Eclipses. *A&A*, 311:793–802, July 1996. (Cited on page: 322)

[186] B. P. Flannery and E. P. J. van den Heuvel. On the Origin of the Binary Pulsar PSR 1913+16. *A&A*, 39:61–67, February 1975. (Cited on page: 5)

[187] E. Fonseca, B. C. Andersen, M. Bhardwaj, P. Chawla, D. C. Good, A. Josephy, V. M. Kaspi, K. W. Masui, R. Mckinven, D. Michilli, Z. Pleunis, K. Shin, S. P. Tendulkar, K. M. Bandura, P. J. Boyle, C. Brar, T. Cassanelli, D. Cubranic, M. Dobbs, F. Q. Dong, B. M. Gaensler, G. Hinshaw, T. L. Land ecker, C. Leung, D. Z. Li, H. H. Lin, J. Mena-Parra, M. Merryfield, A. Naidu, C. Ng, C. Patel, U. Pen, M. Rafiei-Ravandi, M. Rahman, S. M. Ransom, P. Scholz, K. M. Smith, I. H. Stairs, K. Vanderlinde, P. Yadav, and A. V. Zwaniga. Nine New Repeating Fast Radio Burst Sources from CHIME/FRB. *ApJL*, 891(1):L6, March 2020. doi: 10.3847/2041-8213/ab7208. (Cited on pages: 41, 178, and 179)

[188] D. Foreman-Mackey, D. W. Hogg, D. Lang, and J. Goodman. Emcee: The MCMC Hammer. *PASP*, 125(925):306, March 2013. doi: 10.1086/670067. (Cited on pages: 112 and 296)

[189] C. Fransson and A. C. Fabian. X-Ray Induced Shocks in Stellar Winds. *A&A*, 87:102–108, July 1980. (Cited on page: 322)

[190] B. M. Gaensler, C. Kouveliotou, J. D. Gelfand, G. B. Taylor, D. Eichler, R. A. M. J. Wijers, J. Granot, E. Ramirez-Ruiz, Y. E. Lyubarsky, R. W. Hunstead, D. Campbell-Wilson, A. J. van der Horst, M. A. McLaughlin, R. P. Fender, M. A. Garrett, K. J. Newton-McGee, D. M. Palmer, N. Gehrels, and P. M. Woods. An Expanding Radio Nebula Produced by a Giant Flare from the Magnetar SGR 1806–20. *Nature*, 434(7037):1104–1106, April 2005. doi: 10.1038/nature03498. (Cited on page: 45)

[191] V. Gajjar, A. P. V. Siemion, D. C. Price, C. J. Law, D. Michilli, J. W. T. Hessels, S. Chatterjee, A. M. Archibald, G. C. Bower, C. Brinkman, S. Burke-Spolaor, J. M. Cordes, S. Croft, J. E. Enriquez, G. Foster, N. Gizani, G. Hellbourg, H. Isaacson, V. M. Kaspi, T. J. W. Lazio, M. Lebofsky, R. S. Lynch, D. MacMahon, M. A. McLaughlin, S. M. Ransom, P. Scholz, A. Seymour, L. G. Spitler, S. P. Tendulkar, D. Werthimer, and Y. G. Zhang. Highest Frequency Detection of FRB 121102 at 4-8 GHz Using the Breakthrough Listen Digital Backend at the Green Bank Telescope. *ApJ*, 863(1):2, Aug 2018. doi: 10.3847/1538-4357/aad005. (Cited on pages: 41, 122, 158, 164, 168, 172, 173, 179, 182, 192, and 205)

[192] F. P. Gavriil and V. M. Kaspi. Long-term Rossi X-Ray Timing Explorer Monitoring of Anomalous X-Ray Pulsars. *ApJ*, 567(2):1067–1076, March 2002. doi: 10.1086/338698. (Cited on page: 38)

[193] F. P. Gavriil, V. M. Kaspi, and P. M. Woods. Magnetar-like X-Ray Bursts from an Anomalous X-Ray Pulsar. *Nature*, 419(6903):142–144, September 2002. doi: 10.1038/nature01011. (Cited on pages: 6 and 36)

[194] F. P. Gavriil, V. M. Kaspi, and P. M. Woods. A Comprehensive Study of the X-Ray Bursts from the Magnetar Candidate 1E 2259+586. *ApJ*, 607(2): 959–969, June 2004. doi: 10.1086/383564. (Cited on page: 37)

[195] F. P. Gavriil, M. E. Gonzalez, E. V. Gotthelf, V. M. Kaspi, M. A. Livingstone, and P. M. Woods. Magnetar-like Emission from the Young Pulsar in Kes 75. *Science*, 319(5871):1802, March 2008. doi: 10.1126/science.1153465. (Cited on pages: 40 and 76)

[196] N. Gehrels, G. Chincarini, P. Giommi, K. O. Mason, J. A. Nousek, A. A. Wells, N. E. White, S. D. Barthelmy, D. N. Burrows, L. R. Cominsky, K. C. Hurley, F. E. Marshall, P. Mészáros, P. W. A. Roming, L. Angelini, L. M. Barbier, T. Belloni, S. Campana, P. A. Caraveo, M. M. Chester, O. Citterio, T. L. Cline, M. S. Cropper, J. R. Cummings, A. J. Dean, E. D. Feigelson,

E. E. Fenimore, D. A. Frail, A. S. Fruchter, G. P. Garmire, K. Gendreau, G. Ghisellini, J. Greiner, J. E. Hill, S. D. Hunsberger, H. A. Krimm, S. R. Kulkarni, P. Kumar, F. Lebrun, N. M. Lloyd-Ronning, C. B. Markwardt, B. J. Mattson, R. F. Mushotzky, J. P. Norris, J. Osborne, B. Paczynski, D. M. Palmer, H. S. Park, A. M. Parsons, J. Paul, M. J. Rees, C. S. Reynolds, J. E. Rhoads, T. P. Sasseen, B. E. Schaefer, A. T. Short, A. P. Smale, I. A. Smith, L. Stella, G. Tagliaferri, T. Takahashi, M. Tashiro, L. K. Townsley, J. Tueller, M. J. L. Turner, M. Vietri, W. Voges, M. J. Ward, R. Willingale, F. M. Zerbi, and W. W. Zhang. The Swift Gamma-Ray Burst Mission. *ApJ*, 611(2):1005–1020, August 2004. doi: 10.1086/422091. (Cited on page: 286)

[197] K. C. Gendreau, Z. Arzoumanian, P. W. Adkins, C. L. Albert, J. F. Anders, A. T. Aylward, C. L. Baker, E. R. Balsamo, W. A. Bamford, S. S. Benegalrao, D. L. Berry, S. Bhalwani, J. K. Black, C. Blaurock, G. M. Bronke, G. L. Brown, J. G. Budinoff, J. D. Cantwell, T. Cazeau, P. T. Chen, T. G. Clement, A. T. Colangelo, J. S. Coleman, J. D. Coopersmith, W. E. Dehaven, J. P. Doty, M. D. Egan, T. Enoto, T. W. Fan, D. M. Ferro, R. Foster, N. M. Galassi, L. D. Gallo, C. M. Green, D. Grosh, K. Q. Ha, M. A. Hasouneh, K. B. Heefner, P. Hestnes, L. J. Hoge, T. M. Jacobs, J. L. Jørgensen, M. A. Kaiser, J. W. Kellogg, S. J. Kenyon, R. G. Koenecke, R. P. Kozon, B. LaMarr, M. D. Lambertson, A. M. Larson, S. Lentine, J. H. Lewis, M. G. Lilly, K. A. Liu, A. Malonis, S. S. Manthripragada, C. B. Markwardt, B. D. Matonak, I. E. Mcginnis, R. L. Miller, A. L. Mitchell, J. W. Mitchell, J. S. Mohammed, C. A. Monroe, K. M. Montt de Garcia, P. D. Mulé, L. T. Nagao, S. N. Ngo, E. D. Norris, D. A. Norwood, J. Novotka, T. Okajima, L. G. Olsen, C. O. Onyeachu, H. Y. Orosco, J. R. Peterson, K. N. Pevear, K. K. Pham, S. E. Pollard, J. S. Pope, D. F. Powers, C. E. Powers, S. R. Price, G. Y. Prigozhin, J. B. Ramirez, W. J. Reid, R. A. Remillard, E. M. Rogstad, G. P. Rosecrans, J. N. Rowe, J. A. Sager, C. A. Sanders, B. Savadkin, M. R. Saylor, A. F. Schaeffer, N. S. Schweiss, S. R. Semper, P. J. Serlemitsos, L. V. Shackelford, Y. Soong, J. Struebel, M. L. Vezie, J. S. Villasenor, L. B. Winternitz, G. I. Wofford, M. R. Wright, M. Y. Yang, and W. H. Yu. The Neutron Star Interior Composition Explorer (NICER): Design and Development. In J.-W. A. den Herder, T. Takahashi, and M. Bautz, editors, *Space Telescopes and Instrumentation 2016: Ultraviolet to Gamma Ray*, volume 9905 of *Society of Photo-Optical Instrumentation Engineers (SPIE) Conference Series*, page 99051H, July 2016. doi: 10.1117/12.2231304. (Cited on page: 143)

[198] M. Geyer and A. Karastergiou. The Frequency Dependence of Scattering Imprints on Pulsar Observations. *MNRAS*, 462(3):2587–2602, November 2016. doi: 10.1093/mnras/stw1724. (Cited on page: 29)

[199] A. M. Ghez, S. Salim, N. N. Weinberg, J. R. Lu, T. Do, J. K. Dunn, K. Matthews, M. R. Morris, S. Yelda, E. E. Becklin, T. Kremenek, M. Milosavljevic, and J. Naiman. Measuring Distance and Properties of the Milky Way's Central Supermassive Black Hole with Stellar Orbits. *ApJ*,

689(2):1044–1062, Dec 2008. doi: 10.1086/592738. (Cited on pages: 256 and 261)

[200] J. A. Gil, J. Kijak, and J. H. Seiradakis. On the Two-dimensional Structure of Pulsar Beams. *A&A*, 272:268–276, May 1993. (Cited on pages: xxii and 12)

[201] S. Gillessen, F. Eisenhauer, T. K. Fritz, H. Bartko, K. Dodds-Eden, O. Pfuhl, T. Ott, and R. Genzel. The Orbit of the Star S2 Around Sgr A* from Very Large Telescope and Keck Data. *ApJL*, 707(2):L114–L117, December 2009. doi: 10.1088/0004-637X/707/2/L114. (Cited on page: 117)

[202] S. Gillessen, F. Eisenhauer, S. Trippe, T. Alexand er, R. Genzel, F. Martins, and T. Ott. Monitoring Stellar Orbits Around the Massive Black Hole in the Galactic Center. *ApJ*, 692(2):1075–1109, Feb 2009. doi: 10.1088/0004-637X/692/2/1075. (Cited on pages: 256 and 261)

[203] T. Gold. Rotating Neutron Stars as the Origin of the Pulsating Radio Sources. *Nature*, 218(5143):731–732, May 1968. doi: 10.1038/218731a0. (Cited on page: 5)

[204] P. Goldreich and W. H. Julian. Pulsar Electrodynamics. *ApJ*, 157:869, August 1969. doi: 10.1086/150119. (Cited on page: 10)

[205] M. Gonzalez and S. Safi-Harb. Chandra Detection of the High Magnetic Field Radio Pulsar J1119–6127 in the Supernova Remnant G292.2–0.5. *ApJL*, 591: L143–L146, July 2003. doi: 10.1086/377070. (Cited on page: 76)

[206] M. E. Gonzalez, V. M. Kaspi, F. Camilo, B. M. Gaensler, and M. J. Pivovaroff. Unusual Pulsed X-Ray Emission from the Young, High Magnetic Field Pulsar PSR J1119–6127. *ApJ*, 630(1):489–494, September 2005. doi: 10.1086/432032. (Cited on pages: 83 and 84)

[207] J. Goodman and J. Weare. Ensemble Samplers with Affine Invariance. *Communications in Applied Mathematics and Computational Science*, 5(1):65–80, January 2010. doi: 10.2140/camcos.2010.5.65. (Cited on pages: 112 and 296)

[208] M. E. Goossens, A. J. Bird, S. P. Drave, A. Bazzano, A. B. Hill, V. A. McBride, V. Sguera, and L. Sidoli. Discovering a 5.72-d Period in the Supergiant Fast X-Ray Transient AX J1845.0–0433. *MNRAS*, 434(3):2182–2187, September 2013. doi: 10.1093/mnras/stt1166. (Cited on page: 312)

[209] C. Gordon and O. Macías. Dark Matter and Pulsar Model Constraints from Galactic Center Fermi-LAT Gamma-Ray Observations. *Phys. Rev. D*, 88(8): 083521, Oct 2013. doi: 10.1103/PhysRevD.88.083521. (Cited on page: 261)

[210] E. V. Gotthelf and J. P. Halpern. The Spectral Evolution of Transient Anomalous X-Ray Pulsar XTE J1810–197. *ApJ*, 632(2):1075–1085, October 2005. doi: 10.1086/432709. (Cited on page: 133)

[211] E. V. Gotthelf, J. P. Halpern, J. A. J. Alford, T. Mihara, H. Negoro, N. Kawai, S. Dai, M. E. Lower, S. Johnston, M. Bailes, S. Osłowski, F. Camilo, H. Miyasaka, and K. K. Madsen. The 2018 X-Ray and Radio Outburst of Magnetar XTE J1810–197. *ApJL*, 874(2):L25, April 2019. doi: 10.3847/2041-8213/ab101a. (Cited on pages: 133, 134, 137, and 140)

[212] E. Göğüș, L. Lin, Y. Kaneko, C. Kouveliotou, A. L. Watts, M. Chakraborty, M. A. Alpar, D. Huppenkothen, O. J. Roberts, G. Younes, and A. J. van der Horst. Magnetar-like X-Ray Bursts from a Rotation-powered Pulsar, PSR J1119–6127. *ApJL*, 829(2):L25, October 2016. doi: 10.3847/2041-8205/829/2/L25. (Cited on pages: 76 and 83)

[213] K. Gourdji, D. Michilli, L. G. Spitler, J. W. T. Hessels, A. Seymour, J. M. Cordes, and S. Chatterjee. A Sample of Low-energy Bursts from FRB 121102. *ApJL*, 877(2):L19, June 2019. doi: 10.3847/2041-8213/ab1f8a. (Cited on pages: 163, 164, 171, 172, 179, and 192)

[214] E. GöğüŞ , P. M. Woods, C. Kouveliotou, J. van Paradijs, M. S. Briggs, R. C. Duncan, and C. Thompson. Statistical Properties of SGR 1900+14 Bursts. *ApJL*, 526(2):L93–L96, December 1999. doi: 10.1086/312380. (Cited on page: 37)

[215] E. Göğüş, P. M. Woods, C. Kouveliotou, J. van Paradijs, M. S. Briggs, R. C. Duncan, and C. Thompson. Statistical Properties of SGR 1806–20 Bursts. *ApJL*, 532(2):L121–L124, April 2000. doi: 10.1086/312583. (Cited on page: 37)

[216] F. Graham Smith, A. G. Lyne, and C. Jordan. The 1997 Event in the Crab Pulsar Revisited. *MNRAS*, 410(1):499–503, January 2011. doi: 10.1111/j.1365-2966.2010.17459.x. (Cited on page: 120)

[217] S. A. Grebenev, A. J. Bird, S. V. Molkov, S. Soldi, P. Kretschmar, R. Diehl, C. Budz-Joergensen, and B. McBreen. IGR J16493–4348 - A Radiopulsar or a New X-Ray Binary. *The Astronomer's Telegram*, 457:1, April 2005. (Cited on page: 281)

[218] T. Güver and F. Özel. The Relation Between Optical Extinction and Hydrogen Column Density in the Galaxy. *MNRAS*, 400(4):2050–2053, December 2009. doi: 10.1111/j.1365-2966.2009.15598.x. (Cited on page: 316)

[219] T. Güver, E. Göğüș, E. Vurgun, T. Enoto, K. C. Gendreau, T. Sakamoto, E. V. Gotthelf, Z. Arzoumanian, S. Guillot, G. K. Jaisawal, C. Malacaria, and W. A. Majid. NICER Observations of the 2018 Outburst of XTE J1810–197. *ApJL*, 877(2):L30, June 2019. doi: 10.3847/2041-8213/ab212d. (Cited on pages: 133, 137, 144, and 149)

[220] W. A. Götz and H. J. Druckmüller. A fast digital radon transform—an efficient means for evaluating the hough transform. *Pattern Recognition*, 29 (4):711–718, 1996. (Cited on page: 218)

[221] T. H. Hankins, J. A. Eilek, and G. Jones. The Crab Pulsar at Centimeter Wavelengths. II. Single Pulses. *ApJ*, 833(1):47, December 2016. doi: 10.3847/1538-4357/833/1/47. (Cited on page: 120)

[222] M. M. Hanson, P. S. Conti, and M. J. Rieke. A Spectral Atlas of Hot, Luminous Stars at 2 Microns. *ApJS*, 107:281, November 1996. doi: 10.1086/192366. (Cited on page: 315)

[223] L. K. Hardy, V. S. Dhillon, L. G. Spitler, S. P. Littlefair, R. P. Ashley, A. De Cia, M. J. Green, P. Jaroenjittichai, E. F. Keane, P. Kerry, M. Kramer, D. Malesani, T. R. Marsh, S. G. Parsons, A. Possenti, S. Rattanasoon, and D. I. Sahman. A Search for Optical Bursts from the Repeating Fast Radio Burst FRB 121102. *MNRAS*, 472(3):2800–2807, December 2017. doi: 10.1093/mnras/stx2153. (Cited on page: 41)

[224] C. He, C. Y. Ng, and V. M. Kaspi. The Correlation Between Dispersion Measure and X-Ray Column Density from Radio Pulsars. *ApJ*, 768(1):64, May 2013. doi: 10.1088/0004-637X/768/1/64. (Cited on page: 78)

[225] K. E. Heintz, J. X. Prochaska, S. Simha, E. Platts, W.-f. Fong, N. Tejos, S. D. Ryder, K. Aggerwal, S. Bhandari, C. K. Day, A. T. Deller, C. D. Kilpatrick, C. J. Law, J.-P. Macquart, A. Mannings, L. J. Marnoch, E. M. Sadler, and R. M. Shannon. Host Galaxy Properties and Offset Distributions of Fast Radio Bursts: Implications for Their Progenitors. *ApJ*, 903(2):152, November 2020. doi: 10.3847/1538-4357/abb6fb. (Cited on page: 177)

[226] D. J. Helfand, S. Chatterjee, W. F. Brisken, F. Camilo, J. Reynolds, M. H. van Kerkwijk, J. P. Halpern, and S. M. Ransom. VLBA Measurement of the Transverse Velocity of the Magnetar XTE J1810–197. *ApJ*, 662(2):1198–1203, June 2007. doi: 10.1086/518028. (Cited on pages: 135, 145, and 153)

[227] G. W. Henry, G. W. Marcy, R. P. Butler, and S. S. Vogt. A Transiting "51 Peg-like" Planet. *ApJL*, 529(1):L41–L44, January 2000. doi: 10.1086/312458. (Cited on page: 8)

[228] J. W. T. Hessels, S. M. Ransom, I. H. Stairs, P. C. C. Freire, V. M. Kaspi, and F. Camilo. A Radio Pulsar Spinning at 716 Hz. *Science*, 311(5769):1901–1904, March 2006. doi: 10.1126/science.1123430. (Cited on page: 7)

[229] J. W. T. Hessels, L. G. Spitler, A. D. Seymour, J. M. Cordes, D. Michilli, R. S. Lynch, K. Gourdji, A. M. Archibald, C. G. Bassa, G. C. Bower, S. Chatterjee, L. Connor, F. Crawford, J. S. Deneva, V. Gajjar, V. M. Kaspi, A. Keimpema, C. J. Law, B. Marcote, M. A. McLaughlin, Z. Paragi, E. Petroff, S. M. Ransom, P. Scholz, B. W. Stappers, and S. P. Tendulkar. FRB 121102 Bursts Show Complex Time–Frequency Structure. *ApJL*, 876(2):L23, May 2019. doi: 10.3847/2041-8213/ab13ae. (Cited on pages: 158, 159, 167, 168, 173, 174, 178, 179, 182, 192, and 205)

[230] A. Hewish, S. J. Bell, J. D. H. Pilkington, P. F. Scott, and R. A. Collins. Observation of a Rapidly Pulsating Radio Source. *Nature*, 217(5130):709–713, February 1968. doi: 10.1038/217709a0. (Cited on pages: 5 and 21)

[231] A. B. Hill, A. J. Dean, R. Landi, V. A. McBride, A. de Rosa, A. J. Bird, A. Bazzano, and V. Sguera. Probing the Nature of IGR J16493–4348: Spectral and Temporal Analysis of the 1–100 keV Emission. *MNRAS*, 385(1):423–429, March 2008. doi: 10.1111/j.1365-2966.2008.12849.x. (Cited on pages: 282 and 316)

[232] W. C. G. Ho and N. Andersson. Rotational Evolution of Young Pulsars Due to Superfluid Decoupling. *Nature Physics*, 8(11):787–789, November 2012. doi: 10.1038/nphys2424. (Cited on page: 13)

[233] G. B. Hobbs, R. T. Edwards, and R. N. Manchester. TEMPO2, A New Pulsar-timing Package - I. An Overview. *MNRAS*, 369(2):655–672, June 2006. doi: 10.1111/j.1365-2966.2006.10302.x. (Cited on page: 145)

[234] D. Hooper and L. Goodenough. Dark Matter Annihilation in the Galactic Center as Seen by the Fermi Gamma Ray Space Telescope. *Physics Letters B*, 697(5):412–428, Mar 2011. doi: 10.1016/j.physletb.2011.02.029. (Cited on pages: 260 and 261)

[235] D. Hooper and T. Linden. Origin of the Gamma Rays from the Galactic Center. *Phys. Rev. D*, 84(12):123005, Dec 2011. doi: 10.1103/PhysRevD.84.123005. (Cited on pages: 260 and 261)

[236] D. Hooper, I. Cholis, T. Linden, J. M. Siegal-Gaskins, and T. R. Slatyer. Millisecond Pulsars Cannot Account for the Inner Galaxy's GeV Excess. *Phys. Rev. D*, 88(8):083009, Oct 2013. doi: 10.1103/PhysRevD.88.083009. (Cited on pages: 260 and 261)

[237] S. Horiuchi, M. Kaplinghat, and A. Kwa. Investigating the Uniformity of the Excess Gamma Rays Towards the Galactic Center Region. *JCAP*, 2016(11):053, Nov 2016. doi: 10.1088/1475-7516/2016/11/053. (Cited on page: 261)

[238] J. H. Horne and S. L. Baliunas. A Prescription for Period Analysis of Unevenly Sampled Time Series. *ApJ*, 302:757, March 1986. doi: 10.1086/164037. (Cited on page: 288)

[239] A. W. Hotan, W. van Straten, and R. N. Manchester. PSRCHIVE and PSRFITS: An Open Approach to Radio Pulsar Data Storage and Analysis. *PASA*, 21(3):302–309, January 2004. doi: 10.1071/AS04022. (Cited on pages: 165 and 182)

[240] L. J. M. Houben, L. G. Spitler, S. ter Veen, J. P. Rachen, H. Falcke, and M. Kramer. Constraints on the Low Frequency Spectrum of FRB 121102. *A&A*, 623:A42, March 2019. doi: 10.1051/0004-6361/201833875. (Cited on pages: 172, 179, and 196)

[241] C.-P. Hu, Y. Chou, C. Y. Ng, L. C.-C. Lin, and D. C.-C. Yen. Evolution of Spin, Orbital, and Superorbital Modulations of 4U 0114+650. *ApJ*, 844(1): 16, July 2017. doi: 10.3847/1538-4357/aa79a3. (Cited on page: 324)

[242] R. A. Hulse and J. H. Taylor. Discovery of a Pulsar in a Binary System. *ApJL*, 195:L51–L53, January 1975. doi: 10.1086/181708. (Cited on page: 5)

[243] L.-W. Hung, R. C. Hickox, B. S. Boroson, and S. D. Vrtilek. Suzaku X-Ray Spectra and Pulse Profile Variations During the Superorbital Cycle of LMC X–4. *ApJ*, 720(2):1202–1214, September 2010. doi: 10.1088/0004-637X/720/2/1202. (Cited on page: 324)

[244] K. Hurley, T. Cline, E. Mazets, S. Barthelmy, P. Butterworth, F. Marshall, D. Palmer, R. Aptekar, S. Golenetskii, V. Il'Inskii, D. Frederiks, J. McTiernan, R. Gold, and J. Trombka. A Giant Periodic Flare from the Soft γ-Ray Repeater SGR1900+14. *Nature*, 397(6714):41–43, January 1999. doi: 10.1038/16199. (Cited on pages: 6, 36, 37, 132, and 140)

[245] K. Hurley, S. E. Boggs, D. M. Smith, R. C. Duncan, R. Lin, A. Zoglauer, S. Krucker, G. Hurford, H. Hudson, C. Wigger, W. Hajdas, C. Thompson, I. Mitrofanov, A. Sanin, W. Boynton, C. Fellows, A. von Kienlin, G. Lichti, A. Rau, and T. Cline. An Exceptionally Bright Flare from SGR 1806–20 and the Origins of Short-duration γ-Ray Bursts. *Nature*, 434(7037):1098–1103, April 2005. doi: 10.1038/nature03519. (Cited on pages: 6, 36, and 37)

[246] A. I. Ibrahim, C. B. Markwardt, J. H. Swank, S. Ransom, M. Roberts, V. Kaspi, P. M. Woods, S. Safi-Harb, S. Balman, W. C. Parke, C. Kouveliotou, K. Hurley, and T. Cline. Discovery of a Transient Magnetar: XTE J1810–197. *ApJL*, 609(1):L21–L24, July 2004. doi: 10.1086/422636. (Cited on pages: 132 and 146)

[247] K. Ioka and B. Zhang. A Binary Comb Model for Periodic Fast Radio Bursts. *ApJL*, 893(1):L26, April 2020. doi: 10.3847/2041-8213/ab83fb. (Cited on pages: 178 and 204)

[248] G. L. Israel, T. Belloni, L. Stella, Y. Rephaeli, D. E. Gruber, P. Casella, S. Dall'Osso, N. Rea, M. Persic, and R. E. Rothschild. The Discovery of Rapid X-Ray Oscillations in the Tail of the SGR 1806–20 Hyperflare. *ApJL*, 628(1):L53–L56, July 2005. doi: 10.1086/432615. (Cited on page: 38)

[249] G. L. Israel, P. Esposito, N. Rea, S. Dall'Osso, F. Senziani, P. Romano, V. Mangano, D. Götz, S. Zane, A. Tiengo, D. M. Palmer, H. Krimm, N. Gehrels, S. Mereghetti, L. Stella, R. Turolla, S. Campana, R. Perna, L. Angelini, and A. de Luca. The 2008 October Swift Detection of X-ray Bursts/Outburst from the Transient SGR-like AXP 1E 1547.0–5408. *MNRAS*, 408(3):1387–1395, November 2010. doi: 10.1111/j.1365-2966.2010.17001.x. (Cited on page: 36)

[250] G. L. Israel, A. Belfiore, L. Stella, P. Esposito, P. Casella, A. De Luca, M. Marelli, A. Papitto, M. Perri, S. Puccetti, G. A. R. Castillo, D. Salvetti, A. Tiengo, L. Zampieri, D. D'Agostino, J. Greiner, F. Haberl, G. Novara, R. Salvaterra, R. Turolla, M. Watson, J. Wilms, and A. Wolter. An Accreting Pulsar with Extreme Properties Drives an Ultraluminous X-Ray Source in NGC 5907. *Science*, 355(6327):817–819, February 2017. doi: 10.1126/science.aai8635. (Cited on page: 8)

[251] G. L. Israel, A. Papitto, P. Esposito, L. Stella, L. Zampieri, A. Belfiore, G. A. Rodríguez Castillo, A. De Luca, A. Tiengo, F. Haberl, J. Greiner, R. Salvaterra, S. Sandrelli, and G. Lisini. Discovery of a 0.42-s Pulsar in the Ultraluminous X-Ray Source NGC 7793 P13. *MNRAS*, 466(1):L48–L52, March 2017. doi: 10.1093/mnrasl/slw218. (Cited on page: 8)

[252] J. C. Jackson. Parameters of Cen X–3 Deduced from Observations of Its Accretion Wake. *MNRAS*, 172:483–492, September 1975. doi: 10.1093/mnras/172.3.483. (Cited on page: 322)

[253] K. Jahoda, J. H. Swank, A. B. Giles, M. J. Stark, T. Strohmayer, W. Zhang, and E. H. Morgan. In-orbit Performance and Calibration of the Rossi X-Ray Timing Explorer (RXTE) Proportional Counter Array (PCA). In O. H. Siegmund and M. A. Gummin, editors, *EUV, X-Ray, and Gamma-Ray Instrumentation for Astronomy VII*, volume 2808 of *Society of Photo-Optical Instrumentation Engineers (SPIE) Conference Series*, pages 59–70, October 1996. doi: 10.1117/12.256034. (Cited on page: 284)

[254] K. Jahoda, C. B. Markwardt, Y. Radeva, A. H. Rots, M. J. Stark, J. H. Swank, T. E. Strohmayer, and W. Zhang. Calibration of the Rossi X-Ray Timing Explorer Proportional Counter Array. *ApJS*, 163(2):401–423, April 2006. doi: 10.1086/500659. (Cited on pages: 284 and 285)

[255] C. Jain, B. Paul, and A. Dutta. Discovery of a Short Orbital Period in the Supergiant Fast X-Ray Transient IGR J16479–4514. *MNRAS*, 397(1): L11–L15, July 2009. doi: 10.1111/j.1745-3933.2009.00668.x. (Cited on page: 322)

[256] P. A. Jenke, M. H. Finger, C. A. Wilson-Hodge, and A. Camero-Arranz. Orbital Decay and Evidence of Disk Formation in the X-Ray Binary Pulsar OAO 1657–415. *ApJ*, 759(2):124, November 2012. doi: 10.1088/0004-637X/759/2/124. (Cited on page: 310)

[257] H. M. Johnston and S. R. Kulkarni. On the Detectability of Pulsars in Close Binary Systems. *ApJ*, 368:504, February 1991. doi: 10.1086/169715. (Cited on pages: 230 and 234)

[258] S. Johnston, M. Kramer, D. R. Lorimer, A. G. Lyne, M. McLaughlin, B. Klein, and R. N. Manchester. Discovery of Two Pulsars Towards the Galactic

Centre. *MNRAS*, 373(1):L6–L10, November 2006. doi: 10.1111/j.1745-3933.2006.00232.x. (Cited on pages: 88, 256, 257, and 259)

[259] A. Josephy, P. Chawla, E. Fonseca, C. Ng, C. Patel, Z. Pleunis, P. Scholz, B. C. Andersen, K. Bandura, M. Bhardwaj, M. M. Boyce, P. J. Boyle, C. Brar, D. Cubranic, M. Dobbs, B. M. Gaensler, A. Gill, U. Giri, D. C. Good, M. Halpern, G. Hinshaw, V. M. Kaspi, T. L. Landecker, D. A. Lang, H. H. Lin, K. W. Masui, R. Mckinven, J. Mena-Parra, M. Merryfield, D. Michilli, N. Milutinovic, A. Naidu, U. Pen, M. Rafiei-Ravand i, M. Rahman, S. M. Ransom, A. Renard, S. R. Siegel, K. M. Smith, I. H. Stairs, S. P. Tendulkar, K. Vanderlinde, P. Yadav, and A. V. Zwaniga. CHIME/FRB Detection of the Original Repeating Fast Radio Burst Source FRB 121102. *ApJL*, 882(2):L18, September 2019. doi: 10.3847/2041-8213/ab2c00. (Cited on pages: 164, 168, 174, 178, and 192)

[260] P. C. Joss and S. A. Rappaport. Neutron Stars in Interacting Binary Systems. *ARA&A*, 22:537–592, January 1984. doi: 10.1146/annurev.aa.22.090184.002541. (Cited on page: 312)

[261] P. M. W. Kalberla, W. B. Burton, D. Hartmann, E. M. Arnal, E. Bajaja, R. Morras, and W. G. L. Pöppel. The Leiden/Argentine/Bonn (LAB) Survey of Galactic HI. Final Data Release of the Combined LDS and IAR Surveys with Improved Stray-radiation Corrections. *A&A*, 440(2):775–782, September 2005. doi: 10.1051/0004-6361:20041864. (Cited on page: 316)

[262] L. Kaper, A. van der Meer, M. van Kerkwijk, and E. van den Heuvel. Measuring the Masses of Neutron Stars. *The Messenger*, 126:27–31, December 2006. (Cited on pages: 312 and 315)

[263] V. M. Kaspi. Grand Unification of Neutron Stars. *PNAS*, 107(16):7147–7152, April 2010. doi: 10.1073/pnas.1000812107. (Cited on pages: 33 and 83)

[264] V. M. Kaspi and A. M. Beloborodov. Magnetars. *ARA&A*, 55(1):261–301, August 2017. doi: 10.1146/annurev-astro-081915-023329. (Cited on pages: 33, 88, and 132)

[265] V. M. Kaspi, J. H. Taylor, and M. F. Ryba. High-precision Timing of Millisecond Pulsars. III. Long-term Monitoring of PSRs B1855+09 and B1937+21. *ApJ*, 428:713, June 1994. doi: 10.1086/174280. (Cited on page: 228)

[266] V. M. Kaspi, F. P. Gavriil, P. M. Woods, J. B. Jensen, M. S. E. Roberts, and D. Chakrabarty. A Major Soft Gamma Repeater-like Outburst and Rotation Glitch in the No-longer-so-anomalous X-Ray Pulsar 1E 2259+586. *ApJL*, 588(2):L93–L96, May 2003. doi: 10.1086/375683. (Cited on pages: 36 and 85)

[267] V. M. Kaspi, R. F. Archibald, V. Bhalerao, F. Dufour, E. V. Gotthelf, H. An, M. Bachetti, A. M. Beloborodov, S. E. Boggs, F. E. Christensen,

W. W. Craig, B. W. Grefenstette, C. J. Hailey, F. A. Harrison, J. A. Kennea, C. Kouveliotou, K. K. Madsen, K. Mori, C. B. Markwardt, D. Stern, J. K. Vogel, and W. W. Zhang. Timing and Flux Evolution of the Galactic Center Magnetar SGR J1745–2900. *ApJ*, 786(2):84, May 2014. doi: 10.1088/0004-637X/786/2/84. (Cited on page: 256)

[268] J. I. Katz. Two Kinds of Stellar Collapse. *Nature*, 253(5494):698–699, February 1975. doi: 10.1038/253698a0. (Cited on page: 8)

[269] J. I. Katz. Are Fast Radio Bursts Made by Neutron Stars? *MNRAS*, 494(1): L64–L68, May 2020. doi: 10.1093/mnrasl/slaa038. (Cited on page: 204)

[270] E. F. Keane. The Future of Fast Radio Burst Science. *Nature Astronomy*, 2:865–872, October 2018. doi: 10.1038/s41550-018-0603-0. (Cited on pages: xxviii, 49, and 158)

[271] E. F. Keane, B. W. Stappers, M. Kramer, and A. G. Lyne. On the Origin of a Highly Dispersed Coherent Radio Burst. *MNRAS*, 425(1):L71–L75, September 2012. doi: 10.1111/j.1745-3933.2012.01306.x. (Cited on page: 40)

[272] M. J. Keith, S. Johnston, L. Levin, and M. Bailes. 17- and 24-GHz Observations of Southern Pulsars. *MNRAS*, 416(1):346–354, September 2011. doi: 10.1111/j.1365-2966.2011.19041.x. (Cited on pages: 96 and 267)

[273] R. Kelley, S. Rappaport, and R. Petre. A Determination of the Orbit of GX 301–2. *ApJ*, 238:699–709, June 1980. doi: 10.1086/158026. (Cited on page: 309)

[274] J. A. Kennea, D. N. Burrows, C. Kouveliotou, D. M. Palmer, E. Göğüş, Y. Kaneko, P. A. Evans, N. Degenaar, M. T. Reynolds, J. M. Miller, R. Wijnands, K. Mori, and N. Gehrels. Swift Discovery of a New Soft Gamma Repeater, SGR J1745–29, Near Sagittarius A*. *ApJL*, 770(2):L24, June 2013. doi: 10.1088/2041-8205/770/2/L24. (Cited on pages: 89, 121, and 257)

[275] J. A. Kennea, A. Y. Lien, F. E. Marshall, D. M. Palmer, T. G. R. Roegiers, and B. Sbarufatti. Swift Detection of a SGR Burst from PSR 1119–6127. *The Astronomer's Telegram*, #9274, July 2016. (Cited on page: 76)

[276] J. A. Kennea, A. P. Beardmore, K. L. Page, and D. M. Palmer. SGR 1935+2154: Swift Detection of Enhanced X-Ray Emission and Dust Scattered Halo. *The Astronomer's Telegram*, #13679:1, April 2020. (Cited on page: 157)

[277] F. Kirsten, M. P. Snelders, M. Jenkins, K. Nimmo, J. van den Eijnden, J. W. T. Hessels, M. P. Gawroński, and J. Yang. Detection of Two Bright Radio Bursts from Magnetar SGR 1935+2154. *Nature Astronomy*, November 2020. doi: 10.1038/s41550-020-01246-3. (Cited on pages: xxviii, 49, 178, and 205)

[278] G. Koenigsberger, E. Moreno, and F. Cervantes. Tidal Forces and Variability in Close Binary Stars: The β-factor. In K. van der Hucht, A. Herrero, and C. Esteban, editors, *A Massive Star Odyssey: from Main Sequence to Supernova*, volume 212, page 101, January 2003. (Cited on page: 324)

[279] G. Koenigsberger, L. Georgiev, E. Moreno, M. G. Richer, O. Toledano, G. Canalizo, and A. Arrieta. The X-Ray Binary 2S0114+650=LSI+65 010. A Slow Pulsar or Tidally-induced Pulsations? *A&A*, 458(2):513–522, November 2006. doi: 10.1051/0004-6361:20065305. (Cited on page: 324)

[280] D. T. Koh, L. Bildsten, D. Chakrabarty, R. W. Nelson, T. A. Prince, B. A. Vaughan, M. H. Finger, R. B. Wilson, and B. C. Rubin. Rapid Spin-up Episodes in the Wind-fed Accreting Pulsar GX 301–2. *ApJ*, 479(2):933–947, April 1997. doi: 10.1086/303929. (Cited on pages: 304 and 310)

[281] M. Kolonko, J. Gil, and K. Maciesiak. On the Pulse-width Statistics in Radio Pulsars. *A&A*, 428:943–951, December 2004. doi: 10.1051/0004-6361:20034399. (Cited on page: 228)

[282] M. Konacki and A. Wolszczan. Masses and Orbital Inclinations of Planets in the PSR B1257+12 System. *ApJL*, 591(2):L147–L150, July 2003. doi: 10.1086/377093. (Cited on page: 8)

[283] R. Kothes, X. Sun, B. Gaensler, and W. Reich. A Radio Continuum and Polarization Study of SNR G57.2+0.8 Associated with Magnetar SGR 1935+2154. *ApJ*, 852(1):54, January 2018. doi: 10.3847/1538-4357/aa9e89. (Cited on page: 158)

[284] C. Kouveliotou, S. Dieters, T. Strohmayer, J. van Paradijs, G. J. Fishman, C. A. Meegan, K. Hurley, J. Kommers, I. Smith, D. Frail, and T. Murakami. An X-Ray Pulsar with a Superstrong Magnetic Field in the Soft γ-Ray repeater SGR1806–20. *Nature*, 393(6682):235–237, May 1998. doi: 10.1038/30410. (Cited on page: 36)

[285] C. Kouveliotou, T. Strohmayer, K. Hurley, J. van Paradijs, M. H. Finger, S. Dieters, P. Woods, C. Thompson, and R. C. Duncan. Discovery of a Magnetar Associated with the Soft Gamma Repeater SGR 1900+14. *ApJL*, 510(2):L115–L118, January 1999. doi: 10.1086/311813. (Cited on page: 36)

[286] K. Koyama, R. Hoshi, and F. Nagase. X-Ray Observations of the Extraordinary Pulsar 1E 2259+586. *PASJ*, 39:801–807, January 1987. (Cited on page: 36)

[287] M. Kramer, A. Jessner, O. Doroshenko, and R. Wielebinski. Observations of Pulsars at 7 Millimeters. *ApJ*, 488(1):364–367, October 1997. doi: 10.1086/304706. (Cited on page: 120)

[288] M. Kramer, B. Klein, D. Lorimer, P. Müller, A. Jessner, and R. Wielebinski. The Effelsberg Search for Pulsars in the Galactic Centre. In M. Kramer, N. Wex, and R. Wielebinski, editors, *IAU Colloq. 177: Pulsar Astronomy - 2000 and Beyond*, volume 202 of *Astronomical Society of the Pacific Conference Series*, page 37, January 2000. (Cited on pages: 88 and 257)

[289] M. Kramer, D. C. Backer, J. M. Cordes, T. J. W. Lazio, B. W. Stappers, and S. Johnston. Strong-field Tests of Gravity Using Pulsars and Black Holes. *New Astron. Rev.*, 48(11-12):993–1002, Dec 2004. doi: 10.1016/j.newar.2004.09.020. (Cited on pages: lii and 264)

[290] M. Kramer, A. G. Lyne, J. T. O'Brien, C. A. Jordan, and D. R. Lorimer. A Periodically Active Pulsar Giving Insight Into Magnetospheric Physics. *Science*, 312(5773):549–551, April 2006. doi: 10.1126/science.1124060. (Cited on page: 121)

[291] M. Kramer, I. H. Stairs, R. N. Manchester, M. A. McLaughlin, A. G. Lyne, R. D. Ferdman, M. Burgay, D. R. Lorimer, A. Possenti, N. D'Amico, J. M. Sarkissian, G. B. Hobbs, J. E. Reynolds, P. C. C. Freire, and F. Camilo. Tests of General Relativity from Timing the Double Pulsar. *Science*, 314(5796): 97–102, October 2006. doi: 10.1126/science.1132305. (Cited on pages: 241, 244, and 262)

[292] H. A. Krimm, S. T. Holland, R. H. D. Corbet, A. B. Pearlman, P. Romano, J. A. Kennea, J. S. Bloom, S. D. Barthelmy, W. H. Baumgartner, J. R. Cummings, N. Gehrels, A. Y. Lien, C. B. Markwardt, D. M. Palmer, T. Sakamoto, M. Stamatikos, and T. N. Ukwatta. The Swift/BAT Hard X-Ray Transient Monitor. *ApJS*, 209(1):14, November 2013. doi: 10.1088/0067-0049/209/1/14. (Cited on pages: 287 and 288)

[293] M. A. Krishnakumar, D. Mitra, A. Naidu, B. C. Joshi, and P. K. Manoharan. Scatter Broadening Measurements of 124 Pulsars at 327 MHz. *ApJ*, 804(1): 23, May 2015. doi: 10.1088/0004-637X/804/1/23. (Cited on page: 25)

[294] L. Kuiper, P. Jonker, W. Hermsen, and K. O'Brien. Chandra Imaging of IGR J16493–4348. *The Astronomer's Telegram*, 654:1, November 2005. (Cited on page: 281)

[295] T. B. H. Kuiper, M. Franco, S. Smith, G. Baines, L. J. Greenhill, S. Horiuchi, T. Olin, D. C. Price, D. Shaff, L. P. Teitelbaum, S. Weinreb, L. White, and I. Zaw. The 17–27 GHz Dual Horn Receiver on the NASA 70 m Canberra Antenna. *JAI*, 8(4):1950014, January 2019. doi: 10.1142/S2251171719500144. (Cited on page: 265)

[296] S. R. Kulkarni, E. O. Ofek, J. D. Neill, Z. Zheng, and M. Juric. Giant Sparks at Cosmological Distances? *ApJ*, 797(1):70, December 2014. doi: 10.1088/0004-637X/797/1/70. (Cited on page: 45)

[297] P. Kumar, R. M. Shannon, S. Osłowski, H. Qiu, S. Bhandari, W. Farah, C. Flynn, M. Kerr, D. R. Lorimer, J. P. Macquart, C. Ng, C. J. Phillips, D. C. Price, and R. Spiewak. Faint Repetitions from a Bright Fast Radio Burst Source. *ApJL*, 887(2):L30, December 2019. doi: 10.3847/2041-8213/ab5b08. (Cited on page: 177)

[298] P. Kumar, R. M. Shannon, C. Flynn, S. Osłowski, S. Bhandari, C. K. Day, A. T. Deller, W. Farah, J. F. Kaczmarek, M. Kerr, C. Phillips, D. C. Price, H. Qiu, and N. Thyagarajan. Extremely Band-Limited Repetition from a Fast Radio Burst Source. *MNRAS*, 500(2):2525–2531, January 2021. doi: 10.1093/mnras/staa3436. (Cited on pages: 177 and 192)

[299] H. C. Lambert and B. J. Rickett. On the Theory of Pulse Propagation and Two-Frequency Field Statistics in Irregular Interstellar Plasmas. *ApJ*, 517(1): 299–317, May 1999. doi: 10.1086/307181. (Cited on pages: 31 and 122)

[300] J. G. Laros, E. E. Fenimore, R. W. Klebesadel, J. L. Atteia, M. Boer, K. Hurley, M. Niel, G. Vedrenne, S. R. Kane, C. Kouveliotou, T. L. Cline, B. R. Dennis, U. D. Desai, L. E. Orwig, A. V. Kuznetsov, R. A. Sunyaev, and O. V. Terekhov. A New Type of Repetitive Behavior in a High-energy Transient. *ApJL*, 320: L111, September 1987. doi: 10.1086/184985. (Cited on page: 35)

[301] C. J. Law, F. Yusef-Zadeh, W. D. Cotton, and R. J. Maddalena. Green Bank Telescope Multiwavelength Survey of the Galactic Center Region. *ApJS*, 177 (1):255–274, July 2008. doi: 10.1086/533587. (Cited on page: 91)

[302] C. J. Law, M. W. Abruzzo, C. G. Bassa, G. C. Bower, S. Burke-Spolaor, B. J. Butler, T. Cantwell, S. H. Carey, S. Chatterjee, J. M. Cordes, P. Demorest, J. Dowell, R. Fender, K. Gourdji, K. Grainge, J. W. T. Hessels, J. Hickish, V. M. Kaspi, T. J. W. Lazio, M. A. McLaughlin, D. Michilli, K. Mooley, Y. C. Perrott, S. M. Ransom, N. Razavi-Ghods, M. Rupen, A. Scaife, P. Scott, P. Scholz, A. Seymour, L. G. Spitler, K. Stovall, S. P. Tendulkar, D. Titterington, R. S. Wharton, and P. K. G. Williams. A Multi-telescope Campaign on FRB 121102: Implications for the FRB Population. *ApJ*, 850(1):76, Nov 2017. doi: 10.3847/1538-4357/aa9700. (Cited on pages: 158, 164, 167, 172, 174, 179, and 192)

[303] C. J. Law, B. J. Butler, J. X. Prochaska, B. Zackay, S. Burke-Spolaor, A. Mannings, N. Tejos, A. Josephy, B. Andersen, P. Chawla, K. E. Heintz, K. Aggarwal, G. C. Bower, P. B. Demorest, C. D. Kilpatrick, T. J. W. Lazio, J. Linford, R. Mckinven, S. Tendulkar, and S. Simha. A Distant Fast Radio Burst Associated with Its Host Galaxy by the Very Large Array. *ApJ*, 899(2):161, August 2020. doi: 10.3847/1538-4357/aba4ac. (Cited on page: 177)

[304] K. Lazaridis, A. Jessner, M. Kramer, B. W. Stappers, A. G. Lyne, C. A. Jordan, M. Serylak, and J. A. Zensus. Radio Spectrum of the AXP J1810–197 and of Its Profile Components. *MNRAS*, 390(2):839–846, October 2008. doi: 10.1111/j.1365-2966.2008.13794.x. (Cited on pages: 96 and 121)

[305] T. J. W. Lazio and J. M. Cordes. Hyperstrong Radio-wave Scattering in the Galactic Center. II. A Likelihood Analysis of Free Electrons in the Galactic Center. *ApJ*, 505(2):715–731, October 1998. doi: 10.1086/306174. (Cited on pages: 116, 117, and 272)

[306] T. J. W. Lazio and J. M. Cordes. A VLA Survey for Compact Radio Sources in the Galactic Center. *ApJS*, 174(2):481–498, February 2008. doi: 10.1086/521676. (Cited on page: 121)

[307] D. A. Leahy, W. Darbro, R. F. Elsner, M. C. Weisskopf, P. G. Sutherland, S. Kahn, and J. E. Grindlay. On Searches for Pulsed Emission with Application to Four Globular Cluster X-Ray Sources: NGC 1851, 6441, 6624 and 6712. *ApJ*, 266:160–170, March 1983. doi: 10.1086/160766. (Cited on page: 302)

[308] F. Lebrun, J. P. Leray, P. Lavocat, J. Crétolle, M. Arquès, C. Blondel, C. Bonnin, A. Bouère, C. Cara, T. Chaleil, F. Daly, F. Desages, H. Dzitko, B. Horeau, P. Laurent, O. Limousin, F. Mathy, V. Mauguen, F. Meignier, F. Molinié, E. Poindron, M. Rouger, A. Sauvageon, and T. Tourrette. ISGRI: The INTEGRAL Soft Gamma-Ray Imager. *A&A*, 411:L141–L148, November 2003. doi: 10.1051/0004-6361:20031367. (Cited on page: 281)

[309] L. C. Lee and J. R. Jokipii. Strong Scintillations in Astrophysics. II. A Theory of Temporal Broadening of Pulses. *ApJ*, 201:532–543, October 1975. doi: 10.1086/153916. (Cited on pages: 31 and 113)

[310] S. K. Lee, M. Lisanti, B. R. Safdi, T. R. Slatyer, and W. Xue. Evidence for Unresolved γ-Ray Point Sources in the Inner Galaxy. *Phys. Rev. Lett.*, 116 (5):051103, Feb 2016. doi: 10.1103/PhysRevLett.116.051103. (Cited on pages: lii and 261)

[311] K. Lefever, J. Puls, and C. Aerts. Statistical Properties of a Sample of Periodically Variable B-type Supergiants. Evidence for Opacity-driven Gravity-mode Oscillations. *A&A*, 463(3):1093–1109, March 2007. doi: 10.1051/0004-6361:20066038. (Cited on pages: lxi, 314, 318, and 320)

[312] L. Levin, M. Bailes, S. Bates, N. D. R. Bhat, M. Burgay, S. Burke-Spolaor, N. D'Amico, S. Johnston, M. Keith, M. Kramer, S. Milia, A. Possenti, N. Rea, B. Stappers, and W. van Straten. A Radio-loud Magnetar in X-Ray Quiescence. *ApJL*, 721(1):L33–L37, September 2010. doi: 10.1088/2041-8205/721/1/L33. (Cited on pages: 7, 33, 88, 96, 120, and 132)

[313] L. Levin, M. Bailes, S. D. Bates, N. D. R. Bhat, M. Burgay, S. Burke-Spolaor, N. D'Amico, S. Johnston, M. J. Keith, M. Kramer, S. Milia, A. Possenti, B. Stappers, and W. van Straten. Radio Emission Evolution, Polarimetry and Multifrequency Single Pulse Analysis of the Radio Magnetar PSR J1622–4950. *MNRAS*, 422(3):2489–2500, May 2012. doi: 10.1111/j.1365-2966.2012.20807.x. (Cited on pages: 84, 95, 118, 120, and 121)

[314] L. Levin, A. G. Lyne, G. Desvignes, R. P. Eatough, R. Karuppusamy, M. Kramer, M. Mickaliger, B. W. Stappers, and P. Weltevrede. Spin Frequency Evolution and Pulse Profile Variations of the Recently Re-Activated Radio Magnetar XTE J1810–197. *MNRAS*, 488(4):5251–5258, October 2019. doi: 10.1093/mnras/stz2074. (Cited on pages: 146 and 205)

[315] Y. Levin, A. M. Beloborodov, and A. Bransgrove. Precessing Flaring Magnetar as a Source of Repeating FRB 180916.J0158+65. *ApJL*, 895(2):L30, June 2020. doi: 10.3847/2041-8213/ab8c4c. (Cited on page: 204)

[316] A. M. Levine, S. Rappaport, R. Remillard, and A. Savcheva. X1908+075: A Pulsar Orbiting in the Stellar Wind of a Massive Companion. *ApJ*, 617(2): 1284–1295, December 2004. doi: 10.1086/425567. (Cited on page: 305)

[317] W. Lewandowski, K. Rożko, J. Kijak, B. Bhattacharyya, and J. Roy. The Study of Multi-frequency Scattering of 10 Radio Pulsars. *MNRAS*, 454(3):2517–2528, December 2015. doi: 10.1093/mnras/stv2159. (Cited on pages: 25 and 29)

[318] H. W. Lilliefors. On the kolmogorov-smirnov test for normality with mean and variance unknown. *J. Am. Stat. Assoc.*, 62(318):399–402, Jun. 1967. (Cited on page: 106)

[319] M.-X. Lin, R.-X. Xu, and B. Zhang. Oscillation-driven Magnetospheric Activity in Pulsars. *ApJ*, 799(2):152, February 2015. doi: 10.1088/0004-637X/799/2/152. (Cited on page: 85)

[320] T. Linden. Known Radio Pulsars Do Not Contribute to the Galactic Center Gamma-Ray Excess. *Phys. Rev. D*, 93(6):063003, Mar 2016. doi: 10.1103/PhysRevD.93.063003. (Cited on page: 261)

[321] B. Link, R. I. Epstein, and K. A. van Riper. Pulsar Glitches as Probes of Neutron Star Interiors. *Nature*, 359(6396):616–618, October 1992. doi: 10.1038/359616a0. (Cited on page: 38)

[322] K. Liu and R. Eatough. Few and Far Between. *Nature Astronomy*, 1:812–813, Dec 2017. doi: 10.1038/s41550-017-0327-6. (Cited on page: 262)

[323] K. Liu, N. Wex, M. Kramer, J. M. Cordes, and T. J. W. Lazio. Prospects for Probing the Spacetime of Sgr A* with Pulsars. *ApJ*, 747(1):1, March 2012. doi: 10.1088/0004-637X/747/1/1. (Cited on page: 262)

[324] K. Liu, R. P. Eatough, N. Wex, and M. Kramer. Pulsar–Black Hole Binaries: Prospects for New Gravity Tests with Future Radio Telescopes. *MNRAS*, 445(3):3115–3132, Dec 2014. doi: 10.1093/mnras/stu1913. (Cited on pages: 256, 261, 262, and 263)

[325] O. Löhmer, M. Kramer, D. Mitra, D. R. Lorimer, and A. G. Lyne. Anomalous Scattering of Highly Dispersed Pulsars. *ApJL*, 562(2):L157–L161, December 2001. doi: 10.1086/338324. (Cited on page: 113)

[326] O. Löhmer, A. Jessner, M. Kramer, R. Wielebinski, and O. Maron. Observations of Pulsars at 9 Millimetres. *A&A*, 480(3):623–628, March 2008. doi: 10.1051/0004-6361:20066806. (Cited on page: 120)

[327] D. R. Lorimer. Binary and Millisecond Pulsars. *Living Reviews in Relativity*, 8(1):7, November 2005. doi: 10.12942/lrr-2005-7. (Cited on pages: xxii, xxiii, 12, and 18)

[328] D. R. Lorimer and M. Kramer. *Handbook of Pulsar Astronomy*. Cambridge University Press, Cambridge, UK, 2012. (Cited on pages: xxiv, xlv, 22, 26, 28, 54, 95, 221, 222, 223, 231, and 270)

[329] D. R. Lorimer, M. Bailes, M. A. McLaughlin, D. J. Narkevic, and F. Crawford. A Bright Millisecond Radio Burst of Extragalactic Origin. *Science*, 318 (5851):777, Nov 2007. doi: 10.1126/science.1147532. (Cited on pages: xxvi, 40, 46, and 163)

[330] R. V. E. Lovelace, J. M. Sutton, and E. E. Salpeter. Digital Search Methods for Pulsars. *Nature*, 222(5190):231–233, April 1969. doi: 10.1038/222231a0. (Cited on page: 221)

[331] W. Lu and P. Kumar. On the Radiation Mechanism of Repeating Fast Radio Bursts. *MNRAS*, 477(2):2470–2493, June 2018. doi: 10.1093/mnras/sty716. (Cited on page: 178)

[332] W. Lu, P. Kumar, and B. Zhang. A Unified Picture of Galactic and Cosmological Fast Radio Bursts. *MNRAS*, 498(1):1397–1405, August 2020. doi: 10.1093/mnras/staa2450. (Cited on pages: 178 and 205)

[333] W. Lu, A. L. Piro, and E. Waxman. Implications of CHIME Repeating Fast Radio Bursts. *MNRAS*, August 2020. doi: 10.1093/mnras/staa2397. (Cited on page: 179)

[334] R. Luo, B. J. Wang, Y. P. Men, C. F. Zhang, J. C. Jiang, H. Xu, W. Y. Wang, K. J. Lee, J. L. Han, B. Zhang, R. N. Caballero, M. Z. Chen, X. L. Chen, H. Q. Gan, Y. J. Guo, L. F. Hao, Y. X. Huang, P. Jiang, H. Li, J. Li, Z. X. Li, J. T. Luo, J. Pan, X. Pei, L. Qian, J. H. Sun, M. Wang, N. Wang, Z. G. Wen, R. X. Xu, Y. H. Xu, J. Yan, W. M. Yan, D. J. Yu, J. P. Yuan, S. B. Zhang, and Y. Zhu. Diverse Polarization Angle Swings from a Repeating Fast Radio Burst Source. *Nature*, 586(7831):693–696, October 2020. doi: 10.1038/s41586-020-2827-2. (Cited on page: 177)

[335] R. S. Lynch, R. F. Archibald, V. M. Kaspi, and P. Scholz. Green Bank Telescope and Swift X-Ray Telescope Observations of the Galactic Center

Radio Magnetar SGR J1745–2900. *ApJ*, 806(2):266, June 2015. doi: 10.1088/0004-637X/806/2/266. (Cited on pages: 89, 106, and 119)

[336] A. Lyne, L. Levin, B. Stappers, M. Mickaliger, G. Desvignes, and M. Kramer. Intense Radio Flare from the Magnetar XTE J1810–197. *The Astronomer's Telegram*, #12284:1, December 2018. (Cited on pages: 132 and 133)

[337] A. G. Lyne and R. N. Manchester. The Shape of Pulsar Radio Beams. *MNRAS*, 234:477–508, October 1988. doi: 10.1093/mnras/234.3.477. (Cited on pages: xxii and 12)

[338] A. G. Lyne and D. J. Thorne. Anomalous Scattering in the Crab Nebula. *MNRAS*, 172:97–108, July 1975. doi: 10.1093/mnras/172.1.97. (Cited on page: 118)

[339] A. G. Lyne, A. Brinklow, J. Middleditch, S. R. Kulkarni, and D. C. Backer. The Discovery of a Millisecond Pulsar in the Globular Cluster M28. *Nature*, 328(6129):399–401, July 1987. doi: 10.1038/328399a0. (Cited on page: 8)

[340] A. G. Lyne, M. Burgay, M. Kramer, A. Possenti, R. N. Manchester, F. Camilo, M. A. McLaughlin, D. R. Lorimer, N. D'Amico, B. C. Joshi, J. Reynolds, and P. C. C. Freire. A Double-Pulsar System: A Rare Laboratory for Relativistic Gravity and Plasma Physics. *Science*, 303(5661):1153–1157, February 2004. doi: 10.1126/science.1094645. (Cited on page: 241)

[341] Y. Lyubarsky. A Model for Fast Extragalactic Radio bursts. *MNRAS*, 442: L9–L13, July 2014. doi: 10.1093/mnrasl/slu046. (Cited on page: 45)

[342] M. Lyutikov. Radio Emission from Magnetars. *ApJL*, 580(1):L65–L68, November 2002. doi: 10.1086/345493. (Cited on page: 159)

[343] M. Lyutikov and S. Popov. Fast Radio Bursts from Reconnection Events in Magnetar Magnetospheres. *arXiv e-prints*, art. arXiv:2005.05093, May 2020. (Cited on page: 159)

[344] M. Lyutikov, M. V. Barkov, and D. Giannios. FRB Periodicity: Mild Pulsars in Tight O/B-Star Binaries. *ApJL*, 893(2):L39, April 2020. doi: 10.3847/2041-8213/ab87a4. (Cited on page: 204)

[345] Y. Maan. *Tomographic Studies of Pulsar Radio Emission Cones and Searches for Radio Counterparts of Gamma-Ray Pulsars*. PhD thesis, Indian Institute of Science, July 2013. (Cited on pages: xxii and 11)

[346] Y. Maan, B. C. Joshi, M. P. Surnis, M. Bagchi, and P. K. Manoharan. Distinct Properties of the Radio Burst Emission from the Magnetar XTE J1810–197. *ApJL*, 882(1):L9, September 2019. doi: 10.3847/2041-8213/ab3a47. (Cited on pages: 153, 158, and 205)

[347] K. Maciesiak, J. Gil, and V. A. R. M. Ribeiro. On the Pulse-width Statistics in Radio Pulsars - I. Importance of the Interpulse Emission. *MNRAS*, 414(2): 1314–1328, June 2011. doi: 10.1111/j.1365-2966.2011.18471.x. (Cited on page: 228)

[348] J.-P. Macquart and N. Kanekar. On Detecting Millisecond Pulsars at the Galactic Center. *ApJ*, 805(2):172, Jun 2015. doi: 10.1088/0004-637X/805/2/172. (Cited on page: 258)

[349] J. P. Macquart, N. Kanekar, D. A. Frail, and S. M. Ransom. A High-frequency Search for Pulsars Within the Central Parsec of Sgr A*. *ApJ*, 715(2):939–946, June 2010. doi: 10.1088/0004-637X/715/2/939. (Cited on pages: lv, 88, 257, 259, 269, 272, 273, and 276)

[350] J. P. Macquart, J. X. Prochaska, M. McQuinn, K. W. Bannister, S. Bhandari, C. K. Day, A. T. Deller, R. D. Ekers, C. W. James, L. Marnoch, S. Osłowski, C. Phillips, S. D. Ryder, D. R. Scott, R. M. Shannon, and N. Tejos. A Census of Baryons in the Universe from Localized Fast Radio Bursts. *Nature*, 581 (7809):391–395, May 2020. doi: 10.1038/s41586-020-2300-2. (Cited on page: 177)

[351] A. Magro, A. Karastergiou, S. Salvini, B. Mort, F. Dulwich, and K. Zarb Adami. Real-time, Fast Radio Transient Searches with GPU De-dispersion. *MNRAS*, 417(4):2642–2650, November 2011. doi: 10.1111/j.1365-2966.2011.19426.x. (Cited on page: 218)

[352] D. J. Majaess, D. G. Turner, and D. J. Lane. Characteristics of the Galaxy According to Cepheids. *MNRAS*, 398(1):263–270, September 2009. doi: 10.1111/j.1365-2966.2009.15096.x. (Cited on pages: xxiii and 20)

[353] W. Majid. A Multi-wavelength Campaign to Study Giant Pulses from the Crab Pulsar. In J. van Leeuwen, editor, *Neutron Stars and Pulsars: Challenges and Opportunities after 80 years*, volume 291, pages 322–322, March 2013. doi: 10.1017/S1743921312023988. (Cited on page: 52)

[354] W. A. Majid, C. J. Naudet, S. T. Lowe, and T. B. H. Kuiper. Statistical Studies of Giant Pulse Emission from the Crab Pulsar. *ApJ*, 741(1):53, November 2011. doi: 10.1088/0004-637X/741/1/53. (Cited on pages: 52 and 120)

[355] W. A. Majid, T. Dobreva, J. Kocz, J. Lazio, J. Lippuner, A. B. Pearlman, and T. Prince. High Frequency Radio Observations of PSR J1119–6127. *The Astronomer's Telegram*, #9321, August 2016. (Cited on pages: xiv, 52, and 78)

[356] W. A. Majid, A. B. Pearlman, T. Dobreva, S. Horiuchi, J. Kocz, J. Lippuner, and T. A. Prince. Post-outburst Radio Observations of the High Magnetic Field Pulsar PSR J1119–6127. *ApJL*, 834(1):L2, January 2017. doi: 10.3847/2041-8213/834/1/L2. (Cited on pages: xiii, 33, 40, 52, 72, 75, 121, 165, and 182)

[357] W. A. Majid, A. B. Pearlman, T. A. Prince, S. Horiuchi, C. J. Naudet, J. Kocz, and T. Enoto. High Frequency Radio Observations of the Reactivated Magnetar XTE J1810–197. *The Astronomer's Telegram*, #12353:1, January 2019. (Cited on pages: xiv, 52, and 133)

[358] W. A. Majid, A. B. Pearlman, K. Nimmo, J. W. T. Hessels, T. A. Prince, C. J. Naudet, J. Kocz, and S. Horiuchi. A Dual-band Radio Observation of FRB 121102 with the Deep Space Network and the Detection of Multiple Bursts. *ApJL*, 897(1):L4, July 2020. doi: 10.3847/2041-8213/ab9a4a. (Cited on pages: xiii, 52, 158, 162, 179, 180, 182, 186, 192, 193, 205, and 206)

[359] W. A. Majid, A. B. Pearlman, T. A. Prince, T. Enoto, Z. Arzoumanian, K. Gendreau, C. J. Naudet, J. Kocz, S. Horiuchi, A. K. Harding, W. C. G. Ho, and L. Kuiper. DSN Radio and NICER X-Ray Observations of PSR J1846–0258 Following Its Recent Outburst. *The Astronomer's Telegram*, 13988:1, September 2020. (Cited on pages: xv and 52)

[360] W. A. Majid, A. B. Pearlman, T. A. Prince, C. J. Naudet, and K. Bansal. Significant Flattening of Swift J1818.0–1607's Spectral Index via Dual Radio Frequency Observations with the Deep Space Network. *The Astronomer's Telegram*, 13898:1, July 2020. (Cited on pages: xv and 52)

[361] W. A. Majid, A. B. Pearlman, T. A. Prince, C. J. Naudet, J. Kocz, S. Horiuchi, T. Enoto, and G. Younes. Dual Radio Frequency Observations of Swift J1818.0–1607 with the Deep Space Network. *The Astronomer's Telegram*, 13649:1, April 2020. (Cited on pages: xv, 41, and 52)

[362] R. N. Manchester and J. H. Taylor. Parameters of 61 Pulsars. *Astrophys. Lett.*, 10:67, January 1972. (Cited on page: 23)

[363] R. N. Manchester and J. H. Taylor. *Pulsars*. W. H. Freeman and Company, San Francisco, 1977. (Cited on page: 218)

[364] R. N. Manchester, A. G. Lyne, F. Camilo, J. F. Bell, V. M. Kaspi, N. D'Amico, N. P. F. McKay, F. Crawford, I. H. Stairs, A. Possenti, M. Kramer, and D. C. Sheppard. The Parkes Multi-beam Pulsar Survey - I. Observing and Data Analysis Systems, Discovery and Timing of 100 Pulsars. *MNRAS*, 328(1): 17–35, November 2001. doi: 10.1046/j.1365-8711.2001.04751.x. (Cited on page: 54)

[365] R. N. Manchester, G. B. Hobbs, A. Teoh, and M. Hobbs. The Australia Telescope National Facility Pulsar Catalogue. *AJ*, 129(4):1993–2006, April 2005. doi: 10.1086/428488. (Cited on pages: xxii, xxiii, xxv, xxvi, lv, 8, 15, 17, 19, 20, 43, 44, 78, 80, 269, 272, and 276)

[366] A. Manousakis and R. Walter. The Stellar Wind Velocity Field of HD 77581. *A&A*, 584:A25, December 2015. doi: 10.1051/0004-6361/201526893. (Cited on page: 322)

[367] B. Marcote, Z. Paragi, J. W. T. Hessels, A. Keimpema, H. J. van Langevelde, Y. Huang, C. G. Bassa, S. Bogdanov, G. C. Bower, S. Burke-Spolaor, B. J. Butler, R. M. Campbell, S. Chatterjee, J. M. Cordes, P. Demorest, M. A. Garrett, T. Ghosh, V. M. Kaspi, C. J. Law, T. J. W. Lazio, M. A. McLaughlin, S. M. Ransom, C. J. Salter, P. Scholz, A. Seymour, A. Siemion, L. G. Spitler, S. P. Tendulkar, and R. S. Wharton. The Repeating Fast Radio Burst FRB 121102 as Seen on Milliarcsecond Angular Scales. *ApJL*, 834(2):L8, Jan 2017. doi: 10.3847/2041-8213/834/2/L8. (Cited on pages: 41, 164, 168, 177, 179, 181, 189, and 194)

[368] B. Marcote, K. Nimmo, J. W. T. Hessels, S. P. Tendulkar, C. G. Bassa, Z. Paragi, A. Keimpema, M. Bhardwaj, R. Karuppusamy, V. M. Kaspi, C. J. Law, D. Michilli, K. Aggarwal, B. Andersen, A. M. Archibald, K. Bandura, G. C. Bower, P. J. Boyle, C. Brar, S. Burke-Spolaor, B. J. Butler, T. Cassanelli, P. Chawla, P. Demorest, M. Dobbs, E. Fonseca, U. Giri, D. C. Good, K. Gourdji, A. Josephy, A. Y. Kirichenko, F. Kirsten, T. L. Landecker, D. Lang, T. J. W. Lazio, D. Z. Li, H. H. Lin, J. D. Linford, K. Masui, J. Mena-Parra, A. Naidu, C. Ng, C. Patel, U. L. Pen, Z. Pleunis, M. Rafiei-Ravandi, M. Rahman, A. Renard, P. Scholz, S. R. Siegel, K. M. Smith, I. H. Stairs, K. Vanderlinde, and A. V. Zwaniga. A Repeating Fast Radio Burst Source Localized to a Nearby Spiral Galaxy. *Nature*, 577(7789):190–194, January 2020. doi: 10.1038/s41586-019-1866-z. (Cited on pages: xliii, 157, 163, 167, 177, 179, 181, 191, 193, 194, 195, 196, 197, 198, and 199)

[369] B. Margalit and B. D. Metzger. A Concordance Picture of FRB 121102 as a Flaring Magnetar Embedded in a Magnetized Ion–Electron Wind Nebula. *ApJL*, 868(1):L4, November 2018. doi: 10.3847/2041-8213/aaedad. (Cited on page: 157)

[370] B. Margalit, P. Beniamini, N. Sridhar, and B. D. Metzger. Implications of a Fast Radio Burst from a Galactic Magnetar. *ApJL*, 899(2):L27, August 2020. doi: 10.3847/2041-8213/abac57. (Cited on pages: 50, 178, and 205)

[371] C. B. Markwardt, J. H. Swank, and E. Smith. RXTE Observations of IGR J16283–4838 and IGR J16493–4348. *The Astronomer's Telegram*, 465: 1, April 2005. (Cited on page: 281)

[372] O. Maron, J. Kijak, M. Kramer, and R. Wielebinski. Pulsar Spectra of Radio Emission. *A&AS*, 147:195–203, December 2000. doi: 10.1051/aas:2000298. (Cited on pages: lv, 120, 264, 269, and 276)

[373] V. R. Marthi, T. Gautam, D. Z. Li, H. H. Lin, R. A. Main, A. Naidu, U. L. Pen, and R. S. Wharton. Detection of 15 bursts from the fast radio burst 180916.J0158+65 with the upgraded Giant Metrewave Radio Telescope. *MNRAS*, 499(1):L16–L20, December 2020. doi: 10.1093/mnrasl/slaa148. (Cited on pages: xliii, 179, 190, 193, 195, and 199)

[374] N. Masetti, M. Orlandini, D. dal Fiume, S. del Sordo, L. Amati, F. Frontera, E. Palazzi, and A. Santangelo. The BeppoSAX View of the Galactic High-mass X-Ray Binary 4U 0114+65. *A&A*, 445(2):653–660, January 2006. doi: 10.1051/0004-6361:20053654. (Cited on page: 324)

[375] K. Masui, H.-H. Lin, J. Sievers, C. J. Anderson, T.-C. Chang, X. Chen, A. Ganguly, M. Jarvis, C.-Y. Kuo, Y.-C. Li, Y.-W. Liao, M. McLaughlin, U.-L. Pen, J. B. Peterson, A. Roman, P. T. Timbie, T. Voytek, and J. K. Yadav. Dense Magnetized Plasma Associated with a Fast Radio Burst. *Nature*, 528 (7583):523–525, December 2015. doi: 10.1038/nature15769. (Cited on page: 40)

[376] M. Mayor and D. Queloz. A Jupiter-Mass Companion to a Solar-Type Star. *Nature*, 378(6555):355–359, November 1995. doi: 10.1038/378355a0. (Cited on page: 8)

[377] E. P. Mazets and S. V. Golenetskii. Recent Results from the Gamma-Ray Burst Studies in the KONUS Experiment. *Ap&SS*, 75(1):47–81, March 1981. doi: 10.1007/BF00651384. (Cited on page: 35)

[378] E. P. Mazets, S. V. Golenetskij, and Y. A. Guryan. Soft Gamma-Ray Bursts from the Source B1900+14. *Soviet Astronomy Letters*, 5:343, December 1979. (Cited on page: 36)

[379] E. P. Mazets, S. V. Golentskii, V. N. Ilinskii, R. L. Aptekar, and I. A. Guryan. Observations of a Flaring X-Ray Pulsar in Dorado. *Nature*, 282(5739):587–589, December 1979. doi: 10.1038/282587a0. (Cited on pages: 6, 35, and 37)

[380] P. M. McCulloch, P. A. Hamilton, J. G. Ables, and A. J. Hunt. A Radio Pulsar in the Large Magellanic Cloud. *Nature*, 303:307–308, May 1983. doi: 10.1038/303307a0. (Cited on page: 7)

[381] M. M. McKinnon. The Analytical Solution to the Temporal Broadening of a Gaussian-shaped Radio Pulse by Multipath Scattering from a Thin Screen in the Interstellar Medium. *PASP*, 126(939):476, May 2014. doi: 10.1086/676975. (Cited on pages: 27 and 123)

[382] M. A. McLaughlin and J. M. Cordes. Searches for Giant Pulses from Extragalactic Pulsars. *ApJ*, 596(2):982–996, October 2003. doi: 10.1086/378232. (Cited on pages: 104, 151, and 181)

[383] S. Mereghetti and L. Stella. The Very Low Mass X-Ray Binary Pulsars: A New Class of Sources? *ApJL*, 442:L17, March 1995. doi: 10.1086/187805. (Cited on page: 36)

[384] S. Mereghetti, D. Götz, A. von Kienlin, A. Rau, G. Lichti, G. Weidenspointner, and P. Jean. The First Giant Flare from SGR 1806–20: Observations

Using the Anticoincidence Shield of the Spectrometer on INTEGRAL. *ApJL*, 624(2):L105–L108, May 2005. doi: 10.1086/430669. (Cited on page: 37)

[385] S. Mereghetti, V. Savchenko, C. Ferrigno, D. Götz, M. Rigoselli, A. Tiengo, A. Bazzano, E. Bozzo, A. Coleiro, T. J. L. Courvoisier, M. Doyle, A. Goldwurm, L. Hanlon, E. Jourdain, A. von Kienlin, A. Lutovinov, A. Martin-Carrillo, S. Molkov, L. Natalucci, F. Onori, F. Panessa, J. Rodi, J. Rodriguez, C. Sánchez-Fernández, R. Sunyaev, and P. Ubertini. INTEGRAL Discovery of a Burst with Associated Radio Emission from the Magnetar SGR 1935+2154. *ApJL*, 898(2):L29, August 2020. doi: 10.3847/2041-8213/aba2cf. (Cited on pages: 143 and 157)

[386] S. Mereghetti, V. Savchenko, D. Gotz, J. Rodriguez, L. Ducci, C. Ferrigno, E. Bozzo, J. Borkowski, and A. Bazzano. INTEGRAL IBIS and SPI-ACS Detection of a Hard X-Ray Counterpart of the Radio Burst from SGR 1935+2154. *The Astronomer's Telegram*, #13685:1, April 2020. (Cited on page: 157)

[387] B. D. Metzger, E. Berger, and B. Margalit. Millisecond Magnetar Birth Connects FRB 121102 to Superluminous Supernovae and Long-duration Gamma-Ray Bursts. *ApJ*, 841(1):14, May 2017. doi: 10.3847/1538-4357/aa633d. (Cited on pages: 121, 157, and 178)

[388] B. D. Metzger, B. Margalit, and L. Sironi. Fast Radio Bursts as Synchrotron Maser Emission from Decelerating Relativistic Blast Waves. *MNRAS*, 485(3):4091–4106, May 2019. doi: 10.1093/mnras/stz700. (Cited on page: 173)

[389] D. Michilli and J. W. T. Hessels. SpS: Single-pulse Searcher, June 2018. (Cited on page: 166)

[390] D. Michilli, J. W. T. Hessels, R. J. Lyon, C. M. Tan, C. Bassa, S. Cooper, V. I. Kondratiev, S. Sanidas, B. W. Stappers, and J. van Leeuwen. Single-pulse Classifier for the LOFAR Tied-Array All-Sky Survey. *MNRAS*, 480(3):3457–3467, November 2018. doi: 10.1093/mnras/sty2072. (Cited on page: 166)

[391] D. Michilli, A. Seymour, J. W. T. Hessels, L. G. Spitler, V. Gajjar, A. M. Archibald, G. C. Bower, S. Chatterjee, J. M. Cordes, K. Gourdji, G. H. Heald, V. M. Kaspi, C. J. Law, C. Sobey, E. A. K. Adams, C. G. Bassa, S. Bogdanov, C. Brinkman, P. Demorest, F. Fernand ez, G. Hellbourg, T. J. W. Lazio, R. S. Lynch, N. Maddox, B. Marcote, M. A. McLaughlin, Z. Paragi, S. M. Ransom, P. Scholz, A. P. V. Siemion, S. P. Tendulkar, P. van Rooy, R. S. Wharton, and D. Whitlow. An Extreme Magneto-ionic Environment Associated with the Fast Radio Burst Source FRB 121102. *Nature*, 553(7687):182–185, January 2018. doi: 10.1038/nature25149. (Cited on pages: 121, 122, 157, 158, 164, 178, 179, and 206)

[392] J. Middleditch and J. Kristian. A Search for Young, Luminous Optical Pulsars in Extragalactic Supernova Remnants. *ApJ*, 279:157–161, April 1984. doi: 10.1086/161876. (Cited on page: 232)

[393] A. H. Minter, F. Camilo, S. M. Ransom, J. P. Halpern, and N. Zimmerman. Neutral Hydrogen Absorption Toward XTE J1810–197: The Distance to a Radio-emitting Magnetar. *ApJ*, 676(2):1189–1199, April 2008. doi: 10.1086/529005. (Cited on pages: 132, 135, and 153)

[394] V. Morello, E. D. Barr, B. W. Stappers, E. F. Keane, and A. G. Lyne. Optimal Periodicity Searching: Revisiting the Fast Folding Algorithm for Large-scale Pulsar Surveys. *MNRAS*, 497(4):4654–4671, August 2020. doi: 10.1093/mnras/staa2291. (Cited on page: 221)

[395] E. Moreno, G. Koenigsberger, and O. Toledano. Line Profile Variability from Tidal Interactions in Binary Systems. *A&A*, 437(2):641–656, July 2005. doi: 10.1051/0004-6361:20041995. (Cited on page: 324)

[396] K. Mori, E. V. Gotthelf, S. Zhang, H. An, F. K. Baganoff, N. M. Barrière, A. M. Beloborodov, S. E. Boggs, F. E. Christensen, W. W. Craig, F. Dufour, B. W. Grefenstette, C. J. Hailey, F. A. Harrison, J. Hong, V. M. Kaspi, J. A. Kennea, K. K. Madsen, C. B. Markwardt, M. Nynka, D. Stern, J. A. Tomsick, and W. W. Zhang. NuSTAR Discovery of a 3.76 S Transient Magnetar Near Sagittarius A*. *ApJL*, 770(2):L23, June 2013. doi: 10.1088/2041-8205/770/2/L23. (Cited on pages: 89 and 258)

[397] V. S. Morozova, B. J. Ahmedov, and O. Zanotti. Explaining Radio Emission of Magnetars via Rotating and Oscillating Magnetospheres of Neutron Stars. *MNRAS*, 419(3):2147–2155, January 2012. doi: 10.1111/j.1365-2966.2011.19866.x. (Cited on page: 85)

[398] D. Morris, M. Kramer, C. Thum, R. Wielebinski, M. Grewing, J. Penalver, A. Jessner, G. Butin, and W. Brunswig. Pulsar Detection at 87 GHz. *A&A*, 322:L17–L20, June 1997. (Cited on page: 120)

[399] D. C. Morris, R. K. Smith, C. B. Markwardt, R. F. Mushotzky, J. Tueller, T. R. Kallman, and K. S. Dhuga. Suzaku Observations of Four Heavily Absorbed HMXBs. *ApJ*, 699(1):892–901, July 2009. doi: 10.1088/0004-637X/699/1/892. (Cited on pages: 282 and 316)

[400] D. J. Mullan. Corotating Interaction Regions in Stellar Winds. *ApJ*, 283:303–312, August 1984. doi: 10.1086/162307. (Cited on page: 325)

[401] E. Nespoli, J. Fabregat, and R. E. Mennickent. K-Band Spectroscopy of IGR J16493–4348. *The Astronomer's Telegram*, 1396:1, February 2008. (Cited on page: 282)

[402] E. Nespoli, J. Fabregat, and R. E. Mennickent. Unveiling the Nature of IGR J16493–4348 with IR Spectroscopy. *A&A*, 516:A106, June 2010. doi: 10.1051/0004-6361/201014348. (Cited on pages: 282, 314, 315, 316, and 323)

[403] C. Ng, D. J. Champion, M. Bailes, E. D. Barr, S. D. Bates, N. D. R. Bhat, M. Burgay, S. Burke-Spolaor, C. M. L. Flynn, A. Jameson, S. Johnston, M. J. Keith, M. Kramer, L. Levin, E. Petroff, A. Possenti, B. W. Stappers, W. van Straten, C. Tiburzi, R. P. Eatough, and A. G. Lyne. The High Time Resolution Universe Pulsar Survey - XII. Galactic Plane Acceleration Search and the Discovery of 60 Pulsars. *MNRAS*, 450(3):2922–2947, July 2015. doi: 10.1093/mnras/stv753. (Cited on pages: lvi and 278)

[404] C. Y. Ng and V. M. Kaspi. High Magnetic Field Rotation-powered Pulsars. In E. Göğüş, T. Belloni, and Ü. Ertan, editors, *Astrophysics of Neutron Stars 2010: A Conference in Honor of M. Ali Alpar*, volume 1379 of *American Institute of Physics Conference Series*, pages 60–69, September 2011. doi: 10.1063/1.3629486. (Cited on page: 83)

[405] K. Nimmo, J. W. T. Hessels, A. Keimpema, A. M. Archibald, J. M. Cordes, R. Karuppusamy, F. Kirsten, D. Z. Li, B. Marcote, and Z. Paragi. Highly Polarized Microstructure from the Repeating FRB 20180916B. *Nature Astronomy*, March 2021. doi: 10.1038/s41550-021-01321-3. (Cited on page: 177)

[406] G. I. Ogilvie and G. Dubus. Precessing Warped Accretion Discs in X-Ray Binaries. *MNRAS*, 320(4):485–503, February 2001. doi: 10.1046/j.1365-8711.2001.04011.x. (Cited on page: 324)

[407] K. Oh, M. Koss, C. B. Markwardt, K. Schawinski, W. H. Baumgartner, S. D. Barthelmy, S. B. Cenko, N. Gehrels, R. Mushotzky, A. Petulante, C. Ricci, A. Lien, and B. Trakhtenbrot. The 105-Month Swift-BAT All-sky Hard X-Ray Survey. *ApJS*, 235(1):4, March 2018. doi: 10.3847/1538-4365/aaa7fd. (Cited on page: 281)

[408] S. A. Olausen and V. M. Kaspi. The McGill Magnetar Catalog. *ApJS*, 212 (1):6, May 2014. doi: 10.1088/0067-0049/212/1/6. (Cited on pages: 84, 88, and 132)

[409] S. A. Olausen, W. W. Zhu, J. K. Vogel, V. M. Kaspi, A. G. Lyne, C. M. Espinoza, B. W. Stappers, R. N. Manchester, and M. A. McLaughlin. X-Ray Observations of High-B Radio Pulsars. *ApJ*, 764(1):1, February 2013. doi: 10.1088/0004-637X/764/1/1. (Cited on page: 37)

[410] R. M. O'Leary, M. D. Kistler, M. Kerr, and J. Dexter. Young Pulsars and the Galactic Center GeV Gamma-Ray Excess. *arXiv e-prints*, art. arXiv:1504.02477, Apr 2015. (Cited on page: 261)

[411] J. R. Oppenheimer and G. M. Volkoff. On Massive Neutron Cores. *Physical Review*, 55(4):374–381, February 1939. doi: 10.1103/PhysRev.55.374. (Cited on page: 3)

[412] F. Özel. Surface Emission from Neutron Stars and Implications for the Physics of Their Interiors. *Reports on Progress in Physics*, 76(1):016901, January 2013. doi: 10.1088/0034-4885/76/1/016901. (Cited on pages: 137 and 142)

[413] F. Pacini. Energy Emission from a Neutron Star. *Nature*, 216(5115):567–568, November 1967. doi: 10.1038/216567a0. (Cited on page: 5)

[414] D. M. Palmer. A Forest of Bursts from SGR 1935+2154. *The Astronomer's Telegram*, #13675:1, April 2020. (Cited on page: 157)

[415] D. M. Palmer, S. Barthelmy, N. Gehrels, R. M. Kippen, T. Cayton, C. Kouveliotou, D. Eichler, R. A. M. J. Wijers, P. M. Woods, J. Granot, Y. E. Lyubarsky, E. Ramirez-Ruiz, L. Barbier, M. Chester, J. Cummings, E. E. Fenimore, M. H. Finger, B. M. Gaensler, D. Hullinger, H. Krimm, C. B. Markwardt, J. A. Nousek, A. Parsons, S. Patel, T. Sakamoto, G. Sato, M. Suzuki, and J. Tueller. A Giant γ-Ray Flare from the Magnetar SGR 1806–20. *Nature*, 434(7037):1107–1109, April 2005. doi: 10.1038/nature03525. (Cited on pages: 132 and 140)

[416] I. E. Papadakis and A. Lawrence. Improved Methods for Power Spectrum Modelling of Red Noise. *MNRAS*, 261:612, April 1993. doi: 10.1093/mnras/261.3.612. (Cited on page: 299)

[417] D. Parent, M. Kerr, P. R. den Hartog, M. G. Baring, M. E. DeCesar, C. M. Espinoza, E. V. Gotthelf, A. K. Harding, S. Johnston, V. M. Kaspi, M. Livingstone, R. W. Romani, B. W. Stappers, K. Watters, P. Weltevrede, A. A. Abdo, M. Burgay, F. Camilo, H. A. Craig, P. C. C. Freire, F. Giordano, L. Guillemot, G. Hobbs, M. Keith, M. Kramer, A. G. Lyne, R. N. Manchester, A. Noutsos, A. Possenti, and D. A. Smith. Observations of Energetic High Magnetic Field Pulsars with the Fermi Large Area Telescope. *ApJ*, 743:170, December 2011. doi: 10.1088/0004-637X/743/2/170. (Cited on pages: 76 and 84)

[418] E. Parent, V. M. Kaspi, S. M. Ransom, M. Krasteva, C. Patel, P. Scholz, A. Brazier, M. A. McLaughlin, M. Boyce, W. W. Zhu, Z. Pleunis, B. Allen, S. Bogdanov, K. Caballero, F. Camilo, R. Camuccio, S. Chatterjee, J. M. Cordes, F. Crawford, J. S. Deneva, R. Ferdman, P. C. C. Freire, J. W. T. Hessels, F. A. Jenet, B. Knispel, P. Lazarus, J. van Leeuwen, A. G. Lyne, R. Lynch, A. Seymour, X. Siemens, I. H. Stairs, K. Stovall, and J. Swiggum. The Implementation of a Fast-folding Pipeline for Long-period Pulsar Searching in the PALFA Survey. *ApJ*, 861(1):44, July 2018. doi: 10.3847/1538-4357/aac5f0. (Cited on page: 224)

[419] A. B. Pearlman, W. A. Majid, S. Horiuchi, J. Kocz, J. Lippuner, and T. A. Prince. Magnetar-like Spectral Index Flattening of the High Magnetic Field

Pulsar PSR J1119–6127. *The Astronomer's Telegram*, 9870:1, Dec 2016. (Cited on pages: xiv and 52)

[420] A. B. Pearlman, W. A. Majid, S. Horiuchi, J. Kocz, J. Lippuner, and T. A. Prince. Magnetar-like Activity and Radio Emission Variability from the High Magnetic Field Pulsar PSR J1119–6127. In *AAS/High Energy Astrophysics Division #16*, AAS/High Energy Astrophysics Division, page 109.17, Aug 2017. (Cited on page: 52)

[421] A. B. Pearlman, W. A. Majid, T. A. Prince, S. Horiuchi, J. Kocz, T. J. W. Lazio, and C. J. Naudet. High Frequency Radio Observations of the Reactivated Magnetar PSR J1622–4950. *The Astronomer's Telegram*, 10581:1, Jul 2017. (Cited on pages: xiv and 52)

[422] A. B. Pearlman, W. A. Majid, T. A. Prince, J. Kocz, and S. Horiuchi. Pulse Morphology of the Galactic Center Magnetar PSR J1745–2900. *ApJ*, 866(2): 160, October 2018. doi: 10.3847/1538-4357/aade4d. (Cited on pages: xiii, 52, 87, 132, 150, 153, 157, 158, 165, 173, 178, 182, 186, 205, and 273)

[423] A. B. Pearlman, J. B. Coley, R. H. D. Corbet, and K. Pottschmidt. The Orbital Parameters of the Eclipsing High-mass X-Ray Binary Pulsar IGR J16493–4348 from Pulsar Timing. *ApJ*, 873(1):86, March 2019. doi: 10.3847/1538-4357/aaf001. (Cited on pages: xiii and 280)

[424] A. B. Pearlman, W. A. Majid, and T. A. Prince. Observations of Radio Magnetars with the Deep Space Network. *Advances in Astronomy*, 2019: 6325183, June 2019. doi: 10.1155/2019/6325183. (Cited on pages: xiii, xxv, 35, 51, 52, 72, 133, 144, 165, 180, 182, and 263)

[425] A. B. Pearlman, W. A. Majid, T. A. Prince, C. J. Naudet, J. W. T. Hessels, K. Nimmo, J. Kocz, and S. Horiuchi. Detection of Multiple Radio Bursts from FRB 121102 Using the Deep Space Network. *The Astronomer's Telegram*, #13235, October 2019. (Cited on pages: xv, 52, 164, 179, and 182)

[426] A. B. Pearlman, W. A. Majid, T. A. Prince, K. Bansal, S. Horiuchi, R. Stephenson, C. J. Naudet, and J. Kocz. A Search for Radio Bursts and Periodic Radio Emission from SGR 1830–0645 Using the Deep Space Network. *The Astronomer's Telegram*, 14102:1, October 2020. (Cited on pages: xv and 52)

[427] A. B. Pearlman, W. A. Majid, T. A. Prince, C. J. Naudet, K. Bansal, and S. Horiuchi. Detection of Radio Pulsations from Swift J1818.0–1607 Simultaneously at 8.3 and 31.9 GHz with the Deep Space Network. *The Astronomer's Telegram*, 13966:1, August 2020. (Cited on pages: xv and 52)

[428] A. B. Pearlman, W. A. Majid, T. A. Prince, C. J. Naudet, and J. Kocz. A Search for Radio Bursts and Periodic Emission from SGR 1935+2154 at High Radio Frequencies Using the Deep Space Network. *The Astronomer's Telegram*, 13713:1, May 2020. (Cited on pages: xv and 52)

[429] A. B. Pearlman, W. A. Majid, T. A. Prince, K. Nimmo, J. W. T. Hessels, C. J. Naudet, and J. Kocz. Multiwavelength Radio Observations of Two Repeating Fast Radio Burst Sources: FRB 121102 and FRB 180916.J0158+65. *ApJL*, 905(2):arXiv:2009.13559, December 2020. doi: 10.3847/2041-8213/abca31. (Cited on pages: xiii, 41, 52, and 176)

[430] A. B. Pearlman, W. A. Majid, T. A. Prince, P. S. Ray, J. Kocz, S. Horiuchi, C. J. Naudet, T. Güver, T. Enoto, Z. Arzoumanian, K. C. Gendreau, and W. C. G. Ho. Bright X-Ray and Radio Pulses from a Recently Reactivated Magnetar. *arXiv e-prints*, art. arXiv:2005.08410, May 2020. (Cited on pages: xiii, 52, 131, 178, 182, 186, and 205)

[431] U.-L. Pen and L. Connor. Local Circumnuclear Magnetar Solution to Extragalactic Fast Radio Bursts. *ApJ*, 807(2):179, July 2015. doi: 10.1088/0004-637X/807/2/179. (Cited on pages: 121 and 157)

[432] T. T. Pennucci, A. Possenti, P. Esposito, N. Rea, D. Haggard, F. K. Baganoff, M. Burgay, F. Coti Zelati, G. L. Israel, and A. Minter. Simultaneous Multi-band Radio and X-Ray Observations of the Galactic Center Magnetar SGR 1745–2900. *ApJ*, 808(1):81, July 2015. doi: 10.1088/0004-637X/808/1/81. (Cited on pages: 95, 96, 120, and 121)

[433] R. Perna and E. V. Gotthelf. Constraints on the Emission and Viewing Geometry of the Transient Anomalous X-Ray Pulsar XTE J1810–197. *ApJ*, 681(1):522–529, July 2008. doi: 10.1086/588211. (Cited on page: 139)

[434] E. Petroff, E. F. Keane, E. D. Barr, J. E. Reynolds, J. Sarkissian, P. G. Edwards, J. Stevens, C. Brem, A. Jameson, S. Burke-Spolaor, S. Johnston, N. D. R. Bhat, P. C. S. Kudale, and S. Bhandari. Identifying the Source of Perytons at the Parkes Radio Telescope. *MNRAS*, 451(4):3933–3940, August 2015. doi: 10.1093/mnras/stv1242. (Cited on page: 41)

[435] E. Petroff, E. D. Barr, A. Jameson, E. F. Keane, M. Bailes, M. Kramer, V. Morello, D. Tabbara, and W. van Straten. FRBCAT: The Fast Radio Burst Catalogue. *PASA*, 33:e045, September 2016. doi: 10.1017/pasa.2016.35. (Cited on pages: xxv, xxvi, 40, 43, 44, 157, 163, and 177)

[436] E. Petroff, J. W. T. Hessels, and D. R. Lorimer. Fast Radio Bursts. *A&A Rev.*, 27(1):4, May 2019. doi: 10.1007/s00159-019-0116-6. (Cited on pages: 40, 157, 163, and 177)

[437] J. Petrović, P. D. Serpico, and G. Zaharijas. Millisecond Pulsars and the Galactic Center Gamma-Ray Excess: The Importance of Luminosity Function and Secondary Emission. *JCAP*, 2015(2):023, Feb 2015. doi: 10.1088/1475-7516/2015/02/023. (Cited on page: 261)

[438] J. A. Petterson. Hercules X–1: A Neutron Star with a Twisted Accretion Disk? *ApJL*, 201:L61–L64, October 1975. doi: 10.1086/181942. (Cited on page: 324)

[439] E. Pfahl and A. Loeb. Probing the Spacetime Around Sagittarius A* with Radio Pulsars. *ApJ*, 615(1):253–258, Nov 2004. doi: 10.1086/423975. (Cited on pages: 256, 257, 261, and 262)

[440] M. Pilia, M. Burgay, A. Possenti, A. Ridolfi, V. Gajjar, A. Corongiu, D. Perrodin, G. Bernardi, G. Naldi, G. Pupillo, F. Ambrosino, G. Bianchi, A. Burtovoi, P. Casella, C. Casentini, M. Cecconi, C. Ferrigno, M. Fiori, K. C. Gendreau, A. Ghedina, G. Naletto, L. Nicastro, P. Ochner, E. Palazzi, F. Panessa, A. Papitto, C. Pittori, N. Rea, G. A. R. Castillo, V. Savchenko, G. Setti, M. Tavani, A. Trois, M. Trudu, M. Turatto, A. Ursi, F. Verrecchia, and L. Zampieri. The Lowest-frequency Fast Radio Bursts: Sardinia Radio Telescope Detection of the Periodic FRB 180916 at 328 MHz. *ApJL*, 896(2):L40, June 2020. doi: 10.3847/2041-8213/ab96c0. (Cited on pages: xliii, 179, 190, 193, 195, and 199)

[441] J. D. H. Pilkington, A. Hewish, S. J. Bell, and T. W. Cole. Observations of Some Further Pulsed Radio Sources. *Nature*, 218(5137):126–129, April 1968. doi: 10.1038/218126a0. (Cited on page: 5)

[442] D. Pines and M. A. Alpar. Superfluidity in Neutron Stars. *Nature*, 316(6023): 27–32, July 1985. doi: 10.1038/316027a0. (Cited on page: 38)

[443] F. Pintore, S. Mereghetti, P. Esposito, R. Turolla, A. Tiengo, N. Rea, F. Bernardini, and G. L. Israel. The 11 Yr of Low Activity of the Magnetar XTE J1810–197. *MNRAS*, 483(3):3832–3838, March 2019. doi: 10.1093/mnras/sty3378. (Cited on page: 133)

[444] E. Platts, A. Weltman, A. Walters, S. P. Tendulkar, J. E. B. Gordin, and S. Kandhai. A Living Theory Catalogue for Fast Radio Bursts. *Phys. Rep.*, 821:1–27, August 2019. doi: 10.1016/j.physrep.2019.06.003. (Cited on pages: 42, 157, 163, and 178)

[445] N. Pol, M. T. Lam, M. A. McLaughlin, T. J. W. Lazio, and J. M. Cordes. Estimates of Fast Radio Burst Dispersion Measures from Cosmological Simulations. *ApJ*, 886(2):135, December 2019. doi: 10.3847/1538-4357/ab4c2f. (Cited on pages: xxvii and 48)

[446] S. B. Popov and K. A. Postnov. Hyperflares of SGRs as an Engine for Millisecond Extragalactic Radio Bursts. In H. A. Harutyunian, A. M. Mickaelian, and Y. Terzian, editors, *Evolution of Cosmic Objects through their Physical Activity*, pages 129–132, November 2010. (Cited on page: 42)

[447] K. Postnov, N. Shakura, R. Staubert, A. Kochetkova, D. Klochkov, and J. Wilms. Variable Neutron Star Free Precession in Hercules X–1 from Evolution of RXTE X-Ray Pulse Profiles with Phase of the 35-d Cycle. *MNRAS*, 435(2):1147–1164, October 2013. doi: 10.1093/mnras/stt1363. (Cited on page: 324)

[448] P. Predehl and J. H. M. M. Schmitt. X-Raying the Interstellar Medium: ROSAT Observations of Dust Scattering Halos. *A&A*, 500:459–475, January 1995. (Cited on pages: 316 and 320)

[449] J. X. Prochaska, J.-P. Macquart, M. McQuinn, S. Simha, R. M. Shannon, C. K. Day, L. Marnoch, S. Ryder, A. Deller, K. W. Bannister, S. Bhandari, R. Bordoloi, J. Bunton, H. Cho, C. Flynn, E. K. Mahony, C. Phillips, H. Qiu, and N. Tejos. The Low Density and Magnetization of a Massive Galaxy Halo Exposed by a Fast Radio Burst. *Science*, 366(6462):231–234, October 2019. doi: 10.1126/science.aay0073. (Cited on pages: 157, 163, and 177)

[450] D. Psaltis, N. Wex, and M. Kramer. A Quantitative Test of the No-hair Theorem with Sgr A* Using Stars, Pulsars, and the Event Horizon Telescope. *ApJ*, 818(2):121, February 2016. doi: 10.3847/0004-637X/818/2/121. (Cited on page: 262)

[451] K. M. Rajwade, D. R. Lorimer, and L. D. Anderson. Detecting Pulsars in the Galactic Centre. *MNRAS*, 471(1):730–739, October 2017. doi: 10.1093/mnras/stx1661. (Cited on page: 91)

[452] K. M. Rajwade, M. B. Mickaliger, B. W. Stappers, C. G. Bassa, R. P. Breton, A. Karastergiou, and E. F. Keane. Limits on Absorption from a 332-MHz Survey for Fast Radio Bursts. *MNRAS*, 493(3):4418–4427, April 2020. doi: 10.1093/mnras/staa616. (Cited on page: 180)

[453] K. M. Rajwade, M. B. Mickaliger, B. W. Stappers, V. Morello, D. Agarwal, C. G. Bassa, R. P. Breton, M. Caleb, A. Karastergiou, E. F. Keane, and D. R. Lorimer. Possible Periodic Activity in the Repeating FRB 121102. *MNRAS*, 495(4):3551–3558, May 2020. doi: 10.1093/mnras/staa1237. (Cited on pages: xi, 179, 205, and 206)

[454] S. Ranasinghe, D. A. Leahy, and W. Tian. New Distances to Four Supernova Remnants. *Open Physics Journal*, 4:1–13, June 2018. doi: 10.2174/1874843001804010001. (Cited on page: 158)

[455] J. M. Rankin. Toward an Empirical Theory of Pulsar Emission. VI. The Geometry of the Conal Emission Region. *ApJ*, 405:285, March 1993. doi: 10.1086/172361. (Cited on pages: xxii and 12)

[456] S. M. Ransom. *New Search Techniques for Binary Pulsars*. PhD thesis, Harvard University, January 2001. (Cited on pages: 55, 78, 79, 80, 91, 92, 145, 150, and 186)

[457] S. M. Ransom, S. S. Eikenberry, and J. Middleditch. Fourier Techniques for Very Long Astrophysical Time-series Analysis. *AJ*, 124(3):1788–1809, September 2002. doi: 10.1086/342285. (Cited on pages: 228, 232, and 233)

[458] S. M. Ransom, J. M. Cordes, and S. S. Eikenberry. A New Search Technique for Short Orbital Period Binary Pulsars. *ApJ*, 589(2):911–920, June 2003. doi: 10.1086/374806. (Cited on pages: 228, 232, and 244)

[459] S. M. Ransom, J. W. T. Hessels, I. H. Stairs, P. C. C. Freire, F. Camilo, V. M. Kaspi, and D. L. Kaplan. Twenty-One Millisecond Pulsars in Terzan 5 Using the Green Bank Telescope. *Science*, 307(5711):892–896, February 2005. doi: 10.1126/science.1108632. (Cited on page: 241)

[460] V. Ravi. The Prevalence of Repeating Fast Radio Bursts. *Nature Astronomy*, 3: 928–931, July 2019. doi: 10.1038/s41550-019-0831-y. (Cited on pages: 164 and 177)

[461] V. Ravi and A. Loeb. Explaining the Statistical Properties of Fast Radio Bursts with Suppressed Low-frequency Emission. *ApJ*, 874(1):72, March 2019. doi: 10.3847/1538-4357/ab0748. (Cited on pages: 179 and 180)

[462] V. Ravi, M. Catha, L. D'Addario, S. G. Djorgovski, G. Hallinan, R. Hobbs, J. Kocz, S. R. Kulkarni, J. Shi, H. K. Vedantham, S. Weinreb, and D. P. Woody. A Fast Radio Burst Localized to a Massive Galaxy. *Nature*, 572 (7769):352–354, August 2019. doi: 10.1038/s41586-019-1389-7. (Cited on pages: 157, 163, and 177)

[463] N. Rea, G. L. Israel, R. Turolla, P. Esposito, S. Mereghetti, D. Götz, S. Zane, A. Tiengo, K. Hurley, M. Feroci, M. Still, V. Yershov, C. Winkler, R. Perna, F. Bernardini, P. Ubertini, L. Stella, S. Campana, M. van der Klis, and P. Woods. The First Outburst of the New Magnetar Candidate SGR 0501+4516. *MNRAS*, 396(4):2419–2432, July 2009. doi: 10.1111/j.1365-2966.2009.14920.x. (Cited on page: 36)

[464] N. Rea, P. Esposito, R. Turolla, G. L. Israel, S. Zane, L. Stella, S. Mereghetti, A. Tiengo, D. Götz, E. Göğüş, and C. Kouveliotou. A Low-magnetic-Field Soft Gamma Repeater. *Science*, 330(6006):944, November 2010. doi: 10. 1126/science.1196088. (Cited on page: 39)

[465] N. Rea, P. Esposito, J. A. Pons, R. Turolla, D. F. Torres, G. L. Israel, A. Possenti, M. Burgay, D. Viganò, A. Papitto, R. Perna, L. Stella, G. Ponti, F. K. Baganoff, D. Haggard, A. Camero-Arranz, S. Zane, A. Minter, S. Mereghetti, A. Tiengo, R. Schödel, M. Feroci, R. Mignani, and D. Götz. A Strongly Magnetized Pulsar Within the Grasp of the Milky Way's Supermassive Black Hole. *ApJL*, 775(2):L34, October 2013. doi: 10.1088/2041-8205/775/2/L34. (Cited on page: 89)

[466] N. Rea, G. L. Israel, J. A. Pons, R. Turolla, D. Viganò, S. Zane, P. Esposito, R. Perna, A. Papitto, G. Terreran, A. Tiengo, D. Salvetti, J. M. Girart, A. Palau, A. Possenti, M. Burgay, E. Göğüş, G. A. Caliandro, C. Kouveliotou, D. Götz, R. P. Mignani, E. Ratti, and L. Stella. The Outburst Decay of the Low

Magnetic Field Magnetar SGR 0418+5729. *ApJ*, 770(1):65, June 2013. doi: 10.1088/0004-637X/770/1/65. (Cited on page: 39)

[467] B. J. Rickett. Interstellar Scattering and Scintillation of Radio Waves. *ARA&A*, 15:479–504, January 1977. doi: 10.1146/annurev.aa.15.090177.002403. (Cited on page: 25)

[468] B. J. Rickett. Radio Propagation Through the Turbulent Interstellar Plasma. *ARA&A*, 28:561–605, January 1990. doi: 10.1146/annurev.aa.28.090190.003021. (Cited on page: 32)

[469] G. H. Rieke and M. J. Lebofsky. The Interstellar Extinction Law from 1 to 13 Microns. *ApJ*, 288:618–621, January 1985. doi: 10.1086/162827. (Cited on pages: 315, 316, and 320)

[470] P. Romano. Seven Years with the Swift Supergiant Fast X-Ray Transients Project. *JHEAp*, 7:126–136, September 2015. doi: 10.1016/j.jheap.2015.04.008. (Cited on page: 282)

[471] K. R. Sand, V. Gajjar, M. Pilia, S. Kudale, B. C. Joshi, V. S. Jagtap, A. Ray, A. Deshpande, B. Bijay, B. Dey, B. Kalita, D. Bandyopadhyay, D. Jena, D. Bhattacharya, G. Waratkar, G. Wagle, J. Singha, M. Bagchi, M. P. Surnis, S. Bhat, S. Mishra, S. Konar, and Y. Maan. Low-frequency Detection of FRB180916 with the uGMRT. *The Astronomer's Telegram*, #13781, June 2020. (Cited on pages: xliii, 179, 190, 193, 195, and 199)

[472] J. D. Scargle. Studies in Astronomical Time Series Analysis. II. Statistical Aspects of Spectral Analysis of Unevenly Spaced Data. *ApJ*, 263:835–853, December 1982. doi: 10.1086/160554. (Cited on page: 290)

[473] J. D. Scargle. Studies in Astronomical Time Series Analysis. III. Fourier Transforms, Autocorrelation Functions, and Cross-correlation Functions of Unevenly Spaced Data. *ApJ*, 343:874, August 1989. doi: 10.1086/167757. (Cited on page: 289)

[474] P. A. G. Scheuer. Amplitude Variations in Pulsed Radio Sources. *Nature*, 218(5145):920–922, June 1968. doi: 10.1038/218920a0. (Cited on page: 25)

[475] D. H. F. M. Schnitzeler, R. P. Eatough, K. Ferrière, M. Kramer, K. J. Lee, A. Noutsos, and R. M. Shannon. Radio Polarimetry of Galactic Centre Pulsars. *MNRAS*, 459(3):3005–3011, July 2016. doi: 10.1093/mnras/stw841. (Cited on page: 89)

[476] P. Scholz and Chime/Frb Collaboration. A Bright Millisecond-timescale Radio Burst from the Direction of the Galactic Magnetar SGR 1935+2154. *The Astronomer's Telegram*, #13681:1, April 2020. (Cited on page: 157)

[477] P. Scholz and V. M. Kaspi. The 2009 Outburst of Magnetar 1E 1547–5408: Persistent Radiative and Burst Properties. *ApJ*, 739(2):94, October 2011. doi: 10.1088/0004-637X/739/2/94. (Cited on page: 37)

[478] P. Scholz, V. M. Kaspi, and A. Cumming. The Long-term Post-outburst Spin Down and Flux Relaxation of Magnetar Swift J1822.3–1606. *ApJ*, 786(1): 62, May 2014. doi: 10.1088/0004-637X/786/1/62. (Cited on page: 38)

[479] P. Scholz, L. G. Spitler, J. W. T. Hessels, S. Chatterjee, J. M. Cordes, V. M. Kaspi, R. S. Wharton, C. G. Bassa, S. Bogdanov, F. Camilo, F. Crawford, J. Deneva, J. van Leeuwen, R. Lynch, E. C. Madsen, M. A. McLaughlin, M. Mickaliger, E. Parent, C. Patel, S. M. Ransom, A. Seymour, I. H. Stairs, B. W. Stappers, and S. P. Tendulkar. The Repeating Fast Radio Burst FRB 121102: Multi-wavelength Observations and Additional Bursts. *ApJ*, 833(2): 177, Dec 2016. doi: 10.3847/1538-4357/833/2/177. (Cited on pages: 41, 164, 167, 168, 178, and 192)

[480] P. Scholz, S. Bogdanov, J. W. T. Hessels, R. S. Lynch, L. G. Spitler, C. G. Bassa, G. C. Bower, S. Burke-Spolaor, B. J. Butler, S. Chatterjee, J. M. Cordes, K. Gourdji, V. M. Kaspi, C. J. Law, B. Marcote, M. A. McLaughlin, D. Michilli, Z. Paragi, S. M. Ransom, A. Seymour, S. P. Tendulkar, and R. S. Wharton. Simultaneous X-Ray, Gamma-Ray, and Radio Observations of the Repeating Fast Radio Burst FRB 121102. *ApJ*, 846(1):80, Sep 2017. doi: 10.3847/1538-4357/aa8456. (Cited on pages: 163, 164, and 179)

[481] P. Scholz, F. Camilo, J. Sarkissian, J. E. Reynolds, L. Levin, M. Bailes, M. Burgay, S. Johnston, M. Kramer, and A. Possenti. Spin-down Evolution and Radio Disappearance of the Magnetar PSR J1622–4950. *ApJ*, 841(2): 126, June 2017. doi: 10.3847/1538-4357/aa73de. (Cited on pages: 38, 121, 146, and 205)

[482] P. Scholz, A. Cook, M. Cruces, J. W. T. Hessels, V. M. Kaspi, W. A. Majid, A. Naidu, A. B. Pearlman, L. G. Spitler, K. M. Bandura, M. Bhardwaj, T. Cassanelli, P. Chawla, B. M. Gaensler, D. C. Good, A. Josephy, R. Karuppusamy, A. Keimpema, A. Y. Kirichenko, F. Kirsten, J. Kocz, C. Leung, B. Marcote, K. Masui, J. Mena-Parra, M. Merryfield, D. Michilli, C. J. Naudet, K. Nimmo, Z. Pleunis, T. A. Prince, M. Rafiei-Ravandi, M. Rahman, K. Shin, K. M. Smith, I. H. Stairs, S. P. Tendulkar, and K. Vanderlinde. Simultaneous X-Ray and Radio Observations of the Repeating Fast Radio Burst FRB 180916.J0158+65. *ApJ*, 901(2):165, October 2020. doi: 10.3847/1538-4357/abb1a8. (Cited on pages: xiv, 52, 163, 179, 181, 185, 190, 193, 195, and 332)

[483] A. Schwarzenberg-Czerny. On the Advantage of Using Analysis of Variance for Period Search. *MNRAS*, 241:153–165, November 1989. doi: 10.1093/mnras/241.2.153. (Cited on page: 302)

[484] S. C. Searle, R. K. Prinja, D. Massa, and R. Ryans. Quantitative Studies of the Optical and UV Spectra of Galactic Early B Supergiants. I. Fundamental Parameters. *A&A*, 481(3):777–797, April 2008. doi: 10.1051/0004-6361:20077125. (Cited on pages: lxi, 313, 314, 315, 318, 320, and 321)

[485] J. H. Seiradakis, W. Reich, R. Wielebinski, A. N. Lasenby, and F. Yusef-Zadeh. Radio Continuum Observations of the Galactic Centre at 4.75 and 10.7 GHz. *A&AS*, 81:291–302, Dec 1989. (Cited on pages: lii and 257)

[486] J. F. Sepinsky, B. Willems, V. Kalogera, and F. A. Rasio. Interacting Binaries with Eccentric Orbits. III. Orbital Evolution Due to Direct Impact and Self-accretion. *ApJ*, 724(1):546–558, November 2010. doi: 10.1088/0004-637X/724/1/546. (Cited on page: 314)

[487] M. Serylak, B. W. Stappers, P. Weltevrede, M. Kramer, A. Jessner, A. G. Lyne, C. A. Jordan, K. Lazaridis, and J. A. Zensus. Simultaneous Multifrequency Single-pulse Properties of AXP XTE J1810–197. *MNRAS*, 394(1):295–308, March 2009. doi: 10.1111/j.1365-2966.2008.14260.x. (Cited on pages: 106, 120, and 152)

[488] F. D. Seward, P. A. Charles, and A. P. Smale. A 6 Second Periodic X-Ray Source in Carina. *ApJ*, 305:814, June 1986. doi: 10.1086/164294. (Cited on page: 36)

[489] A. Seymour, D. Michilli, and Z. Pleunis. DM_phase: Algorithm for Correcting Dispersion of Radio Signals, October 2019. (Cited on page: 166)

[490] B. C. Seymour and K. Yagi. Probing Massive Scalar and Vector Fields with Binary Pulsars. *Phys. Rev. D*, 102(10):104003, November 2020. doi: 10.1103/PhysRevD.102.104003. (Cited on page: 262)

[491] R. M. Shannon and S. Johnston. Radio Properties of the Magnetar Near Sagittarius A* from Observations with the Australia Telescope Compact Array. *MNRAS*, 435:L29–L32, August 2013. doi: 10.1093/mnrasl/slt088. (Cited on pages: 84, 88, 89, and 95)

[492] R. M. Shannon, J. P. Macquart, K. W. Bannister, R. D. Ekers, C. W. James, S. Osłowski, H. Qiu, M. Sammons, A. W. Hotan, M. A. Voronkov, R. J. Beresford, M. Brothers, A. J. Brown, J. D. Bunton, A. P. Chippendale, C. Haskins, M. Leach, M. Marquarding, D. McConnell, M. A. Pilawa, E. M. Sadler, E. R. Troup, J. Tuthill, M. T. Whiting, J. R. Allison, C. S. Anderson, M. E. Bell, J. D. Collier, G. Gürkan, G. Heald, and C. J. Riseley. The Dispersion-Brightness Relation for Fast Radio Bursts from a Wide-field Survey. *Nature*, 562(7727):386–390, October 2018. doi: 10.1038/s41586-018-0588-y. (Cited on pages: 40 and 177)

[493] S. L. Shapiro, S. A. Teukolsky, and I. Wasserman. Implications of the Millisecond Pulsar for Neutron Star Models. *ApJ*, 272:702–707, September 1983. doi: 10.1086/161332. (Cited on page: 7)

[494] A. Siemion, M. Bailes, G. Bower, J. Chennamangalam, J. Cordes, P. Demorest, J. Deneva, G. Desvignes, J. Ford, D. Frail, G. Jones, M. Kramer, J. Lazio, D. Lorimer, M. McLaughlin, S. Ransom, A. Roshi, M. Wagner, D. Werthimer, and R. Wharton. A Search for Pulsars in the Central Parsecs of the Galactic Center. In J. van Leeuwen, editor, *Neutron Stars and Pulsars: Challenges and Opportunities after 80 years*, volume 291, pages 57–57, March 2013. doi: 10.1017/S1743921312023149. (Cited on pages: 88 and 257)

[495] J. H. Simonetti, M. Kavic, D. Minic, U. Surani, and V. Vijayan. A Precision Test for an Extra Spatial Dimension Using Black-Hole–Pulsar Binaries. *ApJL*, 737(2):L28, August 2011. doi: 10.1088/2041-8205/737/2/L28. (Cited on page: 263)

[496] L. L. Smarr and R. Blandford. The Binary Pulsar: Physical Processes, Possible Companions, and Evolutionary Histories. *ApJ*, 207:574–588, July 1976. doi: 10.1086/154524. (Cited on page: 5)

[497] L. G. Spitler, J. M. Cordes, J. W. T. Hessels, D. R. Lorimer, M. A. McLaughlin, S. Chatterjee, F. Crawford, J. S. Deneva, V. M. Kaspi, R. S. Wharton, B. Allen, S. Bogdanov, A. Brazier, F. Camilo, P. C. C. Freire, F. A. Jenet, C. Karako-Argaman, B. Knispel, P. Lazarus, K. J. Lee, J. van Leeuwen, R. Lynch, S. M. Ransom, P. Scholz, X. Siemens, I. H. Stairs, K. Stovall, J. K. Swiggum, A. Venkataraman, W. W. Zhu, C. Aulbert, and H. Fehrmann. Fast Radio Burst Discovered in the Arecibo Pulsar ALFA Survey. *ApJ*, 790(2): 101, Aug 2014. doi: 10.1088/0004-637X/790/2/101. (Cited on pages: 40, 164, 168, 177, and 205)

[498] L. G. Spitler, K. J. Lee, R. P. Eatough, M. Kramer, R. Karuppusamy, C. G. Bassa, I. Cognard, G. Desvignes, A. G. Lyne, B. W. Stappers, G. C. Bower, J. M. Cordes, D. J. Champion, and H. Falcke. Pulse Broadening Measurements from the Galactic Center Pulsar J1745–2900. *ApJL*, 780(1):L3, January 2014. doi: 10.1088/2041-8205/780/1/L3. (Cited on pages: 88, 89, 96, 112, 117, 118, 123, 258, 259, and 273)

[499] L. G. Spitler, P. Scholz, J. W. T. Hessels, S. Bogdanov, A. Brazier, F. Camilo, S. Chatterjee, J. M. Cordes, F. Crawford, J. Deneva, R. D. Ferdman, P. C. C. Freire, V. M. Kaspi, P. Lazarus, R. Lynch, E. C. Madsen, M. A. McLaughlin, C. Patel, S. M. Ransom, A. Seymour, I. H. Stairs, B. W. Stappers, J. van Leeuwen, and W. W. Zhu. A Repeating Fast Radio Burst. *Nature*, 531(7593): 202–205, Mar 2016. doi: 10.1038/nature17168. (Cited on pages: 41, 122, 158, 164, 167, 168, 177, 192, and 205)

[500] L. G. Spitler, W. Herrmann, G. C. Bower, S. Chatterjee, J. M. Cordes, J. W. T. Hessels, M. Kramer, D. Michilli, P. Scholz, A. Seymour, and A. P. V. Siemion. Detection of Bursts from FRB 121102 with the Effelsberg 100 M

Radio Telescope at 5 GHz and the Role of Scintillation. *ApJ*, 863(2):150, Aug 2018. doi: 10.3847/1538-4357/aad332. (Cited on pages: 164 and 179)

[501] H. Spruit and E. S. Phinney. Birth Kicks as the Origin of Pulsar Rotation. *Nature*, 393(6681):139–141, May 1998. doi: 10.1038/30168. (Cited on page: 12)

[502] D. H. Staelin. Fast Folding Algorithm for Detection of Periodic Pulse Trains. *IEEE Proceedings*, 57:724–725, January 1969. doi: 10.1109/PROC.1969.7051. (Cited on pages: xlv, 212, 218, 220, 221, 223, and 224)

[503] J. Standish, E. M. The Observational Basis for JPL's DE 200, the Planetary Ephemerides of the Astronomical Almanac. *A&A*, 233(1):252–271, July 1990. (Cited on page: 285)

[504] K. Stovall, B. Allen, S. Bogdanov, A. Brazier, F. Camilo, F. Cardoso, S. Chatterjee, J. M. Cordes, F. Crawford, J. S. Deneva, R. Ferdman, P. C. C. Freire, J. W. T. Hessels, F. Jenet, D. L. Kaplan, C. Karako-Argaman, V. M. Kaspi, B. Knispel, R. Kotulla, P. Lazarus, K. J. Lee, J. van Leeuwen, R. Lynch, A. G. Lyne, E. Madsen, M. A. McLaughlin, C. Patel, S. M. Ransom, P. Scholz, X. Siemens, I. H. Stairs, B. W. Stappers, J. Swiggum, W. W. Zhu, and A. Venkataraman. Timing of Five PALFA-discovered Millisecond Pulsars. *ApJ*, 833(2):192, December 2016. doi: 10.3847/1538-4357/833/2/192. (Cited on page: 14)

[505] T. E. Strohmayer and A. L. Watts. Discovery of Fast X-Ray Oscillations During the 1998 Giant Flare from SGR 1900+14. *ApJL*, 632(2):L111–L114, October 2005. doi: 10.1086/497911. (Cited on page: 38)

[506] M. Sugizaki, F. Nagase, K. Torii, K. Kinugasa, T. Asanuma, K. Matsuzaki, K. Koyama, and S. Yamauchi. Discovery of an 11-s X-Ray Pulsar in the Galactic-plane Section of the Scorpius Constellation. *PASJ*, 49:L25–L30, October 1997. doi: 10.1093/pasj/49.5.L25. (Cited on page: 36)

[507] S. Suvorova, L. Sun, A. Melatos, W. Moran, and R. J. Evans. Hidden Markov Model Tracking of Continuous Gravitational Waves from a Neutron Star with Wandering Spin. *Phys. Rev. D*, 93(12):123009, June 2016. doi: 10.1103/PhysRevD.93.123009. (Cited on page: 218)

[508] J. Swank and C. Markwardt. Populations of Transient Galactic Bulge X-Ray Sources. In H. Inoue and H. Kunieda, editors, *New Century of X-Ray Astronomy*, volume 251 of *Astronomical Society of the Pacific Conference Series*, page 94, January 2001. (Cited on page: 285)

[509] J. Taylor, Joseph H. Millisecond Pulsars: Nature's Most Stable Clocks. *IEEE Proceedings*, 79:1054–1062, Jul 1991. (Cited on page: 262)

[510] J. H. Taylor. A Sensitive Method for Detecting Dispersed Radio Emission. *A&AS*, 15:367, June 1974. (Cited on page: 218)

[511] J. H. Taylor. Pulsar Timing and Relativistic Gravity. *Philosophical Transactions of the Royal Society of London Series A*, 341(1660):117–134, October 1992. doi: 10.1098/rsta.1992.0088. (Cited on pages: 145 and 304)

[512] J. H. Taylor and D. R. Stinebring. Recent Progress in the Understanding of Pulsars. *ARA&A*, 24:285–327, January 1986. doi: 10.1146/annurev.aa.24.090186.001441. (Cited on page: 7)

[513] J. H. Taylor, L. A. Fowler, and P. M. McCulloch. Measurements of General Relativistic Effects in the Binary Pulsar PSR 1913+16. *Nature*, 277 (5696):437–440, February 1979. doi: 10.1038/277437a0. (Cited on pages: 5 and 262)

[514] J. H. Taylor, A. Wolszczan, T. Damour, and J. M. Weisberg. Experimental Constraints on Strong-field Relativistic Gravity. *Nature*, 355(6356):132–136, Jan 1992. doi: 10.1038/355132a0. (Cited on page: 262)

[515] S. P. Tendulkar, V. M. Kaspi, and C. Patel. Radio Nondetection of the SGR 1806–20 Giant Flare and Implications for Fast Radio Bursts. *ApJ*, 827 (1):59, August 2016. doi: 10.3847/0004-637X/827/1/59. (Cited on page: 45)

[516] S. P. Tendulkar, C. G. Bassa, J. M. Cordes, G. C. Bower, C. J. Law, S. Chatterjee, E. A. K. Adams, S. Bogdanov, S. Burke-Spolaor, B. J. Butler, P. Demorest, J. W. T. Hessels, V. M. Kaspi, T. J. W. Lazio, N. Maddox, B. Marcote, M. A. McLaughlin, Z. Paragi, S. M. Ransom, P. Scholz, A. Seymour, L. G. Spitler, H. J. van Langevelde, and R. S. Wharton. The Host Galaxy and Redshift of the Repeating Fast Radio Burst FRB 121102. *ApJL*, 834(2):L7, Jan 2017. doi: 10.3847/2041-8213/834/2/L7. (Cited on pages: 41, 164, 177, 179, and 189)

[517] S. P. Tendulkar, A. Gil de Paz, A. Y. Kirichenko, J. W. T. Hessels, M. Bhardwaj, F. Ávila, C. Bassa, P. Chawla, E. Fonseca, V. M. Kaspi, A. Keimpema, F. Kirsten, T. J. W. Lazio, B. Marcote, K. Masui, K. Nimmo, Z. Paragi, M. Rahman, D. R. Payá, P. Scholz, and I. Stairs. The 60 pc Environment of FRB 20180916B. *ApJL*, 908(1):L12, February 2021. doi: 10.3847/2041-8213/abdb38. (Cited on page: 179)

[518] J. Terrell, W. D. Evans, R. W. Klebesadel, and J. G. Laros. Periodicity of the γ-Ray Transient Event of 5 March 1979. *Nature*, 285(5764):383–385, June 1980. doi: 10.1038/285383a0. (Cited on page: 36)

[519] The CHIME/FRB Collaboration, M. Amiri, K. Bandura, P. Berger, M. Bhardwaj, M. M. Boyce, P. J. Boyle, C. Brar, M. Burhanpurkar, P. Chawla, J. Chowdhury, J. F. Cliche, M. D. Cranmer, D. Cubranic, M. Deng, N. Denman, M. Dobbs, M. Fandino, E. Fonseca, B. M. Gaensler, U. Giri, A. J. Gilbert, D. C. Good, S. Guliani, M. Halpern, G. Hinshaw, C. Höfer, A. Josephy, V. M. Kaspi, T. L. Landecker, D. Lang, H. Liao, K. W. Masui, J. Mena-Parra, A. Naidu, L. B. Newburgh, C. Ng, C. Patel, U. L. Pen, T. Pinsonneault-Marotte, Z. Pleunis, M. Rafiei Ravandi, S. M. Ransom, A. Renard, P. Scholz,

K. Sigurdson, S. R. Siegel, K. M. Smith, I. H. Stairs, S. P. Tendulkar, K. Vand erlinde, and D. V. Wiebe. The CHIME Fast Radio Burst Project: System Overview. *ApJ*, 863(1):48, August 2018. doi: 10.3847/1538-4357/aad188. (Cited on pages: 179 and 218)

[520] The CHIME/FRB Collaboration, M. Amiri, K. Bandura, M. Bhardwaj, P. Boubel, M. M. Boyce, P. J. Boyle, C. . Brar, M. Burhanpurkar, T. Cassanelli, P. Chawla, J. F. Cliche, D. Cubranic, M. Deng, N. Denman, M. Dobbs, M. Fandino, E. Fonseca, B. M. Gaensler, A. J. Gilbert, A. Gill, U. Giri, D. C. Good, M. Halpern, D. S. Hanna, A. S. Hill, G. Hinshaw, C. Höfer, A. Josephy, V. M. Kaspi, T. L. Landecker, D. A. Lang, H. H. Lin, K. W. Masui, R. Mckinven, J. Mena-Parra, M. Merryfield, D. Michilli, N. Milutinovic, C. Moatti, A. Naidu, L. B. Newburgh, C. Ng, C. Patel, U. Pen, T. Pinsonneault-Marotte, Z. Pleunis, M. Rafiei-Ravandi, M. Rahman, S. M. Ransom, A. Renard, P. Scholz, J. R. Shaw, S. R. Siegel, K. M. Smith, I. H. Stairs, S. P. Tendulkar, I. Tretyakov, K. Vanderlinde, and P. Yadav. A Second Source of Repeating Fast Radio Bursts. *Nature*, 566(7743):235–238, January 2019. doi: 10.1038/s41586-018-0864-x. (Cited on pages: 41, 177, 178, 179, and 192)

[521] The CHIME/FRB Collaboration, B. C. Andersen, K. Bandura, M. Bhardwaj, P. Boubel, M. M. Boyce, P. J. Boyle, C. Brar, T. Cassanelli, P. Chawla, D. Cubranic, M. Deng, M. Dobbs, M. Fandino, E. Fonseca, B. M. Gaensler, A. J. Gilbert, U. Giri, D. C. Good, M. Halpern, A. S. Hill, G. Hinshaw, C. Höfer, A. Josephy, V. M. Kaspi, R. Kothes, T. L. Landecker, D. A. Lang, D. Z. Li, H. H. Lin, K. W. Masui, J. Mena-Parra, M. Merryfield, R. Mckinven, D. Michilli, N. Milutinovic, A. Naidu, L. B. Newburgh, C. Ng, C. Patel, U. Pen, T. Pinsonneault-Marotte, Z. Pleunis, M. Rafiei-Ravandi, M. Rahman, S. M. Ransom, A. Renard, P. Scholz, S. R. Siegel, S. Singh, K. M. Smith, I. H. Stairs, S. P. Tendulkar, I. Tretyakov, K. Vanderlinde, P. Yadav, and A. V. Zwaniga. CHIME/FRB Discovery of Eight New Repeating Fast Radio Burst Sources. *ApJL*, 885(1):L24, November 2019. doi: 10.3847/2041-8213/ab4a80. (Cited on pages: 41, 158, 159, 171, 177, 178, 179, 182, 192, 193, and 196)

[522] The CHIME/FRB Collaboration, M. Amiri, B. C. Andersen, K. M. Bandura, M. Bhardwaj, P. J. Boyle, C. Brar, P. Chawla, T. Chen, J. F. Cliche, D. Cubranic, M. Deng, N. T. Denman, M. Dobbs, F. Q. Dong, M. Fand ino, E. Fonseca, B. M. Gaensler, U. Giri, D. C. Good, M. Halpern, J. W. T. Hessels, A. S. Hill, C. Höfer, A. Josephy, J. W. Kania, R. Karuppusamy, V. M. Kaspi, A. Keimpema, F. Kirsten, T. L. Landecker, D. A. Lang, C. Leung, D. Z. Li, H. H. Lin, B. Marcote, K. W. Masui, R. Mckinven, J. Mena-Parra, M. Merryfield, D. Michilli, N. Milutinovic, A. Mirhosseini, A. Naidu, L. B. Newburgh, C. Ng, K. Nimmo, Z. Paragi, C. Patel, U. L. Pen, T. Pinsonneault-Marotte, Z. Pleunis, M. Rafiei-Ravandi, M. Rahman, S. M. Ransom, A. Renard, P. Sanghavi, P. Scholz, J. R. Shaw, K. Shin, S. R. Siegel, S. Singh, R. J.

Smegal, K. M. Smith, I. H. Stairs, S. P. Tendulkar, I. Tretyakov, K. Vanderlinde, H. Wang, X. Wang, D. Wulf, P. Yadav, and A. V. Zwaniga. Periodic Activity from a Fast Radio Burst Source. *Nature*, 582(7812):351–355, June 2020. doi: 10.1038/s41586-020-2398-2. (Cited on pages: xliii, xliv, 158, 172, 179, 182, 190, 191, 192, 193, 194, 195, 196, 197, 198, 199, 201, 203, 204, 206, and 207)

[523] The CHIME/FRB Collaboration, B. C. Andersen, K. M. Bandura, M. Bhardwaj, A. Bij, M. M. Boyce, P. J. Boyle, C. Brar, T. Cassanelli, P. Chawla, T. Chen, J.-F. Cliche, A. Cook, D. Cubranic, A. P. Curtin, N. T. Denman, M. Dobbs, F. Q. Dong, M. Fandino, E. Fonseca, B. M. Gaensler, U. Giri, D. C. Good, M. Halpern, A. S. Hill, G. F. Hinshaw, C. H"ofer, A. Josephy, J. W. Kania, V. M. Kaspi, T. L. Landecker, C. Leung, D. Z. Li, H.-H. Lin, K. W. Masui, R. McKinven, J. Mena-Parra, M. Merryfield, B. W. Meyers, D. Michilli, N. Milutinovic, A. Mirhosseini, M. M"unchmeyer, A. Naidu, L. B. Newburgh, C. Ng, C. Patel, U.-L. Pen, T. Pinsonneault-Marotte, Z. Pleunis, B. M. Quine, M. Rafiei-Ravandi, M. Rahman, S. M. Ransom, A. Renard, P. Sanghavi, P. Scholz, J. R. Shaw, K. Shin, S. R. Siegel, S. Singh, R. J. Smegal, K. M. Smith, I. H. Stairs, C. M. Tan, S. P. Tendulkar, I. Tretyakov, K. Vanderlinde, H. Wang, D. Wulf, and A. V. Zwaniga. A Bright Millisecond-duration Radio Burst from a Galactic Magnetar. *Nature*, 587(7832):54–58, November 2020. doi: 10.1038/s41586-020-2863-y. (Cited on pages: viii, xxvii, 7, 33, 48, 50, 177, 178, and 205)

[524] C. Thompson and R. C. Duncan. The Soft Gamma Repeaters as Very Strongly Magnetized Neutron Stars - I. Radiative Mechanism for Outbursts. *MNRAS*, 275(2):255–300, July 1995. doi: 10.1093/mnras/275.2.255. (Cited on pages: 39 and 88)

[525] C. Thompson and R. C. Duncan. The Soft Gamma Repeaters as Very Strongly Magnetized Neutron Stars. II. Quiescent Neutrino, X-Ray, and Alfven Wave Emission. *ApJ*, 473:322, December 1996. doi: 10.1086/178147. (Cited on pages: 36, 39, and 88)

[526] C. Thompson, M. Lyutikov, and S. R. Kulkarni. Electrodynamics of Magnetars: Implications for the Persistent X-Ray Emission and Spin-Down of the Soft Gamma Repeaters and Anomalous X-Ray Pulsars. *ApJ*, 574(1):332–355, July 2002. doi: 10.1086/340586. (Cited on page: 39)

[527] T. W. J. Thompson, J. A. Tomsick, R. E. Rothschild, J. J. M. in't Zand, and R. Walter. Orbital Parameters for the X-Ray Pulsar IGR J16393–4643. *ApJ*, 649(1):373–381, September 2006. doi: 10.1086/506251. (Cited on pages: 306 and 308)

[528] T. W. J. Thompson, J. A. Tomsick, J. J. M. in 't Zand, R. E. Rothschild, and R. Walter. The Orbit of the Eclipsing X-Ray Pulsar EXO 1722–363. *ApJ*, 661(1):447–457, May 2007. doi: 10.1086/513458. (Cited on page: 306)

[529] D. Thornton, B. Stappers, M. Bailes, B. Barsdell, S. Bates, N. D. R. Bhat, M. Burgay, S. Burke-Spolaor, D. J. Champion, P. Coster, N. D'Amico, A. Jameson, S. Johnston, M. Keith, M. Kramer, L. Levin, S. Milia, C. Ng, A. Possenti, and W. van Straten. A Population of Fast Radio Bursts at Cosmological Distances. *Science*, 341(6141):53–56, July 2013. doi: 10.1126/science.1236789. (Cited on page: 40)

[530] R. C. Tolman. Static Solutions of Einstein's Field Equations for Spheres of Fluid. *Physical Review*, 55(4):364–373, February 1939. doi: 10.1103/PhysRev.55.364. (Cited on page: 3)

[531] H. Tong, W. Wang, and H.-G. Wang. Periodicity in Fast Radio Bursts Due to Forced Precession by a Fallback Disk. *RAA*, 20(9):142, September 2020. doi: 10.1088/1674-4527/20/9/142. (Cited on page: 204)

[532] P. Torne, R. P. Eatough, R. Karuppusamy, M. Kramer, G. Paubert, B. Klein, G. Desvignes, D. J. Champion, H. Wiesemeyer, C. Kramer, L. G. Spitler, C. Thum, R. Gusten, K. F. Schuster, and I. Cognard. Simultaneous Multi-frequency Radio Observations of the Galactic Centre Magnetar SGR J1745–2900. *MNRAS*, 451:L50–L54, July 2015. doi: 10.1093/mnrasl/slv063. (Cited on pages: 89 and 95)

[533] P. Torne, G. Desvignes, R. P. Eatough, R. Karuppusamy, G. Paubert, M. Kramer, I. Cognard, D. J. Champion, and L. G. Spitler. Detection of the Magnetar SGR J1745–2900 Up to 291 GHz with Evidence of Polarized Millimetre Emission. *MNRAS*, 465(1):242–247, February 2017. doi: 10.1093/mnras/stw2757. (Cited on pages: 34, 89, 95, 121, and 205)

[534] P. Torne, J. Macías-Pérez, B. Ladjelate, A. Ritacco, M. Sánchez-Portal, S. Berta, G. Paubert, M. Calvo, G. Desvignes, R. Karuppusamy, S. Navarro, D. John, S. Sánchez, J. Peñalver, M. Kramer, and K. Schuster. Detection of the Magnetar XTE J1810–197 at 150 and 260 GHz with the NIKA2 Kinetic Inductance Detector Camera. *A&A*, 640:L2, August 2020. doi: 10.1051/0004-6361/202038504. (Cited on page: 205)

[535] L. J. Townsend, M. J. Coe, R. H. D. Corbet, and A. B. Hill. On the Orbital Parameters of Be/X-Ray Binaries in the Small Magellanic Cloud. *MNRAS*, 416(2):1556–1565, September 2011. doi: 10.1111/j.1365-2966.2011.19153.x. (Cited on page: 315)

[536] A. I. Tsygan. Corequakes of Neutron Stars and Soft γ-ray bursts. *A&A*, 44 (1):21–24, November 1975. (Cited on page: 42)

[537] P. Ubertini, F. Lebrun, G. Di Cocco, A. Bazzano, A. J. Bird, K. Broenstad, A. Goldwurm, G. La Rosa, C. Labanti, P. Laurent, I. F. Mirabel, E. M. Quadrini, B. Ramsey, V. Reglero, L. Sabau, B. Sacco, R. Staubert,

L. Vigroux, M. C. Weisskopf, and A. A. Zdziarski. IBIS: The Imager on-board INTEGRAL. *A&A*, 411:L131–L139, November 2003. doi: 10.1051/0004-6361:20031224. (Cited on page: 281)

[538] D. A. Uzdensky and A. Spitkovsky. Physical Conditions in the Reconnection Layer in Pulsar Magnetospheres. *ApJ*, 780(1):3, January 2014. doi: 10.1088/0004-637X/780/1/3. (Cited on page: 119)

[539] M. van der Klis and J. M. Bonnet-Bidaud. The Orbital Parameters and the X-Ray Pulsation of Vela X–1 (4U 0900–40). *A&A*, 135:155–170, June 1984. (Cited on page: 323)

[540] M. H. van Kerkwijk, J. van Paradijs, and E. J. Zuiderwijk. On the Masses of Neutron Stars. *A&A*, 303:497, November 1995. (Cited on pages: 312 and 315)

[541] G. Vasisht and E. V. Gotthelf. The Discovery of an Anomalous X-Ray Pulsar in the Supernova Remnant Kes 73. *ApJL*, 486(2):L129–L132, September 1997. doi: 10.1086/310843. (Cited on page: 36)

[542] S. Vaughan. A Simple Test for Periodic Signals in Red Noise. *A&A*, 431: 391–403, February 2005. doi: 10.1051/0004-6361:20041453. (Cited on page: 299)

[543] V. Venkatraman Krishnan, M. Bailes, W. van Straten, N. Wex, P. C. C. Freire, E. F. Keane, T. M. Tauris, P. A. Rosado, N. D. R. Bhat, C. Flynn, A. Jameson, and S. Osłowski. Lense-Thirring Frame Dragging Induced by a Fast-rotating White Dwarf in a Binary Pulsar System. *Science*, 367(6477): 577–580, January 2020. doi: 10.1126/science.aax7007. (Cited on page: 244)

[544] T. K. Vintsyuk. Speech discrimination by dynamic programming. *Cybernetics*, 4(1):52–57, 1968. (Cited on page: 215)

[545] K. Virkler, J. Kocz, M. Soriano, S. Horiuchi, J. L. Pineda, and T. McNichols. A Broadband Digital Spectrometer for the Deep Space Network. *ApJS*, 251 (1):1, November 2020. doi: 10.3847/1538-4365/abbace. (Cited on pages: liii and 267)

[546] A. J. Viterbi. Error bounds for convolutional codes and an asymptotically optimum decoding algorithm. *IEEE Trans. Inf. Theory*, 13(2):260–269, 1967. (Cited on page: 215)

[547] A. L. Watts and T. E. Strohmayer. Detection with RHESSI of High-frequency X-Ray Oscillations in the Tail of the 2004 Hyperflare from SGR 1806–20. *ApJL*, 637(2):L117–L120, February 2006. doi: 10.1086/500735. (Cited on page: 38)

[548] R. F. Webbink. PSR 1913+16: Endpoints of Speculation. A Critical Discussion of Possible Companions and Progenitors. *A&A*, 41:1, June 1975. (Cited on page: 5)

[549] W. Wegner. Intrinsic Colour Indices of OB Supergiants, Giants and Dwarfs in the UBVRIJHKLM System. *MNRAS*, 270:229–234, September 1994. doi: 10.1093/mnras/270.2.229. (Cited on pages: 315 and 320)

[550] J. M. Weisberg and Y. Huang. Relativistic Measurements from Timing the Binary Pulsar PSR B1913+16. *ApJ*, 829(1):55, September 2016. doi: 10.3847/0004-637X/829/1/55. (Cited on pages: xxi and 6)

[551] J. M. Weisberg, D. J. Nice, and J. H. Taylor. Timing Measurements of the Relativistic Binary Pulsar PSR B1913+16. *ApJ*, 722(2):1030–1034, October 2010. doi: 10.1088/0004-637X/722/2/1030. (Cited on page: 5)

[552] P. Weltevrede, S. Johnston, and C. M. Espinoza. The Glitch-induced Identity Changes of PSR J1119–6127. *MNRAS*, 411:1917–1934, March 2011. doi: 10.1111/j.1365-2966.2010.17821.x. (Cited on pages: 76, 80, and 84)

[553] N. Wex and S. M. Kopeikin. Frame Dragging and Other Precessional Effects in Black Hole Pulsar Binaries. *ApJ*, 514(1):388–401, March 1999. doi: 10.1086/306933. (Cited on page: 262)

[554] WFIRST Astrometry Working Group, R. E. Sanderson, A. Bellini, S. Casertano, J. R. Lu, P. Melchior, M. Libralato, D. Bennett, M. Shao, J. Rhodes, S. T. Sohn, S. Malhotra, S. Gaudi, S. M. Fall, E. Nelan, P. Guhathakurta, J. Anderson, and S. Ho. Astrometry with the Wide-Field Infrared Space Telescope. *Journal of Astronomical Telescopes, Instruments, and Systems*, 5:044005, October 2019. doi: 10.1117/1.JATIS.5.4.044005. (Cited on page: 262)

[555] R. S. Wharton, S. Chatterjee, J. M. Cordes, J. S. Deneva, and T. J. W. Lazio. Multiwavelength Constraints on Pulsar Populations in the Galactic Center. *ApJ*, 753(2):108, Jul 2012. doi: 10.1088/0004-637X/753/2/108. (Cited on pages: 257, 259, and 260)

[556] N. E. White, K. O. Mason, P. Giommi, L. Angelini, G. Pooley, G. Branduardi-Raymont, P. G. Murdin, and J. V. Wall. A 25 min Modulation from the Vicinity of the Unusually Soft X-Ray Source X0142+614. *MNRAS*, 226: 645–654, June 1987. doi: 10.1093/mnras/226.3.645. (Cited on page: 36)

[557] R. Wielebinski, A. Jessner, M. Kramer, and J. A. Gil. First Detection of Pulsars at mm-wavelengths. *A&A*, 272:L13–L16, May 1993. (Cited on page: 120)

[558] I. P. Williamson. Pulse Broadening Due to Multiple Scattering in the Interstellar Medium. *MNRAS*, 157:55, January 1972. doi: 10.1093/mnras/157.1.55. (Cited on pages: 25 and 110)

[559] I. P. Williamson. Pulse Broadening Due to Multiple Scattering in the Interstellar Medium–II. *MNRAS*, 163:345, January 1973. doi: 10.1093/mnras/163.4.345. (Cited on page: 25)

[560] I. P. Williamson. Pulse Broadening Due to Multiple Scattering in the Interstellar Medium–III. *MNRAS*, 166:499–512, March 1974. doi: 10.1093/mnras/166.3.499. (Cited on page: 25)

[561] R. Willingale, R. L. C. Starling, A. P. Beardmore, N. R. Tanvir, and P. T. O'Brien. Calibration of X-Ray Absorption in Our Galaxy. *MNRAS*, 431(1): 394–404, May 2013. doi: 10.1093/mnras/stt175. (Cited on page: 316)

[562] C. Winkler, T. J. L. Courvoisier, G. Di Cocco, N. Gehrels, A. Giménez, S. Grebenev, W. Hermsen, J. M. Mas-Hesse, F. Lebrun, N. Lund, G. G. C. Palumbo, J. Paul, J. P. Roques, H. Schnopper, V. Schönfelder, R. Sunyaev, B. Teegarden, P. Ubertini, G. Vedrenne, and A. J. Dean. The INTEGRAL Mission. *A&A*, 411:L1–L6, November 2003. doi: 10.1051/0004-6361:20031288. (Cited on page: 281)

[563] P. Wojdowski, G. W. Clark, A. M. Levine, J. W. Woo, and S. N. Zhang. Quasi-periodic Occultation by a Precessing Accretion Disk and Other Variabilities of SMC X–1. *ApJ*, 502(1):253–264, July 1998. doi: 10.1086/305893. (Cited on page: 324)

[564] A. Wolszczan. Confirmation of Earth-Mass Planets Orbiting the Millisecond Pulsar PSR B1257+12. *Science*, 264(5158):538–542, April 1994. doi: 10.1126/science.264.5158.538. (Cited on page: 8)

[565] A. Wolszczan and D. A. Frail. A Planetary System Around the Millisecond Pulsar PSR 1257+12. *Nature*, 355(6356):145–147, January 1992. doi: 10.1038/355145a0. (Cited on page: 8)

[566] K. S. Wood, J. P. Norris, P. Hertz, B. A. Vaughan, P. F. Michelson, K. Mitsuda, W. H. G. Lewin, J. van Paradijs, W. Penninx, and M. van der Klis. Searches for Millisecond Pulsations in Low-mass X-Ray Binaries. *ApJ*, 379: 295, September 1991. doi: 10.1086/170505. (Cited on page: 232)

[567] P. M. Woods, C. Kouveliotou, J. van Paradijs, M. H. Finger, and C. Thompson. BEPPOSAX Observations of SGR 1900+14 in Quiescence and During an Active Period. *ApJL*, 518(2):L103–L106, June 1999. doi: 10.1086/312085. (Cited on page: 36)

[568] P. M. Woods, C. Kouveliotou, E. Göğüş, M. H. Finger, J. Swank, C. B. Markwardt, K. Hurley, and M. van der Klis. Large Torque Variations in Two Soft Gamma Repeaters. *ApJ*, 576(1):381–390, September 2002. doi: 10.1086/341536. (Cited on page: 38)

[569] P. M. Woods, C. Kouveliotou, F. P. Gavriil, V. M. Kaspi, M. S. E. Roberts, A. Ibrahim, C. B. Markwardt, J. H. Swank, and M. H. Finger. X-Ray Bursts from the Transient Magnetar Candidate XTE J1810–197. *ApJ*, 629(2):985–997, August 2005. doi: 10.1086/431476. (Cited on pages: 36, 132, and 142)

[570] O. Wucknitz. Probing Interstellar Scattering Towards the Galactic Centre with Pulsar VLBI. In A. Tarchi, M. Giroletti, and L. Feretti, editors, *Proc. 12th European VLBI Network Symp. and Users Meeting*, page 66. Trieste: SISSA, 2014. (Cited on page: 117)

[571] K. Yagi, L. C. Stein, and N. Yunes. Challenging the Presence of Scalar Charge and Dipolar Radiation in Binary Pulsars. *Phys. Rev. D*, 93(2):024010, January 2016. doi: 10.1103/PhysRevD.93.024010. (Cited on page: 263)

[572] S. Yamasaki, S. Kisaka, T. Terasawa, and T. Enoto. Relativistic Fireball Reprise: Radio Suppression at the Onset of Short Magnetar Bursts. *MNRAS*, 483(3):4175–4186, March 2019. doi: 10.1093/mnras/sty3388. (Cited on page: 143)

[573] W. M. Yan, N. Wang, R. N. Manchester, Z. G. Wen, and J. P. Yuan. Single-pulse Observations of the Galactic Centre Magnetar PSR J1745–2900 at 3.1 GHz. *MNRAS*, 476(3):3677–3687, May 2018. doi: 10.1093/mnras/sty470. (Cited on page: 89)

[574] Z. Yan, Z.-Q. Shen, X.-J. Wu, R. N. Manchester, P. Weltevrede, Y.-J. Wu, R.-B. Zhao, J.-P. Yuan, K.-J. Lee, Q.-Y. Fan, X.-Y. Hong, D.-R. Jiang, B. Li, S.-G. Liang, Q.-B. Ling, Q.-H. Liu, Z.-H. Qian, X.-Z. Zhang, W.-Y. Zhong, and S.-H. Ye. Single-pulse Radio Observations of the Galactic Center Magnetar PSR J1745–2900. *ApJ*, 814(1):5, November 2015. doi: 10.1088/0004-637X/814/1/5. (Cited on pages: 89, 96, 100, 106, and 107)

[575] H. Yang and Y.-C. Zou. Orbit-induced Spin Precession as a Possible Origin for Periodicity in Periodically Repeating Fast Radio Bursts. *ApJL*, 893(2): L31, April 2020. doi: 10.3847/2041-8213/ab800f. (Cited on page: 204)

[576] Y.-P. Yang and B. Zhang. Dispersion Measure Variation of Repeating Fast Radio Burst Sources. *ApJ*, 847(1):22, September 2017. doi: 10.3847/1538-4357/aa8721. (Cited on page: 174)

[577] J. M. Yao, R. N. Manchester, and N. Wang. A New Electron-density Model for Estimation of Pulsar and FRB Distances. *ApJ*, 835(1):29, January 2017. doi: 10.3847/1538-4357/835/1/29. (Cited on pages: xxiii, xxv, xxvi, 16, 19, 23, 42, 43, and 47)

[578] G. Younes, C. Kouveliotou, and O. Roberts. GBM Observation of SGR-like Burst from the Direction of PSR 1119–6127. *GRB Coordinates Network*, #19736, January 2016. (Cited on page: 76)

[579] G. Younes, T. Guver, T. Enoto, Z. Arzoumanian, K. Gendreau, C.-P. Hu, P. S. Ray, C. Kouveliotou, S. Guillot, W. C. G. Ho, E. C. Ferrara, and C. Malacaria. Burst Forest from SGR 1935+2154 as Detected with NICER. *The Astronomer's Telegram*, #13678:1, April 2020. (Cited on page: 157)

[580] Q. Yuan and B. Zhang. Millisecond Pulsar Interpretation of the Galactic Center Gamma-Ray Excess. *JHEAp*, 3:1–8, Sep 2014. doi: 10.1016/j.jheap.2014.06.001. (Cited on pages: 260 and 261)

[581] B. Zackay and E. O. Ofek. An Accurate and Efficient Algorithm for Detection of Radio Bursts with an Unknown Dispersion Measure, for Single-dish Telescopes and Interferometers. *ApJ*, 835(1):11, January 2017. doi: 10.3847/1538-4357/835/1/11. (Cited on page: 218)

[582] J. J. Zanazzi and D. Lai. Periodic Fast Radio Bursts with Neutron Star Free Precession. *ApJL*, 892(1):L15, March 2020. doi: 10.3847/2041-8213/ab7cdd. (Cited on page: 204)

[583] B. Zhang, A. K. Harding, and A. G. Muslimov. Radio Pulsar Death Line Revisited: Is PSR J2144–3933 Anomalous? *ApJL*, 531(2):L135–L138, March 2000. doi: 10.1086/312542. (Cited on pages: xxii and 17)

[584] C. F. Zhang, J. C. Jiang, Y. P. Men, B. J. Wang, H. Xu, J. W. Xu, C. H. Niu, D. J. Zhou, X. Guan, J. L. Han, P. Jiang, K. J. Lee, D. Li, L. Lin, J. R. Niu, P. Wang, Z. L. Wang, R. X. Xu, W. Yu, B. Zhang, and W. W. Zhu. A Highly Polarised Radio Burst Detected from SGR 1935+2154 by FAST. *The Astronomer's Telegram*, #13699:1, May 2020. (Cited on pages: 159, 178, and 205)

[585] F. Zhang, Y. Lu, and Q. Yu. On the Existence of Pulsars in the Vicinity of the Massive Black Hole in the Galactic Center. *ApJ*, 784(2):106, Apr 2014. doi: 10.1088/0004-637X/784/2/106. (Cited on page: 262)

[586] S. N. Zhang, S. L. Xiong, C. K. Li, X. B. Li, Y. L. Tuo, M. Y. Ge, X. F. Zhao, S. Xiao, S. M. Jia, J. Y. Nie, H. S. Zhao, Q. Luo, B. Li, C. Cai, Y. Tan, W. C. Xue, F. J. Lu, L. M. Song, C. Z. Liu, Y. Chen, X. L. Cao, Y. P. Xu, T. P. Li, L. Lin, and B. Zhang. Insight-HXMT X-Ray and Hard X-Ray Detection of the Double Peaks of the Fast Radio Burst from SGR 1935+2154. *The Astronomer's Telegram*, #13696:1, May 2020. (Cited on page: 157)

[587] Y. G. Zhang, V. Gajjar, G. Foster, A. Siemion, J. Cordes, C. Law, and Y. Wang. Fast Radio Burst 121102 Pulse Detection and Periodicity: A Machine Learning Approach. *ApJ*, 866(2):149, Oct 2018. doi: 10.3847/1538-4357/aadf31. (Cited on pages: 164, 179, and 182)

[588] P. Zhou, X. Zhou, Y. Chen, J.-S. Wang, J. Vink, and Y. Wang. Revisiting the Distance, Environment, and Supernova Properties of SNR G57.2+0.8 That Hosts SGR 1935+2154. *ApJ*, 905(2):99, December 2020. doi: 10.3847/1538-4357/abc34a. (Cited on page: 158)

[589] I. Y. Zolotukhin, M. Bachetti, N. Sartore, I. V. Chilingarian, and N. A. Webb. The Slowest Spinning X-Ray Pulsar in an Extragalactic Globular Cluster. *ApJ*, 839(2):125, April 2017. doi: 10.3847/1538-4357/aa689d. (Cited on page: 8)